Adsorption technologies for the recycling of fluoride. Hydrometallurgical remediation of spent potlining and hypercrosslinked polymeric extractants

Thomas Robshaw

A thesis submitted in partial fulfilment of the requirements for the degree of Doctor of Philosophy

The University of Sheffield
Faculty of Engineering
Department of Chemical and Biological Engineering

01 July 2020

Abstract

Fluorite (CaF_2) is a critical natural reserve and industrial fluoride recycling is of global importance. This work approaches the problem on two fronts. First, modification of a hydrometallurgical treatment system for spent potlining (SPL); a fluoride-rich, toxic, solid aluminium industry waste. Second, fluoride adsorption by metallated, porous, hydrophilic hypercrosslinked polymers (HHCPs).

To ameliorate hydrometallurgical SPL treatment, an adsorption system is investigated, to selectively extract fluoride from a mixed leachate stream. A lanthanum-loaded chelating resin (La-MTS9501) is chosen for this purpose and its uptake characteristics are investigated. La-MTS9501 co-extracts fluoride and aluminium from simulated SPL leachate via adsorption of aqueous aluminium hydroxyfluoride (AHF) complexes, which chelate to the La centres via bridging fluoride or oxide ligands, with additional weaker interactions at higher leachate concentrations. Uptake was described best by multilayer and heterogeneous isotherm models. The theoretical maximum fluoride uptake capacity (q_{max}) was 145 $mg \cdot g^{-1}$ and the uptake followed pseudo second-order kinetics, with film-diffusion likely being rate-controlling. In dynamic column simulations, fluoride breakthrough was well-described by the Dose-Response model and dynamic loading capacity was 66.7 $mg \cdot g^{-1}$.

Real SPL samples were leached via a two-step treatment using 1M NaOH with added H_2O_2, then 0.5 M H_2SO_4, which solubilised the majority fluoride content of numerous samples, of different mineral composition. The good dynamic column performance achieved with a simulant feed was retained with real SPL leachate. The fluoride and aluminium were selectively eluted from the column, using 1 M NaOH, with few problematic cocontaminants. Synthetic cryolite could potentially be attained from this feed by precipitation. A first-order technicoeconomic model suggested that, with some process optimisation, the enhanced hydrometallurgical system could offset its fixed-CAPEX within six years.

Microporous hydrophilic hypercrosslinked polymers termed "HHCP1" and "HHCP2" were synthesised respectively from 2,2'-biphenol and bisphenol A monomers. These materials had high exchange capacities of up to 6.34 $mmol \cdot g^{-1}$ and unexpectedly broad pK_a ranges. Polymers were loaded with calcium, to create fluoride selectivity, achieved by covalent bonding and unexpectedly by the formation of $CaCO_3$, from adsorbed atmospheric CO_2. Fluoride was extracted by conversion of the bound Ca species to CaF_2. HHCP1 retained a high surface area after metallation and had a theoretical q_{max} of 267 $mg \cdot g^{-1}$. HHCP2 was converted to a surface-functionalised material and had lesser capacity, but faster uptake kinetics. Both polymers could be used in a dynamic column system and were selective in mixed anions uptake experiments, although phosphate was co-extracted. They could also be successfully regenerated in a two-step treatment, using HNO_3, then re-metallation, over four cycles of use.

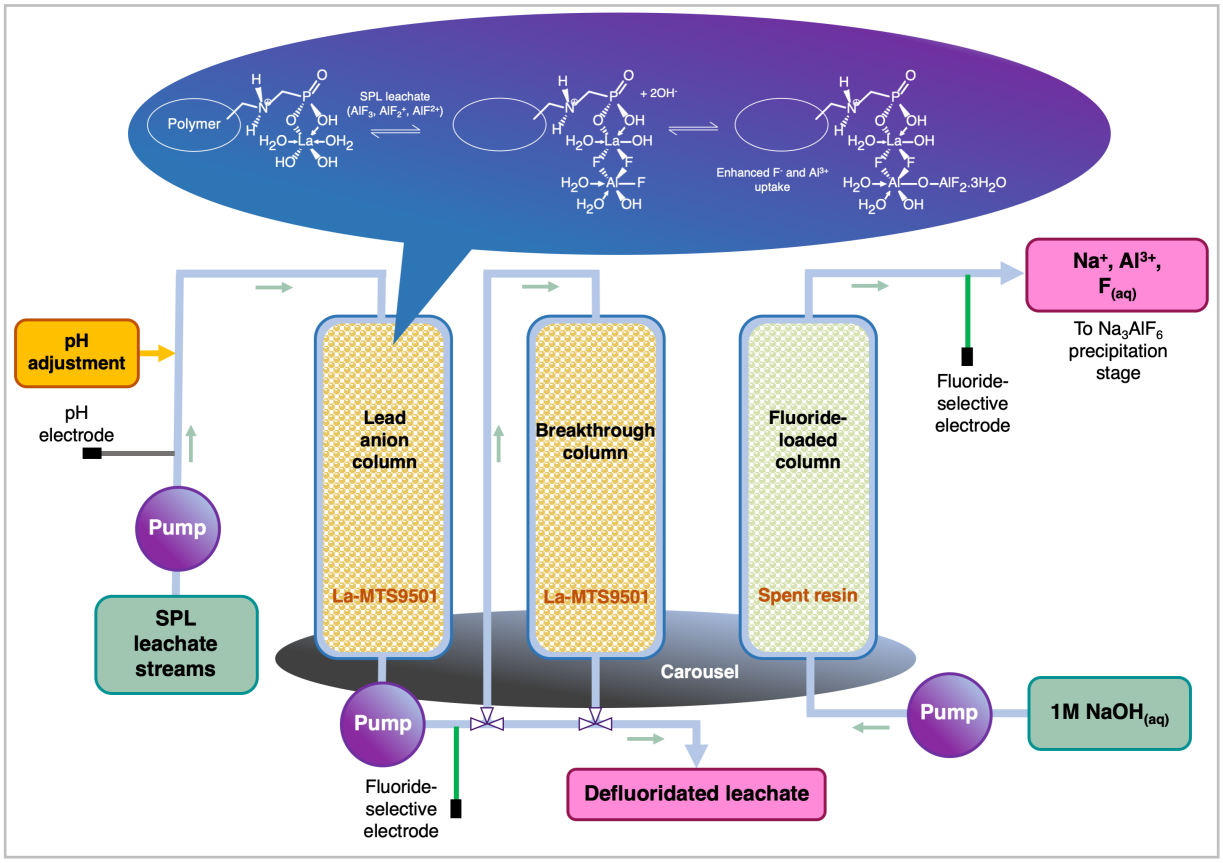
Polymer
SPL leachate
(AlF3, AlF2+, AlF2+)
+ 2OH-
Enhanced F- and Al3+ uptake
pH adjustment
pH electrode
Pump
SPL leachate streams
Lead anion column
La-MTS9501
Breakthrough column
La-MTS9501
Fluoride-loaded column
Spent resin
Carousel
Fluoride-selective electrode
Na+, Al3+, F(aq)
To Na3AlF6 precipitation stage
Pump
1M NaOH(aq)
Pump
Fluoride-selective electrode
Defluoridated leachate

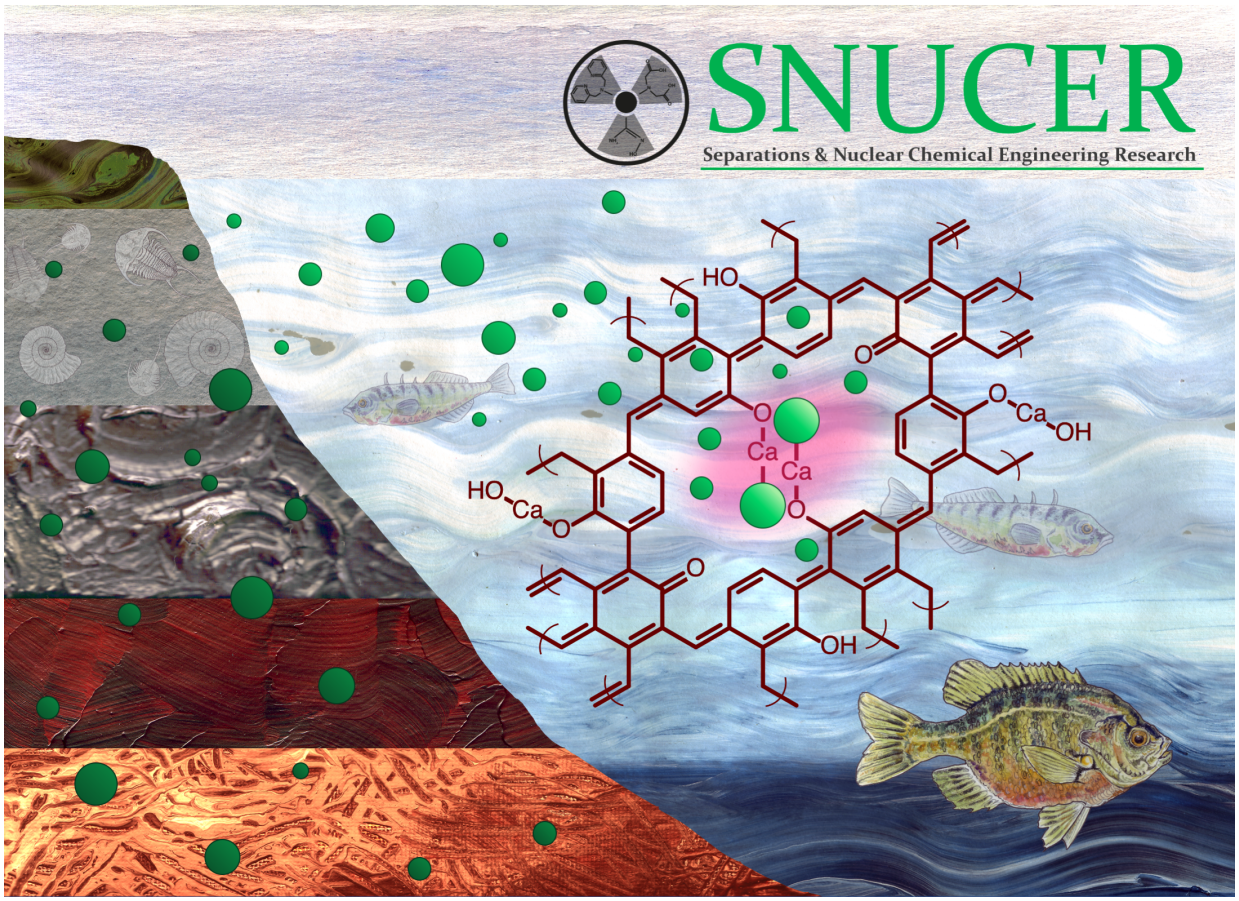
SNUCER
Separations & Nuclear Chemical Engineering Research

Acknowledgments

I would like to thank my supervisor Dr Mark Ogden for his constant support, encouragement and good humour over the last four years, for being a true professional role model and for believing in me from the start. I also thank my second supervisor Dr Robert Dawson for going above and beyond his pastoral responsibilities and welcoming me into his research group. Sorry I mistook you for a student at the interview Rob- take it as a complement. Special thanks to Mum, Dad, Grandma and Kat for being there when I needed you and helping get me back on the right track after my first "career" choice. You helped me see that I was an awful retail manager, but a pretty good research scientist.

I also thank:

Nawfal Al-Dulami
Dr Zarah Alqahtani
Dr James Amphlett
Dr Charlie Appleby-Mallinder
Prof Steven Armes
Carl Atkinson
Dan Barton
Dr James Bezzina (the greatest Australian ever)
Keith Bonser
Prof Lee Brammer
Dr Adam "Cay-ner"
Glyn Coxhill
Dr Denis Cumming
Dr Jennifer Dick
Dr Jonathan Foster
Dr Joe Gaunt
Sion Griffiths
Dr Debbie Hammond
Dr Katie Hu
Dr Leanne Ingram
Dr Alex James
Dr Oli Johnson
Fiona Lambert
Prof Graham Leggett
Dr Alisyn Nedoma
Dr Sarah Pepper
Dr Alex Riley
Duncan Schofield
Dr Cheryl Shaw
Supakorn Tantisriyanurak
Sudhir Tukra
Archibald Waller

Table of Contents

List of common abbreviations used (alphabetical)

Term	Abbreviation
Aluminium hydroxyfluoride	AHF
Aminomethyl phosphonic acid	AMP
Capital expenditure	CAPEX
Conjugated microporous polymer	CMP
Covalent organic framework	COF
Divinylbenzene	DVB
Dubinin-Radushkevich	D-R
European Union	EU
Extended x-ray absorption fine structure	EXAFS
Formaldehyde dimethylacetal	FDA
Freight on board	FOB
Hall-Héroult	HH
Hard-soft-acid-base	HSAB
Hypercrosslinked polymer	HCP
Inductively-coupled plasma mass spectrometry	ICP-MS
Inductively-coupled plasma optical emission spectroscopy	ICP-OES
Infra-red	IR
Ion chromatography	IC
Ion-exchange	IX
Ion-selective electrode	ISE
Lanthanum-loaded Puromet™ MTS9501 resin	La-MTS9501
Low caustic leaching and liming	LCLL
Metal organic framework	MOF
Metric tonne	T
Microporous organic polymer	MOP
Nuclear magnetic resonance	NMR
Polymer of intrinsic microporosity	PIM
Powder X-ray diffraction	PXRD
Pregnant leach solution	PLS
Pseudo first-order	PFO
Pseudo second-order	PSO
Rare earth element	REE
Reduction/oxidation	REDOX
Rio Tinto Alcan	RTA
Scanning electron microscope/microscopy	SEM
Spent potlining	SPL
Strong acid cation	SAC
Strong base anion	SBA
Thermogravimetric analysis	TGA
United States Geological Survey	USGS
Weak acid cation	WAC
Weak base anion	WBA
X-ray photoelectron spectroscopy	XPS

List of figures

List of Tables

Declaration

I, the author, confirm that the Thesis is my own work. I am aware of the University's Guidance on the Use of Unfair Means (www.sheffield.ac.uk/ssid/unfair-means). This work has not been previously been presented for an award at this, or any other, university.

Parts of this thesis appear in the following publications:

T.J. Robshaw, S. Tukra, D.B Hammond, G.J Leggett and M.D. Ogden, "Highly efficient fluoride extraction from simulant leachate of spent potlining via La-loaded chelating resin. An equilibrium study", *Journal of Hazardous Materials,* 2019, **361**, 200-209 (doi.org/10.1016/j.jhazmat.2018.07.036).

T.J. Robshaw, R. Dawson, K. Bonser and M.D. Ogden, "Towards the implementation of an ion-exchange system for recovery of fluoride commodity chemicals. Kinetic and dynamic studies", *Chemical Engineering Journal*, 2019, **367**, 149-159 (doi.org/10.1016/j.cej.2019.02.135).

T.J. Robshaw, K. Bonser, G. Coxhill, R. Dawson, and M.D. Ogden, "Development of a combined leaching and ion-exchange system for valorisation of spent potlining waste", *Waste and Biomass Valorization*, 2020, **11**, 5467-5481 (doi.org/10.1007/s12649-020-00954-1).

T.J. Robshaw, A.M. James, D.B. Hammond, J. Reynolds, R. Dawson and M.D. Ogden, "Calcium-loaded hydrophilic hypercrosslinked polymers for extremely high defluoridation capacity via multiple uptake mechanisms", *Journal of Materials Chemistry A*, 2020, **8**, 7130-7144 (doi.org/10.1039/c9ta12285k).

Dedication

This thesis is dedicated to Katty and Edmond. Eddie, I hope one day you will read this and be proud of Dad.

1. Introduction

1.1. Fluoride in the environment

Fluoride is the ionised form of the element fluorine. Because of the high electronegativity of elemental fluorine (7 L shell electrons), its anionic form is ubiquitous in nature, both in aqueous environments and in mineralogy. Fluoride is geologically abundant, having a concentration of 429-610 $mg \cdot kg^{-1}$ in The Earth's continental crust [1]. In the hydrosphere, fluoride is far less common, with an average concentration of only ~1.3 $mg \cdot L^{-1}$ in seawater, and is even less abundant in freshwater [2]. However, fluoride can be easily mobilised into groundwater in contact with localised mineral deposits [3, 4]. Water can also be contaminated by fluoride anthropogenically, due to accidental or deliberate release of solid or aqueous waste-streams from multiple different industries [3, 5, 6]. As a result, sources of freshwater have been found to contain as much as 2,800 $mg \cdot kg^{-1}$ fluoride [7] and humans, animals and plants in many areas of the world are subject to overexposure to, or overconsumption of fluoride.

1.2. Fluoride and health

Fluoride, in controlled amounts, is a desirable dietary supplement for humans and livestock. It is beneficial for human dental protection against cavities when consumed at an approximate rate of 0.05 $mg \cdot kg^{-1}$(body mass)$\cdot day^{-1}$ [8]. However, excessive consumption (0.1-7 $mg \cdot kg^{-1} \cdot day^{-1}$), can cause dental fluorosis, characterised by undesirable staining and mottling of the teeth [8]. Chronic over-consumption leads to skeletal fluorosis. Bone strength is permanently reduced and brittleness increased, promoting the likelihood of fractures and skeletal deformity. In areas with substantial fluoride groundwater contamination, such as rural India and China, cases in humans are still commonplace [9, 10]. Cattle are generally the most susceptible livestock to skeletal fluorosis and excess fluoride can also adversely affect live weight gain in pigs [11, 12].

1.3. Fluorite and its economic importance

Fluorite (CaF_2) is the most abundant naturally occurring form of fluorine on Earth. It is classified as either "acid-grade" (≥97% purity) or "metallurgical-grade" (80-96%). Worldwide, two thirds of all fluorspar processing requires acid-grade material [13]. Acid-grade is so named because the mineral is treated with concentrated sulphuric acid to produce HF and is thus the source of most fluro-chemicals used in laboratories and industry, such as flurosilicic acid, SiF_4 and hydroflurocarbons (HFCs) [14].

The global fluorite industry is volatile. Exports were previously dominated by China, who accounted for 64% of total production in 2014 [15]. However, this fell to 55% by 2018 [13] and recent years have seen the emergence of Mexico as the principal exporter (888 kT in 2018 [13]). The United States Geological Survey (USGS) estimated there to be ~310 MT geological fluorite remaining

globally, with a current mining rate of ~6 MT·yr^{-1} [16]. Even assuming no significant future increase in mining capacity, this equates to a remaining supply of only 50 years' worth. Fluorite was thus recognised as one of 20 critical global minerals by the EU in 2014 [17] and one of 35 such materials in 2018 by the US [16].

1.4. Primary aluminium production

Aluminium is the most widely produced non-ferrous metal in the world. Estimated global production in 2018 was 64.3 MT, which is over 2.5 times the reported production in 1998 [18]. The market is dominated by China, which enjoys a ~55% share, although every continent currently has appreciable production. Al has uses primarily as a lightweight, yet strong building material. It has a density of 2.7 g·cm^{-3} and is commonly alloyed with Cu, Mg, Mn, Si, Sn and Zn, producing materials with a tensile strength of >300 MPa [19].

Production of Al begins with the conversion of bauxite ore into alumina (Al_2O_3). Crude bauxite contains ~30-54 % alumina, the rest being silica, iron oxides and TiO_2. It is subjected to the Bayer process, which involves first crushing and milling, then gentle heating with NaOH in a pressurised vessel at 170-180°C. A filtering step removes the iron oxides as "red mud", which leaves $NaAl(OH)_4$ in solution. This is cooled and seeded with $Al(OH)_3$ crystals, then a final heating in a rotary kiln yields pure alumina [20].

The reduction of alumina to Al metal is achieved via the Hall-Héroult (HH) process, first introduced in 1886 [21]. This takes place in a large electrolytic cell, a schematic of which is shown in Figure 1.1. The alumina is dissolved in a bath of molten cryolite (Na_3AlF_6), which contains an excess of AlF_3, forming a eutectic mixture, which lowers the melting point of pure alumina from 2054°C to ~900°C. The cryolite ionises to form Na^+ and AlF_6^{3-} ions, with the purpose of the AlF_3 being to stabilise the latter species and control the degree of dissociation into AlF_4^- and F^-, as AlF_6^{3-} is the active species in the alumina dissolution process [22]. Both cryolite and AlF_3 are produced from metallurgical-grade fluorite. Other minor additives to the bath include fluorite itself and occasionally LiF, which further control the bath temperature and improve conductivity. The overall REDOX reactions involved can be described by Equations 1.1 and 1.2.

$$2Al_2O_3 + 3C \rightarrow 4Al + 3CO_2 \quad \textbf{(Eqn. 1.1.)}$$

$$Al_2O_3 + 3C \rightarrow 2Al + 3CO \quad \textbf{(Eqn. 1.2.)}$$

The reduced molten Al metal sits on top of the cathode surface and is periodically siphoned off, then formed into blocks or sheets. Although the molten Al itself actually acts as the cathode during cell operation, the carbon cell lining is commonly termed "the cathode".

The Al industry is extremely polluting and energy-intensive. The energy requirements for Al production are ~13.5-16 kWh·T^{-1} [18] and CO_2 emissions are 12-17 T CO_2·T^{-1} [23]. Both factors can mainly be attributed to the HH process [24]. There is therefore much interest in reducing the overall efficiency and sustainability of the industry [24, 25]. It can be seen in Figure 1.1 that the Al smelting also causes volatilisation of fluoride. However, in modern plants, >99% of the fluoride ($NaAlF_{4(g)}$) is captured by a gas treatment centre and <1% escapes to the atmosphere as HF [26]

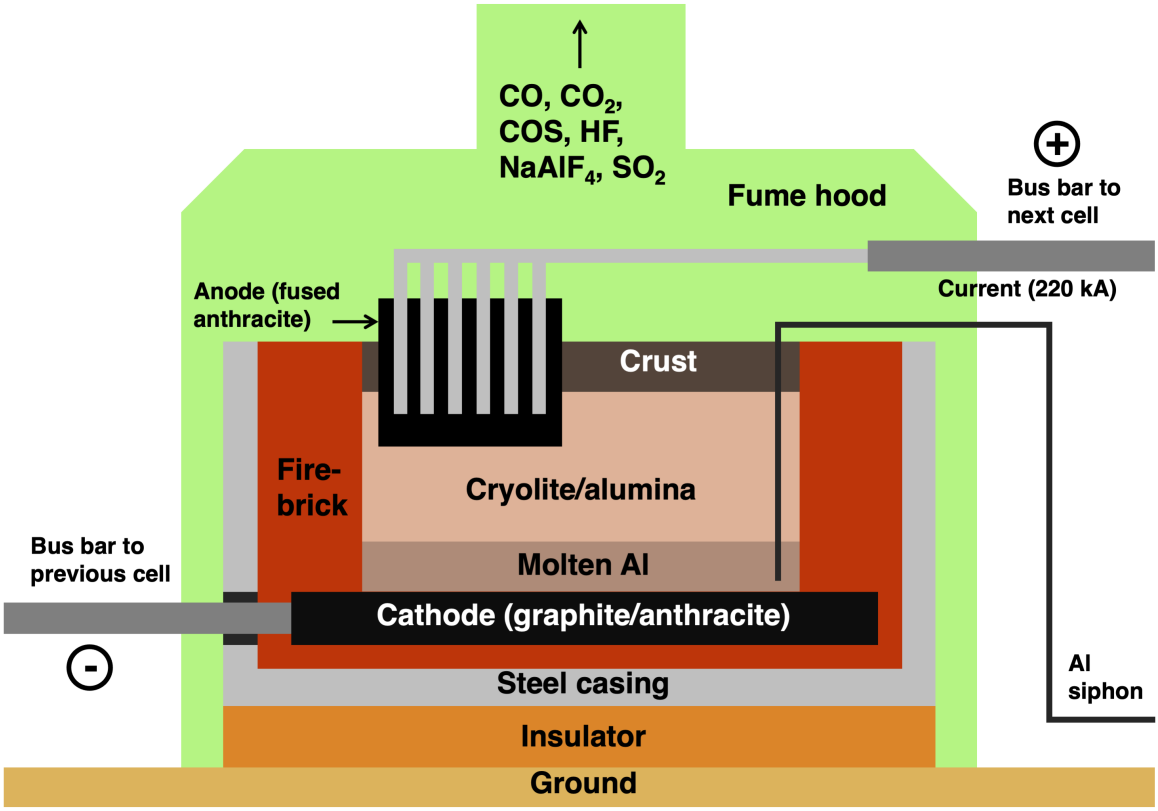

Fig. 1.1. Simplified schematic of a Hall-Heroult cell for primary Al production.

1.5. Spent potlining (SPL)

1.5.1. Formation

SPL is formed from the cathodic lining and refractory surrounding of HH cells. Whilst the cathode is not itself consumed via the REDOX reactions, the lining is degraded over time, due to the harsh reaction conditions of the electrolyte bath. The initial attack is by gaseous sodium ions, which diffuse into the graphite and anthracite lattices and intercalate with the carbon layers [27]. This causes expansion of the lattice, placing the cathode blocks under mechanical stress. Minute fissures form, into which further contaminants from the cryolite bath may then leach and crystallise. The phenomenon is termed “sodium swelling” and results in a volume increase of ≤0.85%, dependant on current density [28]. The pot eventually fails due to more severe cracking or a decline in the quality of aluminium produced. HH cells last for 3-8 years, depending on cell design and fabrication [29], at which point, the cell is drained and rehabilitated. This entails excavating the exhausted cathode material, the steel bus bar and at least some of the firebrick lining underneath. The extent

of the reaction front can be seen in Figure 1.2. The resulting waste material is known industrially as “spent potlining” (SPL). The predominantly carbon fraction is referred to as “first-cut” material and the cementious fraction as “second-cut”. The decommissioning of HH cells requires a pneumatic hammer to break up the potlining [30] and as a result, the two fractions are not easily separated.

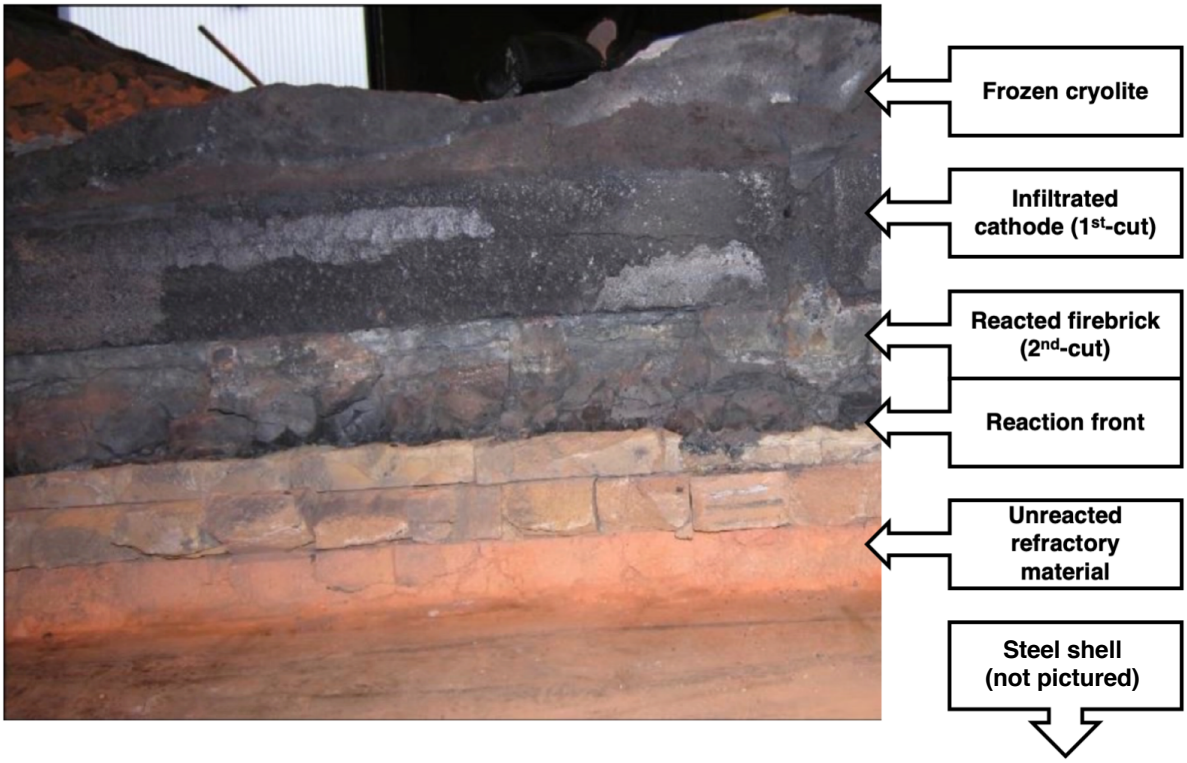

Fig. 1.2. Cross-section of a decommissioned HH cell, showing the extent of contamination of the lining material. Adapted from [31].

The total mass of SPL generated per tonne of Al produced varies widely, according to the efficiency of the HH cell design, but the average is generally agreed to be ~22-25 kg [32-34]. This infers that >1.5 MT of SPL was created by the industry in 2019. Some estimates are much higher (~4 MT) [35].

1.5.2. Composition and hazards

Both the cathodic lining and refractory material below are heavily contaminated during the lifespan of a HH cell, to the point where their chemistry is substantially altered, due to penetration of the electrolytic bath chemicals. Table 1.1 shows the approximate composition of mixed-cut SPL. These ranges are inclusive of all widely used HH cell designs and have been quoted in the literature as being accurate representations [34]. Some SPL samples from other studies have however been found to contain ≤60% carbon and ≤5% SiO_2 [36], which is unsurprising, given that there will be regional variations in how the cells are decommissioned and the cuts are separated. It is however known that mixed-cut SPL represents the largest total fraction of the waste (~54% mass) [37].

Table 1.1. The composition range of mixed-cut SPL. All values, apart from those indicated, are taken from Holywell and Bréault [32].

Component	Normal % composition range	Major chemical phases
Carbon	38–50	Graphite, carbonate
Fluorides	10.9–18.0	Na_3AlF_6, NaF, CaF_2
Sodium	12.5–16.3	Na_3AlF_6, NaF
Aluminium	11.0–13.6	Al_2O_3, $NaAl_{11}O_{17}$, Al (metallic)
Iron	2.9–4.3	Fe_2O_3
Calcium	1.3–2.4	CaF_2
Cyanides	0.05–0.50	NaCN, $Na_3[Fe(CN)_6]$
Titanium	~0.2	TiB_2
Silicon [38]	17.8–20.8	SiO_2
Sulfur [21]	1.5–2.5	Sulfate

Other important species, though not present in large quantities, are Al_4C_3 and AlN [21]. These, along with metallic Al and Na, are highly reactive with water and form hydroxides and volatile gases, according to Equations 1.3-1.7.

$$2\ Na + 2H_2O \rightarrow H_2 + 2\ NaOH \quad \textbf{(Eqn. 1.3.)}$$
$$Al_4C_3 + 6H_2 \rightarrow 3CH_4 + 2\ Al_2O_3 \quad \textbf{(Eqn. 1.4.)}$$
$$2Al + 3H_2O \rightarrow 3H_2 + Al_2O_3 \quad \textbf{(Eqn. 1.5.)}$$
$$2Al + 2NaOH + 2\ H_2O \rightarrow 3H_2 + 2NaAlO_2 \quad \textbf{(Eqn. 1.6.)}$$
$$2AlN + 3H_2O \rightarrow 2NH_3 + Al_2O_3 \quad \textbf{(Eqn. 1.7.)}$$

Because of Equations 1.3 and 1.7, the leachate of untreated SPL, released to the environment is basic and corrosive. The gases released in Equations 1.3-1.6 are potentially explosive [39] and, if allowed to effuse in closed containers, can ignite and cause fires, for example in the holds of transport ships [40].

Arguably, the most dangerous species present in SPL are fluorides and cyanides. The hazards associated with the former have been discussed in section 1.2. Labile cyanides are formed by reaction of air with freshly-exposed carbonaceous SPL, according to Equation 1.8 [41].

$$2Na + 2C + N_2 \rightarrow 2NaCN \quad \textbf{(Eqn. 1.8.)}$$

Over time, through reactions with water, air and rust, the majority is converted to very stable Fe complexes. These consist of six cyano ligands bound with octahedral geometry to a Fe centre, which may be in either the 2+ (ferrocyanides) or 3+ (ferricyanides) oxidation state [42]. Although these forms are low in toxicity by comparison, they can be degraded by photolysis or strong acid and are still considered dangerous. Labile cyanides are extremely toxic to most organisms, with a mean dose of 50–200 mg being fatal to human adults [43].

Environmental leaching of SPL is known to cause local groundwater contamination. A decommissioned Al smelter in Australia, between 1969 and 1992, stored its SPL waste in an

unsecured (lacking an impermeable lining and exposed to the elements) repository. This caused fluoride concentrations of ≤2,000 mg·L^{-1} in local aquifers in 2015 [5].

Accordingly, SPL is classified as a hazardous wasteform in many countries. This status was first conferred by the Environmental Protection Agency (USA) in 1988, then in Australia, by the Hazardous Waste (Regulation of Exports and Imports) Act 1989, then the European Union Council Directive 91/689/EEC in 1991, among others [32]. SPL is also subject to the Basel Convention ruling (1989), prohibiting cross-boundary movement of toxic waste, unless under a bilateral agreement [44].

1.5.3. SPL and fluoride recycling

Considering Table 1.1, it is clear that there is a large potential valorisation opportunity in the high concentration of fluoride trapped within the waste. Industrial recycling of fluoride is globally very limited. Numerous industries produce aqueous waste streams of high fluoride concentration, yet these are commonly regarded as nuisances, rather than recycling opportunities [45-47]. It is equally clear that fluoride recycling processes require improvement and development, before global fluorite reserves become critically depleted. SPL represents a major opportunity to progress these fronts. It is particularly desirable to recycle the fluoride content of SPL, since the HH process consumes ≤50 kg AlF_3 per tonne of metallic Al produced [48]. Even disregarding the threats presented by SPL to environmental contamination and public safety, it is unacceptable, from a sustainability point of view, that the rich fluoride content is not fully recycled. Given the increasing value of fluorite and derivatives (Figure 1.3), fluoride recycling processes can also potentially add value and improve margins for the primary Al smelting industry [49, 50].

Conservation of mineral reserves can not only be achieved directly, but also by recycling of secondary commodities, which are ultimately produced using fluorite as a feedstock. Cryolite is an example of such commodities. It has no significant geological reserves and is instead produced synthetically, mainly from HF (from acid-grade fluorite) and alumina (Equation 1.9).

$$Al_2O_3 + 6NaOH + 12HF \rightarrow 2Na_3AlF_6 + 9H_2O \qquad \textbf{(Eqn. 1.9.)}$$

Some sources state that modern Al smelters now completely regenerate the cryolite required for the HH process and no longer need to purchase the raw material [51]. Nonetheless, synthetic cryolite market prices have remained high for the past six years (Figure 1.3). No reliable data could be found regarding worldwide production, but a basic internet search reveals a large number of merchants selling various grades of synthetic material. Relatively recent research articles have focussed on recovery of cryolite from fluoride-containing waste-streams [52, 53]. Cryolite is additionally used in abrasives, coatings for welding, ceramic glazes and enamels. It is also the active ingredient of

Kryocide®, an insecticide effective on numerous target species, notably used by many Californian wineries [54].

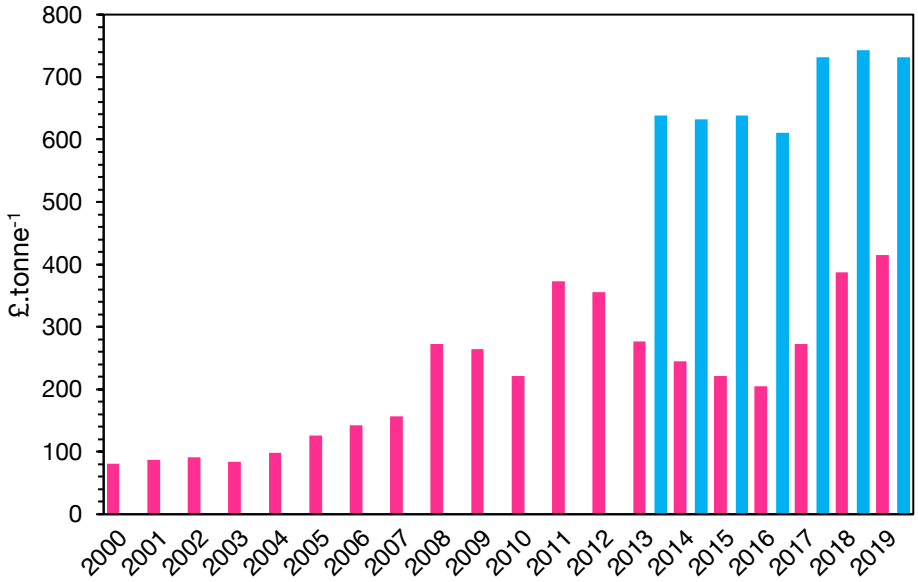

Fig. 1.3. Average market price trends for acid-grade fluorite (pink bars) and synthetic cryolite (blue bars). "Freight on board" price from China, [55].

1.6. Historical and alternative treatments of SPL

SPL is recognised as a hugely significant problem, threatening the future sustainability of the Al smelting industry [44, 56]. It is acknowledged that uncontrolled disposal of SPL was widespread until at least the mid 1990s [30]. Even in 2013, it was thought that ≥75% of SPL produced was disposed of in buildings or refractories open to the elements, with the potential for leaching of contaminants into the environment [32].

A large number of processing solutions for SPL have been attempted, of which, not all have proved economically sustainable [29]. Many focus primarily on conversion of the waste to an environmentally benign form, with fluoride recovery being a secondary aim, if considered at all [57]. This work falls within a hydrometallurgical remit, but other strategies are now briefly described.

1.6.1. Additives for other industries

Untreated SPL has been used as a partial replacement for fuel in cement kilns, where it usefully accelerates clinker-forming reactions by lowering firing temperature [58]. However, the maximum possible addition of SPL to the furnace is 0.5% mass [59] and the kilns required modifications to deal with the SPL addition, due to the sodium content and variability of the material [30]. The main reason for the decline is this practice though, was that the classification of SPL as hazardous waste meant that numerous extra control measures and safety protocol had to be implemented at the handling plants, making the process financially unviable [60, 61].

Efforts were also made in the iron and steel industry to substitute SPL for coke in metallurgical furnaces. However, the high concentration of fluoride in the waste is problematic, as it accelerates degradation of the furnace refractory lining [36]. A further disadvantage is that only first-cut SPL can be used in this employ [62].

SPL may be used as an additive for rock wool and glass wool production. In 2013, Norwegian aluminium smelter Hydro reached an agreement with Rockwool International (Germany) to provide a certain tonnage for conversion into rock wool [63], which finds uses as fireproof insulation materials and media for hydroponic growing. Again, the issue is that only first-cut SPL is suitable for this purpose.

1.6.2. Pyrometallurgical processes

None of the above uses utilise the fluoride content of the waste in a gainful manner. This is not however the case for a number of pyrometallurgical treatment options. Because of the focus of this work, the discussion on pyrometallurgy is limited to industrial solutions only, rather than any laboratory-scale work. These essentially operate on the principle that SPL has a high calorific value (16 $MJ \cdot g^{-1}$ for first-cut samples [64]), which can be used to power a furnace, destroy labile cyanides by thermal oxidation, and volatilise a fraction of the fluorides as HF gas. In some cases, the fluoride was merely trapped as a slurry and not recycled (Alcoa Reynolds, US) [57], or remained in the calcined material (Comalco, Australia) [65]. In others, NaF and AlF_3 were recovered (Alcoa Portland, US and Chalco, China) [29, 38], but the technology in the former was not maintained, due to economics.

It should also be noted that, in addition to "in-house" technology, developed by Al smelters themselves, there are also a number of external companies, which have created pyrometallurgical SPL treatment systems [66]. Such companies charge the smelters a processing fee for shipment and disposal of their SPL waste. However, only commercial literature is available to describe the processes.

Some pyrometallurgical treatments claim to produce zero landfill (Regain Materials, Australia) [67], but the majority result, or resulted, in a sintered landfill product, albeit one that is inert and low in fluoride concentration [29, 68]. The issue from a fluoride recovery perspective is that not all fluoride is volatilised under heating, due to the high temperature required to drive Equation 1.10 to completion, and so remain in the calcined material [69].

$$Na_3AlF_6 + 6H_2O \rightarrow 12HF + Al_2O_3 + 3Na_2O \qquad \textbf{(Eqn. 1.10.)}$$

There is also an obvious environmental impact, or carbon-capture process requirement, from the pyrolysis of the carbonaceous SPL and associated CO_2 production. For these reasons (and also due to the network of research expertise available to the author during production of this thesis), the focus of this work is hydrometallurgical SPL remediation.

1.7. Chemical leaching

Leaching is a key stage of hydrometallurgy. It can be described as the preferential dissolution of one or more components of a solid, via contact with a liquid lixiviant. The chemistry of the process can involve oxidation, such as leaching of platinum group metals from spent autocatalytic converters [70], or reduction, such as recovery of transition metals from exhausted lithium-ion batteries [71] and this influences the choice of lixiviant. In other cases, the leaching simply involves dissolution of the target species, with no change to oxidation state. Dissolution is simply the process by which a solid solute dissolves into a solvent, forming a solution.

Other factors often significant to the leaching process are temperature and the mass ratio of the substance to be leached to the lixiviant [37, 72]. Of particular importance is the particle size of the material. It is generally the case that a small particle size improves the kinetics of leaching, often by several orders of magnitude . Conversely, to achieve smaller particles, more time and energy must be inputted into preparation of the material [73]. Particle size also dictates the design of the leaching vessels, with larger solid fragments being leached by simple percolation tanks, but fine particulates usually having to be pumped through a series of thickeners as a slurry, before solid/liquid separation [73].

1.7.1. Hydrometallurgical industrial SPL treatment

Hydrometallurgical treatment of SPL is a challenging task, because the chemistry of the waste is complex and variable (Table 1.1). It is accepted that both an acidic and caustic leaching stage is required to solubilise even close to 100% of the contaminants [53, 74]. Alumina and cryolite are only soluble in base, while a further two prevalent species, fluorite and diaoyudaoite ($NaAl_4O_{17}$), are only soluble in acid [53].

The first hydrometallurgical treatment of SPL actually predates its hazardous waste classification. SPL was leached with dilute NaOH and the leachate combined with a scrubbing solution, which captured volatiles from the HH electrolysis stage, which in turn enabled precipitation and recovery of cryolite. At the time (early 1970s), this was more economical for the smelter than purchasing synthetic cryolite [60, 75]. The drawbacks to this process were the incomplete leaching, as previously described (~80%) and the timescale of the treatment (>24 hr) [75].

At the time of writing, only two hydrometallurgical systems for SPL are in operation. The BEFESA process is described only by corporate literature and the chemistry of the process is not known [76]. The leaching is performed with unspecified chemicals and output products include fluoride-containing salts, used as flux agents [58].

Rio Tinto Alcan (RTA, Canada) have implemented a “Low-Caustic Leaching and Liming” (LCLL) technology (Figure 1.4), which is one of the few SPL processes to generate fluorite as an output. A limitation of the process is that, although ~100% of the fluoride is leached from the inbound SPL, only the water- and initial caustic-leached fractions are recovered, rather than the total fraction, the fate of which is not precisely addressed in the literature [50]. The fluorite produced by LCLL is of poor quality. The material has a 33% water content and of the dry mass, only 80% purity is claimed [77]. A commercial brochure from RTA suggests the fluorite can be used in the in-house AlF_3 production plant and as a flux in the steel and cement industries, but it is not clear to what extent these goals are actually realised. It is also claimed that the working CAPEX of the process is lower than placing SPL in landfill, which suggests that LCLL currently does not return a net cost benefit to the smelter [77].

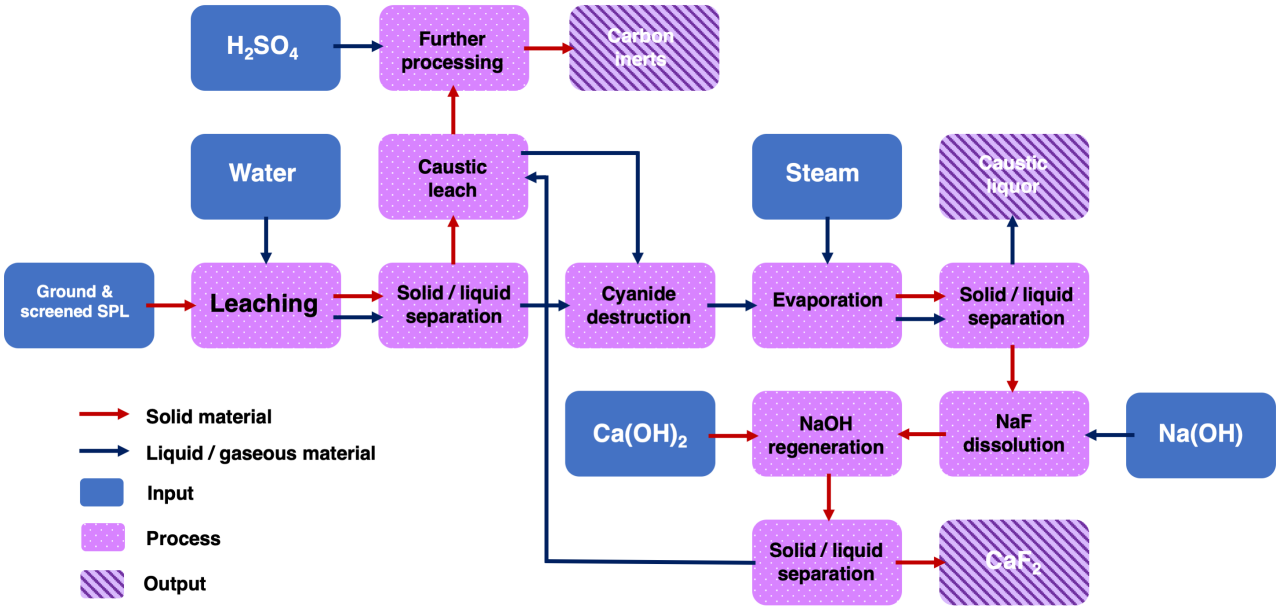

Fig. 1.4. Simplified schematic of the RTA LCLL process [50].

Table 1.2. Overview of recent technologies for SPL processing.

Company	Technology	Throughput ($kT \cdot yr^{-1}$)	Output materials (and destination)	Reference
Hydrometallurgical				
BEFESA	Co-processing with mixed salt slags	N/A	- Inert carbon/cement product (cement/rockwool) - Fluoride salts, mixed with NaCl and KCl (flux agents)	[76]
Rio Tinto Alcan	Four-stage leaching (water, 0.75 M NaOH, H_2SO_4, undefined final stage)	80	- Caustic liquor (Bayer process) - Inert carbon/cement product (fate unknown) - CaF_2 (reused in-house)	[49, 50]
Pyrometallurgical				
Alcoa Portland	Pyrolysis in furnace (1,200ºC), fluidised bed, slag granulation	>10	- Vitrified benign waste (landfill) - AlF_3 (65% pure) and NaF	[29]
Regain Materials	Undefined pyrometallurgical process	12	- Inert materials sold to cement and clay brick industries	[67]
Tetronics International	Single-stage plasma technology	N/A	- Vitrified benign waste (landfill) - Fluoride product (unspecified)	[66]
Combined				
Alcoa Reynolds (Formerly Reynolds Metals, Oregon)	Pyrolysis in rotary kiln (1,000ºC) using limestone and sand, leaching with $Ca(OH)_2$	N/A	- Inert carbon/cement product (landfill) - CaF_2 (landfill)	[57]
Rio Tinto Comalco	Calcination (700ºC), leaching with conc. NaOH	10	- Caustic liquor (Bayer process) - Clinker (cement industry) - NaF	[65]
Zhengzhou Light Metal Research Institute / CHALCO	Co-processing with used anodes and bauxite, sintering (rotary furnace)	3	- Inert residue (cement industry) - AlF_3	[68]

A comparison of all known working and recently decommissioned technologies for the treatment of SPL is shown in Table 1.2. Technical references are provided where possible, but for some technologies, due to protection of intellectual property, only corporate literature was freely available to describe the process. It can be seen that in many cases, a similar mixed carbonaceous/cementious product is attained. However, because of the low commercial value of this substance, the costs of distribution mean that landfill may still be the preferred option, depending on the location of the smelter and industrial connections [32]. This demonstrates the difficulty in full valorisation and recycling of SPL and emphasises the need for a more effective fluoride-recovery process.

1.7.2. Laboratory-scale hydrometallurgy

The focus now moves from fully-realised industrial processes to the large number of smaller-scale studies, which have investigated hydrometallurgical methods for the detoxification of SPL (Table 1.3.). The great majority has focussed on first-cut SPL, with the intended outcome being either recovery of a fluoride species [74, 78], or the purification of the graphite fraction for recycling into carbonaceous products [53, 79].

Very few single-stage treatments have been reported. One such study used a chromic acid lixiviant, which was claimed to reduce the residual fluoride concentration to <150 $mg \cdot kg^{-1}$ [80, 81]. However, the strongly oxidising lixiviant caused effusion of HF gas, which would have to be captured by caustic scrubbing, creating a second aqueous wastestream. Dilute NaOH (pH 12) has been investigated as

a single-stage treatment, but the study was confined to second-cut material and the leaching effected only 70-90% removal of fluorides [82]. Leaching of first-cut only SPL by NaOH (3.53 M) has been shown to improve residual carbon purity to ≤95%, with enhancement by ultrasonication [79]. A similar treatment with NaOH (2.5 M) however, produced only 72.7% carbon purity and 96.4% was attained only after a second treatment with HCl (9.7 M) [53]. This is likely a reflection of the diversity of SPL chemical composition, even when different samples are termed the same grade. The latter study also recovered a fraction of fluorides, achieved by mixing caustic and acidic leachates together and precipitating cryolite. The purity was quoted as 97.0%, but the total recovery of fluoride was not stated [83].

Apart from the choice of strong mineral acid and strong base, other lixiviants have included Al^{3+} salts, with the target recovery product being AlF_3 [37, 78, 84, 85]. This has been essayed with both analytical reagents [37] and with Al anodising wastewater [84]. A hydrated aluminium hydroxyfluoride (AHF) product of defined stoichiometry has been attained, which is a precursor to AlF_3 [78, 85]. However, the treatment must be precluded by washing of the waste with water. This solubilises the major NaF fraction [50], which must be recovered by other means, hence reducing the potential yield of AlF_3. A recent study combined the water-wash and Al^{3+} leachate to instead precipitate cryolite as an output product. However, the extent of solubilisation was low (<70%), although cryolite recovery from the solubilised fluoride was 98.4% [72]. Only first-cut SPL has been demonstrably treated using these techniques, which calls into question the feasibility of their implementation on a large scale.
A treatment system involving no caustic leaching has been proposed [74]. However, it requires leaching in three stages and uses hazardous and expensive reagents (HF and fluorosilicic acid).

Overall, the evidence shows that SPL may be cleansed of close to 100% its leachable fluoride content by economical reagents, within an acceptable timeframe. However, the reported high carbon purity of leached SPL refers only to samples where the original material was of first-cut origin. A mixed-cut SPL feed greatly complicates the carbon recovery process: attempts to separate the carbonaceous and cementious SPL fractions by floatation have achieved a carbon purity of only ≤88% [86] and the technology has not yet transitioned to industrial scale [50].

Table 1.3. Comparison of laboratory-scale leaching treatments for SPL.

Treated cut	Number of stages	Lixiviant(s)	Timescale (hr)	Temperature (°C)	Fluoride extraction (mass %)	Reference
First	1	Chromic acid (conc.)	<0.3	100	>99	[81]
Mixed	4	Water, HF, H_2SiF_6 (1 M), water	Not stated	75	Not stated	[74]
Second	1	NaOH (0.01 M)	18	23	89	[82]
First (presumed)	2	NaOH (2.5 M), HCl (9.7 M)	2 x 3	100	97	[53]
First	2	Water, $Al(NO_3)_3$ (0.36 M)	4 + 24	25	76-86	[78]
First	2	Water, Al wastewater & H_2SO_4 (0.7 M)	2 x 4	60	72	[84]
First	2	Water, $Al(NO_3)_3$ (0.36 M) & HNO_3 (0.5 M)	2 x 4	60	96.3	[37]
First	1	NaOH (3.53 M) with ultrasonication	0.67	70	95	[79]
First (presumed)	2	Water, Al wastewater & 1.77 M H_2SO_4	2 x 3	80	98.4	[72]

Where the SPL cut is not stated in the literature, an assignment has been made, based on the reported elemental quantification.

More importantly, for this work, no system yet devised is able to recover close to 100% of the solubilised fluoride from mixed-cut material as a commodity output that will add value to the process. This invites the hypothesis that fluoride recovery potential may be improved by a selective extraction step, from the leachate streams on to a solid-phase adsorbent, followed by elution, to yield a pure and concentrated wastestream.

1.8. Removal of fluoride from water

There are a number of different techniques for the defluoridation of water, reviewed by several authors [87, 88]. Coprecipitation techniques, such as the Nalgonda method are widely used to improve drinking water quality in developing countries [88]. Despite its advantages of simplicity and economical reagents, the method results in large volumes of amorphous sludge, which is unsuitable for fluoride recovery [87]. As has been seen in the literature, the selective precipitation of a fluoride species of potential value is not straightforward [78, 85] and requires some control over the chemical speciation of the aqueous solution. For example, the purity of fluorite precipitated from an impure feed of industrial wastewater was only 78%, whereas that attained from a pure NaF feed solution was >97% [46, 89]. The evidence thus suggests that purification and concentration, followed by precipitation is the most feasible direction for this work.

Electrocoagulation techniques have been shown to remove fluoride as Al or Fe complexes or crystalline salts, again in the form of a sludge [90]. Although the volumes produced are less than via the Nalgonda method, there has been no potential pathway to recovery yet demonstrated. The same is true for membrane filtration [91]. Hence, the only feasible technique to achieve the first step is that of adsorption.

1.9. Adsorption

Adsorption is the phenomenon by which particles in a gas or aqueous phase (the sorbate) become attached to a solid surface and immobilised (the sorbent). Adsorption can be split into two categories: physisorption and chemisorption. In physisorption processes, the sorbate is held to the surface only by Van der Waals interactions. In chemisorption processes, there is a more significant interaction between the valence electrons of sorbate and sorbent, resulting in a chemical bond being formed. Because of this, chemisorption binding is much stronger and harsher conditions are required to cause the desorption of the sorbate. The energy of desorption (E_{des}) for physisorption phenomena is invariably described as being typically <8 $kJ \cdot mol^{-1}$, whereas for chemisorption, it is 8-16 $kJ \cdot mol^{-1}$ [92, 93]. Adsorption is a commonly applied technique in chemical separations and the requirement of the separation influences which type of adsorption is employed. For example, aliphatic volatile organic carbons (VOCs) can easily be captured by an activated carbon sorbent column by physisorption, due to their hydrophobicity [94]. In contrast, the removal of radioiodine from spent nuclear fuel reprocessing off-gas is achieved via selective chemisorption on to silver-loaded adsorbents (forming AgI salt), to prevent competition from the numerous other gaseous species present [95].

Various aspects of adsorption can be explored via laboratory-scale experiments. These are discussed in detail in the respective experimental chapters, particularly with regard to mathematical modelling, but brief introductions are now given.

1.9.1. Thermodynamics

A number of thermodynamic models have been developed to describe different sorbent/sorbate interactions. Common experimental practice is to produce an isotherm from a series of batch experiments, in which known masses of sorbent are contacted by a series of solutions of increasing sorbate concentration and mixed until equilibrium is reached. The equilibrium sorbate concentration in the aqueous phase (C_e, in $mg \cdot L^{-1}$ or $mmol \cdot L^{-1}$) is plotted against its equilibrium concentration in the solid phase sorbent (q_e, in $mg \cdot g^{-1}$ or $mmol \cdot g^{-1}$), demonstrated in Figure 1.5a. If isotherm data can be accurately described by a certain model, then certain physical parameters can be reliably quoted, which gives insight into the adsorption. For example, whether adsorption sites are degenerate, or sorbate species interaction changes as a function of coverage; whether multiple layers of sorbate

can be bound by the same particle, and whether the adsorption is reversible. Isotherms also allow calculation of a theoretical maximal uptake capacity for a given system, which gives an indication as to what sorbate feed concentration range would be most appropriate in a dynamic setup [96].

It should be noted, that the isotherm models used in this work are derived from gas-phase/solid-phase interactions and do not account for heterovalent adsorption. Although such models are still widely used to investigate aqueous adsorption via chelation, complexation and precipitation reactions [96-99], care needs to be taken in stating whether the fundamental assumptions of the model are established. In other words, the fact that a dataset is described well by a certain model does not always determine the mechanism of adsorption beyond reasonable doubt.

1.9.2. Static kinetics

The kinetics of an adsorption system may also be investigated by simple batch experiments, this time by a plot of time verses the sorbate concentration in the sorbent at a given time (q_t, in $mg \cdot g^{-1}$ or $mmol \cdot g^{-1}$), as in Figure 1.5b. Again, various models can be used to attempt to describe the data and their respective accuracies can reveal information about the system. There are known to be five stages to an adsorption process:

1. Transport of sorbate from the bulk of the contact liquid to the sorbent surface
2. Diffusion through the hydrous layer around the sorbent particle (termed “film diffusion”)
3. Diffusion within the particle to an active site where binding will occur (termed “intra-particle diffusion”)
4. Physical or chemical reaction at the active site
5. Diffusion of any displaced species away from the active site

Kinetic data-fitting can reveal which process is rate-limiting overall, or whether different stages of the adsorption dominate at different times [100].

1.9.3. Dynamic kinetics

Dynamic adsorption experiments use a column, packed with the sorbent, of known dimensions, through which an inlet solution, containing the sorbate of interest, is pumped. This creates an “active” area, where the adsorption proceeds, which moves either up or down the column, depending on flow direction, until the sorbent bed is exhausted. As such, the system is not considered to be at equilibrium during column experiments [101]. By collecting fractions of effluent and determining the sorbate concentration over an effluent volume range, a breakthrough curve can be generated via a plot of sorbate effluent concentration, relative to inlet concentration (C_e/C_i) vs volume of effluent (V_{eff} in mL), as in Figure 1.5c Yet again, models can be fitted, which, depending on accuracy, allow

calculation of physical dynamic parameters. For example, the dynamic uptake capacity of the sorbent and the theoretical lifespan of the column, which are useful when engineering adsorption systems.

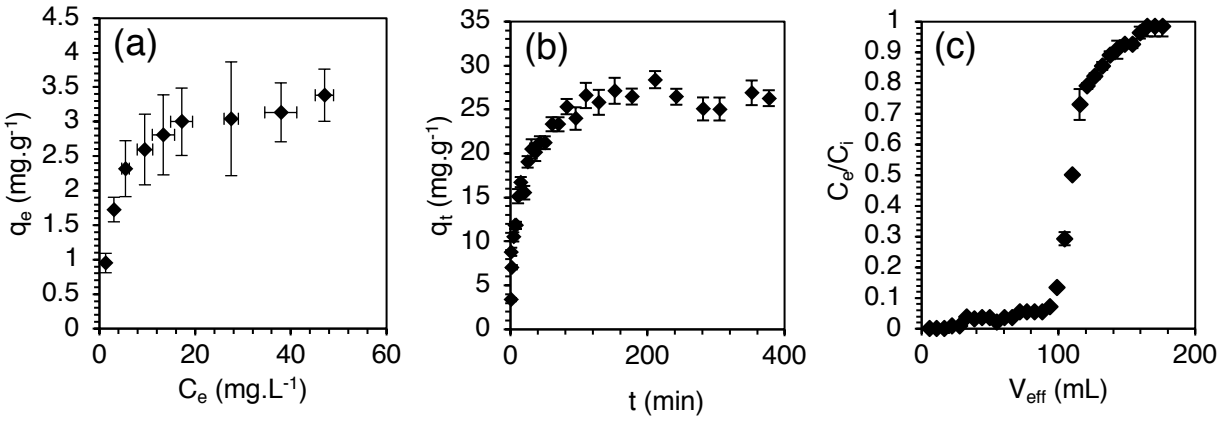

Fig. 1.5. Example data plots of three common adsorption experiments. **(a)** Isotherm. **(b)** Static kinetic. **(c)** Dynamic breakthrough curve. Plots are based on subsequent experimental data, but are included here only for illustrative purposes to show typical data series shapes.

1.9.4. Adsorption applied to SPL waste

The body of literature detailing adsorption of ions from leachate and other liquids, resulting from SPL production, is small. No study has applied adsorption principles to the liquor that might be produced from a hydrometallurgical SPL treatment system. Certain authors have focussed on naturally-produced environmental SPL leachate and selective removal of fluoride, by treatment with $CaCO_3$ and CO_2 in a batch reactor system [33]. Removal was found to be inefficient at atmospheric CO_2 pressure and even at 60 mol% CO_2, the defluoridation of the water did not exceed 97.5%, due to the partial solubility of the CaF_2 formed. Others have attempted defluoridation, after a pretreament with CaO, using activated charcoal, impregnated with a WBA exchanger in liquid form, in a series of dynamic experiments [102]. Although the dynamic fluoride capacity of the exchanger was not determined, it was capable of reducing fluoride concentration in the column eluent to 1 mg·L^{-1}. In both of these cases, chemical analysis in both cases showed the waters studied to have a very low Al^{3+} concentration and also low levels of other potentially competing anions. Therefore, although the adsorbents are certainly shown to remove fluoride from the aqueous phase, the conditions bear little relevance for this work on SPL industrial leachate [74, 85].

1.10. Ion-exchange and commercial ion-exchange resins

Ion-exchange (IX) may be described a reversible process, in which an electrically-charged sorbate ion becomes immobilised on an oppositely-charged active site within the sorbent; in the process, displacing a previously bound ion into the contact solution. The exchangeable ions may be cations

or, as in Equation 1.11, anions. In this equation, M^+ represents an active surface site and A^- and B^- are two different anions.

$$M^+A^-_{(s)} + B^-_{(aq)} \rightleftharpoons M^+B^-_{(s)} + A^-_{(aq)} \quad \textbf{(Eqn. 1.11.)}$$

IX is categorically not chemisorption, as the exchanged species remain in their ionised form and do not chemically bond to the sorbent surface. However, because of the strong electrostatic attraction between oppositely charged species, the strength of binding can often exceed 8 $kJ \cdot mol^{-1}$, for example, in the exchange of protons for divalent metal ions [92]. Conversely, some anion-exchange interactions can be extremely weak, the exchange of chloride for nitrate having been reported as ~40 $J \cdot mol^{-1}$ [103]. The majority of interactions explored in this work are not classical ion-exchange phenomena, but do involve modified ion-exchange resins [104, 105].

The first ion-exchangers observed and documented were actually inorganic in nature. Silicates and aluminosilicates contained in soil were observed to bind ammonium cations from manure, causing the elution of Ca^{2+} ions [106, 107]. However, with the advent of polymers, organic IX resins were synthesised and commercialised (Figure 1.6). The first generation are now commonly referred to as "gel type". They were synthesised by free radical polymerisation of styrene, with a small % of divinylbenzene (DVB), loosely crosslinking the polymer chains [108]. Such resins were able to swell in certain solvents, allowing ionic species access to any functionalities grafted to the polymer chain, but they did not have a measurable surface area. Second-generation resins are termed "macroporous type" (sometimes "macroreticular"). These had an increased % of DVB in the polymer chains and also incorporated porogens in the synthesis, such as caprylic, lauric and palmitic acid, which were removed from the final products, but enabled the resulting structures to have permanent porosity [109]. Gel-type resins generally have a higher exchange capacity and often faster kinetics, but lower mechanical strength (often breaking down under osmotic pressure) and fouling-resistance [101, 110]. Because of this, macroporous resins are usually a better choice for systems where regeneration and reuse of the sorbent beds is practiced.

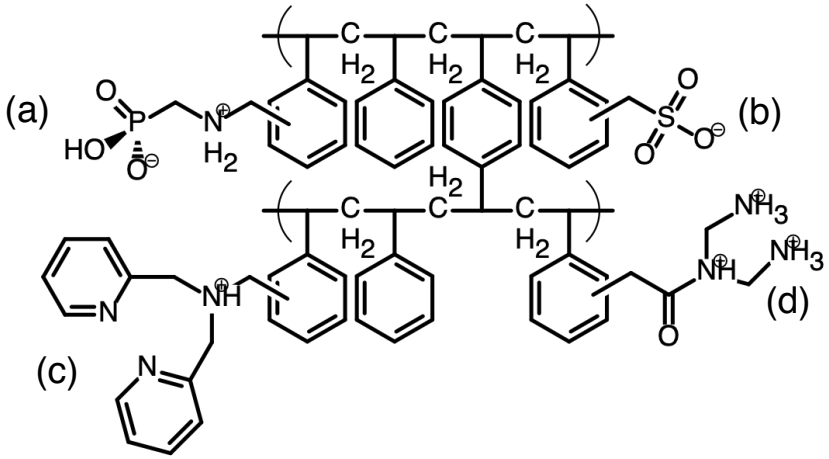

Fig. 1.6. Simplified diagram of a styrene/DVB resin matrix with four illustrative functional groups. **(a)** Aminophosphonic acid. **(b)** Sulfonic acid. **(c)** Bispicolylamine. **(d)** Polyamine.

Commercial IX resins are derived from non-renewable resources and are not the most environmentally-friendly choice of adsorbent; although no reliable E-factor has ever been calculated for the IX industry. They do however have clear pragmatic advantages, which must be considered in the design of a hydrometallurgical system. They can be manufactured to produce a uniform particle size, giving a consistent osmotic column pressure. They have high chemical and mechanical durability, with many resin manufacturers claiming a product lifespan of >10 yr. Moreover, they can be functionalised with a large array of chemical groups, which can be tailored to the adsorption process required; for example, whether selective adsorption of one species is favoured, or complete deionisation of the target aqueous stream [111-113]

The choice of resin functionality is key to the design of a successful water-treatment or resource-recovery circuit. Cation-exchangers are either strong acid cation (SAC) or weak acid cation (WAC). The former has a sulfonic acid functionality, while the latter is often carboxylic or phosphonic acid-based [111]. Weak base anion (WBA) resins are based on amines, usually 2° or 3° [114]. Finally, strong base anion (SBA) resins have permanently quaternised ammonium functional groups. Functionalities may also be chelating in nature, binding to the target ion via multiple donor atoms. Because of this, some resins will selectively uptake certain cations, despite being classified as anion-exchangers. For example, DOWEX™ M4195 is used for the removal of Cu^{2+} ions, but is technically a WBA resin [96].

1.10.1. IX anion selectivity

Selectivity refers to the preferential uptake by a sorbent of one solution-phase sorbate over another in a mixed-species contact solution. Both types of anion-exchanger are governed by clear rules of selectivity in this regard, with SBA resins being more profoundly affected [115]. The order of selectivity is shown below. It can be seen that there are two main influencing factors, these being ionic charge (a 2- anion generally binds more strongly than a 1-) and the size of the ion (a larger, more hydrophobic anion is usually more easily desolvated and adsorbed).

Oxalate > SO_4^{2-} > I^- > NO_3^- > CrO_4^{2-} > Br^- > SCN^- > Cl^- > F^-

The selectivity series illustrates that conventional anion-exchange resins will not be suitable for the application of selectively removing fluoride from SPL leachate, since the anions of all three common mineral acids are all higher in the series than fluoride. This can be seen in multiple studies, which have investigated defluoridation of water, using either conventional anion-exchangers or alternative sorbents with amine or ammonium functionality, as they are invariably shown to be non-selective in mixed species uptake experiments. This is the case for adsorbents such as chitosan, possessing principally amino/acetamido functional groups [116], SBA IX resins [117] and WBA IX resins [118].

In all of these cases, the addition of such common anions as chloride, nitrate and sulfate to the aqueous contact solutions decreased the observed fluoride capacity. The latter case is especially problematic, given that H_2SO_4 is one of the LCLL lixiviants and would therefore be present at macro concentrations in SPL leachate.

1.11. Metallated adsorbents

To overcome selectivity issues within a given system, sorbents may be strategically loaded with a given metal, which then binds the target sorbate, with a stronger interaction than a conventional IX functionality. The metal itself is commonly bound with an IX or chelating interaction [119, 120]. A range of sorbates may be captured in this way. For example, a Cu-loaded IX resin has been used for adsorption of aqueous tartaric acid, which chelates to the metal centres [121]. Alkali metal-loaded microporous polymers have been used for carbon dioxide capture, taking advantage of the favourability of formation of the metal carbonates [120]. For anion removal, fluoride has been a very common target for metallated adsorbents [119, 122, 123], with a small number of studies into iodide uptake also existing [124, 125].

Such adsorbents work on the principle of hard-soft-acid-base (HSAB) theory. Smaller metal ions with high charge density attract smaller, less polarisable anionic ligands. Larger, more diffuse metal ions attract larger, more polarisable anionic ligands. Another key consideration in metal selection is that it must have sufficient valance to exchange at least one ligand for the target anionic sorbate, whilst still remaining coordinated to the resin surface. Equation 1.12 shows the possible ligand-exchange equilibria, which can occur with such systems (L = ligand, M = trivalent metal).

$$[\text{L-M}(\text{H}_2\text{O})_{\text{n-m}}(\text{OH})_{\text{m}}]^{(\text{n-2})-} + \text{qF}^- \rightleftharpoons [\text{L-M}(\text{H}_2\text{O})_{\text{n-m}}(\text{OH})_{\text{m-q}}\text{F}_{\text{q}}]^{(\text{m-2})-} + \text{qOH}^- \qquad \textbf{(Eqn. 1.12.)}$$

The relative strengths of these interactions require consideration. For example, if the solubility product (K_{sp}) of the metal-sorbate salt is very low and/or the binding interaction between metal and functionality is weak, then salt crystallisation and precipitation is likely upon the sorbent surface [97]. The presence of any fine particulates in a dynamic column system cause pressure drop [101], so this phenomenon can be problematic.

Table 1.4. Comparison of the fluoride uptake performances of several metallated IX resins and other adsorbents.

Metal-loaded resins					
Resin (functional group)	**Loaded metal**	**Optimum pH**	**Max initial [F^-] ($mg \cdot L^{-1}$)**	**Max F^- uptake ($mg \cdot g^{-1}$)**	**Reference**
Amberlite 200CT (sulfonic acid)	La	5.5-6	unspecified	25.5	Fang *et al.*, 2003 [123]
Amberlite 200CT (sulfonic acid)	La or Ce	2-7	15	25.5	Luo & Inoue, 2004 [126]
Duolite C466 (iminodiacetic acid)	Al	7	10	1.875	Prabhu & Meenakshi, 2014 [127]
Duolite C466 (iminodiacetic acid)	La or Ce	7	10	4.52-4.76	Prabhu & Meenakshi, 2014 [127]
Duolite C467 (aminophosphonic)	Al	5-7	50	1.98	Ku *et al.*, 2011 [128]
Indion FR10 (sulfonic acid)	La or Ce	7	11	0.456-0.470	Viswanathan & Meenakshi, 2008 [129]
Purolite S940 (aminophosphonic)	Al	2.5	50	12.2	Bhatt *et al.*, 2004 [130]
Purolite S950 (aminophosphonic)	Al	2.5	50	6.02	Bhatt *et al.*, 2004 [130]
Bespoke (aminophosphonic)	La	3.5	50	31.1	Kanesato *et al.*, 1988 [119]
Bespoke (aminophosphonic)	Al	2.5-4	21	11.2	Popat *et al.*, 1994 [131]
Bespoke (hydroxamic acid)	Ce	4	95	9.5	Haron & Wan Yuuns, 2001 [132]
Other sorbents					
Support matrix	**Loaded metal**	**Optimum pH**	**Max initial [F^-] ($mg \cdot L^{-1}$)**	**Max F^- uptake $mg \cdot g^{-1}$)**	**Reference**
Activated alumina	La	4-8	20	6.7	Cheng *et al.*, 2014 [133]
Activated carbon	La	7	80	9.96	Vences-Alvarez *et al.*, 2015 [9]
Cellulose	Ce	3	10	0.416	Sarkar & Santra, 2015 [134]
Chitosan	Mixed lanthanides	unspecified	20	4.73	Liang *et al.*, 2013 [135]
Chitosan	Pr	7	10	15.9	Kusrini *et al.*, 2015 [136]
Palygoirskite zeolite	Al and La	unspecified	60	1.04	Lyu *et al.*, 2016 [137]

There are a vast number of possible adsorbent supports for the investigation of selective sorbate uptake via metallation (Table 1.4), of which one type is investigated in detail in this work (section 1.15). However, in terms of the quick and efficient installation of a dynamic fluoride extraction circuit within an existing hydrometallurgical treatment system, commercial IX resins are the clear media of choice, having been developed and optimised over many years for such purposes (section 1.10).

1.12. Aminomethylphosphonic acid resins

The aminomethyl phosphonic acid (AMP) functionality, pictured in Figure 1.7, is of high importance in the field of IX, due to its complexation and selectivity properties [138].

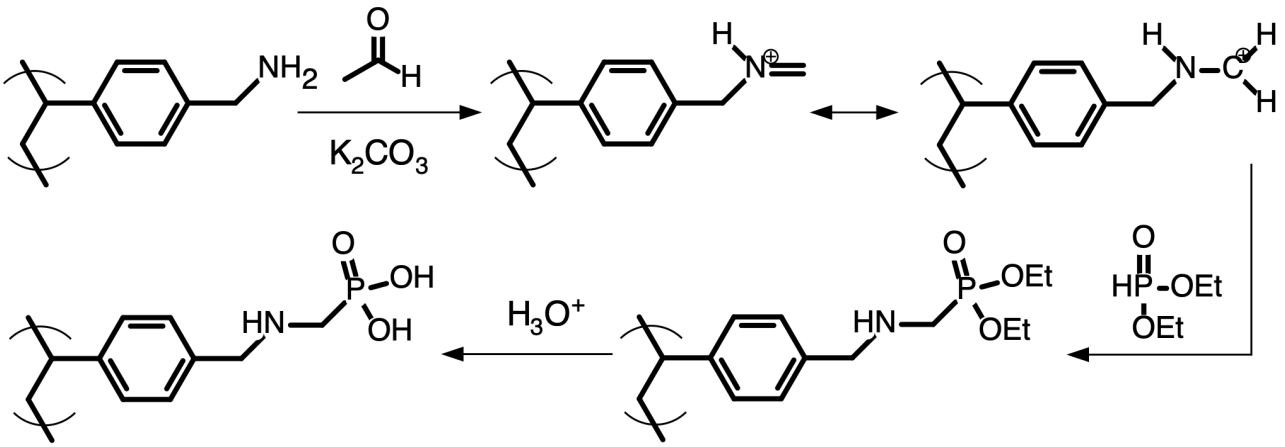

Fig. 1.7. Synthesis of the aminomethylphosphonic acid (AMP) functionality.

The chelating properties of condensed phosphonates for multivalent metal ions have been known since the 1950s. For example, Martell and Calvin reported the logK value for formation of a Ce/pyrophosphoric acid complex as 16.7, while the value for the equivalent Na complex was 2.35 [139]. However, the AMP ligand was first successfully incorporated into a polymeric resin in 1958 by Kennedy and Ficken [140]. This was achieved, following the general method of Fields for synthesis of aminophosphonate esters [141] by reaction of crosslinked (aminomethyl)polystyrene with acetaldehyde, to yield a polyimine, which in turn, reacted quantitatively with diethylphosphite. After this, ester-hydrolysis yielded the functional group (Figure 1.7). The initial targeted use for the resulting resins was in removal of Cu and other transition metals [140, 142, 143]. However, they were later found to be excellent for lanthanide and actinide extraction [144-146]. Currently, AMP resins are available from numerous commercial manufacturers [147] and there is research interest in the attachment of the group to other types of novel adsorbent scaffolds, although it is not always clear what the perceived advantage of this strategy is over conventional IX resins [147, 148]. Notably, a natural biopolymer, derived from fruit waste, has been shown to load metal ions and remove fluoride from solution almost as efficiently as a commercial cation-exchange resin [123].

The binding mechanism of cations to the AMP group is still a subject of some uncertainty. It was originally postulated that the amine nitrogen and one of the phosphoryl oxygens were the donor atoms and that the ligand carried a formal 1- charge [140]. However, later spectroscopic work with transition metals suggested that coordination occurred mainly with both phosphoryl oxygens and no involvement from the nitrogen [142]. Subsequent work considered the effect of pH on the system, as well as metal-ligand stability constants, and concluded that at moderate pH ranges, there are probably numerous bound species in equilibrium, including metal centres held between two AMP groups [147, 149].

The AMP functionality appears a better choice for this work than a phosphonic acid group. This is not stated based on comparisons of binding affinity for multivalent metal (since no such comparisons

exist in the literature). Indeed, as was discussed in the previous section, the presence of the N atom in the AMP group may actually be a complicating factor in an IX system, if the purpose is selective fluoride uptake, as it would relatively act as an anion-exchange site, if not coordinated to a metal ion. Rather, the problem is that although the phosphonic acid group will certainly bind many metal ions via chelation [139, 150, 151], commercial phosphonic acid-functionalised resins generally also contain a % of sulfonic acid loading, such as Purolite S957 [146], which is done to increase the hydrophilicity of the pores and facilitate transport of sorbate ions, enhancing kinetics. However, in this instance, the sulfonic acid groups would bind the loading metal ions with weaker interactions and allow the leaching of aqueous metal fluoride complexes upon contact with the SPL leachate. This is the reason that sulfonic acid SAC resins were disregarded, despite their benefits of economy and high potential loading capacity (Table 1.3). We also did not consider the other common chelating functionality, the iminodiacetic acid (IDA) group, since it is established that larger ions cannot fit into the functional group cavity and therefore only bind via a weaker IX interaction [152]. This would again likely result in column leaching and make the process inherently wasteful. Thus, using an IDA resin would exclude our ultimate loading ion of choice (see 1.13).

AMP resins have been identified by previous researchers as suitable adsorbents for metal pre-loading (specifically Al and La) and selective fluoride capture [128, 130, 131], as the chelating interaction appears to be sufficient to allow Equation 1.12 to proceed, without the metal ions detatching from the AMP group. As early as 1988, Kanesato *et al*. demonstrated that a La-loaded AMP resin could extract fluoride from solution in a dynamic system, with undetectable levels of La bleeding from the column. They furthermore demonstrated that the column did not decrease in efficiency over several loading and stripping cycles, using NaOH as the fluoride-eluting reagent [119]. Subsequent studies, also using metallated AMP resins (Table 1.4) have unfortunately demonstrated negligible advances, either in the performance of the resin, the integration of the IX process within unit operations, or investigating and proving the uptake mechanisms. Such studies will provide some reference points for the forthcoming work. However, as shall be discussed, the selective defluoridation of SPL leachate provides a very different challenge to what these articles present.

1.12.1. Puromet® MTS9501

MTS9501 (previously known as S950+), from manufacturer Purolite, is one of the most widely available AMP chelating resins and has been the object of several studies, specifically on Co and Ni removal [92, 153] and radionuclides U and Th [154]. The Al loaded form has even been subject to preliminary investigations for fluoride uptake [130]. In this study, S950 was surprisingly found to have a rather lower capacity for fluoride than another Purolite AMP resin, S940 (no longer commercially available), which had a different crosslinking % and lower moisture retention. Unfortunately, the

reasons behind the disparity in performance were not investigated. Nonetheless, the modified resin showed good selectivity towards fluoride in the presence of competing anions [130]. MTS9501 is a macroreticular resin and is therefore optimised for use in repeated adsorption/desorption cycles and possesses high resistance to fouling [111, 138]. This makes it a good candidate to withstand the harsh chemical conditions of SPL leachate streams.

1.13. Choice of loading metal for fluoride extraction

Chelating resins have proved a popular choice in the design of extractants for fluoride. The strong interaction between metal and functional group reduces the possibility of the metal ions leaching from the adsorbent column, when contacted by inlet solutions of high ionic strength, as certainly would be the case with SPL leachate. The next step is to consider which loading metal ion would be most appropriate for the task. The need for high fluoride capacity restricts the discussion to ions of tri and higher valance. An obvious choice would seem to be Al^{3+}, especially given that appropriate loading solutions would be conveniently available within the primary Al industry. However, the stability constants of AlF_x complexes are very high (Table 1.5). This was thought likely to cause desorption of Al from the resin surface and formation of aqueous AHFs [155]. Furthermore, a harsh regenerant would be necessary for any fluoride recovery attempt, which would again risk leaching of the metal [131].

Table 1.5. Log_{10} of stability constants for the formation of metal fluoride complexes, with respect to the equilibrium $[MF_{n-1}]^z + F^- \rightleftharpoons [MF_n]^{z-1}$. Ionic strength = 1 M. T = 25°C [155, 156].

n	Al	La
1	6.69	2.67
2	5.35	-4.87
3	3.68	-
4	2.75	-

Other potential candidates are the lanthanides, or rare earth elements (REEs). These are also relatively hard acids and have much lesser, yet still significant affinity for fluoride complexation (Table 1.5). MTS9501 has reasonable affinity for REEs (higher than 2+ cations, but lower than Al^{3+} and Fe^{3+} [146]). Across a number of studies, lanthanide-loaded resins have been shown to outperform the Al-loaded equivalents, with a maximum fluoride capacity of 25-30 $mg \cdot g^{-1}$ vs ~12 $mg \cdot g^{-1}$ [127, 130] (Table 1.4). It must be noted however, that no rational explanations as to why this is the case have been given in the literature. Considering Table 1.5, it might be theorised that increasing fluoride concentration in the contact solution will promote the formation of AlF_n complexes, which would detach from the adsorbent surface and solubilise, limiting the uptake capacity; whereas LaF_3 is a solid crystalline species and hence this phenomenon would not occur. There is a general lack of data in the literature with regards to investigation and understanding of uptake mechanisms [97, 129, 157]. A number of other adsorbents have also been successfully loaded with Ln^{3+} ions and

functionalised for fluoride uptake including alumina, activated carbon and chitosan, further demonstrating their applicability for this remit. It can however be seen (Table 1.4) that alternative support materials seem to offer few tangible benefits over IX resins, other than some are derived from more sustainable or low-value resources. Most have a much smaller capacity for defluoridation and this further justifies our choice of MTS9501 resin.

The high market price of most lanthanides excludes them from further consideration. However, this does not apply to lanthanum itself. The "freight on board" price of La_2O_3 from China remained at ~£1,800·T^{-1} in 2017/18, whereas Nd_2O_3 and Pr_2O_3 prices were >£30,000·T^{-1} [158]. The REEs are mined as mixed ores, after which, the individual elements are separated. There is high demand for this mining, as some REEs are greatly sought after for their optical properties [159]. As well as having no widespread commercial use, apart from niche applications such as electrode membranes [160], La is unusual among the REEs in that it can easily be separated from a mixed lanthanides solution by fractional precipitation as a nitrate salt [161]. Overall, La^{3+} ions appear to be a promising choice for loading metal in the envisaged adsorption system.

1.14. Potential for fluoride adsorption from SPL leachate

It has been demonstrated in the literature that commercial IX resins and many other adsorbents can be activated by metallation for improved affinity towards fluoride. This is shown by many of the studies in Table 1.4, which investigated the effect of coexisting anions on the fluoride uptake capacity of the sorbent. In most cases, this was achieved by adding controlled masses of common anions to the uptake solution, with fluoride analysis showing any suppressive effect [119, 127, 129, 130]. Essentially, these experiments have found that chloride, nitrate and sulfate produce zero to mild suppression for La-loaded sorbents, whereas carbonate and bicarbonate cause a significant reduction in uptake. This has been explained by their presence raising the solution pH and forming hydroxide ions, which are competing hard ligands for the metal centres [130]. It has however also been shown that significant quantities of bicarbonate are actually taken up by La-loaded sorbents, suggesting they may compete for ligand-exchange sites [162]. Phosphate has also been shown to suppress fluoride uptake, due to its chelation interaction with the loaded metal [132, 139], although phosphate has not yet been observed at high concentrations in SPL leachate. Certain authors also tested their metallated adsorbents with real aqueous samples; either naturally-occurring or of industrial origin. Some studies used spring water [126, 129], while others focussed on fluorinated electronics industry wastewater [132]. These samples had much lesser ionic strength than SPL leachate, having maximum total dissolved solids of ≤1,200 mg·L^{-1} and so offer limited insight as to what behaviour might be predicted for the experiments in this thesis.

The key knowledge gap however, is the lack of data concerning fluoride uptake in aqueous systems with mixed fluoride speciation; in other words, where complexing metals form stable aqueous fluro-complexes. Given that the [Al^{3+}] of reported SPL leachates is very variable (if quantified at all) [37, 82, 163] and the affinity of this species towards fluoride, it is probable that in the proposed system, free anionic fluoride will have to be captured simultaneously with AHFs, in multiple charge states, as seen in Figure 1.8. [78, 85]. The possible interactions with the metallated resin are unknown and not easily predictable. Furthermore, even if significant uptake is achieved, this is likely to be due to multiple mechanisms of uptake, to the point where simple thermodynamic and kinetic models cannot describe the data, therefore being problematic for process design.

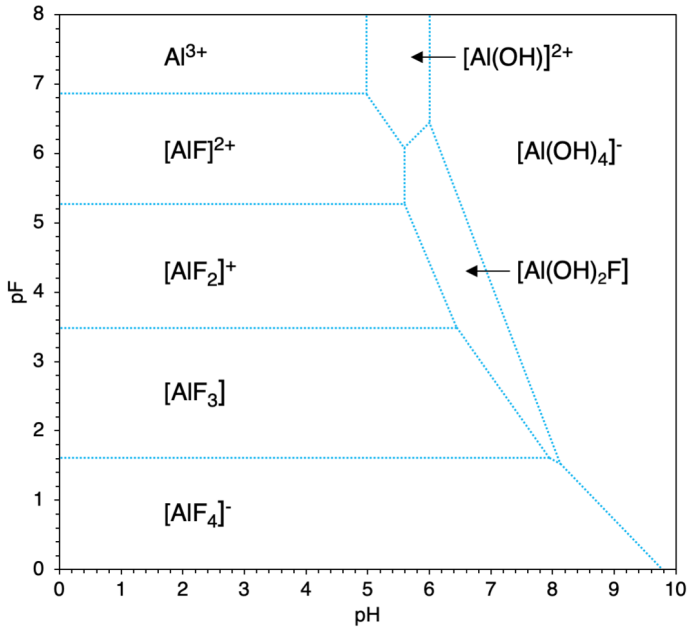

Fig. 1.8. Pourbaix diagram, showing the major aqueous species present, in a Al/O/H/F system, as functions of pH and pF. T = 25°C [164].

Nonetheless, the use of Puromet MTS9501, in La-loaded form is proposed to be a reasonable starting point to begin investigations into this complicated problem.

1.15. Microporous materials

Puromet MTS9501, in common with many commercial resins, possesses large macropores (>50 nm). There are also mesoporous materials, of pore diameter 2-50 nm (many synthesised silicas and silica hybrid materials are mesoporous [165]. Of particular interest however, are microporous materials (pore diameter <2 nm). Such materials can have an extremely high surface area, commonly measured by nitrogen sorption. This property makes them attractive for applications such as catalysis, energy conversion and adsorption, where the number of active sites per mass unit of the material is important [166-168]. There are several types of microporous materials (Figure 1.9); zeolites are inorganic structures, based on aluminosilicates. Zeolites are found in nature but are also synthesised industrially, to more closely control the properties of the materials produced. However, production of zeolites requires an organic or inorganic “templating” molecule [169] and therefore the

process is inherently wasteful. Zeolites do however, offer excellent thermal stability. Metal organic frameworks (MOFs) are a type of coordination polymer, consisting of repeating units of metal ions held together by multifunctional organic ligands, creating a one-, two- or three-dimensional structure. MOFs are attractive research targets, as they can exhibit a remarkably high surface area of >6,000 $m^2 \cdot g^{-1}$ [170]. Some designs in fact, have already been commercialised [171]. However, many MOFs suffer from poor chemical and thermal stability, requiring careful design strategies, such as catenation of the framework [172]. Moreover, their synthesis often requires expensive organic building blocks, which may inhibit further large-scale industrial use.

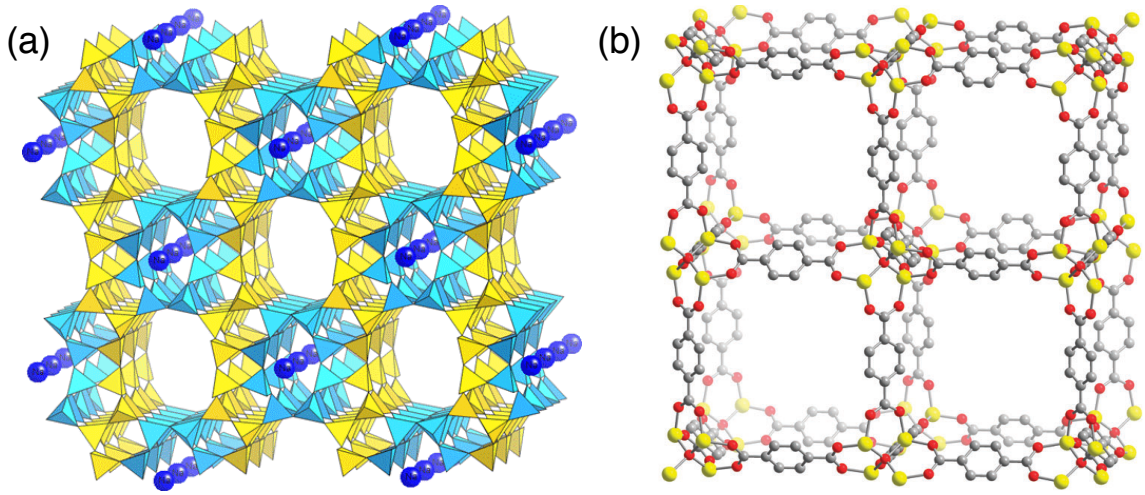

Figure 1.9. (a) Structure of the naturally-occurring zeolite mordenite. Blue and yellow tetrahedra represent silicates and aluminates. Blue spheres are exchangeable cations. Typical surface area = 425 $m^2 \cdot g^{-1}$. **(b)** Structure of "MOF-5", consisting of ZnO_4 nodes (yellow and red) and 1,4-benzodicarboxylate linkers (grey and red). Surface area ≤3,200 $m^2 \cdot g^{-1}$ [173].

1.16. Microporous organic polymers (MOPs)

In contrast to the above, microporous organic polymers (MOPs) are fabricated mainly from light (CHON) elements. MOPs may potentially offer a reasonable compromise of desirable properties, as they have good surface area (≤2,000 $m^2.g^{-1}$ [174]), are composed mainly of stable covalent hydrocarbon bonds and are synthesised by a number of well-understood polymerisation reactions, often involving economical reagents.

The study of MOPs has intensified in recent years and the materials have shown potential in such areas as catalysis [175], drug delivery [176] and gas-phase separation/storage [177, 178]. There has been little work published in the field of contaminant removal from aqueous environments, despite the inherent suitability of the materials for this purpose. In most cases, the species targeted are organic contaminants, such as chemical warfare agents [179] and diesel oil [180]. Ions, such as dissolved heavy metals, are rarely investigated [167].

There are several sub-categories of MOPs (Figure 1.10). These include polymers of intrinsic microporosity (PIMs), which behave akin to solid-state molecular sieves, having contorted structures that are unable to pack efficiently. Covalent organic frameworks (COFs) are unusual in that their structure may be highly ordered and crystalline, whereas most MOPs are amorphous. Conjugated microporous polymers (CMPs) are often based on benzene derivatives. Linkages between monomer units are achieved in such a way that the conjugation of electrons is preserved, creating an extensive delocalised π electron network. As a result, CMPs can exhibit interesting luminescent properties, as their HOMO-LUMO excitation is often readily achieved by common UV light sources. Zhao *et al.* [181] and Li *et al.* [100] have reported boron-based CMPs which, in certain solvents, exhibit a colour change or colour suppression when contacted with the fluoride ion. However, the monomers for CMP synthesis are generally expensive. Such materials may therefore be better candidates for chemosensors, rather than adsorbents.

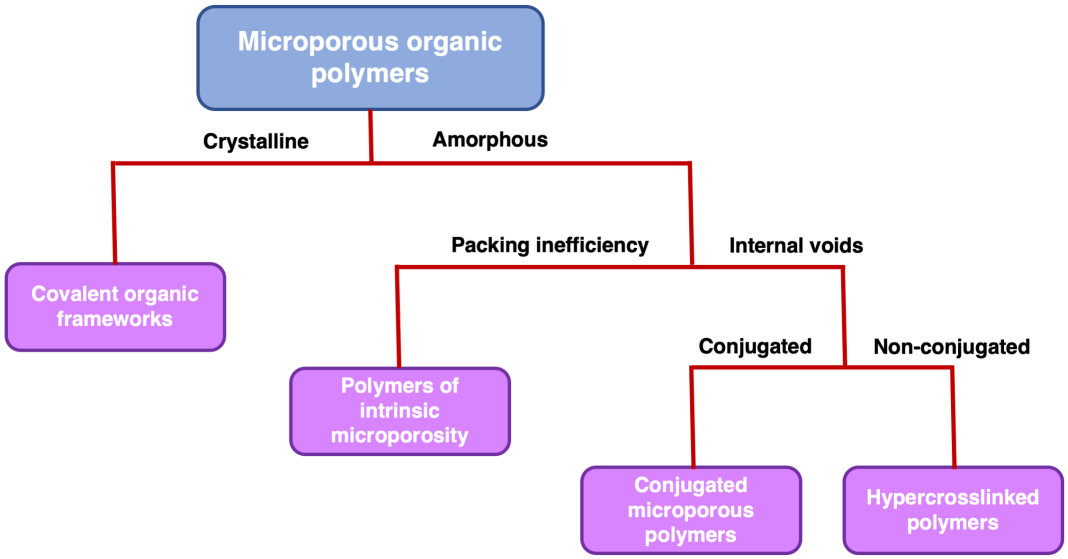

Fig. 1.10. Tree diagram differentiating types of MOPs.

1.17. Hypercrosslinked polymers

A more economical route to novel MOP synthesis may lie in hypercrosslinked polymers (HCPs). These non-conjugated materials may be broadly defined as any polymer with a high degree of cross-linking per monomer unit. The first examples of hypercrosslinked polystyrene, introduced by Davankov *et al.* for example, were >40% cross-linked [182]. These materials, in fact, were remarkably similar in matrix structure to conventional IX resins. Synthesis was achieved by stirring the linear or lightly crosslinked styrene chains in a suitable solvent, typically dichloroethane (DCE). To this was added a Lewis acid metal catalyst, such as $SnCl_4$ or $FeCl_3$, and a crosslinker, which was originally a 1,4-bis(chloromethyl)benzene derivative [182]. During the course of the vigorous Friedel-Crafts alkylation crosslinking reaction, solvent molecules became encapsulated in the forming micropores and, when evaporated, left a rigid structure of high surface area. Later, polymers of

intrinsic functionality were used, by incorporation of vinylbenzyl chloride, rather than styrene into the initial chains [183].

A new strategy for HCP synthesis was introduced in 2011 by Li *et al.* [184], in which the Friedel-Crafts catalyst and cross-linker molecule, commonly formaldehyde dimethylacetal (FDA), is simply introduced to aromatic monomers of rotational symmetry. This procedure is commonly known as "knitting" and the scheme, presented in Figure 1.11, opened doorways to the manufacture of a huge number of possible materials, many based on very economical starting reagents [185-187].

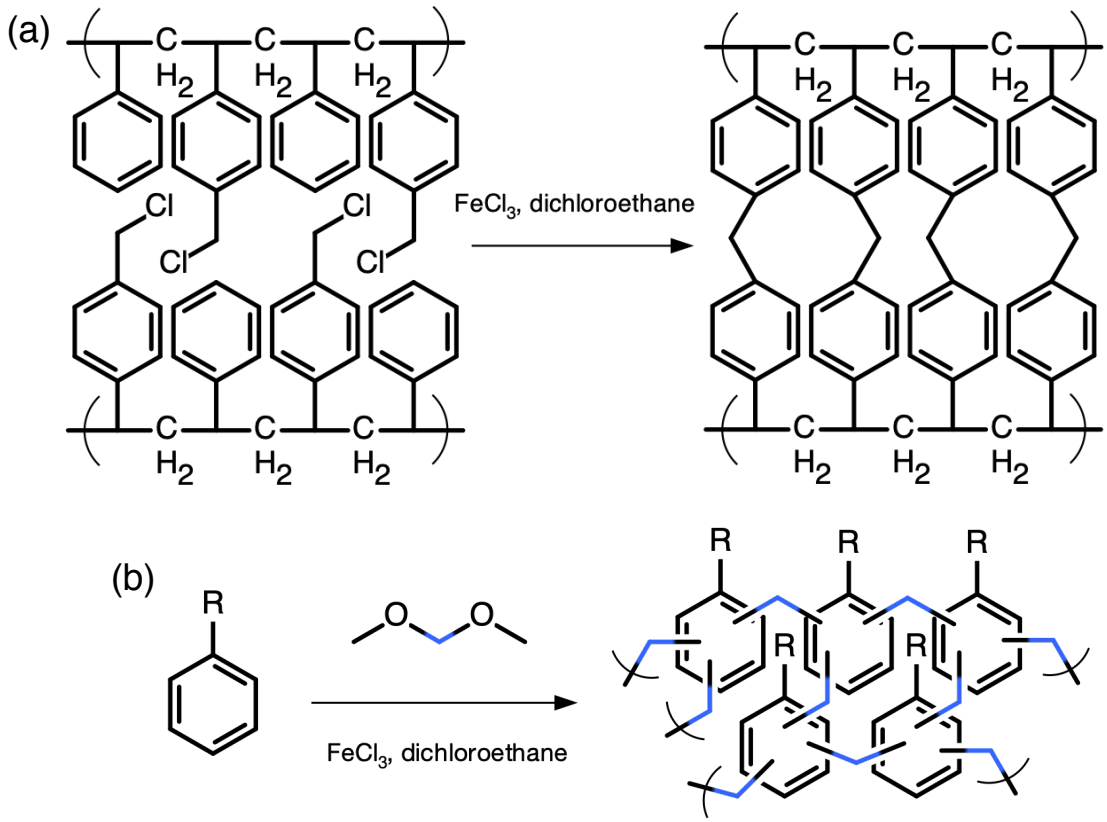

Fig. 1.11. (a) Synthesis of a hypercrosslinked "Davankov" resin using internal crosslinking. **(b)** Synthesis of a "knitted" polybenzene derivative using external crosslinking, both by Friedel-Crafts alkylation.

All HCPs, if polymerised in a relatively large volume of solvent, have areas of meso- and macroporosity, which interconnect the microporous regions [188, 189]. This makes accurate simulations of the pore structures challenging, from a computational modelling perspective [190].

1.17.1. HCPs and MOPs in IX applications

The original intention for hypercrosslinked resins by Davankov *et al.*, appeared to be for use in water treatment, as they reported that a range of functionalities could be incorporated into the materials, noting that they possessed a high exchange capacity of ≤5.35 meq·g^{-1} [182]. However, although such resins were indeed commercialised, their uses are currently restricted to removal of organics from gaseous streams and decolorisation of sugar products (for example, DOWEX™ Optipore and

Purolite® Hypersol-Macronet). Although hydrophilic (sulfonic acid) groups can be present in the networks, this is only to improve wetting and not for ion-capture [191].

In terms of laboratory-scale research, the vast majority of adsorption work has investigated the capture of gas molecules [188, 192], with CO_2 sequestration being a particular focus [193, 194]. Over the course of such work, it has been shown that (relatively) hydrophilic groups and regions can be introduced to polymeric networks without great loss of surface area [184, 195], but this has largely not been capitalised on for aqueous adsorption. Some researchers have used HCPs for the removal of small organic molecules from water, such as chemical warfare emulants [175], phenolic molecules [196] and pesticides, such as oxamyl and methomyl [197]. The latter study notably incorporated -OH groups into the networks, for improved sensitivity. Only a small number of studies have demonstrated IX capabilities for inorganic ions by functionalised HCPs [189, 198]. Both of these mentioned studies formed the hypercrosslinked networks first, then grafted sulfonic acid groups to the polymer support. This led to somewhat low degrees of functionalisation. Li *et al.*, using a Davankov type resin, reported a sulfonic acid group concentration of 1.0 $mmol \cdot g^{-1}$ in the final material [198], while James *et al.*, using the knitting method, reported 3.4 $mmol \cdot g^{-1}$ [189]. This was believed to be due to the functionalising agents not being able to access the micropores, meaning sulfonation occurred mainly in the mesopore regions. The latter study did however find that the HCPs had very high selectivity towards the target ions (Cs^+ and Sr^{2+}), which was attributed to the highly crosslinked structure increasing the influence of de-solvation on selectivity (section 1.10.1).

1.17.2. Potential for metallation of HCPs

A strategy to improve IX capacity for HCPs would be to incorporate the desired functionality into the parent monomers, but surprisingly, this has yet to be demonstrated. Nor has metallation of HCPs been achieved, to create selectivity for a specific anion. Metallation of a CMP has been achieved by Ma *et al.*, with the intention of enhancing the affinity of the material for CO_2. Notably, the metal-loading was achieved post-polymerisation and with relatively small cations (Li^+, Na^+ and Mg^{2+}), without great loss of surface area [120]. Overall, a novel strategy to activate HCPs for fluoride selectivity seems to be feasible. Ma *et al.* used carboxylic acid groups to load metal ions, but this is less feasible for knitted HCPs, as the group is deactivating to aromatic rings. In contrast, phenol derivatives are electrophilic and, although obviously less acidic, they are known to partake in reactions with metal ions to produce phenoxides [199]. In particular, calcium phenoxides are known [200, 201] and these may be attractive species to investigate. Ca^{2+} and fluoride have high, but not irreversible binding affinity (CaF_2 $K_{sp} = 3.9 \times 10^{-11}$). Ca-based adsorbents have been investigated for their defluoridation potential [202, 203] and have even been featured in reviews on the subject [204], although such work has dealt mainly with inorganic materials, rather than metallated organics. Furthermore, if the porosity of the materials can be retained after metallation, fluoride is likely to be

a good sorbate candidate for a microporous sorbent, as its small ionic radius should allow good access to the microporous regions.

1.18. Conclusions on the literature

SPL is a highly challenging wasteform to deal with effectively. There is a growing consensus in the Al smelting industry that uncontrolled and temporary storage solutions historically practiced are no longer sustainable. There is also an increasing appreciation of the potential value of SPL, due to its high fluoride concentration. Fluorite is a critically endangered mineral and efficient recycling of SPL will help to conserve geological reserves of this valuable resource. An in-house recycling treatment could also potentially add value to an Al smelter business, rather than paying for a third party to handle the SPL produced.

Pyrometallurgical treatment of SPL is the most popular processing method, but is undesirable from a CO_2 emission perspective. The only true hydrometallurgical SPL-processing system operational industrially only recycles a partial fluoride component of the waste and recovery products are of low purity. Hence this is an opportunity for further development. The literature has shown that economical lixiviants can be used to solubilise almost the entire fluoride content of SPL, but the key issue is that a multitude of other species are also dissolved, producing complex acidic and basic liquors. Some recovery of fluoride from these leachates has been attempted, but careful precipitation methods are required and there are always limitations imposed on the technique. For example, second-cut and mixed-cut fractions are rarely considered. No strategy has yet been devised that will handle *all* grades of SPL and attempt recovery of *all* the trapped fluorides within the waste and this concept is at the core of the major novelty of this thesis..

To allow realisation of this goal, an IX stage could be introduced to a hydrometallurgical SPL treatment, which would selectively extract aqueous fluoride-bearing species from the SPL leachate. The fluoride would then be eluted as a concentrated and pure aqueous feed, from which a high % recovery should be more feasible, regenerating the sorbent bed in the process. The optimum commercially-available adsorbent for this purpose is a macroporous IX resin, which is designed to tolerate repeated adsorption/regeneration cycles. However, selectivity for fluoride species must be created, since anion-exchangers will preferentially extract all of the other common anions in preference to fluoride. The literature reveals that metallation of a cation-exchanger and appliance of HSAB theory has proved successful in numerous laboratory-scale studies, although there are fewer examples of scaled-up industrial treatments. The combination of La^{3+} ions and AMP functionality seems promising, in terms of strengths of metal/ligand and metal/fluoride binding interactions. It remains to be seen whether such adsorbents will function effectively in complex wastewaters such as SPL leachate. Only a general mechanism for the capture of fluoride, from simple sample matrices

(NaF solution), at low concentrations, has been postulated. It is unknown how the active metal sites would react with a contact solution of mixed fluoride and Al speciation. Previous examples of fluoride adsorption from SPL leachate are very limited and have focussed on removal, rather than recovery.

As well as available technology, the development of novel adsorbents, which offer intrinsic advantages over IX resins, is important to the future of this research field. HCPs are an attractive possibility, partially because their chemical similarity to IX resins makes for intriguing comparisons of adsorption properties. For example, the effects of a microporous structure on the acidity of protonation sites is unknown. Although the first HCPs were designed with aqueous adsorption remits in mind, they are largely under-researched in this area, with gas adsorption and catalysis being more popular choices. HCPs have not been fully developed as ion-exchangers, meaning their intrinsic advantage of high accessible surface area has not been taken advantage of. Fluoride uptake by HCPs has not yet been reported and the same is true for activation of HCPs by metallation, in order to change their IX selectivity.

1.19. Research hypothesis and thesis framework

This thesis proposes in the first instance, that the addition of a selective adsorption system, using a metallated, chelating IX resin, for capture, concentration and then elution of fluoride can be integrated into a hydrometallurgical treatment system for SPL waste. This has the potential to recycle a larger proportion of the fluorides trapped within the waste than is currently achieved and will thus contribute to the future sustainability of the industry. It will also add commercial value to a primary Al smelting business via recovery of a pure, fluoride-containing output product.

It is furthermore proposed that novel adsorbents, based on the first ever metallated HCPs, can function as effective materials for defluoridation and fluoride recovery. Such materials will have a higher capacity than commercial IX resins and merit further attention and development as extractants for water treatment.

1.19.1. Experimental chapters

The first three experimental chapters (2-4) deal with the development of a fluoride adsorption system for SPL leachate, using the afore-mentioned metallated resin. Chapter 5 details the synthesis and investigation of HCPs for fluoride adsorption. SPL is a difficult material to acquire, because of the associated hazards. As a result, Chapters 2 and 3 work with a simulant aqueous leachate, made from defined quantities of analytical reagents. Chapter 4 then deals with real SPL waste.

Chapter 2 begins by exploring the fundamental attributes and limits of the La-loaded MTS9501 resin, using a series of static, thermodynamic fluoride uptake experiments. Key aims were to:

◆ Determine the resin performance and nature of fluoride adsorption at concentrations an order of magnitude above what is commonly reported in the literature.
◆ Compare the adsorption of fluoride on to the resin from aqueous NaF solutions and simulant SPL leachate and understand the similarities and differences, with reference to aqueous speciation.
◆ Propose plausible uptake mechanisms for the above, supported by solid-state spectral analysis.
◆ Examine the sensitivity of the systems to pH changes, given that SPL leachate streams may be acidic, caustic or combined.

Chapter 3 builds on the previous by moving the focus to the kinetics of fluoride uptake, initially with further static experiments, then by miniature column studies, transitioning the system towards its intended industrial application. Key challenges were:
☐ Corroborate or develop the proposed uptake mechanisms from Chapter 2, using the kinetic data.
☐ Ensure the column breakthrough behaviour of the system can be reliably modelled and adsorption kinetics are acceptably rapid.
☐ Investigate the desorption of fluoride and any other co-adsorbed species by generating a full elution profile and use this to establish which fluoride-bearing species should be targeted for isolation and recovery.
☐ Ensure that the metallated resin can be effectively regenerated, using economical reagents.

Chapter 4 illustrates the applicability of the system to real industrial samples, where the composition of the SPL, and thus the leachate, is variable, therefore providing extra challenge. The objectives were:
⭘ Characterise a number of SPL samples by solid-state analysis to gauge its variability.
⭘ Confirm that economical lixiviants and mild conditions were capable of near complete leaching of fluoride from SPL and that the proposed treatments are suitable for processing all fractions of the waste.
⭘ Perform a full speciation analysis of both acidic and caustic leachate, supporting or refuting the need for a two-stage leaching treatment.
⭘ Investigate differences in column breakthrough and elution behaviour, compared to previous work with simulated leachate and adjust the methodology to improve efficiency.
⭘ Perform a first-order technicoeconomic analysis on the proposed process, using experimental data.

Finally, **Chapter 5** details the synthesis, characterisation and testing of the first reported metallated, hydrophilic HCPs, building a full assessment of their potential as defluoridating media. The challenges in this instance were:
✴ Successfully activate HCPs for fluoride capture by metallation and confirm the mechanisms of metal-loading.

✴ Document the impact of the specific microporous polymeric structure and pore characteristics of each sorbent on its IX properties, particularly capacity for fluoride.
✴ Explore the similarities and differences of fluoride uptake, compared to the commercial resin featured in Chapters 2-4, and identify intrinsic advantages of HCPs.
✴ Explore some practicalities for the future use of HCPs in adsorption systems, including column studies, selectivity and possible recycling treatment.

1.19.2. Thesis format

This thesis follows an alternative format, in that all experimental chapters have been submitted and approved for publication. Chapters are therefore presented as they appear in their respective journals. The only exceptions are that certain figures, tables and technical discussions, which necessarily originally appeared in Supporting Information documents, or in rare cases, were left out entirely, to reduce word/page count, are now included in the main research articles, for better continuity. Any non-peer-reviewed material (Chapters 2 and 4 only) is clearly indicated with italic text.

2. Thermodynamic equilibrium studies and mechanistic investigation of adsorption from simulant leachate by La-MTS9501

2.1. Overview of paper

This paper introduces the core concept of appending an IX column system to existing LCLL technology to improve fluoride recycling within the primary Al industry. It begins to build an assessment of the novel La-MTS9501 adsorbent for the required task. The methodology for resin pre-conditioning and the facile loading process with La^{3+} ions are described for the first time. The composition of simulant mixed-cut SPL leachate, which is used throughout Chapters 2 and 3, is also presented.

The uptake of fluoride from the synthesised pregnant leach solution (PLS) is reported in pH-controlled experiments. Isotherms are generated and fitted with two-parameter models, to investigate the nature of the adsorption processes. Results are presented alongside equivalent experiments, using analytical NaF solutions, as a point of comparison to available literature. Isotherm data is collected over low and high concentration ranges, to probe the response of the system to high fluoride concentrations, which has not been previously reported. Solid state analytical methods are used in conjunction, to postulate uptake mechanisms.

It is found that the extraction mechanism is significantly different, depending on the sample matrix. For the NaF system, X-ray photoelectron spectroscopy (XPS) of resin beads, post-contact with the fluoride solution indicated the presence of La complexes with one and two fluoride ligands exchanged; seemingly indicating that the AMP group formally acts as a 1- ligand. This supports the proposed ligand-exchange equilibria shown in Equation 1.11. XPS spectra also appear to show that La^{3+} ions bind to the resin without interaction from the nitrogen atom. In contrast, fluoride is adsorbed from the PLS in conjunction with Al^{3+} and with a lower binding energy than the ligand-exchange reactions observed with NaF solutions. The relevant XPS spectra showed unique La binding environments, indicating that the adsorption still took place upon these active sites.

At higher concentrations, the uptake capacity of the resin unexpectedly continues to rise well beyond the theoretical maximum that would be allowed by La ligand-exchanges, with respect to uptake from both matrices. For NaF solutions, this is shown by X-ray diffractograms to be due to crystallisation processes within the resin pores. the coordinated La species is converted to LaF_3, then further fluoride crystallises upon the adsorbent surface as NaF. The hydrophobic pore interiors and large surface area appear to act to reduce the surface energy penalty associated with nucleation and crystal growth, promoting the crystallisation. For the PLS, the mechanism is less clear, as the species formed are amorphous. However, a combination of XPS of the resin beads and aqueous speciation calculations leads to a prediction of precipitation of AHFs. The proposed mechanism is later modified in Chapter 3, in response to further uptake experiments, but is presented unaltered in this section, to show the development of knowledge through the experimental chapters.

Because of this behaviour, both systems have multilayer adsorption characteristics, with a good fit to the Freundlich isotherm demonstrated. La-MTS9501 extracts fluoride from the simulant PLS with high efficiency (although a lesser theoretical maximum than from equivalent NaF solutions). A working pH range for the system is identified, which appears to be dominated by the favourability of AHF precipitation. Adsorption is unfavourable at both extremes of the pH scale. This indicates that neither acidic, nor alkaline SPL leachate streams would be suitable for IX treatment without either pH adjustment or mixing of the streams. Collectively, this provides the groundwork for the column-based studies featured in Chapter 3.

This paper was submitted to *The Journal of Hazardous Materials* on 14 February 2018, resubmitted in revised form on 6 June 2018 and accepted for publication on 8 July 2018 (doi.org/10.1016/j.jhazmat.2018.07.036).

Notes:

This journal enforces a limit of 6000 words for research articles. Accordingly, several extensions to the discussion have been made, which would ideally have been included in the original article. Some minor additional revisions to the discussion have also been made, due to subsequent data production and analysis after publication. The main research findings and conclusions are not altered by these revisions, but it should be noted that these passages have not been peer-reviewed. For clarity, this new information is indicated with italic text.

The paper refers to the resin as-received from Purolite® as “S950+”, which was its commercial name at time of press.

2.1.1. Author contributions

Thomas J. Robshaw. Experimental work, data interpretation, manuscript writing
Sudhir Tukra. Funding
Dr Deborah B. Hammond. XPS experimental work, technical support and data interpretation
Prof Graham G. Leggett. Provision of XPS facilities and technical support
Dr Mark D. Ogden. Experimental work supervision, manuscript review

"Highly Efficient Fluoride Extraction from Simulant Leachate of Spent Potlining via La-Loaded Chelating Resin. An Equilibrium Study"

Thomas Robshaw[a]*, Sudhir Tukra[b], Deborah Hammond[c], Graham Leggett[c] and Mark D. Ogden[a]

*Corresponding author address:

[a] Separations and Nuclear Chemical Engineering Research (SNUCER), Department of Chemical & Biological Engineering, University of Sheffield, Sheffield, S1 3JD, United Kingdom.

[b] Bawtry Carbon International Ltd., Austerfield, Doncaster, DN10 6QT, United Kingdom.

[c] Department of Chemistry, University of Sheffield, Sheffield, S3 7HF, United Kingdom.

2.2. Abstract

Spent potlining (SPL) hazardous waste is a potentially valuable source of fluoride, which may be recovered through chemical leaching and adsorption with a selective sorbent. For this purpose, the commercially available chelating resin Purolite® S950+ was loaded with lanthanum ions, to create a novel ligand-exchange sorbent. The equilibrium fluoride uptake behaviour of the resin was thoroughly investigated, using NaF solution and a simulant leachate of SPL waste. The resin exhibited a large maximum defluoridation capacity of 149 ± 20 mg·g^{-1} from NaF solution and 145 ± 10 mg·g^{-1} from the leachate, with solution pH being strongly influential to uptake performance. Isotherm and spectral data indicated that both chemisorption and unexpected physisorption processes were involved in the fluoride extraction and suggested that the major uptake mechanism differed in each matrix. The resin demonstrates significant potential in the recovery of fluoride from aqueous waste-streams.

2.2.1. Graphical abstract

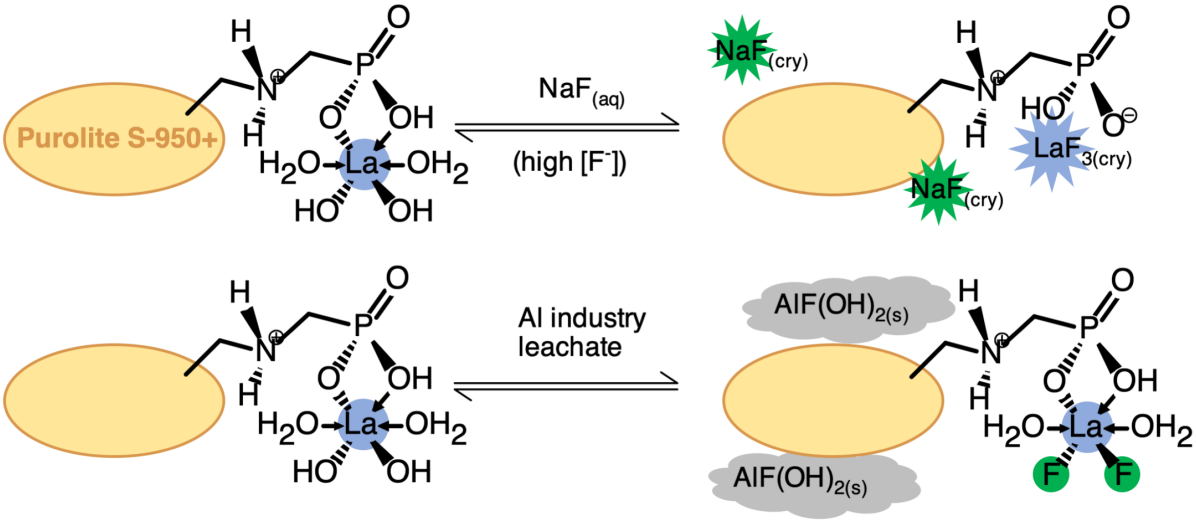

2.2.2. Keywords and research highlights

Spent potlining, Purolite S950+, chelating resin, fluoride uptake, lanthanum.

- ◆ Aqueous fluoride extraction via lanthanum-loaded chelating resin is demonstrated.
- ◆ The uptake mechanism changes, dependant on initial fluoride concentration.
- ◆ Uptake from multi-component leachate occurs mainly via aluminium hydroxyfluoride precipitation.
- ◆ Maximum uptake is greater than previously reported for similar metal-loaded resins.

2.3. Introduction

Spent pot-lining (SPL) is a hazardous, carbonaceous waste product of the primary aluminium industry, formed from the exhausted cathodes of electrolytic cells. Over the lifespan of a cell, contaminants such as cryolite and AlF_3 diffuse through the graphite cathodic lining and ultimately into the refractory material below, causing a degradation in performance [205]. The cell is then decommissioned and the contaminated material excavated. The cathode material is known as "first-cut" SPL and the refractory shell as "second-cut". The amount of SPL currently being generated worldwide is likely in excess of 1 $MT \cdot yr^{-1}$ [18, 60].

The composition of first-cut SPL includes ≤18% fluorides and ≤0.5% cyanides [32], thus presenting a risk of fluorosis and poisoning to both humans and animals [9, 11]. SPL is however, a potentially valuable resource, partially because of its high fluoride concentration. Fluorspar (CaF_2) is the root of practically all major fluro-chemicals and was recognised by the European Union in 2014 as one of the 20 most crucial minerals to recycle effectively in the immediate future [17]. Numerous industrial processes have been devised for the treatment of SPL and recycling of minerals, but at present, only the Rio Tinto Alcan low-caustic leaching and lime (LCLL) process regenerates CaF_2. This involves leaching of ground and screened SPL with water and NaOH, then evaporation to precipitate NaF, before a final treatment with $Ca(OH)_2$ [39]. A percentage of fluoride-bearing compounds are not solubilised by the initial wash [37] and must be leached by a combination of further NaOH and H_2SO_4 to allow safe disposal of the solid residue, yet no fluoride recovery is attempted from these waste-streams. We propose an alternative strategy, in which the separate aqueous leachates are combined, then contacted with a sorbent material that selectively extracts the fluoride.

Many techniques exist for the defluoridation of water. Established precipitation methods however, result in large volumes of low-value slurry, from which fluoride recovery is difficult [87]. Adsorption and ion-exchange techniques are a promising alternative, as the fluoride may be selectively removed under mild conditions, with no waste generated. This has led to numerous fluoride uptake studies, using sorbents such as alumina [206], activated carbon [207], chitosan [208], synthesised microporous polymers [100] and layered double hydroxide clays [209]. Some sorbents may be repeatedly regenerated and reused, with hydroxide treatment being the most common strategy [100,

122]. Commercial anion-exchange resins cannot produce selective uptake, since fluoride is the least selective of all common anions towards such materials [115]. This may be overcome via a cation-exchange or chelating resin, pre-loaded with metal ions, which have a high affinity for fluoride, thereby allowing uptake via the ligand-exchange processes shown in Equation 2.1 [123, 126].

$$[\text{L-M}(\text{H}_2\text{O})_{n-m}(\text{OH})_m]^{(n-2)-} + q\text{F}^- \rightleftharpoons [\text{L-M}(\text{H}_2\text{O})_{n-m}(\text{OH})_{m-q}\text{F}_q]^{(m-2)-} + q\text{OH}^- \quad \textbf{(Eqn. 2.1.)}$$

where L = resin functional group ligand, M = coordinated metal centre and q = 1 or 2. Al itself has been a popular metal for this purpose, given its light molecular weight, abundance and high stability constants associated with AlF_n complexes [155]. The highest reported uptake capacity for Al-loaded resins is ~12 mg fluoride per g resin [130].

Rare earths have been similarly investigated, as they are hard metals, therefore strongly binding fluoride ligands [156]. A barrier to their industrial use for this purpose is their perceived scarcity and high cost. However, this is applicable mainly to Pr and Nd, which are desirable for production of lightweight magnets, used in hybrid car engines [210]. La and Ce in particular, have more limited industrial uses and this is reflected in the market value for their oxides, which remained in the region of £1,400-1,600 T^{-1} throughout 2017. In contrast, Nd and Pr oxide prices were >£30,000 T^{-1} [211].

The most common resin functional groups for La-loading have been either sulfonic or aminophosphonic acids [119, 126, 129], with highest reported uptake capacities being higher than for the Al-loaded equivalents; in the region of 25-30 $mg \cdot g^{-1}$ [127]. Most literature studies on aqueous fluoride extraction focus on uptake from analytical grade NaF solutions [132, 212], sometimes with controlled amounts of competing anions added, or mildly contaminated water from aquifers [129, 132]. However, data for concentrated waste-streams, containing multivalent cations, which may complex fluoride and displace resin-bound metals is lacking. Indeed, this factor compelled us to choose a more expensive chelating resin for the intended purpose, as in solutions of high ionic-strength, the loaded species of a conventional strong acid cation exchanger would be displaced by other cations in the aqueous waste, according to concentration gradients and order of selectivity, hence ruining the fluoride affinity of the resin. The only studies on actual SPL industrial leachate used calcite as a sorbent and focussed on modelling the kinetics of the uptake process [33, 213]. To the best of our knowledge, no work exists on the selective removal of fluoride from leachate of SPL via metal-loaded chelating resin. Additionally, uptake behaviour has only been studied over initial fluoride concentrations <100 $mg \cdot L^{-1}$ (Table 1.3.), whereas the leaching of SPL produces aqueous waste of fluoride concentration >2 orders of magnitude higher [37, 53]. Therefore, from a water-conservation perspective, it is desirable to investigate such uptake conditions, even though the mechanisms of uptake may be complicated. The same applies for simpler NaF-based waste-streams.

Purolite® S950+ is a macroporous, weak acid, chelating resin, consisting of a styrene/divinylbenzene backbone, with aminophosphonic acid functional groups. The Al-loaded form has previously been investigated for fluoride-removal capabilities [130]. A similar Al-loaded resin has been commercialised for industrial use [214], although only as a final water-polishing step, rather than as part of a fluoride-recovery loop. Rare earth-loading has not yet been trialled. We envisage a treatment system (Figure 2.1.) for SPL leachate, using La-modified S950+ columns, with NaOH treatment to elute the fluoride as NaF, then precipitation of CaF_2 with $Ca(OH)_2$ [89]. However, the thermodynamics and kinetics of uptake in such an unusual sample matrix as spent potlining leachate must first be understood. Thus, we report here an investigation into the isotherm behaviour of fluoride uptake on to La-loaded Purolite® S950+, with detailed comparison between PLS and NaF solution matrices.

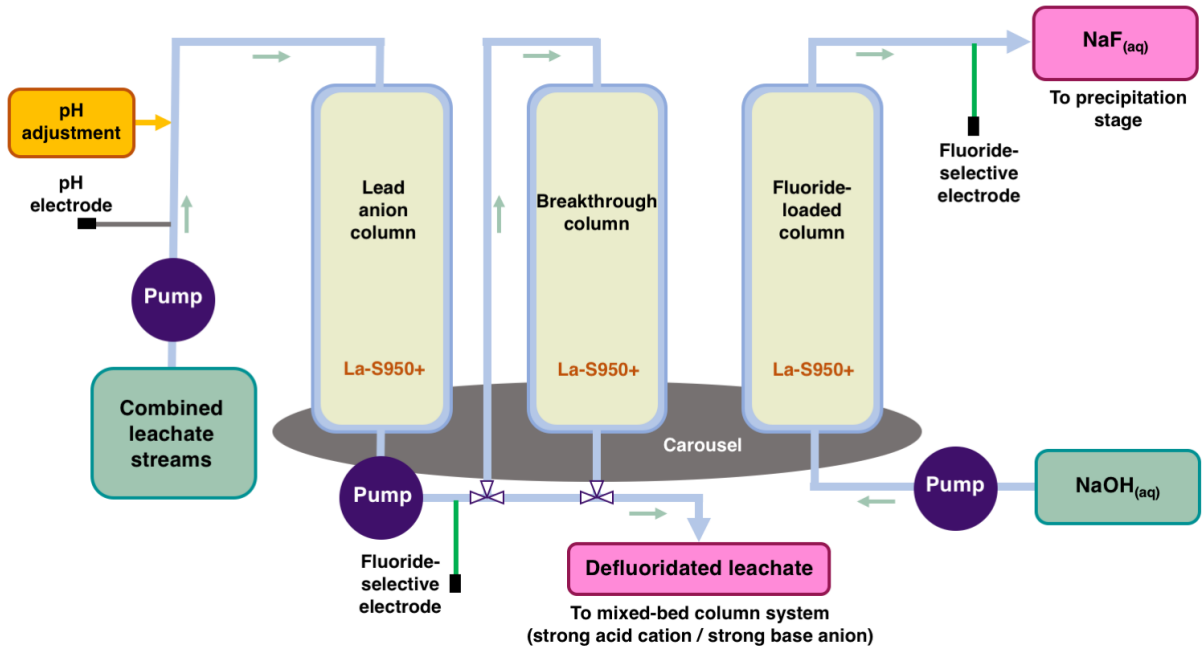

Fig. 2.1. Proposed ion-exchange treatment system for SPL leachate.

2.4. Experimental

2.4.1. Reagents and stock solutions

A simulant pregnant leach solution (PLS) of mixed-cut SPL was prepared, with concentrations calculated from characterisation work of Holywell & Bréault [32], Mahadevan & Ramachandran [21] and Pong *et al.* [74]. The major components of this liquor are given in Table 2.1.

Table 2.1. Composition of SPL simulant leachate pregnant leach solution (PLS).

Component	Concentration ($mg \cdot L^{-1}$)
Fluoride (F^-)	1,500
Carbonate (CO_3^{2-})	750
Chloride (Cl^-)	50
Cyanate (CNO^-)	50
Ferrocyanide ($[Fe(CN)_6]^{4-}$)	50
Sulfate (SO_4^{2-})	2,200
Aluminium (Al^{3+})	1,200
Calcium (Ca^{2+})	200

NaF, $NaHCO_3$, NaCl, NaCNO, $K_4[Fe(CN)_6]$, $(NH_4)_2SO_4$, $Al_2(SO_4)_3$ and $Ca(OH)_2$ (analytical reagent grade) were purchased from commercial suppliers and used without further purification. Sodium and sulfate salts were used where possible, to reflect the leaching agents used in the LCLL process [8]. Reagents were dissolved in deionised water in a polypropylene beaker. The ionic strength of the undiluted leachate was 24.8 $mmol \cdot L^{-1}$, compared to 6.23 $mmol \cdot L^{-1}$ for a NaF solution of equivalent fluoride concentration. The pH was 5.5. Aqueous speciation was carried out using the Aqion software package v6.4.7 [215]. Full methodology is shown in Appendix A, p A1.

2.4.2. Pre-conditioning and metal-loading of the resin

Purolite® S950+ resin was kindly donated by the manufacturer in Na form. Specifications are given in Appendix A, Table A2. Conversion to H form [216] was achieved by contacting 25 g resin (wet mass) with 1 L of 1 M HNO_3 in a Nalgene bottle, which was sealed and placed on an orbital shaker for ≥8 hr at 100 rpm. The resin was then washed with 5 x 200 bed volumes of deionised water (bed volume = minimum volume of water required to fully wet the mass of resin).

The H-S950+ resin was loaded with La by contacting 25 g (wet mass) with 1 L of 10,000 $mg \cdot L^{-1}$ La^{3+} solution, made by dissolving $LaCl_3.7H_2O$ in deionised water. These were agitated and washed, as before, then dried in a 50˚C air-flow oven for a minimum of 24 hr. This resulted in the La-loaded Purolite® S950+ resin, hereafter referred to as La-S950+. La uptake by H-S950+ was determined by analysis of 2,000-15,000 $mg \cdot L^{-1}$ La^{3+} solutions, before and after contact with the resin with a Thermo Scientific iCAP 6000 ICP-OES. Samples were analysed in duplicate and error determined from 2 x standard deviation. Results were compared with similar experimentation, using Ca^{2+} solutions, to gauge the efficiency of La-loading, this being the manufacturer's recommended procedure for determination of S950+ capacity [111].

2.4.3. Batch fluoride extraction from various media

All experiments were carried out at ambient temperature. La-S950+ was handled in hydrated form. Dry mass equivalent was determined by mass-loss upon drying experiments in an air-flow oven at

50°C for >24 hr. In a typical procedure, ~100 mg of La-S950+ (dry mass equivalent) was contacted with 25 mL solution of known fluoride concentration in a 50 mL polypropylene screw-top tube (NaF or PLS solutions were diluted appropriately to achieve the required fluoride concentrations). This was sealed and placed on an orbital shaker at 100 rpm for 24 hr. In controlled pH experiments, the liquor pH was maintained by being adjusted at 10 minute intervals with 0.01-1 M solutions of HCl and NaOH until equilibrium was reached. In all cases, equilibrium pH was within 0.01 unit of initial pH. The fluoride concentration of the solution, before and after resin contact, was determined using a Cole-Palmer fluoride ion-selective electrode. (Appendix A, p A2). The equilibrium fluoride uptake capacity of the resin in mg·g^{-1} (q_e) was determined using Equation 2.2:

$$q_e = (C_i - C_e) \times V/W \qquad \textbf{(Eqn. 2.2.)}$$

where C_i is the initial fluoride concentration of the solution in mg·L^{-1}, C_e is the fluoride concentration of the solution at equilibrium in mg·L^{-1}, V is the volume of solution contacted in L and W is the dry mass of resin used in g.

2.4.4. Determination of uptake behaviour by fitting to isotherm

The uptake behaviour of the system was expected to be dominated by the ligand exchange of aqua and hydroxyl groups for fluorides, coordinated to a finite number of degenerate La centres. We thus fitted batch uptake data to the two-parameter Langmuir isotherm model, represented by Equation 2.3:

$$q_e = \frac{q_{max} K_L C_e}{1 + K_L C_e} \qquad \textbf{(Eqn. 2.3.)}$$

where K_L is a Langmuir isotherm constant and q_{max} is the theoretical saturation capacity of the resin in mg·g^{-1}.

It was however, thought likely that fluoride ions might be bound via multiple interactions with the functionality of the resin, including potentially the protonated amine group at lower pH, and multiple H-bonding interactions [217]. Hence, we also investigated fitting to the empirical Freundlich model (Equation 2.4), which accounts for surface heterogeneity.

$$q_e = K_F C_e^{\,1/n} \qquad \textbf{(Eqn. 2.4.)}$$

where K_F and n are Freundlich isotherm constants. All other terms as per Equations 2.2 and 2.3.

Because of the potential for a non-degenerate energy of adsorption, we also fitted data to the Dubinin-Radushkevich (D-R) isotherm (Equation 2.5), which allows calculation of the desorption energy of uptake, based on a Gaussian distribution [218].

$$q_e = (q_{max}) \exp\left(-B_D \left[RT\ln\left(1 + \frac{1}{C_e}\right)\right]^2\right)$$ (**Eqn. 2.5.**)

where B_D is a D-R isotherm constant in $mol^2 \cdot J^2$, R is the gas constant (8.314 $J \cdot K^{-1} \cdot mol^{-1}$) and T is the temperature in K. The bracket $[RT\ln(1 + 1/C_e)]$ is often described by a single term ε (the Polyani potential) in $J \cdot mol^{-1}$. All other terms as per Equation 2.2.

We finally attempted fitting to the Temkin isotherm (Equation 2.6), which operates on the assumption that the energy of sorption decreases linearly as a function of surface coverage, taking into account possible sorbate-sorbate interactions [218].

$$q_e = B \ln A_T + B \ln C_e$$ (**Eqn. 2.6.**)

where A_T is the equilibrium binding constant and B is a heat of sorption constant. All other terms as per Equation 2.2.

Loading isotherms were determined by the previously described procedure for batch extraction, with solutions of NaF or PLS over a C_i range of 1.5-1,500 $mg \cdot L^{-1}$. Results were averaged from three replicate samples. Errors in C_e values were calculated from 2 x standard deviation and propagated accordingly. Isotherm fitting was achieved with the SOLVER Microsoft Excel programme, following the method of Billo [219].

2.4.5. Co-extraction of other anions and cations

In the case of the PLS, post-resin-contact sample solutions were analysed in comparison to the parent solution, to determine uptake of competing anions and also cations in the system. Cl^-, NO_3^- and SO_4^{2-} were quantified using a Thermo Fisher ICS-900 ion chromatography system (Appendix A, p A5); Al, Ca and Fe via ICP-OES. Leaching of La^{3+} during solution contact was also checked in these analyses.

2.4.6. Solid-state analysis of resin

Samples of resin were first washed of residual NaF or PLS with 10 x 200 bed volumes of deionised water, then ground to a fine slurry, using a mortar and pestle, then dried in an air-flow oven at 50°C for a minimum of 24 hr. XRD analysis was performed using a Bruker D2 Phaser X-ray diffractometer. XRD data was matched using the International Center for Diffraction Data (ICDD) PDF-4+ database [220]. X-ray Photoelectron Spectroscopy (XPS) was carried out using a Kratos Supra instrument. Full operating conditions are detailed in the Appendix A, p A2.

2.5. Results and discussion

2.5.1. Metal-loading of the resin

ICP-OES results determined the Ca^{2+} capacity of the H form of the resin to be 71.3 ± 2.5 mg·g^{-1} (1.78 ± 0.06 mmol·g^{-1}), in close agreement with manufacturer specifications [111]. Similarly, the La^{3+} capacity was found to be 256 ± 2 mg·g^{-1} (1.84 ± 0.01 mmol·g^{-1}). This compares favourably with literature data for aminophosphonic acid resins [119] and for specifically-designed polyacrylamidoxime [221] and amide [222] resins for lanthanide and actinide extraction. A contact solution of 10,000 mg·L^{-1} La^{3+} resulted in optimum loading.

Spectroscopic evidence has suggested that 6- and higher-coordinate metals may chelate to the resin via interactions with both O and N atoms [142]. In this instance, the N 1s XPS spectra (Appendix A, Table A4) demonstrated that there was no interaction between the amines and coordinated metals. Therefore, the La-loading mechanism is likely as shown in Figure 2.2.

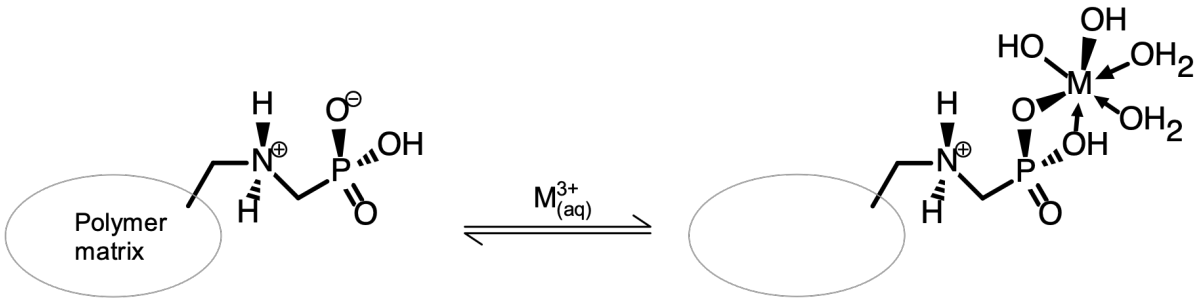

Fig. 2.2. Loading mechanism for La-S950+.

2.5.2. Effect of pH on fluoride uptake

The fluoride uptake of La-S950+ over a pH range of 1-10 is shown in Figure 2.3.

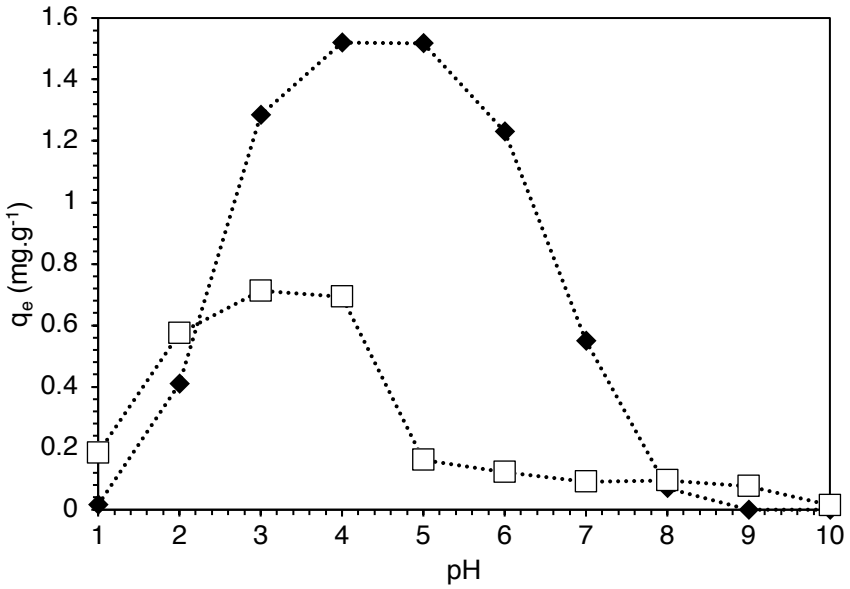

Fig. 2.3. Fluoride uptake of La-S950+ over a pH range of 1-10. F^- C_i = 15 mg·L^{-1}. Error is too small to be graphically represented. Data points represent final equilibrium solution pH. ◆ = PLS. □ = NaF solution.

The solution pH for both sample matrices was significant to the performance of the resin. At low pH, fluoride exists mainly as the stable ion-pair F^-/H_3O^+, making removal from aqueous solution unfavourable [223]. The relatively high uptake from NaF solution at pH 2 was therefore surprising, as the ratio here of $HF:F^-$ was calculated as 1.4:1 [215]. This possibly shows the effect of increased electrostatic attraction, with protonation of the resin surface [128]. At higher pH, the hydroxide ion is a significant competitor for fluoride-binding sites [130, 209]. However, at pH 8, where uptake was negligible for both matrices, the fluoride concentration was still 2 orders of magnitude higher than hydroxide concentration (Appendix A, Table A1). The pK_a of La^{3+} aqua complexes is 8.63 ± 0.05 in 2 M $NaClO_4$ [224]. Therefore $La(OH)_3$ precipitation at a pH > 8.5 may be predicted. However, fluoride exchange clearly became unfavourable at a lower pH than this, possibly indicating modification of the La^{3+} pK_a by the hydrophobic resin surface (i.e. the attachment of a chemical species to an insoluble surface will influence its acidity, compared to a similar solvated species) [96]. The literature shows variance in optimum pH for fluoride uptake on to La-loaded resins, from 3 to 7 [119, 123, 127]. There is also evidence that pK_a values for metal complexes bound to chelating ligands are lower than for monodentate complexes [225]. The specific environment created by the resin support may indeed be influential, but since all the resins used in these studies had similar PS/DVB matrices, this explanation alone is unlikely. It is perhaps more probable that the degree of resin surface charge is influential to the electrostatic attraction of fluoride ions, as this would be influenced to a large degree by the pK_as associated with the different functional groups. Notably, over the pH range for favourable adsorption, a large proportion of fluoride in the PLS system exists as AlF^{2+}, AlF_2^+ and AlF_3 (Table A1), consistent with the literature [128]. This however appeared to enhance, rather than suppress the uptake, which suggested an alternative uptake mechanism was occurring. *It can furthermore be seen from phase diagrams of Al-F-O-H systems (Figure 1.8) that, at low [F^-], the dominant aqueous species at pH 5-6 changes from $[AlF]^{2+}$ to $[Al(OH)]^{2+}$, which is the region where fluoride uptake drops sharply. This phenomenon will be discussed further in due course.*

2.5.3. Practical Operating conditions

Following contact with the resin, the pH of NaF and PLS solutions were observed to quickly decrease to ~4-5 and prior adjustment of pH to this value had no influence on performance. Therefore, rather than lengthen the resin-washing procedure, which would not be practical industrially, subsequent experiments were run at the natural pH of the sample solutions. It was found that the alteration of pH during contact was independent of fluoride uptake, which was expected, since the ligand-exchange mechanism actually releases hydroxide [28,29]. *We conclude that the uncoordinated functional groups of La-S950+ resin simply buffer the aqueous contact solutions to a pH close to their second pK_a value. The pK_as of 1° aminomethylphosphonic acid are available from the NIST database and are reported as $pK_1 = 0.45$, $pK_2 = 5.40$ and $pK_3 = 10.05$ [226]. The pK_as of 2°*

aminomethylphosphonic acids, as a ligand attached to a solid matrix, have also been reported as pK_1 *= 2.0-2.5,* pK_2 *= 5.3-5.60 and* pK_3 *= ~11 [147, 226]. The* pK_1 *and* pK_2 *values refer to the phosphonate group, and* pK_3 *to the amine. From this, we can surmise that the resin buffers sample solutions to a state of equilibrium, in which its* $[LH_2]$ *and* $[LH_3]^+$ *forms coexist (L = aminophosphonic acid ligand). It is interesting to speculate as to whether one of the phosphonate oxygen atoms can still exchange a proton, while still being coordinated to the* La^{3+} *ion (Figure 2.2) and hence contribute to the buffering of aqueous media. As shall be seen (section 2.5.7), each coordinated La centre can bind up to two anionic fluoride ligands, from which it can be inferred that AMP group formally acts as a 1- anionic ligand and therefore one of the phosphonate oxygens may still be protonated after* La^{3+} *loading. An investigation into* Co^{2+} *and* Ni^{2+} *uptake by S950+ at low pH (1-2) found that the number of protons exchanged with the binding of each 2+ metal ion was 1.80 for* Co^{2+} *and 1.41 for* Ni^{2+} *uptake [92], which suggests this is possible. Additionally, IR spectra of AMP resins loaded with a variety of multivalent cations have reported the presence of the P-OH bond stretch at a pH of ~4 [142]. However, such an investigation was beyond the scope of this study. Pragmatically, the resin performs ideally for the fluoride-extraction from PLS remit without any pH adjustment being necessary.*

The amine functionality of aminophosphonic acid resins is known to act as an anion-exchange site [142]. However, uptake experiments (Appendix A, Figure A2) confirmed that uptake of common anions by H-S950+ was negligible (<1 $mg \cdot g^{-1}$ in most cases). Therefore, the amine, and indeed the presence of any uncoordinated phosphonic acid groups appeared to be insignificant to the performance of La-S950+.

In accordance with the literature [208], the uptake efficiency of the resin decreased with increasing resin:solution ratio, although the % extraction increased and easily reached ~100 % at a ratio of 1 g to 25 mL (Appendix A, Figure A3). A ratio of ~100 mg La-S950+ to 25 mL solution was used to ensure high resin efficiency and reasonable accuracy of electrode measurements.

2.5.4. Isotherm behaviour

The fitting of data for fluoride uptake by La-S950+ from NaF solution and from the PLS to the various isotherm models is shown in Figures 2.4-2.5. Figure 2.4 models the data over a low C_i range of 1.5-50 $mg \cdot L^{-1}$, to allow comparison with the literature. Figure 2.5 models the data over a higher C_i range, to more closely simulate industrial conditions. Isotherm parameters were extracted and presented in Tables 2.2 and 2.3. The equilibrium parameter R_L was calculated from Langmuir isotherms, using Equation 2.7:

$$R_L = \frac{1}{1+(1+K_L C_i)} \qquad \textbf{(Eqn. 2.7.)}$$

The mean free energy of desorption (E_{des}, in kJ·mol^{-1}), was calculated from the D-R isotherms using Equation 2.8:

$$E_{des} = \frac{1}{\sqrt{2B_D}} \quad \textbf{(Eqn. 2.8.)}$$

Similarly, the Temkin adsorption energy (b_T, in kJ·mol^{-1}) was calculated from the relevant isotherms with Equation 2.9:

$$b_T = \frac{RT}{B} \quad \textbf{(Eqn. 2.9.)}$$

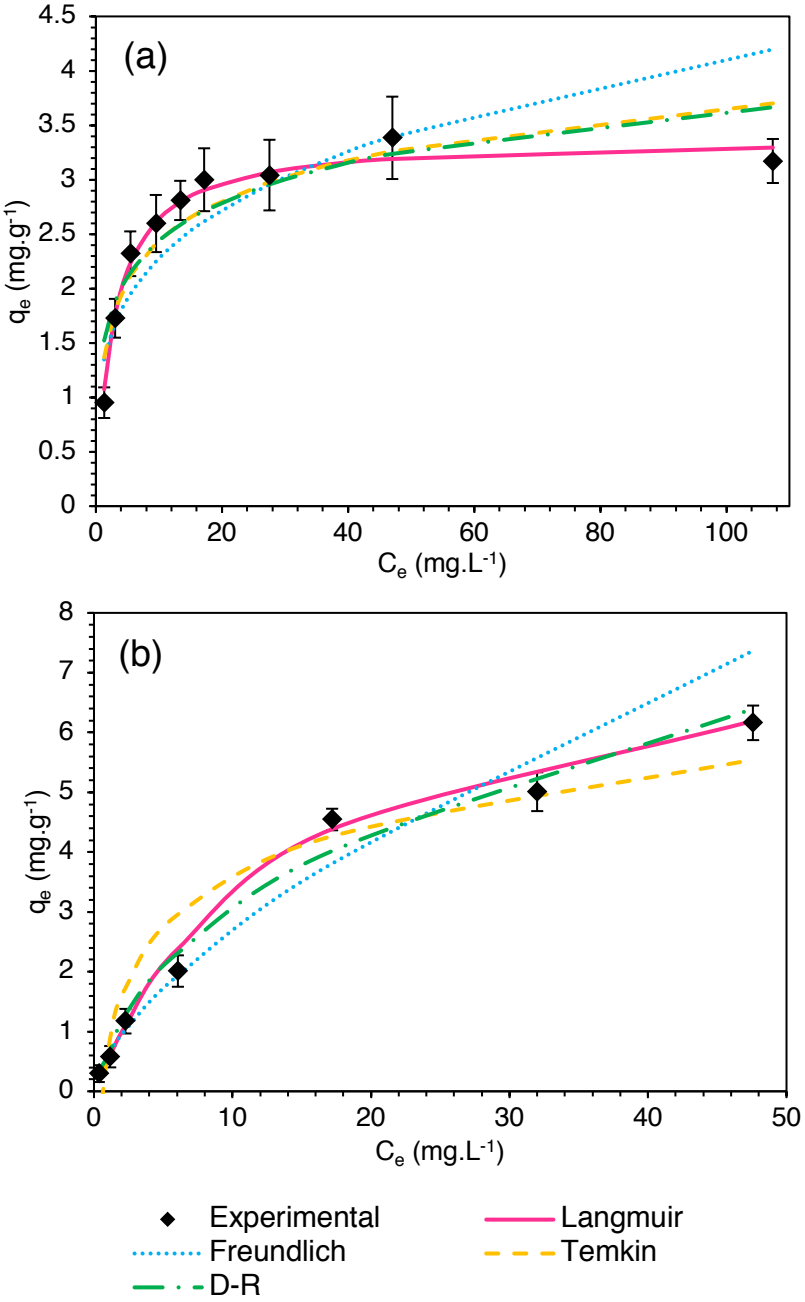

Fig. 2.4. Fluoride uptake of La S950+ fitted to isotherm models from **(a)** NaF solution and **(b)** PLS. F^- C_i range = 1.5-50 mg·L^{-1}.

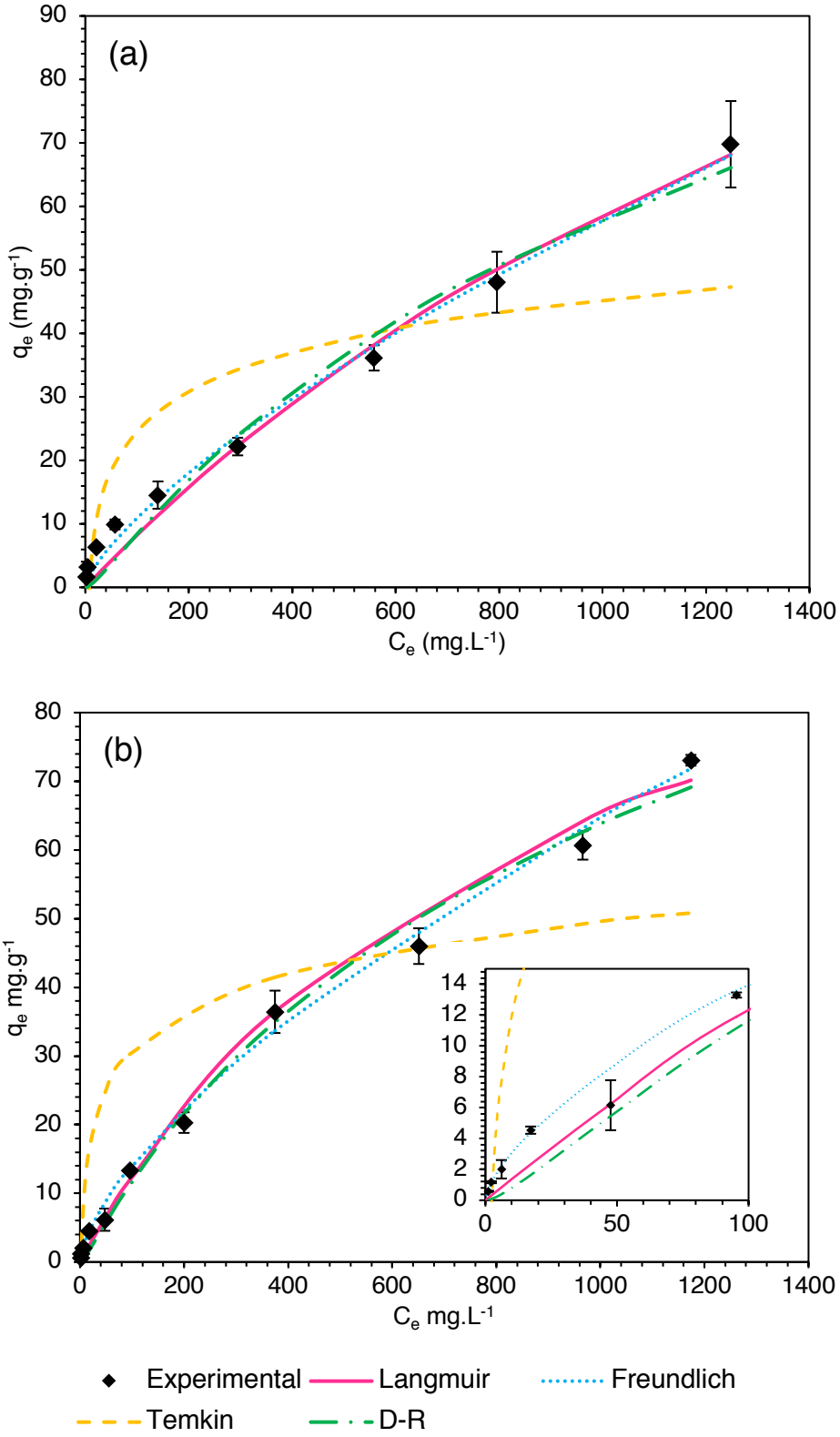

Fig. 2.5. Fluoride uptake of La S950+ fitted to isotherm models from **(a)** NaF solution and **(b)** PLS. F^- C_i range = 10-1,500 mg·L^{-1}. Enlargement shows 1st 6 data points for clarity.

Table 2.2. Isotherm fitting parameters calculated using all models over C_i range of 1.5-50 mg·L^{-1}.

Model	Parameter	NaF	PLS
Langmuir	K_L	0.354 ± 0.033	0.0691 ± 0.0153
	q_{max} (mg·g^{-1})	3.38 ± 0.06	8.08 ± 0.74
	R_L (when C_i = 50 mg·L^{-1})	0.0507 ± 0.0047	0.183 ± 0.030
	R^2	0.999	0.980
Freundlich	K_f	1.26 ± 0.17	0.848 ± 0.073
	n	3.88 ± 0.72	1.90 ± 0.12
	R^2	0.786	0.985
Temkin	A_T	19.1 ± 13.3 x 10^5	3.31 ± 1.4 x 10^4
	B	2.79 ± 0.38 x 10^{-2}	6.61 ± 1.1 x 10^{-2}
	b_T (J·mol^{-1})	88.9 ± 6.1	37.5 ± 6.0
	R^2	0.871	0.908
D-R	B_D	2.20 ± 0.39 x 10^{-9}	5.73 ± 0.56 x 10^{-9}
	q_{max} (mg·g^{-1})	5.27 ± 0.61	22.6 ± 3.6
	E_{des} (kJ·mol^{-1})	15.1 ± 2.7	9.34 ± 0.91
	R^2	0.842	0.978

Table 2.3. Isotherm fitting parameters calculated over C_i range of 10-1,500 mg·L^{-1}.

Model	Parameter (with units where applicable)	NaF	PLS
Langmuir	K_L	4.59 ± 1.67 x 10^{-4}	1.08 ± 0.14 x 10^{-3}
	q_{max} (mg·g^{-1})	187 ± 15	126 ± 10
	R_L (when C_i = 1,500 mg·L^{-1})	0.372 ± 0.135	0.276 ± 0.033
	R^2	0.982	0.976
Freundlich	K_f	0.384 ± 0.042	0.661 ± 0.042
	n	1.38 ± 0.05	1.51 ± 0.03
	R^2	0.993	0.997
Temkin	A_T	2.89 ± 2.2 x 10^3	3.51 ± 3.1 x 10^3
	B	0.474 ± 0.11	0.501 ± 0.090
	b_T (J·mol^{-1})	5.22 ± 1.2	4.94 ± 0.89
	R^2	0.744	0.775
D-R	B_D	1.70 ± 0.20 x 10^{-8}	1.49 ± 0.10 x 10^{-8}
	q_{max} (mg·g^{-1})	149 ± 20	145 ± 10
	E_{des} (kJ·mol^{-1})	5.42 ± 0.63	5.80 ± 0.38
	R^2	0.987	0.991

The uptake of fluoride from NaF solution was very well described by the Langmuir equation up to a C_i of ~ 50 mg·L^{-1}, but at higher C_i, the Freundlich model provided better description. Uptake from the PLS also fit the Freundlich model well over higher C_i, but at low C_i, the fit for both models was similar.

The data suggest that at low C_i, fluoride uptake from NaF solution is controlled by monolayer formation, via the expected aqua/fluoride ligand-exchange process, but at higher C_i, an unexpected multilayer physisorption interaction takes over, causing the greatly enhanced q_{max} values reported. Uptake from the PLS also seems to involve multilayer adsorption and moreover, the mechanism appears to dominate the uptake behaviour at lower C_i. In support of this, the Langmuir-derived R_L values (a measure of favourability of adsorption), did not significantly change, depending on C_i, for the PLS matrix, but was much greater at low C_i than at high C_i for the NaF matrix.

For both matrices, the Freundlich n values of >1 indicated a degree of heterogeneity of binding sites on the resin surface [227]. This again suggested more than one uptake process was operating and also that uptake was more favourable at higher C_i [228].

Langmuir-calculated q_{max} values in this instance were not as great as the largest reported in the literature for metal-loaded resins over similar C_i ranges (Table 1.3). However, over the higher C_i range, not previously investigated, q_{max} values were >4 times greater than has yet been reported. The data overall suggested that such resins could operate successfully in more concentrated waste-streams than have previously been considered.

The attempted data-fitting to the D-R isotherm was an interesting exercise, as the fit is excellent for the PLS at both concentration ranges and for NaF solutions at high concentration. However, the model did not describe well the uptake from NaF solutions at low concentrations (Tables 2.2 and 2.3). The D-R model was originally conceived to describe uptake by porous adsorbents, hence why it is often successfully used to model the behaviour of ion-exchange resins [96, 229]. The model is based on the assumption that adsorption proceeds, not via formation of single or multiple monolayers, but by the progressive filling of the sorbent pores [230]. The uptake of fluoride via ligand-exchange (Figure 2.3) is a surface phenomenon, so would not reasonably be expected to exhibit D-R isotherm behaviour. From this we can postulate that ligand-exchange may be the prevalent mechanism for NaF solutions at low C_i, but not for the other three experiments. Notably the E_{des} value returned in this instance (15.1 kJ·mol^{-1}) was much greater than for the other three experiments and could indicate the proposed ligand-exchanges (despite the poor fit). Values of <8 kJ·mol^{-1} are generally interpreted as indicating physisorption phenomena, while values >8 kJ·mol^{-1} imply either ion-exchange or chemisorption [92, 96]. Onyango et al. *reported a value of 11.3-12.1 kJ·mol^{-1} for the uptake of fluoride by an Al-loaded zeolite, which was proposed to be a ligand-exchange process [93]. At higher C_i, the uptake from NaF solutions appears to clearly switch to a physisorption mechanism, whereas for the PLS, the uptake process appears to be less dependent on C_i and could represent more than one mechanism acting simultaneously.*

In comparison to the other models, the Temkin isotherm was not the most appropriate to describe the data in any experiment. From this, it can be inferred that, assuming there are interactions between bound sorbate molecules, the enthalpy of adsorption will decrease exponentially as a function of coverage, rather than linearly [231]. Because of the poor agreement, we do not draw any conclusions from the calculated sorption energy values and they are presented only for the sake of a full dataset.

2.5.5. Co-uptake of other ions and leaching of La from PLS

Ion chromatography and ICP-OES results showing uptake of the major coexisting anions and cations in the PLS are presented in Table 2.4.

Table 2.4. Uptake of co-ions by La-S950+ from PLS under standard experimental conditions.

Species	**Undiluted PLS**		**1/10 diluted PLS**	
	q_e (mg·g^{-1})	**q_e (mmol·g^{-1})**	**q_e (mg·g^{-1})**	**q_e (mmol·g^{-1})**
F^-	73.1 ± 0.8	3.85 ± 0.02	13.3 ± 0.2	0.700 ± 0.001
Cl^-	< 0.1	<0.01	<0.1	<0.01
SO_4^{2-}	5.88 ± 0.04	0.0612 ± 0.0004	0.430 ± 0.032	4.48 ± 0.17 x 10^{-3}
Al^{3+}	57.4 ± 0.2	0.645 ± 0.006	7.56 ± 0.08	0.280 ± 0.003
Ca^{2+}	0.429 ± 0.042	0.0107 ± 0.0010	0.0979 ± 0.0101	2.44 ± 0.23 x 10^{-3}
Fe^{2+} (as $[Fe(CN)_6]^{4-}$)	1.47 ± 0.08	0.0263 ± 0.002	0.224 ± 0.082	4.01 ± 1.45 x 10^{-3}
La^{3+}	-0.959 ± 0.040	-6.90 ± 0.02 x 10^{-3}	-0.199 ± 0.008	-1.44 ± 0.06 x 10^{-3}

The only cation taken up in appreciable amounts was Al^{3+}. This suggested that a possible uptake mechanism was chelation of Al^{3+} complexes with coordinated fluoride ligands to vacant aminophosphonic acid sites. However, this is unlikely, since the metal-loading data suggested the resin was fully-saturated with La. Another considered possibility was precipitation of aluminium hydroxyfluorides (AHFs) on to the resin surface. AHFs have the general formula $AlF_n(OH)_{3-n}.xH_2O$ and precipitate over a pH range (4.5-5.5) similar to our observed optimum for fluoride removal (Figure 2.3) [78]. They are a possible precursor to AlF_3 [85], which is consumed in large quantities via the aluminium smelting electrolysis process. The small amount of La^{3+} leaching was thought to be due to displacement by Al^{3+} or Ca^{2+} [154]. The effect is not sufficiently severe that the performance of the resin would be notably affected over several cycles, since it is well-known that fluoride can be eluted via hydroxide treatment without significant metal leaching [119].

The uptake of SO_4^{2-} may be explained by the anion-exchange behaviour of the amine in the resin functionality, which would be protonated throughout the uptake process [147, 226]. Prior to contact with the PLS, the counter-anion to this group would be either NO_3^-, from the acid preconditioning, or Cl^-, from the treatment with $LaCl_3$. SO_4^{2-} is above both these anions in the established order of selectivity for SBA and WBA resins [115], which accounts for its uptake. No data is available on the selectivity of $[Fe(CN)_6]^{4-}$, compared to common anions, but it may be predicted to bind strongly, due to large ionic radius and high valance. The uptake was not sufficient for these species to be detected in XPS analysis (Appendix A, Table A4).

2.5.6. XRD analysis

XRD spectra of La-S950+ samples are shown in Figure 2.6. Whilst most samples exhibited no crystalline character, the post-NaF contact sample, where C_i = 1,500 mg·g^{-1}, clearly produced peaks corresponding to the LaF_3, lattice [220], indicating precipitation of this species. This has been

previously reported for mineral-based sorbents [228], but not in the case of metal-loaded ion-exchange resins. Crystalline NaF was also unexpectedly present, suggesting that, in addition to the surface La^{3+}/F^- interaction, fluoride was also taken up by the diffusion of Na^+ and F^- into the pores of the resin beads and crystallisation of NaF. No similar examples were found in the literature, but the uptake from NaF solution definitively cannot be explained by LaF_3 precipitation alone, since the F:La molar ratio on the resin following uptake experiments at high C_i was <<3:1. It must be assumed that the hydrophobic pore environment reduces NaF solubility. This partially explains the observed change to multi-layer adsorption when C_i > 50 mg·L^{-1}. The lack of crystalline NaF in the post-PLS-contact sample supported the hypothesis that the dominant mechanism of fluoride uptake in this matrix did not involve free aqueous fluoride. Crystalline AHFs [78] were also not observed.

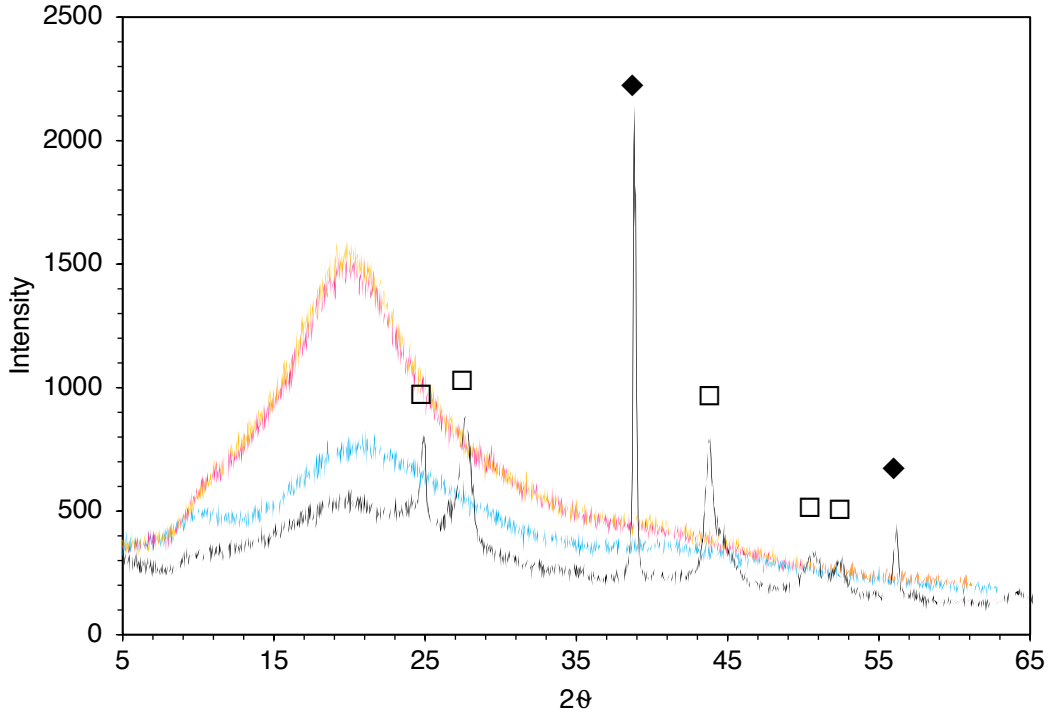

Fig. 2.6. XRD spectra of La-S950+ resin at various process stages. Post-contact samples were derived from 0.1 g resin, contacted with 25 ml NaF solution or PLS. | = pre-fluoride contact. | = post-PLS contact, C_i = 1500 mg·L^{-1}. | = post-NaF contact, C_i = 50 mg·L^{-1}. | = post-NaF contact, C_i = 1,500 mg·L^{-1}. ◆ = NaF crystal lattice. □ = LaF_3 crystal lattice.

2.5.7. XPS analysis

XPS high-resolution spectra for various elements of interest are seen in Figures 2.7-2.9. Survey scans and full characterisation are found in Appendix A, Tables A3 and A4 and Figure A1. The N 1s spectra (Figure 2.7) show the protonated quaternary ammonium nitrogens of the AMP functionality, with a binding energy of ~399.9 eV. The NO_3^- counter-anions are also represented, with binding energy of 402.1-402.6 eV. Notably, the binding energy of the quaternary ammonium environment does not change significantly upon La coordination to the resin, suggesting that it remains protonated, rather than forming a coordination bond to the La centre. Previous XPS studies, for

example Lavallee *et al.* [232] have shown that the N 1s binding energy alters by ≤0.8 eV upon abstraction of a proton and formation of a coordination bond to a metal centre. This evidence supports the notion that the nitrogen atom does not interact with the La centres, as shown in Figure 2.2.

The Al 2p spectrum of PLS-treated resin (Figure 2.8a) showed a single peak, of binding energy consistent with spectra reported by Stosiek *et al*. [233] for amorphous $AlF(OH)_2$. There was no evidence of chelated Al. This was supported by the O 1s spectra (Figures. 2.8b-d), which revealed two different O environments for untreated and NaF-treated La-S950+, the first at ~531.5 eV corresponding to P=O, NO_3^-, P-O-La and La-O-H; the second at ~533 eV, corresponding to P-O-H. For PLS-treated La-S950+, the spectrum was instead dominated by a single O environment, indicating an O-rich surface precipitate and again consistent with $AlF(OH)_2$ formation [233], suggesting that this is the dominant precipitate species. Although a crystalline precipitate might be predicted [85, 234], it is known that gelatinous hydrated $Al(OH)_3$ will precipitate favourably, over crystalline species at lower solution pH [235].

The La 3d spectra (Figures 2.9a-c) showed the expected two separated spin orbit components, each with multiplet splitting. The spectrum for the sample contacted with 1,500 $mg \cdot L^{-1}$ fluoride as NaF demonstrated a new La environment at a binding energy of 837.4 eV, corresponding to LaF_3 [236] and in agreement with XRD data. *The two minor environments at 829.9 and 833.5 eV may be assigned to chelated La centres with either one or two fluoride ligands exchanged. However, the PLS-treated sample exhibited two further unique La environments (831.9 and 836.2 eV), which also could not be matched in the literature and may represent La centres directly bonding with AHFs via fluoride or hydroxide bridging ligands. This possibility is discussed in detail in Chapter 3, following analysis of further adsorption data.*

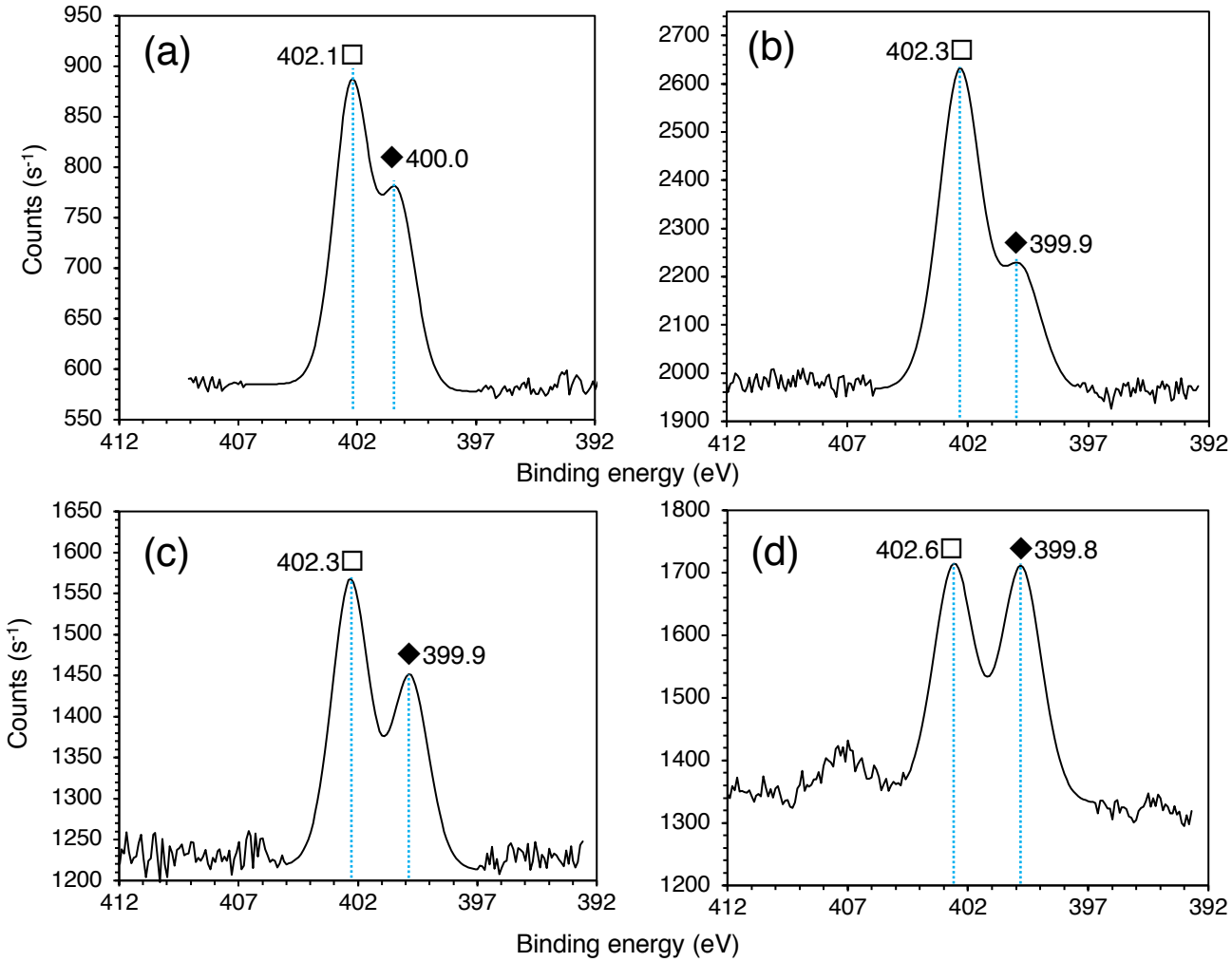

Fig. 2.7. High resolution N 1s spectra for the resin at various process stages: **(a)** H-S950+, **(b)** untreated La-S950+, **(c)** La-S950+ treated with NaF, [F^-] = 1,500 mg·L^{-1} and **(d)** La-S950+ treated with PLS, [F^-] = 1,500 mg·L^{-1}. ◆ = protonated ammonium. □ = nitrate.

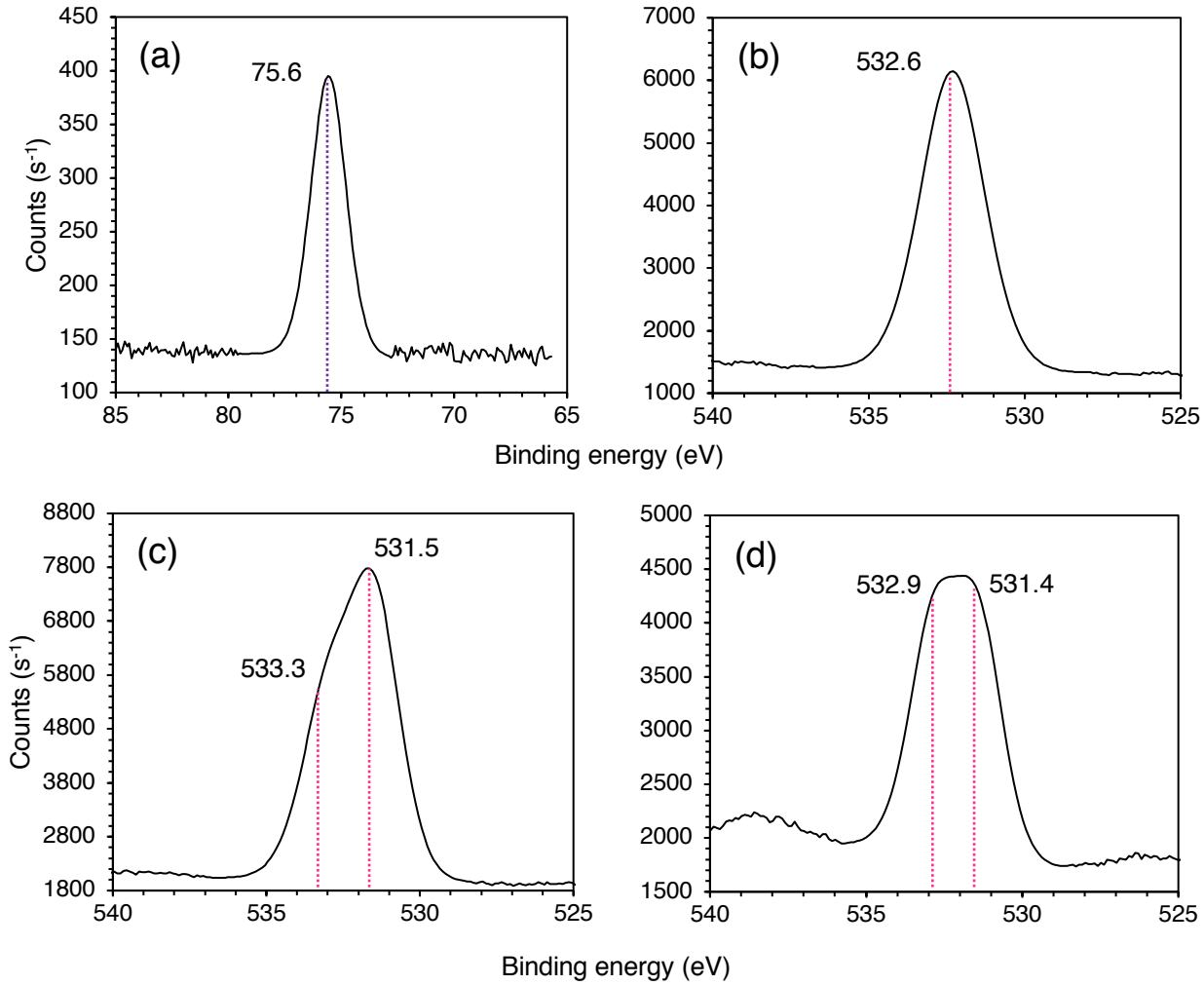

Fig. 2.8. XPS spectra of La-S950+ **(a)** Al 2p, post-PLS-contact, [F^-] = 1,500 mg·L^{-1}. **(b)** O 1s, post-PLS-contact, [F^-] = 1,500 mg·L^{-1}. **(c)** O 1s, untreated resin, **(d)** O 1s, post-NaF solution-contact, [F^-] = 1,500 mg·L^{-1}.

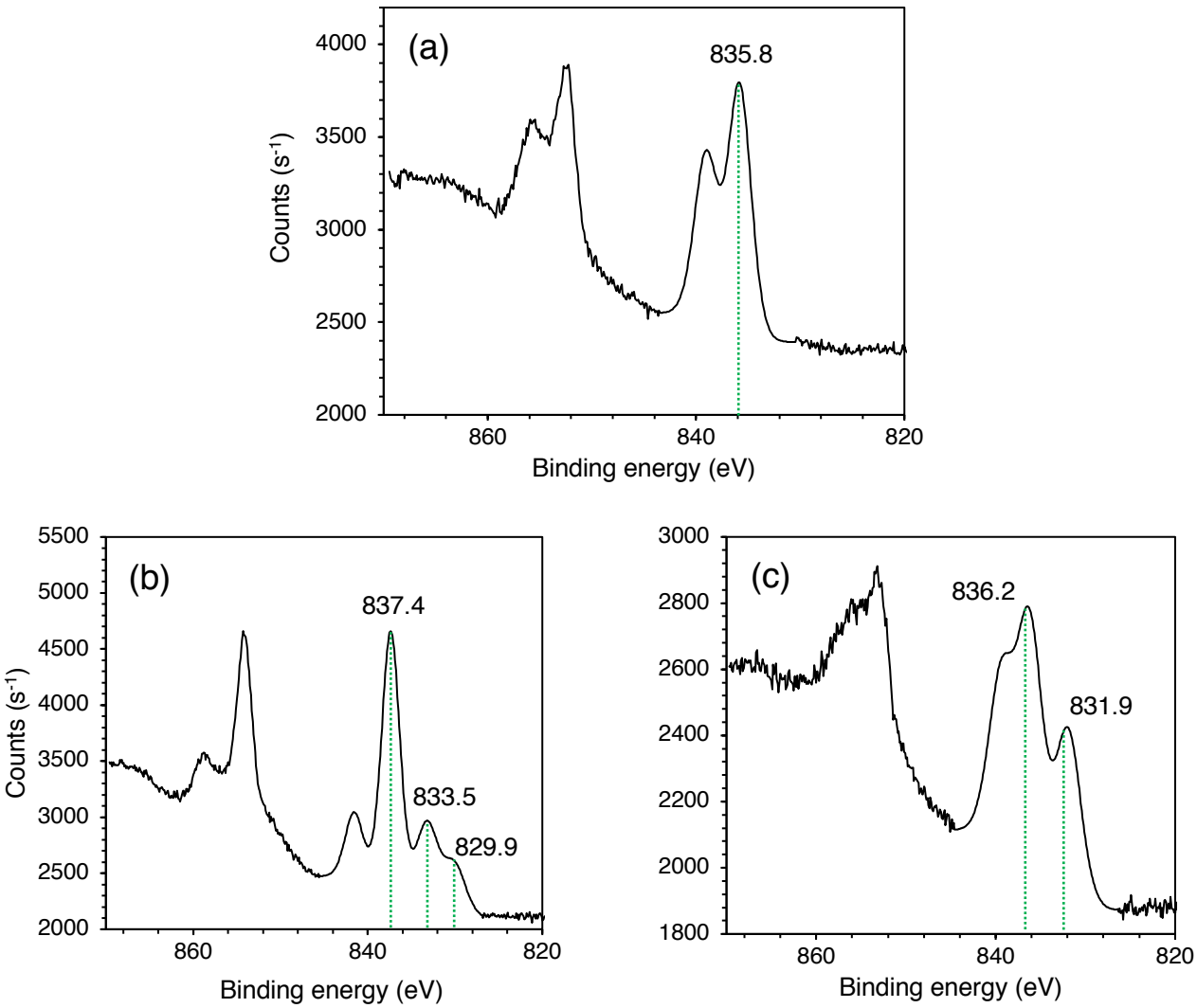

Fig. 2.9. La 3d5/2 XPS spectra of La-S950+ **(a)** Untreated resin, **(b)** Post-NaF solution-contact, [F^-] = 1,500 mg·L^{-1}. **(c)** Post-PLS-contact, [F^-] = 1,500 mg·L^{-1}.

2.5.8. Proposed Uptake mechanism

Taking into account all uptake and spectral data, the likely fluoride removal mechanisms for the two matrices are presented in Figure 2.10. For the NaF solution matrix at low C_i, La-S950+ uptake appears to operate via the ligand-exchange process widely reported in the literature [127, 129, 132, 212], hence the good agreement with the classical Langmuir model. For the same matrix at high C_i, a combination of LaF_3 precipitation and NaF physisorption appears to be prevalent, resulting in better agreement with the Freundlich isotherm. This may be of interest for recovery of fluoride from concentrated aqueous waste-streams without high levels of complexing and hard acid cations. For the PLS matrix, uptake appears to proceed via a combination of ligand-exchange and $AlF(OH)_2$ precipitation, with the latter becoming more prevalent at higher C_i and hence better suiting description by the Freundlich model. Such behaviour would certainly complicate potential fluoride recovery. However, recovered AlF_3 precursor chemicals would be more economically desirable, from

an industry point of view, than CaF_2 as there is a direct pathway to recycling back into the Al electrolysis process.

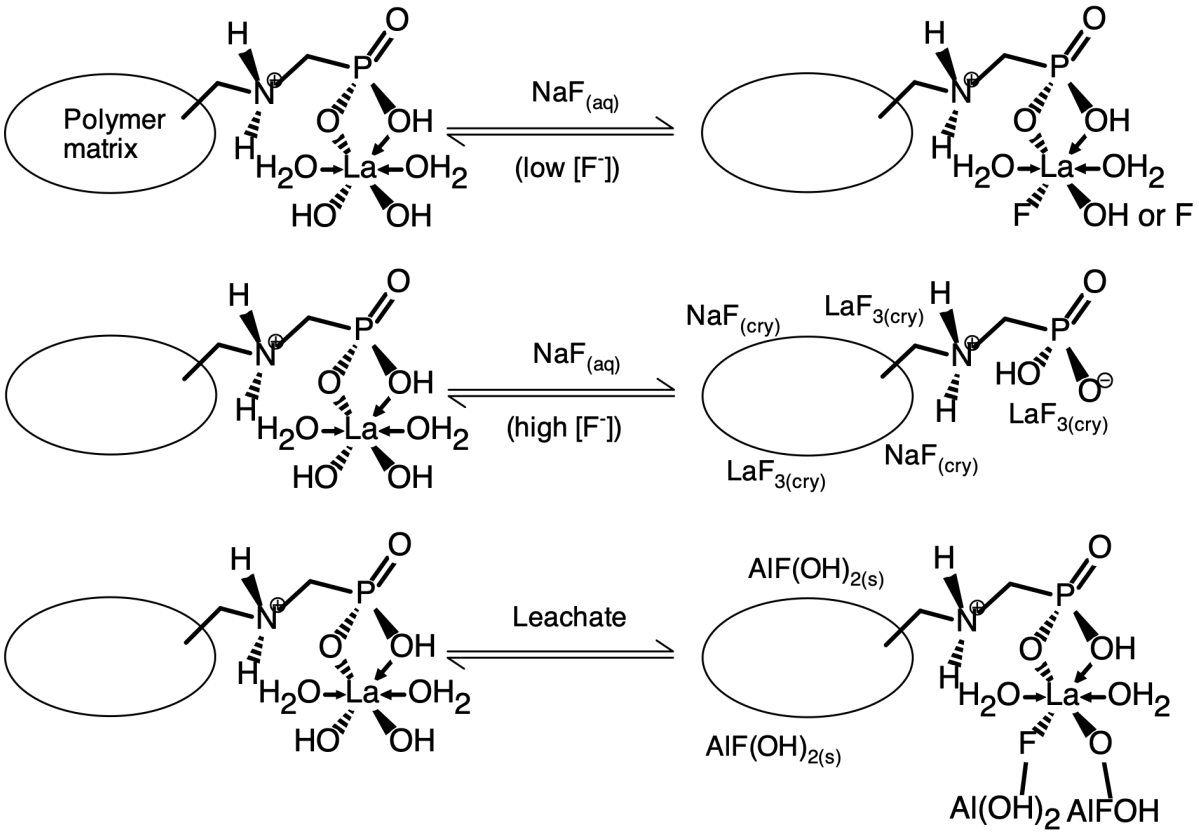

Fig. 2.10. Proposed fluoride uptake mechanisms for the 2 matrices. "cry" = crystalline. Note: The full La 1st coordination sphere is not shown for clarity. La generally has a coordination number of 9-10 [237].

2.6. Conclusions

The aminophosphonic acid chelating resin Purolite® S950+ has been chemically modified with La^{3+} ions to produce a novel sorbent for fluoride uptake from aqueous media. In batch extraction studies from NaF solutions and simulant Al industry leachate of high ionic strength, the resin has shown a greater uptake capacity that has previously been reported for similar sorbents. At low C_i ranges, uptake is dominated by a chemisorption ligand-exchange process. At higher C_i ranges, uptake is apparently enhanced by precipitation of LaF_3 and NaF in the first case and by amorphous $AlF(OH)_2$ precipitation in the second. This may complicate the elution of fluoride as analytically pure solutions, but also allow recovery of AlF_3 for Al smelting, which would be a desirable recycling outcome. Proposed uptake mechanisms are supported by isotherm and spectral data.

Purolite® S950+ is an inexpensive sorbent (retail price = £120·L^{-1}, equating to ~£80·kg^{-1}) and this, coupled with the relative cheapness of La_2O_3 means that La-S950+ compares favourably with traditional fluoride sorbents such as alumina (typical retail price = £540·kg^{-1}). Overall, La-S950+ is a highly effective fluoride sorbent and a promising potential industrial use for La metal. To move this work towards industrial implementation, the kinetics of the $AlF(OH)_2$ precipitation require further

investigation. Dynamic studies, regeneration and performance over repeated cycles are furthermore important parameters for the suitability of an ion-exchange resin for industrial use and are the object of our current research.

2.7. Acknowledgements

The authors would like to thank Dr Sarah Pepper of the SNUCER group, University of Sheffield, for ICP-OES analysis. We thank The Sheffield Surface Analysis Centre, University of Sheffield, for acquisition of XPS data. We also gratefully acknowledge Purolite® for their donation of the S950+ resin. This work was financed jointly by the EPSRC (Grant no. EP/L016281/1) and Bawtry Carbon International Ltd.

3. Static and dynamic kinetic investigations of uptake from simulant leachate and steps towards industrial implementation

3.1. Overview of paper

In Chapter 2, it is demonstrated that the La-MTS9501 resin possesses abnormally high capacity for fluoride from the simulant PLS and therefore the potential efficiency for the intended adsorption system is high. It is also seen that the ligand-exchange uptake mechanism for fluoride extraction by metallated resins, which was previously postulated by numerous researchers, is likely not the dominant uptake process for solutions of high [Al^{3+}]. Nonetheless, the means of extraction were not fully clarified in Chapter 2. All that is proved is that first, the La species formed on the resin surface are not equivalent to those resulting from the ligand-exchange processes. Second, that Al is co-adsorbed by the resin in significant quantities. Third, that the binding energy associated with uptake from the PLS system is rather lower than that associated with ligand-exchange uptake, from which we may predict that the stable AlF_3, AlF_2^+ and AlF^{2+} aqueous species are not dissociated as part of the fluoride adsorption process. Clearly more work is needed to understand the chemistry of the process.

This partially provides the impetus for the work described in Chapter 3. A detailed analysis of the static kinetics of the system is presented, with fluoride uptake from the PLS and from equivalent NaF solutions modelled across a broad concentration range and at different temperatures. This allows determination of rate constants for the adsorption process and mapping of how these change in response to experimental parameters. Broadly speaking, the fluoride removal from both sample matrices follows pseudo second-order kinetics, with intraparticle-diffusion and/or chemical reaction being the rate-limiting step. Although these two traits did not help to differentiate the adsorption mechanisms between the two systems, it was possible to determine activation energy values for the uptake. These revealed that uptake from the PLS proceeded by a lower energy pathway than the ligand-exchange interaction, which offered strong evidence that the aluminium fluoride complexes were binding to the resin, without dissociation. Unlike Chapter 2, the co-adsorption of Al was studied in detail in some experiments, with mapping of the ratio of bound F^- and Al^{3+}, which further evidenced this postulation. The likely mechanism is therefore modified to a chelating interaction between bound La^{3+} centres and aqueous Al^{3+} complexes, through the sharing of bridging ligands. At higher C_i, further AHFs are proposed to bind to the still active adsorption sites, through further bridging ligands, but with progressively weaker interactions. The uptake essentially becomes driven by the concentration gradient, as seen in the isotherms of Chapter 2. This ultimately would result in a large amorphous mass of coordinated AHFs developing around the La^{3+} centres. This would be a disordered structure of varying stoichiometry (because the uptake of AHFs changes the F^-:Al^{3+} ratio and therefore the speciation over the course of the uptake), which explains why no crystalline species are detectable in the spent resin.

The second major development in this chapter is the consideration of how the proposed system would work in its industrial setting. This is initiated by dynamic experiments, whereby the synthetic PLS is passed through a miniature (6.0 mL) column of La-MTS9501. In these experiments, the resin is seen to perform sufficiently, as the breakthrough curves produced can be easily modelled, the theoretical column lifespan (in terms of the Yoon-Nelson model T_{50} value) can be calculated with some degree of accuracy and the extracted dynamic uptake capacity was almost as high as the figure attained in static systems at equivalent C_i. Again, Al uptake closely correlates to fluoride, in support of the mechanistic postulation, whereas the uptake of small quantities of Ca^{2+} and co-anions in the system is very dissimilar, again confirming that AHFs are the dominant adsorbed species. Elution profiles of Al and fluoride are also attained by passing NaOH solution through the loaded columns. These initial experiments are only partially successful, in that the two target species may be eluted partially independently of the other adsorbed cocontaminants, but the resulting fluoride concentration in the effluent stream is actually rather lower than the inlet solution and a large volume of eluent is required for the task. This would complicate fluoride recovery efforts as precipitation of any species would not be feasible at such a low concentration and partial evaporation would be needed. This provides a clear target for improvement, which is addressed in Chapter 4, when experimentation with real SPL leachate begins. However, the elution experiments do produce some crucial findings. First, that the mass-balancing of the system is essentially well-resolved, as ~96% of the fluoride and ~100% of the Al loaded on to the column can be eluted from it. Therefore, the potential efficiency of the system is extremely high. Second, the chemical processes of the elution can be rationalised and agree with the proposed uptake mechanism. Third, it is established beyond reasonable doubt that cryolite is the most feasible recovery product for the planned operating conditions. Fourth, that there are a number of different strength binding interactions between the AHFs and the active sites on the resin; some desorption is possible simply by changing the concentration gradient and some requires elution with NaOH. This explains why in Chapter 2 the adsorption was seen to be heterogeneous and multi-layer in character and why the desorption energy changed as a function of PLS concentration.

Finally, the durability of the resin is tested over a series of batch adsorption/desorption cycles and, in common with previous literature, it is found that there is no loss in performance for fluoride extraction

This paper was submitted to *The Chemical Engineering Journal* on 24 December 2018, resubmitted in revised form on 16 February 2019 and accepted for publication on 19 February 2019 (doi.org/10.1016/j.cej.2019.02.135).

3.1.1. Author contributions

Thomas J. Robshaw. Experimentation and manuscript writing

Dr Robert Dawson. Manuscript review

Keith Bonser. Funding and manuscript writing support (AI industry technicoeconomics)

Dr Mark D. Ogden. Experimentation oversight and manuscript review

"Towards the implementation of an ion-exchange system for recovery of fluoride commodity chemicals. Kinetic and dynamic studies"

Thomas Robshaw[a]*, Robert Dawson[b], Keith Bonser[c] and Mark D. Ogden[a]

*Corresponding author address:

[a] Separations and Nuclear Chemical Engineering Research (SNUCER), Department of Chemical & Biological Engineering, University of Sheffield, Sheffield, S1 3JD, United Kingdom.

[b] Department of Chemistry, University of Sheffield, Sheffield, S3 7HF, United Kingdom.

[c] Bawtry Carbon International Ltd., Austerfield, Doncaster, DN10 6QT, United Kingdom.

3.2. Abstract

Spent potlining (SPL), a hazardous waste product from primary aluminium production, presents an important opportunity to recycle fluoride and conserve global fluorspar reserves. A novel strategy for treatment of the waste requires a selective fluoride-removal step from aqueous leachate. This has been demonstrated, using a Lanthanum-loaded chelating resin, in a series of kinetic and dynamic studies, with a view to industrial implementation. Kinetics could be described by the pseudo second-order model and uptake from SPL leachate was considerably higher than from equivalent NaF solutions, although observed rate constants were an order of magnitude less. Uptake of coexisting species and activation energy calculations indicated that a novel complexation interaction between La centres and aqueous aluminium hydroxyfluorides dominated the uptake process. The resin operated efficiently in column studies, with a dynamic fluoride uptake capacity of 66.7 mg·g^{-1}, calculated by the Dose-Response model, which produced the best fit to the data. The attained elution profile suggested that fluoride recovery by cryolite precipitation would be feasible, which could be recycled back into primary aluminium production or exploited as a commodity. The resin was found to have high durability in performance studies over repeated batch treatments.

3.2.1. Graphical Abstract

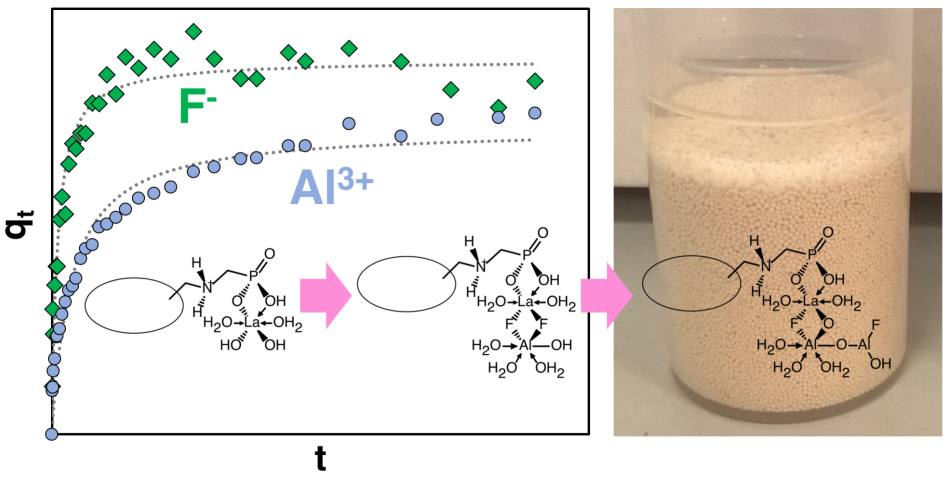

3.2.2. Keywords and Research Highlights

Spent potlining, fluoride recovery, chelating resin, aluminium hydroxyfluorides, lanthanum, cryolite

- ◆ Kinetics of fluoride uptake from spent potlining simulant leachate are demonstrated.
- ◆ Activation energy for fluoride adsorption via metal-loaded resin is reported.
- ◆ Resin-bound La ions may chelate with aqueous aluminium hydroxyfluorides.
- ◆ Column performance is well-described by Dose-Response model.
- ◆ From elution data, recovery of synthetic cryolite is targeted.

3.3. Introduction

Fluorspar (CaF_2) is one of 27 critical raw materials, in terms of global supply-risk and economic importance [238]. It is the raw feedstock for the majority of industrial fluro-chemicals, including the commercial polymers Teflon and Nafion [14]. Fluoride is also projected to be used in future generations of high power-density batteries [239]. Industrial recycling of fluoride is globally very limited, with fluoride-bearing waste streams generally viewed as nuisances to dispose of, rather than recycling opportunities [45-47].

The primary aluminium smelting industry creates ~1.3 million tonnes per year of spent potlining (SPL) waste. This is a hazardous material, comprising of “first-cut” (carbonaceous) and “second-cut” (cementious) fractions. The former in particular, is a rich and untapped source of labile fluorides (≤18%) [32]. It is particularly desirable to recycle the fluoride content of SPL, since the Hall-Hèroult electrolysis process for alumina reduction consumes ≤50 kg AlF_3 per tonne of metallic aluminium produced [48]. The main component of the Hall-Hèroult electrolysis bath is cryolite (Na_3AlF_6), which is increasingly a by-product of modern Al smelters, rather than consumed as a raw material [51]. It is nonetheless a valuable commodity chemical and still purchased in large quantities by the industry globally [240]. The market prices for AlF_3 and cryolite, which are both produced from fluorspar, are on global long-term upwards trends, due to continued high demand and inefficient fluorine recycling [241]. Most current industrial methods for SPL treatment are pyrometallurgical and focus on its conversion to an environmentally benign form via calcination or vitrification, hence not recycling a large fraction of the trapped fluorides [65, 67, 68].

Hydrometallurgical treatment systems are rare, with the low caustic leaching and lime (LCLL) process used by Rio Tinto Alcan being the only industrial example [50]. It is however known that first-cut SPL may be almost completely cleansed of its fluoride content via a simple two-step leach, using NaOH, then H_2SO_4 solutions [39, 53]. These two leachate streams may then be combined, producing a liquor of high aqueous fluoride concentration and also containing many co-existing anions and complexing metal cations.

Our current work focusses on implementing an ion-exchange system to selectively remove the fluoride from this multi-component leachate, consisting of sorbent-filled columns, through which the leachate is pumped. We chose to investigate metal-loaded cation resins for this purpose, since these materials are easily modified, have been optimised for column-based systems, are economical and have good potential for regeneration [126, 129, 214]. Several studies have also used the more economical lanthanides (La and Ce) for sorbent modification for fluoride selectivity. Modified materials include ion-exchange resins [127], alumina [133, 212] and chitosan [135, 136]. However, the aqueous systems studied generally had low fluoride concentration ranges and either low or uncertain ionic strength and appeared to be conducted with polishing or detoxifying applications in mind. Meenakshi and Viswanathan studied the performance of commercial ion-exchange resins over a fluoride concentration range of 2-10 $mg \cdot L^{-1}$ and conducted a field trial on a water source of ~500 $mg \cdot L^{-1}$ total dissolved solids [117]. Wassay *et al.* observed the performance of a lanthanide-modified alumina in the removal of fluoride from semiconductor production wastewater, in which the most concentrated co-anion was NO_3^- at ~390 $mg \cdot L^{-1}$ [212]. Oke *et al.* showed the industrial implementation of an Al-loaded ion-exchange resin column for treatment of an aqueous waste stream from a chemical manufacturer. However, the system was downstream of an independent precipitation unit, which greatly reduced the inlet fluoride concentration [214]. Further examples of the aqueous systems studied are seen in Appendix B, Table B1. None of the studies cited produced an elution profile to investigate how the adsorbed fluoride might be removed from a column in a purer form, to allow its recovery, We were unable to find any documentation of fluoride removal, by ion-exchange, from waste streams of high $[Al^{3+}]$, which profoundly changes the chemistry of the solution, due to its high fluoride affinity [78].

To extract the fluoride from SPL leachate, we chose an aminophosphonic acid resin, Purolite MTS9501, loaded with La^{3+} ions, hypothesising that the chelating functionality would be a sufficiently strong interaction to allow the resin to perform in the challenging conditions of aqueous SPL leachate, with minimal La^{3+} leaching. Initial isotherm studies in fact suggested that the resin was effective even in highly concentrated liquor ($[F^-] \leq 1{,}500$ $mg \cdot L^{-1}$), producing a maximum uptake capacity of >120 $mg \cdot g^{-1}$ (calculated by Langmuir isotherm). This was significantly greater than previous published data for metal-loaded resins [97, 129, 131], although smaller than the figure for uptake from NaF solution alone, which was 187 $mg \cdot g^{-1}$. The results appeared to be due to a combination of the expected La^{3+} ligand-exchange functionality and unexpected precipitation of amorphous aluminium hydroxyfluoride (AHF) complexes within the resin macropores [104]. The unusual co-uptake of fluoride and aluminium led to the hypothesis that cryolite or AlF_3 recovery could be possible through known technology [53, 78, 242]. This would significantly reduce the demand by the aluminium industry for geological fluorspar. Uptake from simple NaF solutions alone also

produced unexpected phenomena, as fluoride was taken up not only by ligand-exchange, but also LaF_3 and NaF precipitation. The heterogeneity of the postulated adsorption mechanisms is shown in Figure 3.1.

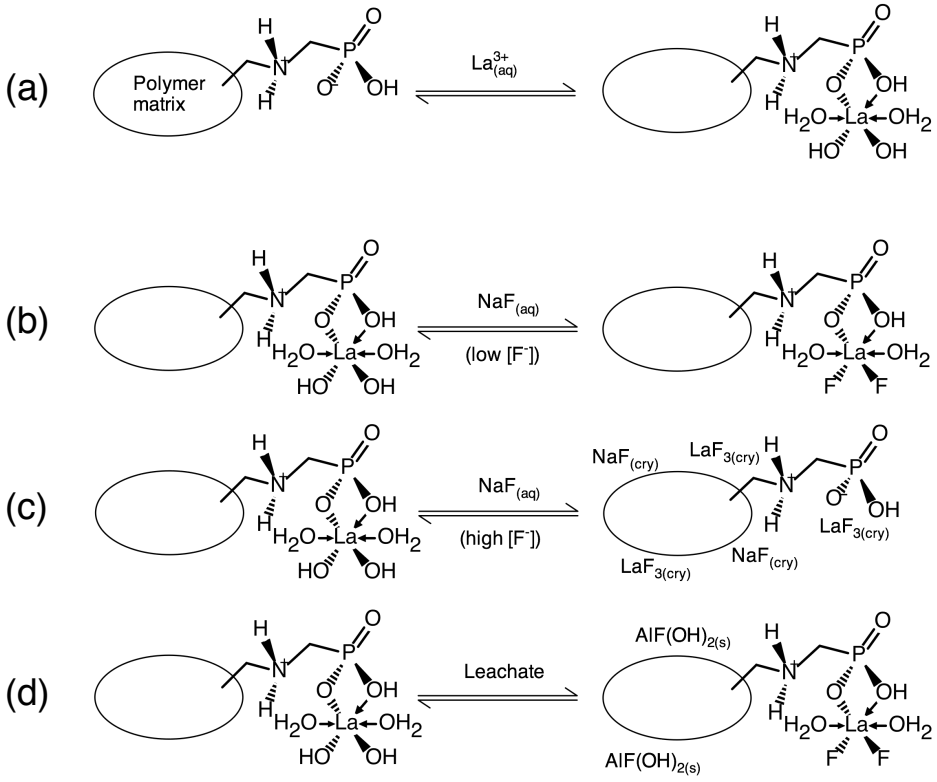

Fig. 3.1. Previously proposed mechanisms of fluoride uptake onto La-MTS9501 resin [104]. **(a)** pre-loading of MTS9501 with La^{3+}. **(b)** contact with dilute NaF solutions, showing the known ligand-exchange process. **(c)** contact with concentrated NaF solutions, showing LaF_3 crystallisation and NaF salt precipitation. **(d)** contact with leachate, showing ligand-exchange and precipitation processes. "cry" = crystalline.

However, to assess La-MTS9501 resin for its intended purpose requires understanding of the kinetic behaviour of the system, specifically with respect to the effects of temperature and concentration, and particularly, given the unusual uptake mechanism proposed. Performance in dynamic operations is also crucial, including breakthrough behaviour and the fluoride and aluminium elution profiles which may be attained. We therefore report here on the kinetic and dynamic behaviour of fluoride uptake via La-MTS9501 treatment with a SPL simulant leachate stream, including, for the first time, a calculation of the activation energy for fluoride uptake by a metal-loaded ion-exchange resin. The focus of the research remains on the performance of La-MTS9501 when contacted with undiluted leachate of high ionic strength. We hope, in this way to continue to establish fundamental understanding of the nature of fluoride uptake in solutions of high Al^{3+} concentration, which has not previously been reported. We also aim to understand, from elution data, which commodity chemicals may be feasibly recovered via the proposed hydrometallurgical process, which again is yet unreported.

Similarly to our previous work, uptake behaviour from analytical NaF solutions and at higher dilutions are also presented, for better understanding of uptake mechanisms, valid comparison to the literature and other potential fluoride recycling routes.

3.4. Experimental

3.4.1. Materials and Reagents

A liquor was prepared, to simulate the leachate produced by contact of mixed-cut SPL with dilute NaOH, followed by dilute H_2SO_4, as per the LCLL process [50]. In addition to high concentrations of Na^+ and SO_4^{2-}, the liquor contained 1,500 mg.L^{-1} fluoride and 1,200 mg·L^{-1} Al^{3+}. Synthesis and concentrations of co-ions are given in Appendix B, Table B2. Aqueous speciation was determined using the Aqion software package v6.4.7. [215]. See Appendix B p B2 for inputted parameters and results. Concentrations were derived from characterisation of first-cut SPL material by previous studies and assuming ~100% leaching of contaminants was possible [32, 38, 74]. For comparative work, NaF solutions were made up by dissolving the required amount of NaF salt in deionised water. Purolite™ MTS9501 resin was kindly donated by Purolite. Physical parameters are found in the Appendix B, Table B5. The resin was converted to its protonated form by batch treatment of ~25 g resin (wet mass) with 1 L of 1 M HNO_3, then loaded with La^{3+} ions by batch treatment of the same with 1 L of 10 g·L^{-1} La^{3+} solution, made by dissolving $LaCl_3.7H_2O$ in deionised water. As previously established, this resulted in a maximal La-loading of 256 mg·g^{-1} (1.84 mmol·g^{-1}) [104]. The La-MTS9501 resin was washed with 5 x 200 bed volumes (BVs) of deionised water (bed volume = equivalent water volume to that of a given resin mass) and dried for 24 hr in an air-flow oven at 50°C. Relevant parameters for the modified resin, from equilibrium studies, are found in Appendix B, Table B6.

3.4.2. Kinetic Experiments

Kinetic data was acquired for fluoride removal from the leachate at dilutions of 1/100 ($[F^-] \approx 15$ mg·L^{-1}), 1/30 ($[F^-] \approx 50$ mg·L^{-1}), 1/10 ($[F^-] \approx 150$ mg·L^{-1}), 1/3 ($[F^-] \approx 500$ mg·L^{-1}) and as-prepared ($[F^-] \approx$ 1,500 mg·L^{-1}). Data was similarly acquired from NaF solutions of equivalent $[F^-]$. An additional experiment was performed at $[F^-] \approx 5{,}000$ mg·L^{-1}, to examine a system dominated by NaF precipitation over ligand-exchange processes and its effect on kinetic parameters.

In kinetic experiments, a 1 L Nalgene® bottle, containing 500 mL of NaF solution or simulant leachate and a large magnetic stirrer, was held, via a clamp, in a 2 L polypropylene beaker, containing tap water and also fitted with a large magnetic stirrer. This was placed on a combined stirrer/hotplate and heated to the desired temperature or cooled with ice. A thermometer was used to ensure the temperature of the bath did not fluctuate by >1°C. 5.0 g La-MTS9501 (dry mass) was placed in the

fluoride-bearing solutions and left to stir for up to 72 hr. At predetermined time periods, 50 μL aliquots were removed from the bottle. The total volume removed from the bottle did not exceed 5.0 mL and the lid was closed between samplings. Most experiments were conducted at 20°C, the range being 2-43°C. The pH of experimental solutions was not adjusted.

The aliquots were diluted by a factor of ≥100 and their fluoride concentration was analysed using a Sciquip fluoride ion-selective electrode (ISE). Each sample also contained 50% ionic strength adjustment buffer (Appendix B, p B4). The Al, and Ca concentration of a number of leachate samples (without added buffer) was determined, using a Thermo Scientific iCAP 6000 ICP-OES. The concentrations of co-existing anions Cl^-, NO_3^- and SO_4^{2-} were quantified using a Metrohm 883 Basic IC plus ion chromatography (IC) system (Appendix B, p B5).

3.4.3. Dynamic Experiments

Breakthrough curves for the two matrices were attained for an inlet fluoride concentration of 15 and 1,500 $mg \cdot L^{-1}$. 1.96 g La-MTS9501 (dry mass) was placed inside a 10 mL polypropylene syringe, fitted with two porous frits, both above and below the resin bed. This was connected to a Watson Marlow 120U peristaltic pump using Watson Marlow Marprene® tubing of 0.8 mm internal diameter, which pumped NaF solution or simulant leachate through the column in a reverse-flow system. The eluent was fed to an automated fraction-collector (Bio Rad, model 2110), which was set to collect fractions of 0.5 BVs (3 mL). The pump was previously calibrated over a period of one day to give a linear flow rate of one BV (6 mL) per hr. Fractions were diluted by a factor ≥ 10 and were analysed by ISE, ICP-OES and IC as previously described.

In elution experiments, a similar dry mass of La-MTS9501, fully-loaded with fluoride or mixed leachate contaminants via the breakthrough technique, was set up as previously described. Loaded species were eluted using the same flow rate as for breakthrough experiments. Eluent used, in order, were deionised water, 0.01 M NaOH, 1 M NaOH and 3 M HCl. Concentrations of fluoride and co-anions were determined by IC, as previously described. Concentrations of Al and Ca were determined by ICP-OES, also as previously stated.

3.4.4. Solid-state analysis of resin

Samples of MTS9501 resin at various process stages were first washed with 10 x 200 BVs of deionised water, then ground to a fine slurry, using a mortar and pestle, then dried in an air-flow oven at 50°C for a minimum of 24 hr. X-ray diffraction (XRD) analysis was performed using a Bruker D2 Phaser X-ray diffractometer. Thermogravimetric analysis (TGA) was conducted using a Perkin Elmer Pyris1. Further details are in Appendix B, p B5.

3.4.5. Investigation of uptake behaviour by fitting to kinetic models

The uptake of fluoride and co-contaminants in the leachate at various time intervals was determined via Equation 3.1:

$$q_t = (C_i - C_t)\ x\ V/W \quad \textbf{(Eqn. 3.1.)}$$

where q_t is the fluoride uptake capacity of the resin at a given time, C_i is the initial fluoride concentration of the solution in mg·L^{-1}, C_t is the fluoride concentration of the solution at equilibrium in mg·L^{-1} at a given time, V is the volume of solution contacted in L and W is the dry mass of resin used in g. Fluoride ligand-exchange uptake data has previously been proposed to obey well both pseudo first-order and pseudo second-order kinetics [136, 212]. Therefore we chose to fit the data to the commonly used Lagergren pseudo first-order (PFO) [243] and Blanchard pseudo second-order (PSO) [244] rate equations (3.2 and 3.3):

$$q_t = q_e\left(1 - e^{-k_1 t}\right) \quad \textbf{(Eqn. 3.2.)}$$

$$q_t = \frac{k_2 q_e^2 t}{1 + k_2 q_e t} \quad \textbf{(Eqn. 3.3.)}$$

where q_e is the uptake capacity at equilibrium, t is time in minutes and k_1 and k_2 are the pseudo first- and second-order rate constants in min^{-1} and g·mg^{-1}·min^{-1}. Model-fitting was achieved using the Microsoft Excel SOLVER add-in (GRG nonlinear engine) [34]. Additional parameters, derived from PFO and PSO equations, were calculated using Equations 3.4 and 3.5:

$$t_{1/2} = \frac{1}{k_n q_e} \quad \textbf{(Eqn. 3.4.)}$$

$$h_0 = k_2 q_e^2 \quad \textbf{(Eqn. 3.5.)}$$

where n = 1 or 2, corresponding to PFO or PSO equations, $t_{1/2}$ is the sorption half-time (min) and h_0 is the initial sorption rate (mg·g^{-1}·min^{-1}) All other parameters are as previously described. The k values attained from experiments at different temperatures were used to create Arrhenius plots, using Equation 3.6:

$$k = Ae^{\frac{-E_a}{RT}} \quad \textbf{(Eqn. 3.6.)}$$

Where A is the pre-exponential factor, E_a is the activation energy for the process (J·mol^{-1}), R is the gas constant (8.314 J·K^{-1}·mol^{-1}) and T is the experimental temperature (K).

At high fluoride concentrations in particular, such uptake systems are influenced by diffusion processes, as the concentration gradient increasingly dominates the behaviour [35]. We therefore checked agreement of data to the Boyd film-diffusion model [245], shown in Equation 3.7

$$\ln(1 - F) = k_{fd}t \quad \textbf{(Eqn. 3.7.)}$$

where F is the fractional attainment of equilibrium at time t and k_{fd} is the film-diffusion rate constant (min^{-1}). Therefore, in a plot of $-\ln(1-C_t/C_i)$ vs t, a linear gradient would indicate that the uptake rate is controlled by the movement of the adsorbate through the hydrous film layer surrounding the adsorbent particles (film-diffusion). A non-linear gradient would suggest the rate is controlled by the movement of adsorbate ions within the pores of the resin beads (intraparticle-diffusion), or the chemical reaction at the surface (note this is applicable only at low solute concentrations ~1 $mmol \cdot L^{-1}$) [245, 246]. We also determined the agreement of the data with the intraparticle diffusion model [247], seen in Equation 3.8:

$$q_t = k_{id}t^{1/2} + C \quad \textbf{(Eqn. 3.8.)}$$

where k_{id} is the intraparticle-diffusion rate constant ($mg \cdot g^{-1} \cdot min^{-1/2}$) and C is a constant relating to the thickness of the adsorbent film layer. Data plots of q_t vs $t^{1/2}$ were produced. It is accepted that, if such a plot has a linear gradient and passes through the origin, the adsorption is entirely controlled by intraparticle-diffusion [92, 248]. We finally studied the adherence of the uptake to the Elovich model [249], applying the Chien and Clayton simplification [250], which has frequently been applied to chemisorption-dominated systems [248]. This is shown in Equation 3.9:

$$q_t = \frac{1}{\beta}\ln(t) + \frac{1}{\beta}\ln(\alpha\beta) \quad \textbf{(Eqn. 3.9.)}$$

where α is the initial rate constant ($mg \cdot g^{-1} \cdot min^{-1}$) and β is a desorption constant ($mg \cdot g^{-1}$). Hence, if a plot of q_t vs ln(t) produces a linear gradient, the system may be described by the Elovich equation. This is often interpreted to mean that adsorption involves two or three simultaneous first-order reactions [250]. Closeness of fit with these three models was estimated via linear regression, to derive R^2 values.

3.4.6. Investigation of uptake behaviour by fitting to dynamic models

The breakthrough data were fitted to a number of commonly applied models, again using SOLVER and non-linear regression. The Dose-Response model [251], which, as shall be seen, provided the best description of fluoride breakthrough, is shown in Equations 3.10 and 3.11.

$$\frac{C}{C_i} = 1 - \frac{1}{1+\left(\frac{V_{ef}}{b}\right)^a} \quad \textbf{(Eqn. 3.10.)}$$

$$q_0 = \frac{bC_i}{m} \quad \textbf{(Eqn. 3.11.)}$$

In these equations V_{ef} is the volume of solution eluted from the column (mL), a and b are constants of the Dose-Response model, q_0 is the theoretical maximum uptake capacity of the resin in a dynamic environment (mg·g^{-1}) and m is the dry mass of resin (g).

The Thomas model is shown in Equation 3.12:

$$\frac{C}{C_i} = \frac{1}{1+e^{\left(\frac{k_{Th}}{Q}\right)(q_0 m - C_i V_{ef})}} \quad \textbf{(Eqn. 3.12.)}$$

where C = concentration of the species of interest in the effluent at a given time (mg·L^{-1}), C_i = concentration in the inlet to the column (mg·L^{-1}), k_{Th} = Thomas rate constant (mL·min^{-1}·mg^{-1}), Q = flow rate (mL·min^{-1}). Other terms are as per the Dose-Response model.

The Adams-Bohart model is shown in Equation 3.13:

$$\ln\left(\frac{C}{C_i}\right) = k_{AB} C_i t - \frac{k_{AB} N_0 Z}{v} \quad \textbf{(Eqn. 3.13.)}$$

where k_{AB} = Adams-Bohart kinetic constant (mL·mg^{-1}·min^{-1}), t = time (min), N_0 = theoretical maximum uptake capacity of the hydrated resin (mg·mL^{-1}), Z = bed depth of column (cm) and v = linear flow rate (mL·min^{-1}). All other terms as previously described. It should be noted that, for the Adams-Bohart equation, data-fitting was performed only as far as the end of the linear section of the breakthrough curve, because of the known limitations of this model [252].

Finally, the Yoon-Nelson model is shown in Equation 3.14:

$$\frac{C}{C_i} = \frac{1}{1+e^{k_{YN}(\tau - t)}} \quad \textbf{(Eqn. 3.14.)}$$

where k_{YN} = Yoon-Nelson rate constant (min^{-1}) and τ = the time at which $C/C_i = 0.5$ (min). All other terms as previously described.

From elution data, the total masses of fluoride, Al and Ca eluted were found by calculating the area underneath the respective elution profiles and comparing to the total mass of each species loaded on to the column. This in turn was calculated from the Dose-Response model q_0 values attained, allowing an approximate % recovery to be derived.

3.4.7. Batch fluoride extraction experiments and resin regeneration attempts

Additional batch experiments were carried out, at ambient temperature, to corroborate kinetic and dynamic data. In certain experiments the initial [Al^{3+}] was altered, by controlling the addition of $Al_2(SO_4)_3$ in the synthetic leachate, with all other factors being kept constant.

In a typical procedure, ~100 mg of La-MTS9501 (dry mass) was contacted with 25 mL solution of known fluoride concentration in a 50 mL polypropylene screw-top tube. This was sealed and placed on the orbital shaker at 100 rpm for 24 hr. Solutions were analysed via ISE, as previously described. The equilibrium uptake capacity of the resin (q_e) in $mg \cdot g^{-1}$ was estimated using Equation 3.15:

$$q_e = (C_i - C_e) \times V/W \qquad \textbf{(Eqn. 3.15.)}$$

where C_e is the fluoride concentration of the solution at equilibrium in $mg \cdot L^{-1}$ and all other terms as per Equation 3.1.

The resin was regenerated by batch treatment of ~25 g resin (wet mass) with 1 L 0.01 M NaOH solution. Contact time was 1.0 hr. The regenerated resin was washed 5 times with 200 bed volumes of deionised water and dried for 24 hr in an air-flow oven at 50°C before being reused. The approximate maximum uptake capacity of the resin by batch treatment with as-prepared simulant leachate ($[F^-] \approx 1500\ mg \cdot L^{-1}$) was determined over five cycles of regeneration. At the end of the five cycles, the resin was further contacted, using the same technique, with 3 M HCl, returning it to the protonated form. It was then re-loaded with La^{3+} as previously described, and uptake capacity was again determined. Analysis was performed in triplicate and results averaged.

3.5. Results and Discussion

3.5.1. Investigation of Uptake Kinetics from media at various concentrations

In the case of the as-prepared liquor, Al kinetic data was acquired to attempt to further understanding of the uptake mechanism of the system. Ca data was acquired for comparison, as previous work had revealed that it was taken up in small amounts (<0.5 $mg \cdot g^{-1}$) in thermodynamic studies [104], yet was not believed to play a role in the fluoride uptake mechanism.

For fluoride uptake, both from leachate and NaF solutions, the full range of R^2 values from linear data plots previously described, for film-diffusion, intraparticle-diffusion and Elovich models are shown in Appendix B, Table B7. The two diffusion-controlled model plots produced curved gradients for all fluoride uptake experiments. The average R^2 values attained for Boyd plots were 0.295 (leachate) and 0.336 (NaF solutions), indicating that intraparticle-diffusion and/or chemical reaction were influential to the rate of adsorption [246] For intraparticle-diffusion plots, the R^2 values were 0.723 (leachate) and 0.620 (NaF solutions). This suggests that, under these experimental conditions, the intraparticle-diffusion step was not rate-limiting for the fluoride transfer on to the resin over the experimental timeframe. Similar data have been observed previously for uptake of rare earth metal ions by macroporous resins [253], which is unsurprising, as a macroporous internal structure should ensure rapid transport of the adsorbate to binding sites The plot of q_t vs $t^{1/2}$ yielded a curve in many cases (Appendix B, Figures B8b and B16b). This has been proposed to indicate that boundary-layer

diffusion, intraparticle diffusion and chemical reaction dominated at different uptake stages [254, 255]. There was no indication of the rate-determining step changing from film- to intraparticle-diffusion at higher fluoride C_i, as was originally shown by Boyd *et al*. [245].

The Elovich model, gave a reasonable description of the data in many cases, but for other experiments was not sufficient. The average R^2 value for leachate experiments was 0.911 (range = 0.852-0.995), and for NaF solution experiments was 0.826 (range = 0.669-0.958). A strongly linear gradient was observed specifically in the plot of q_t vs ln(t) in leachate experiments at high dilutions over some, or all of the experimental timeframe (Appendix B, Figures B4c and B6c). Elovich plots that exhibit sections of linearity, as is the case here, have been proposed to describe heterogeneous adsorption processes [92, 253], which agrees with existing knowledge of this system (Chapter 2).

Calculated parameters from fitting of the same data to the PFO model and the full range of associated R^2 values are also presented in Appendix B, Table B8. The average R^2 value for leachate experiments was 0.897 (range = 0.828–0.960), and for NaF solution experiments was 0.842 (range = 0.785–0.899). The PSO model gave a superior description of the adsorption for nearly all experiments and associated parameters were therefore considered more valid and are shown in Table 3.1.

Table 3.1. SOLVER fitting of fluoride uptake kinetic data to PSO model. Uptake shown from leachate and NaF solutions of various concentrations. Resin dry mass = 5.0 g, initial solution volume = 500 mL, T = 20°C.

Sample	q_e (mg·g^{-1})	k_2 (g·mg^{-1}·min^{-1})	$t_{1/2}$ (min)	h_0	R^2
Leachate 1/100 dilution	0.729 ± 0.012	6.07 ± 0.77 x 10^{-2}	22.6 ± 5.8	3.23 ± 0.82 x 10^{-2}	0.945
Leachate 1/30 dilution	3.78 ± 0.14	3.14 ± 0.492 x 10^{-2}	8.53 ± 2.72	0.355 ± 0.125	0.930
Leachate 1/10 dilution	7.17 ± 0.89	7.28 ± 0.96 x 10^{-3}	21.1 ± 3.5	0.443 ± 0.142	0.968
Leachate 1/3 dilution	16.4 ± 0.2	1.88 ± 0.08 x 10^{-3}	32.6 ± 2.7	0.501 ± 0.042	0.993
Leachate as-prepared	26.4 ± 0.4	4.73 ± 0.73 x 10^{-3}	24.6 ± 4.0	3.3 ± 1.0	0.929
Leachate as-prepared (Al)	21.6 ± 0.30	1.62 ± 0.19 x 10^{-3}	28.6 ± 3.4	0.756 ± 0.090	0.937
Leachate as-prepared (Ca)	1.88 ± 0.02	4.65 ± 0.75 x 10^{-2}	11.5 ± 1.8	0.164 ± 0.026	0.833
NaF solution $C_i \approx 15$ mg·L^{-1}	0.615 ± 0.007	0.546 ± 0.082	2.98 ± 0.45	0.206 ± 0.031	0.951
NaF solution $C_i \approx 50$ mg·L^{-1}	1.68 ± 0.04	0.499 ± 0.019	2.93 ± 0.99	0.390 ± 0.044	0.862
NaF solution $C_i \approx 150$ mg·L^{-1}	3.44 ± 0.03	0.167 ± 0.012	6.68 ± 1.02	2.07 ±0.06	0.944
NaF solution $C_i \approx 500$ mg·L^{-1}	5.07 ± 0.13	0.110 ± 0.031	1.80 ± 0.52	2.82 ± 0.81	0.877
NaF solution $C_i \approx 1{,}500$ mg·L^{-1}	14.0 ± 0.8	2.10 ± 0.83 x 10^{-2}	3.40 ± 1.36	4.12 ± 1.66	0.751
NaF solution $C_i \approx 5{,}000$ mg·L^{-1}	135 ± 3	1.62 ± 0.50 x 10^{-3}	4.58 ± 1.41	29.5 ± 4.57	0.897

Note: For F^- uptake, average R^2 value for leachate experiments was 0.953 and for NaF solution experiments was 0.880.

Kinetic data for fluoride, Al and Ca uptake from the undiluted leachate are shown in Figure 3.2. The corresponding data for NaF solution uptake, where fluoride C_i = 1,500 mg·L^{-1}, is also shown. Data are presented with fitting to the PSO model. Leaching of La was also checked in these experiments and was observed to reach a maximum of ~15 mg·L^{-1} in the leachate medium. Leached La concentration was below detectable limits for the NaF solution medium. The full dataset may be seen in Appendix B, p B6-B17.

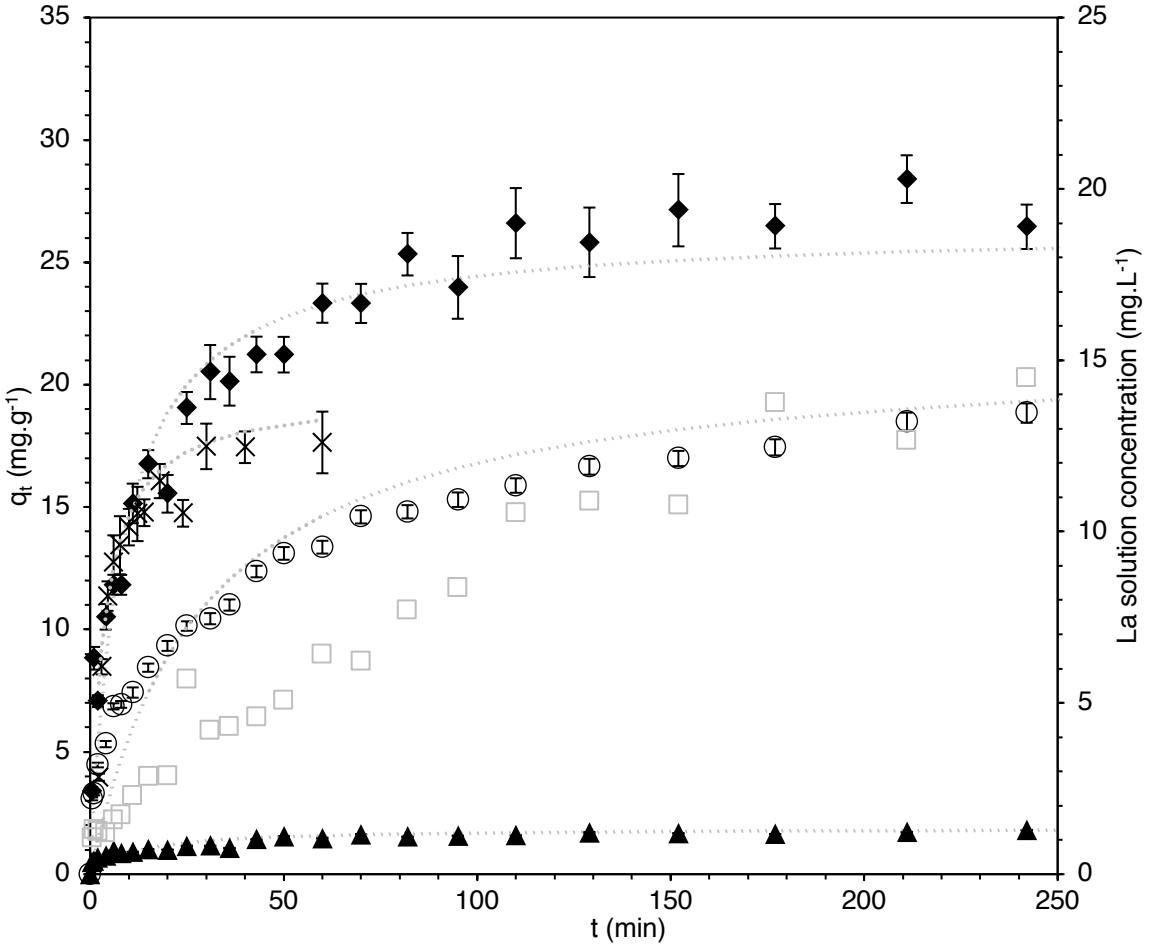

Fig. 3.2. Uptake of fluoride, Al and Ca from as-prepared simulant leachate and NaF solution (fluoride C_i = 1500 mg·L^{-1}) by La-MTS9501 over time, with data fitted to pseudo second-order kinetic model, represented by dotted lines. Includes La-leaching from the resin. Resin dry mass = 5.0 g. Initial solution volume = 500 mL. T = 20°C. ◆ = fluoride from leachate. ○ = Al from leachate. ▲ = Ca from leachate. □ = La loss into leachate (right-hand y axis). × = fluoride from NaF solution. In some cases, error bars too small to be seen.

The reasonable adherence of the fluoride uptake behaviour to PSO kinetics is consistent with an observation by Viswanathan & Meenakshi for similar resins [129] and for many other studies which have used rare earth functionality within other support matrices (Appendix B, Table B1). Further studies have cited the PFO model as suitable for describing fluoride adsorption by ion-exchange resins [123, 128], but as the two models were not directly compared in these cases, it is difficult to conclude whether La-MTS9501 behaves typically or atypically for a metal-loaded resin. In our work, the generally poorer agreement with the PFO model suggested a chemisorption mechanism

dominated over all concentrations tested [154]. It should be noted that we do not propose this based solely on kinetic data, but also on previous X-ray photoelectron spectra, which indicated clear changes to the La bonding environments upon resin-contact with both leachate and NaF solutions [104]. An exception in the data is the case of uptake from NaF solution where $[F^-] \approx 5{,}000$ mg·L^{-1}. This is consistent with our previous results, which suggested that the dominant uptake mechanism from NaF solution changed from chemisorption to physisorption (crystalline NaF precipitation) at very high $[F^-]$.

The attained q_e values via kinetic experiments are much higher for leachate experiments than NaF solution experiments. This is in contrast to the prior equilibrium study, in which our q_{max} values, determined by D-R isotherm-fitting, were similar for the NaF solution [123]. The disparity is likely due to the increased resin:solution ratio in kinetic experiments and results suggested that the practical operating capacity for La-MTS9501 might be considerably higher, when applied to aluminium industry leachate, rather than a simpler matrix. Interestingly, a slight “double plateau” was observed in some NaF solution kinetic data plots (Appendix B, Figures B12 & B15). It is possible that this represents the point where the first OH^-/F^- ligand-exchange is complete on the majority of La centres, since the second exchange is thermodynamically less-favoured and would therefore be slower [123]. This phenomenon has been observed in previous studies, where complexing metals have been used as active sites for fluoride ligand-exchange [128, 162, 206], but does not appear to have been commented on. The behaviour was not observed in all NaF uptake experiments. No double plateau was observed in any leachate uptake experiments, suggesting that the adsorption mechanism did not involve ligand-exchange.

For uptake from NaF solution, the calculated rate constants were considerably higher than previously reported for metal-loaded resins at comparable C_i values [130, 132] and for other rare-earth-functionalised sorbents [133, 135]. This may be partially attributed to the large accessible surface area of the macroporous resin. In support of this, the moisture-content range of MTS9501 (60-68%) is greater than that of commercial equivalent Lewatit® TP260 (58-62%) [111, 256]. The kinetics of uptake from leachate were generally slower by an order of magnitude. This would be expected, given the higher ionic strength of the leachate, as previously stated, which is known to retard adsorption kinetics [257]. As-prepared leachate ionic strength was calculated by Aqion to be 24.8 mmol·L^{-1}, compared to 6.23 mmol·L^{-1} for the NaF solution of equivalent fluoride concentration [215].

The dependence of k_2 values on fluoride C_i for the 2 aqueous systems was examined and is shown in Figure 3.3. The relationship of k_2 with h_0 values is shown in Appendix B, Figure B23.

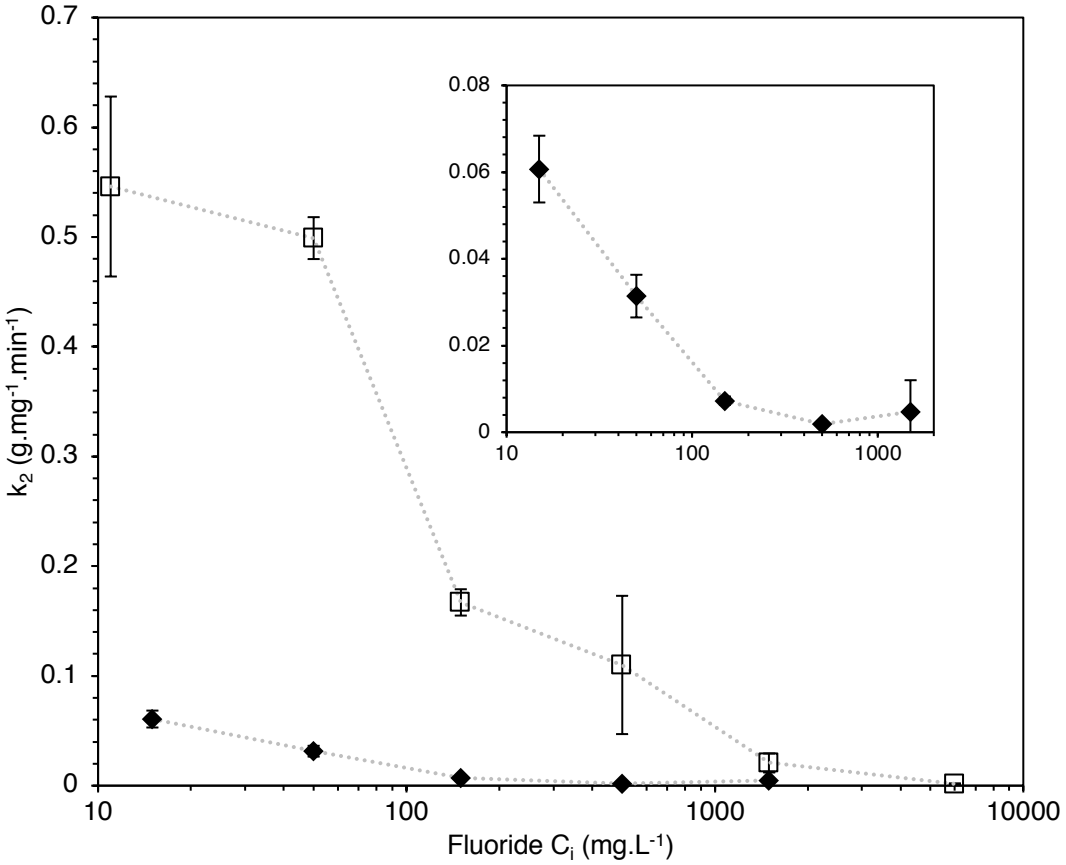

Fig. 3.3. Relationship between fluoride C_i and observed k_2 value for uptake from leachate (◆) and NaF solution (□). x axis is logarithmic for clarity. Enlargement shows change in gradient for leachate matrix.

Figure 3.3 shows that the effect of increasing C_i on the k_2 values was not equivalent for the two matrices. Interestingly, with uptake from leachate, the k_2 value appears to be dependent on the $\log_{10}$ of C_i across the low end of the concentration range, whereas there is minimal correlation for NaF solution uptake. This may be because uptake from NaF solution is dominated by different processes across the C_i range, including ligand-exchange, LaF_3 crystallisation and precipitation [228] and NaF physisorption and crystallisation [97, 104], whereas AHF uptake from leachate is a more homogenous process. It can be seen how, for both matrices, k_2 values approach unity as C_i gets higher, as both mechanisms become more homogeneous (NaF precipitation and poly-AHF complexation) and dependent on concentration gradients. It has been shown that k_2 values are not accurately predicted from C_i values across a wide concentration range [258]. Contrary to our findings, Lv *et al*. studied the effect of changing C_i upon the uptake of fluoride by layered double hydroxide sorbent and reported that k_2 values broadly increased with an increase in C_i, although again, no linear trend was observed [254]. Viswanathan and Meenakshi found no overall trend in the relationship between C_i and k_2 for fluoride uptake by an alumina-chitosan complex, using a C_i range of 9-15 mg·L^{-1} [259]. It can also be observed (Table 3.1) that there is no correlation between fluoride C_i and calculated $t_{1/2}$ values. Interestingly however, the values attained for the as-prepared leachate and 1/100 dilution leachate experiments were almost equivalent. This suggested that operating at

lower dilutions may indeed be practical industrially, from the point of view of rapid and efficient column-loading and the increased fluoride-loading efficiency seen in Chapter 2.

The co-uptake of metal ions data (Figure 3.2) demonstrated that Al and fluoride appeared to be taken up synergistically, or at least in conjunction until the ~200 min stage. This was contrary to expectations, as it was thought that a OH^-/F^- ligand-exchange process would dominate in the first few minutes of adsorption, with negligible Al uptake. This prompted us the examine the molar ratio of the two adsorbed species over time (Figure 3.4). This revealed that apart from a brief period at ~1 min (which may represent the small quantity of free fluoride in the system adsorbing via ligand-exchange), the $F^-:Al^{3+}$ molar ratio remains at ~2.5:1 until ~100 min, then drops gradually to ~1.5:1. This suggests that the dominant mechanism throughout the uptake process is the adsorption of aqueous AHFs. Aqion calculations are in good agreement with this theory (Appendix B, Table B3), since the most prevalent species in solution are AlF_3 and AlF_2^+, hence the ~2.5:1 molar ratio initially observed is sensible. Over time, a slow equilibrium process on the resin surface between 100 and 700 min appears to release some fluoride back into solution at the same time as further AHF adsorption, meaning the ratio tends towards 1:1. This is, in fact, consistent with previous XPS data [104], which indicated that the dominant AHF species on the resin surface, after equilibrium had been reached, was closely related to $AlF(OH)_2$, rather than more fluoride-rich species. The uptake of Ca was seemingly independent of both fluoride and Al, as its k_2 value was an order of magnitude higher. It is possible that Ca^{2+} ions cause changes to La^{3+}/AMP coordination. For example, La centres previously coordinated to multiple AMP groups could undergo a surface rearrangement, to bind with 1:1 stoichiometry and allow some coordination of Ca. The leaching of La into the solution is too minor to be correlated to the uptake of Al or Ca and is likely a cumulative effect of the high ionic strength liquor.

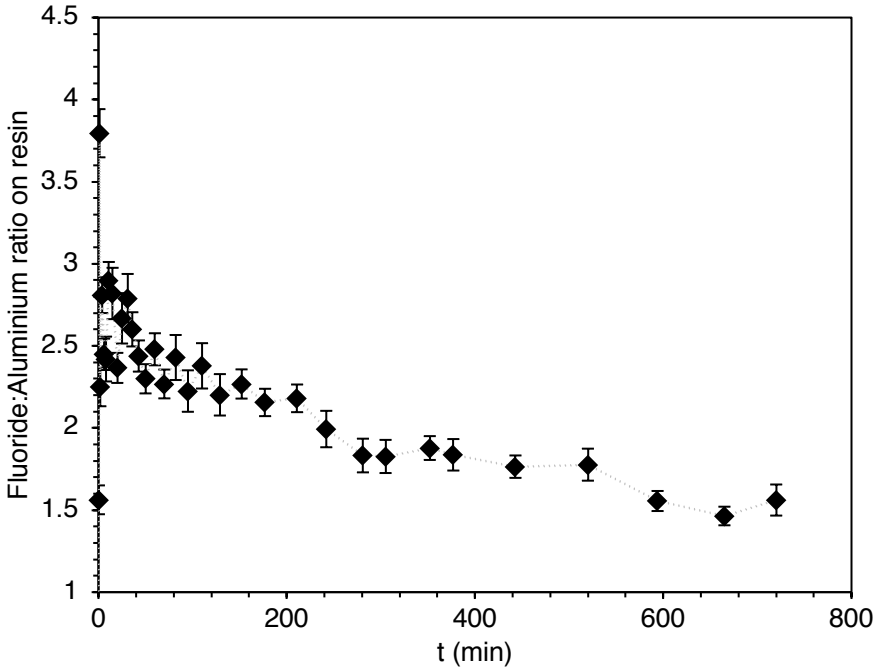

Fig. 3.4. Molar ratio of fluoride:aluminium adsorbed onto the resin and variation over time during kinetic uptake experiment using as-prepared simulant leachate.

3.5.2. Determination of activation energy for the two systems

The full dataset for temperature-varied experiments, in graphical form, is shown in Appendix B, p B18-B21, including parameters calculated from the PSO rate equation. Increasing the temperature of the system increased the rate of fluoride uptake, but resulted in lower q_e values. The effect on q_e was however much less pronounced for uptake from the leachate than for uptake from NaF solutions (Appendix B, Table B9). This infers that the uptake of free fluoride on to the resin was a more exothermic process than AHF complexation (ΔH_f for LaF_3 = -1,732 kJ·mol^{-1}). Viswanathan and Meenakshi observed that q_e values for fluoride uptake by metal-loaded cation-exchange resins similarly decreased with increasing temperature [157].

The k_2 values were subsequently used to produce Arrhenius plots, which are shown, along with the extracted parameters for the leachate and NaF solution matrices in Figure 3.5.

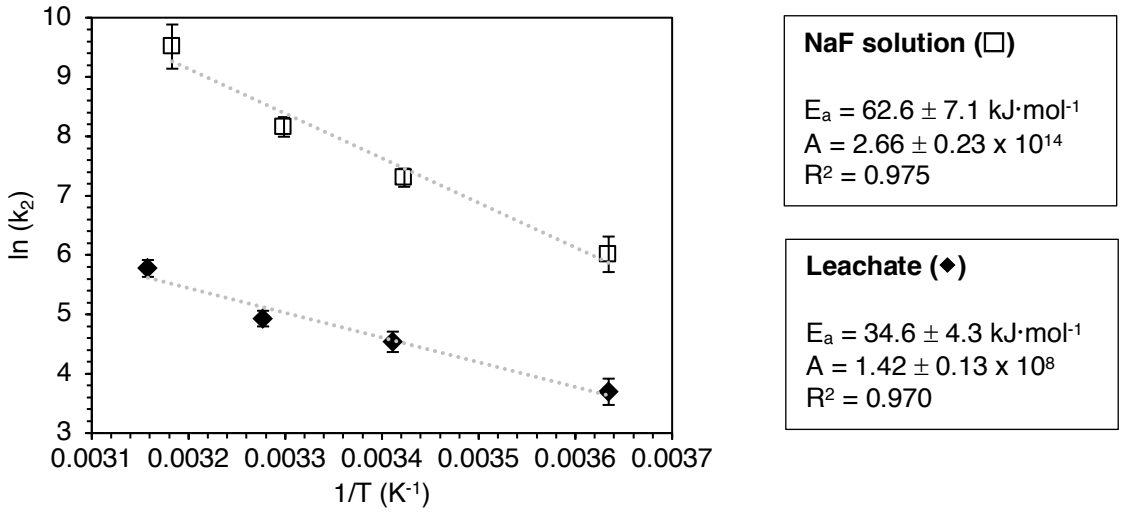

Fig. 3.5. Arrhenius plots for fluoride uptake by La-MTS9501 from leachate (◆) and NaF solution (□). Fluoride C_i = 150 mg·L^{-1}. Resin dry mass = 5.0 g. Initial solution volume = 500 mL. T = 2-43°C.

Experiments to determine E_a values for the two systems were performed at $C_i \approx$ 150 mg·L^{-1} fluoride, to ensure the value attained for NaF solution was representative of the fluoride ligand-exchange reaction only, rather than any crystallisation mechanisms. An XRD spectrum of the resin, post-treatment, confirmed no crystalline species were present (Appendix B, Figure B34). For both matrices, R^2 values for Arrhenius plots were reasonable. The E_a value derived for NaF solution uptake is similar to the figure of 68.7 kJ·mol^{-1} obtained by Na & Park in the uptake of fluoride by $La(OH)_3$ at a similar C_i [228]. The lower E_a value for leachate uptake is nonetheless suggestive of a chemisorption mechanism, since diffusion-controlled processes result in E_a values of <30 kJ·mol^{-1} [49, 50]. We propose that the dominant uptake mechanism from leachate is closely related to the depiction in Figure 3.6, with multi-nuclear complexes formed between P, La and Al centres, with O and F bridging ligands.

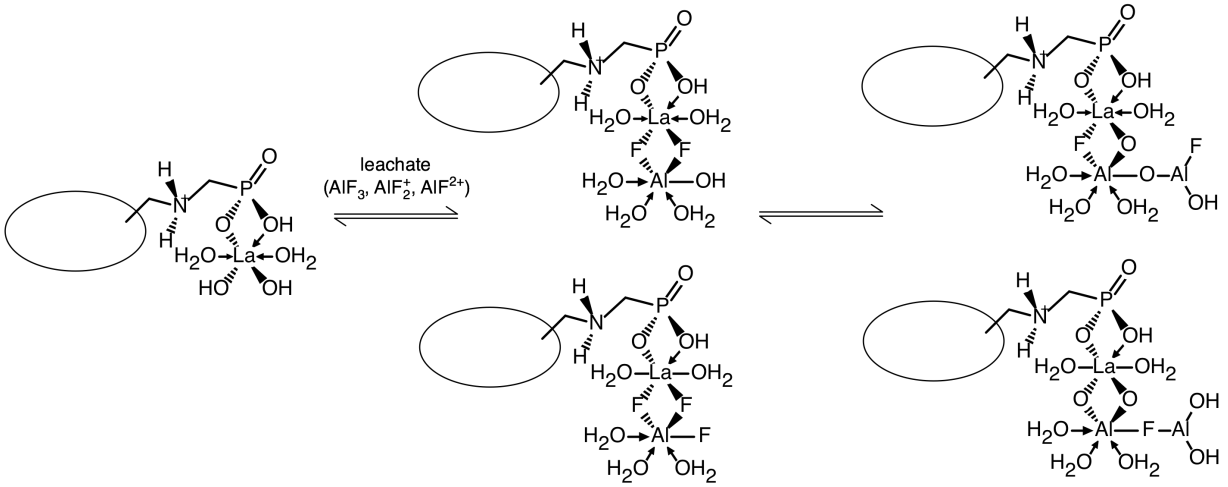

Fig. 3.6. Proposed modified uptake mechanism of fluoride and aluminium from SPL leachate on La-MTS9501. Coordinated waters for secondary AHF complexation are omitted for clarity.

Xu *et al.* have reported a novel La/Al-hydroxide composite material that was spontaneously formed in varying molar ratios in an aqueous environment [260]. Lanthanides are known to partake in multi-nuclear complex formation, with fluoride bridges to first-row transition metals, although complexation with Al has not yet been reported [261]. Lyu *et al.* also investigated modified zeolites for fluoride removal and found that when the material was loaded with both La and Al, a synergistic effect was observed, giving the sorbent a higher capacity than Al or La alone [137]. The lower E_a values in comparison to simple ligand-exchange may be explained by the chelating effect, which may be favoured in high ionic strength conditions [262, 263]. The modified proposed uptake mechanism is consistent with the lack of crystalline AHF species detected on the resin surface and also the unique La environments previously observed in X-ray photoelectron spectroscopy measurements [104]. TGA traces (Appendix B, Figure B35) show a significant difference in the final % mass between pre-treatment and leachate-treated La-MTS9501 samples (30.9 verses 33.5), which could be attributed to the adsorbed Al species, which would essentially be converted to Al_2O_3.

3.5.3. Generation of breakthrough profiles from dynamic experiments

Breakthrough curves for the two matrices were attained for an inlet fluoride concentration of 15 and 1,500 $mg \cdot L^{-1}$ and are shown in Figures 3.7 and 3.8. In the case of the as-prepared leachate experiment, the profiles of Al and Ca were also determined and the concentrations of the other common anions in the effluent were also checked, to monitor the behaviour of coexisting ions, relative to the fluoride breakthrough (Figure 3.9). Leaching of La was checked, but its concentration in the eluent was found to be <0.1 $mg \cdot L^{-1}$ throughout the experiment. Extracted parameters from the Dose-Response model are presented in Table 3.2.

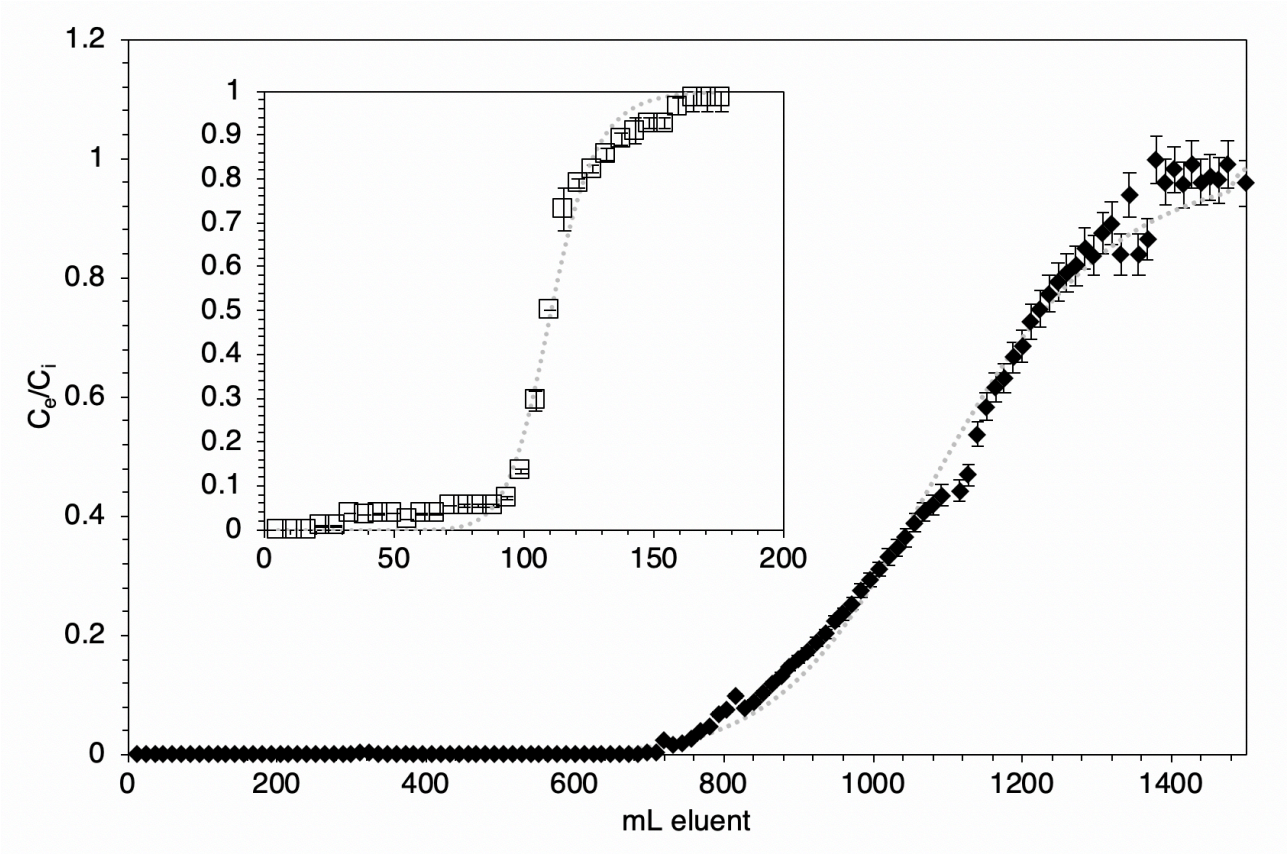

Fig. 3.7. Fluoride breakthrough profile attained by passing 1/100 diluted leachate (◆) and NaF solution of [F^-] ~15 mg·L^{-1} (□) through a La-MTS9501 column. Dotted lines represent Dose-Response model. Resin bed volume = 6.0 mL. Flow rate = 1 BV·hr^{-1}. T = 20°C.

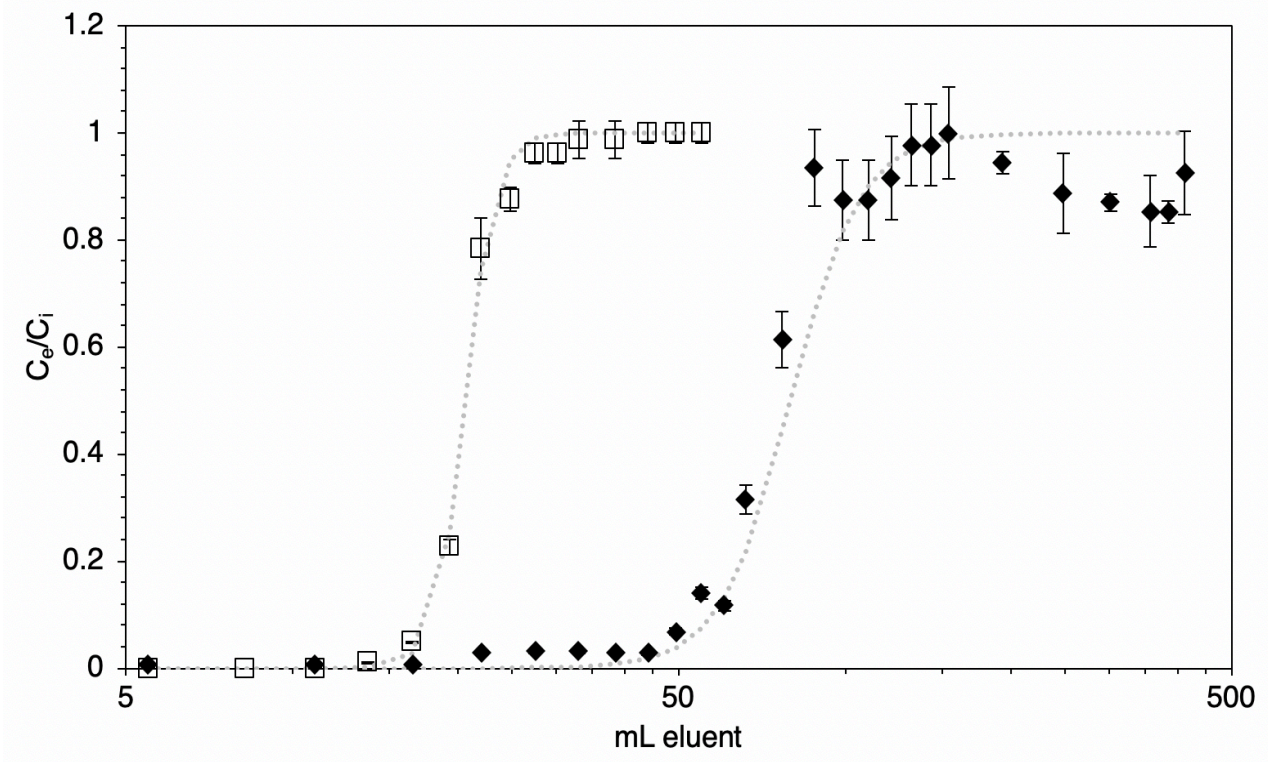

Fig. 3.8. Fluoride breakthrough profile attained by passing as-prepared leachate (◆) and NaF solution of [F^-] ~1,500 mg·L^{-1} (□) through a La-MTS9501 column. x axis is logarithmic for clarity. Dotted lines represent Dose-Response model. Resin bed volume = 6.0 mL. Flow rate = 1 BV·hr^{-1}. T = 20°C.

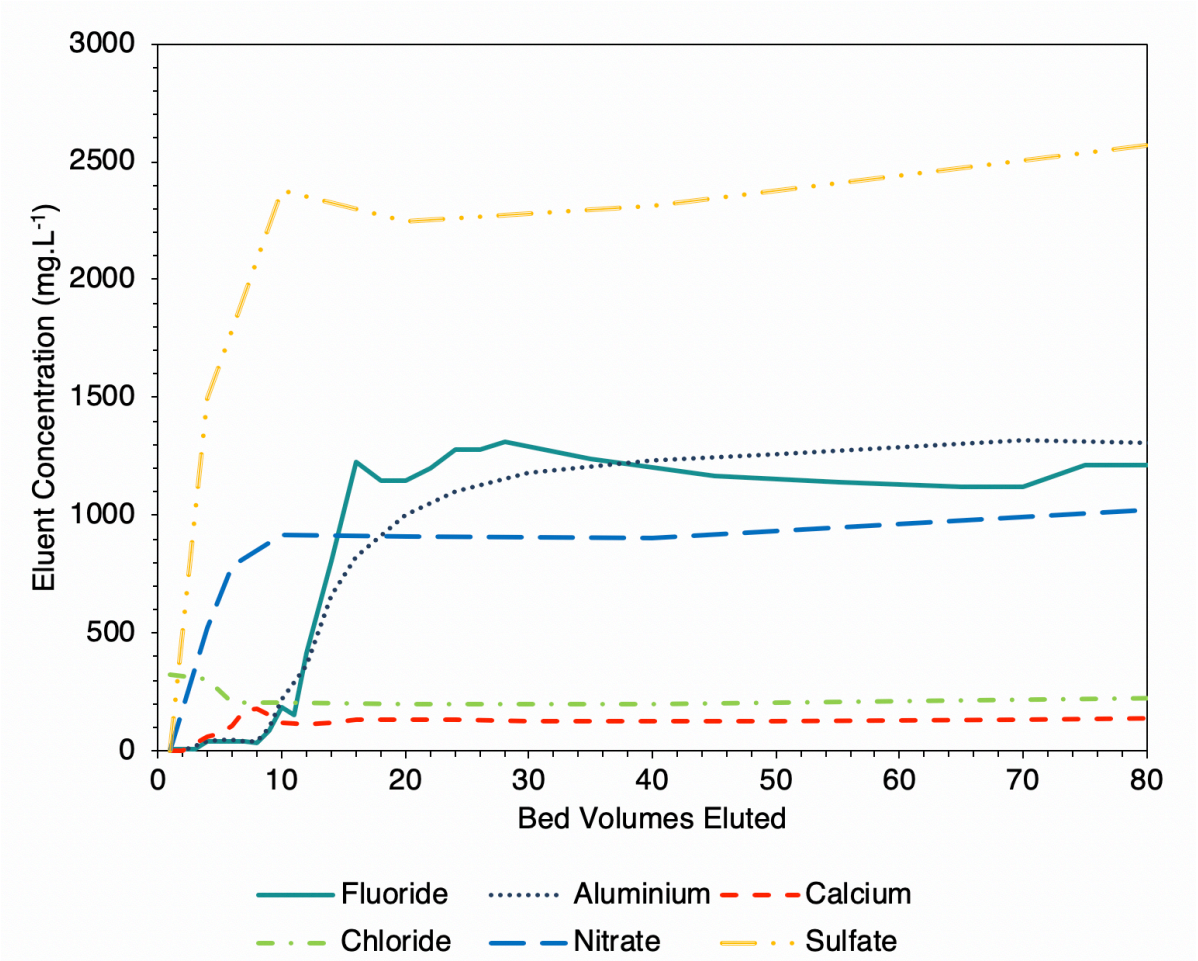

Fig. 3.9. Comparison of co-contaminant concentrations in the effluent during breakthrough experiment with as-prepared leachate. Resin bed volume = 6.0 mL. Flow rate = 1 BV·hr^{-1}. T = 20°C.

Table 3.2. Calculated parameters from Dose-Response model for the systems studied in Figures 3.5-3.9.

Experiment	**Dose-Response model parameters**			
	a	**b**	**q_0 (mg·g^{-1})**	**R^2**
Leachate 1/100 dilution (F^-)	5.35 ± 0.20	1283 ± 126	4.27 ± 0.42	0.964
Leachate as-prepared (F^-)	4.43 ± 0.21	79.6 ± 10.9	66.7 ± 9.1	0.955
Leachate as-prepared (Al)	4.78 ± 0.24	77.0 ± 7.5	26.3 ± 01.7	0.995
Leachate as-prepared (Ca)	3.02 ± 0.40	24.0 ± 5.2	1.75 ± 0.38	0.978
NaF solution ([F^-] ≈ 15 mg·L^{-1})	7.36 ± 0.30	116 ± 27	1.15 ± 0.27	0.964
NaF solution ([F^-] ≈ 1,500 mg·L^{-1})	16.0 ± 0.8	20.6 ± 2.5	20.5 ± 2.5	0.996

For uptake both from NaF solution and leachate, the Dose-Response model provided the best description of breakthrough behaviour. This model is empirical, so no assumptions about fundamental uptake behaviour can be drawn. However, as is common with other dynamic adsorption studies, the model minimises the errors produced by other models [252, 264, 265]. In particular, the Dose-Response equation produced a rather superior fit over a long period of column operation, as the R^2 value for the dilute leachate experiment (1,900 mL eluent) was 0.964 (other models: 0.939 - 0.942). We could not find any previous examples in the literature where this model has successfully been used to describe fluoride breakthrough in a column experiment. Such breakthrough has previously successfully been described by the Thomas model [266], which our results were also in

good agreement with, showing an R^2 range of 0.942 – 0.996 (Appendix B, Table B10). This is predictable, as this model was derived from second-order kinetics, which the sorbent/sorbate interaction was observed to follow in static experiments. From the generally good fits of the Thomas model, it can be concluded that, in a column environment, both free fluoride and AHF adsorption is probably rate-limited not by chemical reaction, but by interfacial mass-transfer [267]. Interestingly, the Thomas kinetic constants (k_{Th}) for leachate fluoride-breakthrough were an order of magnitude lower than for NaF solution breakthrough, which again is comparable to static work. The identical agreement of the data with the Yoon-Nelson model (the two being mathematically analogous) indicates that for both matrices, the breakthrough behaviour can be rationalised as the probability of adsorption for each fluoride ion or AHF complex being proportional to probability of adsorption verses probability of breakthrough [255]. The Adams-Bohart model, whilst being limited, in that it cannot describe the full column breakthrough process [267], was also in good agreement with some data, showing an R^2 range of 0.886 – 0.999 (Appendix B, Table B11). As a result, it is probable that the dynamic adsorption is dependent on both resin residual capacity and fluoride/AHF concentration [252].

In common with static kinetic results, q_0 values, calculated from the Dose-Response model, for the leachate were far larger than for NaF solution (Table 3.2). This suggested that an industrial resin column would work efficiently in its intended function and the superiority was observed at both high and low inlet concentration. Interestingly, in the case of as-prepared leachate, fluoride and Al breakthrough occurs within a similar timeframe, as would be expected given the proposed uptake mechanism. However, q_0 values show a higher molar ratio of F^-:Al^{3+} was taken up in the column study, which is likely because the system does not approach equilibrium, as was the case in static kinetic experiments, so there was not time for the F^-/OH^- reverse ligand-exchange reaction of the coordinated AHFs to proceed (Figure 3.6). The Ca breakthrough curve is dissimilar to Al and fluoride, indicating that Ca^{2+} ions are not similarly involved in fluoride transfer on to the resin and may instead occupy vacant phosphonic acid coordination sites. Coexisting anions NO_3^- and SO_4^{2-} were also observed to breakthrough rapidly, while [Cl^-] in the effluent exceeded that in the inlet solution for a short period. This behaviour may be due to the N atom in the AMP acid group acting as an anion-exchange site, since its deprotonation would not readily occur in these experimental conditions [268]. The counter-ion would originally have been partially Cl^-, due to the $LaCl_3$ treatment of the resin and a certain amount of exchange would be expected, given that NO_3^- and SO_4^{2-} are higher in the established anion selectivity series [115].

3.5.4. Generation of elution profiles from dynamic experiments

The full elution profiles of fluoride, Al and Ca attained from the as-prepared, leachate-loaded La-MTS9501 column are shown in Figure 3.10). A number of BVs were also analysed for pH, Cl^-, NO_3^-

and SO_4^- concentrations and the relationships between these and fluoride and cation concentrations are also shown. The equivalent elution profile for fluoride only, attained from the NaF solution-loaded La-MTS9501 column (fluoride $C_i \approx 1{,}500$ mg·L^{-1}) is shown in Figure 3.11.

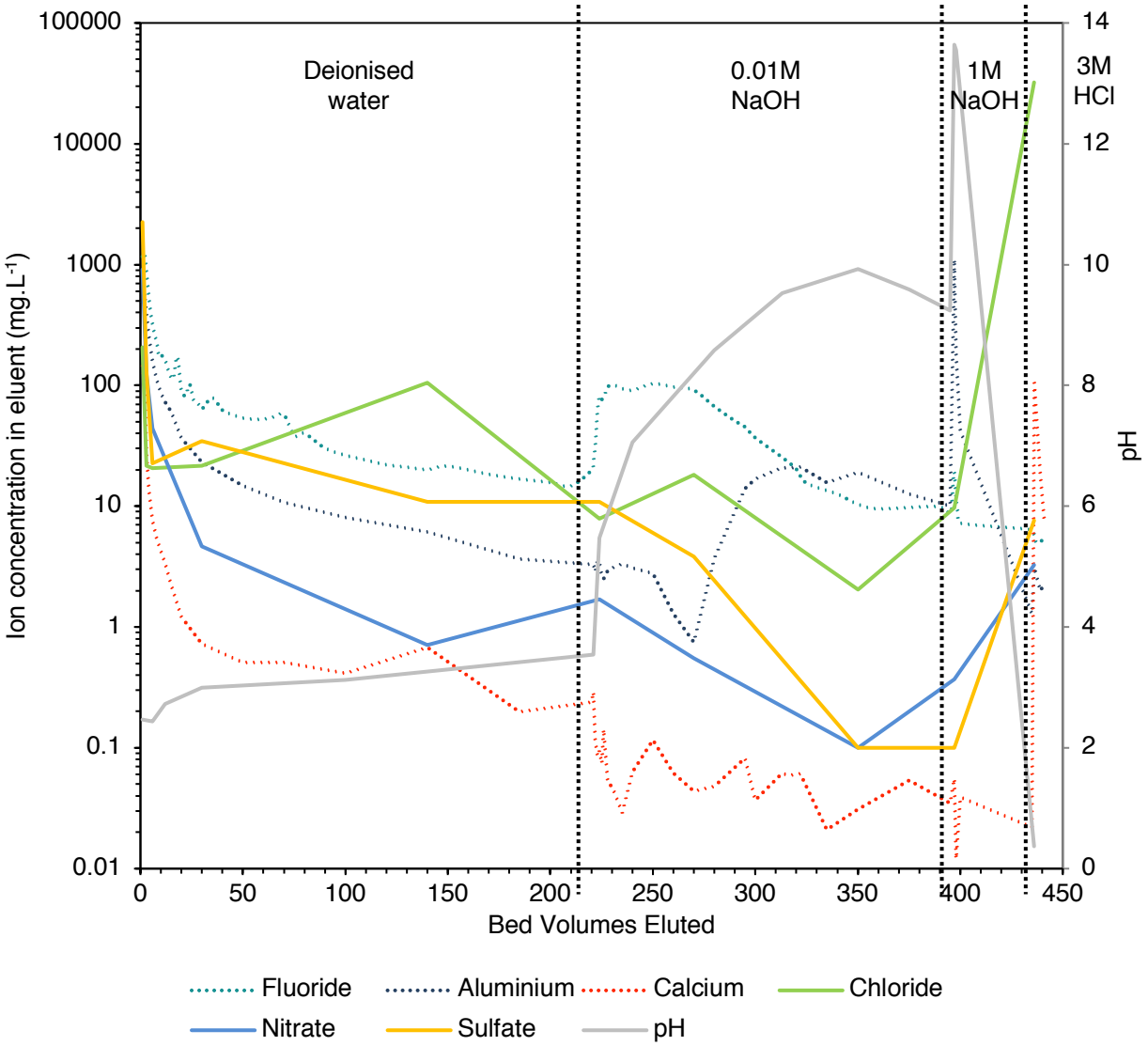

Fig. 3.10. Elution of F^-, Al, Ca, Cl^-, NO_3^- and SO_4^{2-} from leachate-loaded La-MTS9501 column. Y axis is logarithmic for clarity. Vertical lines indicate change in eluent. Resin bed volume = 6.0 mL. Flow rate = 1 BV·hr^{-1}. T = 20°C.

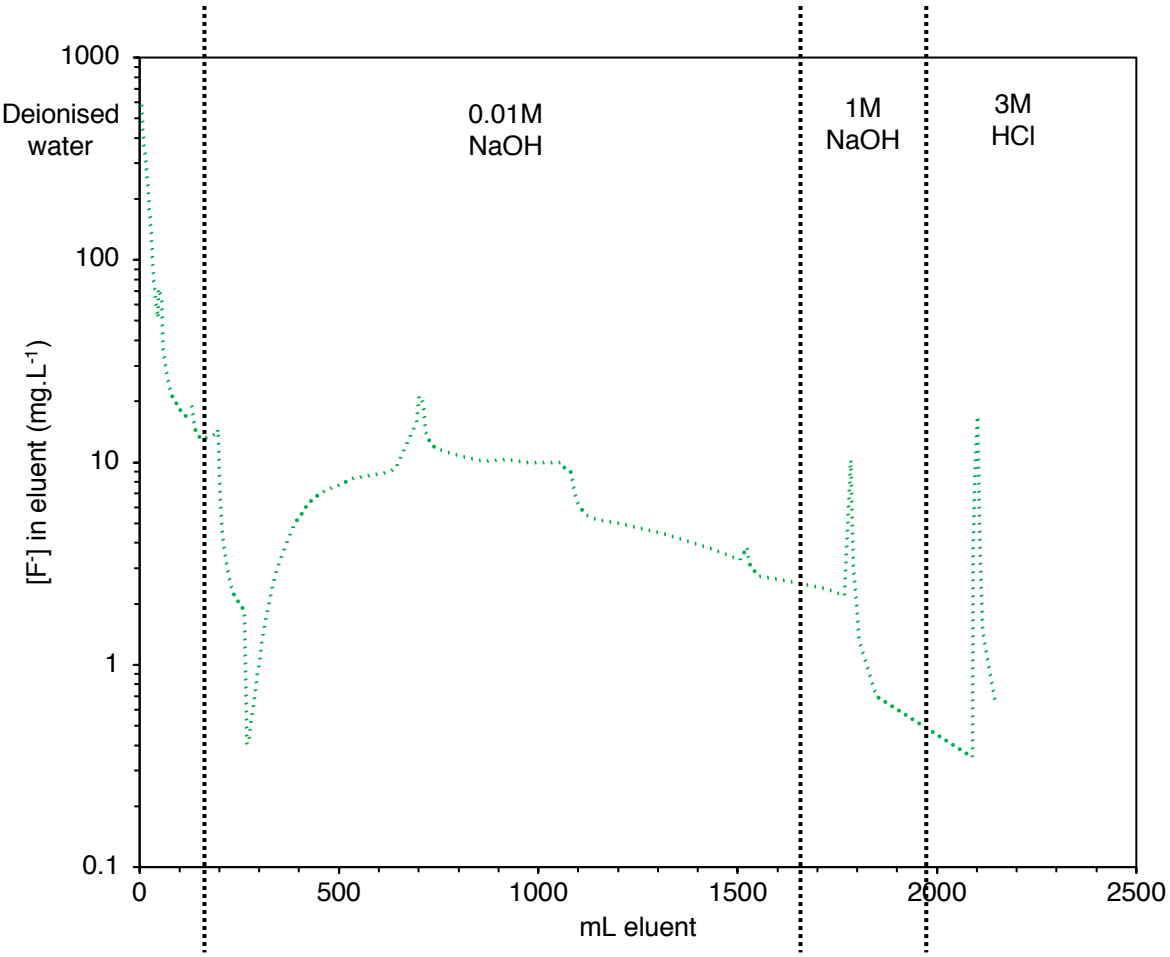

Fig. 3.11. Elution of fluoride from NaF solution-loaded La-MTS9501 column. Y axis is logarithmic for clarity. Vertical lines indicate change in eluent. Resin bed volume = 6.0 mL, flow rate = 1 BV·hr^{-1}. T = 20°C.

Fluoride % recoveries were calculated as 95.7 ± 14% for the leachate-loaded column and 87.1 ± 5.3% for the NaF-loaded column. Al and Ca % recovery were calculated as 106 ± 7% and 109 ± 12% respectively for the leachate-loaded column. This good agreement supports the validity of the Dose-Response model as a tool for predicting breakthrough behaviour for all three species.

Literature sources have reported that metal-loaded resins may be regenerated for fluoride uptake by dilute NaOH treatment [119, 132]. In this instance, for the NaF-loaded column (Figure 3.11), a significant amount of fluoride remained on the resin after the 0.01 M NaOH eluent stage and was only eluted by 1 M NaOH or even remained bound until the La-loading was removed by 3 M HCl. The majority of fluoride eluted very rapidly with deionised water as the eluent, which is likely to represent the weakly-physisorbed crystalline NaF, with elution essentially caused by the change in concentration gradient. The latter stages of the elution suggest a variety of binding sites of different strengths are present on the resin. This is consistent with previous Freundlich isotherm data, which indicated that the resin surface was heterogeneous in energy [104]. The stronger sites may be attributed to fluoride ligands which bridge between two adjacent La centres [261]. The elution peak

caused by 0.01 M NaOH is broad and shallow, suggesting that relatively concentrated NaOH may be a better choice for elution of concentrated, pure fluoride aqueous streams, for CaF_2 precipitation and recovery, since an inlet $[F^-]$ >100 $mg \cdot L^{-1}$ is required for such a process [89]. The peak is also poorly resolved and suggests a number of micro-environments, of slightly different binding energy were present. This agrees with the heterogeneity of the adsorption, proposed in our previous work [104].

The leachate-loaded column (Figure 3.10) exhibited co-elution of fluoride and Al with deionised water as the eluent. Significant fractions of both species were also eluted with NaOH. This again indicates a range of different strength binding sites. Interestingly, although the fluoride effluent concentration increases upon changing the eluent to 0.01 M NaOH, the Al effluent concentration actually falls significantly. This may be explained by a reverse ligand-exchange process, in which -F is replaced by -OH, without dissociation of the proposed binuclear coordinated complexes. The Al then appears to slowly begin to dissociate from the resin surface, before being completely removed by the change to 1 M NaOH. The eluent pH over this timeframe increases from ~6–10 and, as reported by Lisbona and Steel [78], the anionic species $[AlF_3(OH)]^-$ and $[AlF_2(OH)_2]^-$ gradually become dominant over this range in Al/F/H/O systems as pH increases. The behaviour is hence explained, as these species would be exchanged with OH^- ions on the La coordination sites and subsequently elute. The probable changes to the functional group chemistry throughout the elution process are postulated in Figure 3.12.

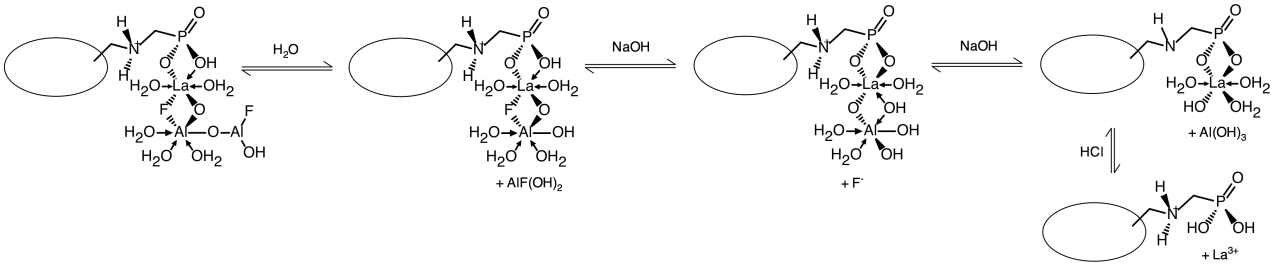

Fig. 3.12. Proposed desorption processes from leachate-loaded La-MTS9501 column with changing eluent.

As seen in Figure 3.10, the pH of the effluent did not rise above 10 until after the eluent change to 1 M NaOH. Hence it can be assumed that the functional group N atoms were not deprotonated until this point and the observed elution of Cl^-, NO_3^- and SO_4^{2-} in the early stages of the experiment was likely due to weak electrostatic interaction of the anions with a positively charged resin surface during loading [128].

3.5.5. Performance of the resin over repeated equilibrium batch cycles

The variations in approximate maximum uptake capacity of the resin over five cycles of regeneration with 0.01 M NaOH is shown in Figure 3.13. The performance of the resin was actually increased slightly, on average, over the sequence of regenerations. We may attribute this to the lesser amount

of Cl^- ions electrostatically associated with the resin surface. The concentration would be substantial during cycle 1 (directly after loading with La^{3+} as $LaCl_3.7H_2O$). Whilst acting only as an outer-sphere ligand, [269] the presence of Cl^- may cause a slight barrier to the La/AHF complexation reaction, which is removed with the NaOH treatment. The results demonstrate the feasibility of use of NaOH as the eluting agent for fluoride commodity chemicals recovery. A further advantage practically, is that the resin could be put straight back into operation, after washing with water, as the high ionic strength liquor naturally buffers the pH towards favourable fluoride uptake conditions [104]. The success of the complete regeneration with acid indicates that the resin could be restored to full effectiveness in the event of any long-term degradation caused by many cycles of NaOH treatment.

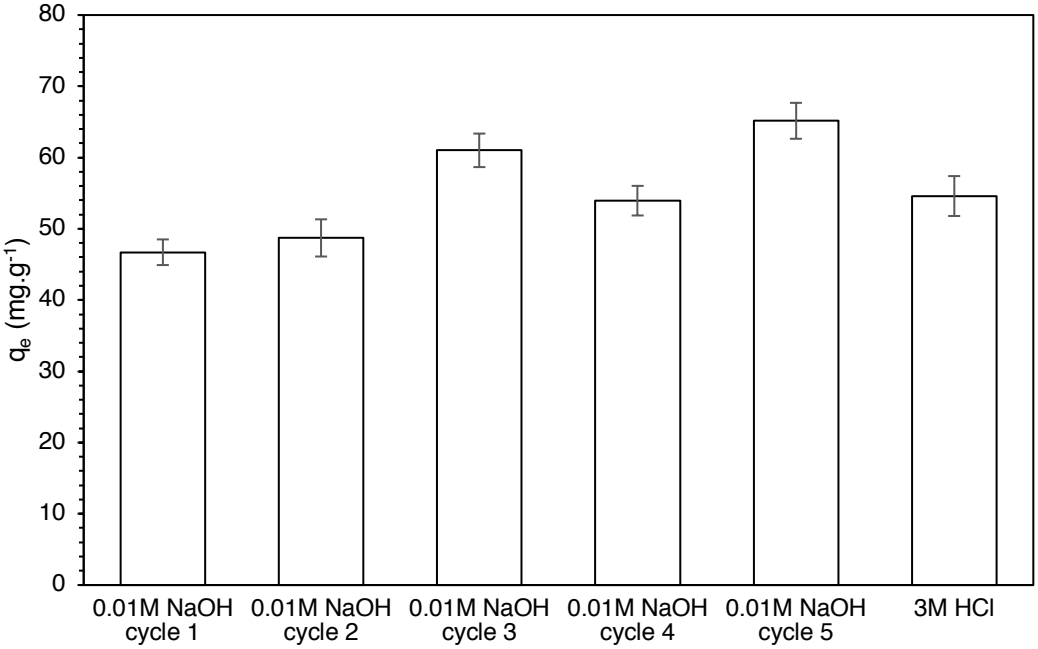

Fig. 3.13. Performance of La-MTS9501 over repeated cycles. Resin dry mass = 100 mg. Sample volume = 25 mL. Contact time = 24 hr. T = 20°C.

3.5.6. Effect of Al^{3+} on resin performance in equilibrium batch studies

The effect of the ratio of F^-:Al^{3+} in the leachate on fluoride uptake in batch experiments is shown in Figure 3.14. This ratio is strongly influential to resin performance with the mass ratio of 1.5:1 F^-:Al^{3+} being very beneficial to fluoride transfer, which is obviously close to the ratio within the SPL leachate (especially considering the small quantity of $Al(OH)_3$ precipitation observed in the preparation of the leachate). Conversely, both very low and very high [Al^{3+}] suppressed the fluoride uptake. The former may be explained by the presence of NO_3^- and SO_4^{2-}, which, as O-donors, may compete for La centre coordination sites with free fluoride, according to concentration gradient laws [270]. The latter is likely because at high [Al^{3+}], the dominant aqueous Al species will be $Al(OH)_3$ (Appendix B, Table B4) [215], which may interact with the aminophosphonic acid group in the same manner as AlF_2^+ and AlF_3. Hence minimal fluoride uptake occurs. Indeed, ICP measurements of the 500 mg·L^{-1} Al^{3+} sample solution indicated an Al q_e of 32.4 mg·g^{-1}, whereas fluoride uptake was negligible.

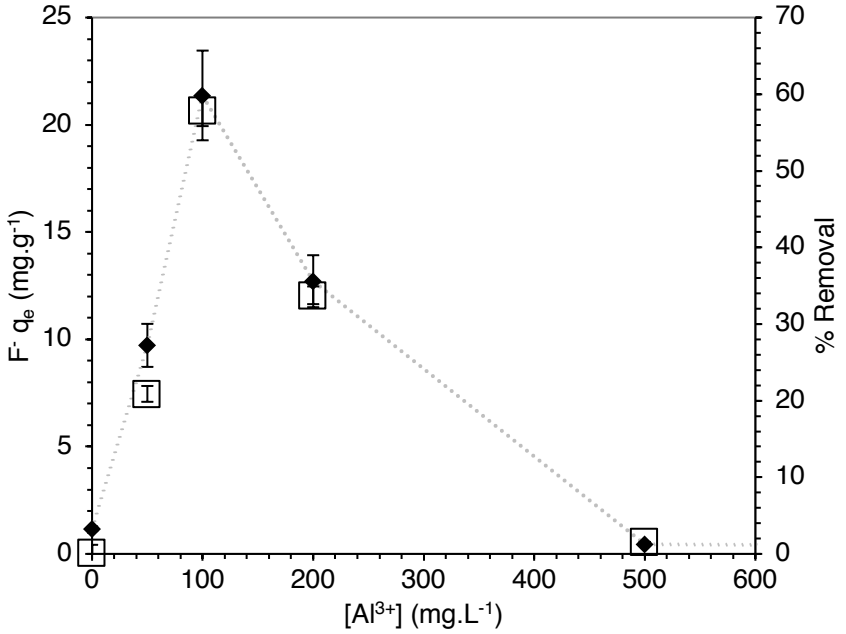

Fig. 3.14. Fluoride uptake of La-MTS9501with varying Al^{3+} concentration in the liquor. Dilution = 1/10 (initial $[F^-] \approx 150$ mg·L^{-1}. Resin dry mass = 100 mg. Sample volume = 25 mL. Contact time = 24 hr. T = 20°C. ◆ = uptake. □ = % removal.

The F^-:Al^{3+} ratio is clearly of concern from an applied perspective, as the composition of SPL and hence the derived leachate is variable, depending on smelter type and cell decommissioning process [32]. The ratio could however, be monitored by in-situ analysis of the leachate feedstock by fluoride ISE, since $[Al^{3+}]$ can be simultaneously determined [271]. The ratio may be altered by addition of Al salts. Also, primary Al production results in gaseous HF formation, which is captured by a caustic scrubbing solution. This stream could also be used for control of the ratio.

3.5.7. Pathways to recovery of commodity products from the eluent

A desirable recovery product from SPL leaching would be the AlF_3 precursor $AlF_2OH.H_2O$, which may be reacted with gibbsite ($Al(OH)_3$) and anhydrous HF to produce the desired product . However, the precipitation of $AlF_2OH.H_2O$ has been shown to require a specific F^-:Al ratio of 1.6:1 and must be achieved starting with a concentrated acidic initial solution, followed by careful raising of the pH, to avoid undesirable co-precipitation of sodium-containing species [85]. The resulting $[F^-]$ and $[Al^{3+}]$ achieved in Figure 3.10 with deionised water as the eluent would not be sufficient and an evaporation step would be required. Elution with deionised water, followed by strong acid is an option, but would lead to complete loss of La from the resin. The most feasible recovery strategy would be as follows: The column would be first eluted with deionised water, to eject the undesirable Ca and anions. As seen in Figure 3.10, the eluent produced here is still fluoride-rich and could be partially recycled back into the lead ion-exchange column after a secondary desalination treatment with a strong-base anion resin column, hence conserving the fluoride in this fraction. The eluent would then change to 1 M

NaOH, which would produce a concentrated and pure aqueous stream of Na^+, F^- and Al^{3+}. Synthetic cryolite could then be readily precipitated from this solution by lowering the pH [53, 272]. The total masses of fluoride and Al eluted during the NaOH eluent stage were 49.2 and 26.2 mg respectively (Figure 3.10). This equates to an approximate F^-:Al^{3+} molar ratio of ~2.5:1, which is feasible for cryolite precipitation [85]. Although not as valuable as AlF_3, cryolite is nonetheless a desirable commodity for Al smelting and indeed other uses outside the industry [272]. Unlike AlF_3, it does not require a calcination step after precipitation, merely requiring drying at ~40°C [240]. Al smelters have historically captured waste fluoride from the Hall-Héroult process as HF by caustic scrubbers and cryolite is attained from this feed by addition of $Al_2(SO_4)_3$ [273]. The advantage of our proposed process (aside from the effective treatment of SPL and recycling of the additional fluoride reserves within the material) is that there would already be a source of Al in the feed. The purity of the material would also likely exceed current industrial grades. Bulk cryolite purchased from merchants tends to be ~85% purity, whereas Figure 3.10 shows that the concentrations of potentially co-precipitating species (SO_4^{2-} and Ca) in the eluent are low.

3.6. Conclusions

We have investigated the kinetic and dynamic behaviour of fluoride uptake by a novel, Lanthanum-loaded aminophosphonic acid chelating resin La-MTS9501, with a view to instigating an ion-exchange treatment for the recovery of fluoride commodity products from spent potlining leachate. In kinetic tests, fluoride removal from simulant leachate was considerably greater than from NaF solutions, but uptake rate constants were slower by an order of magnitude. Both systems however, could be described by pseudo second-order kinetics. Activation energies for the uptake processes were calculated and indicated that the uptake mechanism for the leachate was a much lower energy process. This may be explained by a novel chelation interaction between resin-bound La centres and aqueous AlF^{2+}, AlF_2^+, and AlF_3 complexes, forming multi-nuclear coordination species and leading to the enhanced uptake.

In dynamic studies La-MTS9501 again demonstrated a large loading capacity, with breakthrough behaviour well-described by the Dose-Response model. This supports previous work in concluding that solutions of high initial fluoride concentration may be treated efficiently by an ion-exchange column process. Stripping behaviour for both matrices was unusual, with the loaded fluoride eluting over a number of stages with changes to the eluent. The NaF-loaded column profile was dominated by slow elution of crystallised NaF, while the leachate-loaded column profile suggested first, desorption of weakly-bound AHFs, followed by a reverse F^-/OH^- ligand-exchange process and finally dissociation of the La/AHF complexes. By studying the co-elution of contaminants and pH of the eluent, it was concluded that synthetic cryolite was a feasible recovery product for the process. Puromet™ MTS9501 is an economical sorbent and is available in industrial quantities for ~£12·L^{-1}

(~£8·kg^{-1}) and was shown in this study to perform robustly over 5 loading/stripping cycles. It is hoped that this work will contribute towards development of an optimum hydrometallurgical treatment system for spent potlining and thus contribute to preservation of global fluorspar reserves.

Notes: We refer throughout this article to the commercial resin used as "Purolite™ MTS9501". Our previous work, using the same resin refers to the material as "Purolite® S950+", which was its original commercial title. The price of the adsorbent is an approximate value, provided by an associate from the company. The price of £120 L^{-1} quoted in Chapter 2 is the retail price for an analytical quantity.

Acknowledgements

The authors thank all members of the SNUCER group, University of Sheffield, for their support of this work; in particular Dr Sarah Pepper, for ICP-OES analysis. Thanks to Mr Rob Hanson (Department of Chemistry, University of Sheffield), for TGA training. Thanks to Mr Duncan Schofield and Mr Keith Penny (Department of Chemical and Biological Engineering, University of Sheffield) for IC training. We also gratefully acknowledge Purolite® for their donation of the MTS9501 resin.

Funding

This work was supported by the EPSRC (Grant no. EP/L016281/1) and Bawtry Carbon International Ltd.

4. Characterisation and leaching of SPL waste with accompanying industrial process simulation via column studies

4.1. Overview of paper

Chapter 3 has further clarified the novel uptake mechanism of AHF complexes from simulant SPL leachate and shown that the large theoretical equilibrium fluoride capacity can indeed be translated into high efficiency in dynamic column experiments. This paper now addresses the two significant shortfalls in experimental work presented so far. The first is that the same simulant leachate was used in experiments throughout Chapters 2 and 3. Although it was a necessary measure to keep the elemental composition of the PLS constant, for the sake of corroboration between thermodynamic and kinetic data, it is of course not particularly industrially realistic. This is because, as is suggested in Chapter 1, the elemental makeup of the parent SPL would be expected to vary widely, depending on origin and the extent of separation of cuts.

The second issue is that it was not proven that an aqueous stream can be eluted from the La-MTS9501 column containing aluminium and fluoride at sufficient concentrations to make cryolite precipitation feasible. Therefore, the key process valorisation step requires further development.

The paper begins with a characterisation suite of the SPL samples received from Trimet Aluminium. This confirms the prediction made in Chapter 1 that, without careful intervention in the cell decommissioning process, the compositional variation in even a small SPL sample will be considerable. Accordingly, sub-samples are identified of predominantly first-cut and predominantly mixed-cut, to allow comparisons with a wider field of literature. Although there was some agreement with previous work in terms of major crystalline phases identified in the material (graphite, cryolite and diaoyudaoite), there were some interesting anomalies. For example, silicon carbide and sodium silicate hydrate have not been reported before in SPL samples. Also, alumina was not detected. This further confirms the variations in the incoming wastestream that might be expected in a hydrometallurgical SPL treatment plant and underlines the magnitude of the SPL challenge.

The choice of lixiviants (NaOH, then H_2SO_4) essentially does not deviate greatly from the LCLL process. The [NaOH] was 1 M verses 0.75 M. No information was available on the exact concentration of H_2SO_4 used in the LCLL process. However, this paper usefully demonstrates that relatively mild conditions (1 M NaOH and 0.5 M H_2SO_4) appear to successfully solubilise the hazardous contaminants of the waste, not only fluoride, but also a number of heavy metals, to the same degree as the harsher treatments outlined in Chapter 1. As might be predicted, the resulting combined leachate was more complex than the simulant PLS, with a high Si concentration that was not previously accounted for. Furthermore, the sulfate concentration was an order of magnitude higher than in previous work and the F^-/Al^{3+} ratio rather higher. The proportion of fluoride solubilised by the alkaline leach only was surprisingly high (>95%, whereas 70-90% was expected from the

literature). This may be due to the oxidising potential of the H_2O_2, which was included as an essential safety precaution against labile cyanide.

The La-MTS9501 column performs with an efficiency considerably above expectations. The calculated total dynamic uptake capacities of 31.7 and 37.6 $mg \cdot g^{-1}$ were lower than the figure of 66.7 $mg \cdot g^{-1}$ reported in Chapter 3. However, as has been seen throughout the experimental chapters, the efficiency of the resin, in terms of static and dynamic q_{max}, is essentially dependent on the fluoride and aluminium concentrations in the leachate. In this case, the inlet fluoride concentration was <30% of the concentration of the PLS in Chapter 3, yet the dynamic q_{max} values were ~50% in comparison, despite more challenging conditions. Interestingly, the kinetics of column breakthrough are affected by the higher ionic strength of the leachate, causing breakthrough to occur in two discrete stages and requiring modification of the modelling. This however usefully reveals the heterogeneous nature of the adsorption of the AHFs discussed in previous chapters. Importantly, the resin is efficient in uptake from a feed solution of both high and low F^-/Al^{3+} ratio. This parameter appears to have less significance to column operation than was suggested in Chapter 3. The key progression is in the column elution experiment. Here, the choice of eluents was changed from Chapter 3, resulting in well-resolved, chromatographic peaks for fluoride and Al. Hence, if the correct eluting fractions are conserved, the resulting solution is greatly enriched in fluoride and Al concentration (and almost free of cocontaminants) compared to the inlet. There are undoubtedly still barriers to implementing the system industrially. Removal of Si from the outlet would be necessary, as it would likely interfere with cryolite recovery. Also, a significant fluoride fraction is washed from the column by initial elution with water, along with numerous cocontaminants and a secondary recycling process would be desirable to ensure its recovery. Nonetheless, there are feasible methods described to circumvent these problems and the groundwork is laid for the next step of the intended process, this being the precipitation of cryolite and completion of the fluoride-recovery loop.

This paper was submitted to *Waste and Biomass Valorization* on 8 August 2019, resubmitted in revised form on 31 December 2019 and accepted for publication on 3 February 2020 (doi.org/10.1007/s12649-020-00954-1).

Note:

An addition has been made to this chapter in the form of a technicoeconomic assessment of the proposed adsorption process. This was not included in the version of the research article, due to being outside the scope of the journal. The additional text is italicised for clarity and it should be noted that no part of the assessment has been peer-reviewed.

4.1.1. Author contributions

Thomas J. Robshaw. Experimentation and manuscript writing

Keith Bonser. Funding and manuscript writing support (Al industry technicoeconomics)

Glyn Coxhill. Funding and manuscript writing support (Al industry technicoeconomics)

Dr Robert Dawson. Pastoral support

Dr Mark D. Ogden. Experimentation oversight and manuscript review

"Development of a combined leaching and ion-exchange system for valorisation of spent potlining waste"

Thomas Robshaw[a]*, Keith Bonser[c], Glyn Coxhill[b], Robert Dawson[c] and Mark D. Ogden[a]

*Corresponding author address:

[a] Separations and Nuclear Chemical Engineering Research (SNUCER), Department of Chemical & Biological Engineering, University of Sheffield, Sheffield, S1 3JD, United Kingdom.

[b] Bawtry Carbon International Ltd., Austerfield, Doncaster, DN10 6QT, United Kingdom.

[c] Department of Chemistry, University of Sheffield, Sheffield, S3 7HF, United Kingdom.

4.2. Abstract

This work aims to contribute to addressing the global challenge of recycling and valorising spent potlining; a hazardous solid waste product of the aluminium smelting industry. This has been achieved using a simple two-step chemical leaching treatment of the waste, using dilute lixiviants, namely NaOH, H_2O_2 and H_2SO_4, and at ambient temperature. The potlining and resulting leachate were characterised by spectroscopy and microscopy to determine the success of the treatment, as well as the morphology and mineralogy of the solid waste. This confirmed that the potlining samples were a mixture of contaminated graphite and refractory materials, with high variability of composition. A large quantity of fluoride was solubilised by the leaching process, as well as numerous metals, some of them toxic. The acidic and caustic leachates were combined and the aluminium and fluoride components were selectively extracted, using a modified ion-exchange resin, in fixed-bed column experiments. The resin performed above expectations, based on previous studies, which used a simulant feed, extracting fluoride efficiently from leachates of significantly different compositions. Finally, the fluoride and aluminium were coeluted from the column, using NaOH as the eluent, creating an enriched aqueous stream, relatively free from contaminants, from which recovery of synthetic cryolite can be attempted. Overall, the study accomplished several steps in the development of a fully-realised spent potlining treatment system.

4.2.1. Graphical Abstract

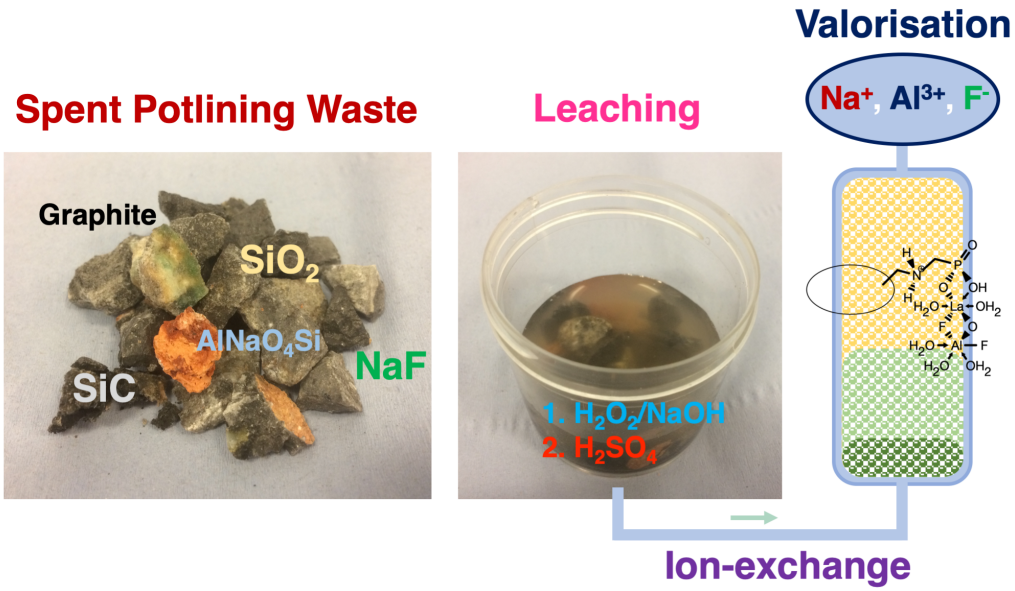

4.2.2. Keywords and Statement of Novelty

Spent potlining, leaching, ion-exchange, fluoride, aluminium, resource recovery

This research aims to address the issue of spent potlining (SPL) recycling in the primary aluminium industry. SPL is a hazardous waste product formed on a MT annual scale, yet also an important valorisation opportunity, being rich in valuable fluoride. Our work is unique in integrating an ion-exchange step into a chemical leaching system. It is a rare example of targeted contaminant removal and recovery from a real hazardous industrial aqueous stream and it is an unprecedented use of a commercial ion-exchange resin. We believe this work will be of interest not only to technical persons within the aluminium industry, but also the broader fields of hydrometallurgy, adsorption and general solid waste treatment.

4.3. Introduction

Spent potlining (SPL) is a hazardous waste product of aluminium smelting operations, which is generated at the end of the lifespan of a smelter electrolysis cell. There are two distinct fractions, these being “first-cut”, composed mainly of graphitic material from exhausted cathode blocks, and “second-cut”, formed mainly of cement and brick. Both cuts are heavily contaminated with fluoride-bearing compounds, with reported fluoride concentrations ≤20% [32]. Various other chemical species are also present, including ≤1% cyanides [33]. Estimates for the average mass of SPL generated per tonne of aluminium produced vary between 7 and 50 kg [72], but an average of ~25 kg is frequently given [56, 60]. The estimated global production of aluminium in 2018 was 64.3 MT, meaning ~1.61 MT of SPL was also created [18]. Of this, it is estimated that 50-75% of the waste was deposited either in landfill facilities or over-ground buildings [32, 274].

Hazardous waste status has been conferred on SPL in a number of countries, due to its leachable fluoride and cyanide components and potential to evolve flammable mixtures of ammonia, methane and hydrogen gases [60, 275]. A number of utilisation strategies have been developed for the waste: SPL may be added to cement clinker kilns, to improve firing conditions [58]. It can be partially substituted for fluorite (CaF_2) in Arc furnaces for steelmaking [276], or used as an additive in pig iron and rock wool production [63, 277]. The issue with all such employments is that only relatively small amounts of SPL may be used, otherwise process complications ensue [36, 58]. Accordingly, various detoxification systems for SPL are also in use, with the goal of converting the waste to an environmentally-benign form. Most are pyrometallurgical, taking advantage of the high chemical energy value of SPL, which has been reported as $\leq$16 $MJ \cdot g^{-1}$ for first-cut samples [64]. The waste may be combusted [65], or sintered with cement and bauxite [38]. This volatilises a fraction of the SPL fluoride content as HF, which can be captured by a scrubber, and recycled [38, 65]. These however cause the emission of CO_2, which must either be captured or released into the atmosphere. The only operational hydrometallurgical process is the low caustic leaching and lime (LCLL) method developed by Rio Tinto Alcan. This has a throughput capacity of 80,000 $T \cdot yr^{-1}$ and produces an inert carbon/cement mixture, which can be used as an aggregate for building, and fluorite, which can be reused by smelters [50].

The LCLL process recovers the fraction of fluorides which are water- and caustic-leached from SPL. Lisbona *et al.* however, showed that many fluoride compounds remain within the SPL matrix after these stages [37]. Fluoride is rapidly becoming a scarce resource, as the only major natural reserves are in the form of geological fluorite, of which there are <53 years-worth remaining globally. Fluorite has been classified as a “critical” mineral by the European Union for future conservation since 2014 [17] and its market price is on a long-term upwards trend [241]. Therefore, there is a clear impetus for a more efficient hydrometallurgical treatment, which will solubilise and moreover, *recover* a greater fraction of the fluoride content of SPL.

A number of different leaching treatments for SPL have been researched. Only a very small number of single-step treatments have been proposed, one using chromic acid as the lixiviant [80]. This reduced the fluoride content in the solid output to <150 $mg \cdot kg^{-1}$, but an estimated 10-11% alumina (Al_2O_3) remained in the waste. Al^{3+} salts, in acidic conditions, have also been favoured as lixiviants [37]. The advantage of this approach is that an aluminium hydroxyfluoride (AHF) hydrate product can be precipitated from the leachate, which may then be converted to AlF_3 and recycled directly back into aluminium smelters [85]. However, it has thus far achieved only 76–86% fluoride extraction [78, 84]. Dilute caustic leaching has also been investigated and found to extract 70–90% of the total fluoride content of SPL [82]. More recently, caustic leaching has been enhanced by ultrasonication

techniques, as shown by Xiao *et al.* [79]. This technique has afforded a solid residue of ≤94.7% carbon. It should however be noted that the SPL used in this study was first-cut material only and the majority fraction of SPL excavated from decommissioned smelter cells is a mixture of first- and second-cut [37]. It is generally recognised that multi-step leaching is required to reduce the concentrations of fluoride and other contaminants in the solid residue to a level safe to landfill [50, 53]. Shi *et al.* used leaching conditions of 2.5 M NaOH, then 9.7 M HCl, both at 100°C, attaining carbon of 96.4% purity [53]. Li *et al.* achieved a carbon purity of 95.5% after a leaching treatment using first, deionised water and second, acidic aluminium anodizing wastewater [72]. However, the SPL used in the instance was again first-cut in origin. The residual fluoride concentration in the carbon residue was also not reported. Neither previous study addressed the issue of labile cyanide destruction in the leachate. It is arguably necessary, from an environmental and economic perspective, that an optimum treatment system should recover close to 100% of the trapped fluorides within SPL waste. It should furthermore deal effectively with all grades of the waste, rather than a selected fraction.

Our research group has conceptualised a treatment system, capable of dealing with all SPL cuts (Figure 4.1). It aims to mobilise >95% of fluoride-bearing contaminants via a two-step leach. The two leachate streams are then combined, whilst ensuring minimal precipitation, producing a liquor of high ionic strength. This however is likely too complex to afford recovery of commodity chemicals of high purity by precipitation. This is seen in the fact that the fluorite currently produced by the LCLL process, which is procured by leaching the SPL with only water and NaOH, achieves a purity of ≤87% [50]. Therefore, an ion-exchange step must be introduced, to immobilise the fluorides selectively upon a solid-phase extractant, allowing potential co-precipitating species to elute. The fluorides are then themselves eluted as an analytically pure and concentrated solution, from which precipitation of high-purity output commodities should be possible. A lanthanum-loaded, chelating, weak acid cation-exchange (WAC) resin was chosen for this purpose. The chemical functionality, modification and uptake behaviour has been reported in previous work and is beyond the scope of this study. However, key information is seen in Appendix C, Figures C1–C2. The adsorbent has extracted fluoride from a simulated SPL leachate with an efficiency of 126-145 $mg \cdot g^{-1}$ (depending on thermodynamic model used) via a unique complexation reaction between La centres and aqueous aluminium hydroxyfluorides (AHFs) [104]. It was also observed to load efficiently in simulated industrial conditions using a mini resin column [105]. We were able to elute a solution of aluminium and fluoride ions, relatively free of cocontaminants, from which it was calculated that synthetic cryolite (Na_3AlF_6) was a viable recovery product. Cryolite is the major component of the Al electrolysis bath. Modern smelter technology has led to improved recycling techniques in recent years, with some sources stating that bulk cryolite purchases are not necessary for the most efficient

plants [51]. Nonetheless, the market price of synthetic cryolite is projected to remain high in the medium-term, due to the ever-increasing demand for Al metal, and is consistently higher than that of fluorite [55].

Hence, the major novelty and improvement of our proposed system over existing technology is that almost all of the SPL fluoride content is valorised, rather than merely a small fraction. It therefore has the potential to not only contribute towards efficient fluoride recycling, but also add economic value to Al smelting operations.

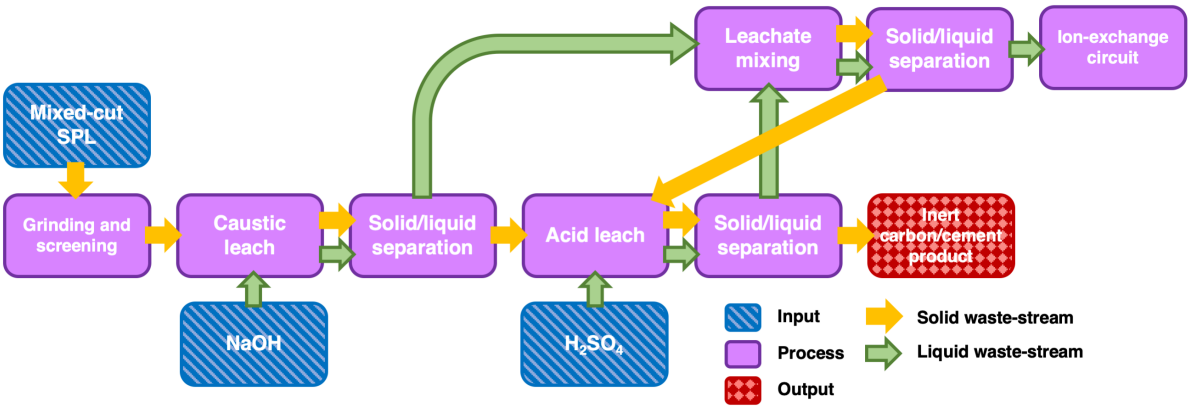

Fig. 4.1. Simplified flow diagram showing the leaching side of the proposed SPL treatment system.

It must be noted however, that the elution behaviour of our column system was not optimised and it is vital to prove that the ion-exchange system performs equivalently in treating actual SPL leachate, as opposed to a simplified simulant solution. This article presents a simple, rapid leaching treatment of mixed-cut SPL, which is often eschewed in favour of the less challenging first-cut fraction. The system is based on the principles of the LCLL process, consisting of first, NaOH/peroxide, then H_2SO_4 leaching, at mild concentrations and temperatures. We present characterisation of the SPL waste before and after leaching, showing the efficacy of the treatment. The leachates themselves are also characterised in detail, with attention paid to their anionic make-up, which is a feature inadequately documented in the literature so far. Finally, we demonstrate the feasibility of the proposed ion-exchange circuit implementation via column loading and elution studies. These show that resin uptake performance and the quality of the resulting fluoride/Al-rich liquor actually exceeds results achieved previously with a simulant feed and marks a clear step towards realisation of this system industrially.

4.4. Experimental

4.4.1. Materials and Reagents

Mixed-cut SPL, of various grades and ages, was kindly provided by Trimet Aluminium (Essen, Germany). All purchased reagents were of analytical grade or better. Deionised water was used

throughout. H_2SO_4 and H_2O_2 (30% aqueous solution) were purchased from Sigma Aldrich. NaOH pellets were purchased from Fisher Scientific. Puromet™ MTS9501 was kindly donated by Purolite and converted into La-loaded form (which will be referred to as La-MTS9501) by the procedure previously reported [104].

4.4.2. Preparation of SPL prior to leaching treatment

The as-received SPL ranged from a fragment size of fine powder to pieces ≤5 cm in diameter. The larger pieces were fed into a jaw crusher to be reduced in size. The fractions of each sample were then separated, by sieving, into three grades, these being >9.51 mm (3/8 inch), 1.18-9.51mm and <1.18 mm. Three different samples, which will be designated as A, B and C henceforward, were identified by visual inspection as having significantly different ratios of cementious to carbonaceous material (Appendix C, Figure C3), thus representing reasonable limits of material that could be provided for processing. Previous research has shown that a particle size of ~1.18 mm represents the threshold, below which, leaching treatments are generally not more effective (i.e. further crushing to a smaller particle size does not afford greater fluoride solubilisation) [37]. Therefore, the smaller two grades for samples A, B and C were carried forward to the chemical leaching trials.

4.4.3. Solid-state characterisation of materials

For powder X-ray diffraction (PXRD) spectroscopy and scanning electron microscopy (SEM) analysis, SPL samples, at various process stages, were ground with a mortar and pestle, inside a glove bag. PXRD was performed using a Bruker D2 phaser, with diffractograms matched using the ICDD database [220]. SEM samples were mounted onto Al stubs, using carbon tape and were analysed, without any coating treatment, using a Jeol JSM6010 microscope. Quantification of C, H, N and S for leached samples was performed using a Perkin Elmer 2400 CHNS/ 0 Series II Elemental Analyzer.

4.4.4. Leaching treatment of SPL

All leaching treatments were performed at ambient temperature (~20°C) inside a fume hood. In a typical caustic leaching experiment, 5.0 g SPL was weighed into a large polypropylene beaker, fitted with a large magnetic stirrer. A 100 mL solution of NaOH at pH 11.0, including 10 mL H_2O_2 was added and the suspension was stirred at 200 rpm for 3 hr. In initial studies, the complete oxidation of cyanide was checked using ion chromatography (IC), which is described in section 4.4.5. After this time, the NaOH concentration was increased to 1 M and the total volume to 250 mL. Leaching proceeded for a further 3 hr, after which the suspension was gravity filtered. The leachate was conserved for analysis and subsequent ion-exchange studies. The solid residue was briefly rinsed with 250 mL water, then dried in an air-flow oven at 50°C for a minimum of 24 hr, before being

conserved for future experimentation. In a typical acidic leach, 5.0 g SPL was again weighed into a large polypropylene beaker, with stirrer. To this was added 250 mL 0.5 M H_2SO_4 and the suspension was stirred at 200 rpm for 3 hr. Similar separation procedures to the caustic leach were then used. The solid:liquid ratio was chosen based on the efficiency reported by previous researchers [37, 84] and the aim to match the resulting [F^-] and [Al^{3+}] with the simulant leachate used in previous work. The rinsing water used between leaches was analysed for fluoride and cocontaminant concentration. However, levels were found to be insignificant compared to caustic and acidic leachate and this water was not conserved. In some experiments, small "thief" samples (100 μL) of the progressing leachate were removed from the beaker at various time intervals during the leaching, to allow the increasing fluoride concentration to be monitored. The volume of leachate removed did not exceed 1% of the total.

4.4.5. Characterisation and mixing of leachates

The majority of elemental quantification was achieved by inductively-coupled plasma mass spectroscopy (ICP-MS), using an Agilent 7500CE spectrometer by diluting samples appropriately in a 1% HNO_3 matrix (Trace Select grade). Anions were quantified using a Metrohm 883 Basic IC plus IC system, fitted with a Metrosep A Supp 5- 4 x 150 mm column and using Na_2CO_3/$NaHCO_3$ eluent. Samples were diluted appropriately with deionised water. Fluoride was also quantified by potentiometry, using a Sciquip ion-selective electrode (ISE), using total ionic strength adjustment buffer (TISAB) solution. A number of samples were cross-measured by both methods during data collection and results were consistently in agreement within 2%.

Acidic and basic leachates were combined by pipetting appropriate volumes into polypropylene vials, followed by any necessary pH adjustment, using H_2SO_4 or NaOH. Any precipitates were collected by vacuum filtration of the suspension through a sintered glass funnel, followed by drying of the solids via air-flow oven as previously described. Precipitates were characterised by PXRD, as previously mentioned. Theoretical aqueous speciation data was determined using the Aqion computer programme [215]. Concentrations of each species were inputted to the programme, according to ICP-MS and IC data. Charge balance was achieved by adjusting [Na^+] or [SO_4^{2-}].

4.4.6. Fluoride uptake by La-MTS9501 and elution in fixed-bed column studies

La-MTS9501 resin (5.50 mL wet settled volume, 1.79 g dry mass) was packed into a miniature polypropylene column, fitted with porous frits above and below the resin bed. This was connected, as a reverse-flow system, to a Watson Marlow 120U peristaltic pump, using Watson Marlow Marprene® tubing (0.8 mm internal diameter) A photograph of the set-up is shown in Appendix C, Figure C4. The system was calibrated over a period of 24 hr to give a flow rate of 1.00 bed volume

(BV) per hr (BV = an equivalent volume of inlet solution to that of the mass of the resin bed). The combined leachates were thus passed through the resin column. Eluent was collected in 0.5 BV fractions and analysed for fluoride concentration, via ISE. A number of common dynamic breakthrough models were used to attempt to describe the data (Chapter 3, section 3.4.6). For elution experiments, the loaded resin bed was connected, as before, to an inlet stream of deionised water, followed by 1M NaOH. Eluent was collected and analysed for fluoride concentration as before. Certain fractions were also analysed for Al and selected other elements, via ICP-MS and IC, as previously described. The % recovery of fluoride from the inlet leachate was estimated by calculating the area under the major fluoride elution peak and dividing this by the theoretical uptake capacity of the column, determined from dynamic model-fitting.

4.5. Results and Discussion

4.5.1. Solid-state characterisation

The elemental analysis results for the full range of samples and size fractions is presented in Table 4.1.

Table 4.1. Mass % of C, H, N and S of SPL samples at various process stages, determined by elemental analysis.

Leaching treatment	Sample	Elemental composition (mass %)			
		C	H	N	S
None	A <1.18 mm	6.73	1.16	< 0.01	0.41
None	A 1.18-9.51 mm	4.26	0.73	< 0.01	< 0.1
None	B <1.18 mm	17.52	1.07	< 0.01	< 0.1
None	B 1.18-9.51 mm	7.53	2.27	< 0.01	< 0.1
None	C <1.18 mm	54.71	0.58	< 0.01	< 0.1
None	C 1.18-9.51 mm	33.73	1.11	< 0.01	0.41
Caustic	A <1.18 mm	7.25	0.67	< 0.01	0.26
Caustic	A 1.18-9.51 mm	1.67	0.39	0.01	0.18
Caustic	B <1.18 mm	28.01	0.85	0.12	0.17
Caustic	B 1.18-9.51 mm	19.47	0.69	1.38	0.16
Caustic	C <1.18 mm	78.31	0.41	0.24	0.20
Caustic	C 1.18-9.51 mm	76.42	0.31	0.40	0.20
Caustic + acidic	A < 1.18 mm	7.26	0.57	0.01	0.14
Caustic + acidic	A 1.18-9.51 mm	2.98	0.48	0.02	0.26
Caustic + acidic	B < 1.18 mm	66.06	0.35	0.18	0.50
Caustic + acidic	B 1.18-9.51 mm	27.57	0.33	0.01	0.36
Caustic + acidic	C < 1.18 mm	88.27	0.27	0.19	0.32
Caustic + acidic	C 1.18-9.51 mm	87.21	0.25	0.56	0.36

From the elemental composition of the leached samples, it is seen that the C % of the SPL increases for mixed-cut and mainly first-cut samples, following the acidic leach, as more contaminants are solublised. The H % also decreases significantly for most samples between the leaching treatments, which may suggest the original material contained an organic hydrocarbon component, which dissolves during the treatment (also suggested in PXRD spectra by the amorphous region). The N % is very inconsistent across all samples and the S % actually increases slightly, following the acidic leach, which is likely due to residual SO_4^{2-} not entirely removed by the final water wash. Notably, the C % was always greater in the smaller size fraction, across all samples, but the difference was only

consistently very large in the case of sample B. It would not be possible, for example, to separate the carbonaceous and cementious fractions effectively on the basis of size exclusion. The attained carbon purity for our first-cut samples is slightly lower that reported in some previous work (>90%) [53, 72]. However, since the proposed treatment is designed for mixed-cut SPL, this parameter is of lesser significance. The separation of first-, second- and mixed-cut SPL is a crude process, employing pneumatic hammers to break up the material [30]. Therefore, the quality of separation varies, depending on the individual smelter.

The attained PXRD diffractograms, as expected, showed a large variety of crystalline species in the untreated SPL samples and substantial variation in the amount of mineral contamination between the three samples, relative to their graphitic content (Figure 4.2). In the mixed-cut samples, there was also an amorphous component, which is believed to be closely related to $NaAlSi_3O_8$ (albite) [31]. After the caustic leaching treatment, some crystalline species were absent or obviously reduced in concentration in the diffractograms, but only the full leaching process returned diffractograms that showed principally graphite and only trace levels of contaminants. The effect of the leaching treatment is shown in Figure 4.2. The full array of diffractograms may be seen in Appendix C, Figures C9-C22.

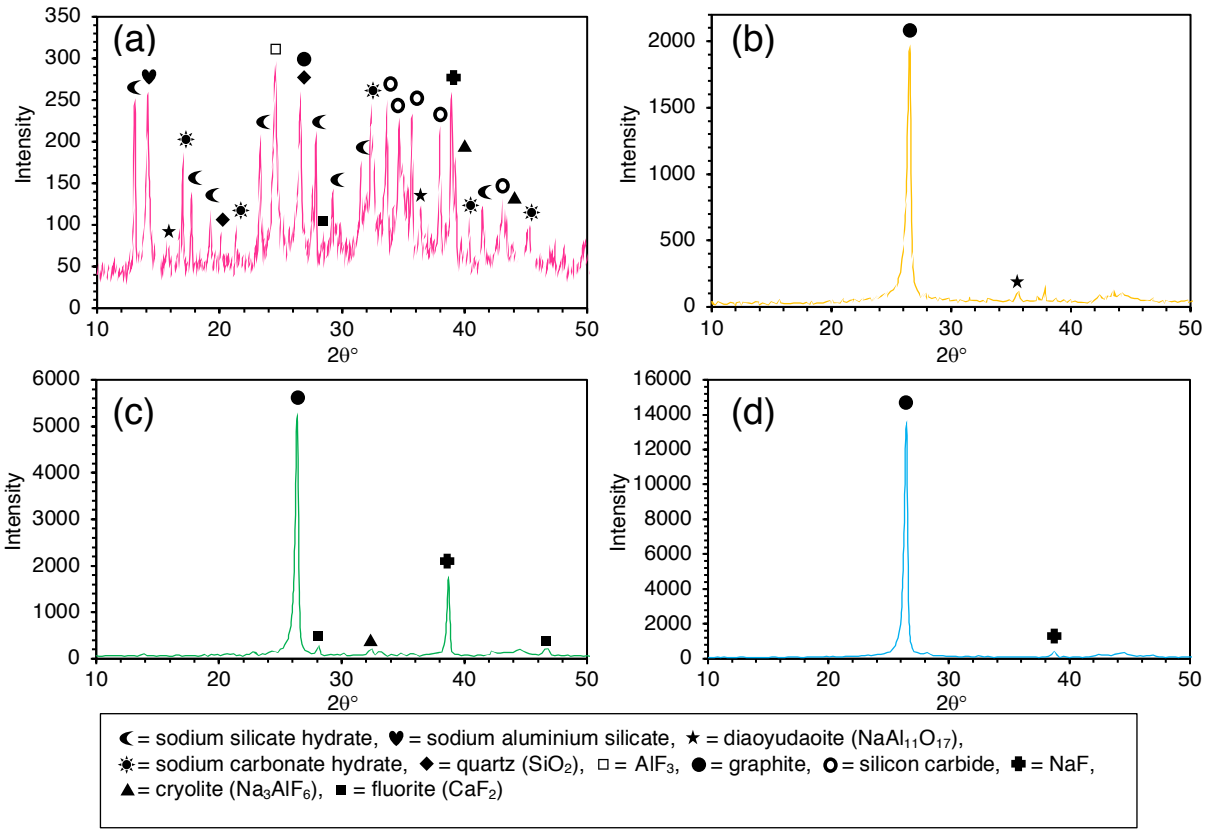

Fig. 4.2. Selected PXRD spectra of SPL samples: **(a)** sample B 1.18-9.51 mm as received, **(b)** sample B 1.18-9.51 mm after full leaching treatment, **(c)** sample C 1.18-9.51 mm as received, **(d)** sample C 1.18-9.51 mm after full leaching treatment.

Compared to previous SPL characterisation attempts, sample C appeared to be relatively free of contamination, with NaF being the only significant species present, apart from graphite. Li *et al*. reported a similar XRD spectrum, for first-cut SPL, to Figure 4.2c [72]. Other researchers have reported high levels of alumina (Al_2O_3), fluorite, cryolite and diaoyudaoite in first-cut material [37, 53]. There have been few attempts to characterise second- or mixed-cut SPL by PXRD, with the exception of Tschope *et al*. [278], who did not find evidence of sodium carbonate hydrate or silicon carbide (SiC). However, the species observed in this instance are predictable, given the known components of a smelting cell. Portland cement and fire brick would be expected to contain a large SiO_2 component [279], whilst the sidewall bricks of a smelting cell can be made entirely of SiC, depending on design [205].

Selected SEM data is seen in Figure 4.3. Again, the full set of micrographs may be viewed in Appendix C, Figures C23-C25. The elemental composition of the material, determined by point EDX analysis in the regions denoted with Greek symbols, is shown in Table 4.2.

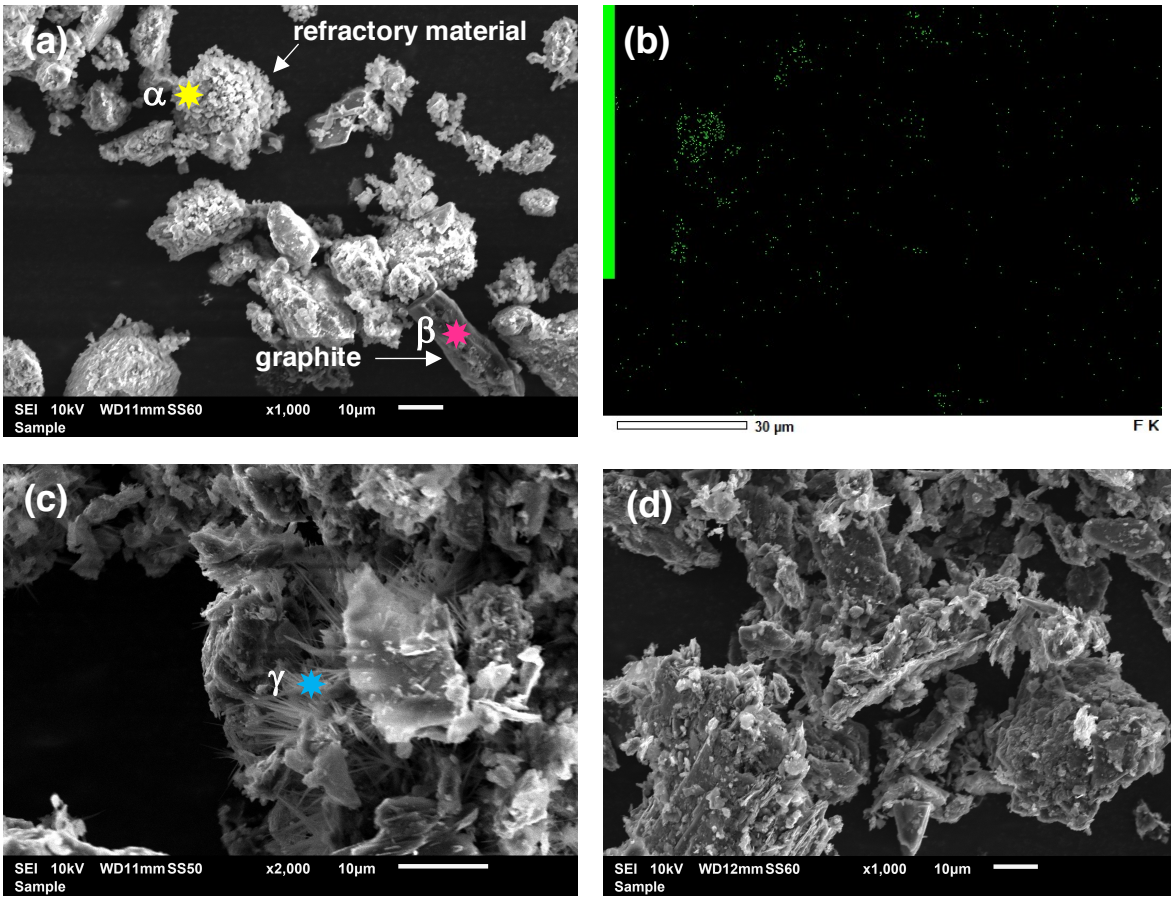

Figure 4.3. SEM images of SPL samples: **(a)** sample A <1.18 mm as received, **(b)** sample A <1.18 mm as received EDX fluorine mapping, **(c)** sample C <1.18 mm as received, **(d)** <1.18 mm after full leaching treatment. α, β and γ symbols denote areas in which point EDX analysis was performed.

Table 4.2. Point EDX analysis of selected regions of SPL samples from SEM images.

Region	Element	Mass %	Atomic %	Sigma	Line
α	O	23.5	31.4	5,050	K
	F	9.60	10.8	1,720	K
	Na	45.9	39.3	12,700	K
	Al	12.1	8.82	2,620	K
	Si	14.0	10.7	34,30	K
β	C	75.2	83.7	31,300	K
	O	12.0	10.0	3,960	K
	Na	8.70	5.06	8,350	K
	Al	1.26	0.63	1,160	K
	Zn	2.91	0.59	1,610	L
γ	C	34.5	45.6	2,440	K
	O	22.6	22.5	2,810	K
	F	16.0	13.4	1,870	K
	Na	26.9	18.6	5930	K

Figure 4.3a confirms that a large fraction of second-cut material was present in sample A. The accompanying EDX mapping (Figure 4.3b) suggested that the distribution of fluorides within the material, at the microscale, was strongly heterogenous. The visible crystalline substance in Figure 4.3c (point γ) appeared to be NaF, according to elemental composition (Table 4.2) and was unsurprisingly absent following the leaching treatment (Figure 4.2d). Needle-like formations of NaF crystals have previously been reported from investigations of exhausted smelter cells [31].

4.5.2. Leachate characterisation

Table 4.3 shows the quantities of major chemical species that were mobilised by the two leaching treatments. Data for the more minor contaminants are shown in Appendix C, Table C1. Na in the caustic leachate and SO_4^{2-} in the acidic leachate are not quantified, as they were present in concentrations of ~1 M, thanks to the choice of leaching reagents. The macro species (Al, Ca, F and Si) can be attributed to the components of the H-H electrolytic bath (cryolite, alumina and CaF_2) or of the firebrick and cement parent material of second-cut SPL (Figure 4.2a). The species present at $mg \cdot kg^{-1}$ concentrations are likely the result of impurities from the parent cathode bars [205], the firebrick and cement cell lining [280] and possibly the metal current-carrying bus bars of the cell.

Table 4.3. Major chemical species leached from each SPL sample, determined by ICP-MS (cations) and IC (anions). Data refer to masses of each species solubilised by individual leaching treatment, relative to mass of as-received or partially-leached SPL contacted by the lixiviant, in units of mg·kg^{-1} unless otherwise stated.

Leaching treatment	Sample	Leached species													
		F^- (%)	NO_3^-	SO_4^{2-}	PO_4^{3-}	Al (%)	Na (%)	Ca (%)	Si (%)	Cu	Fe	K	Ti	Mg	Zr
caustic	A <1.18 mm	5.64	<10	755	152	1.15		0.0372	1.71	0.960	155	1,240	78.7	3.84	<5
caustic	A 1.18-9.51 mm	22.1	<10	480	69.2	0.196		0.0435	1.18	3.28	52.6	612	48.0	11.5	<5
caustic	B <1.18 mm	7.58	<10	785	97.6	1.12		0.0325	1.56	0.936	138	833	53.4	1.87	<5
caustic	B 1.18-9.51 mm	9.72	<10	620	133	2.49		0.0264	1.39	<0.5	65.4	757	83.1	1.65	<5
caustic	C <1.18 mm	9.70	<10	1,150	146	2.00		0.0470	0.409	2.45	102	564	5.39	4.41	<5
caustic	C 1.18-9.51 mm	9.04	<10	3,270	89.3	1.06		0.0383	0.460	<0.5	88.6	394	26.5	3.48	<5
	average	10.6	<10	1,180	114	1.34		0.0374	1.12	1.44	100	734	49.2	4.46	<5
	St. dev.	5.83		1,050	33.7	0.804		0.0074	0.559	1.16	39.9	293	29.9	3.62	
acidic	A <1.18 mm	0.403	3,060		179	4.42	6.43	1.32	4.63	35.8	15,500	2,900	742	845	141
acidic	A 1.18-9.51 mm	0.129	669		164	4.43	8.93	1.99	5.18	5.72	5,550	6,670	794	103	251
acidic	B <1.18 mm	0.364	279		86.0	3.31	4.63	1.20	3.50	14.2	3,540	618	760	814	122
acidic	B 1.18-9.51 mm	0.103	667		<15	2.94	4.03	0.792	3.69	11.2	2,650	102	819	802	88.9
acidic	C <1.18 mm	0.651	2,940		123	1.20	1.27	0.754	0.519	47.6	16,100	178	227	424	16.7
acidic	C 1.18-9.51 mm	0.761	2,930		162	1.25	1.54	0.675	0.401	295	8,090	96.0	150	444	25.3
	average	0.402	2,180		143	2.92	4.47	1.12	2.99	68.3	8,570	1,760	582	727	108
	St. dev.	0.267	1,170		37.9	1.44	2.93	0.500	2.05	112	5,910	2,640	307	242	86.5

The data suggested there was no increase in leaching efficiency between the two size fractions, which would be advantageous industrially, as coarser grinding of the SPL would require less energy input. The approximate composition of the SPL material, derived from the leaching data can be compared to values quoted by Holywell and Bréault [32] (Appendix C, Table C3), which is often referenced in the literature as being an accurate range [34, 104, 274]. The apparent concentrations of Al Fe, Ti and Mg were considerably lower than expected, although it should be noted that our values are based on the total leachable content under the conditions stated (Table 4.3) and should not be considered total quantification values. For example, the Ca and Fe content of the SPL was mainly solubilised by the second acidic leach, but the values in Table 4.3 do not reflect the mass fractions in the original SPL, because a large mass % is solubilised in the first caustic leach. Nonetheless, because nearly all fluoride is solubilised in the initial caustic leach, these specific values are roughly comparable to the literature. It can be seen that the total amount of fluoride in this SPL is lower than has been reported for previous samples. Lisbona *et al.* analysed samples from a now disused smelter in the United Kingdom and found the fluoride concentration to be >19% [37]. Xiao *et al.* reported a concentration of ~13% in a sample sourced from China [79]. These examples however, were both first-cut only material, in which the fluoride and Na content is markedly higher [32]. Given the relatively low fluoride and cyanide contamination identified in this report, it is likely that the original cells were of prebake, rather than Söderberg design [32].

As expected, the majority fraction of the SPL fluoride content was mobilised by the caustic leach [82]. This would have included most of the NaF originally present, which previous studies, and indeed

the LCLL process, have shown to be mainly removed by washing with water [50, 72]. Our work however, shows that both caustic and acidic leaching conditions decrease the quantity of NaF within the solid material (this is seen for example, in Appendix C, Figures C11-C13). NaF is highly water soluble (~4 $g \cdot L^{-1}$ at ambient temperature), hence it is likely that the different lixiviants solubilise different fractions of the SPL matrix, allowing the leaching solution to access further trapped NaF crystals. NaF was only observed in large quantities in sample C, with most fluoride in the other two received samples being more complex species (Figure 4.2a). The other main SPL contaminants soluble in base are cryolite and alumina. The latter was surprisingly not detected in this study, although it is not always present in SPL samples [31]. Major contaminants diaoyudaoite and fluorite, in contrast, are only soluble in acidic conditions. This is seen most clearly in Appendix C, Figure C12.

Although the quantity of fluoride mobilised by the acid leach was, on average, ~20 times less than by the basic leach, it is a necessary step to reduce the fluoride concentration in the residual solid to a level that would allow classification as non-hazardous waste. There are a range of national and international classifications for solid waste-forms, which govern the level of control required with respect to landfill disposal. This paper will refer throughout to criteria used by the European Union (EU Council Decision annex 2003/33/EC) [281]. It can be seen from Table 4.3 that the caustic leaching treatment also does not fully solubilise a number of hazardous metals. Considering an average across all samples studied, the SPL, post-caustic leaching, would contain potentially leachable quantities of fluoride (>4,000 $mg \cdot kg^{-1}$) and selected fractions would contain 295 $mg \cdot kg^{-1}$ Cu, 90 $mg \cdot kg^{-1}$ Cr and 46 $mg \cdot kg^{-1}$ Ni. All of these figures are in excess of the EU maximum allowable levels for 'landfilled hazardous waste', these being 50, 100, 70 and 40 $mg \cdot kg^{-1}$ respectively [281]. This demonstrates the necessity of the acidic leach. This research group plans to conduct future trials on the residual barren SPL samples, after both leaches, to determine leachability of remaining contaminants.

Any labile cyanide originally in the samples was oxidised to cyanate via the initial peroxide treatment, then caustic leachate samples were checked, during IC analysis, for the presence of a cyanate peak. This peak was not detectable above baseline for any of the samples analysed, at a dilution factor of 10. It can therefore be assumed that the great majority of cyanide present in this particular source of SPL was converted to ferrocyanides or ferricyanides, most likely $Na_4Fe(CN)_6$ and $Na_3Fe(CN)_6$, which is known to occur when the waste is exposed to the environment over time [42]. These species may ultimately end up in the ion-exchange circuit and specifically, the wastewater from the fluoride and Al elution process. This water would also contain other toxic species and its potential treatment has been discussed in previous work [105]. However, there is an existing ferro- and ferricyanide-

removal process in the LCLL system, which would be implemented before the ion-exchange step [50].

The anionic composition of the leachates is of particular interest compared to our previous studies, with respect to competition and suppression effects on the uptake of fluoride during the ion-exchange treatment. We predicted a greater NO_3^- concentration, but under-predicted the SO_4^{2-} concentration [104]. This was partially due to considering only the contribution from the acid lixiviant, rather than this and the contribution from the material itself [74]. SO_4^{2-} has only weak affinity for Al^{3+}, but at such high concentrations, $AlSO_4^+$ and $Al(SO_4)_2^-$ are predicted to form [215] and this could partially suppress the formation of aqueous aluminium fluorides, hence interfering with the resin uptake mechanism.

The progression of the leaching treatment over time was determined by quantification of fluoride in the leachate at various time intervals, during leaching of sample B, 1.18-9.51 mm (Figure 4.4). This sample was chosen, due to having both large carbonaceous and cementious components and thus being most representative of fluoride-leaching from bulk SPL material. It can be seen that the largest fraction of fluoride, most likely principally in the form of NaF, is rapidly solubilised by the dilute $NaOH/H_2O_2$ solution. This is unsurprising, given the high level of dissolution reported via water-washing of SPL [84], which can essentially be attributed to the presence of ammonia, sodium carbonate hydrate and other basic species [44], which cause fairly alkaline leaching conditions in-situ. Upon increasing the NaOH concentration to 1 M, dissolution continues more slowly and reaches equilibrium in a total of ~6 hr. Nonetheless, it is clear that significant extra fluoride is mobilised by the increase in base concentration, which confirms that water-washing alone does not lead to full fluoride extraction for mixed-cut SPL. This is in agreement with previous work, focussed on only first-cut SPL [37, 84]. The acidic leaching is more rapid, reaching equilibrium in ~ 2 hr.

In terms of the timescale required for effective leaching, this treatment is comparable to most literature procedures (Appendix C, Table C2). The alkaline H_2O_2 pre-leaching cyanide-oxidation step could possibly be shortened to improve efficiency, but because of the complete absence of labile cyanide in these samples, this could not be assessed. One advantage of this treatment is that it operates at ambient temperature, whereas most studies have performed leaching at elevated temperature, finding the efficiency to be improved [53, 80]. A comparison of laboratory-scale leaching treatments (Appendix C, Table C2) illustrates that our proposed treatment generally uses much higher dilutions of lixiviants than has been previously attempted [53]. Temperature was not considered as a variable in this work, as the uptake capacity of La-MTS9501 decreases at elevated temperature [105]. Hence it would be more practical industrially for both the leaching and ion-exchange sides of the process to operate at ambient temperature.

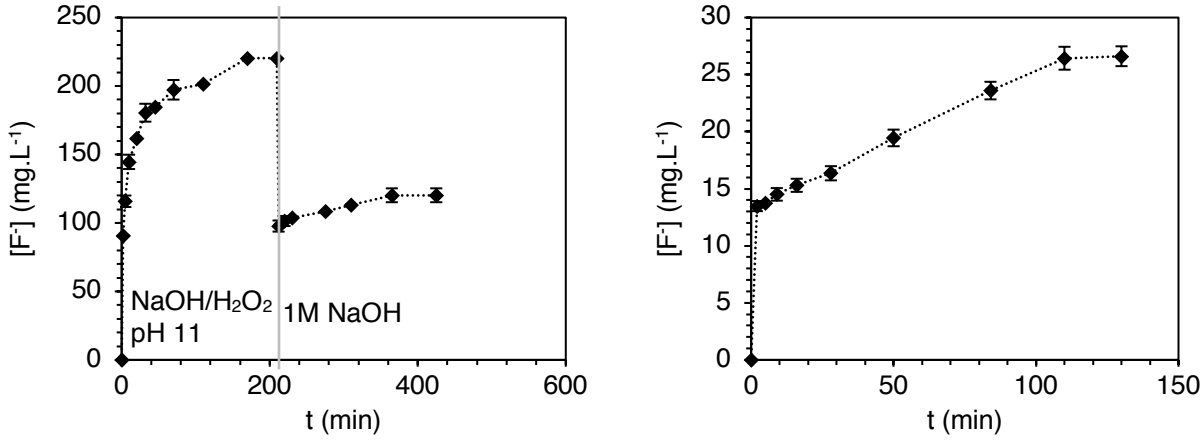

Fig. 4.4. Leaching of fluoride from SPL (Sample B, 1.18-9.51 mm) over time by **(a)** 100 mL $NaOH/H_2O_2$ at pH 11, followed by 250 mL 1M NaOH, **(b)** 250 mL 1M H_2SO_4. Mass of SPL = 2.0 g. T = 20°C. Error bars represent 95% confidence limits derived from three replicate electrode measurements.

The variability of key chemical species concentrations within the range of samples appears to be very high, which is rarely discussed in previous studies. This reinforces the need for the proposed ion-exchange system to handle an inlet stream of variable composition.

4.5.3. Combination of leachates and resulting precipitates

Parameters from the theoretical mixing of caustic and acidic leachates for selected samples and fraction sizes were inputted into the Aqion modelling software. Sample A, <1.18 mm and sample A, 1.18-9.51 mm were chosen, as they represented the limits for the sample range studied, with respect to the F^-:Al^{3+} molar ratio in the final mixed leachate. For sample A, <1.18 mm, this was 1.54 and for sample A 1.18-9.51 mm, it was 7.66. This choice was made because our previous work suggested that the performance of the La-MTS9501 resin was sensitive to this parameter [105]. We also acquired data for sample C, 1.18-9.51 mm, to compare first-cut with mixed-cut leachates. We finally calculated a theoretical average that would be produced by mixing the leachates from all samples and size fractions together. Previous ion-exchange experiments, using synthetic leachate, were run at pH 5.5. However, Aqion predicted substantial precipitation of SiO_2 and CaF_2 under these conditions, which experimental observations, at small scale, appeared to confirm. Therefore, pH was adjusted to 3.0 to minimise any precipitation. Our equilibrium work suggested this would result in a minimal decrease in resin performance [104].

The aqueous speciation results are presented in Table 4.4. For brevity, only major F, Al and S species are shown. It should also be noted that Aqion does not account for Ba, Be, Li, Ti, V, Y and Zr, which would all have been present in the mixed leachates. The associated concentrations would be <10 $mg \cdot L^{-1}$, meaning any significant interference in fluoride or Al uptake behaviour would be minimal.

Table 4.4. Selected Aqion theoretical speciation data for combined leachates, with pH adjusted to 3.0.

Chemical species	Sample A <1.18 mm	Sample A 1.18-9.51 mm	Sample C 1.18-9.51 mm	Average of all samples
	Concentration ($mmol \cdot L^{-1}$)			
AlF^{2+}	5.49	0.0218	6.71×10^{-3}	0.0351
AlF_2^{+}	11.9	2.20	0.904	2.82
AlF_3	1.21	10.5	5.72	10.6
$AlSO_4^{+}$	1.38	1.09×10^{-4}	2.67×10^{-5}	2.35×10^{-4}
$Al(SO_4)_2^{-}$	1.38	1.06×10^{-4}	2.68×10^{-5}	2.36×10^{-4}
$CaSO_4$	2.07	0.329	0.197	0.560
F^{-}	0.0214	1.03	1.36	0.801
HF	0.0145	1.56	1.29	1.00
HSO_4^{-}	3.82	8.57	5.49	7.13
Na^{+}	353	422	476	396
$NaSO_4^{-}$	57.7	67.4	67.4	64.8
SO_4^{2-}	161	162	165	162
Total ionic strength	554	605	581	568

Table 4.4 shows that, at both the lower and upper limit of the F^{-}:Al^{3+} ratio, the dominant fluoride-bearing species is an Al complex, due to the well-known mutual affinity of the two species [282]. This was also the case for the simulant leachate used in previous ion-exchange experiments, which produced excellent resin uptake performance [105]. The real leachates possess greater relative concentrations of AlF_2^{+} and AlF_3, rather than AlF^{2+}. This may be advantageous to resin efficiency, assuming the main complexation reaction involves stoichiometric binding of one AHF with one La centre on the resin surface, as this would lead to the loaded resin being more fluoride-rich (Appendix C, Figure C2). It can also be seen that some leachates contain significant concentrations of free aqueous fluoride and HF. We had not previously examined a system with these species *and* aluminium fluoride complexes co-existing and the effect on uptake behaviour was unknown at this point.

It was found that the most efficient way to combine the two leachate streams was to cautiously add caustic leachate to acidic, whilst maintaining pH below 3.5, to minimise precipitation. The masses of precipitates attained were recorded and are shown in Appendix C, Table C4. The amount of precipitation generally increased with the fraction of second-cut material in the sample. PXRD spectra of selected precipitates from all three samples were examined, namely sample A, 1.18-9.51 mm, sample B, <1.18 mm and sample C <1.18 mm (Appendix C, Figures C29-C32). The only identifiable crystalline component in the spectra was cryolite. There was also an amorphous component, most likely albite and colloidal silica [31, 283], which varied in size between samples, being much lesser for sample C (mainly first-cut). The purity of the cryolite was thus unlikely to be acceptable for resale as a chemical commodity.

A small amount of precipitation appears to be inevitable, upon mixing the caustic and acidic leachates. It would not be feasible to treat acidic and caustic streams individually with La-MTS9501 resin, as it is completely ineffective at extreme pHs [104]. However, it is desirable to avoid loss of fluoride from the leachate by precipitation of impure cryolite, before it enters the ion-exchange

system. There are two potential strategies to negate this. First, the F^-/Al^{3+} ratio could be kept relatively low via addition of aqueous Al^{3+} salts. Anodizing wastewater would be a potential cost-effective candidate for this application [72, 84]. This however, would require monitoring and quantification techniques performed on both leachate streams before mixing [105, 271]. The second strategy would simply be to redissolve the precipitate in the acid leaching vessel, in-lieu of a small quantity of SPL, as suggested in the flow diagram in Figure 4.1.

4.5.4. La-MTS9501 column-loading behaviour

Full breakthrough profiles were attained for column-loading treatment of combined leachates from sample A <1.18 mm and sample A 1.18-9.51 mm (these again being chosen for representing the extremes of the F^-/Al^{3+} molar ratio). The breakthrough behaviour was generally best-modelled as a pair of individual breakthrough curves, seemingly describing two discreet breakthrough stages, though occurring in quick succession. The first breakthrough "plateau" was determined to have been reached after three BVs were analysed, where the fluoride concentration did not vary by >1%. Modelling of the second breakthrough curve was started immediately after this. Column data are shown for sample A <1.18 mm in Figure 4.5 and for sample A 1.18-9.51 mm in Figure 4.6. Parameters for model-fitting are shown in Table 4.5.

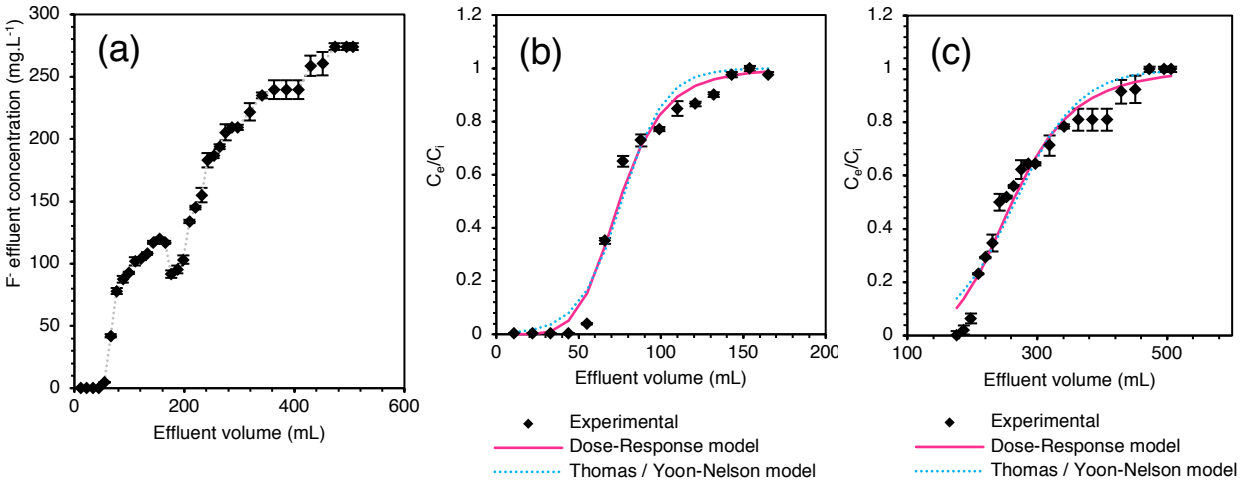

Fig. 4.5. Fluoride breakthrough behaviour via loading of La-MTS9501 resin column from combined leachate of SPL sample A, <1.18 mm size fraction: **(a)** raw data, **(b)** modelling of first breakthrough region, **(c)** modelling of second breakthrough region. Fluoride C_i = 275 mg·L^{-1}. Column volume = 5.50 mL. Resin mass = 1.792 g. Flow rate = 1.00 BV·hr^{-1}. T = 20°C. Error bars represent 95% confidence limits, derived from three replicate electrode measurements.

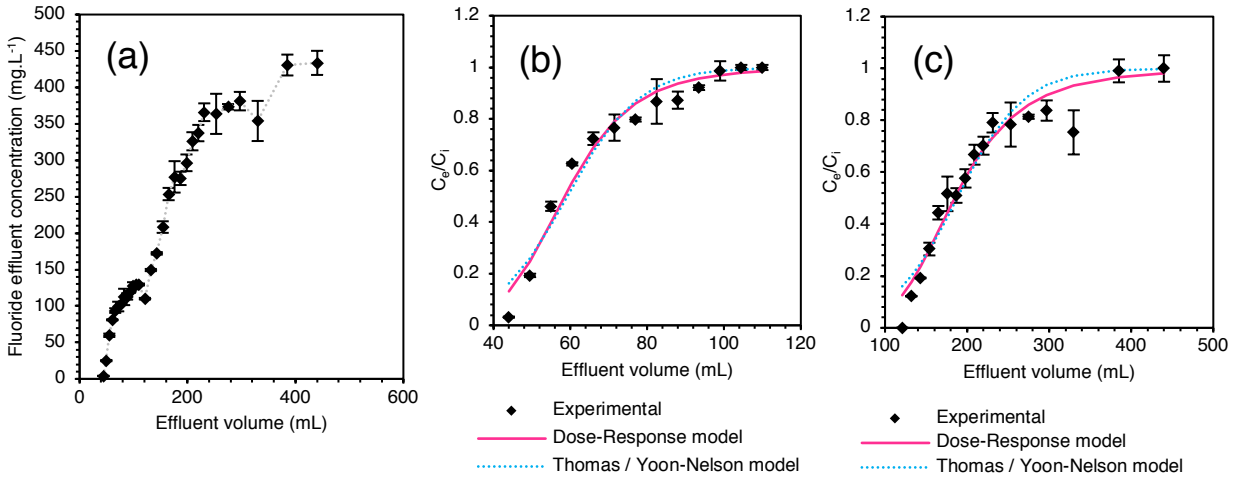

Fig. 4.6. Fluoride breakthrough behaviour via loading of La-MTS9501 resin column from combined leachate of SPL sample A, 1.18-9.51 mm size fraction: **(a)** raw data, **(b)** modelling of first breakthrough region, **(c)** modelling of second breakthrough region. Fluoride C_i = 434 mg·L^{-1}. Other experimental parameters as per Fig. 4.5.

Table 4.5. Extracted parameters from modelling of breakthrough behaviour for leachates of sample A <1.18 mm and sample A 1.18–9.51 mm. For definition of model parameters, see Appendix C, p C4.

Model	Parameter	Breakthrough region	Leachate Sample A <1.18 mm	Sample A 1.18–9.51 mm
Dose-Response	a	first	5.50 ± 0.60	6.60 ± 0.67
	b	first	74.9 ± 1.7	58.5 ± 1.0
	q_0	first	5.01 ± 0.11	4.23 ± 0.07
	R^2	first	0.983	0.969
	a	second	5.45 ± 0.47	4.57 ± 0.48
	b	second	262 ± 4	185 ± 4
	q_0	second	26.7 ± 0.4	33.4 ± 0.7
	R^2	second	0.960	0.947
	R^2	both[a]	0.932	0.959
Thomas	k_{Th}	first	5.78 ± 0.86 (x 10^{-5})	7.60 ± 1.0 (x 10^{-5})
	q_0	first	5.10 ± 0.15	4.28 ± 0.09
	R^2	first	0.971	0.950
	k_{Th}	second	1.02 ± 0.12 (x 10^{-5})	7.00 ± 0.98 (x 10^{-6})
	q_0	second	27.1 ± 0.5	34.0 ± 0.9
	R^2	second	0.937	0.921
	R^2	both[a]	0.942	0.971
Yoon-Nelson	k_{YN}	first	7.56 ± 1.1 (x 10^{-2})	0.107 ± 0.015
	T_{50}	first	76.2 ± 2.2	59.2 ± 1.3
	R^2	first	0.971	0.950
	k_{YN}	second	2.03 ± 0.23 (x 10^{-2})	2.47 ± 0.35 (x 10^{-2})
	T_{50}	second	266 ± 5	188 ± 5
	R^2	second	0.937	0.921
	R^2	both[a]	0.942	0.971

[a] The R^2 values for both breakthrough regions are derived from an attempt to fit a single breakthrough curve to the whole dataset.

The Dose-Response model provided the most accurate modelling of the two breakthrough regions (Table 4.5). This model has previously been observed to minimise the errors produced by other breakthrough models [251, 284]. The resulting maximum dynamic uptake capacity values (q_0, in units of mg·g^{-1}) were therefore considered the most valid to compare the different experiments. These values for sample A <1.18 mm were 5.01 ± 0.11 and 26.7 ± 0.4 mg·g^{-1} respectively for each breakthrough region. For sample A 1.18-9.51 mm, they were 4.23 ± 0.07 and 33.4 ± 0.7 mg·g^{-1}. The leachate of sample A 1.18-9.51 mm however had a significantly greater inlet fluoride concentration

(434 mg·L^{-1}, compared to 275 mg·L^{-1}). Previous work with simulant leachate showed that the q_0 parameter is strongly influenced by this variable [105], so the difference in resin uptake performance is not as great as would be expected. This is especially surprising, given the differences in F^-/Al^{3+} ratio and speciation (Table 4.3). Our previous kinetic work however, suggested that, as the uptake process approaches equilibrium, ligand-exchange reactions occur with the surface-bound AHFs (Appendix C, Figure C2). This causes some release of fluoride back into solution and leads to the dominant adsorbed species tending towards $Al(OH)_2F$, [105]. This may explain the similar resin performance over the two experiments. The calculated concentration of La centres in the resin, from previous experiments, was 1.465 mmol·g^{-1} and assuming stoichiometric binding of one $Al(OH)_2F$ with one La, this equates to a fluoride capacity of 27.84 mg·g^{-1}, which is close to the calculated dynamic uptake values for the 2nd breakthrough regions (Table 4.5).

Our previous work also provided strong evidence that the uptake of AHFs by La-MTS9501 is heterogenous, with an initial chemisorption complexation between La centres and aqueous AHFs, followed by a secondary uptake where further AHFs bind to the existing complexation through much weaker interactions, again involving F or O bridging ligands (Appendix C, Figure C2) [104, 105]. This would explain the two discrete breakthrough regions, the first representing partial fluoride breakthrough with respect to the secondary, weaker interaction; the second representing full saturation of the La centres. In previous work, using simulant leachate, there was not significant evidence of a two-stage breakthrough process [105]. However, the ionic strength of the inlet solution was much greater in this work (554 and 605 mmol·L^{-1} in these experiments verses 24.8 mmol·L^{-1} for the simulant leachate), which is likely to have retarded the adsorption kinetics [257].

Overall, the efficiency of the resin, using SPL leachate, compares well to data produced using a simulant feed and otherwise similar conditions. This produced a q_0 value of 66.7 $\pm$ 9.1 mg·g^{-1}, with the inlet fluoride concentration being substantially higher (1,500 mg·L^{-1}) [105]. It can be concluded that the more complex chemistry and higher ionic strength of the real leachate is not detrimental to resin performance.

4.5.5. La-MTS9501 column-elution behaviour

Elution of the column proceeded first with deionised water, which displaced the residual leachate and also removed the majority of weakly-bound cocontaminant ions. Figure 4.7 shows that this process was complete after ~160 mL eluent (~35 BV). This is mainly due to a quantity of fluoride, which is eluted independently of any Al. This likely represents a reverse ligand-exchange reaction, whereby the bound AHFs are converted to less fluoride-rich species via a change in fluoride concentration gradient (AlF_3 and AlF_2^+ converting to AlF^{2+}) [105, 164] Previously, in experiments with synthetic leachate, we then switched the eluent to 0.01 M NaOH. This resulted in a fairly pure stream

of fluoride and Al, but at unsatisfactory concentrations unsuitable for cryolite recovery [105]. In this work, we immediately switched to 1 M NaOH, with the result being sharp fluoride and Al elution peaks at almost identical retention times. Furthermore, the averaged concentrations of fluoride and Al for the relevant eluent fractions was 658 ± 18 mg·L^{-1} and 807 ± 30 mg·L^{-1} respectively (34.6 ± 0.9 mmol·L^{-1} and 29.9 ± 0.6 mmol·L^{-1}). This appears to support the hypothesis that the dominant resin-bound species has an approximate 1:1 F^-/Al^{3+} molar ratio [105]. To assess the purity of the eluent stream, these fractions were also analysed for all of the cocontaminants present in Table 4.3, again by ICP-MS or IC. The great majority of species were below detectable limits. Those present in significant quantities are shown in Table 4.6.

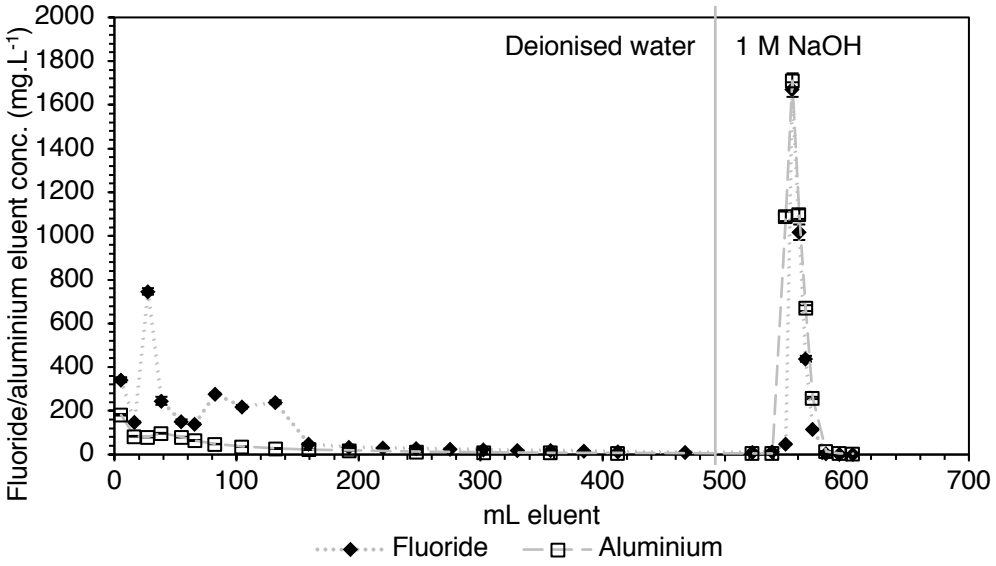

Fig. 4.7. Elution profiles of fluoride and Al from loaded La-MTS9501 column (sample A, <1.18 mm experiment). Original resin mass = 1.792 g. Flow rate = 1.0 BV·hr^{-1}. T = 20°C. Error bars represent 95% confidence limits, derived from duplicate measurements

Table 4.6. Averaged concentrations of fluoride, Al and selected cocontaminants during elution of the major F^- and Al peak, determined by ICP-MS and IC. Experimental conditions as per Figure 4.6.

Species	Concentration (mg·L^{-1})
F^-	658 ± 18
Al	807 ± 30
Na	22,600 ± 400
Ca	2.35 ± 0.05
Si	31.9 ± 0.6
Fe	2.17 ± 0.04
Zn	1.20 ± 0.02
SO_4^{2-}	86.5 ± 1.7
PO_4^{3-}	27.9 ± 0.6

The substantial presence of SO_4^{2-} and PO_4^{3-} can be attributed to deprotonation of the secondary amine in the MTS-9501 functional group [226]. This would preferentially bind SO_4^{2-} and PO_4^{3-} from the leachate during column-loading, due to the high affinity of these two anions for amine

functionalities [115]. Neither anion would be expected to be deleterious to cryolite precipitation. In fact, Na_2SO_4 may be used to add to acidic F^-/Al^{3+} solutions to induce cryolite precipitation [285]. The most problematic species in the solution is likely to be Si, which could feasibly coprecipitate as SiO_2 over the working pH range for cryolite recovery [215], or form polymeric silica colloids [283]. However, there are recognised economical commercial methods for silicon removal from aqueous circuits if necessary, such as the inorganic salt SilStop® [283]. The LCLL process, in fact, already implements a Si removal step from acidic leachate [32]. A key consideration for the proposed process is whether the F^-/Al^{3+} molar ratio produced is appropriate for cryolite precipitation. The literature is somewhat diverse on this point. Chen *et al*. reported that, at a 1:1 ratio, aluminium hydroxyfluoride precipitation dominates over cryolite, although only at pH 5.5 [285], whereas Jiang and Zhou predicted favourable cryolite recovery at the same ratio at pH 9 [240] and Wang *et al.* demonstrated success using a F^-/Al^{3+} molar ratio of ~1:2.55 [52] (although these were achieved by neutralisation of an acidic starting solution). We have considered the molar ratio monitoring and potential adjustment in previous work [105]. It is notable that, in the initial elution from the column with deionised water, $[F^-]$ greatly exceeds $[Al^{3+}]$ and this fraction could potentially be recycled and used for ratio control of the inlet stream, but detailed precipitation studies and optimisation are clearly called for as a next step of the process development. Overall however, the inlet leachate, has been not only purified, but enriched in fluoride. The calculated recovery (with respect to only the main F^- peak), derived from the Dose-Response model q_0 parameter, was 59.0 ± 1.5% and, as mentioned, the initial water wash eluent could potentially be re-treated to further maximise recovery. The quantity of water used also decreased greatly, relative to previous work, from 2,500 mL to 600 mL for elution of a 5.5 mL column [29].

4.5.6. Technicoeconomic assessment

Although the data presented in this article suggest that the proposed adsorption system is feasible from a chemical processing perspective and that it may potentially help to address the issue of global fluoride recycling, any such engineering scheme must also be economically sound. To this end, a technicoeconomic analysis was performed, using the hypothetical scenario of the proposed process being integrated into the existing LCLL system. There were several reasons behind this choice:

- *This greatly improves the simplicity of the analysis, as most of the hydrometallurgical treatment processing steps are already accounted for.*
- *The LCLL process already has methods in place for destruction of labile cyanides and removal of silica from the system, which have been identified as complicating factors in this work.*
- *Part of LCLL requires water to be heated. Therefore, there is the potential to use the calorific value of the large volume of spent resin at the end of its lifespan via known pyrolysis or incineration methods [286].*

The objective of the analysis was to demonstrate to an Al smelter, who is considering a hydrometallurgical treatment for their SPL waste, the potential added value that the adsorption and cryolite production process could contribute, especially if developed further.

It should be noted that the difference in scale between the laboratory experiments presented in this thesis and the calculated volume of resin required to retain the LCLL SPL throughput rate is immense (factor of ~9.5 x 10^7). The laboratory experimental parameters represent an SPL processing rate of 5.5 x 10^{-5} kg·hr^{-1}. The scalability of the technology ideally should be demonstrated by increasing experimental scale successively by a factor of 100, first in larger laboratory experiments (0.0055 kg·hr^{-1}, 0.55 L resin), then at pilot plant scale (0.55 kg·hr^{-1}, 55 L resin) and finally at demonstration plant scale (55 kg·hr^{-1}, 5,500 L resin). A further 100-fold increase of scale would take the process theoretical throughput to the same order of magnitude as the current LCLL system [50]. Nonetheless, the technicoeconomic analysis was regarded as a key deliverable for this thesis.

The approach to the technicoeconomic analysis, in terms of the essential factors considered in the costing, was taken from Peters et al. *[287]. The costing was based on the following: First, an existing technicoeconomic report on a large-scale IX treatment system, commissioned and built in California, 2012 [288]. Second, current freely-available commercial information on the prices of chemical commodities and global freight costs. Third, first-order calculations, based on the data acquired in this study and other pieces of literature relating. Where no resources were available to make a reliable estimate of a certain cost, "Lang factors" [289] were used, which estimate such variables as proportions of the known major equipment spend. Estimation of error margins followed the AACE International Cost Estimate Classification System methodology [290], which determined that a margin of -30% to +50% should be applied to the final calculated capital expenditure (CAPEX) values.*

The following key assumptions were made in preparing the technicoeconomic analysis:

- *The company will not have to make a significant purchase of extra land. The existing plant is already large and IX systems take up a comparatively small footprint [291].*
- *There is an existing water treatment and recycling system in place at the plant, which will be able to treat the barren leachate after cryolite precipitation.*
- *The dynamic efficiency of La-MTS9501 resin can be optimized, so as not to be greatly affected by the scale-up of the process and the increased flow rate required.*

A full breakdown of the analysis, including calculations used, assumptions made and sources consulted, is shown in Appendix C, p C16. A brief summary is seen in Table 4.7.

Table 4.7. *Simplified technicoeconomic assessment for the integration of the proposed technology into the LCLL system and running for the first year of operation.*

Variable	***Value (£ x 10^3)***	***Notes***
Fixed-CAPEX (start-up costs)		
Chemicals	*2,789*	*MTS-9501, $LaCl_3.8H_2O$, NaOH*
Equipment	*1,588*	*IX vessels, $LaCl_3$ mixing and storage tank, pumps*
Installation	*1,176*	*30% proportion of total chemicals and equipment cost*
Miscellaneous	*3,149*	*Control system, instruments, piping and buildings*
Construction and engineering	*1,423*	*66% of major equipment spend*
Contractor fee	*433.5*	*Typically ~4% of fixed-CAPEX*
Contingency	*338.1*	*Standard recommended contingency figure is 2% of fixed-CAPEX x 1.5 for "high-risk" technology (anion-exchange)*
TOTAL	***10,920***	*Low estimate: 7,644; High estimate: 16,380*
Working-CAPEX (running costs) per year		
Consumables	*688.9*	*Buffers, standards, cryolite precipitant, replacement small components*
Electricity	*28.99*	
Waste treatment	*6.611*	*Based on 3% extra plant water capacity*
Labour	*193.3*	*1x experienced IX engineer, 2 x IX technician shift leaders, 2 x IX technicians*
Replacement CaF_2	*3,196*	*Metallurgical grade, imported from Mexico (£231·T^{-1})*
TOTAL	***4,096***	*Low estimate: 2,867; High estimate: 6,144*
Cryolite sales	*6,325*	*Based on current "Freight-on-board" price from merchants in China (£732·T^{-1}). Assumes average [F^-] of SPL = 11% wt., 95% leaching efficiency and 59% recovery from leachate*
PROJECTED ANNUAL EARNINGS	***2,229***	

One major uncertainty in the analysis is that the adsorption system was not tested at different flow rates. It was calculated that a flow rate of 2.74 BV·hr^{-1} would be required to match the throughput of SPL leachate through the plant, whilst retaining its capacity of 80,000 T SPL processed per year . Such a target flow rate is certainly not unrealistic for an industrial IX system and there are multiple large-scale examples in the literature where this parameter has been far higher (18 BV·hr^{-1} for a 789 m^3·min^{-1} throughput [291]). However, La-MTS9501 is a novel adsorbent and it is not known how the kinetics of the uptake mechanism will respond to a considerably greater flow rate than that experimentally tested. The majority of dynamic column studies show that increasing flow rate reduces the capacity of the column, due to reduced contact time of the adsorbate with the resin active sites. This was observed by Ma et al. *for adsorption of fluoride on to bentonite [266]. Perhaps a more accurate comparison would be a column study on adsorption of uranyl complexes by chelation to an ethylenediamine-functionalised resin [265]. In this case, increasing the flow rate by a factor of ~3.85 reduced the q_{max} value by ~15%. Nonetheless, it should be noted that the dynamic uptake capacities observed in this work were not optimised in any way and it is feasible that the effect of flow-rate could be counter-balanced by increasing the [F^-] in the feed, as per Chapter 3. Alternatively, only a fraction of the leachate could be sent to the IX system, with the remainder treated by current LCLL technology (CaF_2 production).*

From a costing perspective, it was found that the lynchpin of the economic success of the process was whether it would be possible to regenerate the NaOH used as eluent for the adsorbed AHFs. Although this experimental work demonstrated the effectiveness of NaOH solution for this purpose, it is a costly reagent. (Table C5). Assuming no regeneration were possible, the elution would require ~ 2bn L of 1 M NaOH per year, at an estimated cost of £21M. Even with process optimization, this could never be economically viable. A survey of the literature suggests that there are low-cost routes to NaOH regeneration, via use of $Ca(OH)_2$ (with gypsum ($CaSO_4$) produced as a side-product) [292]. Such routes start with a Na_2SO_4 solution, which is essentially what would remain in the barren waste-stream for this process, after the maximal recovery of cryolite [72]. In fact, Rio Tinto Alcan already acquires bulk $Ca(OH)_2$ for CaF_2 precipitation [49]. Nonetheless, without experimental data regarding the precipitation of cryolite from the column eluent, which is outside the scope of this work, it is difficult to predict whether caustic recovery would be feasible.

A further notable point, with regard to efficiency, is that in the initial elution column stages, using water as the eluent, the concentration of fluoride in the eluent far exceeds the concentration of Al (Figure 4.7). This invites the possibility that the initial eluent could be subjected to the existing LCLL recovery treatment and allow the continuing production of fluorite [50]. There is reason to believe that, with respect to the current LCLL process, the combined water-wash and caustic leachate streams would be heavily contaminated, given the number of other species we observed in our own alkaline leachate (Table 4.3). Therefore, it is proposed that the quality of CaF_2 produced would likely not decline as a result of this strategy, as the feed would be, if anything, lower inn contaminant concentrations. This would be a great advantage to the smelter, as existing technology would not have to be abandoned/decommissioned. The strategy would also be environmentally sound, as the entire quantity of fluoride leached from the SPL would be recovered as commodity products, apart from the small fraction remaining in the barren eluent, after the precipitation step. There would even be the possibility of switching between combined fluorite/cryolite and fluorite-only production. This would be a considerable asset for the smelter, as it would be able to respond to market price fluctuations for the two minerals, which can be quite severe (Figure 1.3).

With these admittedly large caveats and despite the uncertainties associated with the values in Table 4.7, it can be seen that implementation of the technology, even without any process optimisation, is calculated to begin returning value to the smelter within five years. It should also be noted that several cost factors, although based on available data, are likely to be overestimates. For example, Rio Tinto Alcan will already have an established contract for a supply of bulk CaF_2, so the cost of acquiring the additional material for the HH process, which is "lost" by partially converting the plant to produce cryolite, would be much less than calculated here. Overall, the proposed process has economic, as well as technical potential.

4.6. Conclusions

A simple leaching treatment for spent potlining (SPL) has been developed, with a view to valorisation of the waste, via fluoride and aluminium uptake in an ion-exchange column system, using chemically-modified La-MTS9501 resin. The leaching employs economical lixiviants ($NaOH/H_2O_2$, then H_2SO_4) at high dilutions, works at ambient temperature and is effective for a variety of SPL grades. First-cut and mixed-cut SPL samples, of two different size fractions, were subjected to both stages of the leaching treatment. The SPL was characterised by PXRD and SEM, which confirmed both the strongly heterogeneous nature of the material and the effectiveness of the leaching in terms of mobilising the contaminants. The leaching produced a variety of liquors, which were characterised by ICP-MS and IC, again revealing large differences in elemental composition. Caustic and acidic leachates were combined and pumped through an ion-exchange column to assess the performance of La-MTS9501 with a real industrial leachate feed. The resin performed similarly well in the uptake of fluoride from two inlet solutions of substantially different composition. Dynamic maximum uptake values were in excess of 30 $mg \cdot g^{-1}$ in both cases. The loaded fluoride and aluminium could be coeluted, using 1M NaOH, with minimal cocontaminants, producing an enriched, alkaline solution, with a minimum 59.0% recovery, which will now be taken forward to cryolite precipitation studies. This work confirmed the high selectivity of the resin for uptake of aluminium hydroxyfluorides in a complex industrial liquor of high ionic strength and demonstrated improved process efficiency. *A first-order technicoeconomic analysis suggested that the proposed system could add significant economic value for a smelter currently running, or considering a derivative of the LCLL process.*

Acknowledgements

The authors wish to thank Mr Neil Bramall and Ms Heather Grievson (University of Sheffield, Dept. Chemistry) for ICP-MS and elemental analysis respectively. This work was jointly financed by the Engineering and Physical Sciences Research Council (Grant no. EP/L016281/1) and Bawtry Carbon International. TJR also thanks the Royal Society of Chemistry, Environmental Chemistry Group for support in presenting this work internationally.

5. Investigations into fluoride adsorption characteristics of metallated hypercrosslinked polymers

5.1. Overview of paper

The final experimental chapter moves away from the proposed SPL treatment system and introduces de novo adsorbents for fluoride removal. Although it has been seen that the La-MTS9501 resin is an effective choice for the capture of fluoride, in particular from SPL leachate, there remains a huge body of research focussed on the defluoridation capabilities of novel adsorbents. These sometimes offer intrinsic advantages over existing technology in terms of sustainable production (recycled and naturally-occurring materials are a common choice), but very rarely offer performance advantages, in terms of capacity or selectivity, as is discussed in Chapters 1-4. As will be seen, the metal-loaded polymers reported in this chapter *do* offer potential advantages over the current state of the art.

Metallated HCPs have not previously been characterised and reported. Nor have HCPs of any kind been investigated as adsorbents for fluoride. As a result, this chapter is more focussed on fundamental investigation of the physicochemical properties of novel materials and the impacts on metal-loading and defluoridation behaviour. Uptake experiments were accordingly not performed with SPL leachate, but with NaF solutions with various controlled parameters.

The main distinguishing feature of the microstructure of HCPs, compared to IX resins, is their high surface area and distribution of micro- and mesopores, as opposed to macropores. It is known however, that generally, adding hydrophilic groups and heteroatoms to the polymer matrix, lowers the microporosity. For this reason, rather than attempt to , for example, graft the AMP group to HCP scaffolds, we instead focussed on a very simple phenol functionality for the loading of metal ions, which could be incorporated into the starting monomers and therefore reduce the number of synthetic steps required. A number of different metal ions were trialled to activate the adsorbent for fluoride uptake (this preliminary data is not presented here, for conciseness), but it was found that alkali earth metals, specifically Ca^{2+}, produced greatly superior fluoride capacity than the more obvious choices of Al^{3+} and La^{3+}. With regard to choice of monomers, phenol, the simplest aromatic alcohol, would have been a poor choice for these experiments, as it is difficult to obtain a polymer of high surface area using the conventional Friedel-Crafts crosslinking. Therefore, two common biphenols were chosen, which can be polymerised to generate materials of high porosity: 2,2'-biphenol and 4,4'-(propane-2,2-diyl)diphenol ("bisphenol A"). These monomers are economical; at time of writing, 2,2'-biphenol retails for £154·kg^{-1} (99% purity, Fisher Scientific) and bisphenol A for £42·kg^{-1} (97%, Sigma-Aldrich). Moreover, despite their equivalent functional groups, they are structurally quite dissimilar and therefore allowed study of how changes to the chemistry of the polymer matrix influenced metal-loading and fluoride uptake behaviour. The polymers synthesised from these monomers were termed "hydrophilic hypercrosslinked polymers" (HHCPs).

The paper begins with extensive solid-state analysis, which determined the formation of quinonoid structures in the synthesised polymers. This is caused by dehydrogenation of the crosslinking carbons during polymerisation and this phenomenon gives HCPs their brown coloration. The evidence suggests that the phenol groups are partially incorporated into these structures, demonstrated by metallation changing the colour of the materials. For this reason, the range of protonation constants presented by the materials in potentiometric titrations was far greater than expected. The presence of surprisingly acidic protons in the polymers allowed for proton exchange with -CaOH groups and successful metallation. The degree of Ca-loading was however enhanced by an unexpected mechanism whereby the polymers adsorbed atmospheric CO_2 into their pores when exposed to the environment, which was subsequently converted to $CaCO_3$ upon contact with $Ca(OH)_2$ solution. The most significant difference between the polymers was than the 2,2'-biphenol HHCP (HHCP1) retained much of its surface area after Ca-loading, but the bisphenol A HHCP (HHCP2) was converted to a surface-functionalised adsorbent, as its narrower pore apertures apparently became blocked during loading.

The focus then shifts to the more familiar fluoride uptake studies, in which interesting variations in performance were found. HHCP1 possessed a very high maximum uptake capacity of 267 $mg \cdot g^{-1}$, which is far in excess of the La-MTS9501 resin featured in Chapters 2-4. Moreover, the fluoride is relatively strongly bound, as both covalently-held -CaOH groups and $CaCO_3$ are both ultimately converted to relatively insoluble CaF_2, whereas the NaF formed during uptake by La-MTS9501 was easily desorbed from the resin by deionised water, which would make elution and recovery processes complicated. HHCP2 had a lesser, though still large capacity. It did however exhibit much faster kinetics, as there was no diffusion process through the pores of the adsorbent and maximum uptake was therefore reached rapidly by transport of fluoride to the active surface sites, following PSO kinetics. The fluoride uptake by HHCP1, in contrast, was better described by the multi-step Elovich model. Both materials could be successfully employed in a reverse-flow column system, albeit with a slow inlet flow rate, and displayed good dynamic performance. The variation in uptake performance over a broad pH range was again examined and, in this chapter, was correlated to the degree of surface charge by zeta potential measurements. These experimental results could be rationalised by the variations in Ca environments present between the two polymers. It was also observed that the presence of multiple competing anions was not detrimental to the performance of either adsorbent.

This chapter shows that the strategy of incorporating hydrophilic functionality into the starting monomers can result in a greatly enhanced exchange capacity for the polymeric adsorbent, which in turn can translate to improved fluoride extraction capabilities. Moreover, it is seen that uptake behaviour in HCPs may be controlled by strategically selecting the geometric properties of monomer

materials. This knowledge will hopefully facilitate future development of HCPs as adsorption and IX media.

This paper was submitted to *The Journal of Materials Chemistry A* on 7 November 2019, resubmitted in revised form on 17 January 2020 and accepted for publication on 9 February 2020 (doi.org/10.1039/c9ta12285k).

5.1.1. Author contributions

Thomas J. Robshaw. Synthesis, experimentation, data interpretation and manuscript writing
Dr Alex M. James. Synthesis, N_2 sorption experiments and data processing, manuscript review
Dr Deborah B. Hammond. XPS experimental work, technical support and data interpretation
Jake Reynolds. Synthesis
Dr Robert Dawson. Supervision of synthesis and experimentation
Dr Mark D. Ogden. Supervision of experimentation and manuscript review

"Calcium-loaded hydrophilic hypercrosslinked polymers for extremely high defluoridation capacity via multiple uptake mechanisms"

Thomas J. Robshaw[a,b]*, Alex M. James[a], Deborah B. Hammond[a], Jake Reynolds[a], Robert Dawson[a] and Mark D. Ogden[b]

[a]Department of Chemistry, Dainton Building, University of Sheffield, UK, S3 7HF

[b]Separations and Nuclear Chemical Engineering Research, Department of Chemical and Biological Engineering, Sir Robert Hadfield Building, University of Sheffield, UK, S1 3JD

*Corresponding author: tjrobshaw1@sheffield.ac.uk

5.2. Abstract

Hydrophilic hypercrosslinked porous polymer networks were synthesised from 2,2-biphenol (HHCP1) and bisphenol A (HHCP2) monomers, which were assessed for remediation of highly fluoridated water. As well as being hydrophilic, the hypercrosslinking radically altered the acidity of protonation sites within the polymeric scaffolds. The polymers were metallated to produce novel, hybrid Ca-loaded adsorbents. The metal-loading affected the electron distribution of the quinonoid structures formed during polymerisation. HHCP1 had a greater exchange capacity (6.34 ± 0.17 mmol·g^{-1}) and adsorbed more Ca^{2+}, yet retained much of its original surface area, whereas HHCP2 was rendered non-porous upon metallation. Ca-loading included covalent interactions and formation of crystalline $CaCO_3$ (vaterite), from preferential CO_2 binding under ambient conditions. Both networks were effective defluoridating media, with Ca-loaded HHCP1 exhibiting a capacity among the highest yet reported for any extractant (267 ± 34 mg·g^{-1}). HHCP2-Ca had a lesser capacity of 96.2 ± 10 mg·g^{-1}, but faster uptake kinetics and was more effective at lower concentrations, attributed to stronger binding interactions. Crystalline CaF_2 (fluorite) was the dominant fluoride species formed, from both vaterite and covalently bound Ca. The networks could be used in a dynamic column system, extracted fluoride in the presence of multiple coexisting anions and were regenerable, with a potential pathway demonstrated for recovery of the adsorbed fluoride.

5.2.1. Table of Contents entry

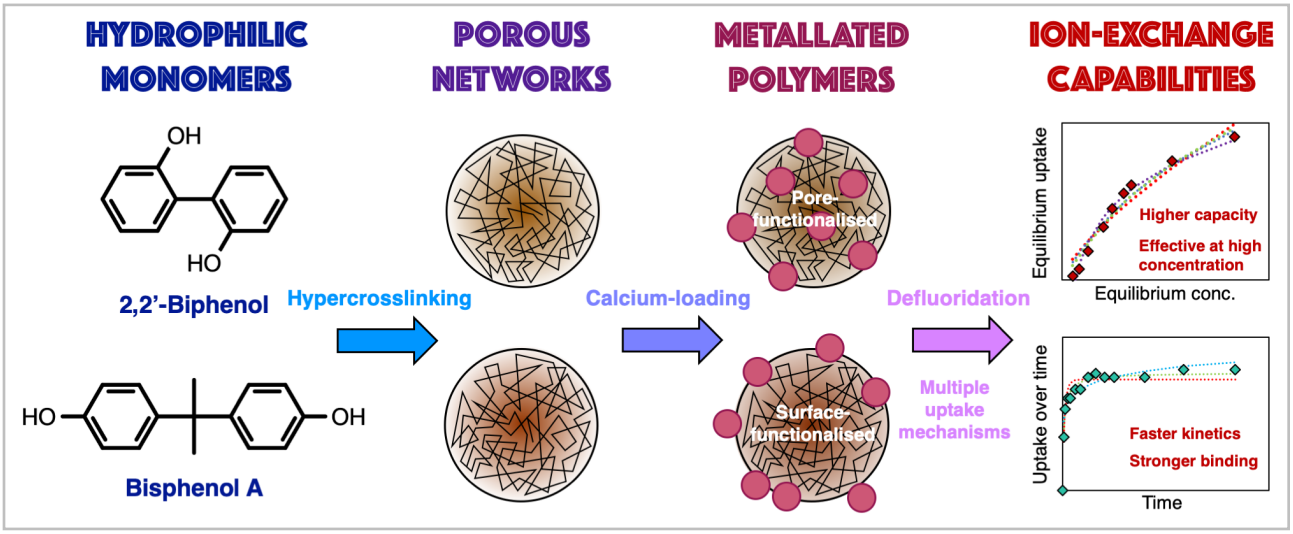

"The first metallated hypercrosslinked polymers have been synthesised, characterised and found to have remarkable capacity for uptake of fluoride ions".

5.3. Introduction

Fluoride is a ubiquitous ionic species in environmental water [4]. The ingestion of small quantities (~0.05 $mg{\cdot}kg^{-1}{\cdot}day^{-1}$) is beneficial to humans, as it protects against dental decay [8]. However, chronic overexposure can lead to skeletal fluorosis, causing permanent contortion of limbs and bone weakness [4, 9]. High fluoride ingestion is also linked to conditions including osteoporosis, infertility, brain damage and cancer [88, 293]. The population forced to drink water exceeding the recommended maximum fluoride concentration (1.5 $mg{\cdot}L^{-1}$) is estimated at >200 million worldwide [88]. Additionally, industries producing problematic fluoride-bearing wastewater include aluminium smelting, photovoltaic manufacturing, uranium enrichment and fertiliser production [50, 294-296].

Although fluoride is abundant (~625 $mg{\cdot}kg^{-1}$) in the Earth's crust, the only commercial extraction methods are mining of fluorite (CaF_2) and recovery from phosphate rock processing [16]. The latter is converted almost exclusively to flurosilicic acid and the former used in steel-making, glass-etching, ceramics and production of HF, which is a feedstock for fine chemicals and industrially-important fluropolymers [14]. The rate of fluorite mining (currently 5.8 $kT{\cdot}yr^{-1}$) is increasing year-upon year [15, 16]. Fluorite was awarded "critical mineral" status by The European Union in 2014 [238]. Fluoride is thus ironically a scarce commodity, as well as a threat to health and environment.

Removal and recovery of fluoride from aqueous waste streams, with cocontaminants, is problematic. Fluoride has high affinity towards common multivalent cations, especially Al^{3+}, so can exhibit complex aqueous speciation [85]. Precipitation techniques yield an amorphous sludge of no commercial value [87]. Membrane technologies have no potential route to recovery [297]. Fluoride

is resistant to removal by commercial anion-exchange resins, being the least selective common anion for weak base and strong base anion functionality [115, 117]. This can be reversed by instead loading a cation-exchanger with multivalent hard acid cations, which selectively bind fluoride via ligand-exchange [97, 118, 157]. However, in solutions of high ionic strength, leaching of the bound cations may occur, necessitating expensive chelating resins for durability [104].

Nonetheless, many fluoride adsorbents have strategically incorporated or loaded such metals into the matrix. Example materials include alumina [133], activated carbon [162] and chitosan [135]. These possessed capacity for fluoride higher than their unmodified equivalents, but an order of magnitude lower than a modified commercial resin (<10 $mg \cdot g^{-1}$ verses >180 $mg \cdot g^{-1}$) [104], due to low degree of functionalisation and/or lack of porosity. The potential leaching of toxic metals into the effluent stream is also problematic for drinking water remediation [297, 298]. There remains a clear need for an economical alternative adsorbent, combining large surface area, high degree of functionalisation and selectivity.

Hypercrosslinked polymers (HCPs) are a sub-class of microporous organic materials, having high surface areas of ≤2,000 $m^2 \cdot g^{-1}$ and robust chemical and thermal stability [190, 299]. They are synthesised by Friedel-Crafts alkylation, whereby multiple aromatic rings are joined together, either by internal crosslinking, usually via chloromethyl substituents, or external, whereby a crosslinking unit (commonly dimethoxymethane) is added to the polymerisation. This creates a dense, permanently porous network with pore diameters commonly 0.5-1.5 nm [190, 300]. The first HCPs were derived from Davankov-type resins and these materials are still commonly reported [196, 301]. A single-step polymerisation was introduced by Li *et al*. [184] in the form of the “knitting” technique, which allows the fusing of small, electrophilic, aromatic monomers to form polymeric networks.

Many HCPs display affinity for CO_2 gas adsorption over N_2, hence being potential candidates for carbon capture and sequestration [185]. They have been applied for removal of organic pollutants [196] and for Pd and Cu catalysis [166]. However, the removal of ionic pollutants from water has been much less widely studied. This strategy has previously involved the grafting of functional groups onto the hypercrosslinked monolith. Li *et al*. [198] functionalised a Davankov HCP with sulfonate groups for uptake of heavy metals. Our research group recently reported a “knitted” HCP via Brönsted acid catalysis, also functionalised with sulfonate, for remediation of Sr and Cs [189]. Maximum theoretical uptake capacities were somewhat lower than expected, being ≤2 $mmol \cdot g^{-1}$ for monovalent ions. This was likely due to incomplete functionalisation, with active sites only being available in the mesopores, and the large metal ions not being able to fully access the micropores [229]. Fluoride, with its small ionic radius, may be an ideal target contaminant for a microporous matrix.

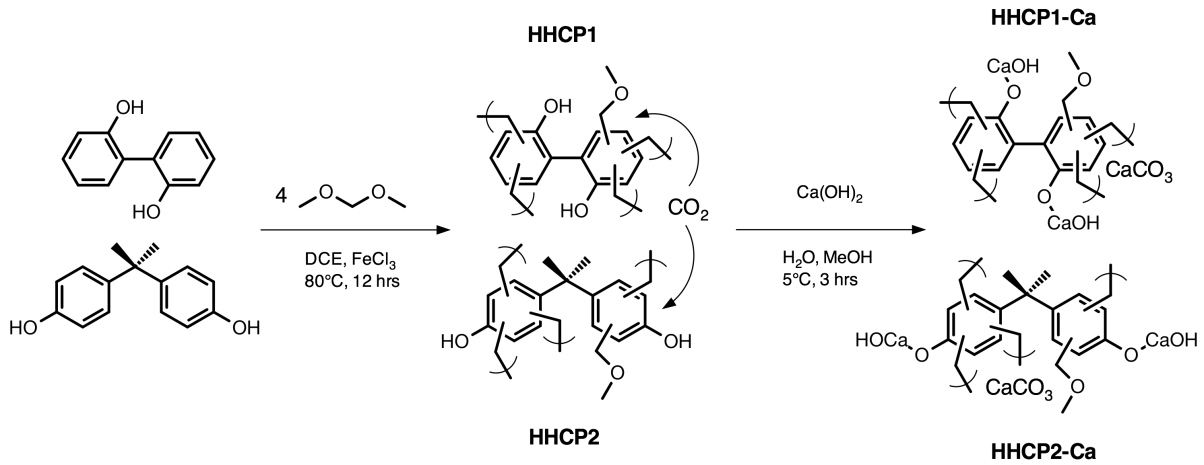

Scheme 5.1. Synthesis of calcium-loaded hydrophilic hypercrosslinked polymers (HHCP1-Ca and HHCP2-Ca from biphenol monomers.

An alternative strategy is to embed functionality within the starting monomers, circumventing the loss of surface area observed with post-synthetic functionalisation [189, 198]. This has been demonstrated in boron-rich conjugated microporous polymers (CMPs), which were selective towards fluoride adsorption, although again, with a moderate uptake capacity of 24 $mg \cdot g^{-1}$ [100]. Ma *et al.* reported a porous organic framework (POF), successfully metallated, post-synthesis [120]. Both these materials however, required costly reagents for the polymerisation. In this paper, we have synergised in-built monomer functionality with strategic metal-loading with Ca to create the first metallated, hypercrosslinked polymers from two economical hydrophilic monomers 2,2'-biphenol, 4,4'-(propane-2,2-diyl)diphenol (bisphenol A) (Scheme 5.1). The hydrophobic monomer biphenyl, having an analogous structure to 2,2'-biphenol, is also concurrently polymerised, contacted with Ca^{2+} ions and characterised, to demonstrate the impact of hydrophilicity on the performance of the materials as defluoridating media. The potential within the strong affinity between fluoride ions and Ca-based mineral adsorbents is shown in a recent review [204]. However, the binding strength is not so great as to cause irreversible adsorption (CaF_2 K_{sp} = 3.9 x 10^{-11}) and should allow facile loading/desorption cycles, since our remit is in potential recovery, as well as defluoridation. Ca^{2+} is also non-toxic and its modest ionic radius (100 pm) theoretically allows access to micropore environments and promotes a high degree of loading.

5.4. Methodology

5.4.1. Chemical reagents

All chemicals were of analytical reagent grade, unless otherwise stated, and used without further purification. For polymer synthesis, biphenyl, 2,2'-biphenol and bisphenol A and $FeCl_3$ (anhydrous) were purchased from Sigma Aldrich. 1,2-dichloroethane (DCE, anhydrous, 99%), dimethoxymethane, $Ca(OH)_2$, and methanol were purchased from Fisher Scientific. For aqueous anion uptake experiments, Na_2CO_3, NaI, $NaNO_3$, Na_2SO_4 and KH_2PO_4 were purchased from Sigma

Aldrich. NaCl and NaF were purchased from Fisher Scientific. KBr (spectroscopic grade) and NaF for fluoride analytical standards (99.999%) were purchased from Acros Organics. Deionised water (>18 MΩ) was used throughout.

5.4.2. Synthesis of HHCPs

In a standard synthetic procedure, a two-necked, round-bottom flask (500 mL), fitted with a stirrer, was charged with the biphenol monomer (30 mmol). This was dissolved in DCE (100 mL) and placed under nitrogen. Dimethoxymethane (10.6 mL, 120 mmol, 4 eq.) was added anhydrously, followed by a slurry of $FeCl_3$ (19.5 g, 120 mmol, 4 eq.) in the minimum quantity of DCE and the mixture was stirred at 80°C for 12 hr. The resulting polymeric mass was washed with further DCE and methanol, then further purified by Soxhlet extraction for 12 hr. It was finally washed with HNO_3 (3 M), then NaOH (1 M), to remove as much of the trapped catalyst as possible, then deionised water until the filtrate pH was neutral, before being dried in a vacuum oven at 60°C overnight. This afforded the final hydrophilic hypercrosslinked polymers (HHCPs) as brown powders. The 2,2'-biphenol polymer was termed HHCP1 (8.07 g, 115%) and the bisphenol A polymer HHCP2 (9.69 g, 117%). For the corresponding biphenyl HCP (HCP1), the same procedure was followed, with 5 eq. of crosslinker and catalyst, and resulted in a yellowy-brown powder (7.25 g, 113%). All yields were calculated on the basis of complete crosslinking occurring at every aromatic -CH- group.

5.4.3. Calcium-loading of HHCPs

In a standard metal-loading procedure, 30 mmol of the HHCP was left in an open vial for 1 hr, to equilibrate with atmospheric gases. It was then placed in a 1:1 solution of water and methanol (2 L) in a polypropylene bottle and left to swell for 1 hr at 18°C. $Ca(OH)_2$ (3.71 g, 50 mmol) was added and the slurry was stirred at 5°C for 3 hr. The polymer was separated by gravity filtration and washed with water until the filtrate pH was neutral (~0.5 L). It was finally dried in a vacuum oven at 60°C, which afforded the final product as a sepia powder (HHCP1-Ca: 11.7 g, HHCP2-Ca: 11.6 g).

5.4.4. Characterisation

Fourier transform infrared (FTIR) spectroscopy was performed using a Perkin-Elmer Spectrum 100. Samples were mixed with KBr (spectroscopic grade, 99.9 %) and pressed into a disk before being measured in transmission mode. Some samples were also measured using an attenuated total refraction (ATR) instrument (Perkin Elmer UATR2).

Elemental analysis (C, H and N) was performed using an Elementar Vario MICRO Cube CHN/S analyser. Cl was quantified by Schöniger oxygen flask combustion and argentometric titration. Other elements were quantified by first, acid digestion of the polymers (HNO_3/$HClO_4$), followed by

appropriate dilution of the solutions and analysis via inductively-coupled plasma mass spectroscopy (ICP-MS), using an Agilent 7500CE mass spectrometer.

Scanning electron microscopy (SEM) images were recorded using an Innspect F50 field emission gun microscope, operating in secondary electron mode. Samples were mounted on carbon tape on Al stubs, without any coating treatment.

Gas sorption parameters were attained using a Micromeritics ASAP 2020Plus analyser. Nitrogen sorption measurements were analysed at -196ºC using ~100 mg of sample. BET surface areas were calculated over a relative pressure range of 0.01-0.11 P/P_0. Error values for surface area measurements were calculated by the Micromeritics Physi ViewCalc programme via non-linear least-squares fitting. Differential pore sizes were calculated using the NLDFT method using the model for Carbon Slit Pores by NLDFT. Samples were degassed at 120°C under dynamic vacuum immediately prior to analysis.

Solid-state NMR analysis was carried out via 1D ^{1}H-^{13}C cross-polarisation magic angle spinning (CP/MAS) experiments, using a Bruker Avance III HD spectrometer.

Powder X-ray diffraction (PXRD) spectra were attained by grinding samples in a mortar and pestle, followed by analysis using a Bruker D2 Phaser X-ray diffractometer, using a single Ni K-β filter. Diffractograms were matched using the International Center for Diffraction Data (ICDD) PDF-4+ database [220].

X-ray photoelectron spectroscopy (XPS) was carried out using a Kratos Supra spectrometer, with a monochromated Al source and two analysis points per sample.

For zeta potential analysis, suspensions of 0.20% Ca-loaded HHCP in 1 mM KCl (w/w) were made up and adjusted to the required pH by addition of HCl or NaOH. Analysis was performed using a Malvern Zetamaster instrument.

Full experimental parameters are found in Appendix D for NMR (p D12) and XPS (p D18).

5.4.5. Determination of exchange capacities and pseudo acid dissociation constants for HHCPs

For all experiments, polymers were vacuum dried immediately prior to analysis and kept in closed containers, to prevent adsorption of CO_2. The apparent exchange capacity of HHCP1 and HHCP2 was determined, in triplicate, using Fisher-Kunin titration for weak acid cation (WAC) resins [302]. The method was unmodified, apart from no adjustment was required for degree of hydration, as the

polymers were not handled in hydrated form. Pseudo stability constants were calculated by potentiometric titrations, using a modified method reported by Ogden *et al.* [96], with a Mettler Toledo T5 Potentiometric Titrator, equipped with a standard pH electrode (DGi115-SC). A suspension of 100 mg polymer in standardized 0.00964 M HCl (50 mL) was titrated, in a closed system, against standardized 0.1008 M NaOH, with titrant additions of 0.02 mL, until the pH reached 11. Ionic strength was maintained at 1.0 M with NaCl and temperature was maintained at 18°C, in order that neither parameter should affect H^+ activity. Titrations were completed within 2 hr and 3 repeat titrations (with pH calibration) for each polymer were acquired.

5.4.6. Fluoride uptake behaviour of HHCP1-Ca and HHCP2-Ca

In a typical static uptake experiment, 100 mg polymer was placed in a polypropylene vial, to which was added 25 mL of NaF solution ($[F^-]$ = 100-2,000 mg·L^{-1}). The sample was sealed and placed on an orbital shaker (200 rpm) for 6 hr, until equilibrium was reached. Samples were passed through a 0.25 μm Whatman syringe filter, before being diluted appropriately for fluoride quantification. This was carried out using a Sciquip ion-selective electrode (ISE). Each sample contained 20% ionic strength adjustment buffer (preparation shown in Appendix D, p D27).

For pH-controlled experiments, samples were made up to close to final volume (22 mL), before pH adjustment was performed by addition of HCl or NaOH (0.0001-1 M). Once the desired pH was reached, samples were agitated, as previously described, for 0.5 hr, and pH was rechecked and adjusted as necessary. This process was repeated for <24 hr until equilibrium was reached, at which point, the volume was finalised and samples treated as before for analysis. For competition experiments, 25 mL of an equimolar solution of F^-, Cl^-, Br^-, I^-, NO_3^-, SO_4^{2-}, PO_4^{3-} and CO_3^{2-} (1.0 mM) was used as the contact media. Samples were diluted appropriately and analysed via anion chromatography, using a Metrohm 883 Basic IC plus, with a Metrosep A Supp 5 150/4.0 column and Na_2CO_3/$NaHCO_3$ eluent (CO_3^{2-} was not quantified, but was added to the contact solution to determine any suppression of fluoride uptake).

In a typical kinetic experiment, 2.00 g polymer was placed in 1 L polypropylene beaker, to which 500 mL NaF solution was added ($[F^-]$ = 2,000 mg·L^{-1}). A timer was immediately started and small aliquots were removed from the beaker and immediately passed through a 0.25 μm Whatman syringe filter, diluted appropriately and analysed by ISE, as previously described. The total volume removed did not exceed 2 mL.

In dynamic experiments (setup shown in Figure D1), polymers were wetted with deionized water and a hydrated volume of 5.50 cm^3 was packed into a polypropylene column. This was connected to a Watson Marlow 120U peristaltic pump, using Watson Marlow Marprene® tubing, which passed an

inlet NaF solution upwards through the column, with a flow rate of 2.75 $mL \cdot hr^{-1}$. The eluent was collected in polypropylene tubes, using a Bio Rad 2110 autosampler and the fractions were diluted appropriately and analysed via ISE, as before.

Two routes were attempted for regeneration of the polymer adsorbents. In the first, ~1 g fluoridated polymer was placed in a 1 L polypropylene bottle and equilibrated with 1 L NaOH (1 M) for 3 hr. The polymer was vacuum-filtered and washed with deionized water until the filtrate pH was neutral (~0.5 L), then dried in a vacuum oven, as previously described, before repeat fluoride uptake experiments were performed. In the second method, ~1 g fluoride-loaded polymer was placed in a 1 L polypropylene bottle and equilibrated with 1 L HCl (1 M) for 3 hr. The polymer was vacuum-filtered and washed with deionized water until the filtrate pH was neutral (~0.5 L). It was then reloaded with Ca, as previously described, before repeat fluoride uptake experiments were performed.

5.5. Results and discussion

5.5.1. Synthesis and Ca-loading of HHCPs

Both HHCPs were prepared in good yields (HHCP1: 115%, HHCP2: 117%). The generic "knitting" technique for small aromatic molecules (Scheme 5.1) was originally reported by Li *et al*. [184]. Analogous materials to the HHCPs were first reported by Dawson *et al.* [185] but our exact synthetic conditions were those described by James *et al.* [189] Additional acidic and alkaline washing steps, unique to this work, ensured maximal removal of any residual Fe species remaining in the networks, as these would have been likely to interact with fluoride during uptake experiments [129]. As with previous literature, yields were above the theoretical maximum, which is attributed to the presence of partially-reacted crosslinker in the final polymers [189, 303]. Ca-loading was performed at 5°C to improve $Ca(OH)_2$ solubility (Scheme 5.1). HHCP1-Ca and HHCP2-Ca showed significant increases in mass upon Ca-loading, as would be expected. The attempted Ca-loading of HCP1 resulted in a modest increase in mass (+ ~6%), which nonetheless suggested that some metal adsorption had occurred by an unexpected mechanism.

5.5.2. Characterisation

Scanning electron micrographs are shown in Figures D5-D7, which show that all networks were composed of <5 μm roughly spherical microparticles, partially fused into much larger agglomerates >10 μm in diameter. This is consistent with previous literature [185]. However, there are some interesting variations between the networks. The average size of microsphere appeared to increase in the order HCP1 > HHCP2 > HHCP1. A possible explanation is that the DCE solvent can better solvate the more hydrophobic networks during the initial gelatinous polymer phase, thereby allowing the microspheres to grow larger before they fully precipitate. A similar phenomenon was reported by

Cooper and Holmes [304]. The HCP1 particles also had a seemingly rougher surface than the biphenol polymers, which is more analogous to CMPs [305]. This may imply the microstructures of HHCP1 and HHCP2 are less ordered. There was no morphological difference detectable upon Ca-loading.

Table 5.1 shows the composition of the networks after polymerisation and also following Ca-loading. All theoretical masses were calculated on the basis of complete crosslinking occurring at every aromatic -CH- group and exchange of both alcoholic protons in the biphenol monomer units for a -CaOH group, which we believed was feasible [200]. HHCP1, HHCP2 and HCP1 possessed a lower C mass % than the expected theoretical figure, which is consistent with previous literature [184, 190]. This has been attributed to the presence of residual $FeCl_3$ trapped in the micropores [185], but the large discrepancies between Cl and Fe mass % suggests this is unlikely and that the Cl becomes otherwise associated during the polymerization. The unaccounted mass % can likely be attributed to extra O content, in the form of partially-reacted crosslinker [303], or atmospheric gases adsorbed under ambient conditions. [185] For HHCP1 and HHCP2, we attempted to adjust the theoretical structure of the biphenol units within the polymer matrix, to rationalise the Ca-loading behaviour (Appendix D, p D5). From these calculations, the extent of Ca-loading was seemingly ~50% of what would be expected if every alcoholic proton was exchanged. However, as shall be seen, Ca-loading was not achieved only via covalent bonding. This does nonetheless explain why the actual C mass % in the metallated polymers was closer to the theoretical values of Table 5.1, because less Ca is adsorbed than expected.

Table 5.1. Elemental composition of the polymer networks. All elements are in units of % mass.

Network	C theoretical	C	H theoretical	H	Ca	Cl	N	Fe
HHCP1	82.1	69.3 ± 0.8	4.27	5.33 ± 0.14	<0.1	1.16 ± 0.13	1.84 ± 0.02	0.0450 ± 0.0003
HHCP2	82.6	65.8 ± 0.1	5.80	4.20 ± 0.02	<0.1	4.38 ± 0.16	<0.1	0.146 ± 0.002
HCP1	95.3	76.0 ± 0.1	4.67	4.28 ± 0.04	<0.1	8.15 ± 0.11	<0.1	0.0326 ± 0.0020
HHCP1-Ca	55.5	58.8 ± 0.4	2.89	4.92 ± 0.14	9.50 ± 0.71	0.365 ± 0.007	1.45 ± 0.01	0.0142 ± 0.0034
HHCP2-Ca	58.7	54.7 ± 0.2	4.12	3.99 ± 0.00	6.39 ± 0.46	3.46 ± 0.16	<0.1	0.1240 ± 0.0010
HCP1 + $Ca(OH)_2$	-	69.8 ± 0.7	-	4.53 ± 0.04	1.31 ± 0.08	4.97 ± 0.02	<0.1	0.0262 ± 0.0006

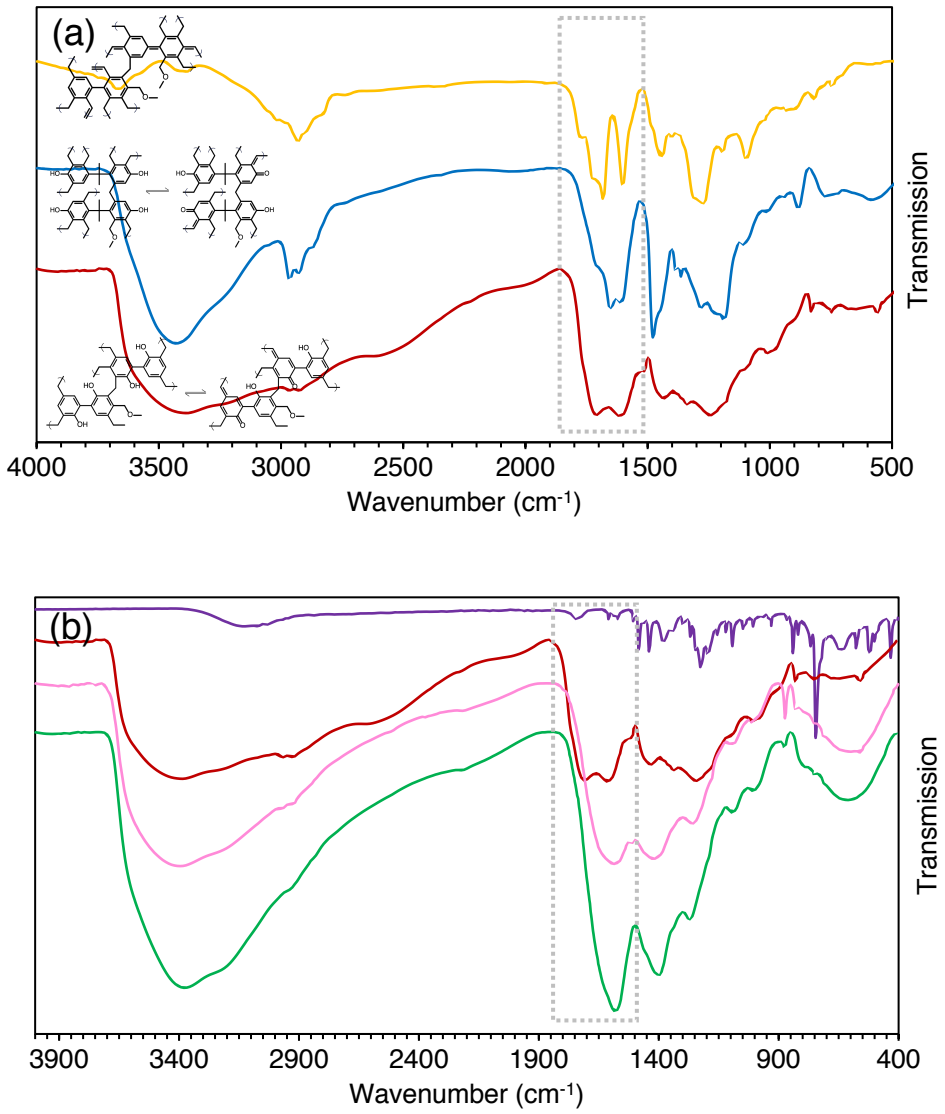

Fig. 5.1. (a) FTIR of HHCP1 (red line), HHCP2 (blue line) and HCP1 (yellow line). **(b)** FTIR of 2,2'-biphenol monomer (purple line), HHCP1 (red line), HHCP1-Ca (pink line) and HHCP1-Ca after treatment with 500 mg L^{-1} fluoride (green line). Quinonoid region is highlighted in each case.

In FTIR spectra, the HHCP networks exhibited broad O-H st. peaks, dissimilar to those of the parent monomers, which suggested that extensive H-bonding took place within the micropores. The HCP1 spectrum revealed the formation of quinonoid areas within the network (strong peaks ~1600-1700 cm^{-1}), due to the Hydride scavenging behaviour of $FeCl_3$, reported by Vinodh *et al.* [301]. Spectra of HHCP1 and HHCP2 also showed quinonoid type peaks, but at slightly higher wavenumbers (Figure 5.1a and Appendix D, p D7-D9), suggesting that the alcohol groups were partially incorporated into the quinonoid structures via resonance donation. In support of this, the Ca-loading of the networks seemingly altered the molecular orbital energy of the quinonoid structures, (Figure 5.1b) due to the phenolic oxygens now forming more polarised covalent bonds with -CaOH groups, which explains the colour change of the materials (Figures D2-D3). To confirm this theory, HHCP1 and HHCP2 were treated with 3 M NaOH, prior to FTIR analysis, to attempt to completely deprotonate the

materials. This caused a striking colour change, with both networks turning black, and again, the quinonoid spectral region was altered, with a new peak appearing at ~1,740 cm^{-1} (Figures D12-D13). This is predictable, since the association of alkali metal cations with phenols is an ionic interaction ($Ar\text{-}O^{-}Na^{+}$), whereas the Ca interaction is a strongly polarized covalent bond (Ar-O-Ca-OH) [200]. These colour and spectral changes were not observed with HCP1 (Figures D4 and D14).

The NMR spectra of HHCP1 and HHCP2 derivatives (Figure D15) supported these observations. Both spectra exhibited an intense peak at δ~120, representing cross-linked aromatic/quinonoid carbons, and a smaller peak at δ ~140, representing phenolic *ipso* carbons; but also a small peak at δ 160-175, which we assign to a second phenolic carbon environment, for which the bonded oxygen atom may be deprotonated with the polymer in an anhydrous state. This shifts upfield and increases with intensity upon metallation, indicating a change in the electronegativity of the oxygen. This strongly de-shielded carbon environment was not seen in spectra of the monomers (Figures D16-D17). Interestingly, there were also changes, upon metal binding, to the small peaks at δ 50-75. These likely represent the aliphatic carbons of partially-reacted crosslinkers (between an aromatic ring and a methoxy group) and could imply that these oxygen atoms also interact with metal ions.

Quantification of the differing optical properties of the networks is beyond the scope of this paper. However, these preliminary findings do indicate that optical properties of HCPs may be controlled by strategic electron-donating or withdrawing groups, which could have ramifications for their use as molecular probes, chemosensors and photovoltaic devices [301]. Figure D18 shows the possible quinonoid structures which could be adopted by HHCP1 and HHCP2 in a manner than would avoid steric hinderance of the -OH groups. It can be seen that this infers differing binding environments for the Ca^{2+} ions between the two networks, which will be discussed in due course.

XRD spectra of the non-metal-loaded networks showed the samples to be completely amorphous, as is common for MOPs [306]. However, diffractograms of HHCP1-Ca, HHCP2-Ca and HCP1 after $Ca(OH)_2$ treatment all showed peaks corresponding to crystalline $CaCO_3$ (vaterite) [220]. A comparison of spectra for samples of Ca-loaded networks after contact with NaF solutions of increasing concentration (Figures D19-D20) showed the growth of CaF_2 (fluorite) peaks, with a corresponding decline in vaterite peaks, thus establishing one of the mechanisms of fluoride extraction. Both 2,2'-biphenol and bisphenol A HCPs have a proven affinity for CO_2 sorption, even with high levels of N_2 and water vapor present (isoteric heats of adsorption = 28-31 $kJ{\cdot}mol^{-1}$) [185]. However, it was unknown whether the networks were equilibrating with atmospheric CO_2 in their non-metallated forms, prior to Ca^{2+} contact, or whether the CO_2 sorption and conversion to $CaCO_3$ took place during $Ca(OH)_2$ treatment, or during exposure to the atmosphere afterwards. An experiment was conducted, described in detail in Appendix D (p D18), which proved that the former

was the case. To the best of our knowledge, the synergistic behaviour of CO_2 adsorption in ambient conditions being converted to a higher degree of functionalisation for an intended application, has not been observed previously in MOPs, although it is predictable, given their high gas adsorption capacity [192, 194] and the favourability of $CaCO_3$ formation (ΔG_f^0 = -1129 kJ·mol^{-1}).

These results demonstrate that hydrophilic HCPs can be essentially activated for enhanced Ca uptake (and almost certainly other alkali earth metals) without the need for high pressure or a pure CO_2 source. It is possible that the metal-loading capacity could be enhanced still further by first exposing the polymers to, for example, a flue gas stream, which may have potential for synergistic industrial process development.

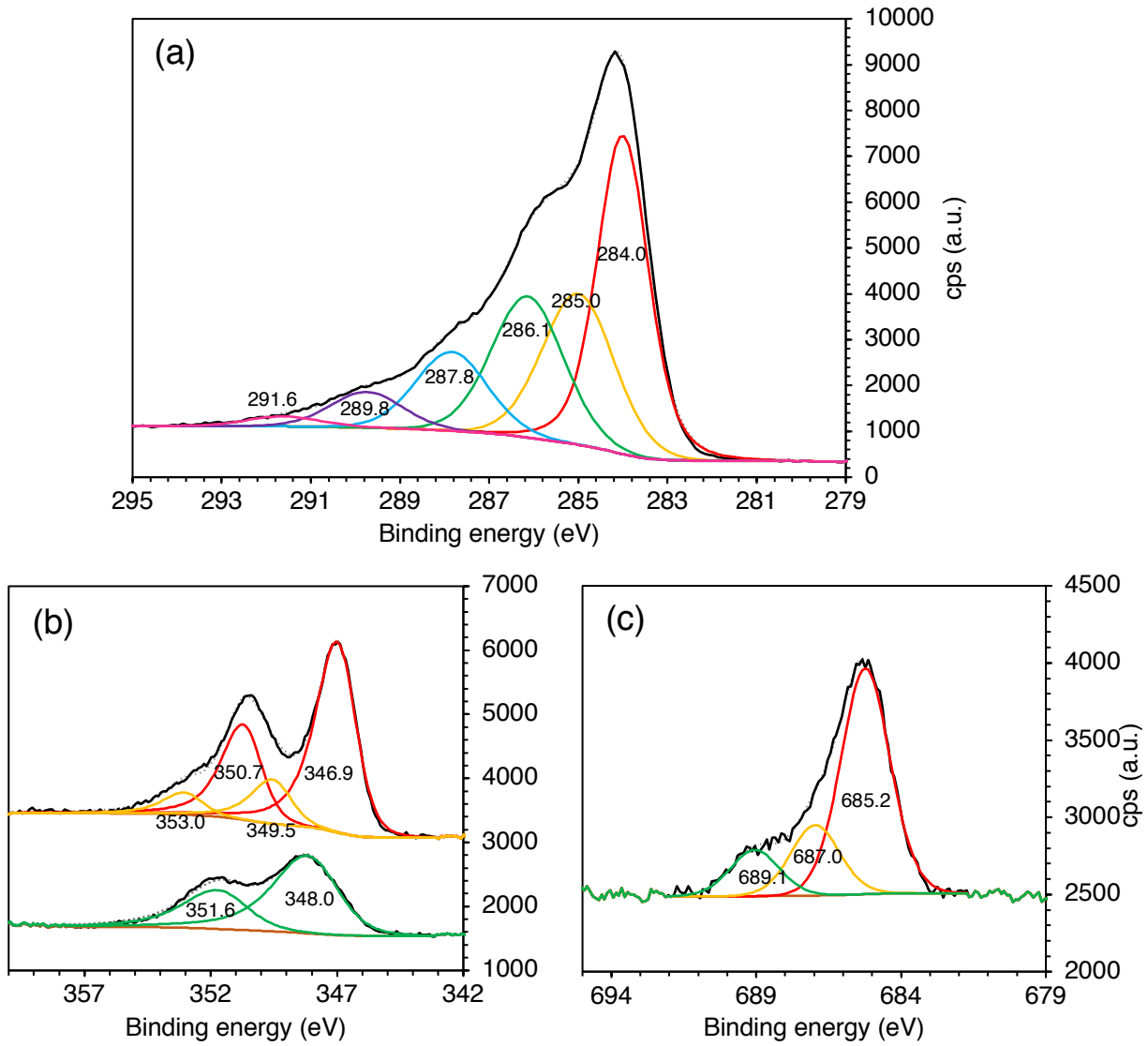

Fig. 5.2. (a) High resolution C 1s XPS spectrum of HHCP1-Ca, with calculated peak-fitting. **(b)** High resolution Ca 2p XPS spectrum of HHCP1-Ca (top) and HHCP1-Ca after contact with 2,000 mg·L^{-1} fluoride solution as NaF (bottom), with calculated peak-fitting. **(c)** High resolution F 1s XPS spectrum of HHCP1-Ca after contact with 2,000 mg·L^{-1} fluoride solution as NaF.

The full dataset for XPS characterisation is seen in Tables D5-D9. Figure 5.2a shows the wide range of C environments present in HHCP1-Ca, detectable by XPS. As expected, the most prevalent species was aromatic sp^2 carbons (284.0 eV). The peak at 285.0 eV was assigned to aliphatic crosslinkers, which had not been hydrogen-scavenged and remained sp^3-hybridised. The peak at 286.1 eV represented C-O carbons of partial crosslinkers. The 287.8 eV environment was midway between the expected binding energy of C-O and C=O carbons respectively. This is thought to represent the *ipso* phenolic carbons and appears to confirm the partial delocalization of the π electron cloud on to the phenolic C-O bond. The most electron-poor environments were at 289.8 eV, which was characteristic of a carbonate ($CaCO_3$) [307], and at 291.6 eV, assigned to a π-π^* satellite. We had no expectations of detecting adsorbed CO_2 in non-metallated samples, but surprisingly, carbonate-like environments were also observed in the spectra of HHCP1, HHCP2 and HCP1. We believe this was due to initial co-uptake of CO_2 and water vapor under ambient conditions [185], followed by HCO_3 formation under the XPS vacuum. Essentially, this can be described as the formation of a Van der Waals H_2O/CO_2 precursor complex, which is catalytically activated by acidic surface sites (the phenol groups in this case) to form carbonic acid, then decomposes to bicarbonate and a proton [308]. The C 1s spectra of HHCP2 polymers and derivatives presented similar carbon environments, but with a higher ratio of aromatised carbons (~50%), while HCP1 samples showed an even higher proportion (~75%), indicating that quinonoid formation was more extensive in these networks. This would explain why the SEM images were suggestive of a more ordered microstructure.

Two distinct environments were observed in the HHCP1-Ca Ca 2p spectrum (Figure 5.2b). The lower binding energy species (346.9 and 350.7 eV) was characteristic of $CaCO_3$ [307, 309]. Given the relative breadth of the peaks, it is believed that this environment also represents the polymer-bound R-O-Ca-OH species. The higher binding energy species (349.5 and 353.0 eV) is unusually electron-poor [310] and may be a result of complex formation via multiple interactions with the quinonoid pseudo-phenoxide groups, acting as neutral ligands [311], with anionic ligands being -OH, or possibly even -Cl or $-NO_3$, based on elemental analysis (Table 5.1, Figure D25). After contact with NaF solutions, the Ca 2p spectrum shows a single environment, corresponding to a CaX_2 salt [310]. However, the breadth of the peaks could again conceal a number of similar environments. Indeed, the F 1s spectrum of HHCP1 (Figure 5.2c) suggests that CaF_2 (685.2 eV) is not the only species present. There are two more unusually electron-poor species present. The peak at 687.0 eV was assigned to an -RO-Ca-F group still bound to the polymer network, while the peak at 689.1 eV could represent a fluoride bridging ligand, held between two Ca centres within the micropores [312]. Electron-poor F species existing as bridging ligands in non-crystalline complexes have previously been reported from XPS probing of metal-loaded polymeric resins [104]. Ca and F environments were similar for HHCP2, but the more electron-poor Ca species was not detected (Table D8), whilst

HCP1 after $Ca(OH)_2$ treatment revealed a small amount of Ca-loading had taken place, likely in the form of $CaCO_3$.

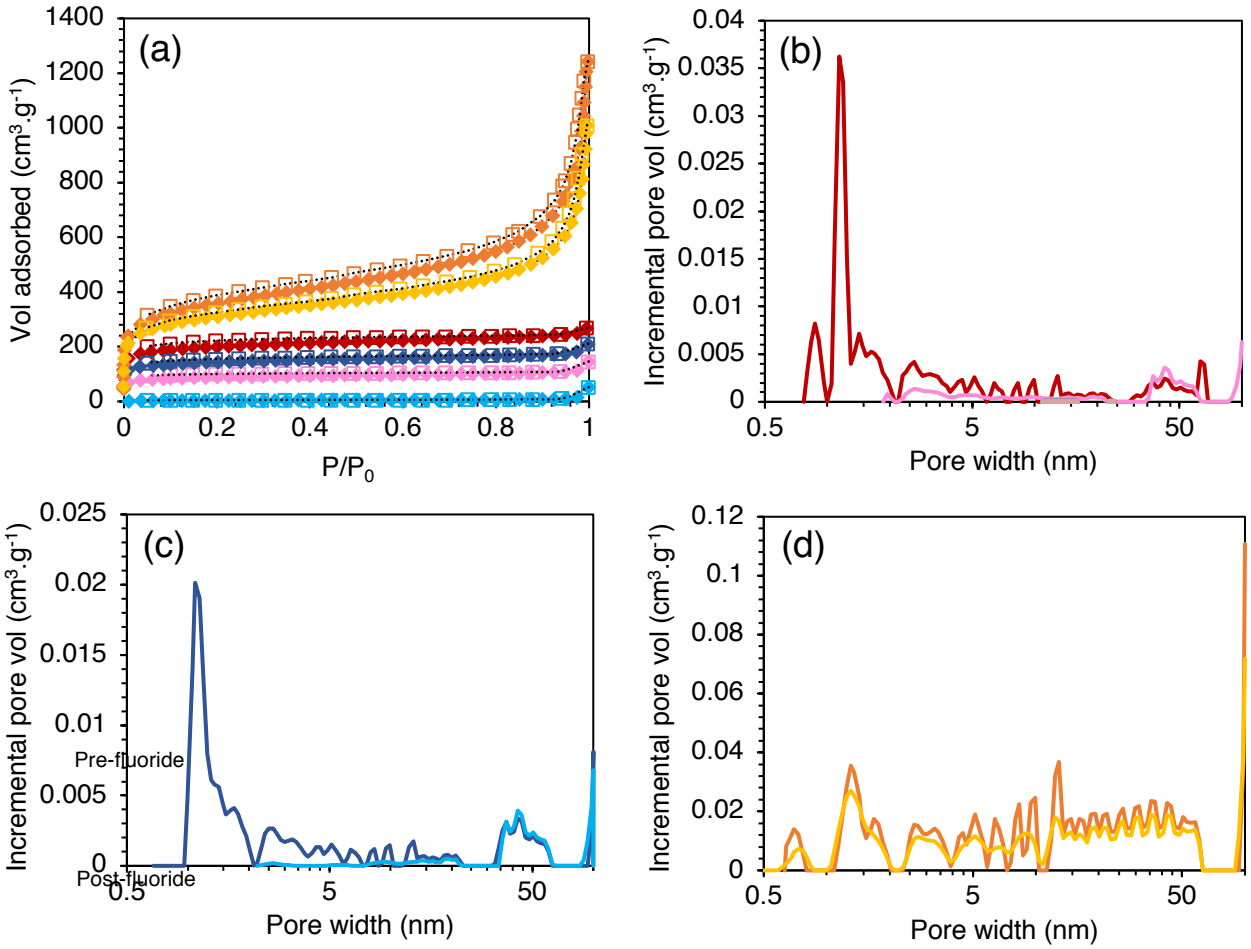

Fig. 5.3. (a) N_2 adsorption/desorption isotherms for ◆□ HHCP1, ◆□ HHCP1-Ca, ◆□ HHCP2, ◆□ HHCP2-Ca, ◆□ HCP1 and ◆□ HCP1 after $Ca(OH)_2$ contact. Diamonds represent adsorption. Squares represent desorption. T = 77 K. **(b)** Pore size distribution, calculated by NLDFT for — HHCP1 and — HHCP1-Ca. **(c)** Pore size distribution for — HHCP2 and — HHCP2-Ca. **(d)** Pore size distribution for — HCP1 and — HCP1-Ca.

Investigation into the pore environments and surface areas of the networks, via N_2 sorption, is shown in Figure 5.3 and Table D10. HHCP1 and HHCP2 exhibited type I isotherms, characteristic of microporous materials. The HCP1 isotherm was type II (more common for macroporous or non-porous materials, but exhibited some type IV character in that a slight hysteresis loop was observed. This is common for HCP powders polymerized in a large volume of solvent, with $FeCl_3$ catalysis, as opposed to polymer monoliths [303] and is commonly interpreted to indicate large mesopores within the samples. HHCP1 and HCP1 had rather higher calculated surface areas than similar networks previously reported, at 748 ± 5 $m^2 \cdot g^{-1}$ and 1,310 ± 1 $m^2 \cdot g^{-1}$,verses 657 $m^2 \cdot g^{-1}$ [185] and 815 $m^2 \cdot g^{-1}$ [184]. HHCP2 had a slightly lesser surface area than the literature equivalent, but was still highly porous (541 ± 4 $m^2 \cdot g^{-1}$ verses 650 $m^2 \cdot g^{-1}$ [185]. Such variation is common in HCP synthesis [184, 185, 189]. Small variations in synthetic technique, such as order of addition and temperature

ramping, likely effect on the prevalence of the competing reactions (crosslinking, partial crosslinking and hydrogen-scavenging). The previous high surface areas reported for these specific biphenol-based polymers was key to our selection of monomers for this study (for example, HCPs based on phenol itself are known to produce lesser surface areas of <400 $m^2 \cdot g^{-1}$ [184], so this monomer was not considered). After attempted Ca-loading, HCP1 showed a modest decrease in surface area to 1140 ± 1 $m^2 \cdot g^{-1}$, due to the $CaCO_3$ formation within the pores. However, the pore size distribution (Figure 5.3d) is very similar to the original polymer. HHCP1-Ca possessed a surface area of 334 $m^2 \cdot g^{-1}$, which was a more pronounced reduction, relative to HHCP1 but HHCP2-Ca had minimal micro- and mesoporosity, with a surface area of merely 17.1 $m^2 \cdot g^{-1}$. Both networks retained their larger mesopore fraction (~40 nm) upon metallation, but HHCP1-Ca also retained some smaller mesopores ~2.5 – 4 nm (Figures 5.3b and 5.3c). This may indicate that HHCP2 has narrower access channels to the mesoporous regions, which are blocked by the relatively large -CaOH groups, which may partially explain the lower Ca-loading (Table 5.1). Ma *et al.* reported alkali metal loading of carboxylated POFS, in which the surface area of the materials decreased according to ionic radius of the loading metal [120]. We have previously sulfonated HCPs and observed that the functionalization appeared to take place mainly in the mesopores of the materials [189]. In this instance, the loss of surface area from Ca chemisorption is from both micropores and mesopores (Table D10), but mainly the former indicating that functionalization was successful throughout the polymer matrix. Notably, HCP1, although having by far the greatest measured surface area, only achieved a small quantity of $CaCO_3$ conversion (Table 5.1), which demonstrates the necessity of not only porosity, but also polar group functionality in creating a suitable hydrophilic extractant for aqueous species.

5.5.3. Ion-exchange capacity and pseudo acid dissociation constants of HHCP1 and HHCP2

The non-metallated HHCPs were assessed for their proton uptake capacity and the apparent range of pK_a values for functional groups present in the networks (Table 5.2). To the best of our knowledge, these are the first such experiments carried out on microporous polymers and were intended to further probe the properties of the micropore environments created, in the context of ion-exchange behaviour. Potentiometric data were fitted, using SOLVER, to models ranging from 1-7 pK_as. (Figure 5.4) The experimental data for the HHCP1 network was best fit by a 4-pK_a model, while corresponding data for HHCP2 most closely agreed with a 5-pK_a model. Increasing the number of pK_as further led to inferior fitting and these results are not presented. As seen in Figure 5.4, a number of models gave feasible fittings to the data within experimental error and these possibilities are shown in Tables D11-D12. It should be noted that, while this technique is versatile, having been applied successfully to polymeric adsorbents [92, 96], it assumes that the molar concentrations of all different acidic groups throughout the adsorbent or ligand are equivalent, which, as has been

discussed, is unlikely in these networks. However, the experiments gave an indication of the variety of acidic environments present within the polymers.

Fig. 5.4. Potentiometic titrations of HHCP1 **(a)** and HHCP2 **(b)**, with least-squares curve-fitting to models allowing for 1 to 5 different pK_as, using Microsoft SOLVER. Error bars represent 95% confidence limits over

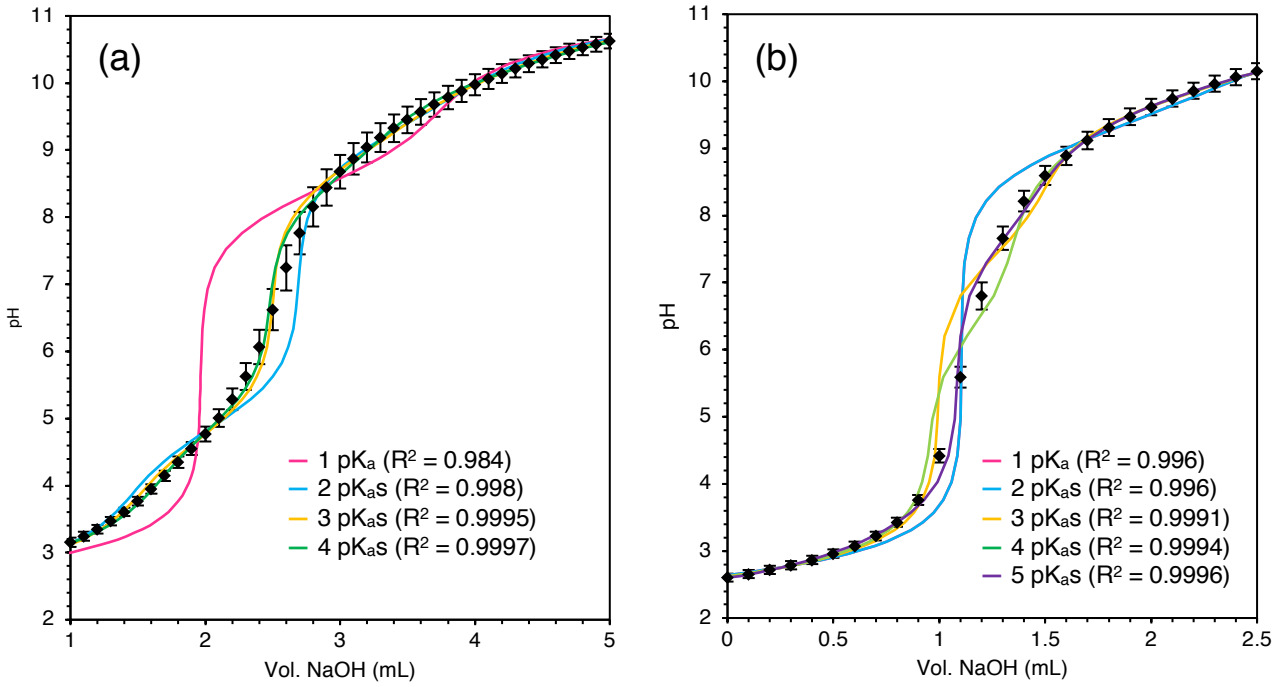

3 replicate titrations. T = 18°C. Ionic strength = 1.00 M. Note: for HHCP2, the 1 pK_a and 2 pK_a model lines are too close to be visually distinguished.

Table 5.2. Fundamental ion-exchange parameters for HHCP1 and HHCP2. Proton capacities calculated from Kunin-Fisher titration. Protonation constants from potentiometric titration, calculated from best fitting models.

Polymer	Proton capacity (mmol·g^{-1})	$Log_{10}K_1$	$Log_{10}K_2$	$Log_{10}K_3$	$Log_{10}K_4$	$Log_{10}K_5$	R^2
HHCP1	6.34 ± 0.17	10.5 ± 0.1	9.99 ± 0.06	8.48 ± 0.05	4.86 ± 0.04		0.9997
HHCP2	4.57 ± 0.25	10.1 ± 0.3	9.90 ± 0.09	9.19 ± 0.20	7.54 ± 0.12	3.33 ± 0.13	0.9996

As would be predicted from the relative masses of Ca-loading, HHCP1 had a significantly greater exchange capacity. Indeed, it is superior in this regard to even the most efficient commercial resins. The polyamine resin Purolite MTS9850 has an anion-exchange capacity of ~6.25 mmol·g^{-1} and the chelating resin Puromet MTS9501 (which has selectivity for alkali earth metals) has a reported cation-exchange capacity of only ~1.83 mmol·g^{-1} [92, 284]. The capacity of HHCP2 was rather lower than expected in comparison, even given the extra mass present in the theoretical repeating unit of the polymer. This would suggest that HHCP2 featured a greater % of partial crosslinking, with the extra methoxy groups adding to the mass (Figure D8). A larger C mass % was observed in HHCP1, suggesting that the O mass % in HHCP2 may be greater (Table 5.1). The range of pK_as observed in both polymers was far greater than expected. Dissociation for phenolic protons typically occurs at pH ~10. However, it is known that the 2 pK_as of 2,2'-biphenol are split, with the first occurring at 7.6 (very close to the predicted $log_{10}K_4$ value for HHCP1) and the second at 13.7, due to an

intramolecular hydrogen bond stabilizing the monoprotonated molecule [313]. For bisphenol A, the first pK_a is expected at 9.73 [314] but to the best of our knowledge, the second has not been reported. It is known however, that many 4,4'-biphenols also exhibit pK_a-splitting behaviour [315]. These data help to explain the pK_{1-3} values observed. The apparent pK_as below pH 5 are more mysterious, being more suggestive of carboxylic acids. Nevertheless, they are predicted by even the simpler models, with fewer pK_as (Tables D11-D12). It is known that hydrophobic environments, such as micropores, can lower pK_a values substantially [92, 96], although not to the degree seen here. It is notable however, that there appear to be similar acidic functionalities present in both networks, which produce slightly lower pK_as in the HHCP2 network (10.1 vs 10.5; 9.90 and 9.19 vs 9.99; 7.54 vs 8.48), which may be assumed to have more hydrophobic pore environments, because of the alkyl bridges between phenol rings. It is also known that 3 vicinal phenol groups will form a stable $[H_2(OPh)_3]^-$ structure through H-bonding [311], which could explain a particularly acidic proton environment (the extent of H-bonding in the networks was clear from FTIR data). Because of the probable pK_a-splitting, half of the phenolic protons in both polymers would not have dissociated under these experimental conditions.

NMR spectra (Figure D15) also support the predicted pK_as, as they suggest the existence of both protonated and deprotonated phenol groups within the polymers in an anhydrous state, having been washed to neutral pH before drying. This implies that one of the phenol groups in each monomer unit is never deprotonated or bound covalently to a metal ion. Yet the degree of deprotonation seems to be greater for the Na-loaded polymers. This is logical, as Na-loading took place using a 3 M NaOH solution, whereas the pH of the Ca-loading solution was limited by the solubility of $Ca(OH)_2$ and therefore the pK_2 values for the biphenols would not be reached [313]. This explains the more pronounced colour change for the Na-loaded polymers, since greater deprotonation and ionization of the phenolic oxygens has occurred, changing the optical properties (Figures D2-D3).

Taking into account elemental analysis, XPS and titration data, the efficiency of Ca^{2+} binding by the expected covalent interactions is seemingly <50%, relative to the number of original phenol groups, with the remainder taking the form of $CaCO_3$. Despite the very high fluoride uptake values achieved by the existing materials, there is clearly scope for further development in terms of potentially increasing the Ca-loading still further.

5.5.4. Equilibrium studies for fluoride-binding to polymers under static conditions

All synthesized networks demonstrated a degree of wettability when immersed in water (Figures D27-D32), in contrast to most HCP networks [189]. The Ca-loading was beneficial to wettability, due to the increase in mass % of polar groups. The order of hydrophilicity was clearly HHCP1 > HHCP2

> HCP1, which may contribute to the differences in Ca-loading and proton capacity, and almost certainly to the acidification of pK_as [96].

We briefly assessed the networks for their fluoride uptake capabilities by batch treatment of samples with 2,000 $mg \cdot L^{-1}$ fluoride solutions (Figure D31). Predictably, from Ca-loading data, HHCP1-Ca and HHCP2-Ca showed large apparent equilibrium uptake capacities (q_e), at >60 $mg \cdot g^{-1}$, which were equal to, or greater than that observed for an Al-loaded ion-exchange resin (representative of a current industrially used adsorbent [214]). Ca-treated HCP1 had a modest uptake capacity, attributed to CaF_2 formation from the trapped $CaCO_3$. HCP1 and HHCP1 also extracted a small quantity of fluoride, which may represent anion-exchange with small quantities of NO_3^- and or Cl^- trapped in the matrices. Following these data, subsequent fluoride uptake work focused solely on HHCP1-Ca and HHCP2-Ca.

We investigated the defluoridation potential of the networks over a broad pH scale and also analysed the corresponding zeta potential of the polymer surfaces (Figures D34-D35). Both networks had a wide working range, with highest fluoride q_e values observed at pH 3-7. Performance decreased at pH >7. This was a gradual decline, in the case of HHCP2-Ca and a more pronounced reduction in the case of HHCP1-Ca. Such behaviour is often attributed to competition from OH^- [130] or to the adsorbent surface acquiring negative charge [162]. In this instance, zeta potential did not correspond exactly with fluoride uptake, as the adsorbents are negatively charged over the whole pH range tested. This was demonstrated by linear dataplots of fluoride uptake verses zeta potential, which produced R^2 values of only 0.183 (HHCP1-Ca) and 0.0092 (HHCP2-Ca). Furthermore, at pH 8, $[F^-]$ is still 6 orders of magnitude above $[OH^-]$, making this explanation alone unlikely. The major uptake mechanisms may roughly be considered as the equilibria $CaCO_3 + 2\ F^- \leftrightharpoons CaF_2 + CO_3^{2-}$ and $RO\text{-}Ca\text{-}OH + 2F^- + H_2O \leftrightharpoons CaF_2 + RO\text{-}H + 2OH^-$ (XPS data suggested that the RO-Ca-F group is an intermediary, with CaF_2 formation being prevalent at higher $[F^-]$). CaF_2 solubility is constantly small at high pH, but increases dramatically at <3 [98, 316], which coincides with the drop in defluoridation behaviour of the polymers (Figures D34-D35). The uptake of fluoride using $CaCO_3$ itself as an adsorbent also becomes gradually more unfavourable at pH >7 [316], similarly to the behaviour of HHCP2. The second equilibrium would be predicted to still be favourable ≤pH 11.5 [317], which is clearly not the case in this instance. However, a hydrophobic pore environment will modify equilibria involving salt precipitation, specifically in polymeric resins [97, 104].

There is limited correlation between defluoridation and zeta potential for both networks at higher pH, with the decrease in surface potential to <-30 mV corresponding to the almost complete loss of fluoride uptake. The zeta potential drop can be related to deprotonation of unreacted (not Ca-loaded) phenol groups which, as has been discussed, will still be present in significant quantities in HHCP1-

Ca and HHCP2-Ca. According to Table 5.2, HHCP1-Ca deprotonation would be expected between pH 8.48 and 10.5, with HHCP2-Ca deprotonation between 9.19 and 10.1; hence the sharper increase in negative surface charge observed. The more acidic pK_as predicted by the modelling would play a lesser role in zeta potential results, as these groups would likely have been successfully converted to -CaOH active sites during metallation. We were unable to find any literature reports on the alkaline hydrolysis of calcium phenoxides or similar species. The comparatively large increase in negative surface charge between pH 8 and 10 for both networks may indeed cause electrostatic repulsion of fluoride. Hence the decreasing uptake [162]. The increasingly positive surface charge at very low pH does not equate to enhanced defluoridation, because the formation of the stable ion-pair F^-/H_3O^+ in solution [223]. Overall, both major uptake mechanisms are evidenced in the pH-dependent behaviour observed.

Because the intended remit of this work was remediation of potable water, rather than specific acidic or alkaline wastestreams, it was decided to run further experimentation at pH 7. Although HHCP2 in particular appeared to have an optimum pH range of 3-4, it was discovered that Ca^{2+} began to leach into solution at pH <3, resulting in equilibrium concentrations >50 mg·L^{-1}. Although expected (indeed, it is an indication of successful conversion of $CaCO_3$ to CaF_2 [316]), this would be undesirable from a water quality point of view.

Fluoride loading isotherms were produced for both networks from initial solution concentrations of 50-2,000 mg·L^{-1}. This is a larger range than is normally investigated, with most studies focussing on concentrations <50 mg·L^{-1} [129, 135, 209]. However, the fluoride concentration range reported in freshwater sources is similarly diverse [3]. Uptake data were fitted to 4 common classical adsorption models. These are presented, along with calculated parameters in Appendix D, p D29-D30.

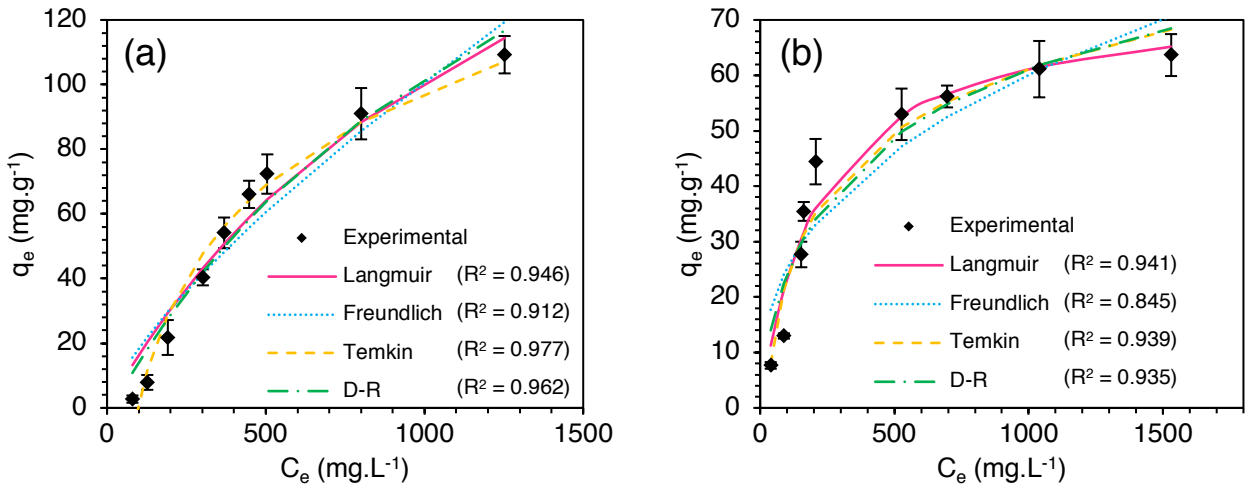

Fig. 5.5. Fluoride loading isotherms for **(a)** HHCP1-Ca and **(b)** HHCP2-Ca with two-parameter isotherm model fitting. Error bars represent 95% confidence limits from 3 replicate samples. D-R = Dubinin-Radushkevich. C_e = equilibrium [F^-]. Polymer mass = 100 mg. Contact solution volume = 25 mL. Initial fluoride concentration = 50-2,000 mg·L^{-1}. Contact time = 6 hr. T = 18°C.

Despite the similar functionalization of the polymers, the isotherms produced were not alike (Figure 5.5). Both isotherms did demonstrate multilayer character, with a good description of the data given by the Temkin model. This infers that adsorption proceeds via interactions between bound and aqueous sorbate, which change in energy as a function of concentration [318]. This may reflect the different strength binding interactions between fluoride and both covalently-held Ca and $CaCO_3$. It could also be reasoned that at lower [F^-] the fluoride ions principally react with the RO-Ca-OH groups, to form the RO-Ca-F intermediate, but as [F^-] increases, the fluoride ions interact further with this adsorbed complex and crystalline CaF_2 becomes the dominant species (Table D8).

Nonetheless, the isotherm for HHCP2-Ca was actually best described by the classical Langmuir model. This may be attributed to the HHCP1 polymer skeleton retaining much of its surface upon Ca-loading, allowing fluoride accumulation within the mesopores. HHCP2 in contrast, is essentially converted to a surface-functionalised medium (Figure 5.3) and therefore, adsorption takes the form of monolayers on the polymer particles (but still with sorbate-sorbate interactions, hence the good Temkin fitting). This would also explain the significantly lower capacity.

The multilayer nature of the fluoride adsorption by HHCP1-Ca is evidenced by the better fitting to the Freundlich isotherm, which empirically describes multilayer phenomena [319]. It is however noted that this model gave the poorest description of the uptake for both polymers. This in itself shows that conversion of $CaCO_3$ to CaF_2 is not the only effective mechanism, as this process in isolation is known to follow the Freundlich isotherm [98].

A reasonable description of adsorption by both networks was given by the Dubinin-Radushkevich (D-R) model. Comparison of the calculated desorption energy (E_{des}) of fluoride binding, calculated via this isotherm, showed that the fluoride was more strongly held by HHCP2-Ca (7.81 $kJ \cdot mol^{-1}$ vs 5.36 $kJ \cdot mol^{-1}$). These are averaged values, assuming a Gaussian energy distribution, so cannot be correlated to specific chemical interactions. They do however suggest that uptake by the HHCP1-Ca system is mainly physisorption (generally <8 $kJ \cdot mol^{-1}$), whereas the HHCP2-Ca system may be more dependent on ion-exchange or chemisorption processes (generally >8 $kJ \cdot mol^{-1}$) [92, 96]. The E_{des} value for fluoride extraction by metal centre ligand-exchange is ~15 $kJ \cdot mol^{-1}$ [104]. It is not appropriate to consider an overall “binding energy” for the conversion of $CaCO_3$ to CaF_2, as it is a complex interaction, which includes adsorption, dissolution and precipitation processes [316]. However, the activation energy for CaF_2 conversion from $CaCO_3$ is rather lower than for the ligand-exchange reaction (~40 $kJ \cdot mol^{-1}$ vs ~60 $kJ \cdot mol^{-1}$) [105, 320]. We therefore predict that the HHCP1-Ca system is more strongly influenced by $CaCO_3$ conversion and the HHCP2-Ca system more influenced by ligand-exchange reactions.

We monitored both the change in [OH^-] and [Ca^{2+}] in NaF solutions at various initial concentrations, after being equilibrated with HHCP1-Ca and HHCP2-Ca samples, as described previously (Figure D36). It was observed that equilibrium [OH^-] increased alongside initial [F^-], possibly providing proof for the ligand-exchange mechanism. From the experimental data of HHCP1-Ca, considerably more OH^- was exchanged at 2,000 mg·L^{-1} F^-, whereas for the HHCP2-Ca data, the difference in OH^- release between 400 mg·L^{-1} and 2,000 mg·L^{-1} F^- was modest. This is concurrent with isotherm data, showing that HHCP2-Ca exchange sites become exhausted at lower [F^-]. For both polymers, the quantity of Ca^{2+} leached reduced markedly in NaF solutions, relative to deionized water. Ca^{2+} dissolution is an essential driving force for the mechanism of CaF_2 formation from $CaCO_3$ [316], but at higher [F^-], the saturation point with respect to CaF_2 is instantly reached in the particle solvation layer [320] and fluorite precipitates in areas of high local surface Ca density, principally at the edges of retreating calcite crystal terraces [316]. This presumably also happens in areas of high covalently-bound Ca concentration, acting as nucleation sites for CaF_2 crystals. similar phenomena have been reported for metallated ion-exchange resins [104]. The overall chemistry of the Ca-loading and fluoride uptake processes are thus elucidated and summarised in Scheme 5.2.

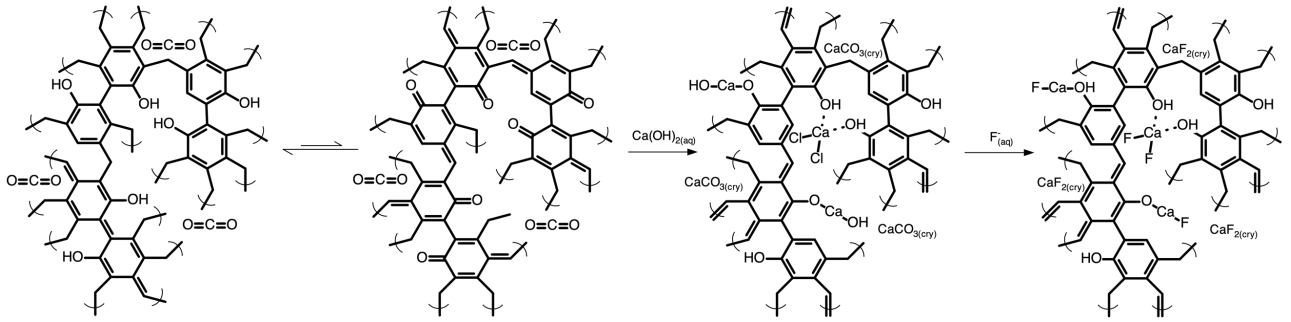

Scheme 5.2. Proposed Ca-loading and fluoride extraction processes of HHCPs, shown using the HHCP1 matrix as an example.

Both polymers had large maximal uptake capacities, calculated by D-R isotherm (HHCP1-Ca = 267 ± 34 mg·g^{-1}; HHCP2-Ca = 96.2 ± 10 mg·g^{-1}), which compare favourably to the literature (Table D14). As far as we are aware, only layered double hydroxide clay adsorbents, which have limited selectivity for fluoride, have recorded higher capacity than these materials (318 ± 6 mg·g^{-1}), [209]. HHCP1-Ca is the superior adsorbent at high [F^-], whereas HHCP2-Ca would be more appropriate at lower [F^-].

5.5.5. Kinetics of fluoride-binding to HHCPs under static conditions

Kinetic data were acquired for the two networks. Similarly to equilibrium data, a number of common models were applied and relevant parameters extracted (Appendix D, p D31-D35). Again, the uptake characteristics for the two networks were different (Figure 5.6a). For the HHCP2-Ca experiment, fluoride extraction rose sharply and quickly reached a plateau, in good agreement with the pseudo second order (PSO) model (R^2 = 0.946). This suggested the rate of adsorption would depend on the fluoride solution concentration and number of active binding sites available on the surface of the

sorbent particles. However, in the case of HHCP1-Ca, the PSO model described the adsorption data less successfully (R^2 = 0.905) and underpredicted the equilibrium uptake capacity. The fluoride uptake again increased sharply, but changed to a more gradual increase from 20-80 min (Figure D37). The Elovich model gave a superior fit (R^2 = 0.971), implying that multiple mechanisms were rate limiting at different contact stages [92]. $CaCO_3$ conversion to CaF_2 is known to be a multistep rate-limiting process [320]. The data fit to diffusion-based models (Figures D38 and D40) suggested that diffusion through the mesopores was unlikely to be rate-limiting and this is supported by other studies involving similar adsorbents [189]. The slower uptake mechanism is thus likely to be the conversion of $CaCO_3$ to CaF_2 within the mesopores.

HHCP2-Ca in particular, exhibited very rapid uptake, reaching ~50% equilibrium capacity ($t_{1/2}$) in ~0.6 min (Table D15). This is more rapid than commercial metallated ion-exchange resins (in defluoridation studies, the lowest $t_{1/2}$ value recorded was 1.8 min) [105, 129]. The observed rate constant is lesser than that reported for the MOF MIL-88A (2.81 x 10^{-2} vs 0.17-7.20 $g \cdot mg^{-1} \cdot min^{-1}$). However, this material had a lesser equilibrium uptake capacity of 40.4 $mg \cdot g^{-1}$ [298].

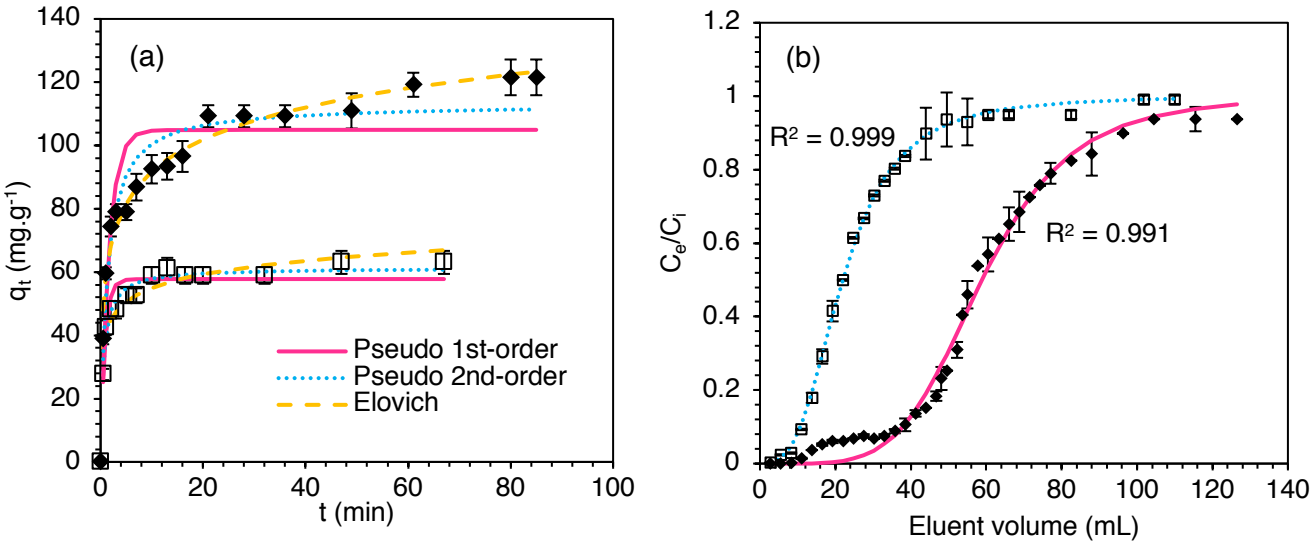

Fig. 5.6. Static and dynamic kinetic data for the networks. **(a)** Fluoride uptake over time by HHCP1-Ca (◆) and HHCP2-Ca (□) with fitting to kinetic models. Polymer mass = 2.00 g. Contact solution initial volume = 500 mL. Initial [F^-] = 2,000 $mg \cdot L^{-1}$. T = 18°C. **(b)** Dynamic fluoride breakthrough curves for HHCP1-Ca (◆) and HHCP2-Ca (□) with fitting to Dose-Response model. Inlet [F^-] = 2,000 $mg \cdot L^{-1}$. T = 18°C. For both datasets, error bars represent 95% confidence limits from 3 replicate electrode measurements.

5.5.6. Dynamic fluoride uptake experiments, using HHCPs as ion-exchange columns

In dynamic operations, the high capacity of the polymers was again demonstrated. Data were fitted to the empirical Dose-Response model (Figure 5.6b) [251], which has previously successfully described fluoride breakthrough with inlet flows of high concentration [105]. This model is empirical in nature but allows calculation of a dynamic sorbent uptake capacity (Table D16). This was found to be 95.8 ± 0.8 $mg \cdot g^{-1}$ for HHCP1-Ca and 58.4 ± 0.4 $mg \cdot g^{-1}$ for HHCP2-Ca, which are close to the

figures observed for static equilibrium experiments at equivalent [F^-]. It can thus be suggested that non-monolithic HCPs are suitable materials for column water treatment systems at low inlet flow rate, despite the small particle size. To the best of our knowledge, this is the first time such performance has been demonstrated.

As seen, data for HHCP1-Ca were not perfectly modelled (Figure 5.6b), as the more heterogeneous adsorption resulted in a two-stage breakthrough, with a weak adsorption site of low capacity becoming exhausted before major breakthrough occurred. The main breakthrough stage was however adequately modelled. A synergistic treatment could use HHCP1-Ca (more effective at high [F^-]) as the lead anion column adsorbent, with HHCP2-Ca as a guard or polishing column (more effective at low [F^-]).

5.5.7. Polymer selectivity for fluoride ions

A successful adsorbent for fluoride remediation must also demonstrate high selectivity for the anion, in order to then elute the captured fluoride as a pure aqueous effluent, from which recovery can be attempted. In the case of contaminated groundwater, there are often positive correlations between concentrations of fluoride and other common anions (Cl^-, PO_4^{3-} and HCO_3^-) [3]. We therefore studied competition and defluoridation-suppression effects of coexisting anions in an equimolar solution. It was observed that both polymers had high affinity for PO_4^{3-}. Indeed, the distribution coefficients (K_D) for PO_4^3 were an order of magnitude higher than for fluoride (Figures D41-D42). Surprisingly though, fluoride uptake was not suppressed by this behaviour, but enhanced, with K_D values increasing from 29.3 to 37.0 (HHCP1-Ca) and 12.3 to 19.5 (HCCP2-Ca). This was unexpected, as previous studies have reported only competitive adsorption processes for these two species [209, 321]. There were no changes to the crystalline species present in samples of the networks, after contact with the mixed anions solution (Figure D23). It is possible that adsorbed PO_4^{3-} leads to the adoption of pseudo hydroxyapatite complexes within the polymer matrix, which is an effective system for defluoridation [204, 322]. These experiments also revealed that Cl^- and NO_3^- were released during the uptake process. This supports the existence of a Ca species, proposed from XPS data, anchored to the network electrostatically, associated with 2 exchangeable anionic ligands. The amount of Cl^- released by HHCP2-Ca was somewhat greater (Table 5.1 shows there was far more Cl present in HHCP2 and HHCP2-Ca than the equivalents) and may help to explain why the desorption energy for this system was more indicative of an ion-exchange process.

5.5.8. Attempted regeneration of adsorbents

Several studies have used dilute NaOH to remove bound fluoride from the adsorbent [105, 323]. In this instance, this treatment was only partially successful (Figure D43), due to the insolubility of the precipitated CaF_2 at high pH. The presence of unreacted fluorite within the networks after NaOH

treatment was confirmed by PXRD, which also showed there was negligible $CaCO_3$ present (Figure D22). Nonetheless, both polymers retained appreciable capacity after 4 cycles of attempted NaOH regeneration, which suggests that the OH^-/F^- ligand-exchange reaction, which *is* reversible [105], is overall the dominant uptake mechanism observed in this work. Notably, HHCP2-Ca lost more of its capacity during the NaOH cycles than HHCP1-Ca, suggesting less reversible adsorption, concurrent with the binding energies observed. In contrast, the acid regeneration process completely restored and in fact increased the performance of both polymers slightly. This may indicate that more NO_3^- anions are introduced to the material, allowing for increased defluoridation by the postulated anion-exchange mechanism. The acid regeneration route of course desorbs the Ca, as well as fluoride, from the polymers. However, this may be advantageous from an applied perspective, since the recovery of fluoride from aqueous streams, as fluorite, requires a source of Ca^{2+} in the feed [50]. It would be necessary to raise the pH of the effluent to cause fluorite precipitation, at which point, recovery should be feasible via fluidized bed treatment [89]. The two regeneration techniques could possibly be used synergistically, with NaOH treatment cycles proceeding until the performance of the polymers falls below an acceptable level, at which point, full acid-regeneration occurs and the combined effluents are pumped to the fluorite recovery stage.

5.6. Conclusions

We have synthesized the first metal-loaded HCPs. Porous networks derived from biphenyl, 2,2'-biphenol and bisphenol A monomers possessed high surface area and exhibited quinonoid character. Following Ca-loading of the hydrophilic systems, the HHCP1-Ca (2,2'-biphenol), surface area was still significant, owing to mesoporosity retention, but HHCP2-Ca (bisphenol A) was converted to a surface-functionalised adsorbent. The metal-loading affected the quinonoid chromophores, altering π cloud delocalization. As well as the expected covalent binding interaction, Ca was loaded by $CaCO_3$ formation, caused by CO_2 uptake by the networks under ambient conditions. This is a new demonstration of how these already-known properties of HCPs may be capitalized on within a different remit. Non-metallated networks had proton capacities larger than for commercial ion-exchange resins and also surprisingly acidic pK_as. The cation-loading environments within the polymer pores were complex and varied, corroborated by spectroscopic techniques.

Both Ca-loaded networks possessed high defluoridation capacities, yet there were differences in loading behaviour in isotherm, kinetic and dynamic investigations. HHCP1-Ca had a greater capacity, but lower adsorption rate constants and uptake adhered more to multilayer thermodynamic models and multi-step kinetic models, due to diffusion of fluoride through the mesopores to the active sites. The dominant adsorbed species was crystalline CaF_2, formed from both $CaCO_3$ and covalently-bound Ca. Accordingly, caustic regeneration of the adsorbents was only partially

successful. However, acid regeneration, followed by Ca-reloading was effective, suggesting a long potential lifespan.

Seemingly small changes in the chemistry of the polymeric matrix have wide-ranging implications for the properties of these materials as ion-exchangers. It is hoped this will stimulate further investigation into the aqueous phase interactions of microporous polymers, which may play an important role in the future management of aqueous fluoride.

5.7. Acknowledgements

The authors thank University of Sheffield associates Mr Keith Penny (Dept. Chemical and Biological Engineering), for ion chromatography technical support, Dr Cheryl Shaw (Sorby Centre), for SEM technical support and Prof Steven Armes (Dept. Chemistry), for zeta potential analysis. TJR acknowledges funding from the EPSRC (Grant no. EP/L016281/1) and Bawtry Carbon International Ltd.

6. Conclusions

6.1. Research hypothesis

The depletion of geological fluorite and lack of efficient industrial recycling processes for aqueous fluoride are globally significant issues. This thesis has hypothesised that the problem may be ameliorated on two fronts, both of which could play a role in the conservation of fluoride. The first is enhanced valorisation of the fluoride trapped within solid SPL waste. This is accomplished via a hydrometallurgical treatment, incorporating a novel adsorption step. The platform for the technology is a commercially-available IX resin, with chemical modification by La^{3+} metallation (La-MTS9501). The second front is by development of microporous HCPs as selective adsorbents for fluoride; the hypothesis being that the combination of high surface area and economic starting materials can result in materials capable of surpassing commercial adsorbents in terms of efficiency and economics. This conclusion will show that evidence presented and discussed in experimental Chapters 2-5 has proven both aspects of the hypothesis correct. The proposed adsorption system demonstrates feasibility, both technically and (with lesser certainty) commercially. Furthermore, metallated HCPs do possess advantages over commercial resins (and other adsorbents), due to their fundamental physicochemical properties.

Much of the progression of knowledge shown in this work has been in elucidating the fundamental chemistry behind the proposed engineering processes. As such, there are application challenges remaining on both fronts, which are identified and addressed in 6.6 “Future work”.

6.2. Fundamental investigations into fluoride adsorption by La-MTS9501 via equilibrium studies and spectroscopic analysis

In initial experiments (Chapter 2), a synthetic PLS was used to simulate the leaching of SPL. Although much simplified compared to real leachate, this solution allowed an assessment of uptake behaviour by La-MTS9501 from systems of mixed F^-/Al^{3+} speciation and at an initial $[F^-]$ an order of magnitude higher than previous literature. It was found that the resin removed fluoride from solution with high efficiency. The static uptake q_{max} was determined as 126 $\pm$ 10 (Langmuir model) and 145 $\pm$ 10 (D-R model) $mg \cdot g^{-1}$. This is an order of magnitude higher than has previously been reported for fluoride extraction via IX resin and the values returned were only slightly below those for fluoride adsorption from analytical NaF solutions, which were 187 $\pm$ 15 (Langmuir model) and 149 $\pm$ 20 (D-R model) $mg \cdot g^{-1}$. The nature of the adsorption changed, depending on [AHF] in the contact solution, meaning it was impossible for any of the two-parameter models assessed to completely describe the process. Nonetheless, the adsorption appeared to switch from a weak chemisorption interaction at lower [AHF] to a physisorption interaction at higher [AHF]. The interaction between resin and AHF was heterogeneous in nature and, through a comparison with uptake from NaF solutions, appeared to be neither OH^-/F^- ligand-exchange, nor precipitation of LaF_3 or NaF. It was discovered at this stage that Al was co-adsorbed on to the resin, but the precise mechanism was yet unclear. However, given

the stability of AHFs vs known LaF_n species, it seemed likely that AHFs did not dissociate and allow ligand-exchange to occur as part of the process.

In addition to the studied PLS system, this chapter also revealed interesting uptake phenomena in simple NaF solutions, beyond the previously-reported ligand-exchanges. Higher [F^-] resulted in both LaF_3 and NaF precipitation within the resin macropores. This evidences how the hydrophobic pore environments of an IX resin, along with pre-existing nucleation sites, in the form of high concentrations of coordinated fluoride, are capable of modifying the solubility constants of inorganic salts and inducing crystallisation. This behaviour led to an artificially high q_{max} value for La-MTS9501 uptake from NaF solutions. Whilst it may be of limited practicality in dynamic column systems, it is possible that the phenomenon could be used advantageously in simple batch treatments of highly fluoridated water.

One of the key parameters of an IX system, the pH of the feed solution, was examined. It was found that the maximal uptake of the resin coincided with a pH range in which solubility of AHFs was reduced. Uptake was minimal at high and low pH, which indicated that recovery of fluoride via adsorption would not be feasible from untreated caustic or acidic leachate alone. Overall, Chapter 2 identifies the potential of La-MTS9501 for the intended remit and lays the foundations for understanding the adsorption mechanisms.

6.3. A pathway towards application of La-MTS9501 via static and dynamic kinetic experiments

Chapter 3 continued with experimentation, using the La-MTS9501/PLS system and gauged its potential in a more industrially-relevant context. However, thanks to the detailed modelling of the uptake of both fluoride and cocontaminants, the work serendipitously further clarified the uptake mechanism. Hence it was shown that AHFs were most likely adsorbed, without dissociation, via sharing of bridging fluoride and oxide ligands with the resin-bound La centres. The interaction was strong at low [AHF], due to chelation, but became weaker at high [AHF] because of subsequent weaker binding of further AHFs, likely via sharing of single bridging ligands. It was noted that the F^-/Al^{3+} molar ratio on the resin did not remain constant over the timespan of the uptake. In other words, the stoichiometry of the adsorbed complex over time did not remain constant. This provided an insight as to why the adsorbed AHFs remained in an amorphous state, as shown in Chapter 2.

Static and dynamic kinetic modelling of the uptake was successful. Static uptake followed PSO kinetics and it was likely that intraparticle-diffusion and possibly chemical reaction were rate-determining at different uptake stages, which is logical, given the strongly heterogeneous adsorption that this work implies. Dynamic uptake could be well-modelled by the empirical Dose-Response equation and the Thomas equation, which again implies that inter-facial mass-transfer was

dynamically rate-limiting. In both static and dynamic conditions, the derived rate constants were seen to decrease with increasing concentration of NaF solution or PLS, although the relationships were not linear. This is essentially because altering the concentration of the contact solutions changes the dominant uptake mechanism, with weaker interactions (and therefore slower adsorption) becoming more prevalent at higher C_i. For NaF solutions, the weak interaction is crystallisation of LaF_3 and NaF. For the PLS, it is likely binding of further AHFs via bridging ligands. In all cases, the kinetics of AHF adsorption were slower than free fluoride adsorption, attributed to a dominant chelation, rather than ligand-exchange interaction.

An elution profile, generated from a spent resin column showed that close to 100% of the loaded fluoride could be accounted for, although the dilute NaOH used as eluent was not sufficient to concentrate the fluoride and Al; only to separate them from other cations and anions in the system. The water-consumption of the elution was also considerable, with ~2,500 mL eluent required in total to completely elute the 5.5 mL column. These two factors represented a clear developmental need for the proposed system. However, the elution profile pointed towards cryolite as being the most convenient and economic recovery product for the system, due to pH and concentrations of fluoride and Al. It was finally shown that La-MTS9501 was capable of being reused over several adsorption/desorption cycles, without loss of performance, using NaOH as regenerant.

6.4. Application of the proposed adsorption system to real SPL waste

Chapter 4 was devoted principally to an investigation of how the La-MTS9501 column system would perform with the leachate of real SPL waste. It attempted to redress some of the practical problems of elution and cryolite recovery identified in the previous chapter. A thorough characterisation of multiple SPL samples was also made and the efficacy of a simple two-stage leaching treatment was examined.

The acquired SPL originated from a single site. It was seen that there were great variations in the compositions of the samples provided. Some samples were clearly of first-cut origin, being predominantly graphite, with fluoride contamination present mainly as NaF. Other samples contained a large proportion of second-cut material and many other crystalline phases were identified by XRD, some of which (SiC and sodium carbonate hydrate) had not previously been reported as major SPL components. This is likely reflective of differing cell decommissioning processes globally and explains the variation in reports of the “average” composition of SPL in the literature.

The leaching treatment used was relatively mild compared to most procedures reported in the literature, being conducted at room temperature and with dilute reagents. The majority of fluoride was solubilised by caustic leaching, but a significant extra fraction was mobilised by the acidic leach, which confirms that the existing LCLL process does not successfully valorise ~100% of the fluoride

content of SPL. This was true for both first-cut and mixed-cut samples. A large number of other species were also solubilised by both leaching stages. This confirmed the need for multiple leaching stages in SPL hydrometallurgy. It also gave insights into why the fluorite currently produced by LCLL is of low purity, because of co-precipitation. Although XRD spectra of fully-leached SPL samples suggested that minimal fluoride-bearing species were present, it must be noted that no quantitative evidence was produced to show that the fluoride in the exhausted SPL was below safe/allowable concentration levels.

It was however clear that the La-MTS9501 column system performed above expectations in the extraction of fluoride and aluminium from the resulting very high ionic strength liquor, with a dynamic uptake capacity of >30 $mg \cdot g^{-1}$. The increased efficiency, relative to the synthetic PLS experiments was essentially attributed to higher proportions of AlF_3 and AlF_2^+ in the leachate, relative to AlF^{2+}. The higher ionic strength and multiple minor species present in the leachate were not deleterious to the fluoride and Al uptake, but did have the effect of retarding the adsorption kinetics. This allowed a visual representation of the two distinct binding interactions, which were proposed, but not proved in Chapter 3; the first a stronger chelation between aqueous AHF and surface-bound La^{3+} centre, the second a weaker binding of further AHFs, probably through a single bridging ligand.

In elution studies, the strategy to change directly from deionised water to 1M NaOH as the eluent was successful, as a large fraction (~59%) of the fluoride loaded on to the column was coeluted with Al in a small number of bed volumes, at higher concentration than in the inlet solution and with no significant cocontaminants, apart from Si. Although incomplete, this marked the start of process optimisation for the proposed cryolite recovery system.

A first-order technicoeconomic analysis of the implemented process vs existing LCLL technology was attempted. It was found that the ability to regenerate the caustic eluent was key to industrial viability and unfortunately, this cannot at present be predicted with any certainty. This is because the technique for recovering cryolite from the fluoride-enriched eluent was outside the scope of this work and has not been investigated. Nonetheless, the assessment showed that the addition of an IX process within hydrometallurgical SPL treatment could provide benefits beyond research novelty; it could improve SPL valorisation efficiency, help in the industrial recycling of fluoride and add commercial value to an Al smelter, within a timeframe of <5 years. However, it should be noted that because of the early developmental stage of the project, all CAPEX values were subject to large margins of error (+50%, -30%) and in the worst-case scenario, the actual annual return, after implementing the IX system, could be minimal.

A flowsheet for the partially-developed process is shown in Figure 6.1. It can be seen by comparison to the original LCLL flow diagram (Figure 1.4) that although complexity and uncertainties are added

to the system, the only additional inputs (albeit with the provisos detailed in section 4.5.6) are the La-MTS9501 resin and the cryolite precipitant. Furthermore, that all original outputs of potential usefulness are retained, with the addition of cryolite to sell as a valuable commodity. Overall, it is felt that the potential of the process to add value and sustainability to a hydrometallurgical SPL treatment is significant.

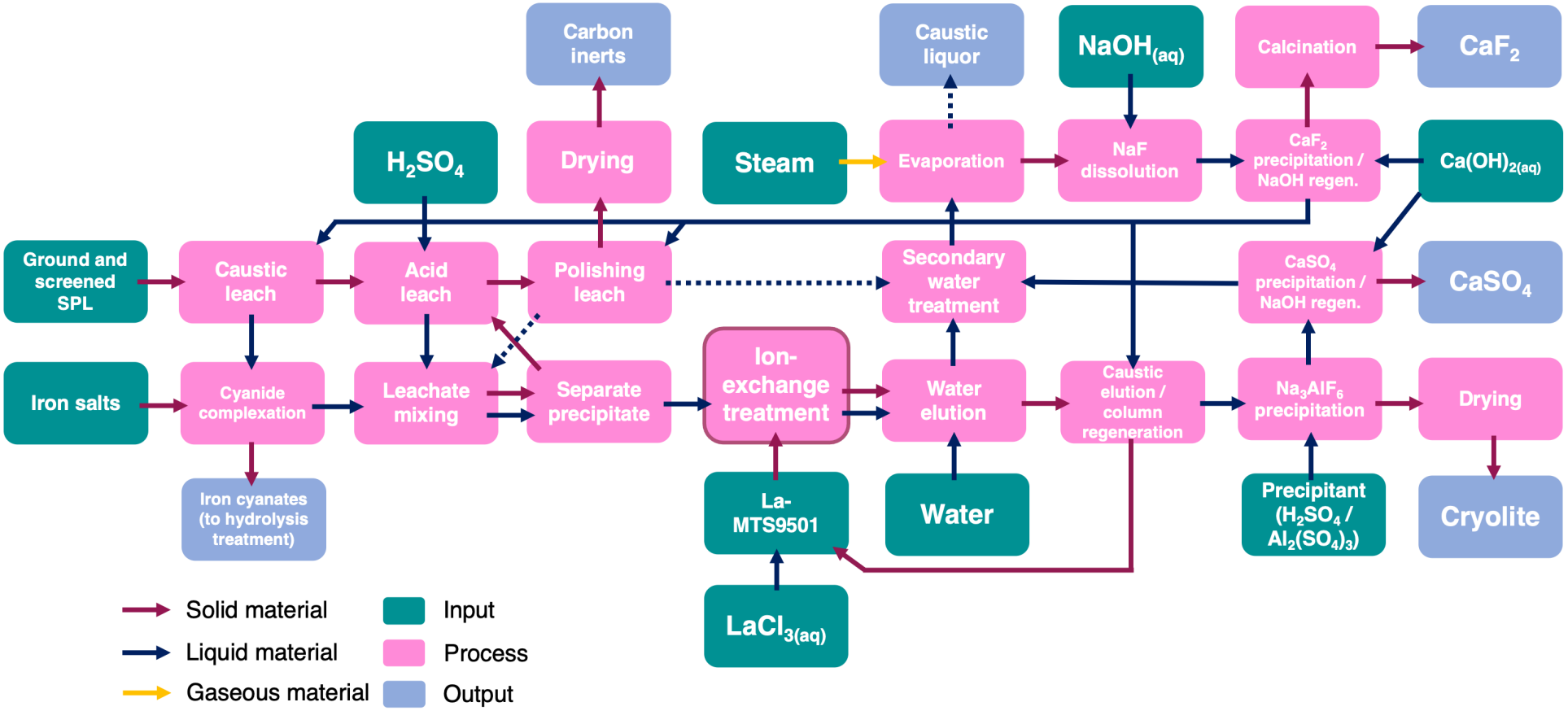

Fig. 6.1. Process flowsheet for the LCLL process, with the proposed IX system implemented. Dotted arrows show possible processes, dependent on the chemical composition of the stream, which is not precisely known at this time.

6.5. Hypercrosslinked polymers and potential to advance IX technology

The secondary strand of this thesis, shown in Chapter 5, was to progress IX technology for the capture of aqueous fluoride on a more fundamental level, via the investigation of de novo adsorbents. The HHCPs synthesised and assessed demonstrated great potential for fluoride remediation. Several other interesting observations were made as to their physicochemical properties, which add to the knowledge base for these materials, both for chemisorption and for other potential applications. It was seen that the HSAB methodology shown in the previous chapters could be applied to microporous adsorbents, although the adsorption mechanisms were not the same as La-MTS9501.

HHCPs were synthesised from appropriate biphenol monomers. Although the polymers were superficially chemically similar, they behaved differently in an aqueous environment in almost every experiment attempted. HHCP1 (2,2'-biphenol polymer) exhibited a higher concentration of acidic groups, with an extremely high exchange capacity of 6.34 $\pm$ 0.17 mmol·g^{-1}, as its greater surface area allowed access to more active -OH moieties. Accordingly, it was more hydrophilic than HHCP2 (bisphenol A polymer). Both polymers possessed high exchange capacities a wide range of acidic groups, which could not be explained by literature data for the parent monomers. The hypercrosslinking process clearly caused the formation of unexpected microenvironments, leading to low pK_a values being found for both systems. The relative hydrophobicity of HHCP2 resulted in generally lower pK_as.

Metallation of the polymers with Ca^{2+} ions was expected to proceed similarly to the loading of MTS-9501 with La^{3+}. However, because of the pK_a-splitting behaviour of the polymers, carried over from the parent monomers, <50% of phenol groups reacted in this way. Yet Ca-loading was still relatively high. This was due to the ability of the polymers to uptake atmospheric CO_2 in ambient conditions. Upon contact with Ca^{2+} ions, this was converted into $CaCO_3$ (vaterite), meaning the metallated HHCPs became hybrid organic/inorganic materials. For HHCP2, this process blocked the pore apertures, converting it to a surface-functionalised adsorbent. HHCP1 only partially lost its porosity. It was noted how metallation changed the colour of the polymeric materials, due to incorporation of the phenolic oxygen atoms into conjugated quinonoid structures. It was proposed this may lead to opportunities to control the optical properties of HCPs.

Because of differences in porosity, there were many variations in fluoride uptake capabilities between the two systems. HHCP1-Ca had a far greater q_{max} of 267 mg·g^{-1} (D-R isotherm), with uptake being better described by multi-layer adsorption models. This is among the highest fluoride-loading capacities ever recorded for an adsorbent and confirms the importance of the measured surface area parameter in the chemisorption capabilities of these adsorbents. It is substantially

higher than the capacity of La-MTS9501 (in NaF solutions) reported in Chapter 2 and that figure was skewed by the NaF precipitation phenomenon. Although interesting, this would potentially be problematic in an applied context, because the fluoride would begin to desorb immediately upon changing the solution concentration gradient, which is not the case for uptake by the polymers. The capacity of HHCP2-Ca was lesser (96.2 $mg \cdot g^{-1}$), though still large, and binding interactions were stronger and better described by the Langmuir model. HHCP2-Ca adsorption could be well-described by 2nd-order kinetics and the adsorption was 3 times as rapid as reported for La-MTS9501. HHCP1-Ca kinetics were slower and better fit by the Elovich model, indicating several different adsorption steps were variously rate-controlling. Overall, the dominant fluoride species formed within the polymers, upon adsorption, was crystalline CaF_2. However, we concluded that the main uptake mechanism for HHCP1-Ca was conversion of the $CaCO_3$ within the micropores, but for HHCP2-Ca, the conversion of covalently-bound -CaOH was dominant. A third mechanism involved a likely ligand-exchange by electrostatically-adsorbed Ca^{2+} centres, which was suggested by release of chloride and nitrate, during the defluoridation process.

From a practical perspective, the HHCPs adsorbed fluoride in the presence of many other competing anions. They did however possess higher affinity for phosphate and the seeming co-extraction mechanism was not investigated further at this time. The polymers exhibited high efficiency in a column system, albeit with a low inlet flow rate. The dynamic q_{max} values of 95.8 $mg \cdot g^{-1}$ (HHCP1-Ca) and 58.4 $mg \cdot g^{-1}$ (HHCP2-Ca) were both greatly in excess of those achieved by La-MTS9501 with a NaF inlet solution. The polymers could be fully regenerated by a two-step treatment, using relatively mild conditions, which could be conducive to the recovery of fluorite

Clearly, many aspects of the anion uptake by HHCPs require further elucidation and their final physical form (fine powders) currently limits their potential in dynamic systems. However, if these issues are addressed, HHCPs do offer fundamental advantages over existing IX technology.

6.6. Future work

6.6.1. Elucidation of the uptake mechanism of AHFs by La-MTS9501

A mechanism for the most fundamentally important uptake process described in this work has been proposed in Chapters 2 and 3, which agrees with all the experimental data collected and is sensible in the chemistry it describes. However, it is important to note that this remains a postulation and there is only limited qualitative evidence that the resin/AHF interaction is as visualised throughout the thesis. A full understanding of the uptake mechanism would clearly inform future research on the removal of fluoride from aqueous solutions with high concentrations of Al^{3+} and other hard, complexing metal ions. It is particularly important why there appears to be two distinct modes of AHF binding to the resin. The adsorption at lower concentrations appears to be much stronger and

requires caustic eluent for desorption. However, at higher concentrations, a much weaker form of binding also occurs, requiring only a change in concentration gradient for elution. As seen in Chapters 3 and 4, this limits the theoretical cryolite yield for the process (although as mentioned, there is potential for this initial eluent to be converted to CaF_2).

Future experiments, rather than using the simulant leachate described in this thesis, would contact the La-MTS9501 resin with a number of solutions, with carefully controlled ratios of Al^{3+} and fluoride. The concentrations could be set so that the dominant Al species in solution changes from $[Al(OH)_4]^-$ to AlF^{2+}, AlF_2^+ and AlF^3. Resin samples could then be treated, as previously mentioned, and analysed by spectroscopy. Further XPS experiments would be helpful to better describe the uptake (for example, as the F^-:Al^{3+} ratio in solution increases, the adsorbed Al complexes should gradually become more fluoride-rich. Therefore a decrease in average binding energy for the Al environment should be observed. Furthermore, if the relative concentrations of La environments also change as a function of F^-:Al^{3+} ratio, this provides strong evidence that there is a direct interaction between La centres and AHFs, as proposed. A second possible set of experiments would maintain the same F^-:Al^{3+} ratio, but gradually increase the concentration of the contact solution. At low [AHF], one would expect the dominant species observed to be coordinated to the resin via two bridging ligands, but at high [AHF], the prevalent species would be the more weakly bound kind. However, the differences in binding energy between the two environments could well be too subtle to be differentiated by XPS.

Another possibly powerful technique would be extended x-ray absorption fine structure (EXAFS) analysis. This could be used to determine the coordination numbers of both La and adsorbed Al environments, which would confirm whether, in the initial stronger binding interaction, the AHF complex acts as a mono- or bidentate ligand around the La centre. It would also determine whether there is significant interaction between the La centre and the AMP nitrogen atom. Solid-state NMR experiments were also considered as a possibility. ^{17}O experiments might be feasible, even with the very low abundance of this isotope, because of the suspected high [O] in an AHF-loaded resin sample. For example, it may be possible to identify oxygen bridging ligands between La and Al centres. ^{139}La is also a possible nucleus to study, to corroborate XPS data, although usually restricted to small complexes, rather than polymeric species with many different micro-environments.

6.6.2. Optimisation of parameters and development of the proposed adsorption system

Clearly, despite the potential of the system, there is research still outstanding on the proposed extension to the hydrometallurgical SPL treatment. The efficacy of the two-stage leaching treatment, in terms of rendering the resulting inert material environmentally benign and compliant, should be checked. There are simple standard protocols for these experiments, such as ISO 18772:2008(en).

The key issue however, is development of a process for precipitating cryolite from the purified liquor, after elution. This is critical to improving the technicoeconomic analysis accuracy. The process may require elevated temperature and/or the addition of a precipitant, both of which add to the cost of the process. As mentioned in Chapter 3, cryolite is much less energy-intensive to dry than either CaF_2 or AlF_3. So this step should at least be straightforward and cost-effective. One must then address the issue of regenerating the NaOH eluent from what would essentially be a barren Na_2SO_4 solution. If established industrial methods are followed, NaOH recovery would be done first by adding a cheap source of $Ca(OH)_2$ and precipitating out $CaSO_4$, which is a low-value by-product. If the resulting NaOH is not of sufficient purity, this can be improved by an additional carbonate post-precipitation. All these steps necessarily add complexity and cost to the proposed treatment. The best solution would be to retain the CaF_2 production side of the process, with lower capacity, and direct the barren caustic waste-stream to the evaporation, or secondary water treatment stage, as shown in Fig. 6.1. If the end result is to make the treatment uneconomical, unfortunately, a cheaper eluent for the La-MTS9501 column, possibly Na_2CO_3, would have to be researched.

Aside from this key technicoeconomic consideration, work should be done to minimise the required throughput of water and volume of MTS9501 that would be purchased (which are huge CAPEX factors), and maximise the recovery of cryolite. This is a difficult balancing act because, as the experimental work has shown, La-MTS9501 resin becomes more efficient (in terms of loading capacity) the higher the [AHF] in the inlet leachate solution. However, the kinetics of uptake become slower and one must bear in mind that the column flow rate needs to be ~7 times greater than has been tested experimentally, to keep the overall plant capacity, in terms of mass of SPL processed per year. Therefore, dynamic experiments at faster flow rate are crucial. Performing column experiments at elevated temperature, to boost the kinetics was considered, but ultimately discounted, due to not only the potential energy cost, but also the fact that static kinetic experiments showed that the q_e of the resin decreased significantly with raised temperature. Another consideration is that higher AHF loading of the La-MTS9501 column ultimately produces more weakly-bound AHFs, which would begin to elute from the column during the washing procedure between loading and elution. If indeed the fluoride content in these column washings could ultimately be recovered as CaF_2, as per the original LCLL process, then this may be a good compromise for the plant and in this case, work should focus on lowering the SPL:lixiviant solution ratios, in order to attain a higher [AHF] concentration in the leachate. If however it is found that the column washings cannot be valorised, the reverse would be true. Handling a more dilute leachate would make it very difficult for the process to be financially viable, because either the SPL throughput would have to be greatly reduced, or the IX capacity of the plant would have to increase still further (at great initial CAPEX). Future research would really have to be conducted with cooperation from RTA to manage the integration of the process and further laboratory-scale work is clearly called for before any scale-

up takes place. This would be done in sequential stages with an approximate scale increase of 100 in each step.

6.6.3. The future for HHCPs

A large number of developmental pathways are possible, to capitalise on the potential of HHCPs for defluoridation capabilities. In terms of the specific systems studied in this thesis, an obvious goal would be to increase the degree of metallation which, although already high in HHCP1-Ca and HHCP2-Ca, was not optimised. Established organometallic techniques could be attempted to synthesise the calcium phenoxide forms of the monomers, but it is not known what their stability would be under the fairly aggressive Friedel-Crafts conditions (the synthesis could also be attempted post-polymerisation). Alternatively, simpler monomers, with only one hydroxyl group per unit, which would not exhibit pK_a-splitting behaviour, could be assessed. For example, 2-naphthol is known to polymerise into a porous material and has a pK_a of ~9.5.

A second option would be to increase the CO_2 loading of the materials, prior to contact with Ca^{2+}. Although the networks synthesised are selective towards CO_2 adsorption, the extent of loading under our experimental conditions would again not have been optimised, because of the impact of N_2 and (especially) water vapour. It would be interesting to explore the benefits of loading the polymers with CO_2 analytically. This behavioural trait of metallated HHCPs may have significant applied potential, as it could facilitate the development of a process which simultaneously removes CO_2 from a gaseous effluent stream and uses it for the remediation of fluoride from an aqueous stream.

It is worth emphasising that both of these steps to increase metal-loading would likely result in a further loss of surface area in HHCP1 derivatives. This parameter would have to be monitored in subsequent experiments because the porosity is key to the novelty of the materials and to the large defluoridation capacity of HHCP1-Ca. A possible strategy would be to investigate the use of porogens in the synthetic procedure, using a similar idea to the design of Davankov-type resins. This would hopefully create regions of macroporosity, interconnecting the microporous regions and hopefully allowing facie access of sorbate ions to the active sites. Again, there are also other possible monomers which may polymerise into materials with wider pore appertures. However, identifying a more appropriate monomer would likely be a case of trial and error, rather than a rational selection process. Very little is known about this aspect of the microstructure of HCPs, which leads into the next possible developmental area.

The determination of protonation constants and N_2 sorption characteristics presented in this work can give insights into sorbent-sorbate interactions. But the conclusions drawn as to the nature of the microenvironments created are merely sensible postulations based on the data and literature

sources. The computer modelling of adsorption processes by HCPs has only been attempted for solid/gas-phase interactions and has not accounted for polar functional groups, nor the dehydrogenation and quinonoid formation processes, which the work in Chapter 5 confirmed. Progression on this front would help to explain why the acidic environments within the polymeric matrices are so different to what would be expected from known data on the parent monomers and if this could be elucidated, the chemisorption properties of HHCPs would be much easier to predict and take advantage of.

A final point is that the macroparticular properties of HHCPs are still a barrier to their application in water treatment. Although we were able to demonstrate a successful column-loading experiment, in reality, the flow-rate required industrially for effective water treatment would be extremely difficult to achieve with such fine particles. Although it is possible to create rigid polymer monoliths by reducing the solvent:monomer ratio, the resulting materials are still very fragile and have only been synthesised at low g scale. One option is to investigate a fluidised bed treatment, which negates the pressure-drop associated with fine particulate beds. Another perhaps more exciting possibility is to look into methods of agglomerating the polymer particles post-synthesis and working towards achieving uniform particle size, which would then make the materials direct competitors for commercial IX resins. This however would have to be achieved with minimal extra mass added to the particles, otherwise the great intrinsic advantage of the materials (their superior exchange capacity) would be lost.

7. References

[1] K.T. Koga, E.F. Rose-Koga, “Fluorine in the Earth and the solar system, where does it come from and can it be found?”, *Comptes Rendus Chimie*, 2018, **21**, 749-756.
[2] Y.H. Li, “Distribution patterns of the elements in the ocean - a synthesis”, *Geochimica et Cosmochimica Acta*, 1991, **55**, 3223-3240.
[3] S. Ali, S.K. Thakur, A. Sarkar, S. Shekhar, “Worldwide contamination of water by fluoride”, *Environmental Chemistry Letters*, 2016, **14**, 291-315.
[4] M. Vithanage, P. Bhattacharya, “Fluoride in the environment: sources, distribution and defluoridation”, *Environmental Chemistry Letters*, 2015, **13**, 131-147.
[5] Government of New South Wales, Department of Health, *Water Fluoridation: Questions and Answers*, Sidney, 2015.
[6] C. Gonzalo, J.A. Camargo, “The impact of an industrial effluent on the water quality, submersed macrophytes and benthic macroinvertebrates in a dammed river of Central Spain”, *Chemosphere*, 2013, **93**, 1117-1124.
[7] K.R. Nair, F. Manji, J.N. Gitonga, “The occurrence and distribution of fluoride in groundwaters of Kenya”, *East African Medical Journal*, 1984, **61**, 503-512.
[8] European Food Safety Authority, Scientific Committee on Food, *Tolerable Upper Intake Levels for Vitamins and Minerals*, EFSA, Parma, 2006.
[9] G.J. Liu, Q.F. Ye, W. Chen, Z.J. Zhao, L. Li, P. Lin, “Study of the relationship between the lifestyle of residents residing in fluorosis endemic areas and adult skeletal fluorosis”, *Environmental Toxicology and Pharmacology*, 2015, **40**, 326-332.
[10] S. Rawlani, S. Rawlani, S. Rawlani, “Assessment of skeletal and non-skeletal fluorosis in endemic fluoridated areas of Vidharbha Region, India: A survey”, *Indian Journal of Community Medicine*, 2010, **35**, 298-301.
[11] P. Senthil Kumar, C. Aravindakshan, “Industrial Fluorosis and Its Effects on Serum Biochemistry and Haemogram in Cattle of Kerala, India”, *Proceedings of the National Academy of Science, India, Section B, Biological Science*, 2015, **85**, 867-872.
[12] X. Tao, Z.R. Xu, Y.Z. Wang, “Effect of excessive dietary fluoride on nutrient digestibility and retention of iron, copper, zinc, and manganese in growing pigs”, *Biological Trace Element Research*, 2005, **107**, 141-151.
[13] IndexBox, *World Fluorspar Market Analysis, Forecast, Size, Trends and Insights*, IndexBox, Walnut, California, 2020.
[14] A. Dreveton, “Manufacture of high-bulk density aluminium fluoride from fluosilicic acid (HBD-AlF_3 from FSA) and AHF”, First Symposium on Innovation and Technology in the Phosphate Industry, Marrakech, 2011.
[15] U.S. Geological Survey, *Mineral Commodity Summaries 2015*, US Government Printing Office, Washington DC, 2015.
[16] M.E. McRae, “Fluorspar”, in: U.S. Geological Survey, *Mineral Commodity Surveys 2019*, USGS, Reston, Virginia, 2018, pp. 60-61.
[17] European Union, *Communication from The Commission to The European Parliament, The Council, The European Economic and Social Committee and The Committee of The Regions on the review of the list of Critical Raw Materials for the EU and the implementation of the Raw Materials Initiative*, EU, Brussels, 2014.
[18] International Aluminium Institute, “Primary Aluminium Production” [online], 2019, http://www.world-aluminium.org/statistics/.
[19] A.C.F. Silva, D.F.O. Braga, M.A.V. de Figueiredo, P. Moreira, “Ultimate tensile strength optimization of different FSW aluminium alloy joints”, *International Journal of Advanced Manufacturing Technology,* 2015, **79**, 805-814.
[20] S. Samal, A.K. Ray, A. Bandopadhyay, “Proposal for resources, utilization and processes of red mud in India - A review”, *International Journal of Mineral Processing*, 2013, **118**, 43-55.
[21] H. Mahadevan, T.R. Ramachandran, “Recent trends in alumina and aluminium production technology”, *Bulletin of Materials Science*, 1996, **19**, 905-920.
[22] W.E. Haupin, “Electrochemistry of the Hall- Héroult process for aluminum smelting”, *Journal of Chemical Education*, 1983, **60**, 279-282.
[23] M. Gautam, B. Pandey, M. Agrawal, “Carbon footprint of aluminum production: emissions and mitigation, *Environmental Carbon Footprints: Industrial Case Studies*, 2018, 197-228.

[24] M. Dutta, S. Mukherjee, “An outlook into energy consumption in large scale industries in India: The cases of steel, aluminium and cement”, *Energy Policy*, 2010, **38**, 7286-7298.
[25] N. Ding, F. Gao, Z.H. Wang, X.Z. Gong, Z.R. Nie, “Environment impact analysis of primary aluminum and recycled aluminium”, *2011 Chinese Materials Conference*, 2012, **27**, 465-474.
[26] T.A. Aarhaug, A.P. Ratvik, Aluminium primary production off-gas composition and emissions: an overview, *Journal of Metals*, 2019, **71**, 2966-2977.
[27] K. Tschope, C. Schøning, T. Grande, “Autopsies of spent pot linings - a revised view”, *Light Metals*, 2009*,* 1085-1090.
[28] A.P. Ratvik, A. Store, A. Solheim, T. Foosnaes, “The effect of current density on cathode expansion during start-up”, *Light Metals*, 2008, 966-971.
[29] K. Mansfield, G. Swayn, J. Harpley, *The Spent Pot Lining Treatment and Fluoride Recycling Project*, Portland Aluminium, Portland, Victoria, 2002.
[30] K. Tschope, “Degradation of cathode lining in Hall-Héroult cells”, [PhD thesis], Department of Materials Science and Engineering, Norwegian University of Science and Technology, Trondheim, 2010.
[31] K. Tschope, C. Schøning, J. Rutlin, T. Grande, “Chemical Degradation of Cathode Linings in Hall-Héroult Cells - An Autopsy Study of Three Spent Pot Linings”, *Metallurgical and Materials Transactions B*, 2012, **43**, 290-301.
[32] G. Holywell, R. Bréault, “An Overview of Useful Methods to Treat, Recover, or Recycle Spent Potlining”, *Journal of The Minerals, Metals and Materials Society*, 2013, **65**, 1441-1451.
[33] S.B. Sleap , B.D. Turner, S.W. Sloan, “Kinetics of fluoride removal from spent pot liner leachate (SPLL) contaminated groundwater”, *Journal of Environmental Chemical Engineering*, 2015, **3**, 2580-2587.
[34] G. Ospina, M.I. Hassan, “Spent Pot Lining Characterization Framework”, *Journal of The Minerals, Metals and Materials Society*, 2017, **69**, 1639-1645.
[35] W.M. Xie, F.P. Zhou, J.Y. Liu, X.L. Bi, Z.J. Huang, Y.H. Li, D.D. Chen, H.Y. Zou, S.Y. Sun, “Synergistic reutilization of red mud and spent pot lining for recovering valuable components and stabilizing harmful element”, *Journal of Cleaner Production*, 2020, **243**, 118624-118635.
[36] L. Gao, S. Mostaghel, S. Ray, K. Chattopadyay, “Using SPL (Spent Pot-Lining) as an Alternative Fuel in Metallurgical Furnaces”, *Metallurgical and Materials Transactions E*, 2016, **3**, 179-188.
[37] D. Lisbona, C. Somerfield, K. Steel, “Leaching of spent pot- lining with aluminium nitrate and nitric acid: Effect of reaction conditions and thermodynamic modelling of solution speciation”, *Hydrometallurgy*, 2013, **134**, 132-143.
[38] V.Y. Bazhin, R.K. Patrin, “Modern methods of recycling spent potlinings from electrolysis baths used in aluminium production”, *Refractories and Industrial Ceramics*, 2011, **52**, 63-65.
[39] R. Bréault, S.P. Poirier, G. Hamel, A. Pucci, “A ‘green’ way to deal with spent pot lining”, *Aluminium International Today*, 2011, 22.
[40] N. Bloxsome, *The Safety Guide 2018. Working Towards a Safer Aluminium Industry*, Quartz, Redhill, Surrey, 2018.
[41] K. Grjotheim, C. Krohn, K. Malinkovsky, K. Matiasovsky, *Thonstad Jomar Aluminium Electrolysis*, Aluminium-Verlag, Dusseldorf, 1982.
[42] Y. Courbariaux, J. Chaouki, C. Guy, “Update on spent potliners treatments: Kinetics of cyanides destruction at high temperature”, *Industrial and Engineering Chemistry Research*, 2004, **43**, 5828-5837.
[43] M.J. Palmieri, J. Luber, L.F. Andrade-Vieira, L.C. Davide, “Cytotoxic and phytotoxic effects of the main chemical components of spent pot-liner: A comparative approach”, *Mutation Research-Genetic Toxicology and Environmental Mutagenesis*, 2014, **763**, 30-35.
[44] B. Cooper, “Applying Industrial Ecology to Address Environmental Concerns Associated with Aluminum Smelter Spent Potlining”, 66th Annual Technical Meeting of the Indian Institute of Metals, Jamshedpur, Jharkhand, India, 2012.
[45] T. Kameda, J. Oba, T. Yoshioka, “Recyclable Mg-Al layered double hydroxides for fluoride removal: Kinetic and equilibrium studies”, *Journal of Hazardous Materials*, 2015, **300**, 475-482.

[46] A. Ezzeddine, A. Bedoui, A. Hannachi, N. Bensalah, “Removal of fluoride from aluminum fluoride manufacturing wastewater by precipitation and adsorption processes”, *Desalination and Water Treatment*, 2015, **54**, 2280-2292.
[47] M. Dessalegne, F. Zewge, N. Pfenninger, C.A. Johnson, I. Diaz, “Layered Double Hydroxide and Its Calcined Product for Fluoride Removal from Groundwater of Ethiopian Rift Valley”, *Water Air and Soil Pollution*, 2016, **227**, 13.
[48] M. Iffert, “Aluminium Smelting Cell Control and Optimisation”, [PhD thesis], School of Chemical Sciences and Engineering, The University of New South Wales, Sydney, Australia, 2007.
[49] G. Hamel, R. Bréault , G. Charest , S. Poirier, B. Boutin, From the “low caustic leaching and liming” process development to the Jonquière spent potlining treatment pilot plant start-up, 5 years of process up-scaling, engineering and commissioning”, *Light Metals*, 2009, 921-925.
[50] L. Birry, S. LeClerc, S. Poirier, “The LCL&L process: A sustainable solution for the treatment and recycling of spent potlining”, *Light Metals*, 2016, 467-471.
[51] H. Kvande, “Production of Primary Aluminium”, in: R. Lumley (Ed.) *Fundamentals of Aluminium Metallurgy; Production, Processing and Applications*, Woodhead Books, Sawston, Cambridge, 2011, pp. 49-69.
[52] L.S. Wang, C.M. Wang, Y. Yu, X.W. Huang, Z.Q. Long, Y.K. Hou, D.L. Cui, “Recovery of fluorine from bastnasite as synthetic cryolite by-product”, *Journal of Hazardous Materials*, 2012, **209**, 77-83.
[53] Z.-N. Shi, W. Li, X.-W. Hu, B.-J. Ren, B.-L. Gao, Z.-W. Wang, “Recovery of carbon and cryolite from spent pot lining of aluminium reduction cells by chemical leaching”, *Transactions of the Nonferrous Metals Society of China*, 2012, **22**, 222-227.
[54] Cerexagri, “Kryocide. Insecticide” [online], 2009, http://fluoridealert.org/wp-content/pesticides/msds/cryolite.label.kryocide.epa.pdf
[55] CEIC, “Accurate macro and micro economic data you can trust” [online], 2019, https://www.ceicdata.com/en.
[56] R. Pawlek, “Spent Potlining: an Update”, in: C.E. Suarez (Ed.) *Light Metals 2012*, Wiley, Hoboken, New Jersey, 2012, pp. 1313-1317.
[57] D.B. Banker, D.G. Brooks, E.R. Cutshall, D.D. Macauley, D.F. Strahan, *Detoxification of Aluminum Spent Potliner by Thermal Treatment, Lime Slurry Quench and Post-Kiln Treatment*, Reynolds Metals Company, Richmond, Virginia, 1992.
[58] D. Miksa, M. Homsak, N. Samec, “Spent potlining utilisation possibilities”, *Waste management and Research: The Journal of The International Solid Wastes and Public Cleansing Association*, 2003, **21**, 467-473.
[59] D.L. Constans, “Primary Aluminum Production Wastes: Spent Aluminum Potliner, K088” [online], 1998, https://gcisolutions.com/GCINotes998.html.
[60] A. Suss, N. Kuznetzova, A. Damaskin, I. Paromova, A. Panov, “Issues of spent carbon potlining processing”, The International Committee for Study of Bauxite, Alumina & Aluminium, United Arab Emirates, 2015.
[61] M. Cencic, I. Kobal, J. Golob, “Thermal hydrolysis of cyanides in spent pot lining of aluminium electrolysis”, *Chemical Engineering & Technology*, 1998, **21**, 523-532.
[62] P. von Kruger, “Use of spent potlining (SPL) in ferro silico manganese smelting”, *Light Metals*, 2011, 275-280.
[63] Ø. Breivik, *From Waste to Resource*, Norsk Hydro, Oslo, 2013.
[64] A.B. Cardoso, “Spent potliner management in primary aluminium production”, 62nd ABM International Annual Congress, Vitoria, Brazil, 2007, 2186-2195.
[65] T. Hopkins, P. Merline, “Comtor Process for Treatment of Spent Potlining”, *Mineral Processing and Extractive Metallurgy Review*, 1995, **15**, 247-255.
[66] Tetronics International, “50 years experience delivering hazardous waste treatment solutions” [online], 2014, https://tetronics.com/assets/Hazardous-Waste-Brochure.pdf.
[67] P. Black, B. Cooper, *A Natural "Industrial Ecology" Based Solution for Spent Potlining: Closing the loop for aluminium in the circular economy*, Regain Services, Victoria, Australia, 2015.

[68] W. Li, X. Chen, “Running results of the SPL detoxifying pilot plant in Chalco”, Light Metals, Aluminium Reduction Technology, Cell Development and Operations - Part 1, Auckland, New Zealand, 2006.
[69] W.X. Li, X.P. Chen, “Chemical stability of fluorides related to spent potlining”, *Light Metals*, 2008, 855-858.
[70] C.A. Nogueira, A.P. Paiva, P.C. Oliveira, M.C. Costa, A.M.R. da Costa, “Oxidative leaching process with cupric ion in hydrochloric acid media for recovery of Pd and Rh from spent catalytic converters”, *Journal of Hazardous Materials*, 2014, **278**, 82-90.
[71] N. Vieceli, C.A. Nogueira, C. Guimaraes, M.F.C. Pereira, F.O. Durao, F. Margarido, “Hydrometallurgical recycling of lithium-ion batteries by reductive leaching with sodium metabisulphite”, *Waste Management*, 2018, **71**, 350-361.
[72] X.M. Li, W.D. Yin, Z. Fang, Q.H. Liu, Y.R. Cui, J.X. Zhao, H. Jia, “Recovery of Carbon and Valuable Components from Spent Pot Lining by Leaching with Acidic Aluminum Anodizing Wastewaters”, *Metallurgical and Materials Transactions B - Process Metallurgy and Materials Processing Science*, 2019, **50**, 914-923.
[73] R.E. Treybal, *Mass-Transfer Operations*, 3rd edition, McGraw-Hill, Singapore, 1981.
[74] T.K. Pong, R.J. Adrien, J. Besida, T.A. O'Donnell, D.G. Wood, “Spent potlining - A hazardous waste made safe”, *Process Safety and Environmental Protection*, 2000, **78**, 204-208.
[75] G. Findeis, “Working up cathode linings from electrolytic cells for aluminium”, in: C. Zellerfield (Ed.) *Environmental Protection in the Aluminium and Non-Ferrous Smelting Industry - Symposium*, Technicopy Ltd., Stonehouse, 1973, pp. 84-93.
[76] C.R. de Veye, “Total recovery of Spent Pot Liner (SPL) using the BEFESA process”, 27th International Aluminium Conference, Moscow, Russia, 2012.
[77] AP Technology, *LCLL, A Breakthrough in the Spent Potlining Treatment Technology*, AP technology/Rio Tinto, Arvida, Canada, 2019.
[78] D.F. Lisbona, K.A. Steel, “Recovery of fluoride values from spent pot-lining: Precipitation of an aluminium hydroxyfluoride hydrate product”, *Separation and Purification Technology*, 2018, **61**, 182-192.
[79] J. Xiao, J. Yuan, Z.L. Tian, K. Yang, Z. Yao, B.L. Yu, L.Y. Zhang, “Comparison of ultrasound-assisted and traditional caustic leaching of spent cathode carbon (SCC) from aluminum electrolysis”, *Ultrasonics Sonochemistry*, 2018, **40**, 21-29.
[80] B. Mazumder, “Chemical oxidation of spent cathode carbon blocks of aluminium smelter plants for removal of contaminants and recovery of graphite value”, *Journal of Scientific and Industrial Research*, 2003, **62**, 1181-1183.
[81] B. Mazumder, S. Rani Devi, “Conceptual Design of a Commercial Spent Pot Liner Treatment Plant”, *International Journal of Engineering and Science*, 2014, **4**, 5-7.
[82] B.I. Silveira, A.E. Dantas, J.E. Blasquez, R.K.P. Santos, “Characterization of inorganic fraction of spent potliners: evaluation of the cyanides and fluorides content”, *Journal of Hazardous Materials*, 2002, **89**, 177-183.
[83] G.A. Senchyk, A.B. Lysenko, K.V. Domasevitch, O. Erhart, S. Henfling, H. Krautscheid, E.B. Rusanov, K.W. Kramer, S. Decurtins, S.X. Liu, “Exploration of a Variety of Copper Molybdate Coordination Hybrids Based on a Flexible Bis(1,2,4-triazole) Ligand: A Look through the Composition-Space Diagram”, *Inorganic Chemistry*, 2017, **56**, 12952-12966.
[84] D.F. Lisbona, C. Somerfield, K.M. Steel, “Leaching of spent pot- lining with aluminum anodizing wastewaters: Fluoride extraction and thermodynamic modelling of aqueous speciation”, *Industrial and Engineering Chemistry Research*, 2012, **51**, 8366-8377.
[85] U. Ntuk, S. Tait, E.T. White, K.M. Steel, “The precipitation and solubility of aluminium hydroxyfluoride hydrate between 30 and 70ºC”, *Hydrometallurgy*, 2015, **155**, 79-87.
[86] J.L. Wang, H.Y. Liu, Y.F. Luo, Q.R. Niu, H. He, S.F. Shen, “Study on harmless and resources recovery treatment technology of waste cathode carbon blocks from electrolytic aluminium”, *Proceedings of the Seventh International Conference on Waste Management and Technology*, 2012, **16**, 769-777.
[87] P. Renuka, K. Pushpanjali, “Review on Defluoridation Techniques of Water”, *International Journal of Engineering and Science*, 2013, **2**, 86-94.

[88] A. Bhatnagar, E. Kumar, M. Sillanpää, “Fluoride removal from water by adsorption- A review”, *Chemical Engineering Journal*, 2011, **171**, 811-840.
[89] R. Aldaco, A. Garea, A. Irabien, “Calcium fluoride recovery from fluoride wastewater in a fluidized bed reactor”, *Water Research*, 2007, **41**, 810-818.
[90] N. Drouiche, S. Aoudj, M. Hecini, N. Ghaffour, H. Lounici, N. Mameri, “Study on the treatment of photovoltaic wastewater using electrocoagulation: Fluoride removal with aluminium electrodes - Characteristics of products, *Journal of Hazardous Materials*, 2009, **169**, 65-69.
[91] S. Ayoob, A.K. Gupta, V.T. Bhat, “A conceptual overview on sustainable technologies for the defluoridation of drinking water”, *Critical Reviews in Environmental Science and Technology*, 2008, **38**, 401-470.
[92] S.E. Pepper, K.R. Whittle, L.M. Harwood, J. Cowell, T.S. Lee, M.D. Ogden, “Cobalt and nickel uptake by silica-based extractants”, *Separation Science and Technology*, 2018, **53**, 1552-1562.
[93] M.S. Onyango, Y. Kojima, O. Aoyi, E.C. Bernardo, H. Matsuda, “Adsorption equilibrium modelling and solution chemistry dependence of fluoride removal from water by trivalent-cation-exchanged zeolite F-9”, *Journal of Colloid and Interface Science*, 2004, **279**, 341-350.
[94] X.Y. Zhang, B. Gao, A.E. Creamer, C.C. Cao, Y.C. Li, “Adsorption of VOCs onto engineered carbon materials: A review”, *Journal of Hazardous Materials*, 2017, **338**, 102-123.
[95] A. Meleshyn, U. Noseck, “Radionuclide inventory of vitrified waste after spent nuclear fuel reprocessing at La Hague”, ASME 2013, 15th International Conference on Environmental Remediation and Radioactive Waste Management, Brussels, Belgium, 2013.
[96] M.D. Ogden, E.M. Moon, A. Wilson, S.E. Pepper, “Application of chelating weak base resin Dowex M4195 to the recovery of uranium from mixed sulfate/chloride media”, *Chemical Engineering Journal*, 2017, **317**, 80-89.
[97] G.J. Millar, S.J. Couperthwaite, D.B. Wellner, D.C. Macfarlane, S.A. Dalzell, “Removal of fluoride ions from solution by chelating resin with imino-diacetate functionality”, *Journal of Water Process Engineering*, 2017, **20**, 113-122.
[98] T.K. Wadhwani, “The mechanism of fluorine removal by calcium salts - part 1”, *Journal of The Indian Institute of Science*, 1954, **36**, 250-258.
[99] T.J. Robshaw, S.M. Griffiths, A. Canner, J.P. Bezzina, D.B. Hammond, S. Van Meurs, M.D. Ogden, “Insights into the interaction of iodide and iodine with Cu(II)-loaded bispicolylamine chelating resin and applications for nuclear waste treatment”, *Chemical Engineering Journal*, 2020, **390**, 124647-124659.
[100] Z.P. Li, H. Li, H. Xia, X.S. Ding, X.L. Luo, X.M. Liu, Y. Mu, “Triarylboron-Linked Conjugated Microporous Polymers: Sensing and Removal of Fluoride Ions”, *Chemistry - A European Journal*, 2015, **21**, 17355-17362.
[101] C.E. Harland, *Ion exchange: theory and practice*, 2nd ed., Royal Society of Chemistry, Cambridge, 1994.
[102] G. Singh, B. Kumar, P.K. Sen, J. Majumdar, “Removal of fluoride from spent pot liner leachate using ion exchange”, *Water Environment Research*, 1999, **71**, 36-42.
[103] M. Chabani, A. Amrane, A. Bensmaili, “Kinetic modelling of the adsorption of nitrates by ion exchange resin”, *Chemical Engineering Journal*, 2006, **125**, 111-117.
[104] T. Robshaw, S. Tukra, D.B. Hammond, G.J. Leggett, M.D. Ogden, “Highly efficient fluoride extraction from simulant leachate of spent potlining via La-loaded chelating resin. An equilibrium study”, *Journal of Hazardous Materials*, 2019, **361**, 200-209.
[105] T.J. Robshaw, R. Dawson, K. Bonser, M.D. Ogden, Towards the implementation of an ion-exchange system for recovery of fluoride commodity chemicals. Kinetic and dynamic studies Chemical Engineering Journal, 2019, **367**, 149-159.
[106] H.S. Thompson, “On the absorbent power of soils”, *Journal of the Royal Agricultural Society of England*, 1850, **11**, 68-74.
[107] J.T. Way, “On the power of soils to absorb manure”, *Journal of the Royal Agricultural Society of England*, 1850, **11**, 313-379.
[108] H. Staudinger, W. Heuer, “Über hochpolymere Verbindungen, 93. Mitteil.: Über das Zerreißen der Faden-Moleküle des Poly-styrols”, *Berichte der Deutschen Chemischen Gesellschaft*, 1934, **67**, 1159-1164.

[109] C.H. McBurney, “Resinous insoluble reaction products of tertiary amines with haloalkylated vinyl aromatic hydrocarbon copolymers”, US patent 2591573, 1952.
[110] J. Huang, S.R. Turner, “Hypercrosslinked Polymers: A Review”, *Polymer Reviews*, 2018, **58**, 1-41.
[111] Purolite, Product data sheet. Puromet MTS9501 [online], 2018, https://www.purolite.com/product-pdf/MTS9501.pdf.
[112] Purolite, Product Data Sheet. Purolite MTS9850 [online], 2019, https://www.purolite.com/product-pdf/MTS9850.pdf.
[113] Purolite, Purolite C145H. Polystyrenic Macroporous Strong Acid Cation Resin. Hydrogen form [online], 2019, https://www.purolite.com/product-pdf/C145H.pdf.
[114] Purolite, Product Data Sheet. Purolite MTS9850 [online], 2019, https://www.purolite.com/product-pdf/MTS9850.pdf.
[115] F.G. Helfferich, *Ion Exchange*, McGraw-Hill, New York, 1962.
[116] N. Viswanathan, C.S. Sundaram, S. Meenakshi, “Development of multifunctional chitosan beads for fluoride removal”, *Journal of Hazardous Materials*, 2009, **167**, 325-331.
[117] S. Meenakshi, N. Viswanathan, “Identification of selective ion-exchange resin for fluoride sorption”, *Journal of Colloid and Interface Science*, 2007, **308**, 438-450.
[118] I.B. Solangi, S. Memon, M.I. Bhanger, “Removal of fluoride from aqueous environment by modified Amberlite resin”, *Journal of Hazardous Materials*, 2009, **171**, 815-819.
[119] M. Kanesato, T. Yokoyama, T.M. Suzuki, “Selective adsorption of fluoride-ion by La(III)-loaded chelating resin having phosphonomethylamino groups”, *Chemistry Letters*, 1988, 207-210.
[120] H.P. Ma, H. Ren, X.Q. Zou, S. Meng, F.X. Sun, G.S. Zhu, “Post-metalation of porous aromatic frameworks for highly efficient carbon capture from CO_2 + N_2 and CH_4 + N_2 mixtures”, *Polymer Chemistry*, 2014, **5**, 144-152.
[121] W. Du, B.C. Pan, P.J. Jiang, Q.R. Zhang, W.M. Zhang, B.J. Pan, Q.J. Zhang, Q.X. Zhang, “Selective sorption and preconcentration of tartaric acid using a copper(II)-bound polymeric ligand exchanger”, *Chemical Engineering Journal*, 2008, **139**, 63-68.
[122] X. Yang, S. Deng, F. Peng, T. Luo, “A new adsorbent of a Ce ion-implanted metal–organic framework (MIL-96) with high-efficiency Ce utilization for removing fluoride from water”, *Dalton Transactions*, 2017, **46**, 1996-2006.
[123] L. Fang, K.N. Ghimire, M. Kuriyama, K. Inoue, K. Makino, “Removal of fluoride using some lanthanum(III)-loaded adsorbents with different functional groups and polymer matrices”, *Journal of Chemical Technology and Biotechnology*, 2003, **78**, 1038-1047.
[124] G. Lefevre, M. Alnot, J.J. Ehrhardt, J. Bessiere, “Uptake of iodide by a mixture of metallic copper and cupric compounds”, *Environmental Science and Technology*, 1999, **33**, 1732-1737.
[125] S.W. Liu, S.H. Kang, H.M. Wang, G.Z. Wang, H.J. Zhao, W.P. Cai, “Nanosheets-built flowerlike micro/nanostructured $Bi_2O_{2.33}$ and its highly efficient iodine removal performances”, *Chemical Engineering Journal*, 2016, **289**, 219-230.
[126] F. Luo, K. Inoue, “The removal of fluoride ion by using metal(III)-loaded Amberlite resins”, *Solvent Extraction and Ion Exchange*, 2004, **22**, 305-322.
[127] S.M. Prabhu, S. Meenakshi, “Effect of metal ions loaded onto iminodiacetic acid functionalized cation exchange resin for selective fluoride removal”, *Desalination and Water Treatment*, 2014, **52**, 2527-2536.
[128] Y. Ku, H.M. Chiou, H.W. Chen, “Removal of fluoride from aqueous solution by aluminum-loaded Duolite C-467 resin”, *Journal of the Chinese Institute of Engineers*, 2011, **34**, 801-807.
[129] N. Viswanathan, S. Meenakshi, “Effect of metal ion loaded in a resin towards fluoride retention”, *Journal of Fluorine Chemistry*, 2008, **129**, 645-653.
[130] D.B. Bhatt, P.R. Bhatt, H.H. Prasad, K.M. Popat, P.S. Anand, “Removal of fluoride ion from aqueous bodies by aluminium complexed amino phosphonic acid type resins”, *Indian Journal of Chemical Technology*, 2004, **11**, 299-303.

[131] K.M. Popat, P.S. Anand, B.D. Dasare, “Selective removal of fluoride ions from water by the aluminium form of the aminomethylphosphonic acid-type ion exchanger”, *Reactive Polymers*, 1994, **23**, 24-32.
[132] M.J. Haron, W.M.Z. Yunus, “Removal of fluoride ion from aqueous solution by a cerium-poly(hydroxamic acid) resin complex”, *Journal of Environmental Science and Health Part A - Toxic/Hazardous Substances & Environmental Engineering*, 2001, **36**, 727-734.
[133] J.M. Cheng, X.G. Meng, C.Y. Jing, J.M. Hao, “La^{3+}-modified activated alumina for fluoride removal from water”, *Journal of Hazardous Materials*, 2014, **278**, 343-349.
[134] M. Sarkar, U. Santra, “Modeling Fluoride Adsorption on Cerium-Loaded Cellulose Bead-Response Surface Methodology, Equilibrium, and Kinetic Studies”, *Water Air and Soil Pollution*, 2015, 2015, **226**, 1-14.
[135] P. Liang, Y. Zhang, D.F. Wang, Y. Xu, L. Luo, “Preparation of mixed rare earths modified chitosan for fluoride adsorption”, *Journal of Rare Earths*, 2013, **31**, 817-822.
[136] E. Kusrini, N. Sofyan, N. Suwartha, G. Yesya, C.R. Priadi, “Chitosan-praseodymium complex for adsorption of fluoride ions from water”, *Journal of Rare Earths*, 2015, **33**, 1104-1113.
[137] Y. Lyu, X.S. Su, S.Y. Zhang, Y.L. Zhang, “Preparation and Characterization of La(III)-Al(III) Co-loaded Hydrothermal Palygorskite Adsorbent for Fluoride Removal from Groundwater”, *Water Air and Soil Pollution*, 2016, **227**, 1-9.
[138] S.D. Alexandratos, “Ion-Exchange Resins: A Retrospective from Industrial and Engineering Chemistry Research”, *Industrial & Engineering Chemistry Research*, 2009, **48**, 388-398.
[139] A.E. Martell, M. Calvin, *Chemistry of the Metal Chelate Compounds*, Prentice-Hall, New York, 1952.
[140] J. Kennedy, G.E. Ficken, “Syntheses of metal-complexing polymers II. Phosphonamide and alpha-aminophosphonate polymers”, *Journal of Applied Chemistry*, 1958, **8**, 465-468.
[141] E.K. Fields, “The synthesis of esters of substituted amino phosphonic acids”, *Journal of the American Chemical Society*, 1952, **74**, 1528-1531.
[142] S.K. Sahni, R. Vanbennekom, J. Reedijk, “A spectral study of transition-metal complexes on a chelating ion-exchange resin containing aminophosphonic acid groups”, *Polyhedron*, 1985, **4**, 1643-1658.
[143] A. Deepatana, M. Valix, “Recovery of nickel and cobalt from organic acid complexes: Adsorption mechanisms of metal-organic complexes onto aminophosphonate chelating resin”, *Journal of Hazardous Materials*, 2006, **137**, 925-933.
[144] S.K. Sahni, J. Reedijk, “Coordination chemistry of chelating resins and ion-exchangers”, *Coordination Chemistry Reviews*, 1984, **59**, 1-139.
[145] B. Esma, A. Omar, D.M. Amine, “Comparative study on lanthanum(III) sorption onto Lewatit TP 207 and Lewatit TP 260”, *Journal of Radioanalytical and Nuclear Chemistry*, 2014, **299**, 439-446.
[146] M.J. Page, K. Soldenhoff, M.D. Ogden, “Comparative study of the application of chelating resins for rare earth recovery”, *Hydrometallurgy*, 2017, **169**, 275-281.
[147] P.N. Nesterenko, O.S. Zhukova, O.A. Shpigun, P. Jones, “Synthesis and ion-exchange properties of silica chemically modified with aminophosphonic acid”, *Journal of Chromatography A*, 1998, **813**, 47-53.
[148] G. Xu, L. Wang, Y.J. Xie, M.L. Tao, W.Q. Zhang, “Highly selective and efficient adsorption of Hg^{2+} by a recyclable aminophosphonic acid functionalized polyacrylonitrile fiber”, *Journal of Hazardous Materials*, 2018, **344**, 679-688.
[149] Y.Z. Hamada, W.R. Harris, “Stability constants and multinuclear NMR measurements of phosphonic acid derivatives with aluminum in aqueous solutions”, *Inorganica Chimica Acta*, 2006, **359**, 1135-1146.
[150] H. Egawa, K. Yamabe, A. Jyo, “Studies on selective adsorption resins. XXXIII. Behavior of macroreticular chelating resins containing phosphinic and / or phosphonic acid groups in the adsorption of trivalent lanthanides”, *Journal of Applied Polymer Science*, 1994, **52**, 1153-1164.
[151] R. Chiarizia, E.P. Horwitz, R.A. Beauvais, S.D. Alexandratos, “Diphonix-CS: A novel combined cesium and strontium selective ion exchange resin”, *Solvent Extraction and Ion Exchange*, 1998, **16**, 875-898.

[152] R.K. Misra, S.K. Jain, P.K. Khatri, “Iminodiacetic acid functionalized cation exchange resin for adsorptive removal of Cr(VI), Cd(II), Ni(II) and Pb(II) from their aqueous solutions”, *Journal of Hazardous Materials*, 2011, **185**, 1508-1512.
[153] W. Sofinska-Chmiel, D. Kolodynska, “Purolite S940 and Purolite S950 in heavy metal ions removal from acidic streams”, *Separation Science and Technology*, 2016, **51**, 2528-2538.
[154] A.J. Canner, S.E. Pepper, M. Hayer, M.D. Ogden, “Removal of radionuclides from a HCl steel decontamination stream using chelating ion exchange resins – Initial studies”, *Progress in Nuclear Energy*, 2018, **104**, 271-279.
[155] R.P. Agarwal, E.C. Moreno, “Stability constants of aluminium fluoride complexes”, *Talanta*, 1971, **18**, 873-880.
[156] M.P. Menon, J. James, “Stability constants for lanthanide fluoride complexes in aqueous solution at 25°C”, *Journal of Solution Chemistry*, 1989, **18**, 735-742.
[157] N. Viswanathan, S. Meenakshi, “Role of metal ion incorporation in ion exchange resin on the selectivity of fluoride”, *Journal of Hazardous Materials*, 2009, **162**, 920-930.
[158] Argus Consulting, *Argus Rare Earths Monthly Outlook 19/6*, Argus, London, 2019.
[159] W. Yantasee, G.E. Fryxell, R.S. Addleman, R.J. Wiacek, V. Koonsiripaiboon, K. Pattamakomsan, V. Sukwarotwat, J. Xu, K.N. Raymond, “Selective removal of lanthanides from natural waters, acidic streams and dialysate”, *Journal of Hazardous Materials*, 2009, **168**, 1233-1238.
[160] M.S. Frant, J.W. Ross, “Use of a total ionic strength adjustment buffer for electrode determination of fluoride in water supplies”, *Analytical Chemistry*, 1968, **40**, 1169-1171.
[161] K.L. Nash, “Separation chemistry for lanthanides and trivalent actinides”, in: K.A. Gschneidner Jr., L. Eyring, G.R. Choppin, G.H. Lander (Eds.) *Handbook on the Physics and Chemistry of Rare Earths*, Elsevier Science, Amsterdam, 1994.
[162] E. Vences-Alvarez, L.H. Velazquez-Jimenez, L.F. Chazaro-Ruiz, P.E. Diaz-Flores, J.R. Rangel-Mendez, “Fluoride removal in water by a hybrid adsorbent lanthanum – carbon”, *Journal of Colloid And Interface Science*, 2015, **455**, 194-202.
[163] J. Yuan, J. Xiao, F.C. Li, B.J. Wang, Z. Yao, B.L. Yu, L.Y. Zhang, “Co-treatment of spent cathode carbon in caustic and acid leaching process under ultrasonic assisted for preparation of SiC”, *Ultrasonics Sonochemistry*, 2018, **41**, 608-618.
[164] B. Tagirov, J. Schott, “Aluminum speciation in crustal fluids revisited”, *Geochimica Et Cosmochimica Acta*, 2001, **65**, 3965-3992.
[165] Z.A. Alothman, “A review: Fundamental aspects of silicate mesoporous materials”, *Materials*, 2012, **5**, 2874-2902.
[166] Z.H. Guan, B.Y. Li, G.L. Hai, X.J. Yang, T. Li, B.E. Tan, “A highly efficient catalyst for Suzuki-Miyaura coupling reaction of benzyl chloride under mild conditions”, *RSC Advances*, 2014, **4**, 36437-36443.
[167] P. Mu, H.X. Sun, Z.Q. Zhu, W.D. Liang, J.H. Liu, A. Li, “Synthesis and properties of nitrogen-containing conjugated microporous polymers”, *Macromolecular Materials and Engineering*, 2016, **301**, 451-456.
[168] Y. Kou, Y.H. Xu, Z.Q. Guo, D.L. Jiang, “Supercapacitive energy storage and electric power supply using an aza-fused pi-conjugated microporous framework”, *Angewandte Chemie - International Edition*, 2011, **50**, 8753-8757.
[169] M. Moliner, F. Rey, A. Corma, “Towards the rational design of efficient organic structure-directing agents for zeolite synthesis”, *Angewandte Chemie - International Edition*, 2013, **52**, 13880-13889.
[170] R. Grunker, V. Bon, P. Muller, U. Stoeck, S. Krause, U. Mueller, I. Senkovska, S. Kaskel, “A new metal-organic framework with ultra-high surface area”, *Chemical Communications*, 2014, **50**, 3450-3452.
[171] MOF Technologies, “MOF manufacturing” [online], 2019, https://www.moftechnologies.com/manufacturing/
[172] H. Jasuja, K.S. Walton, “Effect of catenation and basicity of pillared ligands on the water stability of MOFs”, *Dalton Transactions*, 2013, **42**, 15421-15426.

[173] H.H. Zhao, H.L. Song, L.J. Chou, “Facile synthesis of MOF-5 structure with large surface area in the presence of benzoyl peroxide by room temperature synthesis”, *Materials Chemistry and Physics*, 2014, **143**, 1005-1011.
[174] A.I. Cooper, “Conjugated Microporous Polymers”, *Advanced Materials*, 2009, **21**, 1291-1295.
[175] I. Pulko, J. Wall, P. Krajnc, N.R. Cameron, “Ultra-high surface area functional porous polymers by emulsion templating and hypercrosslinking: Efficient nucleophilic catalyst supports”, *Chemistry - A European Journal*, 2010, **16**, 2350-2354.
[176] H.Y. Zhao, Z. Jin, H.M. Su, X.F. Jing, F.X. Sun, G.S. Zhu, “Targeted synthesis of a 2D ordered porous organic framework for drug release”, *Chemical Communications*, 2011, **47**, 6389-6391.
[177] R.T. Woodward, L.A. Stevens, R. Dawson, M. Vijayaraghavan, T. Hasell, I.P. Silverwood, A.V. Ewing, T. Ratvijitvech, J.D. Exley, S.Y. Chong, F. Blanc, D.J. Adams, S.G. Kazarian, C.E. Snape, T.C. Drage, A.I. Cooper, “Swellable, water- and acid-tolerant polymer sponges for chemoselective carbon dioxide capture”, *Journal of the American Chemical Society*, 2014, **136**, 9028-9035.
[178] X.Y. Wang, Y. Zhao, L.L. Wei, C. Zhang, J.X. Jiang, “Nitrogen-rich conjugated microporous polymers: impact of building blocks on porosity and gas adsorption”, *Journal of Materials Chemistry A*, 2015, **3**, 21185-21193.
[179] C. Wilson, M.J. Main, N.J. Cooper, M.E. Briggs, A.I. Cooper, D.J. Adams, “Swellable functional hypercrosslinked polymer networks for the uptake of chemical warfare agents” *Polymer Chemistry*, 2017, **8**, 1914-1922.
[180] K.V. Rao, S. Mohapatra, T.K. Maji, S.J. George, “Guest-responsive reversible swelling and enhanced fluorescence in a super-absorbent, dynamic microporous polymer”, *Chemistry - A European Journal*, 2012, **18**, 4505-4509.
[181] W.X. Zhao, X.D. Zhuang, D.Q. Wu, F. Zhang, D. Gehrig, F. Laquai, X.L. Feng, “Boron-pi-nitrogen-based conjugated porous polymers with multi-functions”, *Journal of Materials Chemistry A*, 2013, **1**, 13878-13884.
[182] V. Davankov, V. Rogozhin, M. Tsjurupa, “Macronet polystyrene structures for ionites and method of producing same”, US patent 3729457A, 1973.
[183] P. Veverka, K. Jerabek, “Mechanism of hypercrosslinking of chloromethylated styrene-divinylbenzene copolymers”, *Reactive & Functional Polymers*, 1999, **41**, 21-25.
[184] B.Y. Li, R.N. Gong, W. Wang, X. Huang, W. Zhang, H.M. Li, C.X. Hu, B.E. Tan, “A new strategy to microporous polymers: Knitting rigid aromatic building blocks by external cross-linker”, *Macromolecules*, 2011, **44**, 2410-2414.
[185] R. Dawson, L.A. Stevens, T.C. Drage, C.E. Snape, M.W. Smith, D.J. Adams, A.I. Cooper, “Impact of water coadsorption for carbon dioxide capture in microporous polymer sorbents”, *Journal of The American Chemical Society*, 2012, **134**, 10741-10744.
[186] S.J. Xu, K.P. Song, T. Li, B. Tan, “Palladium catalyst coordinated in knitting N-heterocyclic carbene porous polymers for efficient Suzuki-Miyaura coupling reactions”, *Journal of Materials Chemistry A*, 2015, **3**, 1272-1278.
[187] S.W. Yao, X. Yang, M. Yu, Y.H. Zhang, J.X. Jiang, “High surface area hypercrosslinked microporous organic polymer networks based on tetraphenylethylene for CO_2 capture”, *Journal of Materials Chemistry A*, 2014, **2**, 8054-8059.
[188] C.D. Wood, B. Tan, A. Trewin, F. Su, M.J. Rosseinsky, D. Bradshaw, Y. Sun, L. Zhou, A.I. Cooper, “Microporous organic polymers for methane storage”, *Advanced Materials*, 2008, **20**, 1916-1921.
[189] A.M. James, S. Harding, T. Robshaw, N. Bramall, M.D. Ogden, R. Dawson, “Selective environmental remediation of strontium and cesium using sulfonated hyper-cross-linked polymers (SHCPs)” *Applied Materials and Interfaces*, 2019, **11**, 22464-22473.
[190] C.D. Wood, B. Tan, A. Trewin, H.J. Niu, D. Bradshaw, M.J. Rosseinsky, Y.Z. Khimyak, N.L. Campbell, R. Kirk, E. Stockel, A.I. Cooper, “Hydrogen storage in microporous hypercrosslinked organic polymer networks”, *Chemistry of Materials*, 2007, **19**, 2034-2048.
[191] Purolite, “Macronet Adsorbent Resins” [online], 2019, https://www.purolite.com/brand/macronet.

[192] J.Y. Lee, C.D. Wood, D. Bradshaw, M.J. Rosseinsky, A.I. Cooper, “Hydrogen adsorption in microporous hypercrosslinked polymers”, *Chemical Communications*, 2006, **25**, 2670-2672.
[193] R. Dawson, T. Ratvijitvech, M. Corker, A. Laybourn, Y.Z. Khimyak, A.I. Cooper, D.J. Adams, “Microporous copolymers for increased gas selectivity”, *Polymer Chemistry*, 2012, **3**, 2034-2038.
[194] X. Yang, M. Yu, Y. Zhao, C. Zhang, X.Y. Wang, J.X. Jiang, “Hypercrosslinked microporous polymers based on carbazole for gas storage and separation”, *RSC Advances*, 2014, **4**, 61051-61055.
[195] C. Yao, G.Y. Li, Y.H. Xu, “Carboxyl-enriched conjugated microporous polymers: Impact of building blocks on porosity and gas adsorption”, *Acta Physico-Chimica Sinica*, 2017, **33**, 1898-1904.
[196] A.M. Li, Q.X. Zhang, G.C. Zhang, J.L. Chen, Z.H. Fei, F.Q. Liu, “Adsorption of phenolic compounds from aqueous solutions by a water-compatible hypercrosslinked polymeric adsorbent”, *Chemosphere*, 2002, **47**, 981-989.
[197] D. Bratkowska, N. Fontanals, F. Borrull, P.A.G. Cormack, D.C. Sherrington, R.M. Marce, “Hydrophilic hypercrosslinked polymeric sorbents for the solid-phase extraction of polar contaminants from water”, *Journal of Chromatography A*, 2010, **1217**, 3238-3243.
[198] B.Y. Li, F.B. Su, H.K. Luo, L.Y. Liang, B.E. Tan, “Hypercrosslinked microporous polymer networks for effective removal of toxic metal ions from water”, *Microporous and Mesoporous Materials*, 2011, **138**, 207-214.
[199] T.D. Vaden, J.M. Lisy, “Characterization of hydrated Na^+(phenol) and K^+(phenol) complexes using infrared spectroscopy”, *Journal of Chemical Physics*, 2004, **120**, 721-730.
[200] R.H. Schlosberg, C.G. Scouten, “Organic chemistry of calcium - formation and pyrolysis of hydroxycalcium phenoxides”, *Energy & Fuels*, 1988, **2**, 582-585.
[201] C.G. Scouten, H.W. Dougherty, “Organic chemistry of calcium. 3. Steam stripping of metal phenoxides liberates phenol and regenerates the metal hydroxide”, *Industrial & Engineering Chemistry Research*, 1990, **29**, 1721-1725.
[202] N. Sakhare, S. Lunge, S. Rayalu, S. Bakardjiva, J. Subrt, S. Devotta, N. Labhsetwar, “Defluoridation of water using calcium aluminate material”, *Chemical Engineering Journal*, 2012, **203**, 406-414.
[203] M. Chaudhary, A. Maiti, “Defluoridation by highly efficient calcium hydroxide nanorods from synthetic and industrial wastewater”, *Colloids and Surfaces A - Physicochemical and Engineering Aspects*, 2019, **561**, 79-88.
[204] S.K. Nath, R.K. Dutta, “Significance of calcium containing materials for defluoridation of water: a review”, *Desalination and Water Treatment*, 2015, **53**, 2070-2085.
[205] A. Yurkov, *Refractories For Aluminium*, Springer, Basel, 2015.
[206] L.M. Camacho, A. Torres, D. Saha, S.G. Deng, “Adsorption equilibrium and kinetics of fluoride on sol-gel-derived activated alumina adsorbents”, *Journal of Colloid and Interface Science*, 2010, **349**, 307-313.
[207] P. Wu, L. Xia, M. Dai, L.L. Lin, S.X. Song, “Electrosorption of fluoride on TiO_2-loaded activated carbon in water”, *Colloids and Surfaces A - Physicochemical and Engineering Aspects*, 2016, **502**, 66-73.
[208] Y. Vijaya, M.V. Subbaiah, A.S. Reddy, A. Krishnaiah, “Equilibrium and kinetic studies of fluoride adsorption by chitosan coated perlite”, *Desalination and Water Treatment*, 2010, **20**, 272-280.
[209] L. Lv, J. He, M. Wei, D.G. Evans, Z.L. Zhou, “Treatment of high fluoride concentration water by MgAl-CO_3 layered double hydroxides: Kinetic and equilibrium studies”, *Water Research*, 2007, **41**, 1534-1542.
[210] S.R. Trout, Y. Zhilichev, “Effective use of neodymium iron boron magnets, case studies”, Electrical Insulation Conference / Electrical Manufacturing and Coil Winding Conference, IEEE, Cincinnati, 1999.
[211] Argus Consulting, *Argus Rare Earths Monthly Outlook 17/9*, Argus, London, 2017.
[212] S.A. Wasay, S. Tokunaga, S.-W. Park, “Removal of Hazardous Anions from Aqueous Solutions by La(III)- and Y(III)- Impregnated Alumina”, *Separation Science and Technology*, 1996, **31**, 1501-1514.

[213] B.D. Turner, P.J. Binning, S.W. Sloan, “A calcite permeable reactive barrier for the remediation of Fluoride from spent potliner (SPL) contaminated groundwater”, *Journal of Contaminant Hydrology*, 2008, **95**, 110-120.
[214] K. Oke, S. Neumann, B. Adams, “Selective Fluoride Removal”, *Water Today*, 2011, May, 76-80.
[215] H. Kalka, “Aqion: Manual (selected topics)” [online], 2015, http://www.aqion.de/site/98?.
[216] N.v.d.W. Tjaart, P.P. Coetzee, “Distribution coefficients and ion exchange behaviour of some elements with Purolite S-950 in hydrochloric acid”, *Fresenius Journal of Analytical Chemistry*, 1996, **356**, 420-424.
[217] P. Miretzky, A.F. Cirelli, “Fluoride removal from water by chitosan derivatives and composites: A review”, *Journal of Fluorine Chemistry*, 2011, **132**, 231-240.
[218] A.O. Dada, A.P. Olalekan, A.M. Olatunya, O. Dada, “Langmuir, Freundlich, Temkin and Dubinin–Radushkevich Isotherms Studies of Equilibrium Sorption of Zn^{2+} Unto Phosphoric Acid Modified Rice Husk”, *IOSR Journal of Applied Chemistry*, 2012, **3**, 38-45.
[219] E.J. Billo, *Excel for Chemists: A Comprehensive Guide*, 3rd ed., John Wiley, Hoboken, New Jersey, 2004.
[220] T.G. Fawcett, F. Needham, C. Crowder, S. Kabekkodu, “Advanced materials analysis using the powder diffraction file”, 10th National Conference on X-ray Diffraction and ICDD Workshop, Shanghai, China, 2009.
[221] A. Adel, E.E. Ibrahim, Y.A. Fadia, F.H. Mohammed, “Studies on the Uptake of Rare Earth Elements on Polyacrylamidoxime Resins from Natural Concentrate Leachate Solutions”, *Journal of Dispersion Science and Technology*, 2010, **31**, 1128-1135.
[222] M.A. Maheswari, M.S. Subramanian, “Extraction chromatographic method for the separation of actinides and lanthanides using EDHBA grafted AXAD-16 polymer”, *Talanta*, 2005, **65**, 735-742.
[223] P.A. Giguere, S. Turrell, The nature of hydrofluoric acid. A spectroscopic study of the proton-transfer complex $H_3O^+.F^-$, *Journal of The American Chemical Society*, 1980, **102**, 5473-5477.
[224] H. Lopez-Gonzalez, M. Solache-Rios, M. Jimenez-Reyes, J.J. Ramirez-Garcia, A. Rojas-Hernandez, “Effect of chloride ions on the hydrolysis of trivalent lanthanum, praseodymium and lutetium in aqueous solutions of 2 M ionic strength”, *Journal of Solution Chemistry*, 2005, **34**, 427-441.
[225] I. Bertini, C. Luchinat, “Reaction pathways of zinc enzymes and related biological catalysts”, in: I. Bertini, H. Gray, S.J. Lippard, J.S. Valentine (Eds.) *Bioinorganic Chemistry*, University Science Books, Mill Valley, California, 1994, pp. 37-106.
[226] A.E. Martell, R.M. Smith, R.J. Motekaitis, “Critical Stability Constants Database”, A & M University, College Station, Texas, 1997.
[227] I.A.W. Tan, A.L. Ahmad, B.H. Hameed, “Adsorption isotherms, kinetics, thermodynamics and desorption studies of 2,4,6-trichlorophenol on oil palm empty fruit bunch-based activated carbon”, *Journal of Hazardous Materials*, 2009, **164**, 473-482.
[228] C.K. Na, H.J. Park, “Defluoridation from aqueous solution by lanthanum hydroxide”, *Journal of Hazardous Materials*, 2010, **183**, 512-520.
[229] J.T.M. Amphlett, M.D. Ogden, R.I. Foster, N. Syna, K. Soldenhoff, C.A. Sharrad, “Polyamine functionalised ion exchange resins: Synthesis, characterisation and uranyl uptake”, *Chemical Engineering Journal*, 2018, **334**, 1361-1370.
[230] Q.L. Hu, Z.Y. Zhang, “Application of Dubinin-Radushkevich isotherm model at the solid/solution interface: A theoretical analysis”, *Journal of Molecular Liquids*, 2019, **277**, 646-648.
[231] K. Vijayaraghavan, T.V.N. Padmesh, K. Palanivelu, M. Velan, “Biosorption of nickel(II) ions onto *Sargassum wightii*: Application of two-parameter and three-parameter isotherm models”, *Journal of Hazardous Materials*, 2006, **133**, 304-308.
[232] D.K. Lavallee, J. Brace, N. Winograd, “X-ray photoelectron-spectra of n-methyltetraphenylporphyrins - evidence for a correlation of binding-energies with metal-nitrogen bond distances”, *Inorganic Chemistry*, 1979, **18**, 1776-1780.

[233] C. Stosiek, G. Scholz, S.L.M. Schroeder, E. Kemnitz, “Structure and Properties of Noncrystalline Aluminum Oxide-Hydroxide Fluorides”, *Chemistry of Materials*, 2010, **22**, 2347-2356.
[234] J.M. Cowley, T.R. Scott, “Basic fluorides of aluminium”, *Journal of The American Chemical Society*, 1948, **70**, 105-109.
[235] T. Sato, S. Ikoma, F. Ozawa, “Preparation of gelatinous aluminium hydroxide by urea from aqueous solutions containing chloride, nitrate and sulphate of aluminium”, *Journal of Chemical Technology and Biotechnology*, 1980, **30**, 225-232.
[236] S. Selvasekarapandian, M. Vijayakumar, T. Gnanasekaran, S. Fujihara, S. Koji, “Ion conduction studies on LaF_3 thin film by impedance spectroscopy”, *Physica B - Condensed Matter*, 2003, **337**, 52-57.
[237] N.N. Greenwood, A. Earnshaw, *Chemistry of The Elements*, 2nd Ed., Butterworth-Heinemann, Oxford, 1997.
[238] European Commission, *Communication from The Commission to The European Parliament, The Council, The European Economic and Social Committee and The Committee of The Regions. On the 2017 list of Critical Raw Materials for the EU*, European Union, Brussels, 2017.
[239] V. Davis, C. Bates, B. Savoie, Q. Xu, W. Wolf, M. Webb, K. Billings, R. Mckenney, I. Darolles, N. Nair, A. Hightower, D. Rosenberg, A. Musahid, C. Brooks, T. Miller, R. Grubbs, S. Jones, “Room - temperature cycling of metal fluoride electrodes: Liquid electrolytes for high-energy fluoride ion cells”, *Science*, 2018, **362**, 1144-1148.
[240] K. Jiang, K. Zhou, “Recovery of cryolite with high molar ratio from high fluorine-containing wastewater”, *Euro-Mediterranean Journal for Environmental Integration*, 2017, **2**, 22.
[241] Roskill, *Fluorspar. Global Industry, Markets and Outlook 2018*, Roskill Information Services, Wimbledon, 2018.
[242] M.M. Hyland, E.C. Patterson, F. Stevens-McFadden, B.J. Welch, “Aluminium fluoride consumption and control in smelting cells”, *Scandinavian Journal of Metallurgy*, 2001, **30**, 404-414.
[243] S. Lagergren, “Theorie der sogenannten adsorption gelosterstoffe”, *Svenska Vetenskapsakademiens. Handlingar*, 1898, **24**, 1-39.
[244] G. Blanchard, M. Maunaye, G. Martin, “Removal of heavy metals from waters by means of natural zeolites”, *Water Research*, 1894, **18**, 1501-1507.
[245] G.E. Boyd, A.W. Adamson, L.S. Myers Jr., “The exchange adsorption of ions from aqueous solutions by organic zeolites. 11. Kinetics”, *Journal of The American Chemical Society*, 1947, **69**, 2836-2848.
[246] N.T.T. Tu, T.V. Thien, P.D. Du, V.T.T. Chau, T.X. Mau, D.Q. Khieu, “Adsorptive removal of Congo red from aqueous solution using zeolitic imidazolate framework-67”, *Journal of Environmental Chemical Engineering*, 2018, **6**, 2269-2280.
[247] W.J. Weber, J.C. Morris, “Kinetics of adsorption on carbon from solution”, *Journal of the Sanitary Engineering Division*, 1963, **89**, 31-60.
[248] H.N. Tran, S.J. You, A. Hosseini-Bandegharaei, H.P. Chao, “Mistakes and inconsistencies regarding adsorption of contaminants from aqueous solutions: A critical review”, *Water Research*, 2017, **120**, 88-116.
[249] S. Roginsky, Y.B. Zeldovich, “The catalytic oxidation of carbon monoxide on manganese dioxide”, *Acta Physicochimica U.R.S.S.*, 1934, **1**, 554.
[250] S.H. Chien, W.R. Clayton, “Application of Elovich equation to the kinetics of phosphate release and sorption in soils”, *Soil Science Society of America Journal*, 1980, **44**, 265-268.
[251] G.Y. Yan, T. Viraraghavan, M. Chen, “A new model for heavy metal removal in a biosorption column”, *Adsorption Science & Technology*, 2001, **19**, 25-43.
[252] H. Tavakoli, H. Sepehrian, F. Semnani, M. Samadfam, “Recovery of uranium from UCF liquid waste by anion exchange resin CG-400: Breakthrough curves, elution behavior and modeling studies”, *Annals of Nuclear Energy*, 2013, **54**, 149-153.
[253] J.P. Bezzina, M.D. Ogden, E.M. Moon, K.L. Soldenhoff, “REE behavior and sorption on weak acid resins from buffered media”, *Journal of Industrial and Engineering Chemistry*, 2018, **59**, 440-455.

[254] L. Lv, J. He, M. Wei, X. Duan, “Kinetic studies on fluoride removal by calcined layered double hydroxides”, *Industrial & Engineering Chemistry Research*, 2006, **45**, 8623-8628.
[255] E.B. Simsek, U. Beker, B.F. Senkal, “Predicting the dynamics and performance of selective polymeric resins in a fixed bed system for boron removal”, *Desalination*, 2014, **349**, 39-50.
[256] Lanxess, “Product Information: Lewatit TP260” [online], 2011, https://www.lenntech.com/Data-sheets/Lewatit-TP-260-L.pdf.
[257] M.J. Moreira, L.M. Ferreira, “Kinetic studies for sorption of amino acids using a strong anion-exchange resin. Effect of ionic strength”, *Journal of Chromatography A*, 2005, **1092**, 101-106.
[258] Y. Liu, L. Shen, “From Langmuir kinetics to first- and second-order rate equations for adsorption”, *Langmuir*, 2008, **24**, 11625-11630.
[259] N. Viswanathan, S. Meenakshi, “Enriched fluoride sorption using alumina/chitosan composite”, *Journal of Hazardous Materials*, 2010, **178**, 226-232.
[260] R. Xu, M.Y. Zhang, R.J.G. Mortimer, G. Pan, “Enhanced phosphorus locking by novel lanthanum/aluminum-hydroxide composite: implications for eutrophication control, *Environmental Science and Technology*, 2017, **51**, 3418-3425.
[261] T. Birk, K.S. Pedersen, C.A. Thuesen, T. Weyhermuller, M. Schau-Magnussen, S. Piligkos, H. Weihe, S. Mossin, M. Evangelisti, J. Bendix, “Fluoride bridges as structure-directing motifs in 3d-4f cluster chemistry”, *Inorganic Chemistry*, 2012, **51**, 5435-5443.
[262] J.L. Sides, C.T. Kenner, “Effect of pH and ionic strength on the distribution coefficients of alkaline earth metals and nickel with chelating ion-exchange resins”, *Analytical Chemistry*, 1966, **38**, 707-711.
[263] J.T.M. Amphlett, C.A. Sharrad, M.D. Ogden, “Extraction of uranium from non-saline and hypersaline conditions using iminodiacetic acid chelating resin Purolite S930+”, *Chemical Engineering Journal*, 2018, **342**, 133-141.
[264] B. Zhao, Y. Shang, W. Xiao, C. Dou, R. Han, “Adsorption of Congo red from solution using cationic surfactant modified wheat straw in column model”, *Journal of Environmental Chemical Engineering*, 2014, **2**, 40-45.
[265] J.T.M. Amphlett, C.A. Sharrad, R.I. Foster, M.D. Ogden, “Ethylenediamine functionalised ion exchange resin for uranium recovery from acidic mixed sulfate-chloride media: initial column loading studies”, *Journal of the Southern African Institute of Mining and Metallurgy*, 2018, **118**,1251-1257.
[266] Y.X. Ma, F.M. Shi, X.L. Zheng, J. Ma, C.J. Gao, “Removal of fluoride from aqueous solution using granular acid-treated bentonite (GHB): Batch and column studies”, *Journal of Hazardous Materials*, 2011, **185**, 1073-1080.
[267] M.H. Calero, F. Hernáinz, G. Blázquez, G. Tenorio, M.A. Martín-Lara, “Study of Cr (III) biosorption in a fixed-bed column”, *Journal of Hazardous Materials*, 2009, **171**, 886-893.
[268] D. Villemin, M.A. Didi, “Aminomethylenephosphonic acids syntheses and applications (a review)”, *Oriental Journal of Chemistry*, 2015, **31**, 1-12.
[269] V.S. Sastri, J.-C. Bunzli, V. Ramachandra Rao, G.V.S. Rayudu, J.R. Perumareddi, *Modern Aspects of Rare Earths and their Complexes*, Elsevier, Amsterdam, 2003.
[270] J. Knoeck, “Vibrational spectrometric and electrochemical evidence for lanthanum(lll)-nitrate complexes in aqueous solution”, *Analytical Chemistry*, 1969, **41**, 2069-2071.
[271] T.J. Hanson, K.M. Smetana, *Determination of aluminium by four analytical methods*, Atlantic Richfield Hanford Company, Richland, Washington, 1975.
[272] Y. Li, H. Zhang, Z.Q. Zhang, L.M. Shao, P.J. He, “Treatment and resource recovery from inorganic fluoride-containing waste produced by the pesticide industry”, *Journal of Environmental Sciences*, 2015, **31**, 21-29.
[273] M.A. Ford, J.d.B. Cunliff, “An equilibrium model for the precipitation of synthetic cryolite”, *Hydrometallurgy*, 1986, **16**, 283-299.
[274] D. Yu, V. Mambakkam, A.H. Rivera, D. Li, K. Chattopadhyay, “Spent Potlining (SPL): A myriad of opportunities”, *Aluminium International Today*, 2015, September/October, 17-20.
[275] European Union, “Council Directive of 12 December 1991 on hazardous waste (91/689/EEC)”, *Official Journal of the European Communities*, 1991, **L377**, 20-27.

[276] K.G. Deshpande, “Use of spent potlining from the aluminium electrolytic cell as an additive to arc furnace steel melting and cupola iron melting in steel industries”, *Environmental and Waste Management*, 1998, **831**, 129-136.
[277] F. Olsen, “Elkem spent potlining recycling project”, REWAS Global Symposium on Recycling, Waste Treatment and Clean Technology, Warrendale, Pensylvania, 2008.
[278] K. Tschope, A. Store, A. Solheim, E. Skybakmoen, T. Grande, A.P. Ratvik, “Electrochemical wear of carbon cathodes in electrowinning of aluminum”, *Journal of Metals*, 2013, **65**, 1403-1410.
[279] K. Afshinnia, A. Poursaee, “The potential of ground clay brick to mitigate alkali-silica reaction in mortar prepared with highly reactive aggregate”, *Construction and Building Materials*, 2015, **95**, 164-170.
[280] P.-C. Aïtcin, R.J. Flatt, *Science and Technology of Concrete Admixtures*, Woodhead, Cambridge, 2016.
[281] The Council of the European Union, “Council decision of 19 December 2002, establishing criteria and procedures for the acceptance of waste at landfills pursuant to Article 16 of and Annex II to Directive 1999/31/EC (2003/33/EC)”, *Official Journal of the European Communities*, 2003, **L11**, 27-49.
[282] A. Strunecka, O. Strunecky, J. Patocka, “Fluoride plus aluminum: Useful tools in laboratory investigations, but messengers of false information”, *Physiological Research*, 2002, **51**, 557-564.
[283] K.C. Sole, F.K. Crundwell, N. Dlamini, G. Kruger, “Mitigating effects of silica in copper solvent extraction”, 9th Southern African Base Metals Conference, Southern African Institute of Mining and Metallurgy, Livingstone, Zambia, 2018.
[284] D.N.T. Barton, T.J. Robshaw, O. Okusanya, D. Kim, S.E. Pepper, C.A. Sharrad, M.D. Ogden, “Remediation of radioiodine using polyamine anion exchange resins”, *Journal of Industrial and Engineering Chemistry*, 2019, **78**, 210-221.
[285] J.Y. Chen, C.W. Lin, P.H. Lin, C.W. Li, Y.M. Liang, J.C. Liu, S.S. Chen, “Fluoride recovery from spent fluoride etching solution through crystallization of Na_3AlF_6 (synthetic cryolite)”, *Separation and Purification Technology*, 2014, **137**, 53-58.
[286] B.G. Place, *Engineering Study for the Treatment of Spent Ion Exchange Resin Resulting from Nuclear Process Applications*, WHC-EP-0375, westinghouse Hanford Company, Washington, 1990.
[287] M.S. Peters, K.D. Timmerhaus, R.E. West, *Plant Design and Economics for Chemical Engineers*, 5th ed., McGraw-Hill, New York, 2007.
[288] J. Rine, E. Coppola, A. Davis, *Final Report. Demonstration of Regenerable, Large-Scale Ion Exchange System Using WBA Resin in Rialto, CA*, Applied Research Associates/ESTCP, Panama City, 2012.
[289] H.J. Lang, “Cost relationships in preliminary cost estimation”, *Chemical Engineering*, 1947, **54**, 117-121.
[290] AACE International, *Cost Estimate Classification System – As Applied in Engineering, Procurement and Construction for the Process Industries*, 18R-97, AACE, Morgantown, 2020.
[291] J.H. Koon, W.J. Kaufman, *Optimization Of Ammonia Removal By Ion Exchange Using Clinoptilolite*, Environmental Protection Agency/University of California, Berkley, 1971.
[292] K. Ebner, S. Ebner, “Process and plant for converting sodium sulphate into sodium hydroxide”, international patent DE3801382A1, 1989.
[293] World Health Organisation, *Guidelines for Drinking-water Quality*, 4th Ed., WHO Press, Geneva, 2011.
[294] D. Kauspediene, R. Ragauskas, V. Pakstas, A. Gefeniene, “Fluoride and silicon removal from spent glass etching solution by chemical treatment”, *Chemija*, 2017, **28**, 33-38.
[295] N.M. Mourad, T. Sharshar, T. Elnimr, M.A. Mousa, “Radioactivity and fluoride contamination derived from a phosphate fertilizer plant in Egypt”, *Applied Radiation and Isotopes*, 2009, **67**, 1259-1268.

[296] M. Potgieter, J.C. Barry, D.J.v.d. Westhuizen, H.M. Krieg, “Recovery of uranium from nuclear conversion plant waste”, *Journal of the Southern African Institute of Mining and Metallurgy*, 2017, **117**, 785-792.
[297] K.K. Yadav, N. Gupta, V. Kumar, S.A. Khan, A. Kumar, “A review of emerging adsorbents and current demand for defluoridation of water: Bright future in water sustainability”, *Environment International*, 2018, **111**, 80-108.
[298] F. Ke, G. Luo, P.R. Chen, J. Jiang, Q.Y. Yuan, H.M. Cai, C.Y. Peng, X.C. Wan, “Porous metal-organic frameworks adsorbents as a potential platform for defluoridation of water”, *Journal of Porous Materials*, 2016, **23**, 1065-1073.
[299] L.X. Tan, B. Tan, “Hypercrosslinked porous polymer materials: design, synthesis, and applications”, *Chemical Society Reviews*, 2017, **46**, 3322-3356.
[300] B.Y. Li, R.N. Gong, Y.L. Luo, B.E. Tan, “Tailoring the pore size of hypercrosslinked polymers”, *Soft Matter*, 2011, **7**, 10910-10916.
[301] R. Vinodh, P. Hemalatha, M. Ganesh, M.M. Peng, A. Abidov, M. Palanichamy, W.S. Chab, H.T. Jang, “Novel microporous hypercross-linked conjugated quinonoid chromophores with broad light absorption and CO_2 sorption characteristics”, *RSC Advances*, 2014, **4**, 3668-3674.
[302] S. Fisher, R. Kunin, “Routine exchange capacity determinations of ion exchange resins”, *Analytical Chemistry*, 1955, **27**, 1191-1194.
[303] C.D. Wood, B. Tan, A. Trewin, F. Su, M.J. Rosseinsky, D. Bradshaw, Y. Sun, L. Zhou, A.I. Cooper, “Microporous organic polymers for methane storage”, *Advanced Materials*, 2008, **20**, 1916-1921.
[304] A.I. Cooper, A.B. Holmes, “Synthesis of molded monolithic porous polymers using supercritical carbon dioxide as the porogenic solvent”, *Advanced Materials*, 1999, **11**, 1270-1274.
[305] R. Dawson, A. Laybourn, R. Clowes, Y.Z. Khimyak, D.J. Adams, A.I. Cooper, “Functionalized conjugated microporous polymers”, *Macromolecules*, 2009, **42**, 8809-8816.
[306] R. Dawson, D.J. Adams, A.I. Cooper, “Chemical tuning of CO_2 sorption in robust nanoporous organic polymers”, *Chemical Science*, 2011, **2**, 1173-1177.
[307] M. Ni, B.D. Ratner, “Differentiation of calcium carbonate polymorphs by surface analysis techniques – an XPS and TOF-SIMS study”, *Surface Interface Analysis*, 2008, **40**, 1356-1361.
[308] M.A. Henderson, “Evidence for bicarbonate formation on vacuum annealed TiO_2(110) resulting from a precursor-mediated interaction between CO_2 and H_2O”, *Surface Science*, 1998, **400**, 203-219.
[309] F.A. Andersen, L. Brecevic, “Infrared-spectra of amorphous and crystalline calcium-carbonate”, *Acta Chemica Scandinavica*, 1991, **45**, 1018-1024.
[310] B. Demri, D. Muster, “XPS study of some calcium compounds”, *Journal of Materials Processing Technology*, 1995, **55**, 311-314.
[311] K.G. Caulton, M.H. Chisholm, S.R. Drake, K. Folting, J.C. Huffman, W.E. Streib, “Triangular phenoxide aggregates of calcium, strontium, and barium - a comparison”, *Inorganic Chemistry*, 1993, **32**, 1970-1976.
[312] S.L. Benjamin, W. Levason, G. Reid, “Medium and high oxidation state metal/non-metal fluoride and oxide-fluoride complexes with neutral donor ligands”, *Chemical Society Reviews*, 2013, **42**, 1460-1499.
[313] M. Jonsson, J. Lind, G. Merenyi, “Redox and acidity properties of 2,2'- and 4,4'-biphenol and the corresponding phenoxyl radicals, *Journal of Physical Chemistry A*, 2002, **106**, 4758-4762.
[314] Y.H. Li, X.R. Zhai, X.S. Liu, L. Wang, H.R. Liu, H.B. Wang, “Electrochemical determination of bisphenol A at ordered mesoporous carbon modified nano-carbon ionic liquid paste electrode”, *Talanta*, 2016, **148**, 362-369.
[315] M. Ragnar, C.T. Lindgren, N.-O. Nilvebrant, “pK_a - Values of guaiacyl and syringyl phenols related to lignin”, *Journal of Wood Chemistry and Technology*, 2008, **20**, 277-305.

[316] B.D. Turner, P. Binning, S.L.S. Stipp, “Fluoride removal by calcite: Evidence for fluorite precipitation and surface adsorption”, *Environmental Science & Technology*, 2005, **39**, 9561-9568.
[317] W.H. Kang, E.I. Kim, J.Y. Park, ”Fluoride removal capacity of cement paste”, *Desalination*, 2007, **202**, 38-44.
[318] M. Eriksson, I. Lundstrom, L.G. Ekedahl, “A model of the Temkin isotherm behavior for hydrogen adsorption at Pd-SiO_2 interfaces”, *Journal of Applied Physics*, 1997, **82**, 3143-3146.
[319] K.Y. Foo, B.H. Hameed, “Insights into the modeling of adsorption isotherm systems”, *Chemical Engineering Journal*, 2010, **156**, 2-10.
[320] E.T. Pedrosa, L. Boeck, C.V. Putnis, A. Putnis, “The replacement of a carbonate rock by fluorite: Kinetics and microstructure”, *American Mineralogist*, 2017, **102**, 126-134.
[321] L.Y. Chai, Y.Y. Wang, N. Zhao, W.C. Yang, X.Y. You, “Sulfate-doped Fe_3O_4/Al_2O_3 nanoparticles as a novel adsorbent for fluoride removal from drinking water”, *Water Research*, 2013, **47**, 4040-4049.
[322] P. Gasser, Y. Haikel, J.C. Voegel, P. Gramain, “Surface-reactions of hydroxyapatite in the presence of fluoride ions. 2. Effects of calcium and phosphate in saturated solutions”, *Colloids and Surfaces A - Physicochemical and Engineering Aspects*, 1994, **88**, 157-168.
[323] N. Thakur, S.A. Kumar, D.N. Wagh, S. Das, A.K. Pandey, S.D. Kumar, A.V.R. Reddy, “Matrix supported tailored polymer for solid phase extraction of fluoride from variety of aqueous streams”, *Journal of Hazardous Materials*, 2012, **201**, 193-201.

APPENDIX A

"Highly efficient fluoride extraction from simulant leachate of spent potlining via La-loaded chelating resin. An equilibrium study"

SUPPORTING INFORMATION

PLS aqueous speciation data using Aqion version 6.4.7

Experimental

Known concentrations of cations and anions in the PLS at 1/100 dilution, to simulate experimental conditions in section 3.2. of the main research article were inputted into the Aqion software [11]. Appropriate adjustments to pH, [Cl^-] and [Na^+] were made. Necessary adjustments to charge balance were made by adjustment of dissolved inorganic carbon. Output speciation took precipitation of minerals into account.

Results

The concentrations of key aqueous species (these being mainly anions, cations and neutral complexes present in significant quantities and containing Al^{3+} and F^-) are shown in Table A1.

Table A1. Aqion calculations for Al^{3+} and F^- speciation in the PLS at different pHs.

Species	Concentrations (mmol·L^{-1})		
	pH 2	**pH 4**	**pH 8**
AlF^{2+}	0.0228	0.00140	< 0.0001
AlF_2^+	0.163	0.0820	< 0.0001
AlF_3	0.0363	0.132	< 0.0001
$[Al(OH)_4]^-$	< 0.0001	< 0.0001	0.190
F^-	0.0223	0.140	0.785
HF	0.297	0.0428	< 0.0001
H^+	11.0	0.223	< 0.0001
OH^-	< 0.0001	< 0.0001	0.00139

Table A2. Manufacturer specifications for Purolite® S950+ [12].

Parameter	Value
Appearance	Spherical beads, off-white
Commercial equivalents	Duolite® C467 Lewatit® MonoPlus TP 260 Amberlite® IRC 747
Moisture retention	60-68%
Particles <300 μm	≤1%
Reversible swelling H - Na	≤50%
Capacity (Ca^{2+})	74 mg·g^{-1} (1.84 mmol·g^{-1})

Fluoride ion-selective electrode analysis and synthesis of total ionic strength adjustment buffer (TISAB)

The fluoride concentration of solutions before and after resin-contact were analysed using a Cole-Palmer fluoride ion-selective electrode. The electrode was calibrated using standards of known fluoride concentration from 0.1-10 or from 10-100 mg·L^{-1}. These were made by dissolving ≥99.999% NaF, which had been dried in an air-flow oven for a minimum of 24 h, in deionised water. Electrode readings for each sample were averaged from at least three replicates. Error values were calculated from 2 x standard deviation, then propagated as necessary. Each sample contained 50% total ionic strength adjustment buffer and were sufficiently diluted to ensure ionic strength did not vary significantly between samples.

For synthesis of TISAB, all reagents were of analytical grade and used without further purification. In a 1 L beaker, 45.0 g NaCl was dissolved in ~500 mL deionised water, followed by 4.00 g 1,2-Diaminocyclohexanetetraacetic acid hydrate. 57 mL acetic acid were added were added and the water volume increased to ~800 mL. 5 M NaOH was added dropwise, to increase pH to 5.5. The solution was then transferred to a 1 L volumetric flask and water volume increased to exactly 1 L.

Analysis of resin at various process stages by X-ray photoelectron spectroscopy (XPS)

Experimental

Samples were washed, ground and dried as described in the main research article. The samples were mounted for XPS analysis by pressing into In foil.

Analysis was carried out using a Kratos Supra spectrometer, with monochromated Al source and 2 analysis points per sample. The area of analysis was 300 x 700 μm. Charge neutralisation was used throughout. Survey scans were collected between 1200-0 eV binding energy, at 160 eV pass energy, with 1 eV intervals and 300 s per sweep with 2 sweeps being collected. High-resolution Al 2p, C 1s, Cl 2p, F 1s, La 3d and 4d, N 1s, O 1s and P 2p scans were collected over appropriate energy ranges (see spectra), at 20 eV pass energy, with 0.1 eV intervals. For C 1s, F 1s, La 4d and O 1s, 1 x 5 min sweep was collected. For Al 2p, Cl 2p, N 1s and P 2p, 2 x 5 min sweeps were collected and for La

3d, 4 x 5 min sweeps were collected. The increased collection time was due either to reduced sensitivity, extended energy range or both.

Attained data was calibrated for intensity, using a transmission function characteristic of the instrument, then quantified using Schofield theoretical relative sensitivity factors. All data was calibrated relative to a C 1s position of 285.0 eV for aliphatic C environment.

Results and commentary

Table A3. Average surface composition (atomic %), of the resin at various process stages.

Sample	Al	Ca	C	Cl	F	La	N	O	P	Na
H-950+	<0.1	<0.1	76.2	<0.1	<0.1	<0.1	3.8	15.2	4.9	<0.1
La-S950+	<0.1	0.8	74.5	<0.1	<0.1	0.6	3.0	14.6	6.3	<0.1
La-S950+ post-NaF-contact	<0.1	<0.1	69.7	<0.1	6.7	1.6	2.2	10.8	5.0	4.2
La-S950+ post-PLS-contact	3.9	0.3	67.8	<0.1	2.9	0.7	4.2	14.6	5.8	<0.1

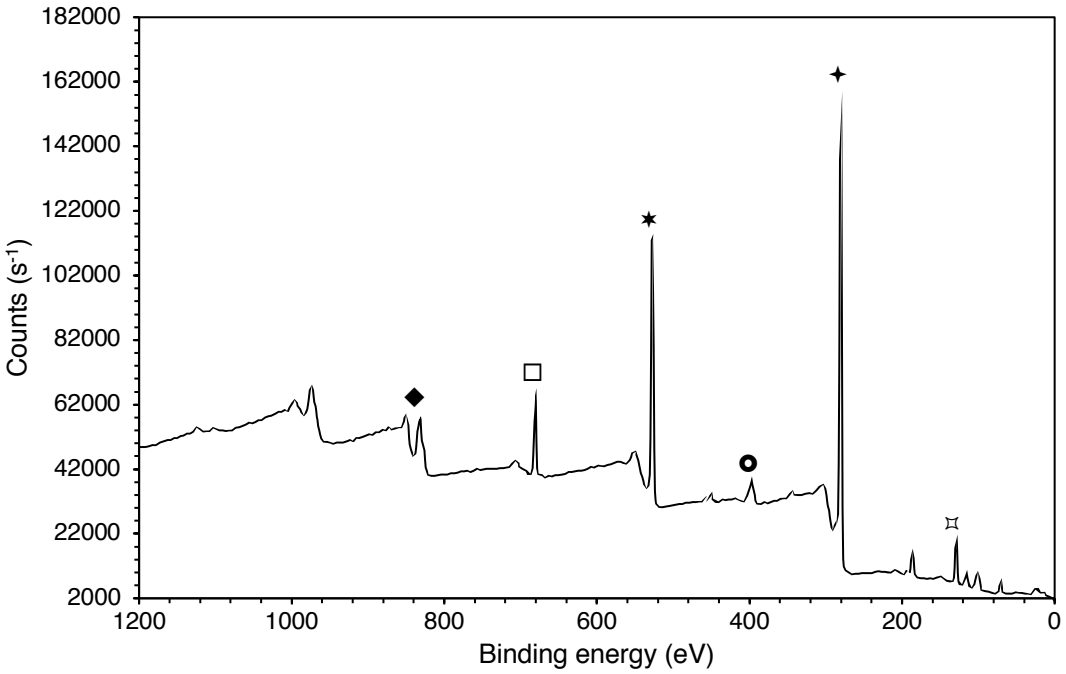

Fig. A1. Survey scan of La-S950+ treated with PLS, [F^-] = 1500 mg·L^{-1}. ◆ = La 3d5/2, □ = F 1s, ✶ = O 1s, ✪ = N 1s, ✦ = C 1s, ⌑ = P 2p.

Table A4. Results of curve-fitting and analysis of N, O and La chemical environments present in samples of H-S950+ and La-S950+ at various process stages.

Sample	Binding energy (eV)	Atomic conc. (%)	Assignment
N 1s			
H-S950+	400.0	39.1	Protonated amine
	402.1	60.9	Nitrate
La-S950+ untreated	399.9	27.4	Protonated amine
	402.3	72.6	Nitrate
La-S950+ NaF-treated	399.9	40.2	Protonated amine
	402.3	59.8	Nitrate
La-S950+ PLS-treated	399.8	50.2	Protonated amine
	402.6	49.8	Nitrate
O 1s			
H-S950+	531.5	49.2	P=O and NO_3^-
	533.0	50.8	P-O-H
La-S950+ untreated	531.5	62.3	P=O, NO_3^-, P-O-La and La-O-H
	533.3	37.7	P-O-H
La-S950+ NaF-treated	531.4	51.6	P=O, NO_3^-, P-O-La and La-O-H
	532.9	48.4	P-O-H*
La-S950+ PLS-treated	532.6	100	$AlF(OH)_2$
La 3d 5/2			
La-S950+ untreated	835.8 / 839.1	100	Coordinated La with OH / H_2O ligands
La-S950+ NaF-treated	829.9 / nd	14.8	Coordinated La with 2 F^- ligands
	833.5 / nd	12.6	Coordinated La with 1 F^- ligand
	837.4 / 841.5	72.6	LaF_3
La-S950+ PLS-treated	831.9 / nd	29.2	Coordinated La with 2 F^- ligands
	836.2 / 839.4	70.8	Coordinated La with 1 F^- ligand

nd = not detectable.

* Due to precipitation of crystalline LaF_3 at high [NaF], the aminophosphonic group is no longer chelated to a metal centre and is presumably reprotonated, consistent with the binding energies observed.

Technical notes

The binding energy of the quaternary ammonium environment does not change significantly upon La coordination to the resin, suggesting that it remains protonated, rather than forming a coordination bond to the La centre. Previous XPS studies [13] have shown that the N 1s binding energy alters by ~0.8 eV upon abstraction of a proton and formation of a coordination bond to a metal centre.

For the untreated La-S950+ samples, the measured binding energy of 835.8 / 839.1 eV matches closely with values for sintered, amorphous lanthanum phosphate samples [14]. The assignments for La complexes with fluoride ligands are given with low confidence, because it is not clear why the addition of strongly electron-withdrawing ligands appears to reduce core electron binding energy. A possibility is that the binding of fluoride significantly decreases the degree of chelation with the phosphonic acid group (this is suggested by the favourability of LaF_3 formation) and this effect overrides the electronegativity of the ligands

Uptake of mixed anions by H-S950+ and La-S950+

Experimental

Equi-mass solutions of F^-, Cl^-, Br^-, NO_3^-, PO_4^{3-} and SO_4^{2-} (150 mg·L^{-1}) were made up by dissolving their Na salts in deionised water ~200 mg of H-S950+ or La-S950+ (dry weights) were contacted with 25 mL mixed anions solution. Pre- and post-contact solution samples were diluted appropriately and analysed by ion-chromatography using a Thermo-Fisher ICS-900, fitted with a Dionex IonPac® AS23 4 x 250 mm column and using Na_2CO_3/$NaHCO_3$ eluent. The instrument was calibrated with solutions of 1-10 mg·L^{-1}, which were diluted from 1,000 mg·L^{-1} analytical standards, purchased from Fisher Scientific. The equilibrium uptake capacity for the various anions (q_e) was calculated using the procedure described in the main research article.

Results

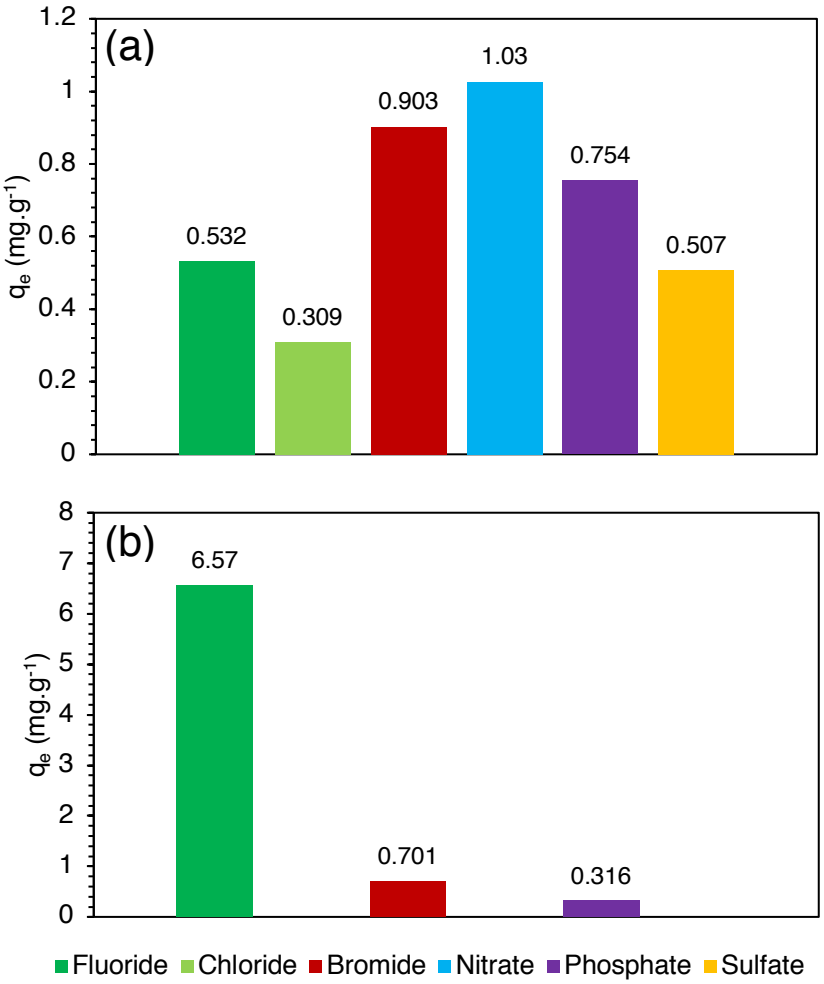

Fig. A2. Uptake of common anions from 150 mg·L^{-1} equi-mass solution by **(a)** H-S950+ resin, **(b)** La-S950+ resin (Cl^-, NO_3^- and SO_4^{2-} uptake were < 0.01 mg·g^{-1}).

Effect of sorbent dose on resin performance

The standard experimental procedure, detailed in section 2.4. of the main research article, was followed, with variation of the mass of La-S950+ from 100-1,000 mg (dry weight), keeping all other variables constant. Results in terms of % fluoride extraction and q_e are presented in Figure A3.

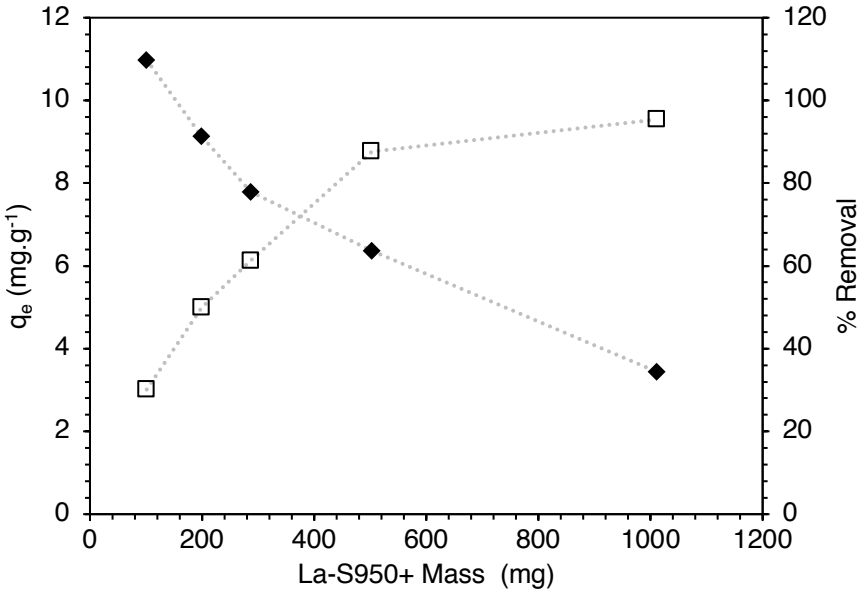

Fig. A3. Fluoride uptake of La-S950+ and % fluoride removal from PLS with varying mass of resin. Liquor dilution = 1/10 (V/V). Volume of liquor = 25 mL. Initial fluoride concentration = 150 mg·g^{-1}. Error is too small to be graphically represented. ◆ = uptake capacity. □ = % removal.

Appendix A References

[1] D.B. Bhatt, P.R. Bhatt, H.H. Prasad, K.M. Popat, P.S. Anand, "Removal of fluoride ion from aqueous bodies by aluminium complexed amino phosphonic acid type resins", *Industrial Journal of Chemical Technology*, 2004, **11**, 299-303.

[2] Y. Ku, H.M. Chiou, H.W. Chen, "Removal of fluoride from aqueous solution by aluminum-loaded Duolite C-467 resin", *Journal of The Chinese. Institute of Engineers*, 2011, **34**, 801-807.

[3] F. Luo, K. Inoue, "The removal of fluoride ion by using metal(III)-loaded Amberlite resins", *Solvent Extraction and Ion Exchange*, 2004, **22**, 305-322.

[4] Z.P. Li, H. Li, H. Xia, X.S. Ding, X.L. Luo, X.M. Liu, Y. Mu, "Triarylboron-linked conjugated microporous polymers: sensing and removal of fluoride ions", *Chemistry: A European Journal*, 2015, **21**, 17355-17362.

[5] N. Viswanathan, S. Meenakshi, "Effect of metal ion loaded in a resin towards fluoride retention", *Journal of Fluorine Chemistry,* 2008, **129**, 645-653.

[6] S.M. Prabhu, S. Meenakshi, "Effect of metal ions loaded onto iminodiacetic acid functionalized cation exchange resin for selective fluoride removal", *Desalination and Water Treatment*, 2014, **52**, 2527-2536.

[7] M.J. Haron, W.M.Z. Yunus, "Removal of fluoride ion from aqueous solution by a cerium-poly(hydroxamic acid) resin complex", *Journal of Environmental Science and Health Part A-Toxic/Hazardous Substances & Environmental Engineering*, 2001, **36**, 727-734.

[8] J.M. Cheng, X.G. Meng, C.Y. Jing, J.M. Hao, "La^{3+}-modified activated alumina for fluoride removal from water", *Journal of Hazardous. Materials*, 2014, **278**, 343-349.

[9] E. Vences-Alvarez, L.H. Velazquez-Jimenez, L.F. Chazaro-Ruiz, P.E. Diaz-Flores, J.R. Rangel-Mendez, “Fluoride removal in water by a hybrid adsorbent lanthanum-carbon”, *Journal of Colloid & Interface Science*, 2015, **455**, 194-202.

[10] P. Liang, Y. Zhang, D.F. Wang, Y. Xu, L. Luo, “Preparation of mixed rare earths modified chitosan for fluoride adsorption”, *Journal of Rare Earths*, 2013, **31**, 817-822.

[11] H. Kalka, “Aqion: Manual (selected topics)” [online], http://www.aqion.de/site/98?, 2015.

[12] Purolite, “Product Data Sheet: Purolite S950” [online], http://www.lenntech.com/Data-sheets/Purolite-S950-L.pdf, 2017.

[13] D.K. Lavallee, J. Brace, N. Winograd, X-ray photoelectron spectra of N-methyltetraphenylporphyrins- evidence for a correlation of binding energies with metal-nitrogen bond distance, *Inorganic Chem*istry, 1979, **18**, 1776-1780.

[14] S. Jørgensen, J.A. Horst, O. Dyrlie, Y. Larring, H. Ræder, T. Norby, “XPS surface analyses of $LaPO_4$ ceramics prepared by precipitation with or without excess of PO_4^{3-}”, *Surface and Interface Analysis*, 2002, **34**, 306-310.

APPENDIX B

"Towards the implementation of an ion-exchange system for recovery of fluoride commodity chemicals. Kinetic and dynamic studies"

SUPPORTING INFORMATION

Overview of previous literature

Table B1. Overview of kinetic studies of fluoride adsorption on to ion-exchange resins and selected other adsorbents with rare earth metal functionality.

Adsorbent	F^- starting concentration ($mg \cdot L^{-1}$)	T (°C)	Best-fitting kinetic model	Calculated rate constant	Ionic strength modifier	Reference
La-loaded sulfonic acid ion-exchange resin	11	30	Pseudo 2nd-order	0.569 $g \cdot mg^{-1} \cdot min^{-1}$	None*	Viswanathan and Meenakshi [1]
Ce-loaded hydroxamic acid ion-exchange resin	95	20	Pseudo 1st-order	0.096 min^{-1}	None*	Haron and Wan Younis [2]
La-impregnated alumina	38	20	Pseudo 1st-order	0.349 min^{-1}	None*	Wasay *et al.* [3]
La-modified activated alumina	10	Not stated	Pseudo 2nd-order	0.019 $g \cdot mg^{-1} \cdot min^{-1}$	NaCl (40 $mmol \cdot L^{-1}$)	Cheng *et al.* [4]
Alumina-chitosan complex	15	30	Pseudo 2nd-order	0.927 $g \cdot mg^{-1} \cdot min^{-1}$	None*	Viswanathan and Meenakshi [5]
Pr-chitosan complex	20	Not stated	Pseudo 2nd-order	0.01 $g \cdot mg^{-1} \cdot min^{-1}$	None*	Kusrini *et al.* [6]
Zr nanoparticles	29	20	Pseudo 2nd-order	1.58 x 10^{-3} $g \cdot mg^{-1} \cdot min^{-1}$	None*	He and Chen [7]

*In these studies, it is stated that the pH of contact fluoride solutions is adjusted with HCl or NaOH, either before or before and during contact with the adsorbent. However, because the natural pH of an aqueous suspension of the adsorbent is not reported, nor the quantities of acid or base added, it is not possible to say what the ionic strength of contact solutions was.

Preparation of simulant SPL leachate

This solution was designed to emulate the leachate, which would be produced by aqueous caustic, then acidic leaching treatment of mixed-cut SPL, followed by mixing of the two streams. For safety reasons, labile CN^- was replaced by CNO^-. The composition of this liquor is given in Table B2.

Table B2. Composition of SPL simulant leachate solution.

Component	Concentration ($mg \cdot L^{-1}$)
Fluoride (F^-)	1500
Aluminium (Al^{3+})	1200
Calcium (Ca^{2+})	200
Carbonate (CO_3^{2-})	750
Chloride (Cl^-)	200
Cyanate (CNO^-)	50
Nitrate (NO_3^-)	800
Sulfate (SO_4^{2-})	2200

NaF, $Al_2(SO_4)_3$, $Ca(OH)_2$, $NaHCO_3$, NaCl, NaCNO, $NaNO_3$ and Na_2SO_4 (all analytical reagent grade) were purchased from commercial suppliers and used without further purification. Na and SO_4^{2-} salts were used where possible, since aqueous NaOH is the leaching agent in the LCLL process [8]. Reagents were dissolved in deionised water in a polypropylene beaker, fitted with a large magnetic stirrer. The natural pH of the liquor, as synthesised, was 5.5. The solution was filtered gravimetrically, to remove a small quantity of precipitated salts (see Table B2).

Calculation of solution speciation using Aqion software

Experimental

Known concentrations of cations and anions in the simulant leachate, to simulate the full range of experimental conditions used were inputted into the Aqion software [9]. Concentrations were calculated from masses of the relevant salts added to the liquor. Necessary adjustments to charge balance were made by adjustment of dissolved inorganic carbon. La-MTS9501 was discovered, in previous work, to buffer contact solutions to pH ~4 [10]. Therefore, this pH was used for most inputs. Output speciation took precipitation of minerals into account.

Results

The ionic strength of the as-prepared leachate was 24.8 $mmol \cdot L^{-1}$. Concentrations of key aqueous species (these being mainly anions, cations and neutral complexes present in significant quantities and containing Al^{3+} and F^-) are shown in Table B3.

Table B3. Aqion calculations for Al^{3+} and F^- speciation in the simulant leachate, both as prepared and at the pH of resin/solution contact.

Species	Concentrations (mmol·L^{-1})	
	As-prepared (pH 5.5)*	**During resin-contact (pH 4.0)**
Al^{3+}	0.0496	0.207
AlF^{2+}	27.7	29.2
AlF_2^+	5.11	10.8
AlF_3	6.04	3.24
$AlSO_4^+$	0.238	0.861
F^-	0.0304	0.016
HF	<0.01	<0.01
H^+	0.00616	0.123

* A precipitate of $Al(OH)_3$ (5.14 mmol·L^{-1}) was predicted, consistent with experimental observations.

A further set of results was attained, in which concentrations inputted matched those of the leachate used in batch experiments with $[Al^{3+}]$ variation (section 3.6. of the main article). The two extremes of the experiment, where $[Al^{3+}] = 0$ and $[Al^{3+}] = 500$ mg·L^{-1} are shown in Table B4. The pH was inputted as 4.0.

Table B4. Aqion calculations for Al^{3+} and F^- speciation in the simulant leachate in experiments with $[Al^{3+}]$ varied and all other factors constant.

Species	Concentrations (mmol·L^{-1})	
	$[Al^{3+}] = 0$	$[Al^{3+}] = 500$ mg·L^{-1}
Al^{3+}	0	12.3
AlF^{2+}	0	7.42
AlF_2^+	0	0.238
AlF_3	0	<0.01
$AlSO_4^+$	0	1.72
F^-	5.95	<0.01
HF	0.872	<0.01
H^+	0.123	0.120

Puromet MTS9501 manufacturer specification

Table B5. Physical and chemical parameters of Puromet™ MTS9501, according to manufacturer specifications [11].

Basic properties	
Matrix	Macroporous Styrene-divinylbenzene
Functional Group	Aminophosphonic – RCH_2 N HCH_2 PO_3
Appearance	Spherical beads
Ionic Form (as shipped)	Na^+
Chemical and physical properties	
Moisture content (Na)%	60-68%
Operating Temperature (Maximum)	90°C, 195°F
Operating pH Range, H^+ Form	2-6
Operating pH Range, Na^+ Form	6-11
Bed Density	710-745 $g{\cdot}L^{-1}$
Particle Density, Moist Na^+ Form	1.13 $g{\cdot}cm^{-3}$
Exchange Capacity (Na^+ Form)	24 g Ca^{2+} $L^{-1}{\cdot}min^{-1}$ at pH 9.5
Reversible Swelling, (H^+ ➔ Na^+) Max	45%
Mean Size Typical	0.60-0.85 mm
Uniformity Coefficient (max.)	1.70
Typical affinity for common cations	
Acidic pH	$H^+ > Fe^{3+} > Pb^{2+} > Cu^{2+} > Zn^{2+}, Al^{3+} > Mg^{2+} > Ca^{2+} > Cd^{2+} > Ni^{2+} > Co^{2+} > Na^+$
Alkaline pH	Cd^{2+}, $Mg^{2+} > Ca^{2+} > Sr^{2+}$, $Al^{3+} > Ba^{2+} >> Na^+$, K^+

Table B6. Relevant physical and chemical parameters of La-loaded Puromet™ MTS9501 (La-MTS9501, as determined in previous work [10].

Parameter	Value
Maximum La-loading ($mg{\cdot}g^{-1}$, $mmol{\cdot}g^{-1}$)	256 ± 2, 1.84 ± 0.01
Approximate moisture content	53%
Optimum pH for fluoride uptake	3
Maximum fluoride capacity, calculated by Langmuir isotherm ($mg.g^{-1}$)	187 ± 15
Selectivity coefficient for F^-, vs Cl^-	2530

Fluoride ion-selective electrode analysis and synthesis of total ionic strength adjustment buffer (TISAB)

The fluoride concentration of solutions before and after resin-contact were analysed using a Cole-Palmer fluoride ion-selective electrode. The electrode was calibrated using standards of known fluoride concentration from 0.1-10 or from 10-100 $mg{\cdot}L^{-1}$. These were made by dissolving ≥99.999% NaF, which had been dried in an air-flow oven for a minimum of 24 hr, in deionised water. Electrode readings for each sample were averaged from at least three replicates. Error values were calculated from 2 x standard deviation, then propagated as necessary. Each sample contained 50% total ionic strength adjustment buffer and were sufficiently diluted to ensure ionic strength did not vary significantly between samples.

For synthesis of TISAB, all reagents were of analytical grade and used without further purification. In a 1 L beaker, 45.0 g NaCl was dissolved in ~500 mL deionised water, followed by 4.00 g 1,2-Diaminocyclohexanetetraacetic acid hydrate. 57 mL acetic acid were added and the water volume increased to ~800 mL. 5 M NaOH was added dropwise, to increase pH to 5.5. The solution was then transferred to a 1 L volumetric flask and water volume increased to exactly 1 L.

Determination of uptake of coexisting anions from simulant leachate in kinetic and dynamic experiments by ion chromatography

Samples of leachate from kinetic and dynamic studies were diluted appropriately and analysed by ion-chromatography using a Metrohm 883 Basic IC plus instrument, fitted with a Metrosep A Supp 5- 4 x 150 mm column and using Na_2CO_3/$NaHCO_3$ eluent. The flow rate was 0.8 $mL{\cdot}min^{-1}$. The instrument was calibrated with standards, made up by dilution of 1000 $mg{\cdot}L^{-1}$ standard solutions of chloride, nitrate and sulfate, purchased from Fisher Scientific. This allowed simultaneous analysis of all 3 anions in one run. The equilibrium uptake capacity for the various anions (q_e) was calculated using the procedure described in the main research article. Relative Standard Deviation for measurements was automatically calculated using the MagIC Net software (v3.1) and error was propagated accordingly.

X-ray diffraction (XRD) and thermogravimetric analysis (TGA) of resin beads at various process stages

XRD data was collected using a Bruker D2 Phaser X-ray powder diffractometer, using a 1 mm divergence slit, 3 mm airscatter screen module mode and 2.5 mm Ni β filter. Data was collected between $2\theta = 10°$ and $2\theta = 80°$. Samples were pressed into Bruker poly(methyl methacrylate) specimen-holders

TGA data was collected using a Perkin Elmer Pyris1. The atmosphere was N_2 at a flow rate of 60 $mL{\cdot}min^{-1}$. Heating rate was $10°C{\cdot}min^{-1}$. The instrument was calibrated using Alumet and Fe Curie points. Samples (~6 mg) were loaded into a ceramic pan.

Investigation of Uptake Kinetics from media at various concentrations

Table B7. Linear fitting of fluoride uptake kinetic data to diffusion-based models. Uptake shown from leachate and NaF solutions of various concentrations. Resin dry mass = 5.0 g, initial solution volume = 500 mL, T = 20°C.

Sample	Film diffusion model R^2	Intra-particle diffusion model R^2	Elovich model R^2
Leachate 1/100 dilution	0.265	0.574	0.852
Leachate 1/30 dilution	0.207	0.880	0.995
Leachate 1/10 dilution	0.365	0.769	0.875
Leachate 1/3 dilution	0.396	0.835	0.952
Leachate as-prepared	0.243	0.556	0.879
Leachate as-prepared (Al)	0.513	0.908	0.966
Leachate as-prepared (Ca)	0.508	0.847	0.957
NaF solution $C_i \approx 15$ mg L^{-1}	0.401	0.739	0.928
NaF solution $C_i \approx 50$ mg L^{-1}	0.190	0.435	0.690
NaF solution $C_i \approx 150$ mg L^{-1}	0.376	0.707	0.958
NaF solution $C_i \approx 500$ mg L^{-1}	0.325	0.650	0.857
NaF solution $C_i \approx 1500$ mg L^{-1}	0.346	0.520	0.669
NaF solution $C_i \approx 5000$ mg L^{-1}	0.380	0.668	0.854

Table B8. SOLVER fitting of fluoride uptake kinetic data to Lagergren pseudo first-order model. Uptake shown from leachate and NaF solutions of various concentrations. Resin dry mass = 5.0 g, initial solution volume = 500 mL, T = 20°C.

Sample	q_e (mg.g^{-1})	k_1 (min^{-1})	$t_{1/2}$ (min)	R^2
Leachate 1/100 dilution	0.653 ± 0.126	3.29 ± 0.66 x 10^{-2}	46.5 ± 12.9	0.960
Leachate 1/30 dilution	3.52 ± 0.41	8.19 ± 0.53 x 10^{-2}	9.31 ± 1.53	0.828
Leachate 1/10 dilution	6.81 ± 1.32	0.133 ± 0.013	3.47 ± 0.46	0.839
Leachate 1/3 dilution	14.4 ±1.4	2.37 ± 0.27 x 10^{-2}	2.93 ± 0.44	0.987
Leachate as-prepared	25.1 ± 5.8	7.20 ± 2.43 x 10^{-2}	0.554 ± 0.226	0.869
Leachate as-prepared (Al)	19.6 ± 3.0	2.43 ± 0.19 x 10^{-2}	2.09 ± 0.36	0.867
Leachate as-prepared (Ca)	1.76 ± 0.41	5.12 ± 0.67 x 10^{-2}	11.1 ± 3.0	0.707
NaF solution $C_i \approx 15$ mg·L^{-1}	0.563 ± 0.151	0.238 ± 0.031	7.47 ± 2.22	0.895
NaF solution $C_i \approx 50$ mg·L^{-1}	1.96 ± 0.71	0.657 ± 0.22	2.51 ± 0.59	0.812
NaF solution $C_i \approx 150$ mg·L^{-1}	3.22 ± 0.73	0.105 ± 0.013	5.34 ± 1.06	0.857
NaF solution $C_i \approx 500$ mg·L^{-1}	4.68 ± 1.6	0.385 ± 0.131	0.556 ± 0.121	0.785
NaF solution $C_i \approx 1500$ mg·L^{-1}	12.1 ± 1.2	0.244 ± 0.085	0.340 ± 0.124	0.801
NaF solution $C_i \approx 5000$ mg·L^{-1}	123 ± 28	0.159 ± 0.054	5.12 ± 1.48 x 10^{-2}	0.899

Graphical data for kinetic uptake experiments are presented in Figures B1-B22. For all experiments Resin dry mass = 5.0 g. Initial solution volume = 500 mL. T = 20°C.

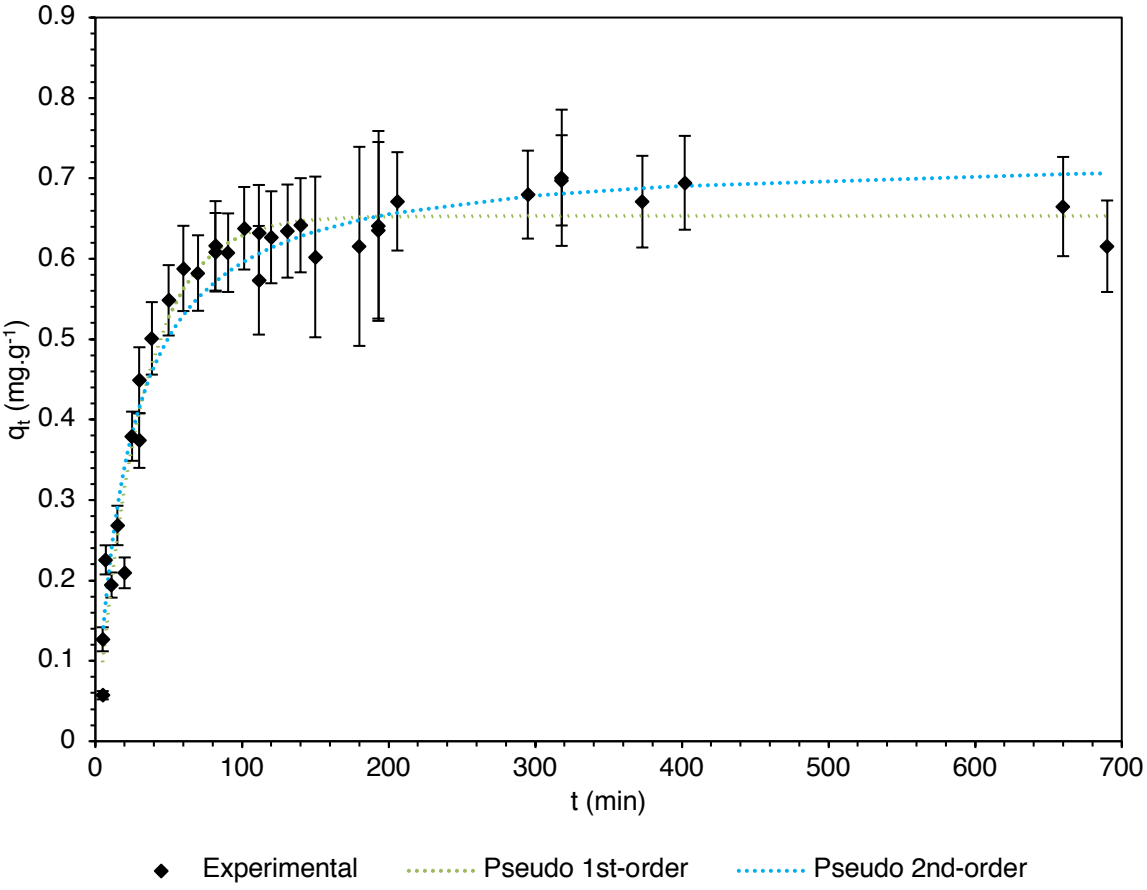

Fig. B1. Simulant leachate 1/100 dilution (Fluoride $C_i \approx 15$ mg·L^{-1}).

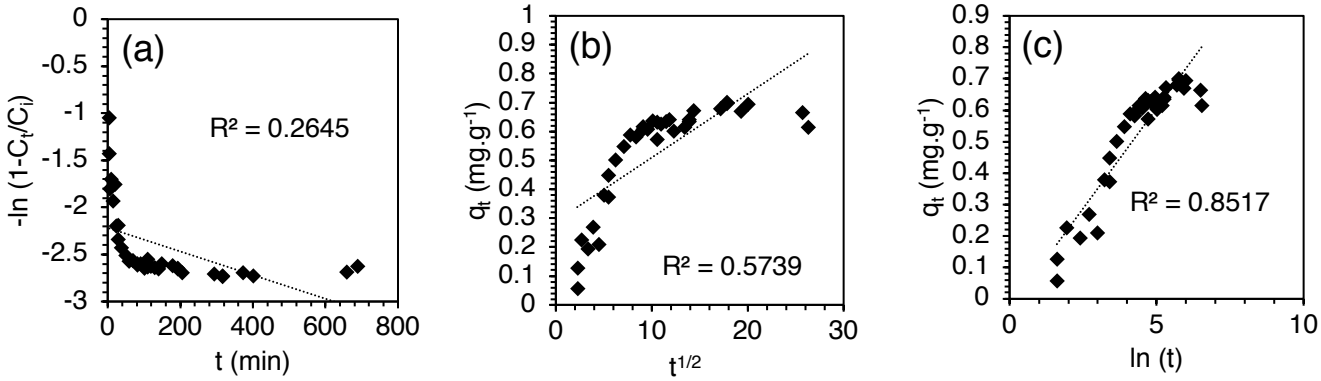

Figs. B2 (a-c). Fitting of above data to film diffusion (left), intraparticle diffusion (centre) and Elovich (right) models.

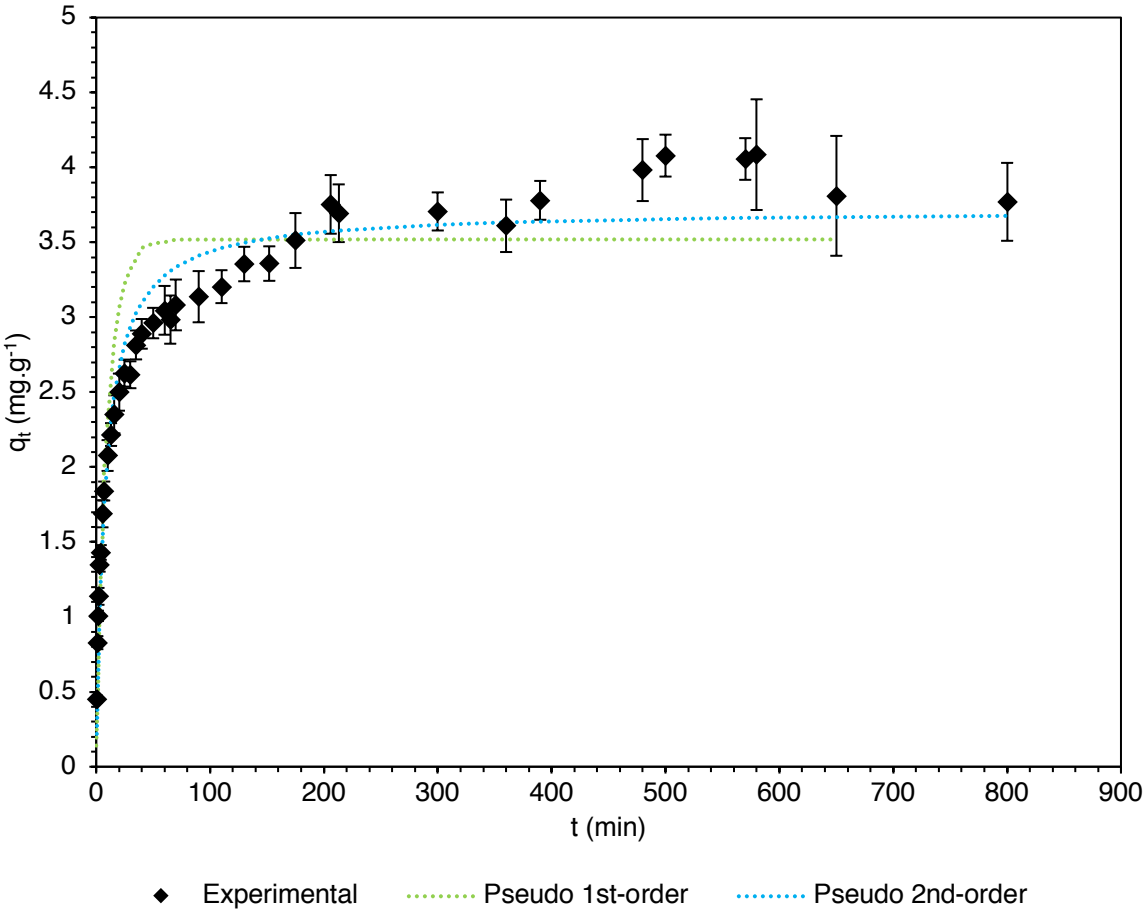

Fig. B3. Simulant leachate 1/30 dilution (Fluoride $C_i \approx 50$ mg·L^{-1}).

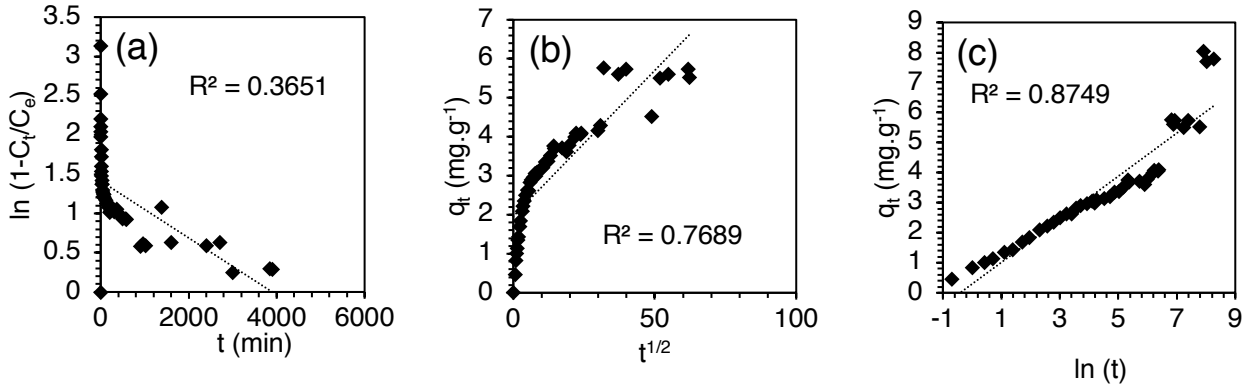

Figs. B4 (a-c). Fitting of above data to film diffusion (left), intraparticle diffusion (centre) and Elovich (right) models.

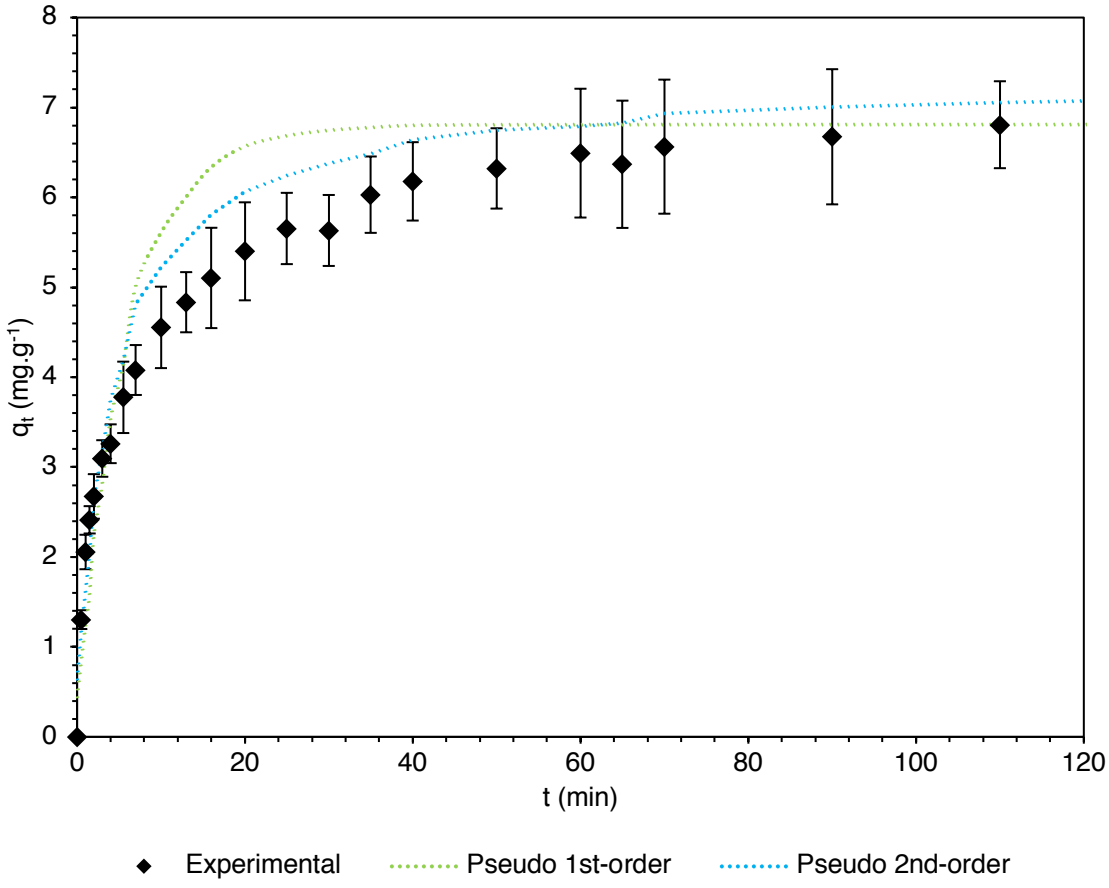

Fig. B5. Simulant leachate 1/10 dilution (Fluoride $C_i \approx 150$ mg·L^{-1}).

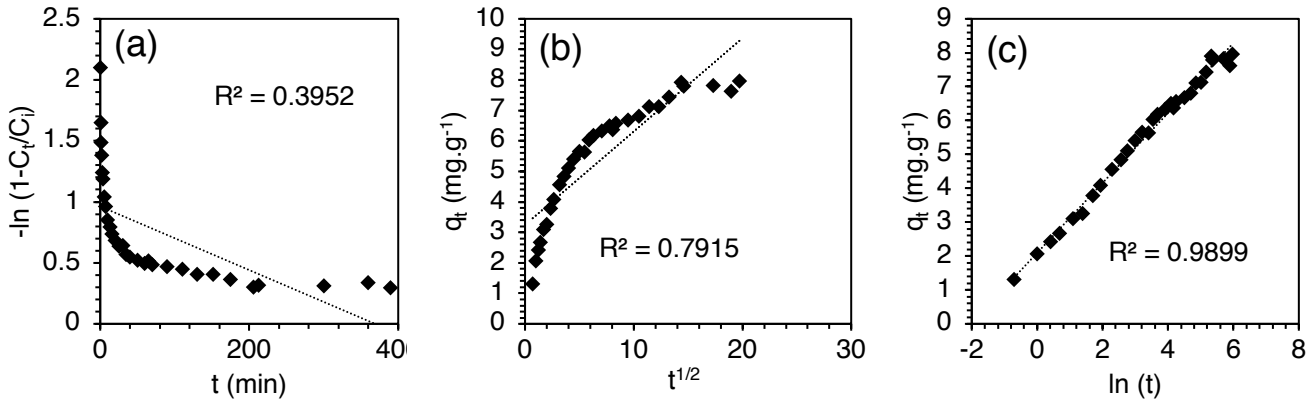

Figs. B6 (a-c). Fitting of above data to film diffusion (left), intraparticle diffusion (centre) and Elovich (right) models.

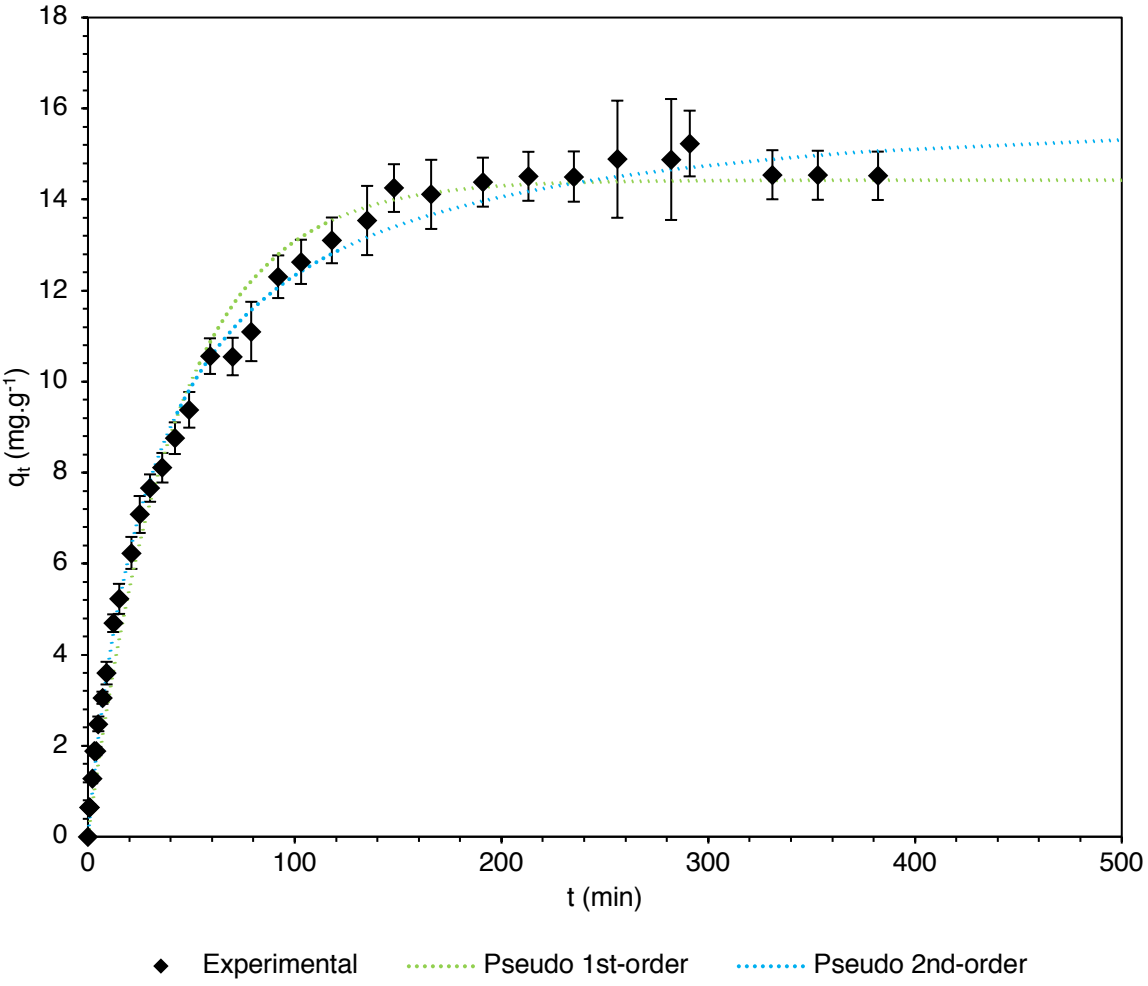

Fig. B7. Simulant leachate 1/3 dilution (Fluoride $C_i \approx 500$ mg·L^{-1}).

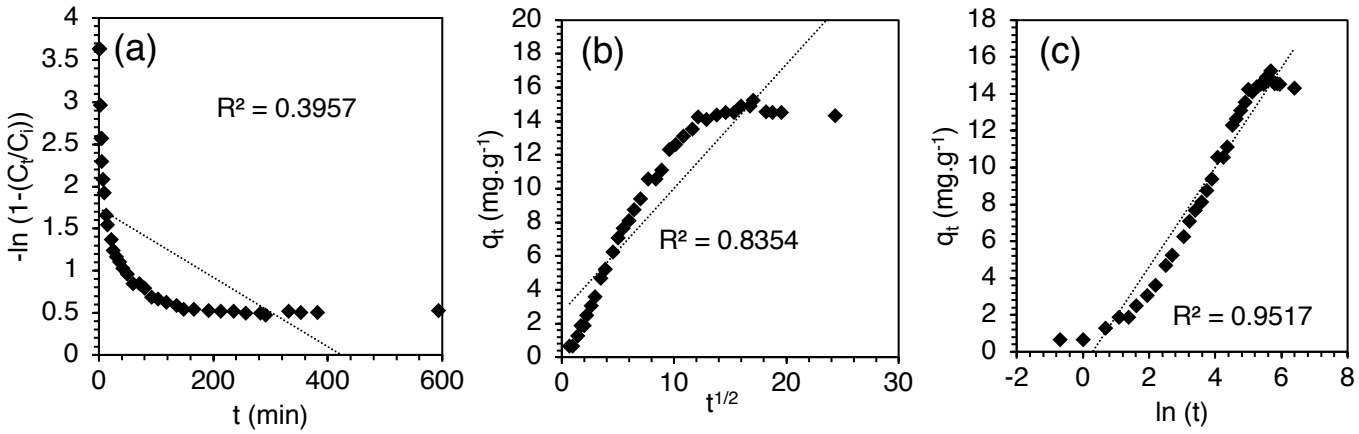

Figs. B8 (a-c). Fitting of above data to film diffusion (left), intraparticle diffusion (centre) and Elovich (right) models.

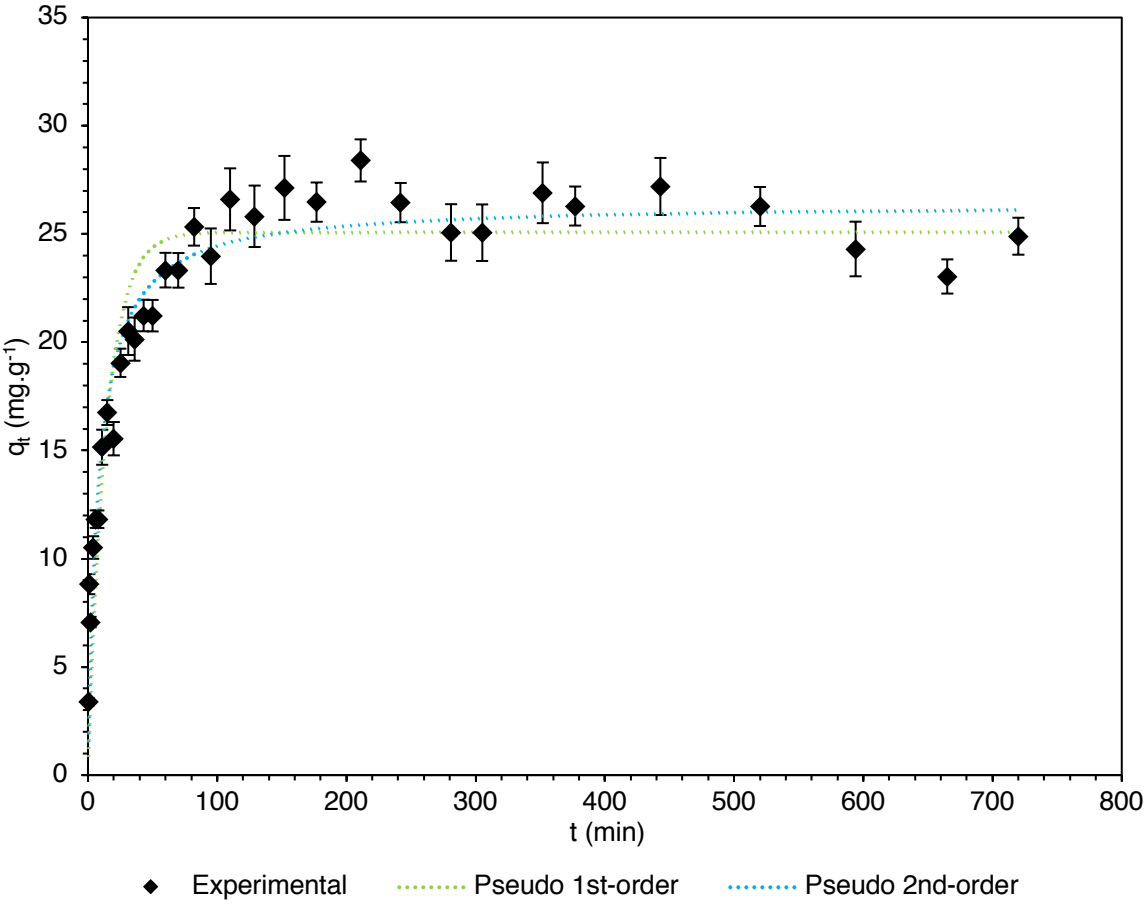

Fig. B9. Simulant leachate as-prepared (Fluoride $C_i \approx 1500$ mg·L^{-1}).

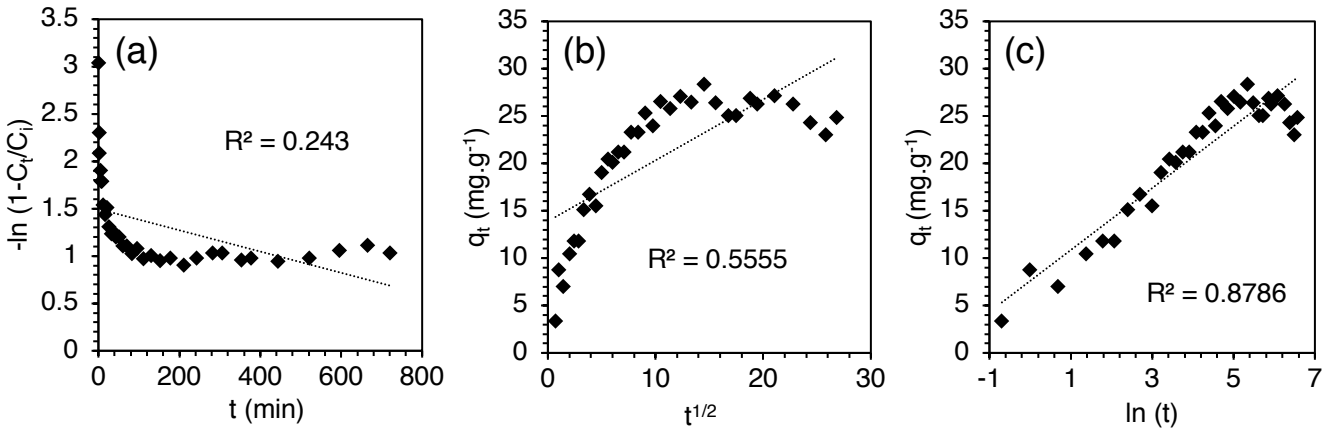

Figs. B10 (a-c). Fitting of above data to film diffusion (left), intraparticle diffusion (centre) and Elovich (right) models.

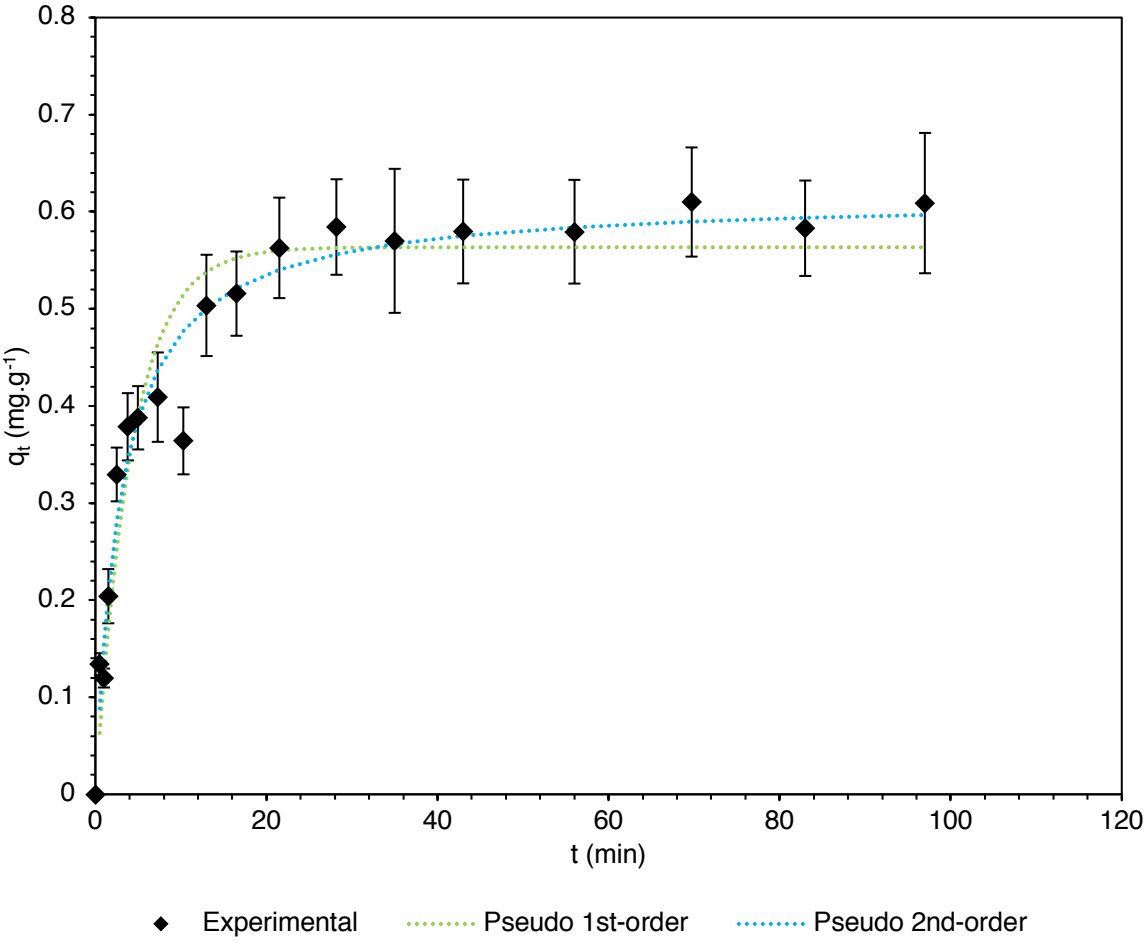

Fig. B11. NaF solution. Fluoride $C_i \approx 15$ mg·L^{-1}.

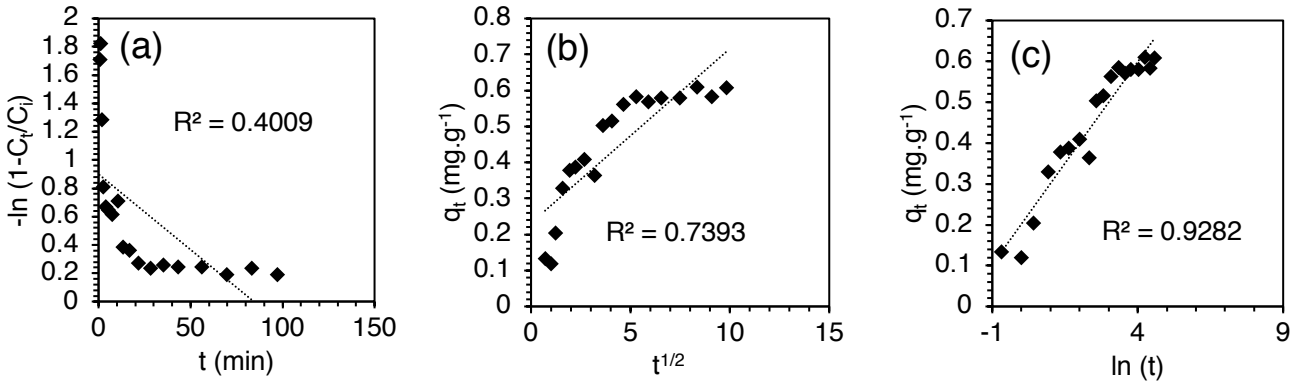

Figs. B12 (a-c). Fitting of above data to film diffusion (left), intraparticle diffusion (centre) and Elovich (right) models.

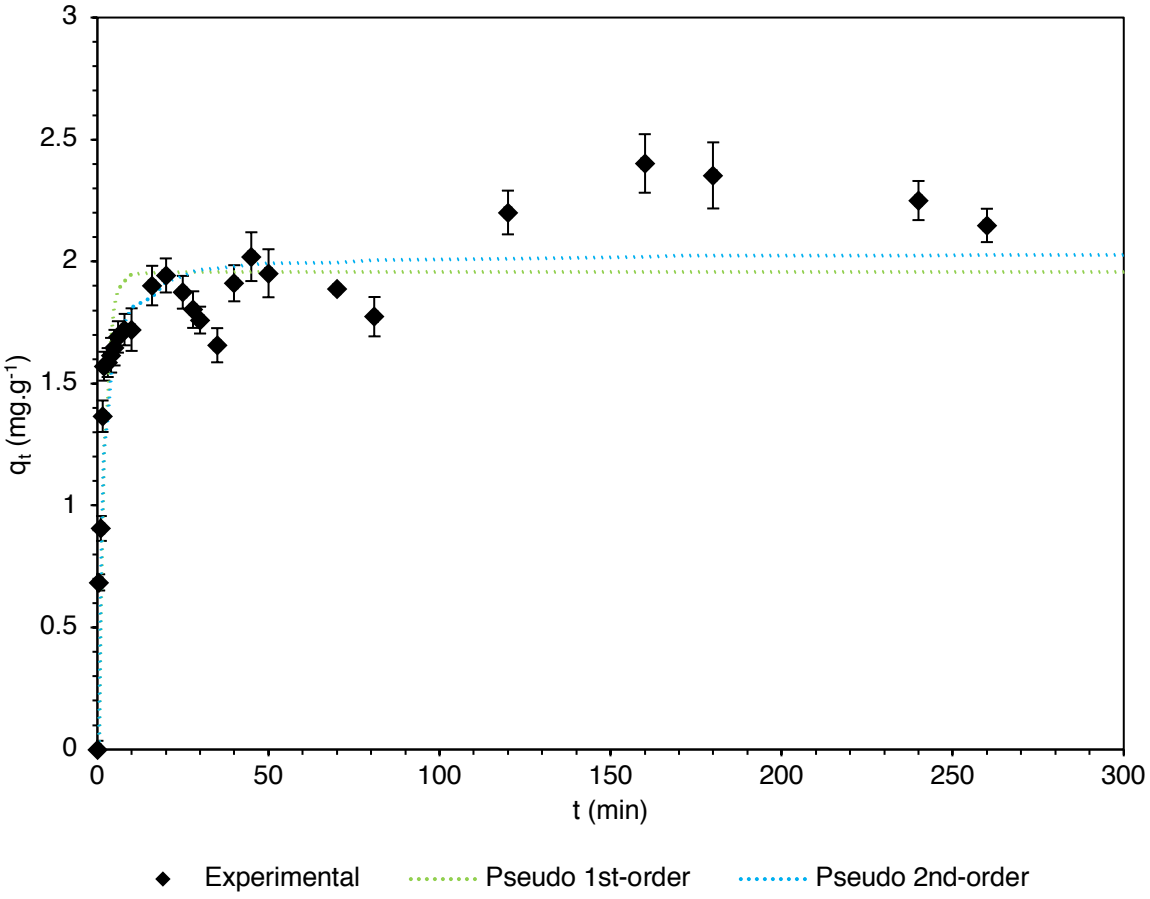

Fig. B13. NaF solution. Fluoride $C_i \approx 50$ mg·L^{-1}.

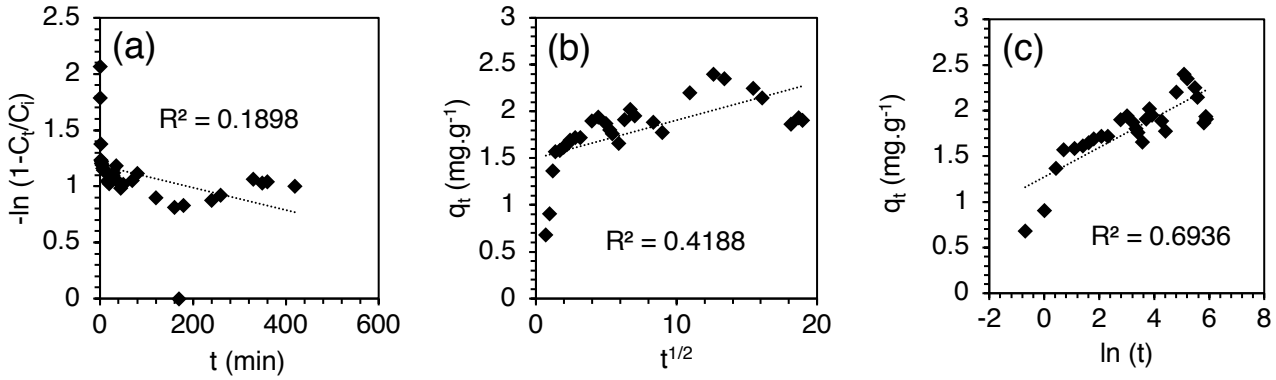

Figs. B14 (a-c). Fitting of above data to film diffusion (left), intraparticle diffusion (centre) and Elovich (right) models.

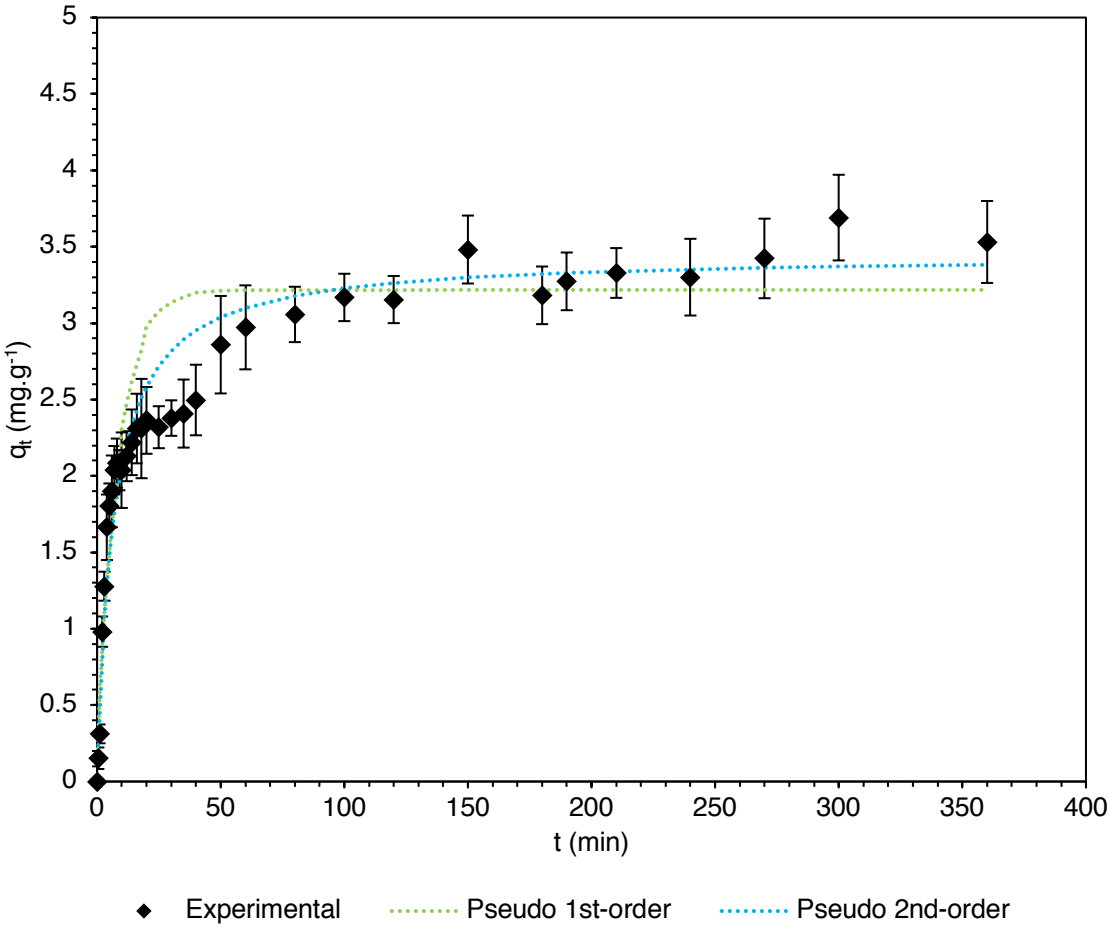

Fig. B15. NaF solution. Fluoride $C_i \approx 150$ mg·L^{-1}.

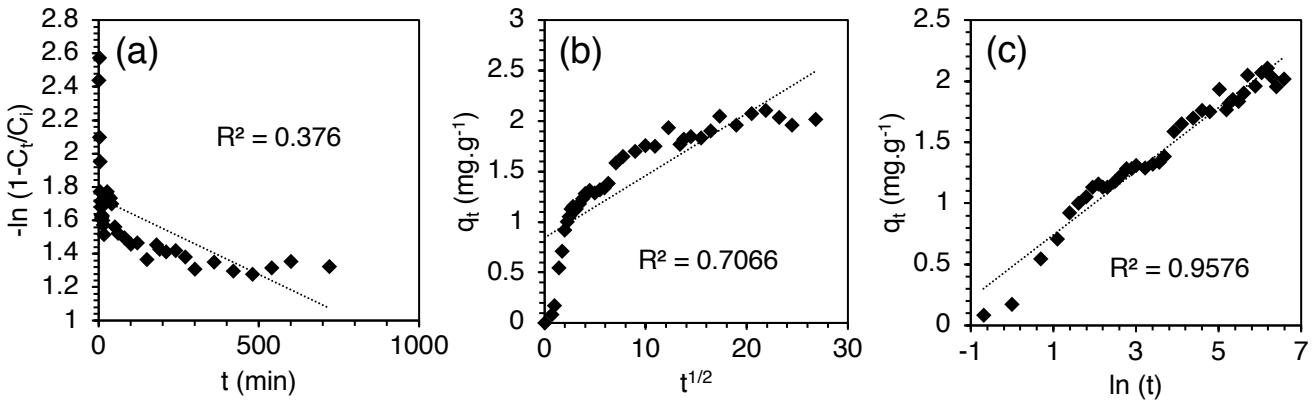

Figs. B16 (a-c). Fitting of above data to film diffusion (left), intraparticle diffusion (centre) and Elovich (right) models.

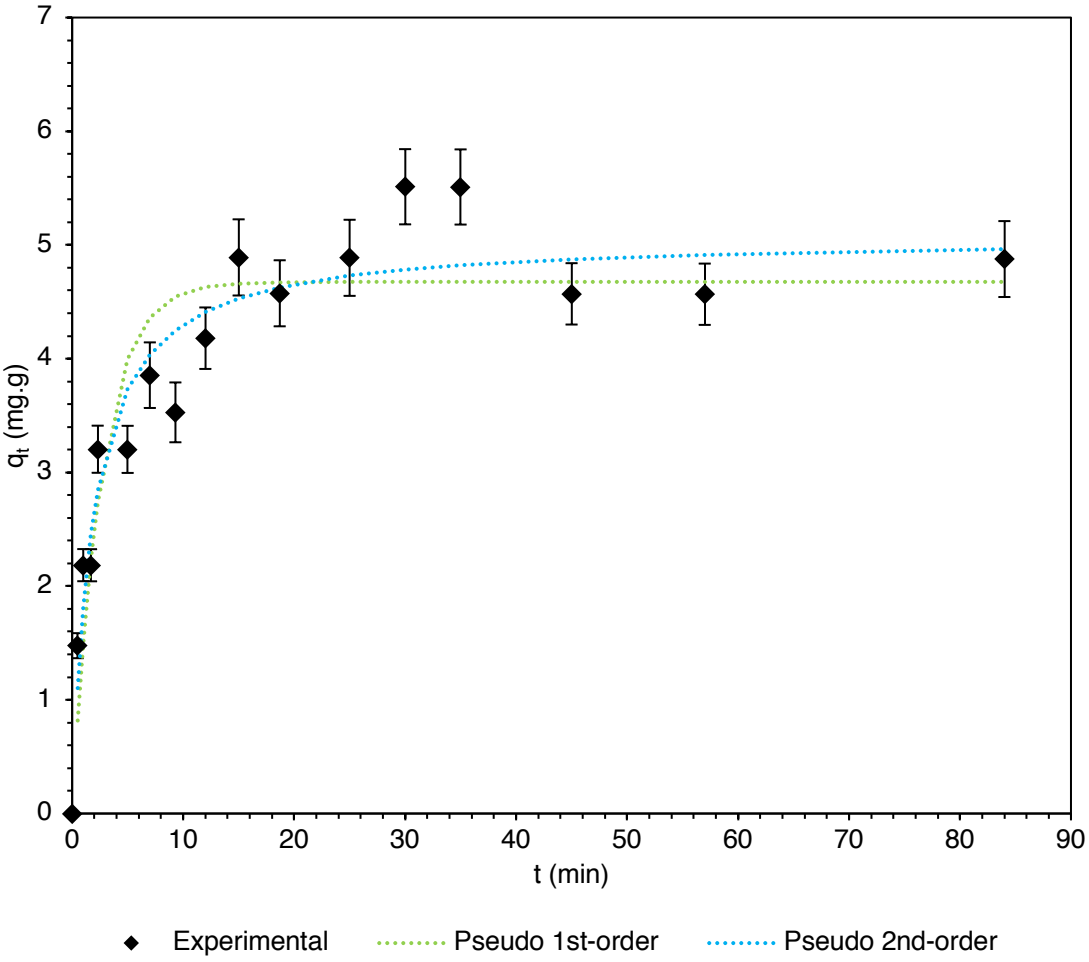

Fig. B17. NaF solution. Fluoride $C_i \approx 500$ mg·L^{-1}.

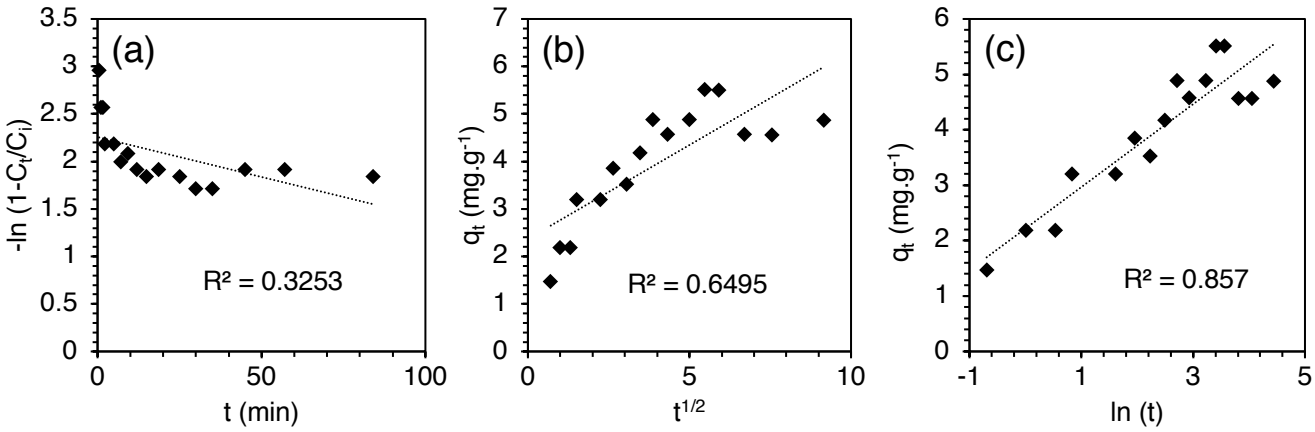

Figs. B18 (a-c). Fitting of above data to film diffusion (left), intraparticle diffusion (centre) and Elovich (right) models.

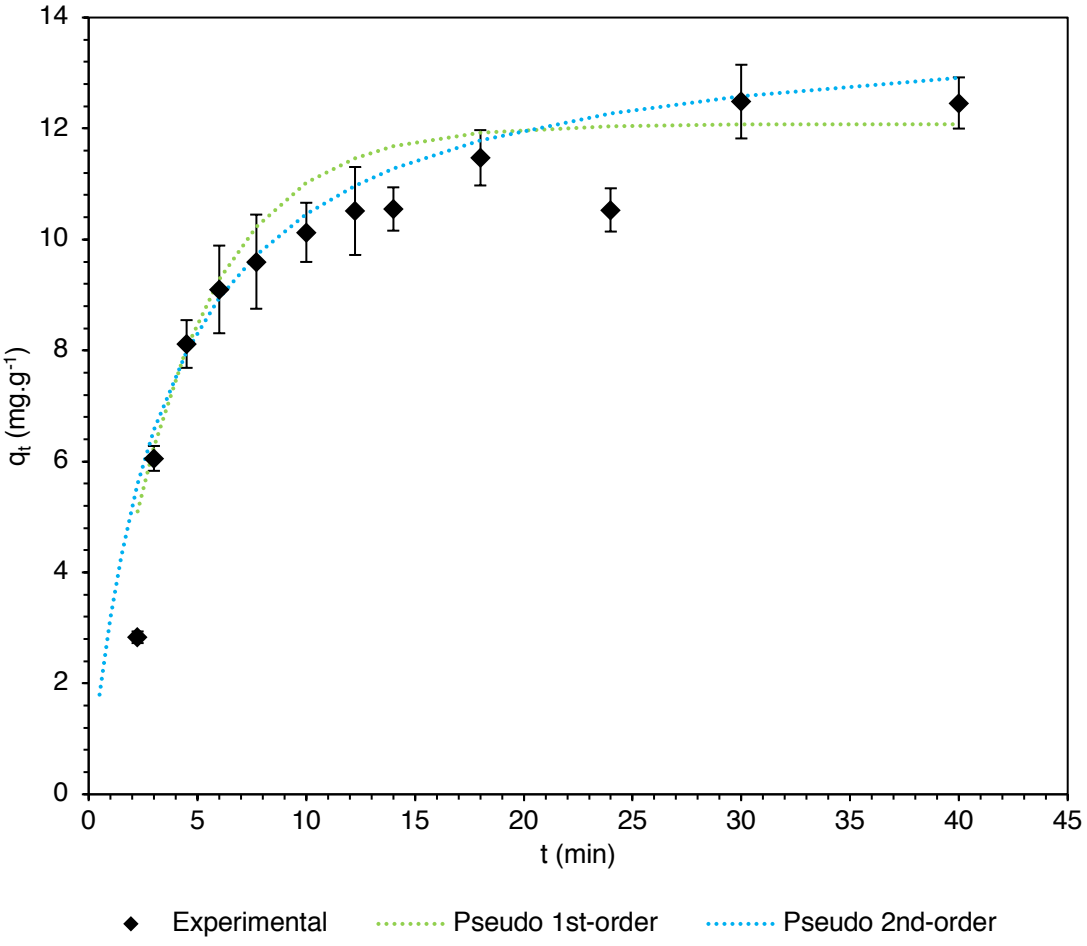

Fig. B19. NaF solution. Fluoride $C_i \approx 1500$ mg·L^{-1}.

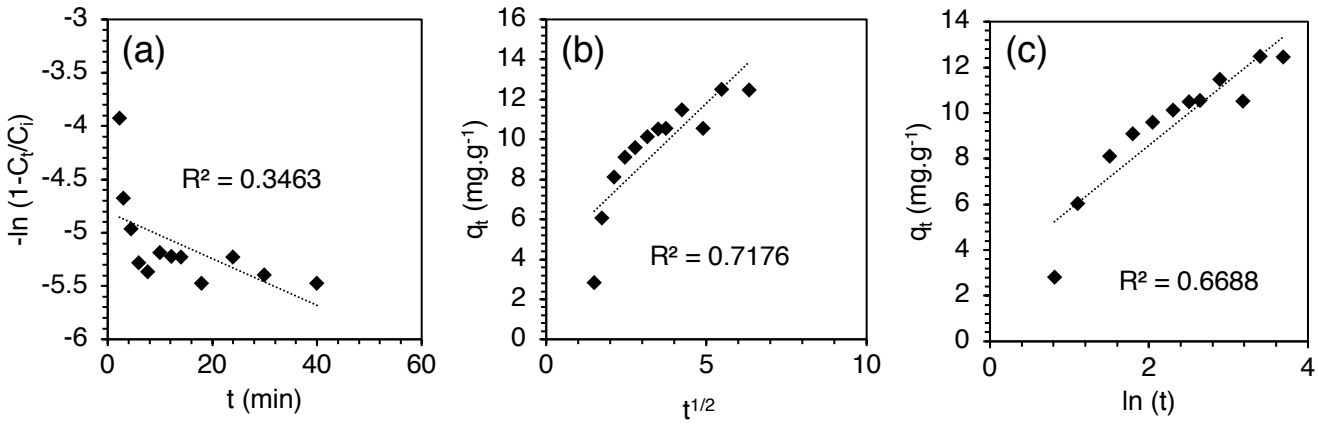

Figs. B20 (a-c). Fitting of above data to film diffusion (left), intraparticle diffusion (centre) and Elovich (right) models.

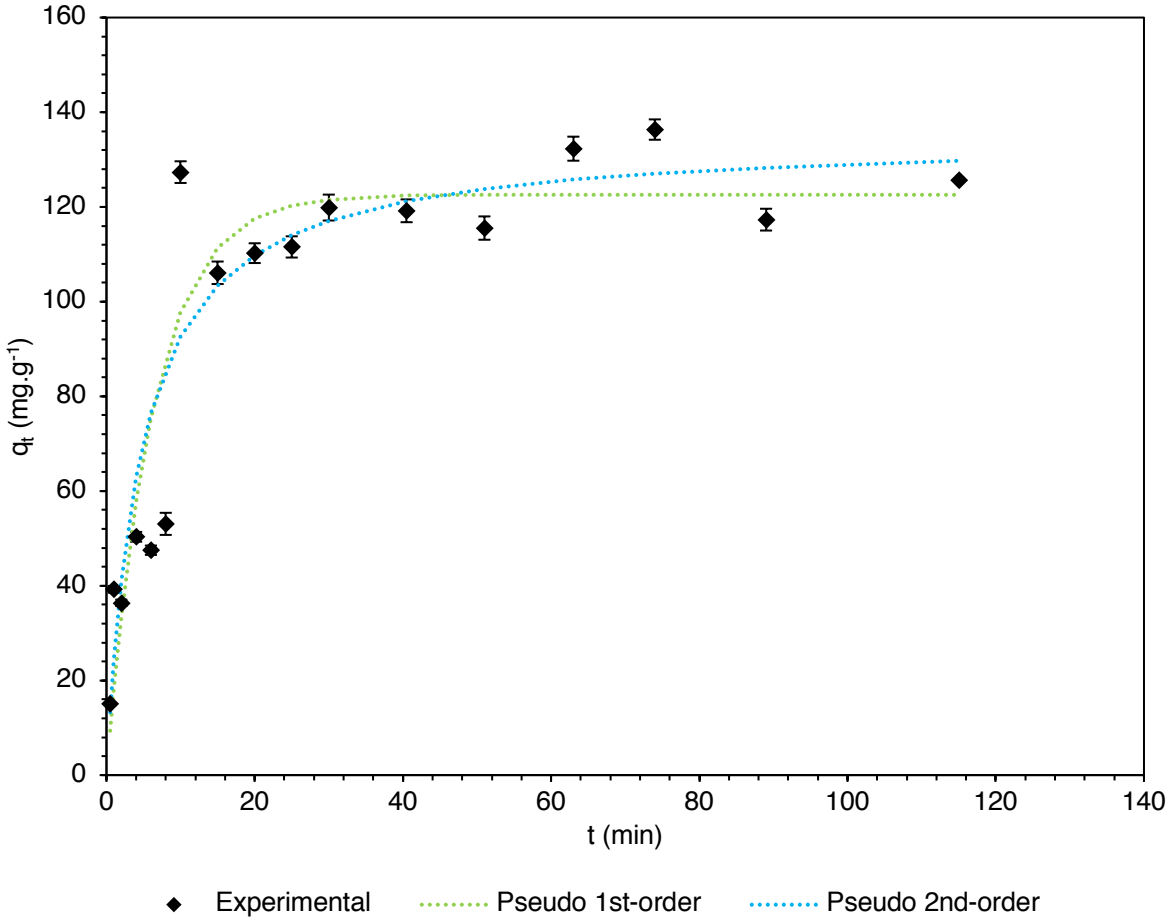

Fig. B21. NaF solution. Fluoride $C_i \approx 5000$ mg·L^{-1}.

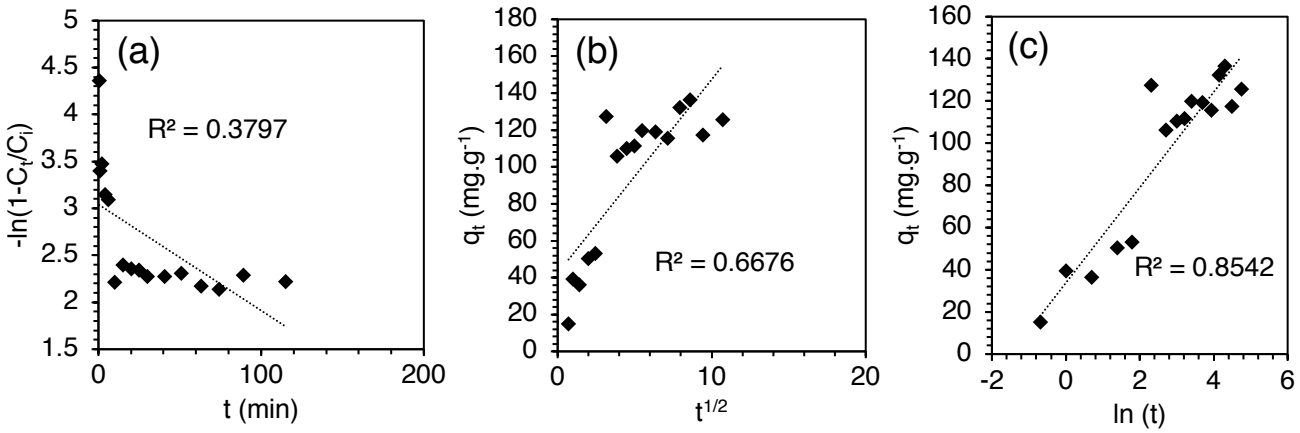

Figs. B22 (a-c). Fitting of above data to film diffusion (left), intraparticle diffusion (centre) and Elovich (right) models.

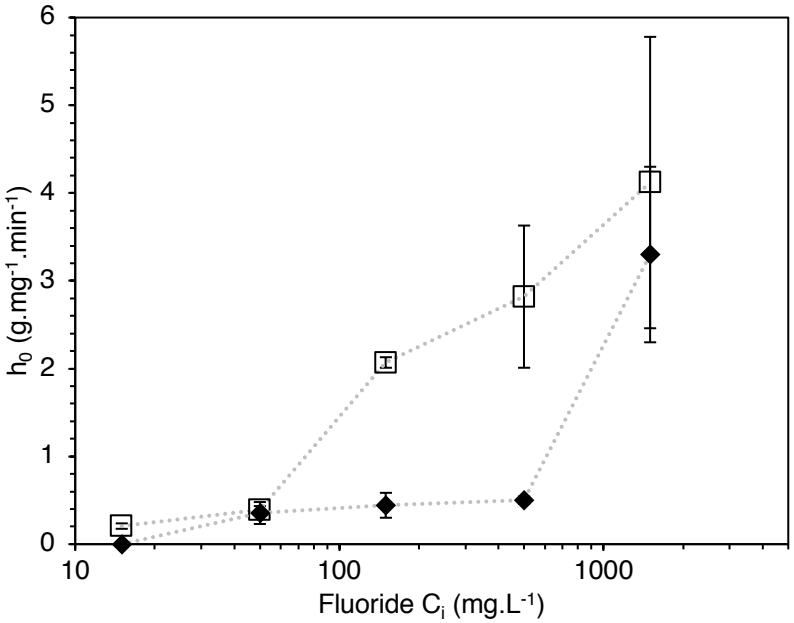

Fig. B23. Relationship between fluoride C_i and observed h_0 value for uptake from leachate (◆) and NaF solution (□). X axis is logarithmic for clarity. The h_0 values were calculated from the pseudo second-order rate equation (see main research article, Table 3.1).

Determination of Uptake Kinetics from media at various temperatures with fixed initial fluoride concentration

Data for kinetic uptake experiments with varied temperature are presented in Figures B24-29. Extracted parameters are shown in Table B9 and Arrhenius plots are as seen in main research article.

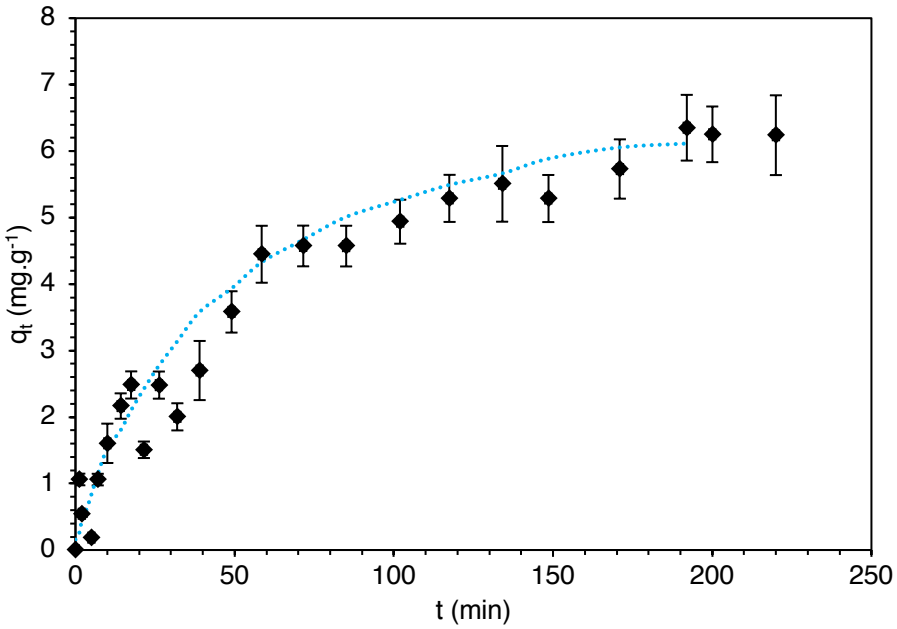

Fig. B24. Simulant leachate 1/10 dilution (Fluoride $C_i \approx 150$ mg·L^{-1}). T = 2°C. Dotted line represents pseudo 2nd-order model.

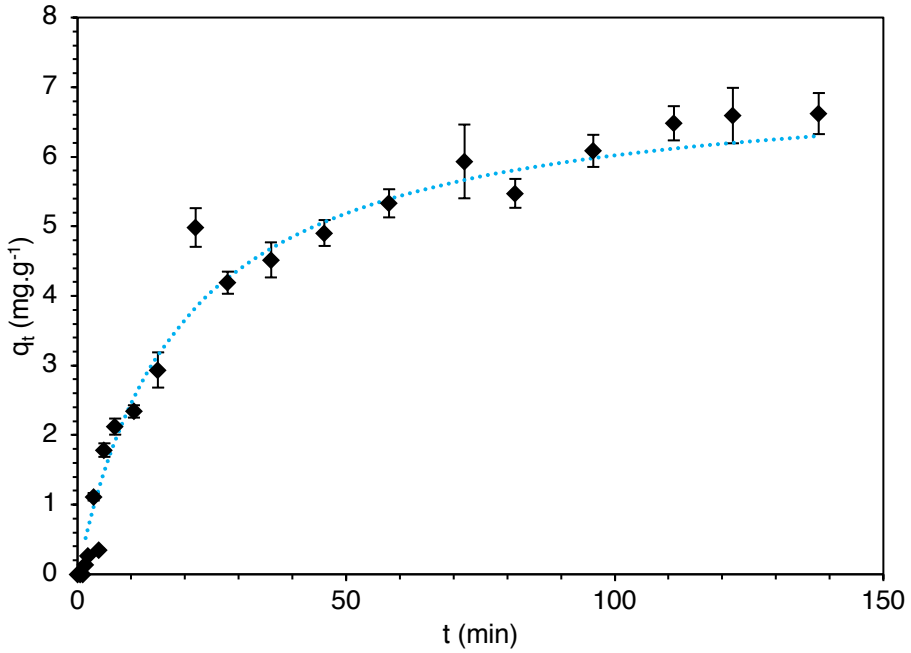

Fig. B25. Simulant leachate 1/10 dilution (Fluoride $C_i \approx 150$ mg·L^{-1}). T = 33°C. Dotted line represents pseudo 2nd-order model.

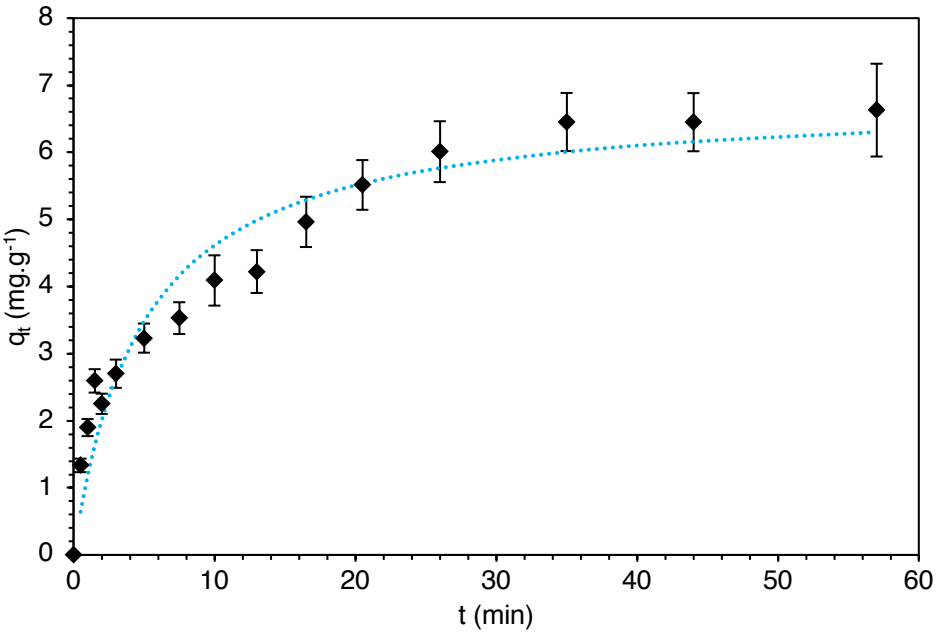

Fig. B26. Simulant leachate 1/10 dilution (Fluoride $C_i \approx 150$ mg·L^{-1}). T = 43°C. Dotted line represents pseudo 2nd-order model.

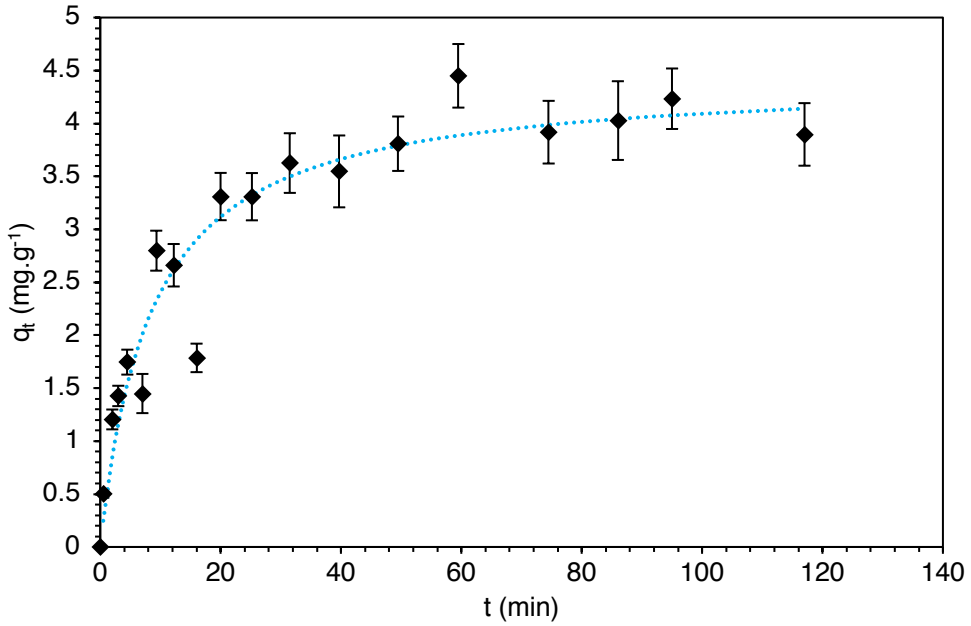

Fig. B27. NaF solution (Fluoride $C_i \approx 150$ mg·L^{-1}). T = 2°C. Dotted line represents pseudo 2nd-order model.

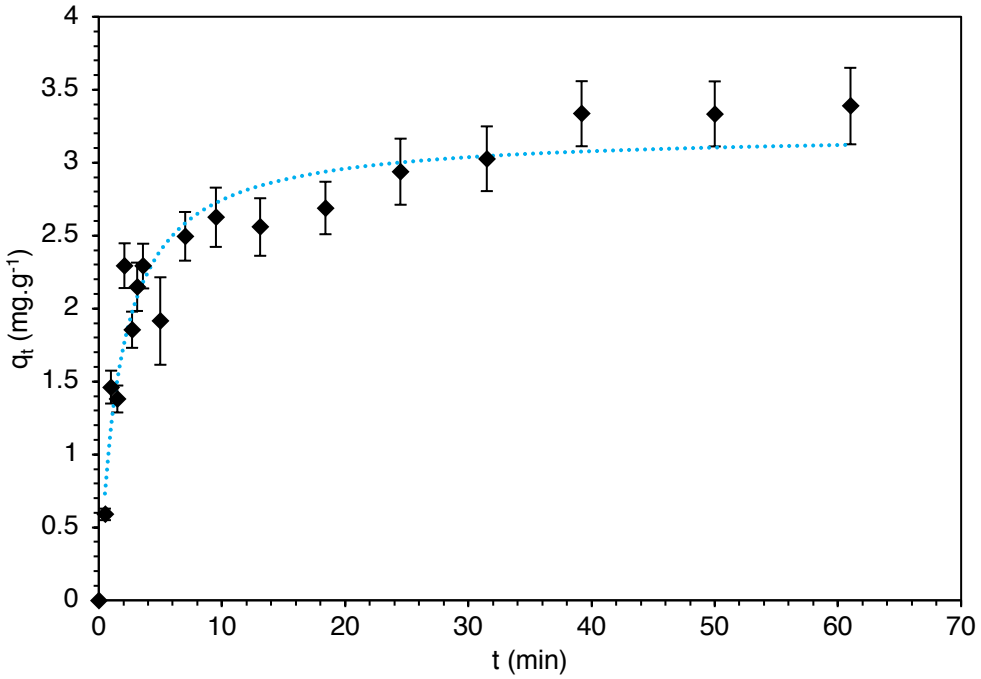

Fig. B28. NaF solution (Fluoride $C_i \approx 150$ mg·L^{-1}). T = 31°C. Dotted line represents pseudo 2nd-order model.

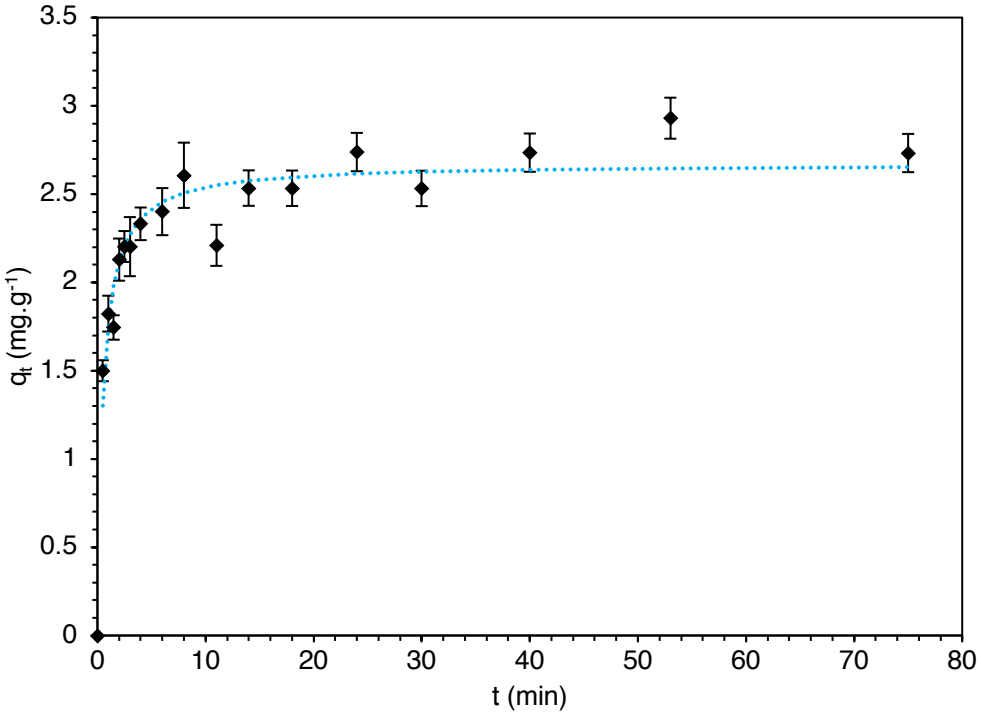

Fig. B29. NaF solution (Fluoride $C_i \approx 150$ mg·L^{-1}). T = 42°C. Dotted line represents pseudo 2nd-order model.

Table B9. Extracted kinetic parameters from temperature-varied experiments.

Sample	**Pseudo second-order model**				
	q_e (mg·g^{-1})	**k_2 (g·mg^{-1}·min^{-1})**	**$t_{1/2}$ (min)**	**h_0**	**R^2**
Leachate 2°C	7.93 ± 0.48	2.12 ± 0.34 (x 10^{-3})	60 ± 10	0.133 ± 0.024	0.953
Leachate 33°C	7.17 ± 0.89	7.3 ± 1.1 (x 10^{-3})	19.2 ± 3.2	0.37 ± 0.13	0.952
Leachate 43°C	6.83 ± 0.22	3.04 ± 0.48 (x 10^{-2})	4.82 ± 0.78	1.42 ± 0.23	0.914
NaF solution 2°C	4.44 ± 0.16	2.15 ± 0.63 (x 10^{-2})	8.5 ± 2.0	0.52 ± 0.13	0.898
NaF solution 31°C	3.21 ± 0.06	0.184 ± 0.030	1.69 ± 0.28	1.90 ± 0.31	0.894
NaF solution 42°C	2.67 ± 0.04	0.71 ± 0.14	0.256 ± 0.096	5.08 ± 0.99	0.899

Breakthrough profiles from dynamic experiments fitted to models

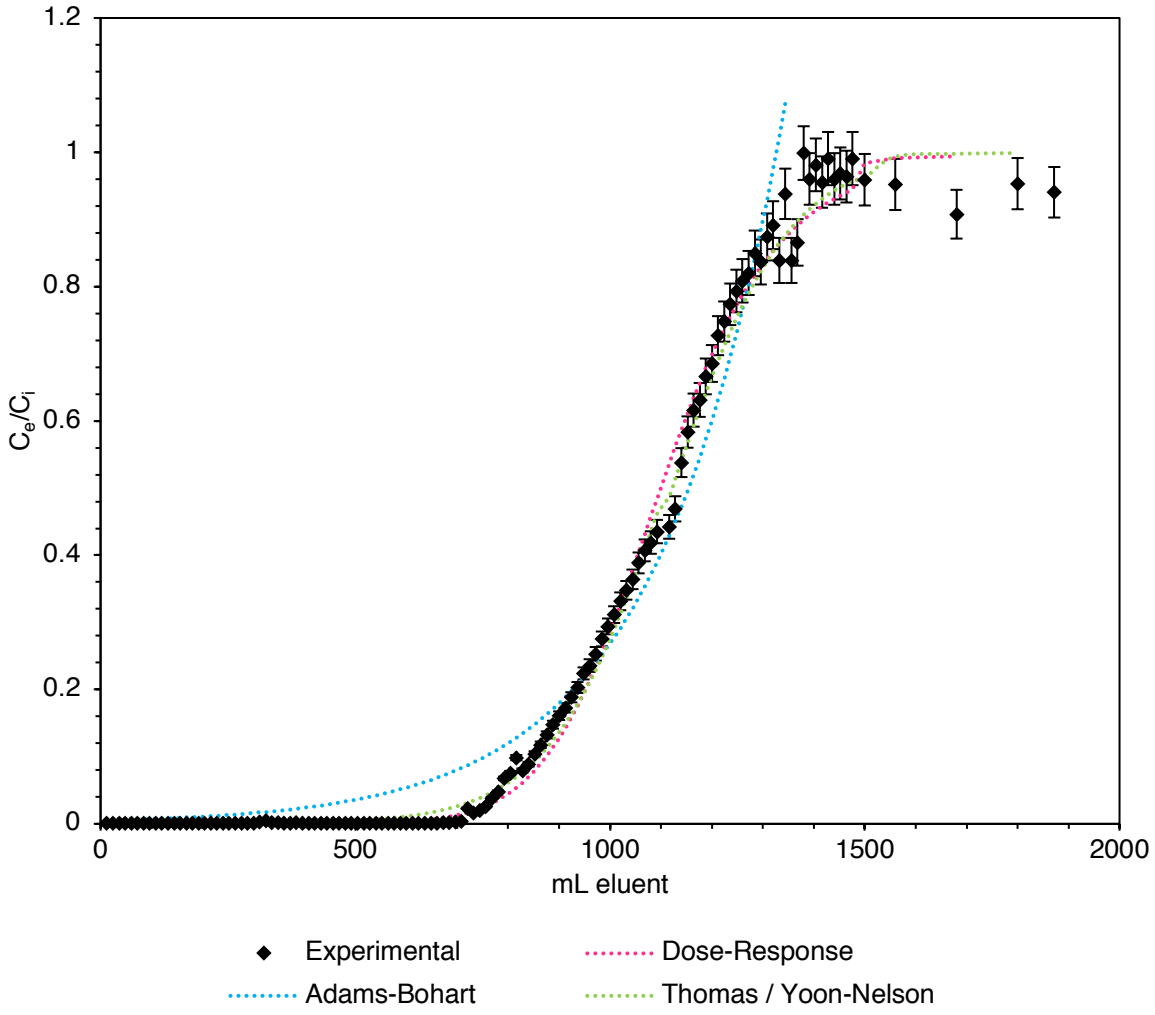

Fig. B30. Breakthrough profile for fluoride with La-MTS9501 column and leachate inlet solution (1/100 dilution, fluoride $C_i \approx 15$ mg·L^{-1}). Dotted lines represent dynamic model fits. Resin BV = 6.0 mL. Flow rate = 1 BV·hr^{-1}. T = 20°C.

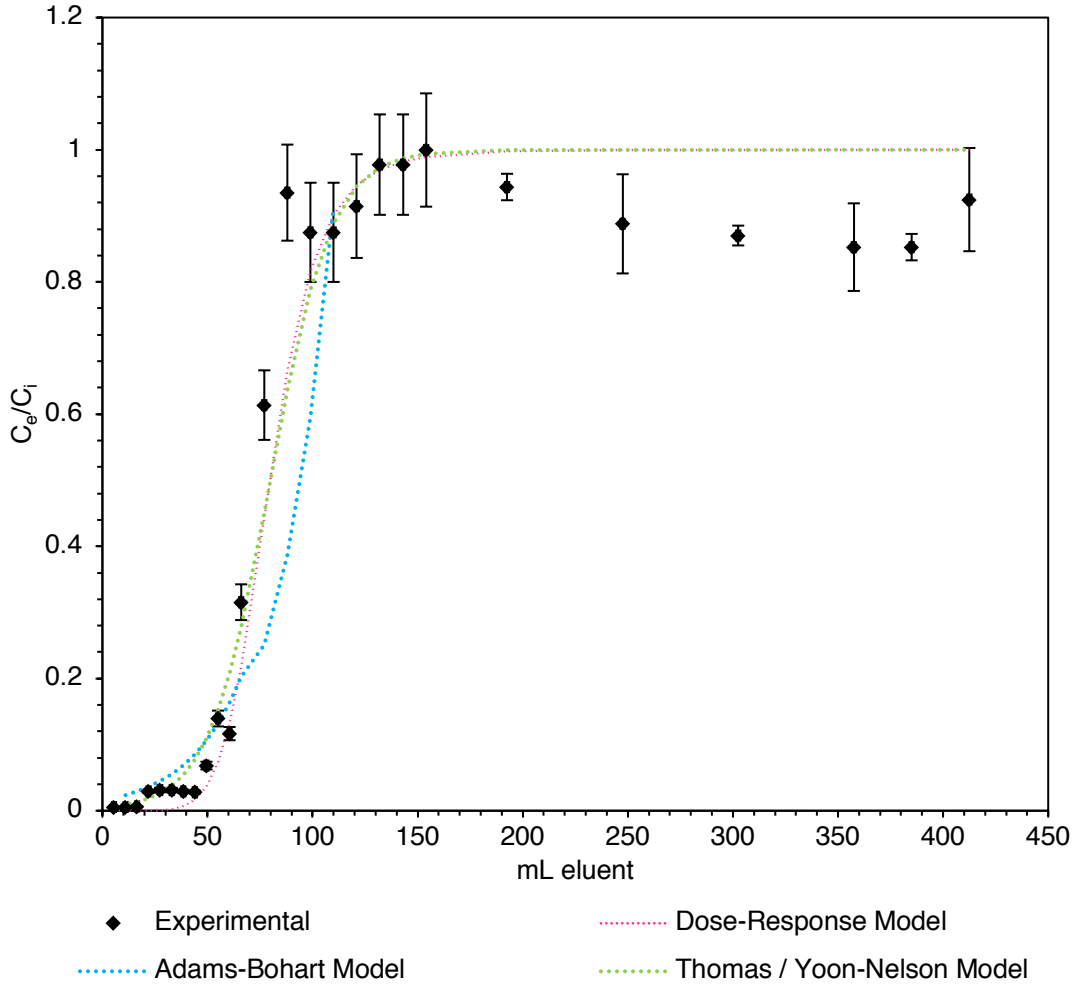

Fig. B31. Breakthrough profile for fluoride with La-MTS9501 column and leachate inlet solution (as-prepared, fluoride $C_i \approx 1500$ mg·L^{-1}). Dotted lines represent dynamic model fits. Resin BV = 6.0 mL. Flow rate = 1 BV·hr^{-1}. T = 20°C.

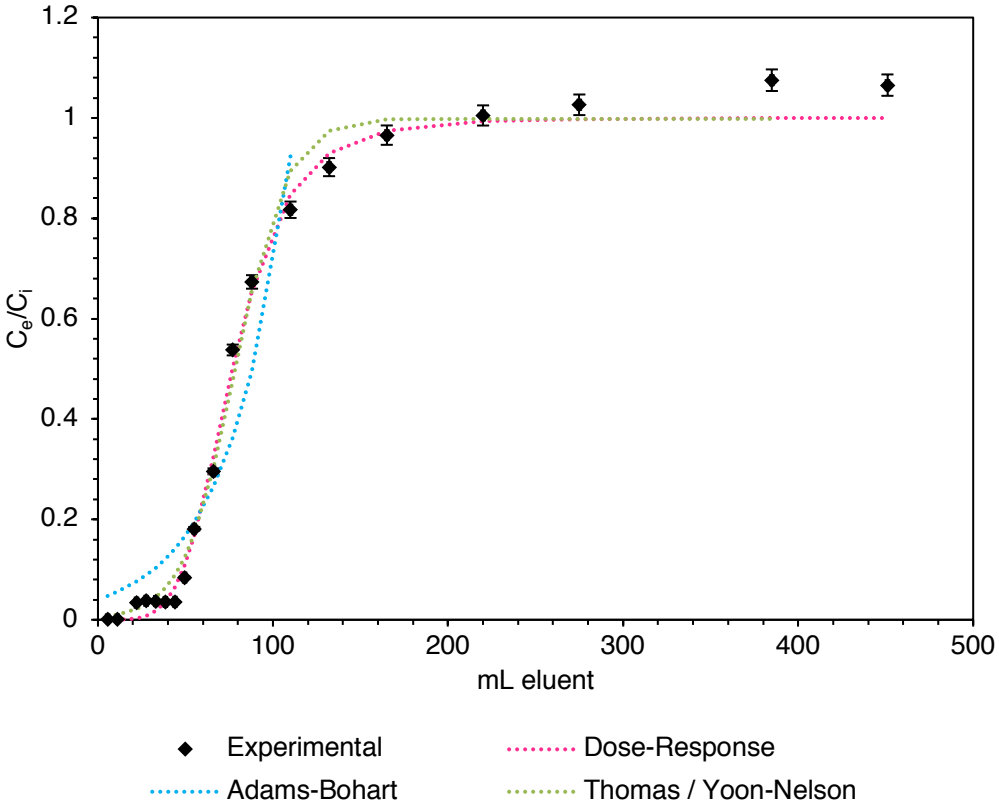

Fig. B32. Breakthrough profile for Al with La-MTS9501 column and leachate inlet solution (as-prepared, fluoride $C_i \approx 1500$ mg·L^{-1}). Dotted lines represent dynamic model fits. Resin BV = 6.0 mL. Flow rate = 1 BV·hr^{-1}. T = 20°C.

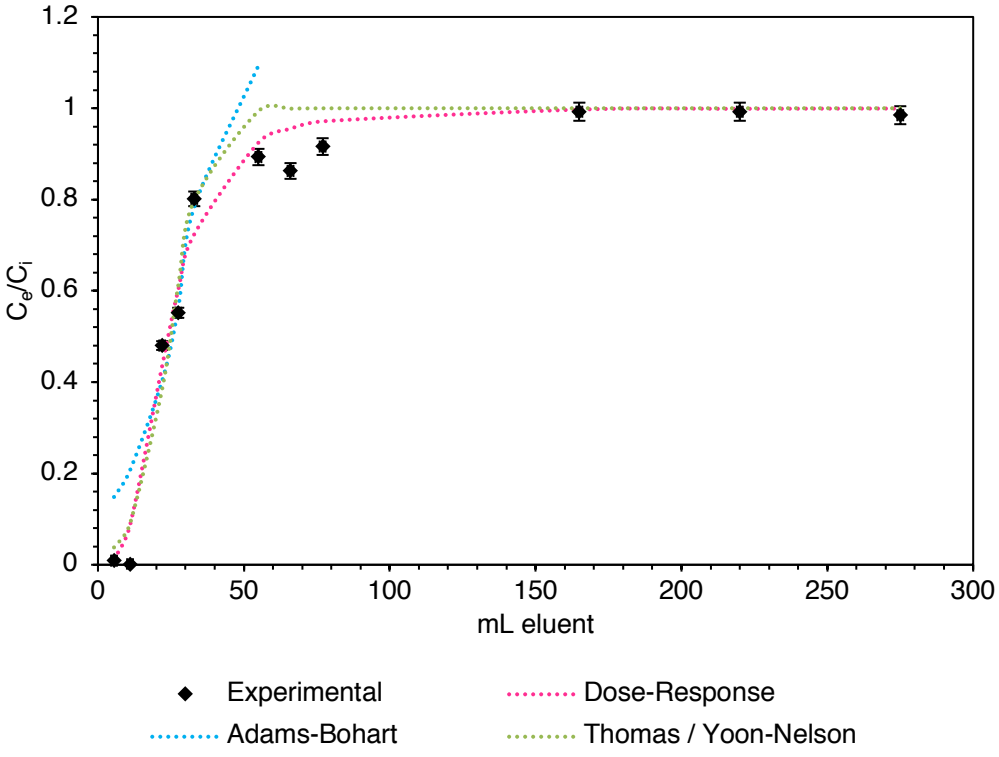

Fig. B33. Breakthrough profile for Ca with La-MTS9501 column and leachate inlet solution (as-prepared, fluoride $C_i \approx 1500$ mg·L^{-1}). Dotted lines represent dynamic model fits. Resin BV = 6.0 mL. Flow rate = 1 BV·hr^{-1}. T = 20°C.

Table B10. Extracted parameters from Thomas model data fitting.

Experiment	Parameters		
	k_{Th} (mL·mg^{-1}·min^{-1})	q_0 (mg·g^{-1})	R^2
Leachate 1/100 dilution (F^-)	7.44 ± 0.24 x 10^{-5}	4.28 ± 0.17	0.942
Leachate as-prepared (F^-)	4.20 ± 0.91 x 10^{-6}	66.9 ± 19.7	0.952
Leachate as-prepared (Al)	1.01 ± 0.10 x 10^{-5}	26.8 ± 3.5	0.988
Leachate as-prepared (Ca)	1.17 ± 0.36 x 10^{-4}	1.81 ± 0.37	0.959
NaF solution ([F^-] ≈ 15 mg·L^{-1})	3.24 ± 0.27 x 10^{-4}	1.16 ± 0.13	0.954
NaF solution ([F^-] ≈ 1500 mg·L^{-1})	4.08 ± 0.27 x 10^{-5}	20.5 ± 2.2	0.996

Table B11. Extracted parameters from Adams-Bohart model data fitting.

Experiment	Parameters		
	k_{AB} (mL·mg^{-1}·min^{-1})	N_0 (mg·mL^{-1})	R^2
Leachate 1/100 dilution (F^-)	4.67 ± 0.16 (x 10^{-5})	1.67 ± 0.04	0.939
Leachate as-prepared (F^-)	2.39 ± 0.16 (x 10^{-6})	27.7 ± 2.1	0.886
Leachate as-prepared (Al)	4.25 ± 0.63 (x 10^{-6})	12.5 ± 2.2	0.880
Leachate as-prepared (Ca)	4.2 ± 1.1 (x 10^{-5})	0.88 ± 0.28	0.919
NaF solution ([F^-] ≈ 15 mg·L^{-1})	4.4 ± 1.2 (x 10^{-4})	0.39 ± 0.11	0.927
NaF solution ([F^-] ≈ 1500 mg·L^{-1})	2.40 ± 0.33 (x 10^{-4})	7.3 ± 1.2	0.999

Table B12. Extracted parameters from Yoon-Nelson model.

Experiment	Parameters		
	k_{YN} (min^{-1})	T_{50} (min)	R^2
Leachate 1/100 dilution (F^-)	1.28 ± 0.04 (x 10^{-2})	530 ± 21	0.942
Leachate as-prepared (F^-)	6.31 ± 0.30 (x 10^{-3})	870 ± 180	0.952
Leachate as-prepared (Al)	6.18 ± 0.58 (x 10^{-3})	860 ± 110	0.988
Leachate as-prepared (Ca)	1.53 ± 0.48 (x 10^{-2})	271 ± 20	0.959
NaF solution ([F^-] ≈ 15 mg·L^{-1})	6.29 ± 0.53 (x 10^{-2})	117 ± 13	0.954
NaF solution ([F^-] ≈ 1500 mg·L^{-1})	7.27 ± 0.49 (x 10^{-2})	225 ± 24	0.996

XRD and TGA experimental data

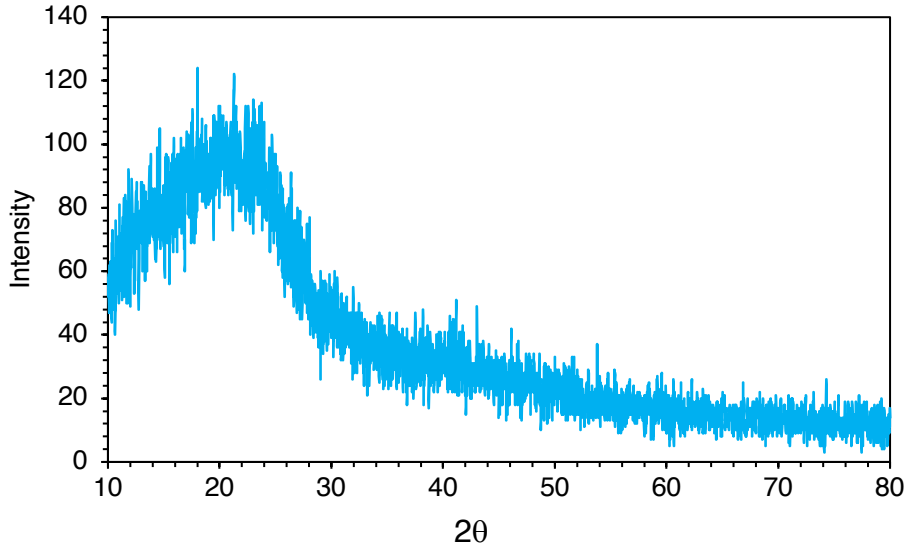

Fig. B34. Powder XRD spectrum of MTS-9501 resin post-contact with NaF solution. Fluoride $C_i \approx 150$ mg·L^{-1} (sample taken after a complete kinetic experiment).

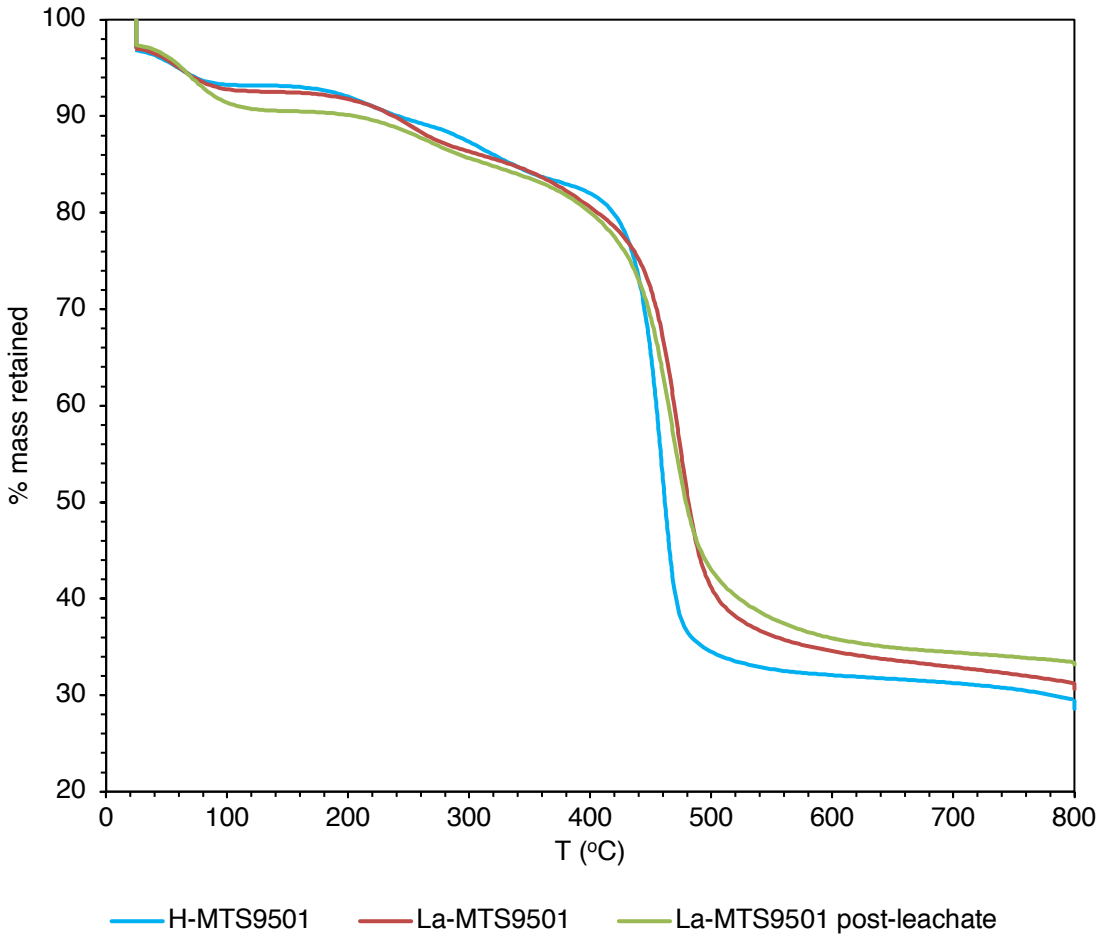

Fig. B35. TGA traces for samples of resin at various process stages. Post-leachate-contact sample was taken from a completed kinetic experiment, using as-prepared leachate (fluoride $C_i \approx 1500$ mg·L^{-1}).

Appendix B References

[1] N. Viswanathan, S. Meenakshi, “Effect of metal ion loaded in a resin towards fluoride retention”, *Journal of Fluorine Chemistry*, 2008, **129**, 645-653.

[2] M.J. Haron, W.M.Z. Yunus, “Removal of fluoride ion from aqueous solution by a cerium-poly(hydroxamic acid) resin complex”, *Journal of Environmental Science and Health Part A-Toxic/Hazardous Substances & Environmental Engineering*, 2001, **36**, 727-734.

[3] S.A. Wasay, S. Tokunaga, S.-W. Park, “Removal of Hazardous Anions from Aqueous Solutions by La(III)- and Y(III)- Impregnated Alumina”, *Separation Science and Technology*, 1996, **31**, 1501-1514.

[4] J.M. Cheng, X.G. Meng, C.Y. Jing, J.M. Hao, “La^{3+}-modified activated alumina for fluoride removal from water”, *Journal of Hazardous Materials*, 2014, **278**, 343-349.

[5] N. Viswanathan, S. Meenakshi, “Enriched fluoride sorption using alumina/chitosan composite”, *Journal of Hazardous Materials*, 2010, **178**, 226-232.

[6] E. Kusrini, N. Sofyan, N. Suwartha, G. Yesya, C.R. Priadi, “Chitosan-praseodymium complex for adsorption of fluoride ions from water”, *Journal of Rare Earths*, 2015, **33**, 1104-1113.

[7] J.S. He, J.P. Chen, “A zirconium-based nanoparticle: Essential factors for sustainable application in treatment of fluoride containing water”, *Journal of Colloid and Interface Science*, 2014, **416**, 227-234.

[8] L. Birry, S. Leclerc, S. Poirier, “The LCL&L process: A sustainable solution for the treatment and recycling of spent potlining”, *TMS (The Minerals, Metals & Materials Society), Light Metals,* 2016, 467-471.

[9] H. Kalka, “Aqion: Manual (selected topics)” [online], http://www.aqion.de/site/98?, 2015.

[10] T. Robshaw, S. Tukra, D.B. Hammond, G.J. Leggett, M.D. Ogden, “Highly efficient fluoride extraction from simulant leachate of spent potlining via La-loaded chelating resin. An equilibrium study”, *Journal of Hazardous Materials*, 2019, **361**, 200-209.

[11] Purolite, “S950 Macroporous Aminophosphonic Chelating Resin (For the selective removal of toxic metal from aqueous solutions). Technical Data” [online], http://www.reskem.com/wp-uploads/2015/04/purolite-s950.pdf, 2017.

APPENDIX C

"Development of a combined leaching and ion-exchange system for valorisation of spent potlining waste"

SUPPORTING INFORMATION

Thomas J. Robshaw, Keith Bonser, Glyn Coxhill, Robert Dawson and Mark D. Ogden

Information on Lanthanum-loaded Puromet™ MTS9501 resin (La-MTS9501)

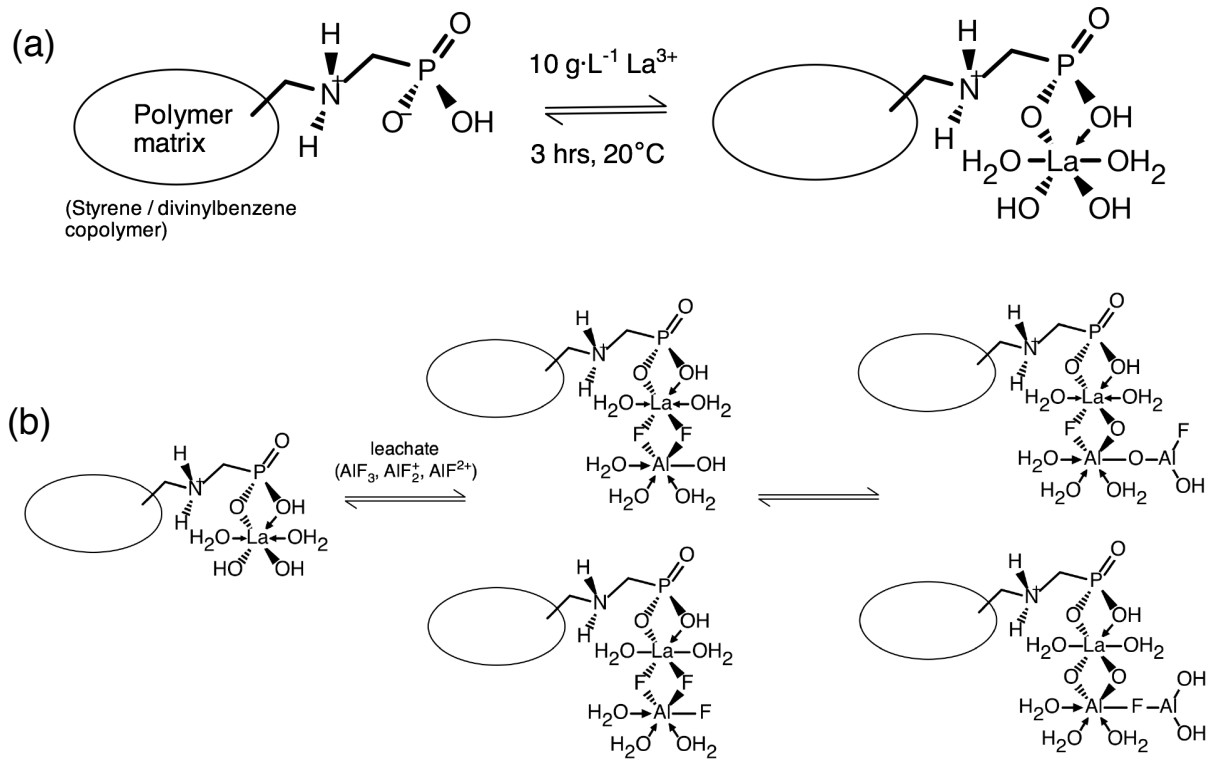

Fig. C1. (a) La-loading mechanism for commercial resin Puromet™ MTS9501 resin, showing chelation of La ion to aminophosphonic acid functionality. **(b)** Probable mechanisms of aluminium hydroxyfluoride (AHF) uptake by La-MTS9501. Initial strong chemisorption interaction between La centre and aqueous AHF, then complexation with further weakly-bound AHFs (coordinating water ligands are omitted for clarity), accompanied by ligand-exchange reactions, resulting in the dominant bound AHF species having stoichiometry of ~$Al(OH)_2F$ [1, 2].

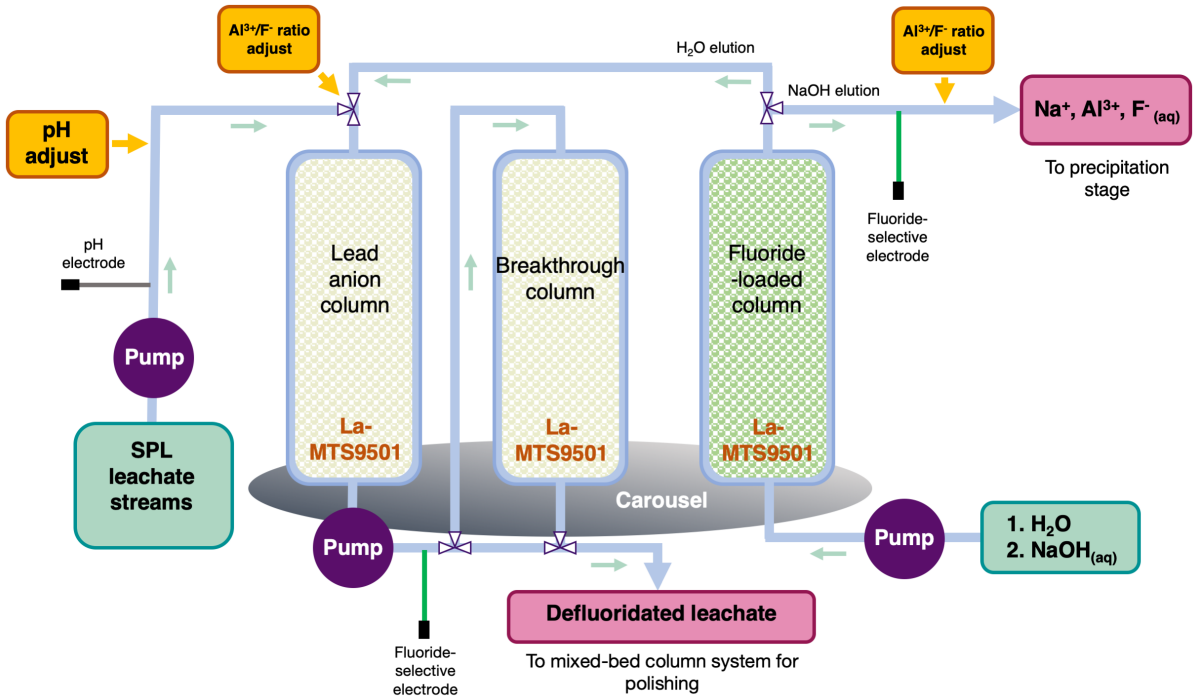

Fig. C2. Conceptual diagram of La-MTS9501 column system for treatment of SPL leachate, derived from previous work [1, 2].

Images of selected SPL samples

Fig. C3. Photographs of the three different unprocessed SPL samples selected for leaching trials. Sample A (left), containing a large fraction of cementious and brick material. Sample B (middle), containing visible cementious material. Sample C (right), appearing to be mainly graphitic material.

Dynamic experiment setup

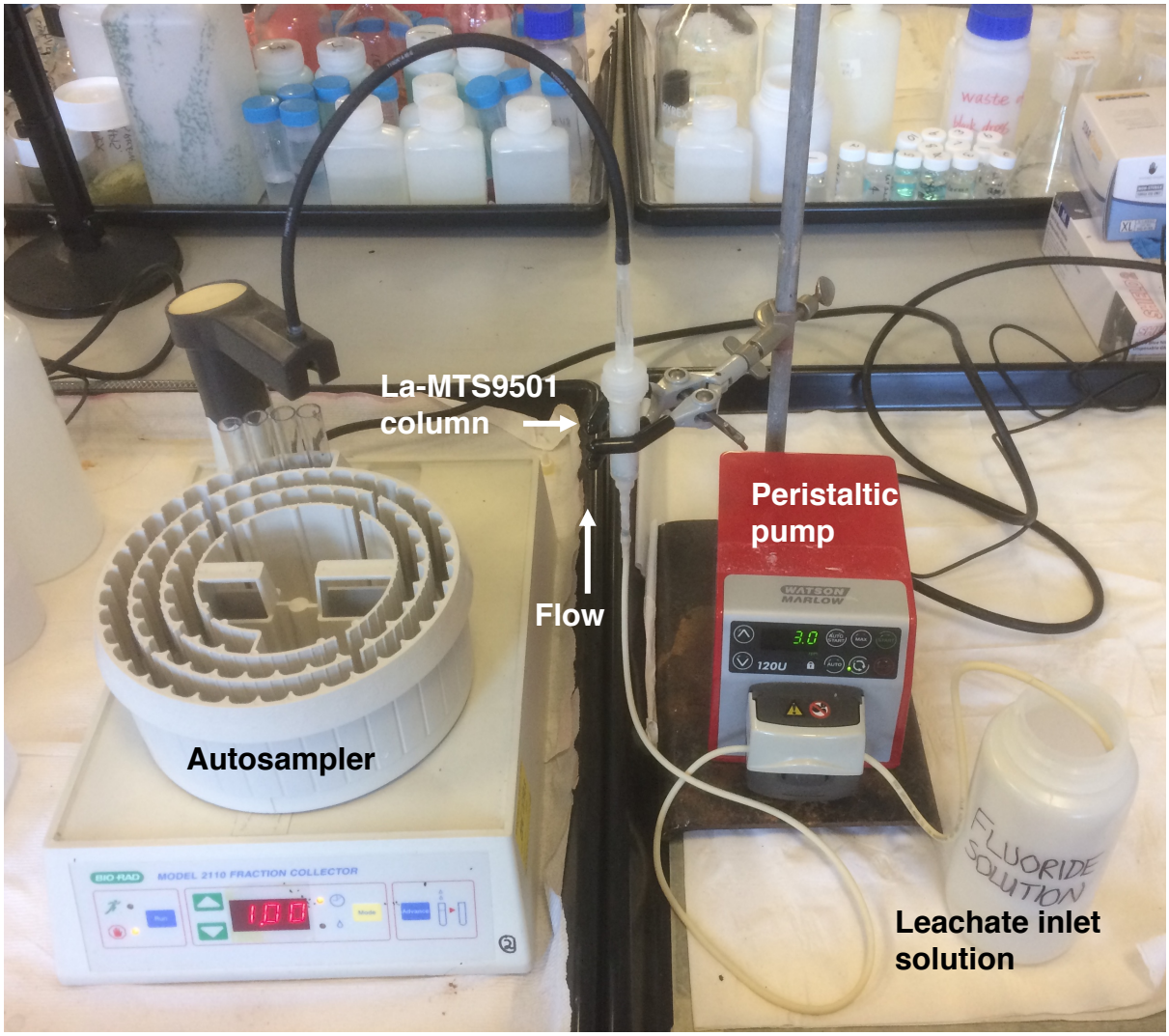

Fig. C4. Experimental setup for a fixed-bed column fluoride-loading experiment.

Dynamic breakthrough models

Dose-response model [3]

$$\frac{C}{C_i} = 1 - \frac{1}{1+\left(\frac{V_{ef}}{b}\right)^a} \quad \textbf{(Eqn. C1)}$$

$$q_0 = \frac{bC_i}{m} \quad \textbf{(Eqn. C2)}$$

In these equations C is the fluoride concentration in the effluent at a given time ($mg \cdot L^{-1}$), C_i is the fluoride concentration in the effluent at full breakthrough ($mg \cdot L^{-1}$), V_{ef} is the volume of solution eluted from the column (mL), a and b are constants of the Dose-Response model, q_0 is the theoretical maximum uptake capacity of the resin in a dynamic environment ($mg \cdot g^{-1}$) and m is the dry mass of resin (g).

Thomas model [4]

$$\frac{C}{C_i} = \frac{1}{1+e^{\left(\frac{k_{Th}}{Q}\right)(q_0 m - C_i V_{ef})}} \quad \textbf{(Eqn. C3)}$$

where k_{Th} = Thomas rate constant ($mL \cdot min^{-1} \cdot mg^{-1}$), Q = flow rate ($mL \cdot min^{-1}$). All other terms as previously described.

Yoon-Nelson model [5]

$$\frac{C}{C_i} = \frac{1}{1+e^{k_{YN}(\tau - t)}} \quad \textbf{(Eqn. C4)}$$

where k_{YN} = Yoon-Nelson rate constant (min^{-1}), t = time (min) and τ = the time at which $C/C_i = 0.5$ (min). All other terms as previously described. It should be noted that the Thomas and Yoon-Nelson models are mathematically analogous. Therefore, their fitting to experimental data using Microsoft SOLVER [6] produces identical R^2 values.

PXRD spectra of SPL samples at various process stages

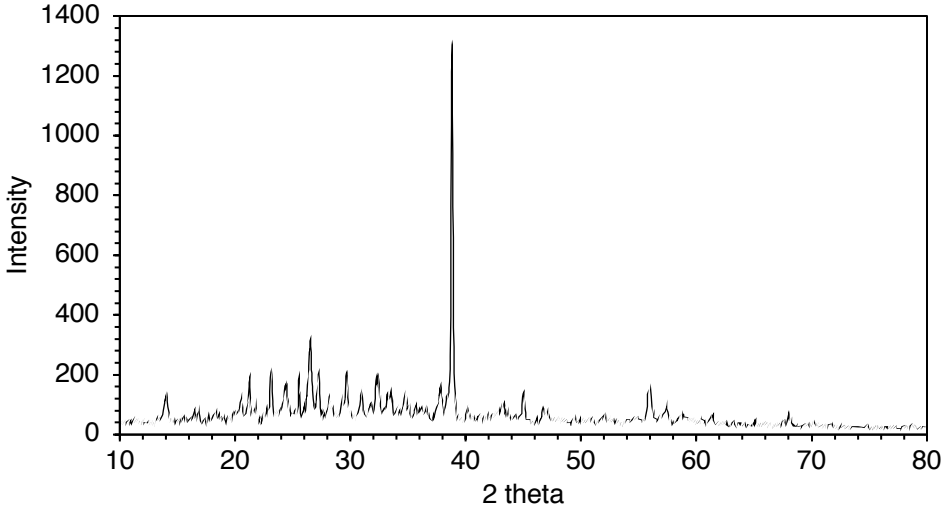

Fig. C5. PXRD spectrum of sample A <1.18 mm size fraction as received.

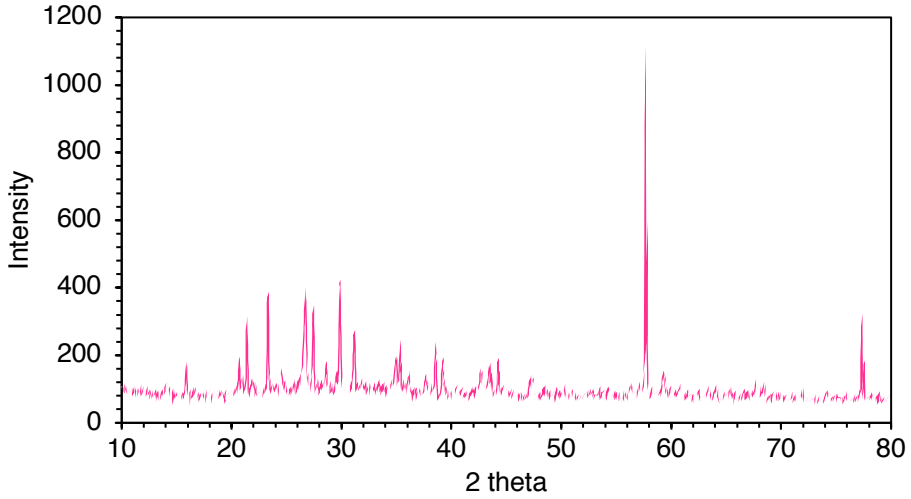

Fig. C6. PXRD spectrum of sample A <1.18 mm size fraction after caustic leaching treatment.

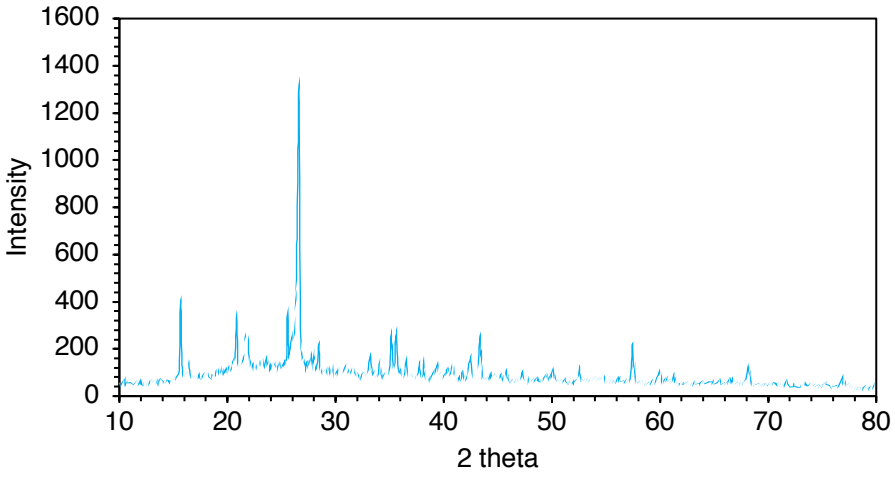

Fig. C7. PXRD spectrum of sample A <1.18 mm size fraction after full leaching treatment.

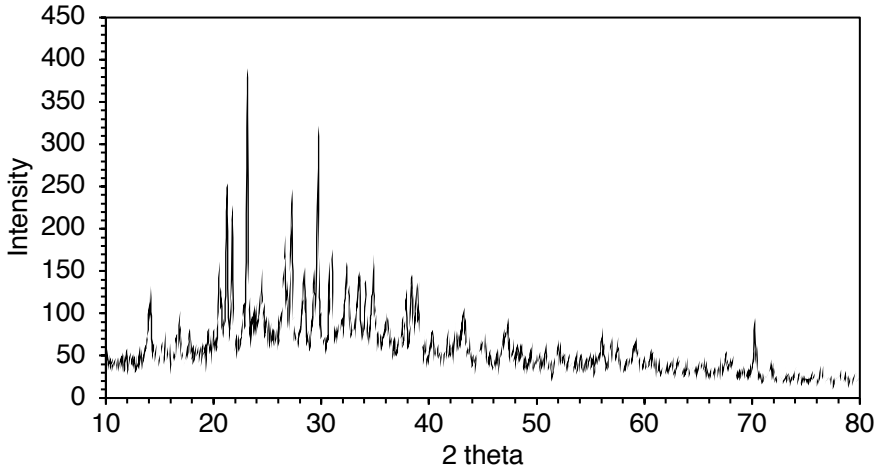

Fig. C8. PXRD spectrum of sample A 1.18–9.51 mm size fraction as received.

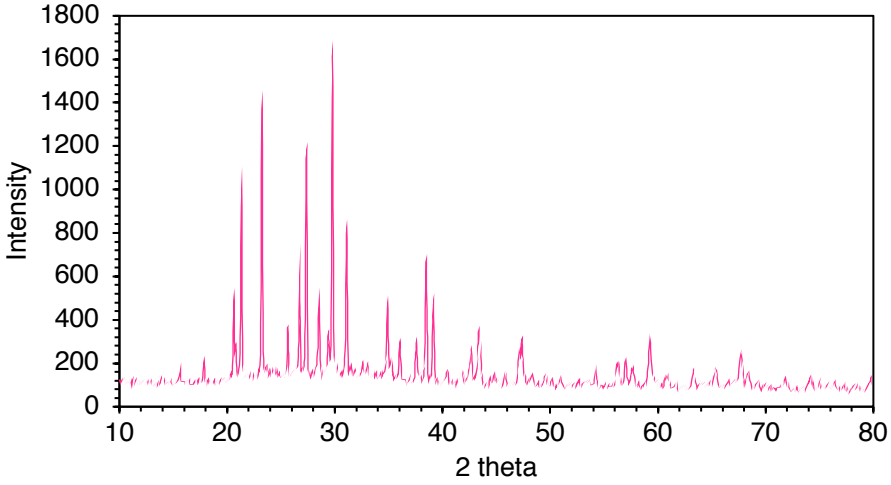

Fig. C9. PXRD spectrum of sample A 1.18–9.51 mm size fraction after caustic leaching treatment.

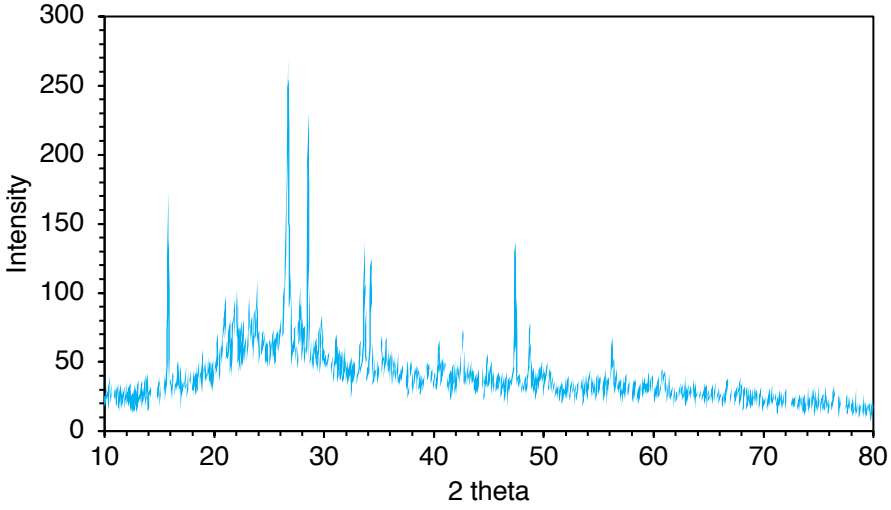

Fig. C10. PXRD spectrum of sample A 1.18–9.51 mm size fraction after full leaching treatment.

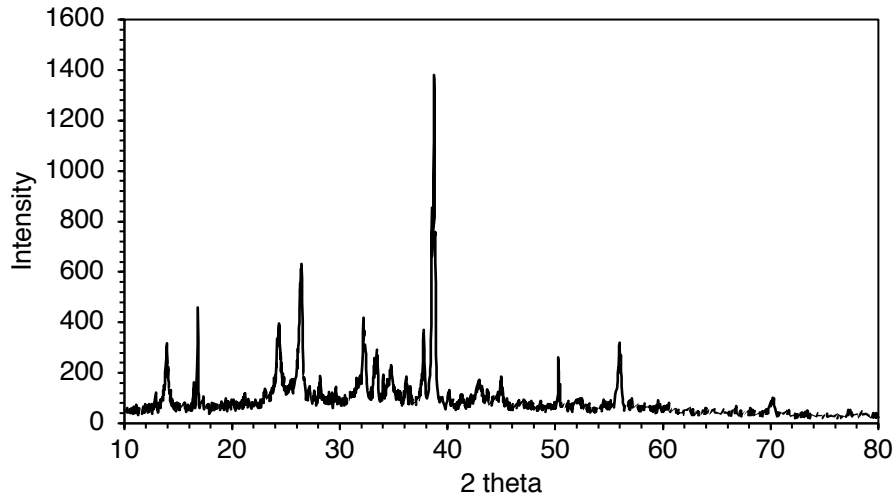

Fig. C11. PXRD spectrum of sample B <1.18 mm size fraction as received.

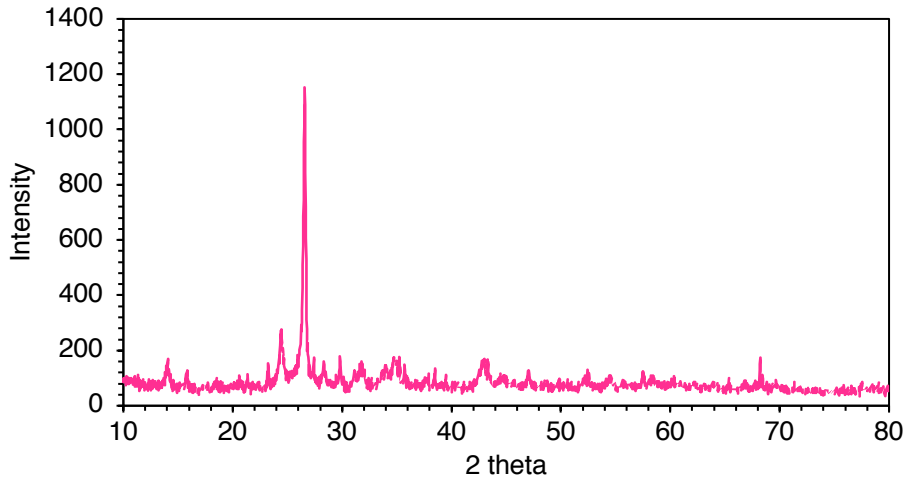

Fig. C12. PXRD spectrum of sample B <1.18 mm size fraction after caustic leaching treatment.

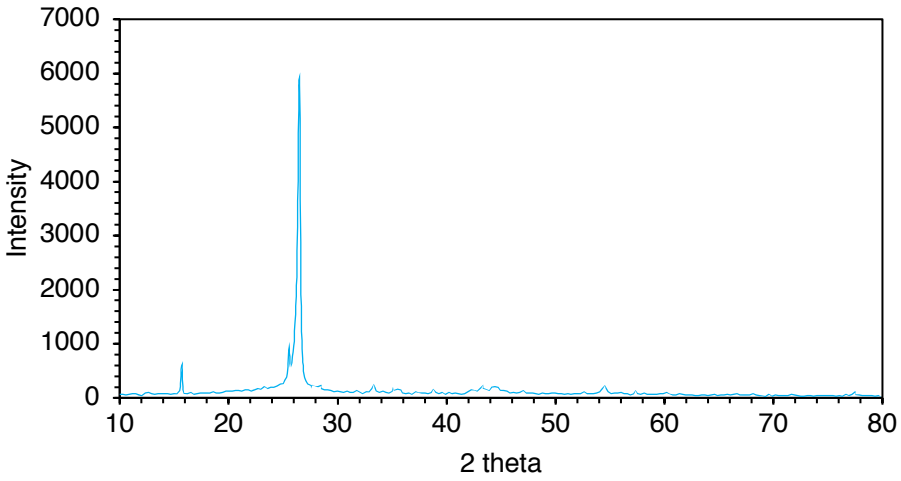

Fig. C13. PXRD spectrum of sample B <1.18 mm size fraction after full leaching treatment.

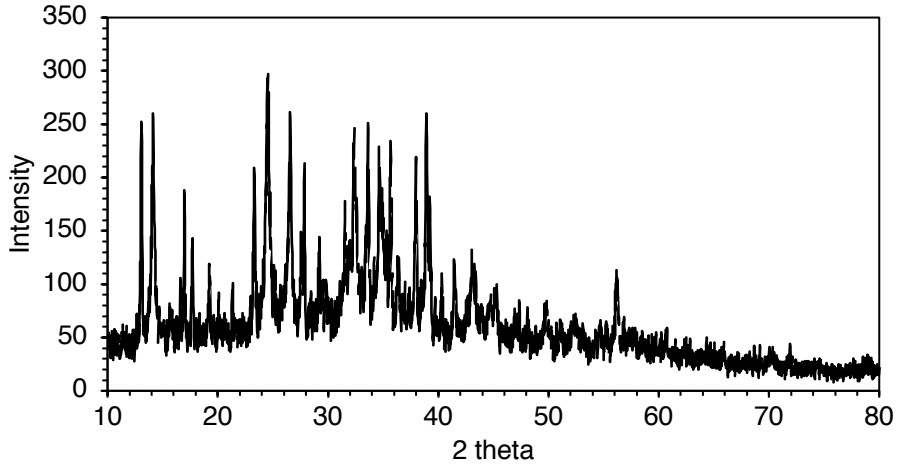

Fig. C14. PXRD spectrum of sample B 1.18-9.51 mm size fraction as received.

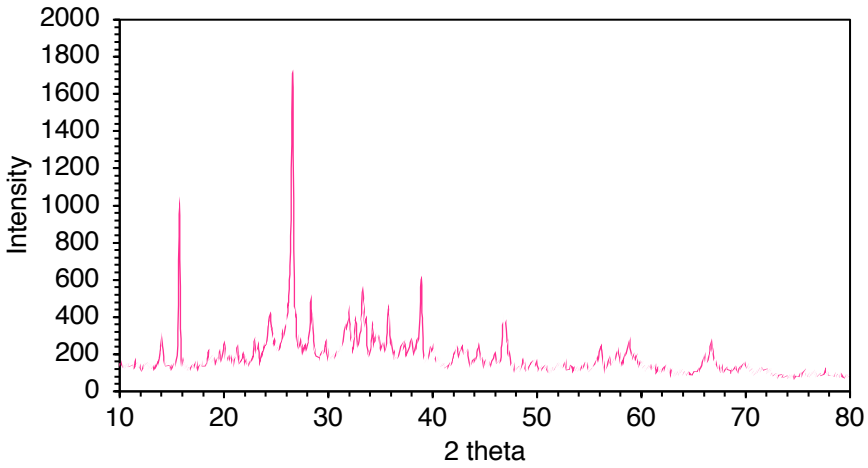

Fig. C15. PXRD spectrum of sample B 1.1–9.51 mm size fraction after caustic leaching treatment.

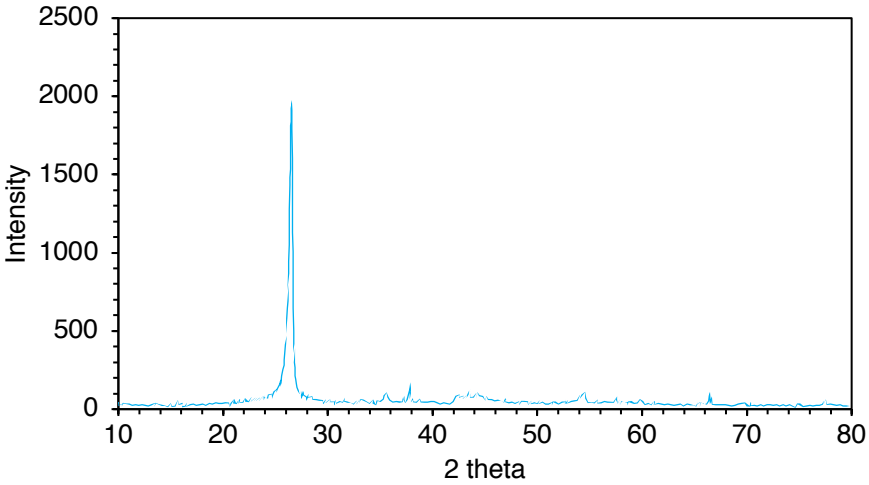

Fig. C16. PXRD spectrum of sample B 1.18–9.51 mm size fraction after full leaching treatment.

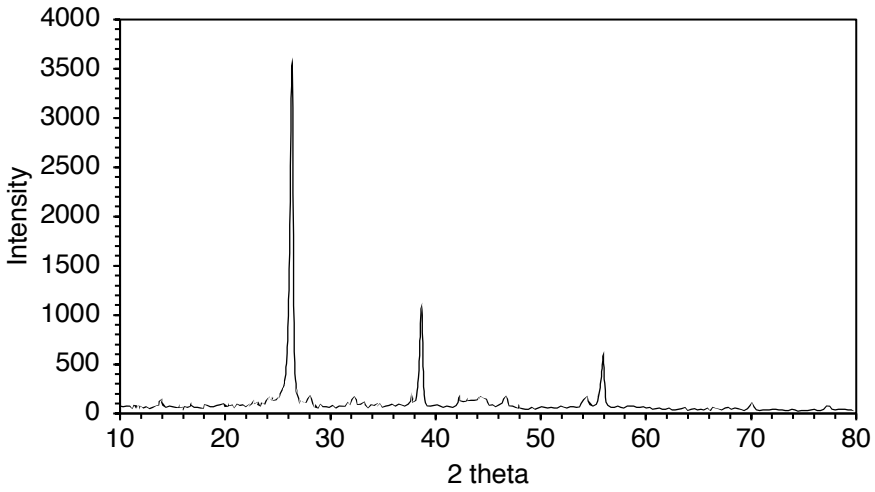

Fig. C17. PXRD spectrum of sample C <1.18 mm size fraction as received.

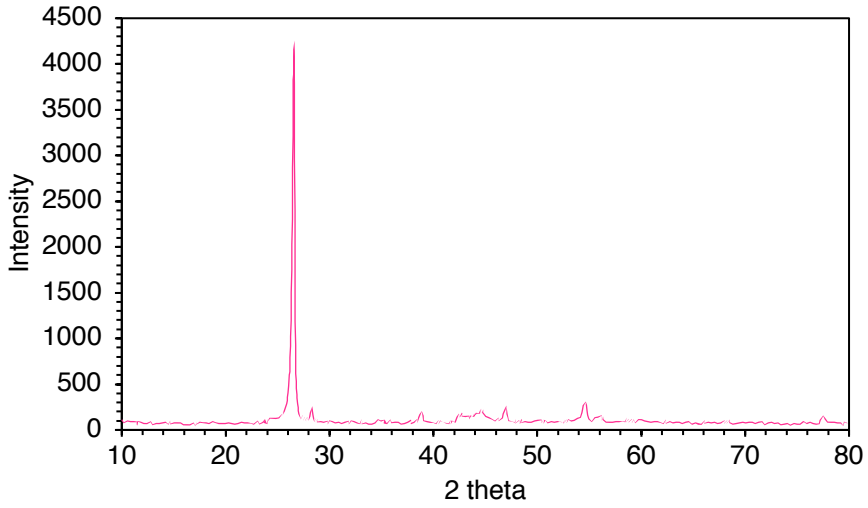

Fig. C18. PXRD spectrum of sample C <1.18 mm size fraction after caustic leaching treatment.

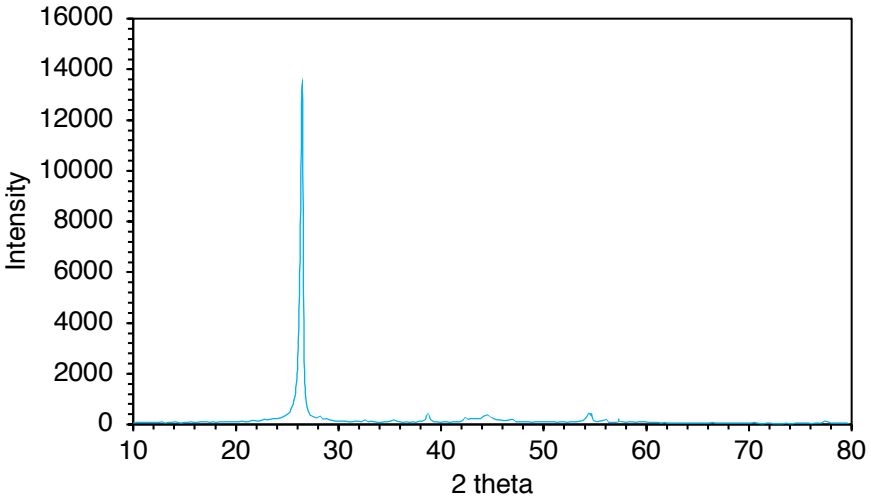

Fig. C19. PXRD spectrum of sample C <1.18 mm size fraction after full leaching treatment.

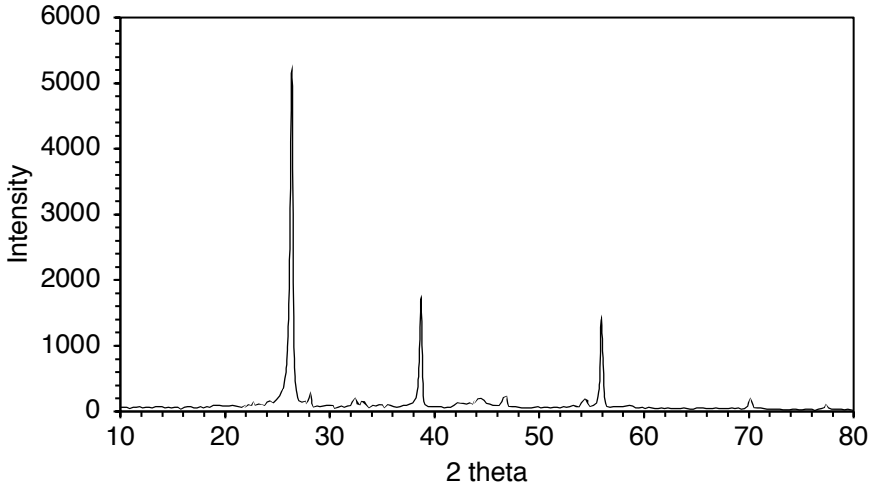

Fig. C20. PXRD spectrum of sample C 1.18–9.51 mm size fraction as received.

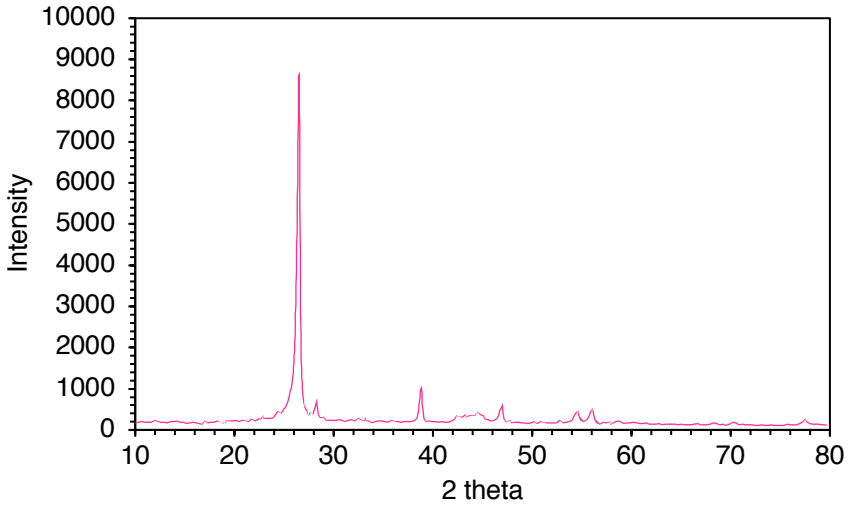

Fig.C21. PXRD spectrum of sample C 1.18–9.51 mm size fraction after caustic leaching treatment.

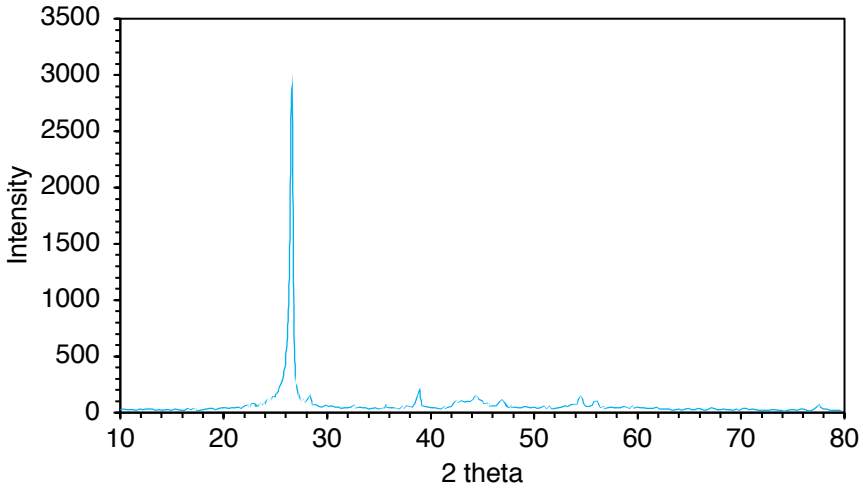

Fig. C22. PXRD spectrum of sample C 1.18–9.51 mm size fraction after full leaching treatment.

Scanning electron microscopy (SEM) images

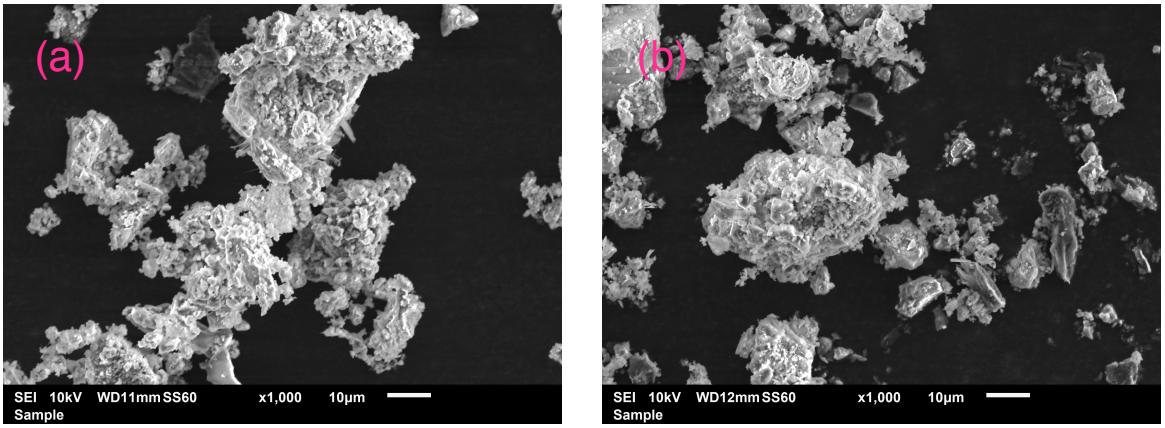

Fig. C23. SEM images of sample A <1.18 mm size fraction before **(a)** and after **(b)** full leaching treatment.

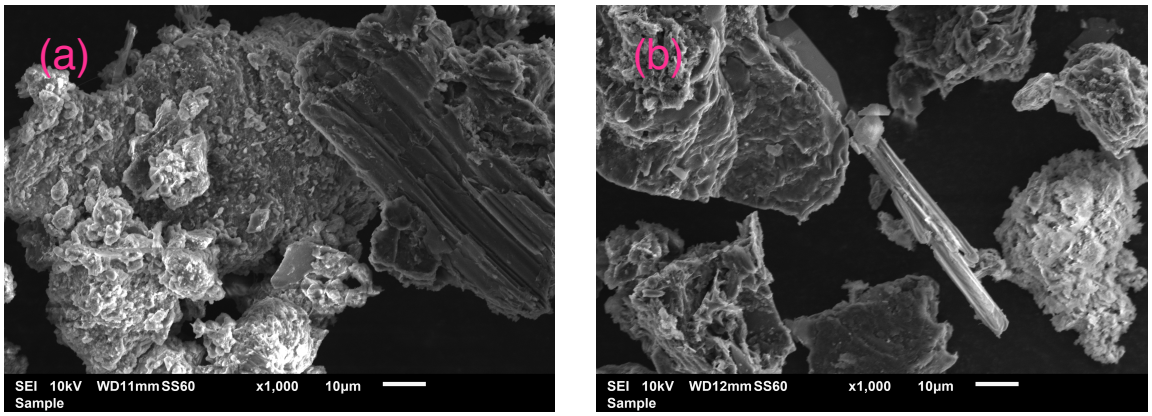

Fig. C24. SEM images of sample B <1.18 mm size fraction before **(a)** and after **(b)** full leaching treatment.

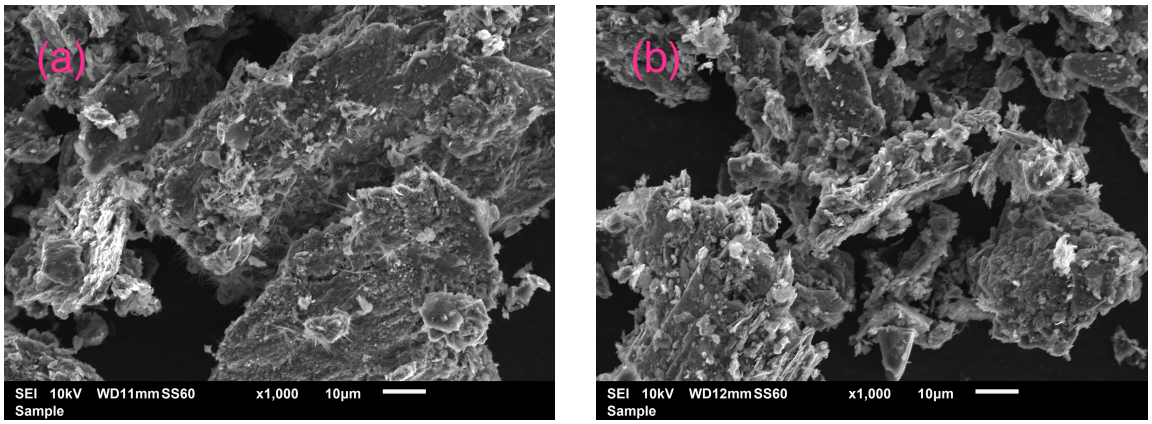

Fig. C25. SEM images of sample C <1.18 mm size fraction before **(a)** and after **(b)** full leaching treatment.

Energy-dispersive X-ray (EDX) spectra from point analysis (performed in conjunction with SEM imaging)

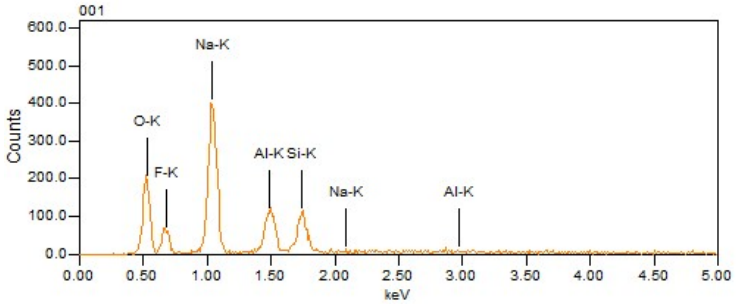

Fig. C26. EDX spectrum for point α (cementious particle) in sample A <1.18 mm size fraction (micrograph in main article, Fig. 4.3).

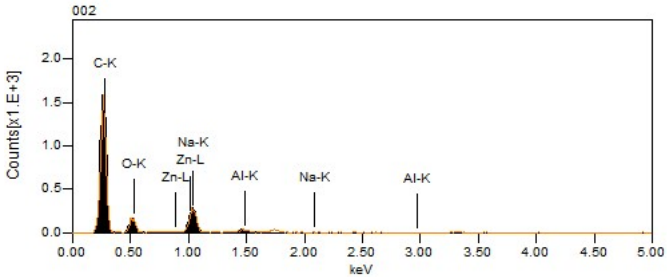

Fig. C27. EDX spectrum for point β (graphite particle) in sample A <1.18 mm size fraction (micrograph in main article, Fig. 4.3).

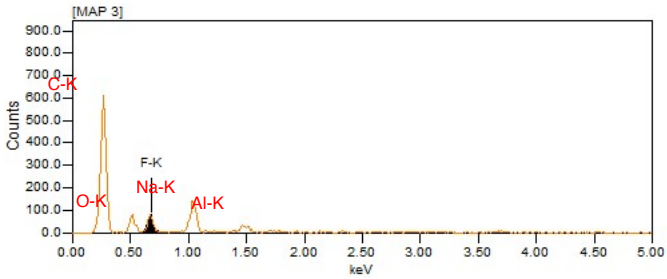

Fig. C28. EDX spectrum for point γ (crystalline region) in sample C <1.18 mm size fraction. Peaks labelled in red were manually assigned (micrograph in main article, Fig. 4.3).

Additional ICP-MS analysis of SPL leachate

Table C1. Quantities of minor chemical species leached from each SPL sample, determined by ICP-MS.

Leaching treatment	Sample	Ni	Ba	Be	Cr	Sr	Li	V	Mn	Y	Zn
caustic	A <1.18 mm	< 5	0.480	0.960	21.6	1.44	18.2	16.3	0.480	< 5	77.8
caustic	A 1.18-9.51 mm	< 5	2.46	< 0.5	6.57	0.821	45.6	7.39	1.64	< 5	60.4
caustic	B <1.18 mm	< 5	0.468	1.87	8.89	1.40	34.6	12.6	0.468	< 5	67.4
caustic	B 1.18-9.51 mm	< 5	0.414	3.31	3.31	0.827	26.5	12.8	0.414	< 5	50.9
caustic	C <1.18 mm	< 5	3.92	4.90	20.1	3.43	27.9	7.84	0.490	< 5	67.6
caustic	C 1.18-9.51 mm	< 5	1.30	2.61	6.08	2.61	24.8	3.91	0.434	< 5	44.7
	average	< 5	1.51	2.36	11.1	1.76	29.6	10.2	0.655	< 5	61.5
	Standard deviation		1.42	1.61	7.78	1.05	9.44	4.54	0.485		12.1
acidic	A <1.18 mm	46.3	9.84	3.60	90.0	57.8	34.8	5.28	133.7	6.24	85.2
acidic	A 1.18-9.51 mm	9.45	7.46	3.23	14.9	64.7	32.1	8.71	42.5	7.71	162
acidic	B <1.18 mm	17.2	5.23	5.65	24.1	62.4	32.0	2.51	58.0	4.61	48.4
acidic	B 1.18-9.51 mm	8.02	4.86	2.67	15.8	33.0	16.5	0.729	18.7	2.43	52.7
acidic	C <1.18 mm	28.1	2.14	4.07	37.9	75.9	19.5	3.43	106	2.36	30.2
acidic	C 1.18 mm-9.51 mm	13.6	2.12	6.58	13.4	55.0	21.5	1.91	47.8	1.91	17.4
	average	20.4	5.28	4.30	32.7	58.1	26.1	3.76	67.2	4.21	66.1
	Standard deviation	14.6	3.02	1.51	29.5	14.3	7.79	2.87	43.2	2.38	52.5

Other SPL leaching treatments described in the literature

Table C2. Comparison of SPL leaching treatments previously reported.

SPL cut	Number of stages	Lixiviant(s)	Length of treatment (hr)	Leaching temperature (°C)	Reference
Mixed	2	1 M NaOH (with H_2O_2), 0.5 M H_2SO_4	3 (x 2) + 2	20	This study
First	1	Concentrated chromic acid	< 0.3	100	[7]
Not stated (presumed mixed)	4	Water, HF, H_2SiF_6, water	Not stated	60 - 90	[8]
Second	1	0.01 M NaOH	18	23	[9]
Not stated (presumed first)	2	2.5 M NaOH, 9.7 M HCl	3 (x 2)	100	[10]
First	2	Water, 0.36 M $Al(NO_3)_3$	4 + 24	25	[11]
First	2	Water, Al anodizing wastewater / 0.7 M H_2SO_4	4 (x 2)	25 - 60	[12]
First	1	NaOH (1.25 M, ultrasound-assisted)	0.67	70	[13]
Not stated (presumed first)	2	Water, Al anodizing wastewater / 1.77 M H_2SO_4	3 (x 2)	80	[14]

Table C3. Composition of SPL from different common smelter cell types [15].

Chemical species (mass %)	Cell type A type prebake	B type prebake	Söderberg
Fluorides	10.9	15.5	18
Cyanides (mg·kg^{-1})	680	4480	1040
Total aluminium	13.6	11	12.5
Metallic aluminium	1	1	1.9
Carbon	50.2	45.5	38.4
Sodium	12.5	16.3	14.3
Calcium	1.3	2.4	2.4
Iron	2.9	3.1	4.3
Lithium	0.03	0.03	0.6
Titanium	0.23	0.24	0.15
Magnesium	0.23	0.09	0.2

Mixing of caustic and acidic leachates and precipitation

Table C4. Masses of precipitate attained from combination of 250 mL caustic leachate and 250 mL acidic leachate, maintaining pH of ~ 3.

Sample	Precipitate mass (g)
A <1.18 mm	0.1039
A 1.18–9.51 mm	0.0993
B <1.18 mm	0.0661
B 1.18–9.51 mm	0.0929
C <1.18 mm	0.0748
C 1.18–9.51 mm	0.0759

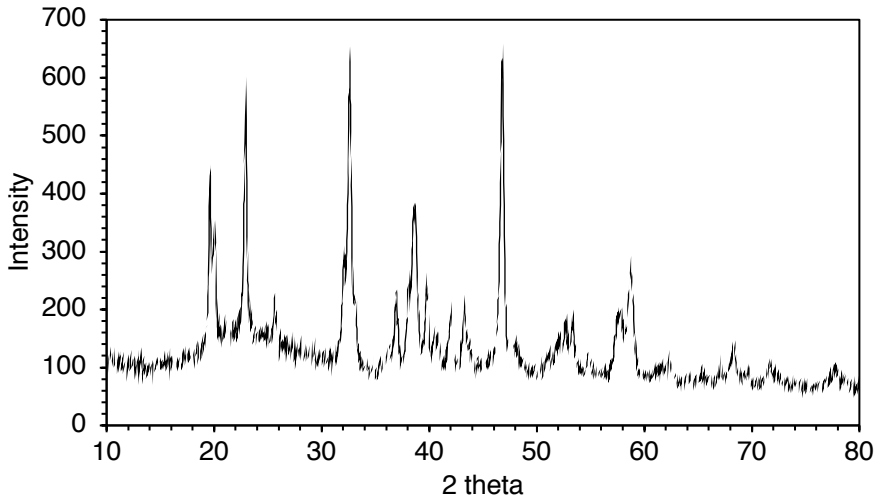

Fig. C29. PXRD spectrum of precipitate obtained by mixing caustic and acidic leachates from treatment of sample A, 1.18–9.51 mm fraction.

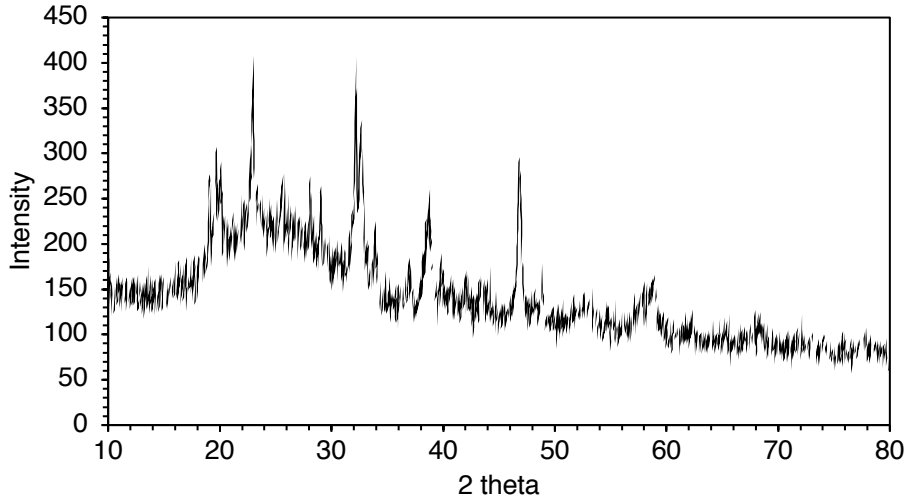

Fig. C30. PXRD spectrum of precipitate obtained by mixing caustic and acidic leachates from treatment of sample B, <1.18 mm fraction.

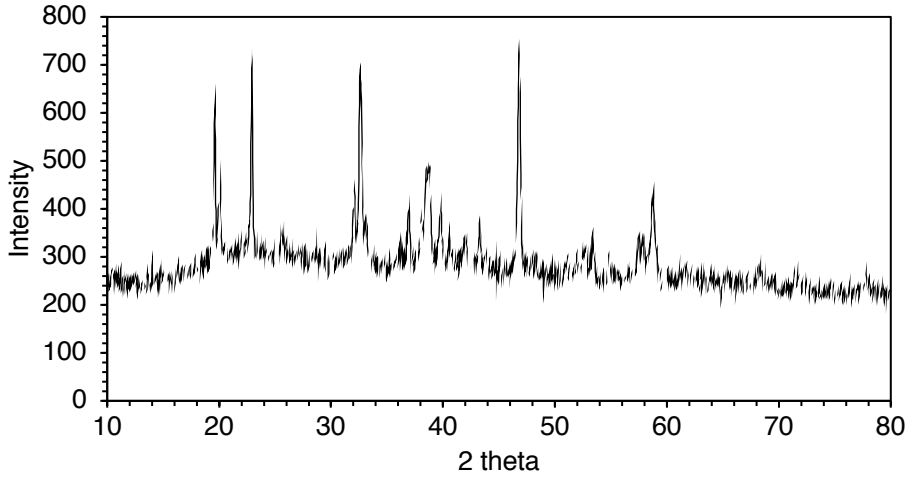

Fig. C31. PXRD spectrum of precipitate obtained by mixing caustic and acidic leachates from treatment of sample C, <1.18 mm fraction.

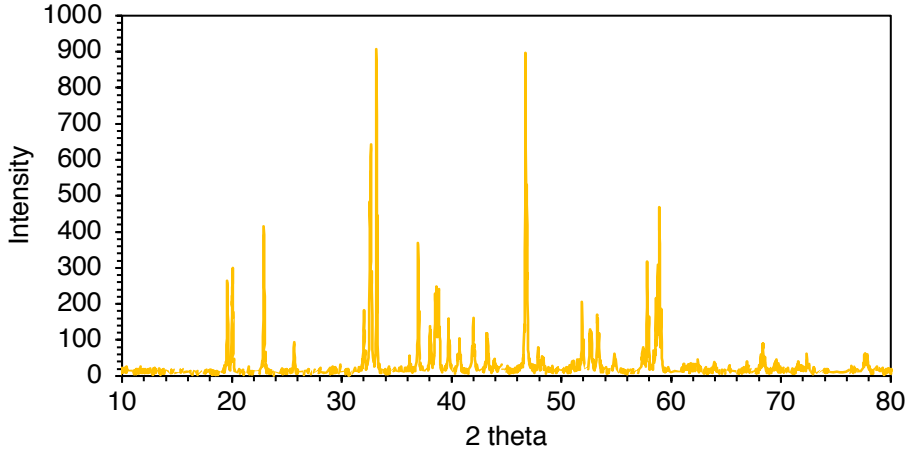

Fig. C32. Literature PXRD spectrum of cryolite from the ICDD for comparison [16].

Full Technicoeconomic analysis

A technicoeconomic analysis was performed for the installation of the proposed adsorption technology within the framework of the existing LCLL process, thereby converting the plant to produce synthetic cryolite, in addition to fluorspar. Costing was performed for both start-up, or fixed-capital expenditure (CAPEX), and continuous running of the technology, or working-CAPEX.

Literature sources and models used to estimate costs

A number of equipment costs were derived from a technical report on the commissioning and installation of a large IX system in North America for the removal of perchlorate from contaminated groundwater in 2013 by Rine et al. *[17]. Although the remit was different to this study and the capacity much lesser (rated at 7.57 $m^3 \cdot min^{-1}$ water treated, verses the required 23.8 $m^3 \cdot min^{-1}$), this was the most appropriate and recent fully-costed system that could be found in the literature. It should be noted that, despite the scale of the proposed system, there have been many much larger schemes previously designed and built (1970s), with capacities in the region of 657-789 $m^3 \cdot min^{-1}$ [18], so the scale of the technology is not unprecedented. However, no detailed costing was available for these projects and the economics of design, commissioning and construction are likely to be significantly different in the present day [19]. The costs derived from [17] have been adjusted to account for inflation, by multiplying by a factor of 1.13.*

It is well known in engineering project management that the relationship between the scale of the design and the cost of design, building and installation is not directly proportionate, because of economies of scale. As a result, for several cost factors, the scale-up formula developed by Peters et al. *has been used [19]. This states that if the cost of a given factor with a known capacity is available, then the cost of an equivalent unit with X times the capacity of the original will be $X^{0.6}$ times the cost of the initial unit. This formula, whilst accepted to be an oversimplification, has been found to be accurate within a tenfold range of capacity (this proposed system is ~3 times larger than that described in Rine* et al. *[17] in terms of water throughput).*

A more detailed costing model for implementation of an IX system, also based on perchlorate removal, has been developed by the US EPA. This is a full computer programme and requires inputs to calculate precise values, which are not possible to estimate from this study. However, certain model parameters are stated in the accompanying document "Work Breakdown Structure-Based Cost Model for Ion Exchange Treatment of Perchlorate in Drinking Water" [20] and can be more easily incorporated into the technicoeconomic analysis. Examples are estimates for shipping costs for bespoke pieces of equipment in North America.

Where possible, estimates for costs, using one of the methods stated, were corroborated by a second estimation, using an additional model. One of the most useful simple techniques for this purpose is the use of "Lang" factors [21]. The premise behind these is that if the cost of major pieces of purchased equipment is known, or reliably estimated, the costs of the other aspects of fixed-CAPEX can be predicted using simple ratios of the equipment value. No major discrepancies (>20%) were found between this model and other estimates. Where there were two or more feasible methods for deriving a cost, the method which calculated the greater expense was chosen.

All costs were converted from US$ to £ by multiplying by a factor of 0.77. All international shipping prices included Canadian customs duty (4%) and goods and services tax (5%). All road freight costs were calculated on the basis of a journey between Montreal port and Rio Tinto Alcan, Jonquière (290 miles x £2.79·mile^{-1}) and assuming trucks can carry 22.7 tonnes of goods (£35.70·T^{-1}).

Estimation of margins of error associated with costs

The various values inputted into the technicoeconomic analysis were derived from the experimental data in this thesis, in addition to the sources and models described in the preceding section. Attempting to accurately propagate the error margins from these multiple sources would be an extremely complex process. Therefore the approach to error estimation followed the AACE International Recommended Practice Cost Estimate Classification System (18R-97) [22]. This framework considers the project stage-gate (projects are grouped into one of five classes, depending on how close they are to full-scale completion). From the AACE classification matrix, this project currently sits in Class 4 ("study of feasibility" stage) and therefore, the expected accuracy of cost estimates is -30% to +50%).

Table C5. *Predicted fixed-CAPEX for implementation of the proposed IX technology into the existing LCLL system.*

Factor	Unit	Price per unit (£)	Units required	Sub-total (£ x 10^3)	Shipping (£ x 10^3)	Total cost (£ x 10^3)	Reference(s)	Notes
Major equipment								
Ion-exchange vessels (18 x 30 m^3)	*m^3*	*2,601*	*540*	*1,405*	*105.0*	*1,510*	*Basic cost taken from Rine* et al. *[17], scaled up using IAEA formula [23] and inflation 2013-2020. Shipping calculated from EPA [20] (£20.33 per cubic metre)*	*The IAEA have developed a specific formula for scaling up the costs of IX reactors, used in this instance*
$LaCl_3$ mixing and holding tank, 114 m^3	*m^3*	*512*	*114*	*58.16*	*2.309*	*60.47*	*Basic cost taken from Rine* et al. *[17], scaled up using Peters* et al. *0.6 power law [19]. Shipping calculated from EPA [20]*	*EPA shipping estimate is £20.33 per m^3*
Pumps (large)	*8.33 $m^3 \cdot min^{-1}$ pump*	*6,337*	*3*	*19.01*	*1.824*	*20.84*	*Quote from Absolute Water Pumps for electric centrifugal pumps, 20 horse power. Shipping calculated from EPA [20] (£608 per large pump)*	*Calculated to be capable of dealing with total flow rate of >15.9 $m^3 \cdot min^{-1}$ (pumping of mixed leachate to IX columns)*
Pumps (small)	*1.38 $m^3 \cdot min^{-1}$ pump*	*1,907*	*18*	*34.33*	*10.94*	*45.27*	*Quote from Absolute Water Pumps for electric centrifugal pumps, 3.0 horse power. Shipping calculated from EPA [20] (£608 per large pump)*	*Calculated to be capable of dealing with total flow rate of >23.8 $m^3 \cdot min^{-1}$ (pumping of mixed leachate and NaOH eluent through IX columns)*
Installation of equipment	*-*	*-*	*-*	*606.1*	*0*	*606.1*	*30% proportion of total equipment and chemicals spend (Rine* et al. *[17])*	*Peters* et al. *similarly suggest a proportion of 28.5% is sensible*
Chemical reagents								
MTS-9501	*m^3*	*10,000*	*260.4*	*2,604*	*0*	*2,604*	*Personal communication from resin manufacturer*	*Delivery by road from US included in estimate*
$LaCl_3.7H_2O$ for pre-loading	*T*	*1,373*	*78*	*107.0*	*71.71*	*178.7*	*Quote from Ganzhou Wanfeng Advanced Materials Technology, Jiangxi, China (FOB price). Bulk freight shipping quote from World Freight Rates (Shanghai to Montreal, £886·tonne^{-1})*	*99.95% purity*
Extra NaOH for elution cycles	*T*	*66.1*	*93.10*	*6.154*	*0*	*6.154*	*Rine* et al. *[17]*	*Price of 25% solution, including shipping within North America*
Other direct plant costs								
Instruments (pH meters)	*probe*	*109*	*25*	*2.725*	*0.195*	*2.920*	*Quote from Omega for industrial-grade, heavy-duty retractable PTFE electrode with lifespan of >16 months. Shipping calculated from EPA [20]*	*EPA shipping estimate is £7.80 for small electrical unit. 1 electrode per IX column outlet plus extras for inlet leachate feed and standbys for calibration etc.*
Instruments (fluoride ISEs)	*probe*	*350*	*25*	*8.750*	*0.195*	*8.945*	*Quote from Turtle Tough for industrial-grade, heavy-duty retractable PTFE electrode with lifespan of >12 months. Shipping calculated from EPA [20]*	*EPA shipping estimate is £7.80 for small electrical unit. 1 electrode per IX column outlet plus extras for inlet leachate feed and standbys for calibration etc.*
Piping and valves	*-*	*-*	*-*	*668.5*	*0*	*668.5*	*Lang factors [21]*	*Typically 31% of major equipment spend*
Electrics (control system)	*-*	*variable*	*30*	*439.0*	*2.400*	*441.4*	*Basic cost taken from Rine* et al. *[17], scaled up using Peters* et al. *0.6 power law [19]. Shipping calculated from EPA [20]*	*EPA shipping estimate is £80 per high-end unit*
Electricity for MTS9501 La preloading cycle	*kWhr*	*0.08701*	*1659*	*0.1444*	*0*	*0.1444*	*Electricity cost (kWhr·m^{-3} water pumped) estimated from Rine* et al. *[17], assuming equivalent efficiency*	*Based on continuous pumping of La^{3+} solution through IX system for 4 hr. Assumptions for electricity usage are as per running costs*
Buildings	*-*	*-*	*-*	*474.4*	*0*	*474.4*	*Lang factors [21]*	*Typically 22% of major equipment spend*
Yard improvement and H&S	*-*	*-*	*-*	*215.6*	*0*	*215.6*	*Lang factors [21]*	*Typically 10% of major equipment spend*
Caustic recycling and cryolite precipitation system (estimate)	*-*	*-*	*-*	*2,000*	*0*	*2,000*		*The main research article explains why accurate estimations of this cost are difficult*
Total direct plant cost	*-*	*-*	*-*	*-*	*-*	***8,824***		
Construction and engineering	*-*	*-*	*-*	*1,423*	*0*	*1,423*	*Lang factors [21]*	*Typically 66% of major equipment spend*
Total direct and indirect cost	*-*	*-*	*-*	*-*	*-*	***10,250***		
Contractor fee	*-*	*-*	*-*	*433.5*	*0*	*356.8*	*Peters* et al. *[19]*	*Typically ~4% of fixed-CAPEX*
Contingency	*-*	*-*	*-*	*338.1*	*-*	*321.0*	*Peters* et al. *[19] and EPA [20]*	*Standard recommended contingency figure is 2% of fixed-CAPEX x 1.5 for "high-risk" technology (anion-exchange)*
TOTAL FIXED-CAPEX	***-***	***-***	***-***	***-***	***-***	***10,920***		*Low estimate: 7,644; High estimate: 16,380*

Table C6. *Predicted working CAPEX for implementation of the proposed IX technology for a single year of operation.*

Factor	**Unit**	**Price per unit (£)**	**Units required**	**Sub-total (£ x 10^3)**	**Shipping (£ x 10^3)**	**Total cost (£ x 10^3)**	**Reference(s)**	**Notes**
$LaCl_3.7H_2O$	T	1,373	10.73	14.73	9.870	24.60	Shipping calculated as per start-up costs.	Quantity required based on La^{3+} leaching data in static kinetic experiments (Chapter 3)
CaF_2	T	252.3	9,830	2,480	715.9	3,196	FOB price taken from averaged data from Industrial Minerals 2019-20. Bulk freight shipping quote from World Freight Rates (Tampico, Mexico to Montreal, £71.49·tonne^{-1})	This refers to the additional CaF_2 that would have to be purchased by the plant for Al smelting, in the LCLL process partial switch-over from CaF_2 to cryolite production.
Electricity	kWhr	0.08701	333,200	28.99	0	28.99	Electricity cost (kWhr·m^{-3} water pumped) estimated from Rine et al. [17], assuming equivalent efficiency	
Consumables and small equipment replacement	various	various	-	164.3	0	164.3	Estimated from Rine et al. [17], scaled up according to increased plant throughput (m^3 water·min^{-1}). Peters et al. [19] 0.6 power law not applied	Replenishment of MTS9501 not included (estimated lifespan 10-15 yr)
Increased aqueous waste treatment/disposal	m^3	0.007132	927,000	6.611	0	6.611	Disposal/treatment cost estimated from Rine et al. [17], scaled up according to increased plant throughput (m^3 water·min^{-1}). Peters et al. [19] 0.6 power law not applied.	Assumes 3% total throughput increase required, due to IX column washing between cycles [24]
Permanent staff	Experienced IX engineer	107,400	1	107.4	0	107.4	Tentatively based on estimates by Rine et al. [17] (1.5-2 persons required for running of 7.57 m^3·min^{-1} system) and Koon and Kaufman [17] (2.5 persons required for 26.3 m^3·min^{-1} system, FTE). Salary estimates provided by Neuvco (averaged data for Canada from >10 sources)	Salaries include Quebec Pension Plan (5.10%) and Employment Insurance (2.268%)
Permanent staff	IX shift-leader	48,320	1	48.32	0	48.32		
Permanent staff	IX technician	37,580	1	37.58	0	37.58		
Caustic recycling and cryolite precipitation system (estimate)	-	-	-	500	0	500.0		Main working cost will be the cryolite precipitant, most likely $Al_2(SO_4)_3$, which is economically priced (<£150·T^{-1})
TOTAL WORKING-CAPEX (yr^{-1})	-	-	-	-	-	**4,096**		Low estimate: 2,867; High estimate: 6,144
Estimated sales from cryolite production	T	732	9083	-6,649	324.2	-6,325	FOB price taken from averaged data from Industrial Minerals 2019-20. Bulk freight shipping quote from World Freight Rates (Montreal, £71.49·T^{-1})	
TOTAL VALUE RETURNED (yr^{-1})	-	-	-	-	-	**-2,229**		

Selected calculations

[A] *The theoretical required throughput of water through the IX circuit was calculated as follows:*

◆ *The LCLL plant processes 80,000 T SPL per year [25] and this capacity should be maintained, if possible.*

◆ *The SPL will be leached with the experimental ratio of 500 mL total lixiviant solution volume to 5 g SPL = 8bn L leachate pumped per year (the ratio currently used by Rio Tinto Alcan may be lower than this, but no data is freely available).*

◆ *The fluoride and Al must also be eluted from the IX columns with 1M NaOH solution. Chapter 4 demonstrates this may be achieved with <50% of the BVs required to load the resin (Figures 4.5 to 4.7), so multiply required capacity by 1.5 = 12bn L total aqueous solution per year.*

◆ *Add 3% extra water for "sweetening off" and washing between cycles [24] = 12.36 bn $L \cdot yr^{-1}$ total capacity. ("sweetening off" refers to the practice of conserving the 1-2 BVs of eluent after the column breakthrough capacity is reached, which displace the inlet solution from the column. These BVs generally have a high concentration of the chemical species being recovered).*

◆ *Plant will run on a 24 hr cycle for 360 days per year.*

$(12.36 \times 10^{10}) / 360 / 24 / 60 = 2.38 \times 10^{4}$ $L \cdot min^{-1}$ = ***$23.8\ m^3 \cdot min^{-1}$****.*

[B] *The total combined volume of the IX vessels required for the plant was calculated as follows:*

◆ *Assume that the average $[F^-]$ in the inlet SPL solid waste-stream is 11% of the total mass, as per Chapter 4 (Table 4.3). Assume 95% of the fluoride is solubilised by the combined leaching treatment. This equates to 8,360 T fluoride solubilised per year.*

◆ *Each IX column to be fully-loaded with fluoride and "sweetened off" ready for the elution cycle in a 4 hr period (demonstrably possible from experimental data in Chapter 3)*

8,360 x 1,000 / 360 / 24 / 6 = 3,870 kg fluoride to be adsorbed per 4 hr cycle.

◆ *From dynamic experiments in Chapter 4, the average dynamic q_e value for uptake of fluoride by La-MTS9501 was ~34.5 $mg \cdot g^{-1}$. This can be multiplied by an experimentally-determined ratio to convert from dry mass to wet settled volume (0.3259) and equates to a capacity of 11.2 $kg \cdot m^{-3}$.*

3870 kg / 11.2 $kg \cdot m^{-3}$ = 344 m^3 La-MTS9501.

Add 1% capacity to account for slightly incomplete counter-flow regeneration.

344 x 1.01 = 348 m³ active La-MTS9501 required.

◆ *Each IX column to be eluted, regenerated and washed, ready for the next loading cycle, in a 2 hr period (see **[A]**). Two columns will operate in tandem, as shown in Figure C33.*

*348 x 1.5 = **522 m³ total La-MTS9501 required** (hence 18 x 30 m³ vessels will be purchased, for 540 m³ total column volume).*

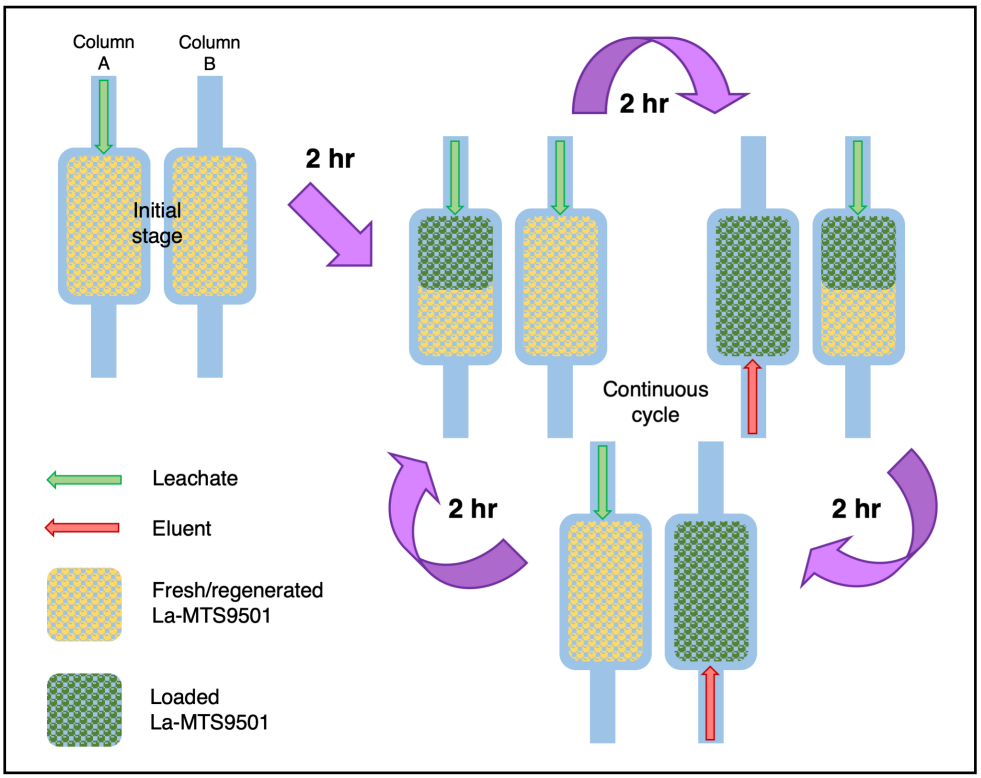

***Fig. C33.** Showing how a pair of IX columns would work in tandem for a continuous loading/elution cycle. The proposed plant would incorporate nine sets of paired columns, to satisfy throughput requirements.*

***[C]** The required flow rate for fluoride-loading and elution of the columns was calculated as follows (this assumes that the flow rates for loading and elution will be equivalent, as they were in Chapters 3 and 4):*

◆ *The theoretical throughput of water for the plant is 23.8 $m^3 \cdot min^{-1}$. = 14,300 $m^3 \cdot hr^{-1}$.*

◆ *Divide by the total volume of La-MTS9501. 1,430 / 522 = **2.74 $BV \cdot hr^{-1}$**.*

***[D]** Puromet™ MTS9501 resin is sold in hydrated Na-form. The volume of resin to be purchased was calculated as follows:*

◆ *From **[B]**, 522 m³ total La-MTS9501 is required. Convert to dm³ and multiply by conversion factor of 0.3259*

$(5.22 \times 10^5) \times 0.3259 = 1.700 \times 10^5$ kg total La-MTS9501 required.

◆ *La-MTS9501 dry mass can be converted to equivalent Na-MTS9501 dry mass via an experimentally-determined ratio of 0.6701.*

1.700 x 10^5 x 0.6701 = ***1.139 x 10^5 kg Na-MTS9501 required****.*

Na-MTS9501 dry mass can be converted to hydrated mass as-received by an experimentally-determined ratio (0.3870). The experimentally-determined calculated density of Na-MTS9501 matches the manufacturer quoted figure (1.130 g·cm^{-3}) [26].

(1.139 x 10^5) / 0.3870 /1.130 = 2.604 x 10^5 dm^3 = ***260.4 m^3 Na-MTS9501 purchased.***

[E] *The potential LCLL cryolite production capacity were estimated as follows (no data was available from Rio Tinto Alcan):*

◆ *Assume a throughput of 80,000 T SPL per year [25], with [F^-] in the inlet of 11% of the total mass.*

◆ *With implementation of the proposed technology, data from Chapter 4 (XRD spectra) suggest that fluoride solubilisation is >95%.*

80,000 x 0.11 x 0.95 = 4,932 T fluoride solubilised per year.

◆ *Data from Chapter 4 (Figure 4.7) suggest that ~59% of the solubilised fluoride could be recovered as a purified aqueous stream. A recent literature study suggests that conversion to cryolite from such a stream can operate with close to 100% efficiency [14].*

4,932 x 0.59 x (209.9 / 114.0) = ***9,083 T cryolite produced.***

[F] *The mass of metallurgical-grade CaF_2 that would have to be purchased in lieu of the material currently produced by the LCLL process and recycled into the H-H process was estimated as follows:*

◆ *Data from Chapter 4 (Table 4.3) suggest that the extent of fluoride dissolution by caustic leaching only would be ~97% of that achieved by the full leaching treatment (It should be noted that this is much higher than is suggested by the literature [9, 10]).*

◆ *Assume that once the IX system is incorporated into the plant, the fraction of column eluent not used for cryolite precipitation can be diverted back to the CaF_2 production stream (therefore only ~59% capacity is actually lost)*

80,000 x 0.11 x 0.95 x 0.97 = 8,109 T fluoride solubilised per year by water and caustic leaching alone

80,000 x 0.11 x 0.95 x 0.41 = 3,428 T fluoride that would still be used for CaF_2 production, with the implementation of the IX process

8,109 – 3,428 = 4,682 T fluoride

◆ *Assume the existing recovery efficiency is ~100%, because of years of process optimization (although it is probably lower).*

4,682 x (78.08 / 38.00) = ***9,619 T fluorite to be replaced****.*

Appendix C References

[1] T.J. Robshaw, S. Tukra, D.B.Hammond, G.J. Leggett, M.D. Ogden, "Highly efficient fluoride extraction from simulant leachate of spent potlining via La-loaded chelating resin. An equilibrium study", *Journal of Hazardous Mater*ials, 2019, **361**, 200-209.

[2] T.J. Robshaw, R. Dawson, K. Bonser, M.D. Ogden, "Towards the implementation of an ion-exchange system for recovery of fluoride commodity chemicals. Kinetic and dynamic studies", *Chemical Engineering Journal*, 2019, **367**, 149-159.

[3] G.Y. Yan, T. Viraraghavan, M. Chen, "A new model for heavy metal removal in a biosorption column", *Adsorption Science and Technology*, 2001, **19**, 25-43.

[4] H.C. Thomas, "Heterogeneous ion exchange in a flowing system", *Journal of the American Chemical Society*, 1944, **66**, 1664-1666.

[5] Y.H. Yoon, J.H. Nelson, "Application of gas adsorption kinetics I. A theoretical model for respirator cartridge service life", *American Industrial Hygiene Association Journal*, 1984, **45**, 509-516.

[6] E.J. Billo, *Excel for Chemists: A Comprehensive Guide*, 2nd ed., Wiley, Hoboken, New Jersey, 2004.

[7] B. Mazumder, "Chemical oxidation of spent cathode carbon blocks of aluminium smelter plants for removal of contaminants and recovery of graphite value", *Journal of Scientific and Industrial Research*, 2003, **62**, 1181-1183.

[8] T.K. Pong, R.J. Adrien, J. Besida, T.A. O'Donnell, D.G. Wood, "Spent potlining - A hazardous waste made safe", *Process Safety and Environmental Protocol*, 2000, **78**, 204-208.

[9] B.I. Silveira, A.E. Dantas, J.E. Blasquez, R.K.P. Santos, "Characterization of inorganic fraction of spent potliners: evaluation of the cyanides and fluorides content", *Journal of Hazardous Materials,* 2002, **89**, 177-183.

[10] Z.-N. Shi, W. Li, X.-W. Hu, B.-J. Ren, B.-L. Gao, Z.-W. Wang, "Recovery of carbon and cryolite from spent pot lining of aluminium reduction cells by chemical leaching" *Transactions of the Nonferrous Metals Society of China*, 2012, **22**, 222-227.

[11] D.F. Lisbona, K.M. Steel, "Recovery of fluoride values from spent pot-lining: Precipitation of an aluminium hydroxyfluoride hydrate product", *Separation and Purification Technology*, 2008, **61**, 182-192.

[12] D.F. Lisbona, C. Somerfield, K.M. Steel, "Leaching of spent pot-lining with aluminum anodizing wastewaters: Fluoride extraction and thermodynamic modeling of aqueous speciation", *Industrial and Engineering Chemistry Research*, 2012, **51**, 8366-8377.

[13] J. Xiao, J.Yuan, Z.L. Tian, K. Yang, Z. Yao, B.L. Yu, L.Y. Zhang, "Comparison of ultrasound-assisted and traditional caustic leaching of spent cathode carbon (SCC) from aluminum electrolysis", *Ultrasonic Sonochemistry* 40, 21-29 (2018)

[14] X.M. Li, W.D. Yin, Z. Fang, Q.H. Liu, Y.R. Cui, J.X. Zhao, H. Jia, "Recovery of Carbon and Valuable Components from Spent Pot Lining by Leaching with Acidic Aluminum Anodizing Wastewaters", *Metallurgical Materials Transactions B - Process Metallurgy and Materials Processing Science*, 2019, **50**, 914-923.

[15] G. Holywell, R. Bréault, "An overview of useful methods to treat, recover, or recycle spent potlining", *Journal of the Minerals Metals and Materials Society*, 2013, **65**, 1441-1451.

[16] T.G. Fawcett, F. Needham, C. Crowder, S. Kabekkodu, “Advanced materials analysis using the powder diffraction file”, 10th National Conference on X-ray Diffraction and ICDD Workshop. Shanghai, China, 2009.
[17] J. Rine, E. Coppola, A. Davis, *FINAL REPORT. Demonstration of Regenerable, Large-scale Ion Exchange System Using WBA Resin in Rialto, CA*, Applied Research Associates/ESTCP, Panama City, 2012.
[18] J.H. Koon, W.J. Kaufman, *Optimization of Ammonia Removal by Ion Exchange Using Clinoptilolite*, Environmental Protection Agency/University of California, Berkley, 1971.
[19] M.S. Peters, K.D. Timmerhaus, R.E. West, *Plant Design and Economics for Chemical Engineers,* 5th ed., McGraw-Hill, New York, 2007.
[20] United States Environmental Protection Agency, *Work Breakdown Structure-Based Cost Model for Ion Exchange Treatment of Perchlorate in Drinking Water*, EPA Office of Water, Washington D.C., 2019.
[21] H.J. Lang, “Cost Relationships in Preliminary Cost Estimation”, *Chemical Engineering*, 1947, **54**, 117-121.
[22] AACE International, *Cost Estimate Classification System – As Applied in Engineering, Procurement and Construction for The Process Industries*, AACE, Morgantown, 2020.
[23] International Atomic Energy Agency, *Operation and Control of Ion-Exchange Processes for Treatment of Radioactive Wastes*, IAEA, Vienna, 1967.
[24] C.E. Harland, *Ion exchange: theory and practice*, 2nd ed., Royal Society of Chemistry, Cambridge, 1994.
[25] L. Birry, S. LeClerc, S. Poirier, “The LCL&L process: A sustainable solution for the treatment and recycling of spent potlining”, *Light Metals*, 2016, 467-471.
[26] Purolite, “S950 Macroporous Aminophosphonic Chelating Resin (For the selective removal of toxic metal from aqueous solutions). Technical Data” [online], http://www.reskem.com/wp-uploads/2015/04/purolite-s950.pdf, 2017.

APPENDIX D

"Calcium-loaded hydrophilic hypercrosslinked polymers for extremely high defluoridation capacity via multiple uptake mechanisms"

SUPPORTING INFORMATION

Thomas J. Robshaw, Alex M. James, Deborah B. Hammond, Jake Reynolds, Robert Dawson and Mark D. Ogden

Diagram of dynamic experiment setup

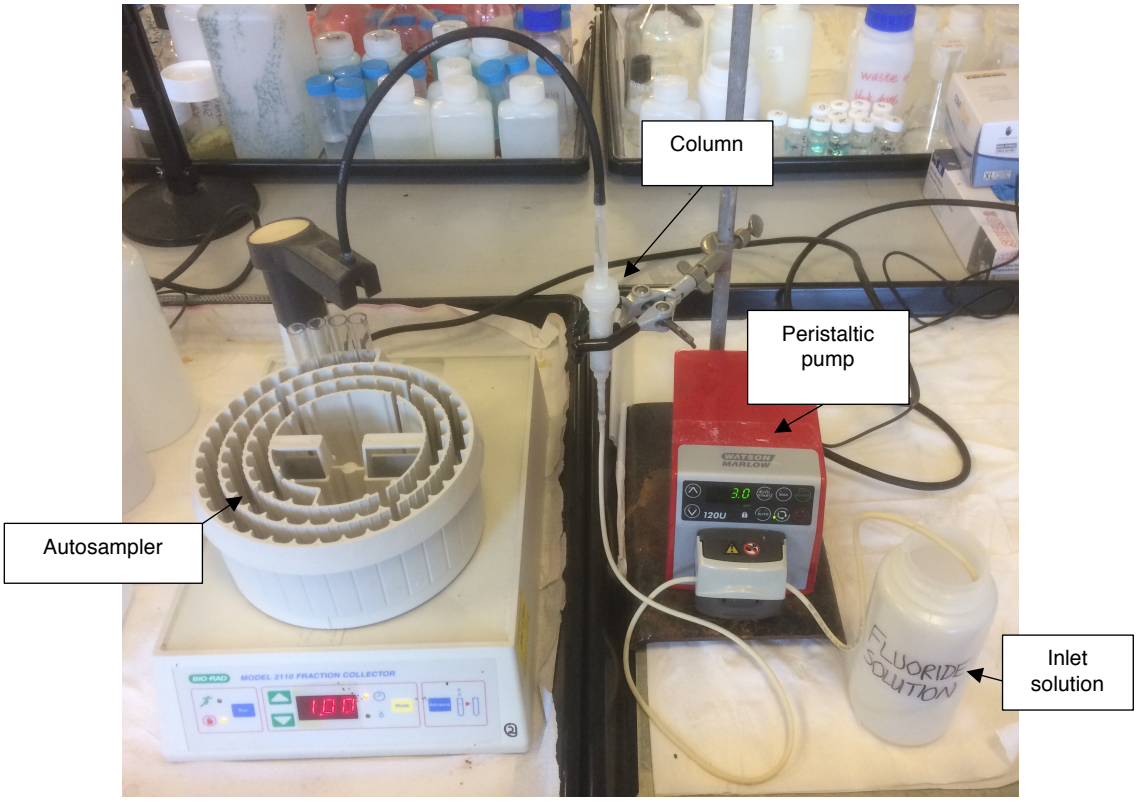

Fig. D1. Photograph of apparatus used for reverse-flow dynamic column experiment.

Photographs of polymer networks

Fig. D2. Photographs of HHCP1 (left), HHCP1-Ca (centre) and HHCP1, NaOH treated (right).

Fig. D3. Photographs of HHCP2 (left), HHCP2-Ca (centre) and HHCP2, NaOH treated (right).

Fig. D4. Photographs of HCP1 (left), HCP1, $Ca(OH)_2$ treated (centre) and HCP1, NaOH treated (right), showing the absence of colour change.

Scanning electron micrographs of polymer networks

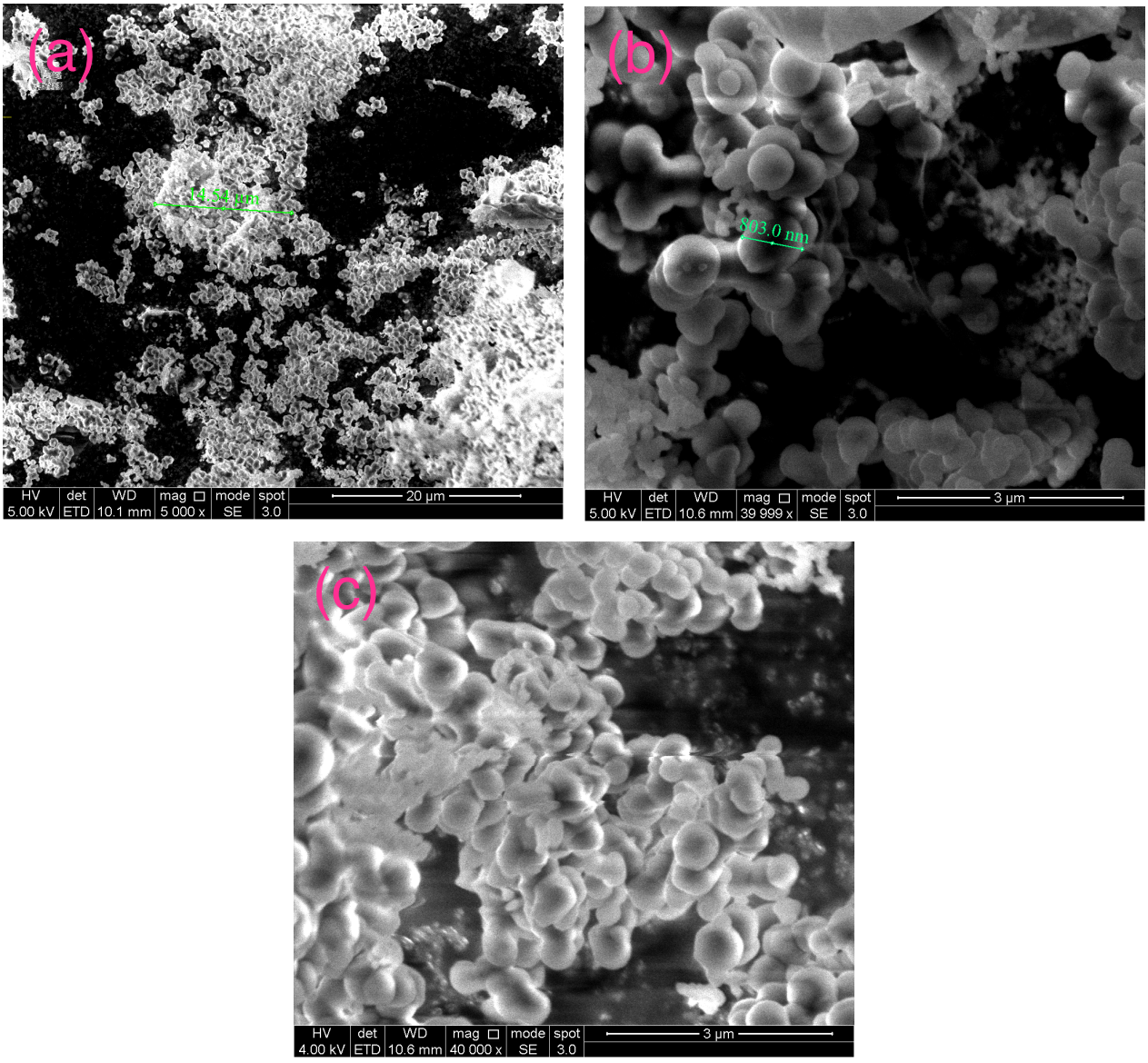

Fig. D5. (a) HHCP1 at low magnification. Measured diameter = 14.54 µm. **(b)** HHCP1 at high magnification. Measured diameter = 803.0 nm. **(c)** HHCP1-Ca at high magnification.

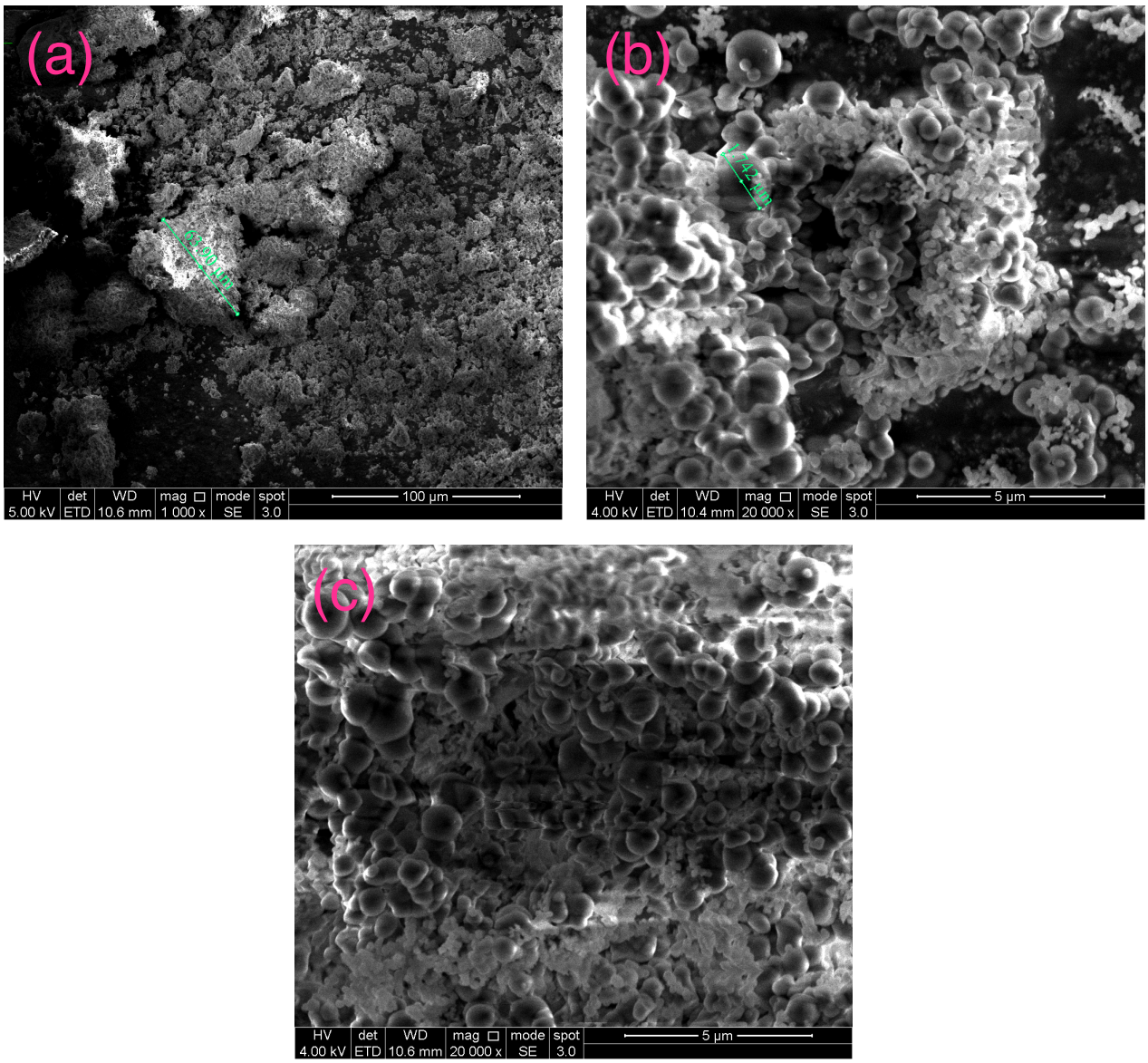

Fig. D6. (a) HHCP2 at low magnification. Measured diameter = 63.90 µm. **(b)** HHCP2 at high magnification. Measured diameter = 1.742 µm. **(c)** HHCP2-Ca at high magnification.

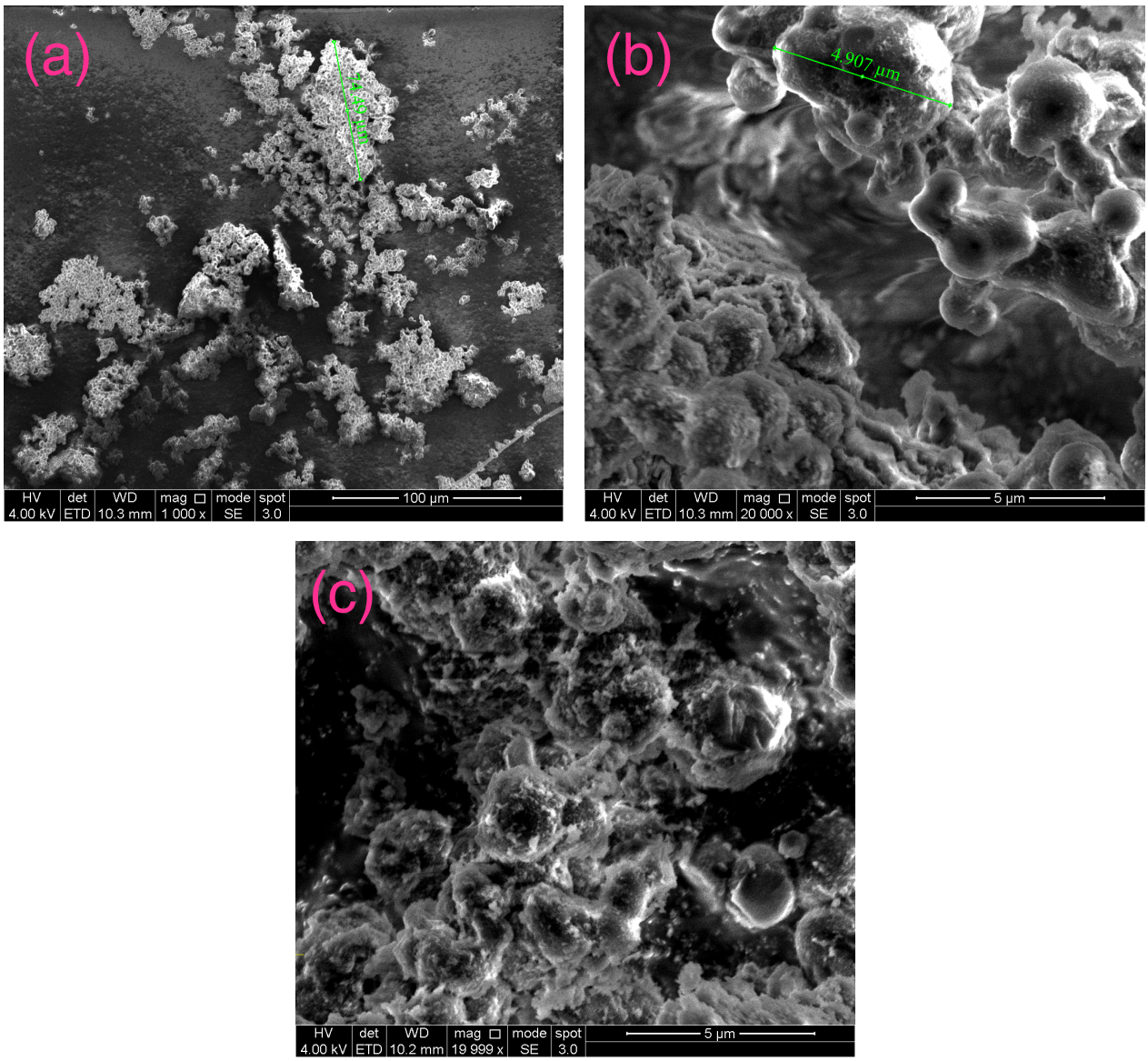

Fig. D7. (a) HCP1 at low magnification. Measured diameter = 74.49 µm. **(b)** HCP1 at high magnification. Measured diameter = 4.907 µm. **(c)** HCP1 + $Ca(OH)_2$ at high magnification.

Calculations for theoretical Ca-loading

The theoretical C and H mass % for the polymers shown in Table 5.1, main article, are based on full crosslinking occurring at every available aromatic carbon in each biphenol unit. Given the differences between theoretical and actual data, these are clearly not realistic structures to base the theoretical maximum Ca-loading capacities on. However, we can add the following modifiers to the theoretical structure: 1. Each HHCP1 biphenol unit includes two partially-reacted crosslinkers. 2. Each HHCP2 unit has four partially-reacted crosslinkers. 3. The Cl and N content of the polymers found in the elemental analysis is in the form of Cl^- and NO_3^- ions. This gives the following theoretical elemental mass % results (Figure D8 and Table D1), which are much closer to the actual results.

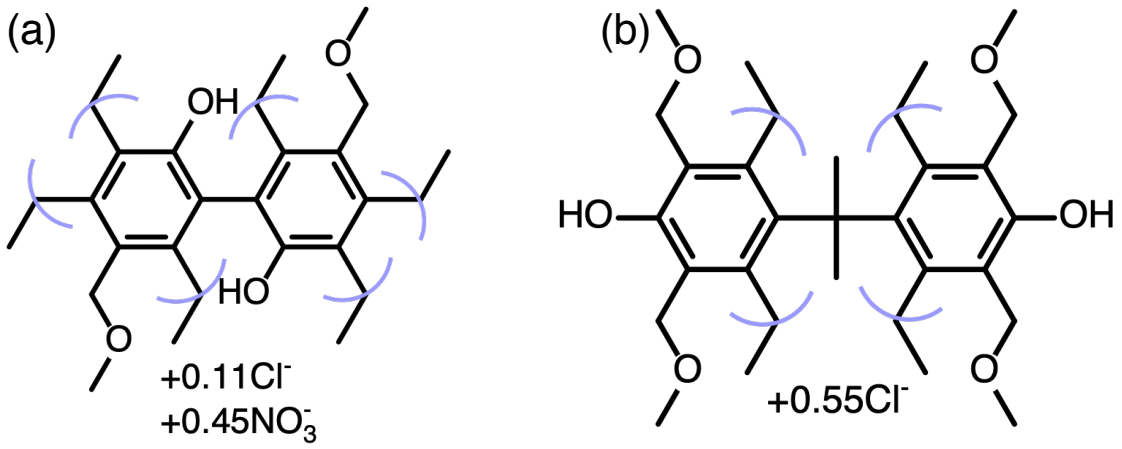

Fig. D8. Approximate structures of biphenol units within **(a)** HHCP1 and **(b)** HHCP2, based on elemental analysis data (Table 5.1, main article).

Table D1. Approximate theoretical elemental composition of HHCP1 and HHCP2, based on the structures proposed in Figure D8. All elements are in units of mass %.

Network	C (% mass)	H	O	Cl	N
HHCP1 (theoretical)	66.7	5.27	25.0	1.14	1.84
HHCP1 (actual)	69.3 ± 0.8	5.33 ± 0.14	Not measured	1.16 ± 0.13	1.84 ± 0.02
HHCP2 (theoretical)	67.0	7.15	21.5	4.35	0
HHCP2 (actual)	65.8 ± 0.1	4.20 ± 0.02	Not measured	4.38 ± 0.16	<0.1

From Table D1, the calculated theoretical concentrations of phenol groups in the materials are 5.85 mmol·g^{-1} for HHCP1 (calculated for $C_{19}H_{18}O_{5.35}N_{0.45}Cl_{0.11}$) and 4.47 mmol·g^{-1} for HHCP2 (calculated for $C_{25}H_{32}O_6Cl_{0.55}$), which are close to the experimental values of 6.34 and 4.57 mmol·g^{-1}. It should be noted that these structures do not account for dehydrogenation and quinonoid formation, or the fact that the polymers immediately start equilibrating with atmospheric gases (CO_2 and H_2O) on exposure to the air [1]. However, we considered them reasonably accurate models to base Ca-loading efficiency on.

Assuming that Ca-loading occurs by the exchange of phenolic protons for -CaOH groups [2], the fully exchanged polymers would exhibit Ca mass % of 17.6 for HHCP1-Ca (calculated for $C_{19}H_{18}O_{7.35}Ca_2N_{0.45}Cl_{0.11}$) and 14.3 for HHCP2-Ca (calculated for $C_{25}H_{32}O_8Ca_2Cl_{0.55}$).

Assuming that Ca-loading is only possible for half of the phenolic protons, the polymers would exhibit Ca mass % of 10.0 for HHCP1-Ca (calculated for $C_{19}H_{18}O_{6.35}CaN_{0.45}Cl_{0.11}$) and 7.92 for HHCP2-Ca (calculated for $C_{25}H_{32}O_7CaCl_{0.55}$). The actual Ca mass % achieved is 9.50 and 6.39 (Table 5.1, main article). However, it is later revealed that a fraction of this is in the form of $CaCO_3$. Therefore, it can

be stated with reasonable confidence that the fraction of phenolic protons in the polymers that actually exchange is <50%.

FT-IR Spectra

Technical note

FT-IR spectra were captured using both a KBr disc method (Perkin Elmer Spectrum 100) and attenuated total refraction (Perkin Elmer UATR2), as it was found that the former technique resulted in better peak intensity at higher wavenumbers, but the latter gave better resolution in the quinonoid stretching region (1,600–1,700 cm^{-1}). All peak assignments are based on KBr disc spectra and we do not make any direct comparisons or deductions based on comparison of the spectra of different polymers run on different instruments.

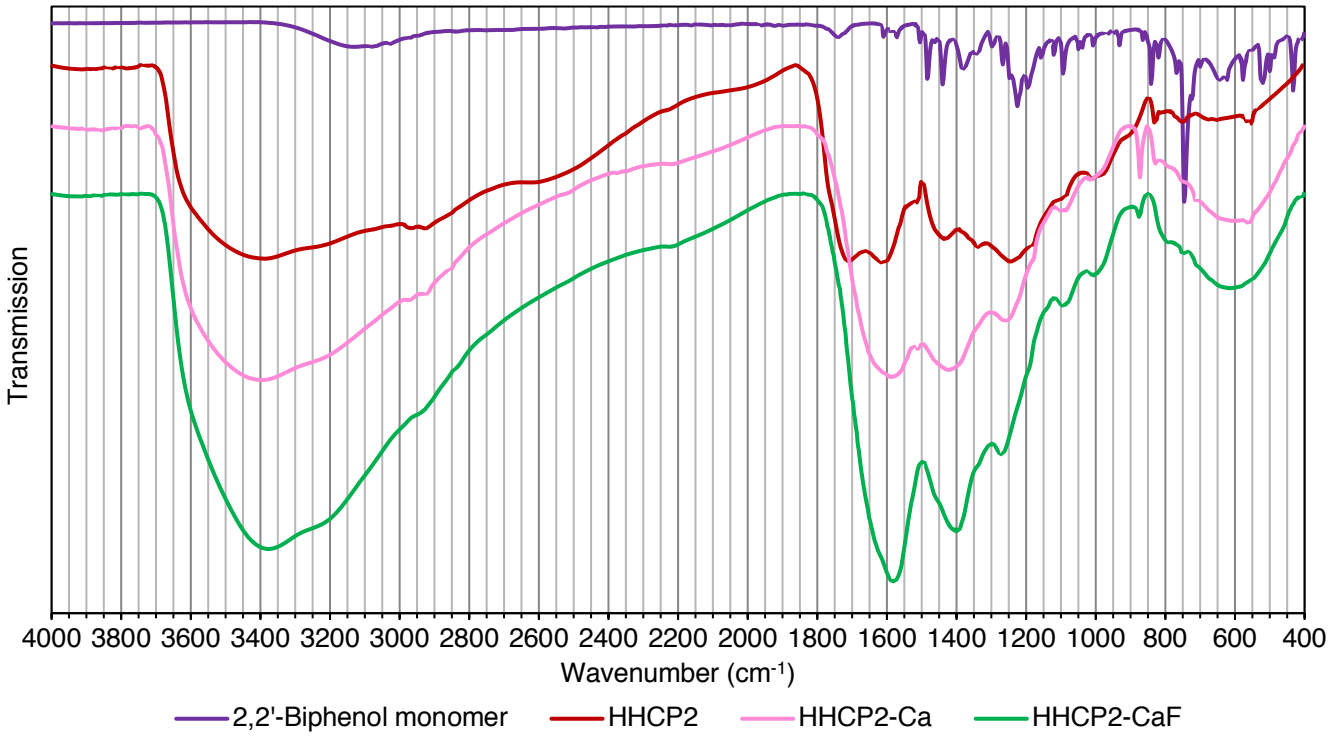

Fig. D9. FTIR spectra of 2,2'-biphenol, HHCP1, HHCP1-Ca and HHCP1-Ca after treatment with 500 $mg \cdot L^{-1}$ fluoride (KBr disc).

Table D2. Peak assignments for 2,2'-biphenol, HHCP1, HHCP1-Ca and HHCP1-Ca after treatment with 500 mg·L^{-1} fluoride.

Sample	Wavenumber (cm^{-1})	Assignment
2,2'-biphenol monomer	3,140	O-H st.
	3,025	Ar C-H st.
	1,735	C=O st. (keto tautomerism)
	1,610, 1,570 and 1,510	Combination bands
	1,480, 1,440 and 1,380	Ar C=C st.
	1,225	Ar C-O st.
	1,195	Ar C-O-H st.
	1,090	Ring breathing
	840 and 745	Ar C-H bend (ortho-substituted)
	640	sp^2 C-H bend (cis alkene, keto tautomerism)
HHCP1	3,400	O-H st. (with H-bonding)
	2,960 and 2,920	sp^3 C-H st.
	1,710 and 1,610	Quinonoid C=C st
	1,510 and 1,440	Ar C=C st.
	1,340	sp^3 C-H bend
	1,245	Ar C-O st.
	1,100	C-O st. (aliphatic ether)
	1,010	Ring breathing
	830 and 750	Quinonoid C-H bend
HHCP1-Ca	1,595	Quinonoid st.
	1,420	Ar C=C st.
	1,255	Ar C-OCa st.
	870	C-O st. (CO_3^{2-})
	600	Ca-O
HHCP1-CaF	1,395	Ar C=C st.
	1,270	Ar C-O st.
	610	Ca-O

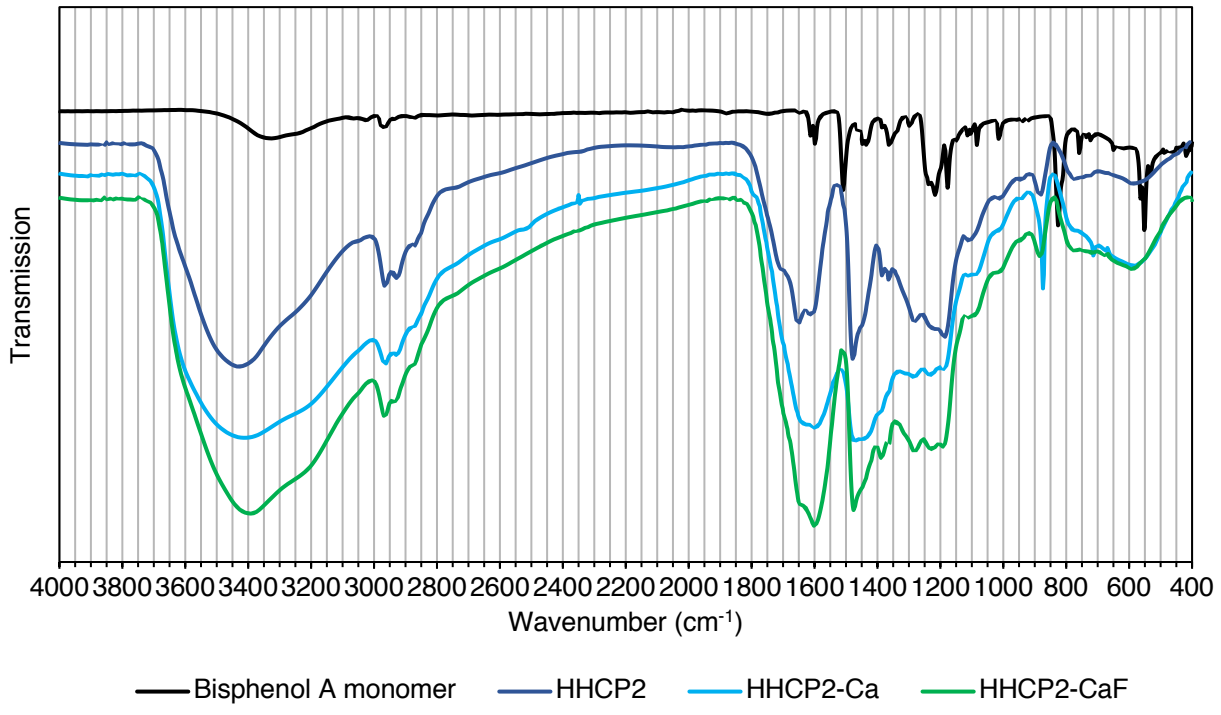

Fig. D10. FTIR spectra of bisphenol A, HHCP2, HHCP2-Ca and HHCP2-Ca after treatment with 500 mg·L^{-1} fluoride (KBr disc).

Table D3. Peak assignments for bisphenol A, HHCP2, HHCP2-Ca and HHCP2-Ca after treatment with 500 mg·L^{-1} fluoride.

Sample	Wavenumber (cm^{-1})	Assignment
Bisphenol A monomer	3,330	O-H st.
	3,025	Ar C-H st.
	2,960	sp^3 C-H st.
	1,750 (w)	C=O st. (keto tautomerism)
	1,610 and 1,600	Combination bands
	1,505, 1,450 and 1,360	Ar C=C st.
	1,300	Ar C-H bend
	1,215	Ar C-O st.
	1,180	Ar C-O-H st.
	1,080 and 1,015	Ring breathing
	825	Ar C-H bend (para-substituted)
	745	Ar C-H bend (para-substituted)
	550	Ring deformation
HHCP2	3,400	O-H st. (with H-bonding)
	2,960 and 2,920	sp^3 C-H st.
	1,710 (shoulder),1,650 and 1,605	Quinonoid C=C st.
	1,480, 1,380 and 1,360	Ar C=C st.
	1,280	Ar C-O st.
	1,185	Ar C-O-H st.
	1,105	C-O st. (aliphatic ether)
	880	Quinonoid C-H bend
HHCP2-Ca	875	C-O st. (CO_3^{2-})
	710	C-O st. (CO_3^{2-})
	590	Ca-O

Note: HHCP2-CaF spectrum is similar to HHCP2-Ca spectrum, due to fluoride-loading being lower than for HHCP1-Ca.

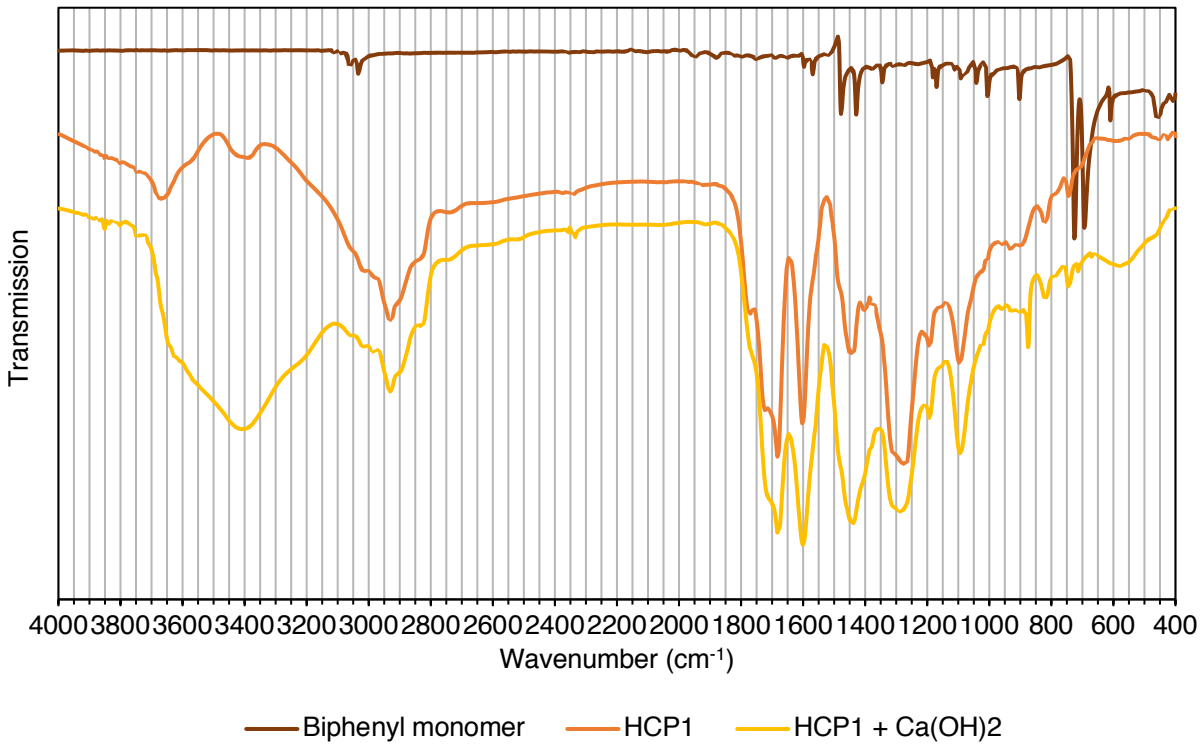

Fig. D11. FTIR spectra of biphenyl, HCP1 and HCP1 after treatment with $Ca(OH)_2$ (KBr disc).

Table D4. Peak assignments for biphenyl, HCP1 and HCP1 after treatment with $Ca(OH)_2$.

Sample	Wavenumber (cm^{-1})	Assignment
Biphenyl monomer	3,060 and 3,030	Ar C-H st.
	1,600 and 1,570	Combination bands
	14,75, 1,430 and 1,340	Ar C=C st.
	1,180 and 1,170	Ar C-H bend
	1,005	Ring breathing
	900 and 725	Ar C-H bend (monosubstituted)
	695, 610 and 460	Ring deformation
HCP1	3,020	sp^2 C-H st.
	2,930	sp^3 C-H st.
	2,825	Aldehyde sp^2 C-H st.
	1,680 and 1,600	Quinonoid st.
	1,440	Ar C=C st.
	1,270	Acyl C-O st. (ester)
	1,190	C-H bend
	1,100	C-O st. (aliphatic ether)
	815	Quinonoid C-H bend
HCP1 + $Ca(OH)_2$	3,400	O-H st. (associated H_2O)
	1,400 (shoulder)	C=O st. (CO_3^{2-})
	875	C-O st. (CO_3^{2-})
	580	Ca-O

Assignments taken from the following references: Andersen & Brecevic [3], Galvan-Ruiz *et al.* [4], Ni & Ratner [5], Steele & Lippincott [6], Ullah *et al.* [7] and Vinodh *et al.* [8].

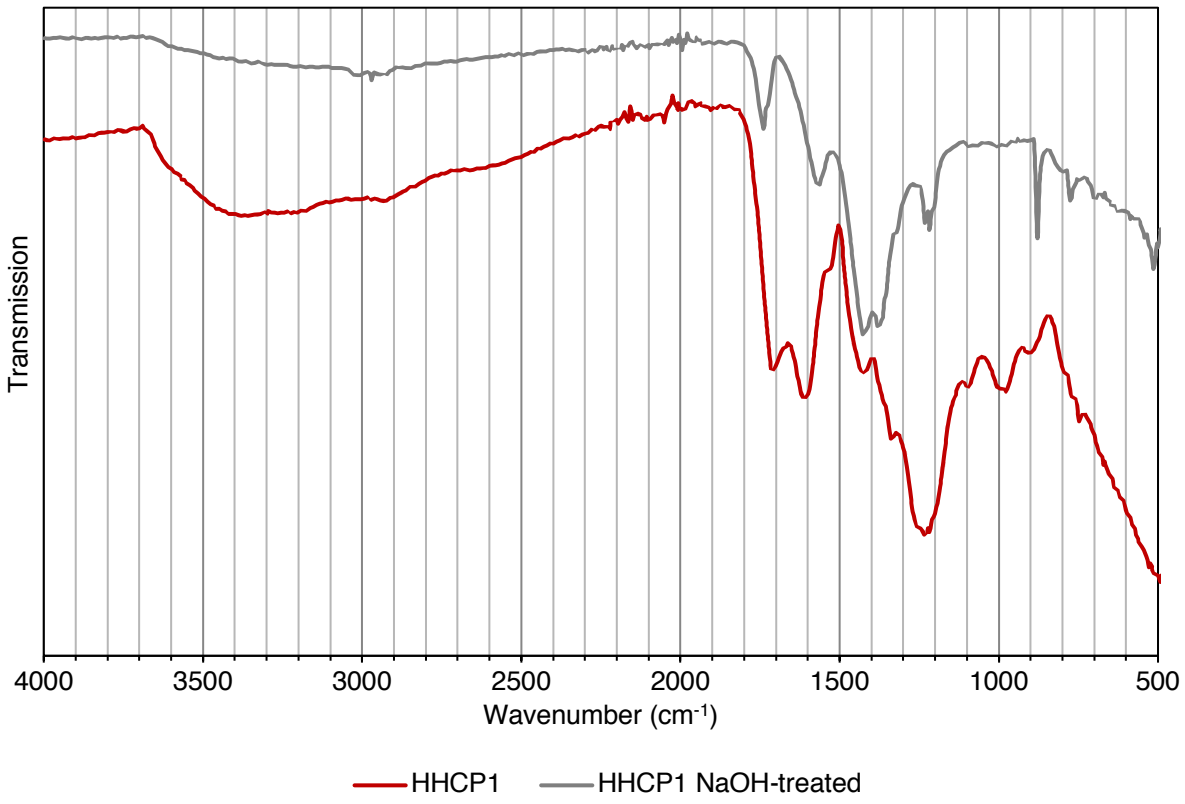

Fig. D12. FTIR spectra of HHCP1 before and after treatment with 3 M NaOH (ATR).

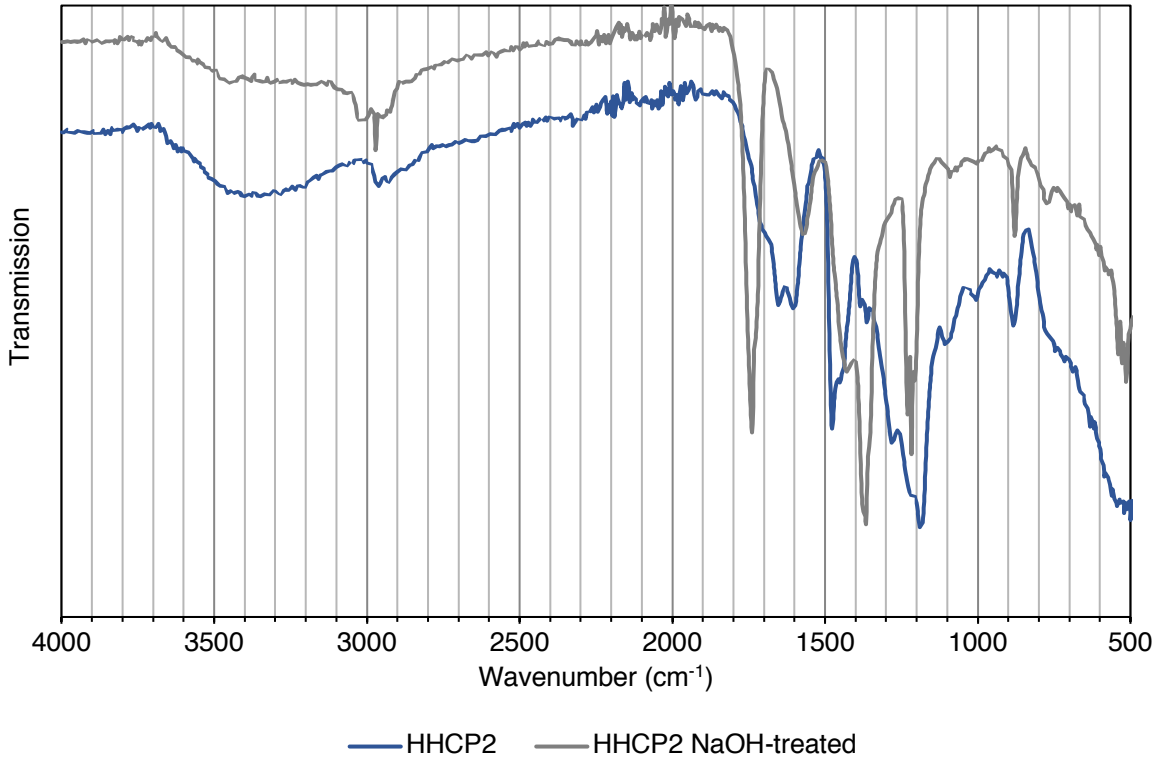

Fig. D13. FTIR spectra of HHCP2 before and after treatment with 3 M NaOH (ATR).

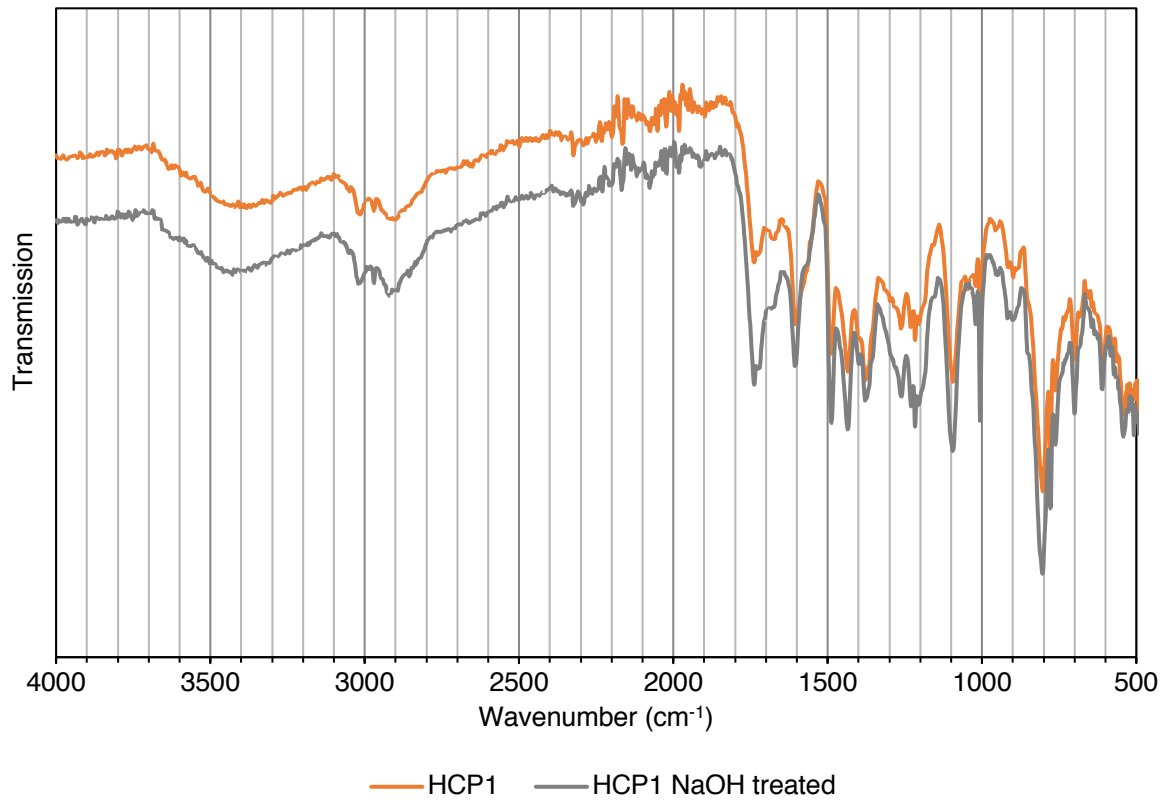

Fig. D14. FTIR spectra of HCP1 before and after treatment with 3 M NaOH (ATR).

Solid state NMR

Experimental parameters

Solid-State NMR samples were packed into 4 mm zirconia rotors and transferred to a Bruker Avance III HD spectrometer. 1D ^{1}H-^{13}C cross-polarisation magic angle spinning (CP/MAS) NMR experiments were measured at 125.76 MHz (500.13 MHz ^{1}H) at a MAS rate of 10.0 kHz. The ^{1}H π/2 pulse was 3.4 µs, and two-pulse phase modulation (TPPM) decoupling was used during the acquisition. The Hartmann-Hahn condition was set using hexamethylbenzene. The spectra were measured using a contact time of 2.0 ms. The relaxation delay D_1 for each sample was individually determined from the proton T_1 measurement ($D_1 = 5 \times T_1$). Samples were collected until sufficient signal to noise was observed, typically greater than 256 scans. The values of the chemical shifts are referred to tetramethylsilane.

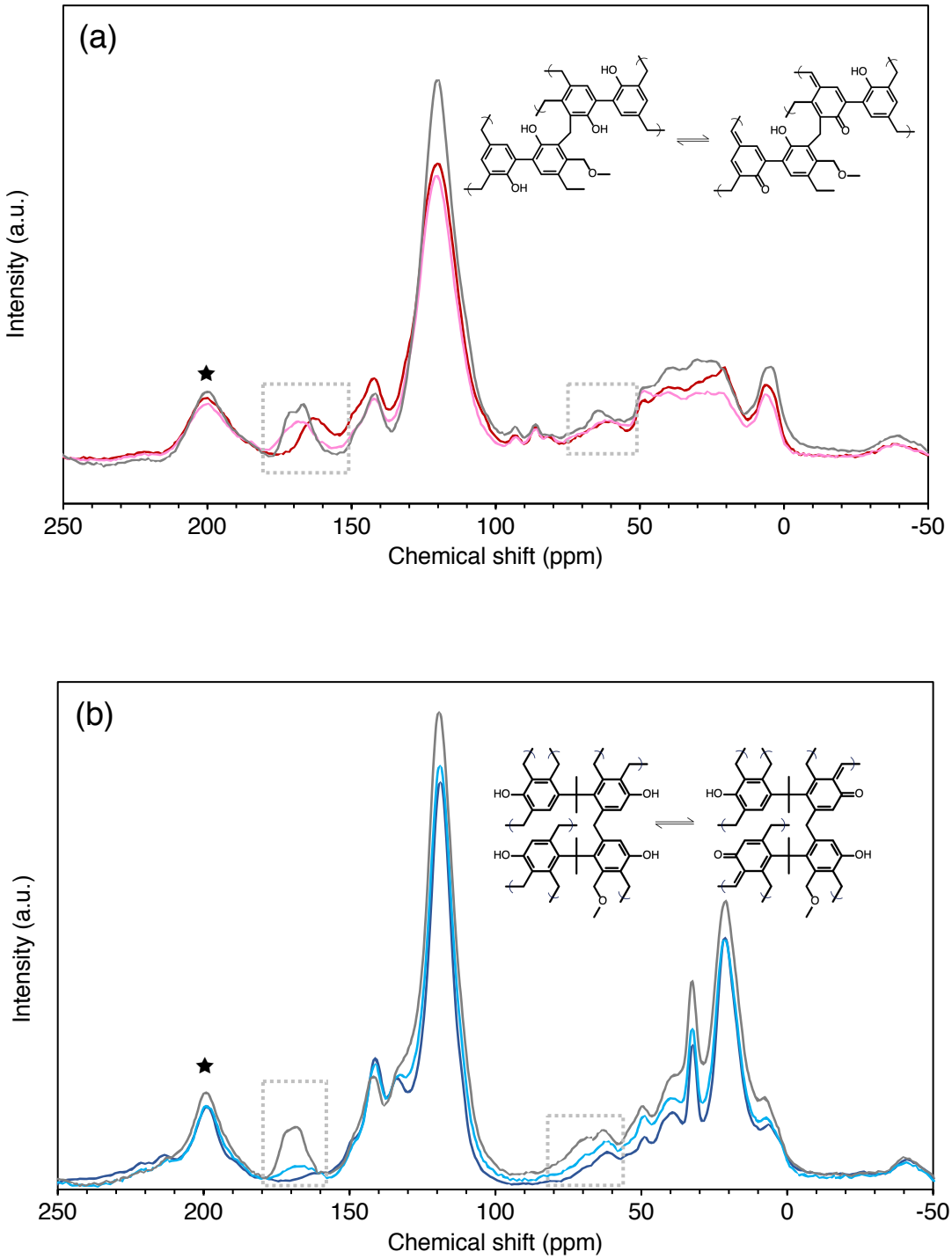

Fig. D15. (a) Solid state NMR spectrum of 2,2'-biphenol-based polymer networks. Red line = HHCP1. Pink line = HHCP1-Ca. Grey line = HHCP1-Na. **(b)** Solid state NMR spectrum of bisphenol A-based polymer networks. Dark blue line = HHCP2. Light blue line = HHCP2-Ca. Grey line = HHCP2-Na. Regions of spectral change are highlighted. ★ = spinning side bands.

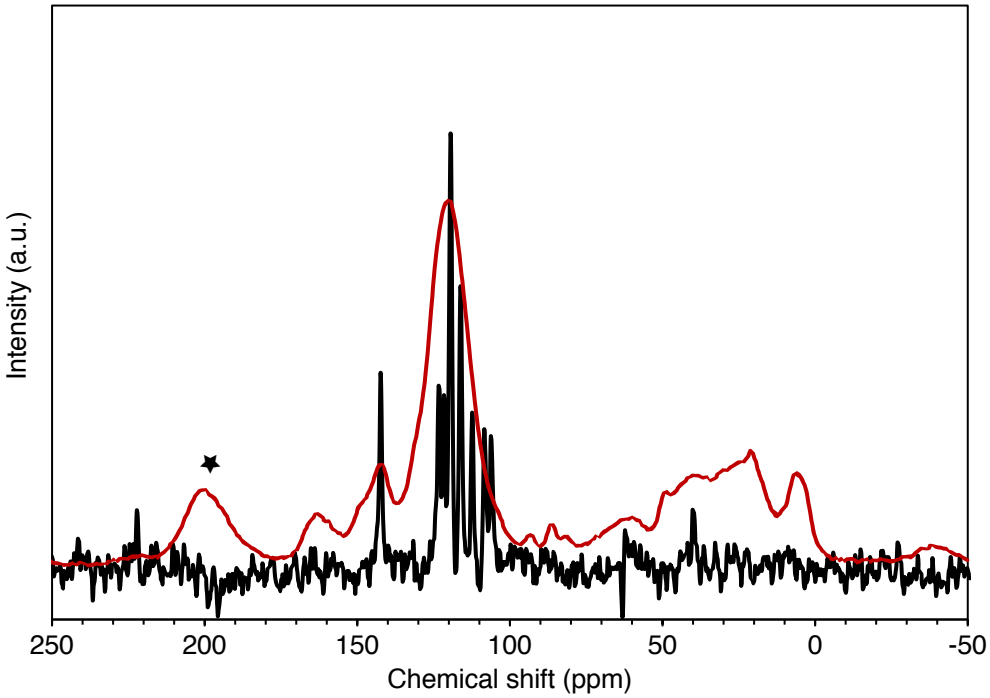

Fig. D16. Solid state NMR spectra of 2,2'-biphenol monomer (black line) and HHCP1 (red line). ★ = spinning side band.

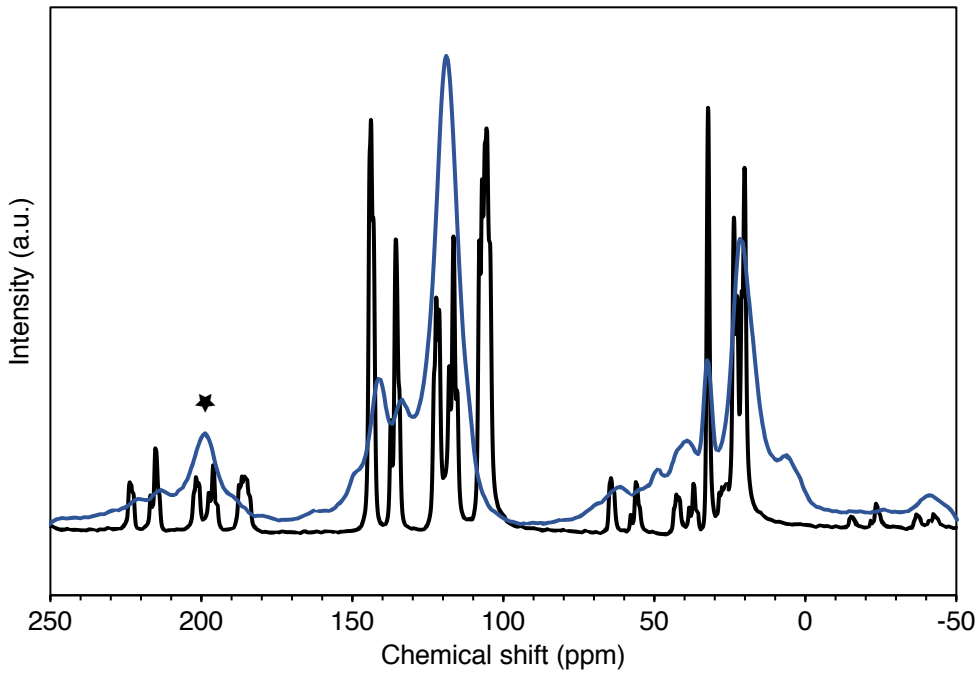

Fig. D17. Solid state NMR spectra of bisphenol A monomer (black line) and HHCP1 (blue line). ★ = spinning side band.

Quinonoid formation within the networks

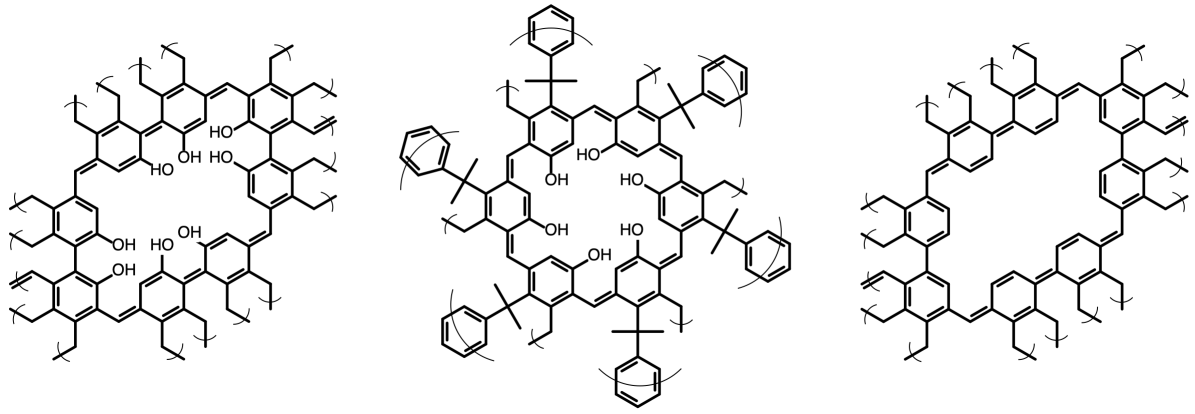

Fig. D18. Potential quinonoid formation in HHCP1 (left), HHCP2 (centre) and HCP1 (right).

Powder X-Ray Diffractograms

In the following diffractograms, ◆ = $CaCO_3$ (vaterite) and □ = CaF_2 (fluorite).

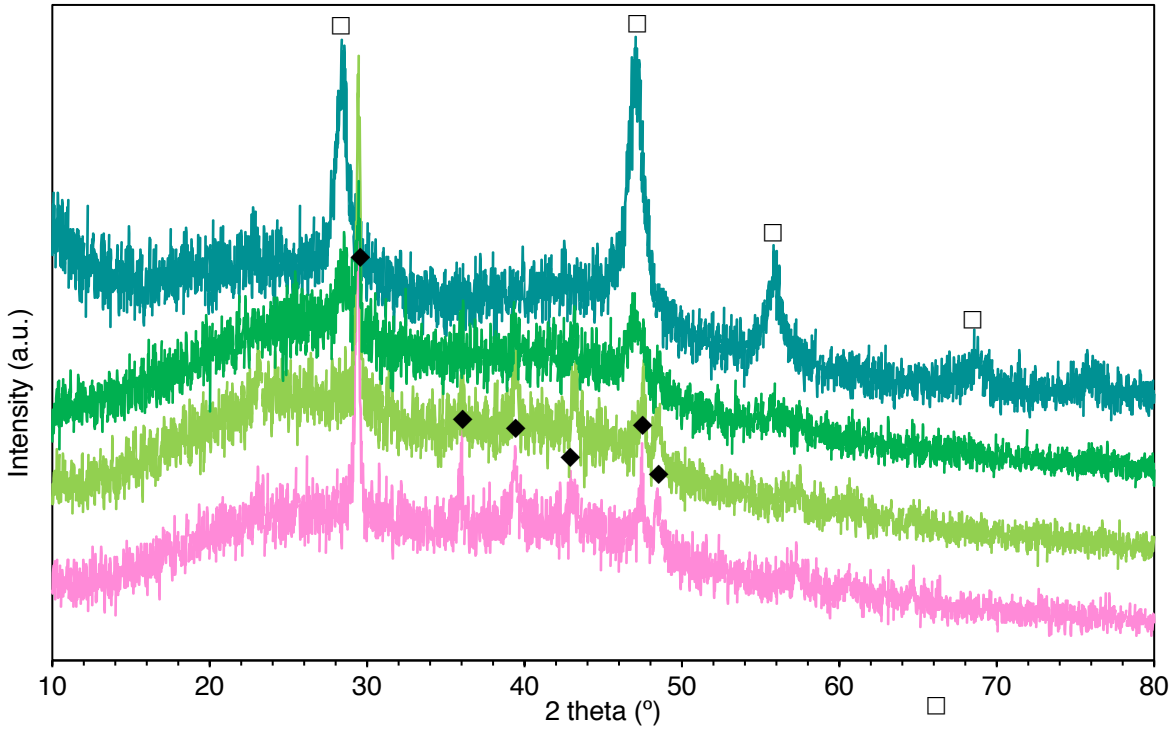

Fig. D19. Samples of HHCP1-Ca at various process stages. **Pink line** = no further treatment. **Yellow-green line** = after contact with 100 mg·L^{-1} fluoride solution. **Green line** = after contact with 400 mg·L^{-1} fluoride solution. **Green-blue line** = after contact with 2,000 mg·L^{-1} fluoride solution (all fluoride solutions made from NaF).

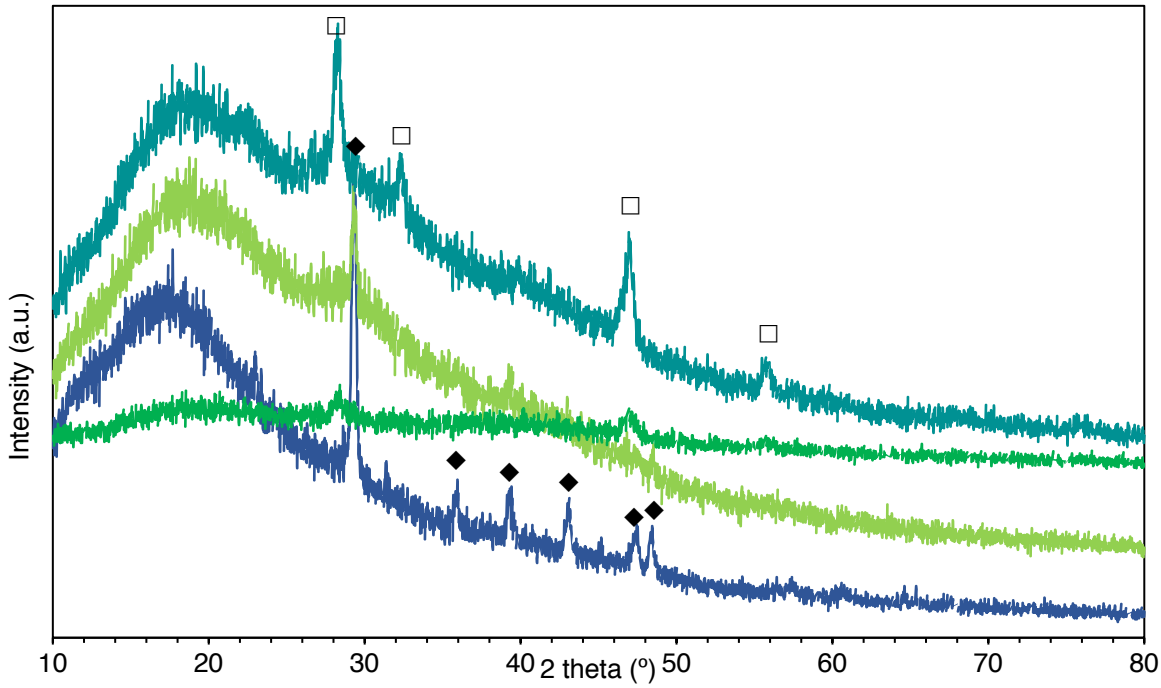

Fig. D20. Samples of HHCP2-Ca at various process stages. **Blue line** = no further treatment. **Yellow-green line** = after contact with 100 mg·L^{-1} fluoride solution. **Green line** = after contact with 400 mg·L^{-1} fluoride solution. **Green-blue** line = after contact with 2,000 mg·L^{-1} fluoride solution (all fluoride solutions made from NaF).

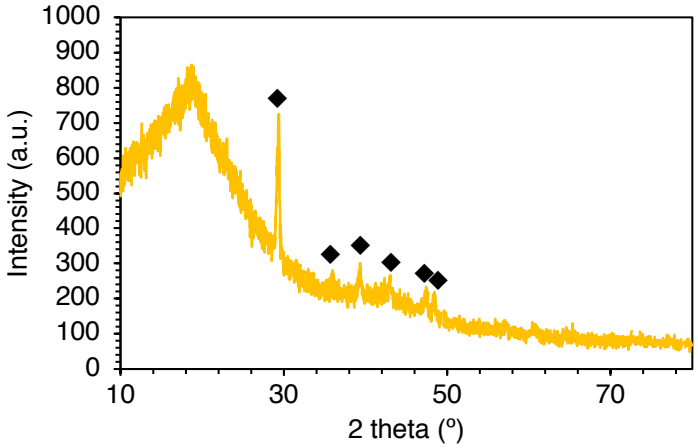

Fig. D21. HCP1 after attempted Ca-loading with $Ca(OH)_2$.

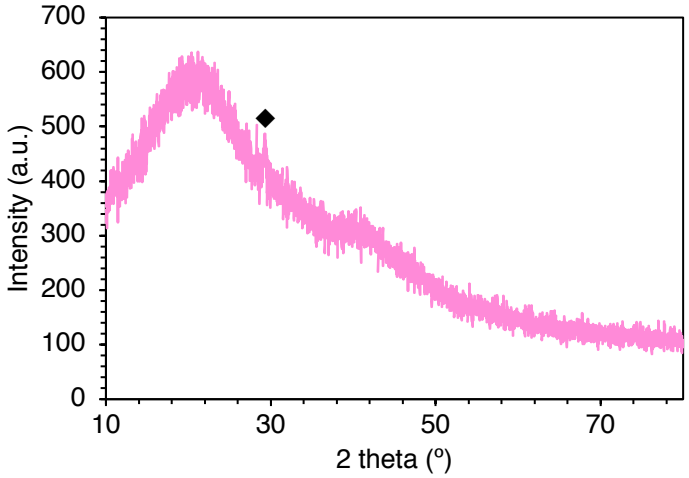

Fig. D22. HHCP1-Ca, made by alternative procedure, whereby a sample of HHCP1 was vacuum-dried, then immediately contacted with $Ca(OH)_2$ solution, then left exposed to the atmosphere for 24 hrs.

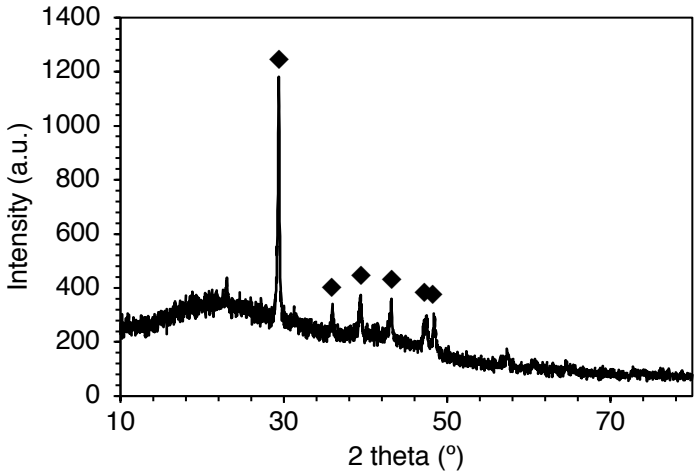

Fig. D23. HHCP1-Ca, after contact with mixed anions solution (1.0 mM F^-, Cl^-, Br^-, I^-, NO_3^-, SO_4^{2-}, $PO_4^{3-}$and CO_3^{2-}).

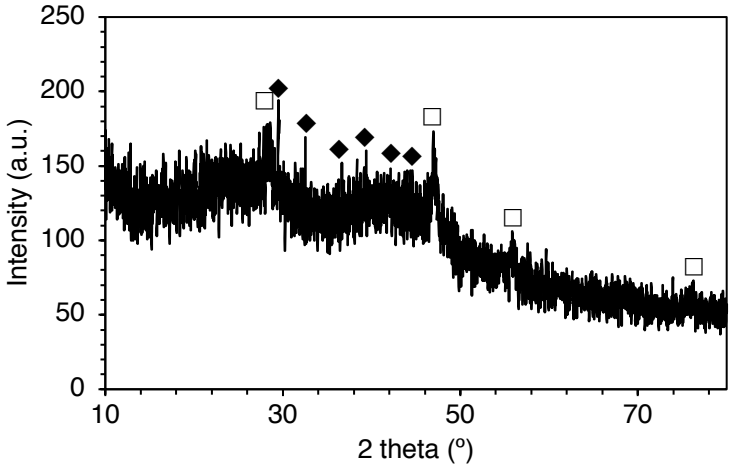

Fig. D24. HHCP1-Ca, after contact with 2,000 mg·L^{-1} fluoride solution, then attempted regeneration with 1 M NaOH solution.

Determination of mechanism of $CaCO_3$ formation in the networks

Two samples of HHCP1-Ca were compared. The first was made as described in the main article, by allowing the HHCP1 sample to equilibrate with atmospheric gases for 24 hr before $Ca(OH)_2$ contact. The sample was washed and dried in the vacuum oven, again as described in the main article, then immediately (within 10 min) was analysed by PXRD. This produced the diffractogram seen in Figure D19. The second sample was placed in the vacuum oven for 24 hr, prior to Ca-loading, then was removed and immediately (within 2 min) contacted with $Ca(OH)_2$ solution, with the sample vessel being kept sealed throughout the process to eliminate interference from atmospheric CO_2. The sample was washed and dried in the vacuum oven, as previously described, then immediately (within 10 min) was analysed by PXRD, which resulted in a completely amorphous spectrum. The sample of HHCP1-Ca was then allowed to equilibrate with the atmosphere for 24 hr, before it was again analysed by PXRD. This produced the spectrum seen in Figure D22, which is almost completely amorphous, with only the major vaterite peak at ~29° being weakly visible. From these data, we concluded that the dominant formation mechanism was the interaction of Ca^{2+}, upon $Ca(OH)_2$ treatment, with previously adsorbed CO_2 molecules.

X-Ray Photoelectron Spectra

Experimental parameters

The samples were all prepared by pushing the submitted HCP and HHCP powders into indium foil.

The analyses were carried out using a Kratos Supra instrument with a monochromated aluminium source, and two analysis points per sample. The analysis area was 700 μm by 300 μm. Charge neutralisation was used throughout. The survey scans were collected between 1200-0 eV, at 1 eV energy resolution, and two 300 second sweeps. High resolution O 1s, C 1s and, where appropriate, F 1s, Fe 2p, Ca 2p, Cl 2p and N 1s scans were collected over an appropriate energy range at 0.1 eV energy resolution. Two 300 seconds sweeps were collected for C 1s, O 1s, F 1s, Cl 2p and N 1s, and four 300 seconds sweeps for Fe 2p and Ca 2p.

The data collected was calibrated in intensity using a transmission function characteristic of the instrument (determined using software from NPL) to make the values instrument-independent. The data was then quantified using theoretical Schofield relative sensitivity factors. All data was calibrated relative to a C 1s position of 285.0 eV for C-C/C-H type carbon environments.

Table D5. Quantification results from XPS survey scans. Monomers are not presented, as the analysis was unreliable, due to volatilisation.

Sample	Elemental composition (atomic %)						
	Na	F	O	N	Ca	C	Cl
HHCP1 (a)	0.1	<0.1	21.1	1.9	0.1	76.3	0.4
HHCP1 (b)	0.1	<0.1	20.8	1.8	0.1	76.8	0.4
HHCP1-Ca (a)	<0.1	<0.1	26.7	1.6	5.3	63.4	0.3
HHCP1-Ca (b)	<0.1	0.1	25.6	1.5	5.1	65.6	0.3
HHCP1-Ca after F^- (400 $mg \cdot L^{-1}$) contact (a)	<0.1	1.9	18.3	2.3	4.3	72.6	0.3
HHCP1-Ca after F^- (400 $mg \cdot L^{-1}$) contact (b)	<0.1	1.5	19.9	2.2	4.4	71.4	0.3
HHCP1-Ca after F^- (2000 $mg \cdot L^{-1}$) contact (a)	<0.1	3.2	17.3	<0.1	3.7	75.0	0.7
HHCP1-Ca after F^- (2000 $mg \cdot L^{-1}$) contact (b)	<0.1	3.1	14.4	<0.1	3.5	75.2	0.8
HHCP2 (a)	<0.1	<0.1	15.4	<0.1	<0.1	83.8	0.8
HHCP2 (b)	<0.1	<0.1	15.9	<0.1	<0.1	83.4	0.6
HHCP2-Ca (a)	<0.1	<0.1	19.7	<0.1	2.7	76.3	0.5
HHCP2-Ca (b)	<0.1	<0.1	19.2	<0.1	2.7	77.2	0.5
HHCP2-Ca after F^- (400 $mg \cdot L^{-1}$) contact (a)	<0.1	5.9	16.3	<0.1	6.2	70.8	0.6
HHCP2-Ca after F^- (400 $mg \cdot L^{-1}$) contact (b)	<0.1	5.9	16.0	<0.1	6.1	71.5	0.3
HHCP2-Ca after F^- (2000 $mg \cdot L^{-1}$) contact (a)	<0.1	9.3	15.1	<0.1	8.4	66.4	0.3
HHCP2-Ca after F^- (2000 $mg \cdot L^{-1}$) contact (b)	<0.1	9.6	15.1	<0.1	8.4	66.2	0.3
HCP1 (a)	<0.1	<0.1	6.3	<0.1	<0.1	92.2	1.4
HCP1 (b)	<0.1	<0.1	6.3	<0.1	<0.1	92.3	1.4
HCP1 + $Ca(OH)_2$ (a)	<0.1	<0.1	10.4	<0.1	0.8	87.5	1.1
HCP1 + $Ca(OH)_2$ (b)	<0.1	<0.1	8.2	<0.1	0.7	90.1	1.1

Table D6. Results of curve-fitting of high-resolution C 1s scans. π-π* satellites not presented. B.E. = binding energy.

Sample	Environment									
	C=C sp_2		Aliphatic sp_3		C-O		C=O		Carbonate	
	B.E. (eV)	Atomic %	B.E. (eV)	Atomic %	B.E. (eV)	Atomic %	B.E. (eV)	Atomic %	B.E. (eV)	Atomic %
HHCP1 (a)	284.0	33.8	285.0	31.7	286.3	20.3	288.2	9.6	290.2	3.4
HHCP1 (b)	284.0	35.7	285.0	30.9	286.4	19.1	288.2	10.1	290.2	3.0
HHCP1-Ca (a)	284.0	36.5	285.0	23.1	286.1	21.5	287.8	12.0	289.8	5.4
HHCP1-Ca (b)	284.0	38.8	285.0	21.0	286.0	21.5	287.8	12.1	289.8	5.2
HHCP1-Ca after F^- (400 mg·L^{-1}) contact (a)	284.0	37.8	285.0	40.4	286.1	9.5	287.6	9.8	289.4	1.8
HHCP1-Ca after F^- (400 mg·L^{-1}) contact (b)	284.0	37.7	285.0	31.3	286.0	14.5	287.6	12.1	289.4	3.1
HHCP1-Ca after F^- (2,000 mg·L^{-1}) contact (a)	284.0	35.0	285.0	31.7	286.3	20.6	287.9	8.0	289.7	2.9
HHCP1-Ca after F^- (2,000 mg·L^{-1}) contact (b)	284.0	41.1	285.0	26.1	286.1	20.5	287.8	7.8	289.8	2.9
HHCP2 (a)	284.3	53.1	285.0	23.4	285.9	14.8	286.9	4.7	288.3	4.1
HHCP2 (b)	284.3	46.7	285.0	25.3	285.9	16.3	286.8	5.7	288.0	6.0
HHCP2-Ca (a)	284.2	46.6	284.8	28.6	285.8	13.2	286.6	6.4	290.7	5.2
HHCP2-Ca (b)	284.2	49.0	284.9	22.5	285.7	13.5	286.5	7.2	287.8	7.8
HHCP2-Ca after F^- (400 mg·L^{-1}) contact (a)	284.2	57.1	285.0	20.0	286.0	11.3	286.6	4.7	287.9	6.8
HHCP2-Ca after F^- (400 mg·L^{-1}) contact (b)	284.3	47.7	284.8	21.7	285.7	15.7	286.6	8.4	288.0	6.6
HHCP2-Ca after F^- (2,000 mg·L^{-1}) contact (a)	284.2	40.3	284.9	23.0	285.7	16.2	286.5	8.7	287.6	11.8
HHCP2-Ca after F^- (2,000 mg·L^{-1}) contact (b)	284.3	56.4	285.2	13.4	286.1	19.8	287.0	3.7	288.0	6.8
HCP1 (a)	284.0	79.9	285.2	9.1	286.2*		4.9*		290.2	6.1
HCP1 (b)	284.0	70.8	285.3	18.4	286.3*		5.1*		290.2	5.8
HCP1 + $Ca(OH)_2$ (a)	284.1	72.7	285.2	12.2	286.4*		6.2*		289.8	8.9
HCP1 + $Ca(OH)_2$ (b)	284.1	82.9	285.1	5.2	286.2*		5.9*		290.5	5.9

*These C-O and C=O environments could not be distinguished.

Technical notes

For C 1s curve-fitting for HHCP1 and derivatives, the sp^2 peak was made asymmetric and allowed to be narrower than the sp^3 peaks, as is typical in polymeric samples. This gave sensible relative ratios of all carbons. The same practice was tried for HHCP2 and derivatives, but this gave illogical carbon ratios (only ~20% sp^2). An alternative sp^2 curve-fitting was tried: instead of assuming a narrower asymmetric peak compared to the sp^3 components, it was fitted as a symmetric peak of equal width to all the other carbon components. No additional calibrations to the energy scale were made and this produced sensible carbon ratios. A narrower and more symmetrical sp^2 peak is commonly seen in graphene type samples and this suggests that quinonoid-formation is more prevalent in HHCP2 than HHCP1. This indeed is also suggested by the relative ratios of sp^2 to sp^3 carbons in XPS spectra and also the much lower than calculated H mass % of HHCP2 (Table D1).

The atomic % of C=C carbons for HHCP1 and HHCP2 polymers and derivatives is somewhat lower than expected, assuming the dehydrogenation and quinonoid formation proposed by Vinodh *et al.* is occurring [8] (suggested by FT-IR data). It is possible that during the polymerisations, the $FeCl_3$

migrates to the relatively hydrophilic pore interiors, rather than the particle surfaces, which are in contact with hydrophobic DCE. For this reason, the surface sites analysed by XPS are likely to contain more aliphatic crosslinkers and partial crosslinkers than aromatised crosslinkers.

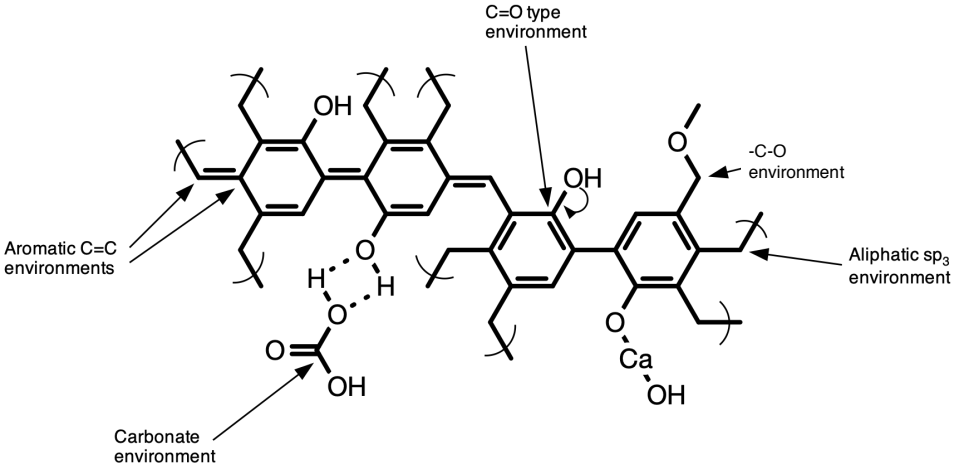

Fig. D25. Structure of HHCP1 with assigned XPS carbon environments.

Table D7. Results of curve-fitting of high-resolution O 1s scans.

Sample	Environment					
	C-O-, Ca-O- and carbonate		C=O		Adsorbed water	
	B.E. (eV)	Atomic %	B.E. (eV)	Atomic %	B.E. (eV)	Atomic %
HHCP1 (a)	531.3	28.1	532.6	58.4	534.3	13.5
HHCP1 (b)	531.3	28.0	532.6	58.1	534.5	13.9
HHCP1-Ca (a)	531.0	51.4	532.5	37.9	534.3	10.7
HHCP1-Ca (b)	531.0	49.7	532.5	39.5	534.3	10.8
HHCP1-Ca after F^- (400 $mg \cdot L^{-1}$) contact (a)	530.8	52.6	532.3	42.4	533.7	5.1
HHCP1-Ca after F^- (400 $mg \cdot L^{-1}$) contact (b)	530.8	49.5	532.3	43.4	533.9	7.1
HHCP1-Ca after F^- (2,000 $mg \cdot L^{-1}$) contact (a)	531.0	24.4	532.5	62.7	534.3	13.0
HHCP1-Ca after F^- (2,000 $mg \cdot L^{-1}$) contact (b)	530.9	22.9	532.5	63.6	534.3	13.6
HHCP2 (a)	531.4	15.2	532.7	84.8		
HHCP2 (b)	531.5	17.2	532.7	82.8		
HHCP2-Ca (a)	531.2	30.1	532.6	69.9		
HHCP2-Ca (b)			532.2	100		
HHCP2-Ca after F^- (400 $mg \cdot L^{-1}$) contact (a)	531.3	29.0	532.6	71.0		
HHCP2-Ca after F^- (400 $mg \cdot L^{-1}$) contact (b)	531.5	30.6	532.9	69.4		
HHCP2-Ca after F^- (2,000 $mg \cdot L^{-1}$) contact (a)	531.3	23.3	532.7	66.6	534.3	10.1
HHCP2-Ca after F^- (2,000 $mg \cdot L^{-1}$) contact (b)			532.4	100		
HCP1 (a)			532.0	100		
HCP1 (b)			532.1	100		
HCP1 + $Ca(OH)_2$ (a)			532.0	100		
HCP1 + $Ca(OH)_2$ (b)			532.1	100		

Table D8. Results of curve-fitting of high-resolution Ca 2p scans.

Sample	Environment											
	RO-Ca-OH and $CaCO_3$				CaF_2				Coordinated CaX_2			
	2p 3/2		2p 1/2		2p 3/2		2p 1/2		2p 3/2		2p 1/2	
	B.E. (eV)	Atom %	B.E. (eV)	Atom %	B.E. (eV)	Atom %	B.E. (eV)	Atom %	B.E. (eV)	Atom %	B.E. (eV)	Atom %
HHCP1-Ca (a)	346.9	54.2	350.7	27.0					349.5	12.5	353.0	6.3
HHCP1-Ca (b)	346.9	55.4	350.6	27.7					349.5	11.3	353.0	5.6
HHCP1-Ca after F^- (400 mg·L^{-1}) contact (a)	347.1	66.7	350.6	33.3								
HHCP1-Ca after F^- (400 mg·L^{-1}) contact (b)	347.0	50.3	350.5	25.1					350.0	16.4	353.5	8.2
HHCP1-Ca after F^- (2,000 mg·L^{-1}) contact (a)					348.0	66.7	351.6	33.3				
HHCP1-Ca after F^- (2,000 mg·L^{-1}) contact (b)					347.9	66.7	351.5	33.3				
HHCP2-Ca (a)	347.4	66.7	351.0	33.3								
HHCP2-Ca (b)	347.4	66.7	351.0	33.3								
HHCP2-Ca after F^- (400 mg·L^{-1}) contact (a)					348.7	66.7	351.9	33.3				
HHCP2-Ca after F^- (400 mg·L^{-1}) contact (b)					348.3	66.7	352.0	33.3				
HHCP2-Ca after F^- (2,000 mg·L^{-1}) contact (a)					348.5	66.7	352.0	33.3				
HHCP2-Ca after F^- (2,000 mg·L^{-1}) contact (b)					348.6	66.7	352.1	33.3				
HCP1 + $Ca(OH)_2$ (a)	347.6	66.7	351.4	33.3								
HCP1 + $Ca(OH)_2$ (b)	347.8	66.7	351.5	33.3								

Table D9. Results of curve-fitting of high-resolution F 1s scans.

Sample	Environment					
	CaF_2		F ligand		F bridging ligand	
	B.E. (eV)	Atomic %	B.E. (eV)	Atomic %	B.E. (eV)	Atomic %
HHCP1-Ca after F^- (400 mg·L^{-1}) contact (a)	685.0	100				
HHCP1-Ca after F^- (400 mg·L^{-1}) contact (b)	684.8	47.0	686.6	53.0		
HHCP1-Ca after F^- (2,000 mg·L^{-1}) contact (a)	685.3	63.7	686.7	26.5	688.6	9.8
HHCP1-Ca after F^- (2,000 mg·L^{-1}) contact (b)	685.2	66.0	687.0	20.6	689.1	13.5
HHCP2-Ca after F^- (400 mg·L^{-1}) contact (a)	685.5	83.4	687.2	16.6		
HHCP2-Ca after F^- (400 mg·L^{-1}) contact (b)	685.7	79.8	687.3	20.2		
HHCP2-Ca after F^- (2,000 mg·L^{-1}) contact (a)	685.4	70.5	686.8	23.9	688.3	5.7
HHCP2-Ca after F^- (2,000 mg·L^{-1}) contact (b)	685.4	78.0	686.4	19.9	688.1	2.1

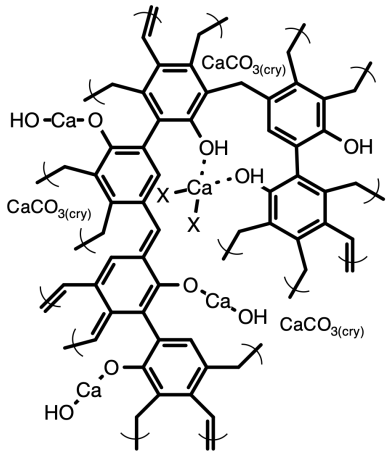

Fig. D26. Structure of HHCP1-Ca showing low B.E. and high B.E. Ca environments. X = OH, Cl or NO_3. Note that after 400 mg·L^{-1} F^- contact, the high B.E. environment becomes more electron-poor, shifting by 0.5 eV, due to the electronegativity of the F ligands.

N_2 sorption measurements

Table D10. Calculated parameters for the polymer networks from N_2 sorption experiments. Sample mass ≈ 100 mg. T = 77 K.

Sample	BET surface area ($m^2 \cdot g^{-1}$)	BET equation R^2	Micropore volume ($cm^3 \cdot g^{-1}$)	Total pore volume ($cm^3 \cdot g^{-1}$)	V_{micro} / V_{total}	Average pore size (nm)	Median pore size (nm)
HHCP1	748 ± 5	0.9999	0.294	0.379	0.776	2.03	0.495
HHCP1-Ca	334 ± 2	0.9999	0.132	0.170	0.776	2.03	0.614
HHCP2	541± 4	0.9999	0.212	0.272	0.779	2.01	0.490
HHCP2-Ca	17.1 ± 0.1	0.9999	0.006	0.018	0.333	4.16	0.781
HCP1	1,310 ± 1	0.9999	0.500	1.161	0.431	3.55	0.574
HCP1 + $Ca(OH)_2$	1,140 ± 1	0.9999	0.437	0.944	0.463	3.31	0.554

Notes: Surface areas were calculated over a P/P_0 range of 0.01 – 0.11 using BET equation. Micropore volume was calculated at P/P_0 = 0.01. Total pore volume was calculated at P/P_0 = 0.95.

Determination of protonation constants

Table D11. pK_a values determined from the 3 best-fitting models for HHCP1. Experimental parameters as described in the main article.

Model	$Log_{10}K_1$	$Log_{10}K_2$	$Log_{10}K_3$	$Log_{10}K_4$	R^2
2 pK_as	9.24 ± 0.06	4.88 ± 0.05			0.9981
3 pK_as	10.2 ± 0.07	8.77 ±0.04	4.73 ± 0.04		0.9995
4 pK_as	10.5 ± 0.1	9.99 ± 0.06	8.48 ± 0.05	4.86 ± 0.04	0.9997

Table D12. pK_a values determined from the 3 best-fitting models for HHCP2. Experimental parameters as described in the main article.

Model	$Log_{10}K_1$	$Log_{10}K_2$	$Log_{10}K_3$	$Log_{10}K_4$	$Log_{10}K_5$	R^2
3 pK_as	9.91 ± 0.09	9.60 ± 0.08	7.38 ± 0.11			0.9991
4 pK_as	9.93 ± 0.19	9.87 ± 0.09	8.87 ± 0.16	6.30 ± 0.14		0.9994
5 pK_as	10.1 ± 0.3	9.90 ± 0.09	9.19 ± 0.20	7.54 ± 0.12	3.33 ± 0.13	0.9996

Note: The 5 pK_a model for HHCP1 and 6 pK_a model for HHCP2 gave R^2 values of 0.9995 and 0.9994, but returned illogical parameters (pK_as with value of 0).

Photographs of aqueous suspensions of polymers

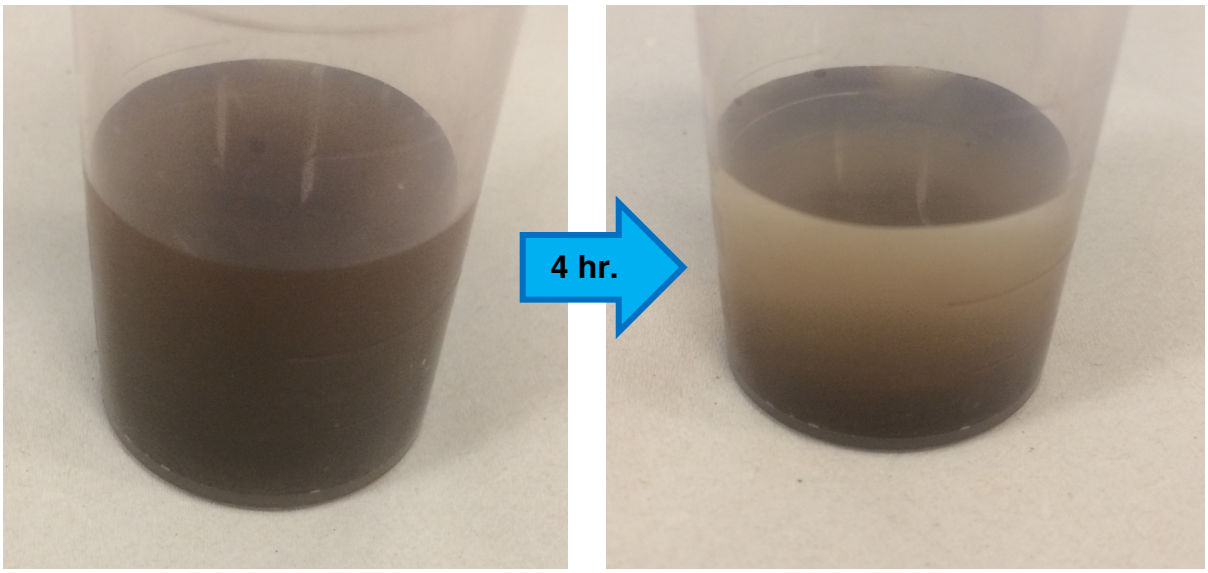

Fig. D27. Aqueous suspensions of HHCP1 after initial contact and after being left to stand for 4 hr.

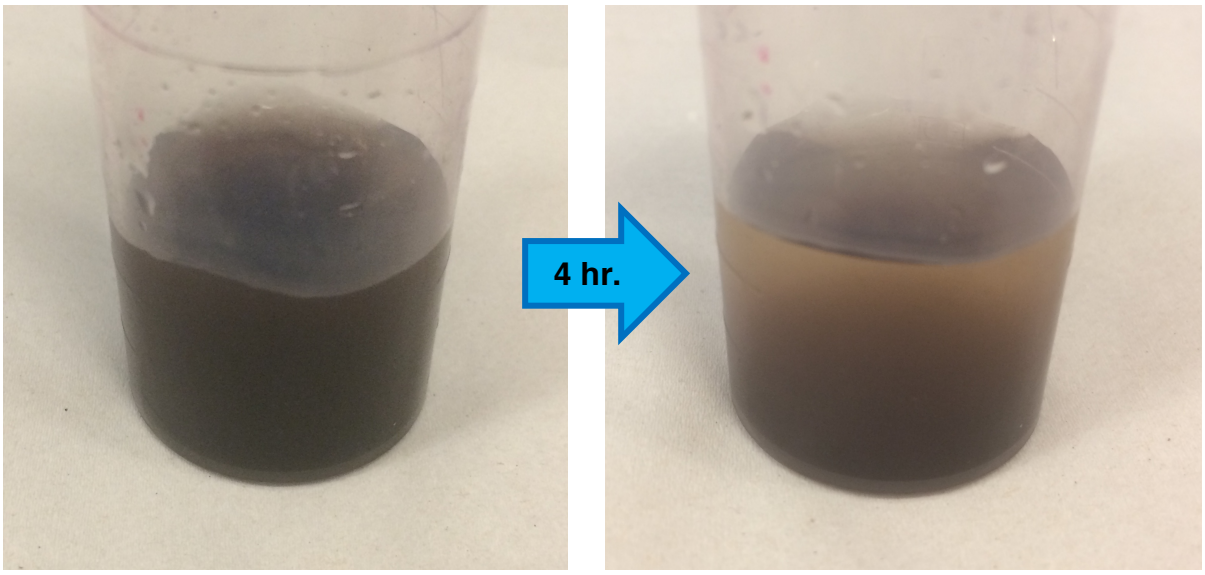

Fig. D28. Aqueous suspensions of HHCP1-Ca after initial contact and after being left to stand for 4 hr.

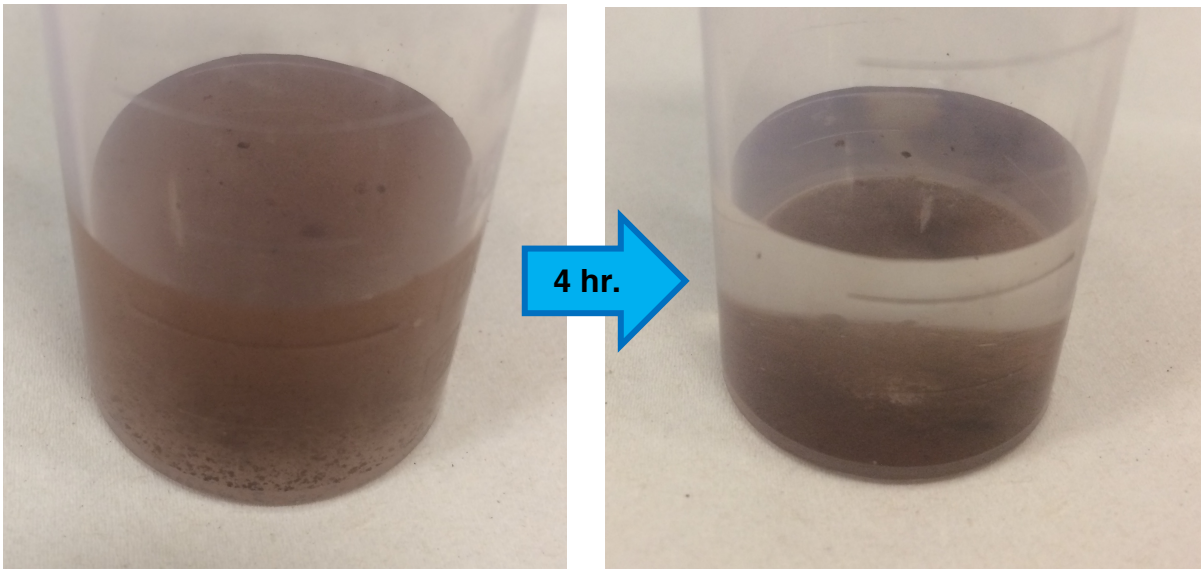

Fig. D29. Aqueous suspensions of HHCP2 after initial contact and after being left to stand for 4 hr.

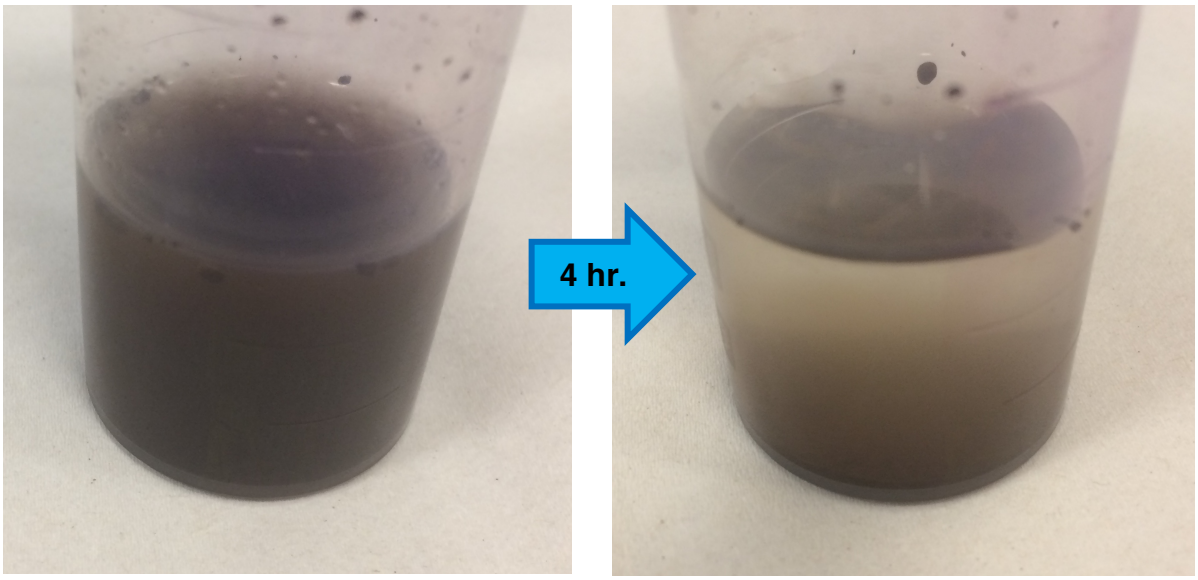

Fig. D30. Aqueous suspensions of HHCP2-Ca after initial contact and after being left to stand for 4 hr.

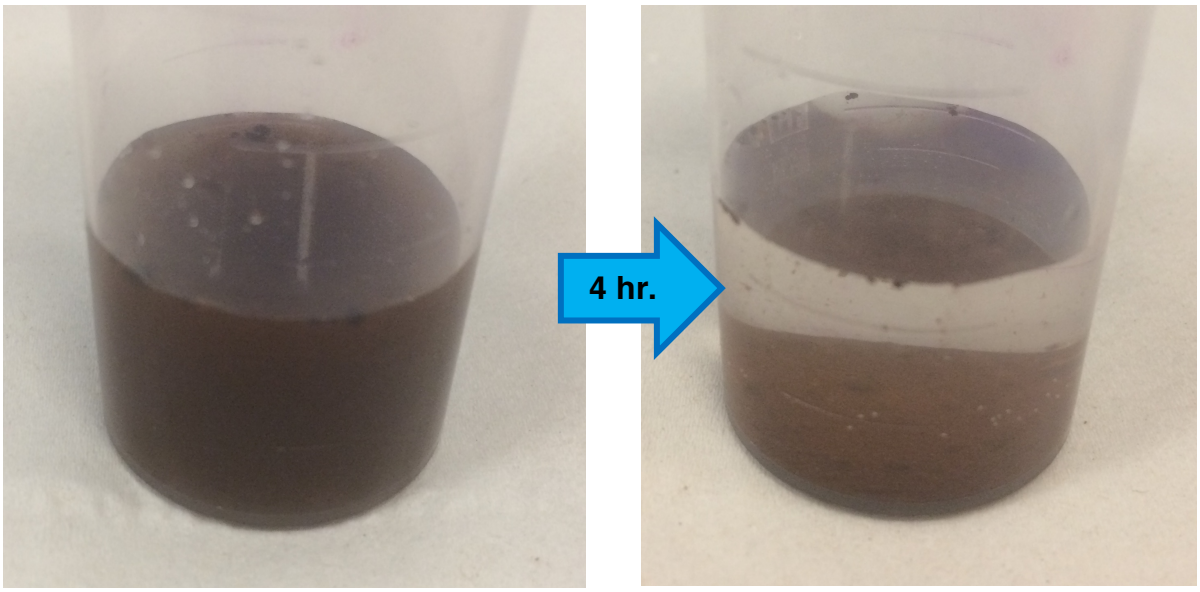

Fig. D31. Aqueous suspensions of HCP1 after initial contact and after being left to stand for 4 hr.

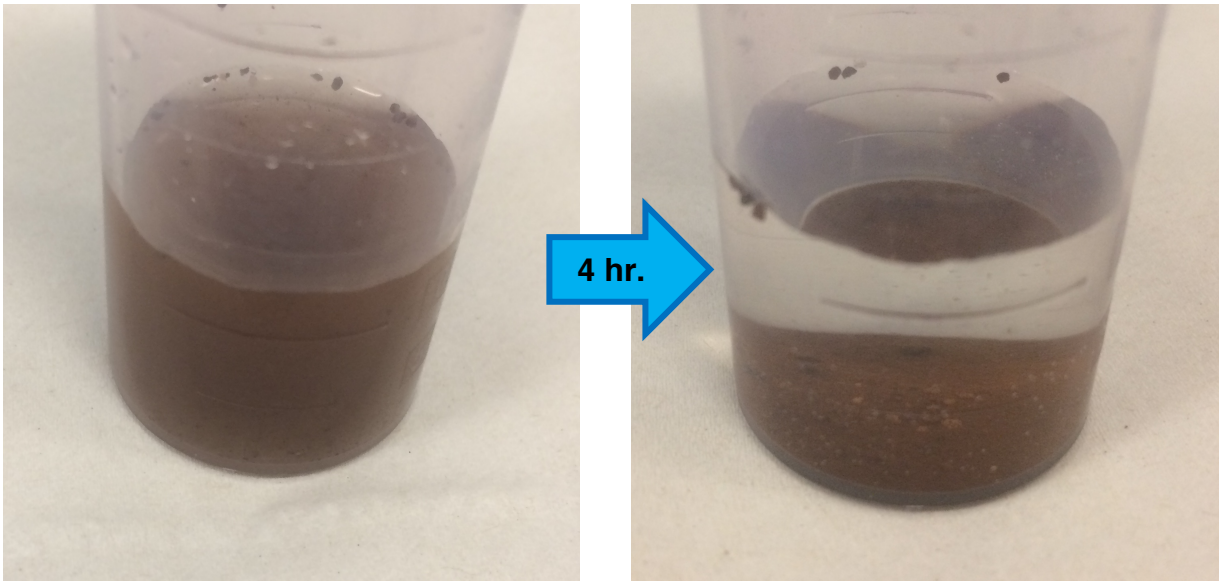

Fig. D32. Aqueous suspensions of HCP1 + $Ca(OH)_2$ after initial contact and after being left to stand for 4 hr.

Fluoride uptake studies

Static uptake experiments were carried out according to the procedure described in the main article. Equilibrium fluoride uptake capacity (q_e) in mg·g^{-1} of the polymers was calculated according to Equation D1,

$$q_e = \frac{(C_1 - C_2)\,V}{m} \qquad \textbf{(Eqn. D1)}$$

where C_1 is the concentration of fluoride in the sample solution before polymer contact (mg L^{-1}), C_2 is the concentration after equilibrium is reached (mg·L^{-1}), V is the volume of solution treated (L) and m is the mass of adsorbent (g).

Fluoride concentration measurements were carried out by ion-selective electrode. A three-point calibration was carried out prior to analysis, using an appropriate range of standards, usually covering two orders of magnitude. These were made by dissolving ≥ 99.999 % NaF, which had been dried in an air-flow oven for a minimum of 24 hr, in deionised water. Recalibration was performed after <10 sample measurements. Each sample contained 50% total ionic strength adjustment buffer (TISAB). For synthesis of TISAB, all reagents were of analytical grade and used without further purification. In a 1 L beaker, 45.0 g NaCl was dissolved in ~500 mL deionised water, followed by 4.00 g 1,2-Diaminocyclohexanetetraacetic acid hydrate. 57 mL acetic acid were added were added and the water volume increased to ~800 mL. 5 M NaOH was added dropwise, to increase pH to 5.5. The solution was then transferred to a 1 L volumetric flask and water volume increased to exactly 1 L.

Assessment of all synthesised networks for fluoride uptake capabilities

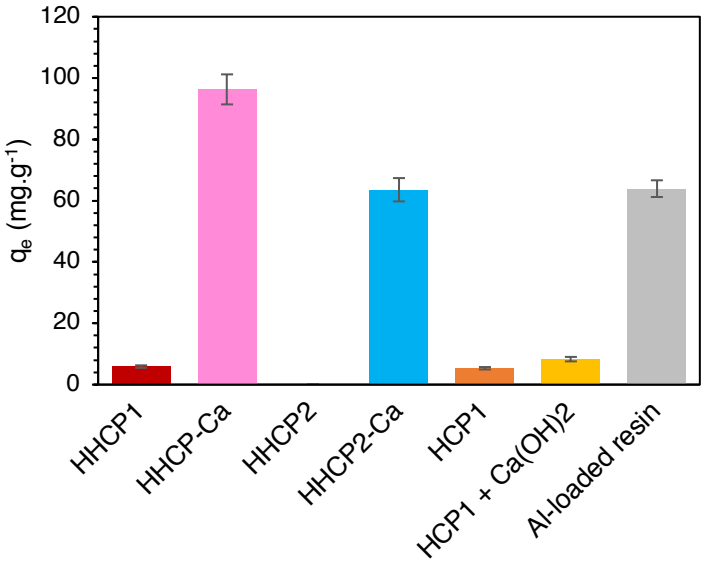

Fig. D33. Calculated equilibrium uptake capacities for all networks from contact with 2,000 mg·L^{-1} fluoride solutions, as NaF. Polymer/resin mass = 100 mg. Volume of solution = 25 mL. Contact time = 24 hr. T = 18°C.

Technical note

The Al-loaded resin was metallated, using the same procedure described in previous work to create a La-loaded resin [9]. The ion-exchange resin used was Puromet® MTS9501, kindly donated from Purolite, and has an aminomethylphosphonic acid chelating functionality.

Fluoride uptake as a function of pH and corresponding surface zeta potential

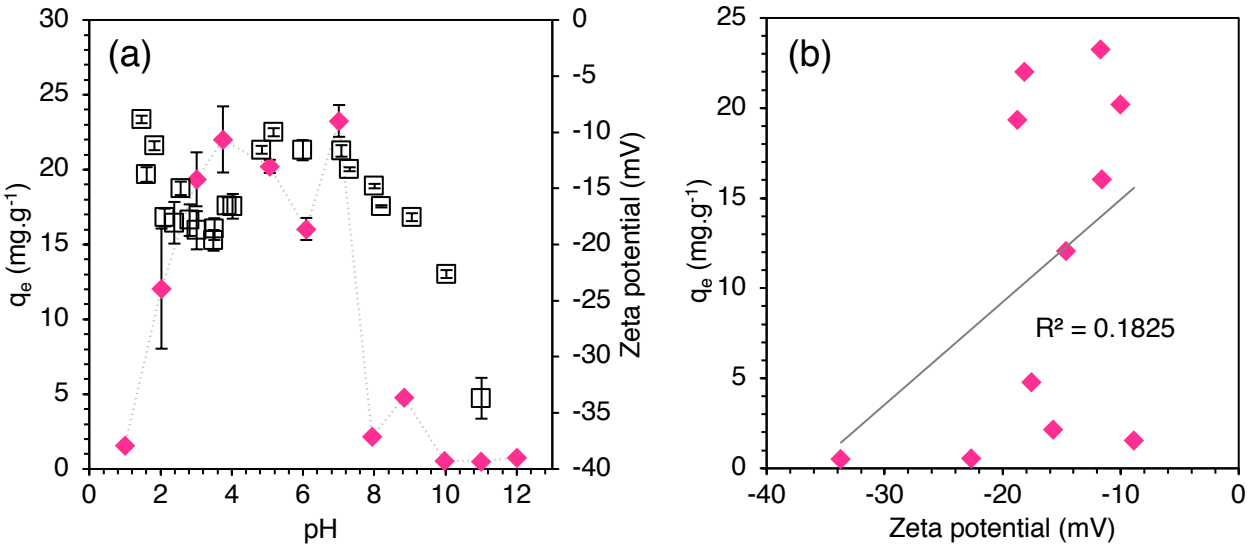

Fig. D34. (a) Equilibrium fluoride uptake of HHCP1-Ca (◆) over pH range 1-12 with corresponding zeta potential (☐) over equivalent pH range. **(b)** Linear plot of fluoride uptake verses zeta potential for samples where pH was equivalent to ± 0.1 pH unit. Error bars represent 95% confidence limits from 2 duplicate samples. Polymer mass = 100 mg. Contact solution volume = 25 mL. Initial fluoride concentration = 100 mg·L^{-1}. Contact time = 6 hr. T = 18°C.

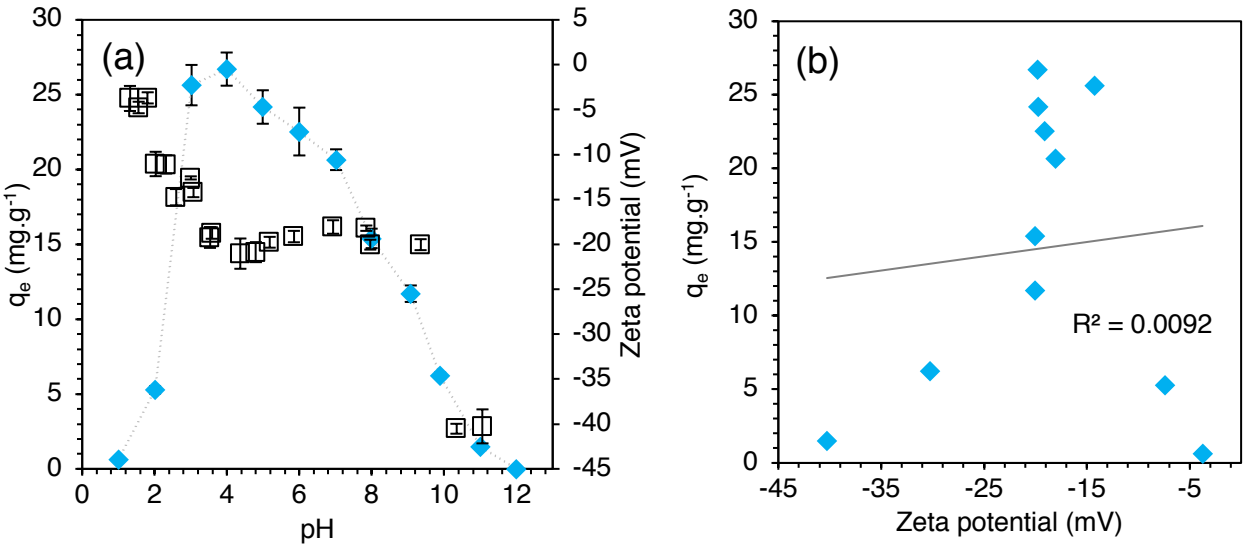

Fig. S35. (a) Equilibrium fluoride uptake of HHCP2-Ca (◆) over pH range 1-12 with corresponding zeta potential (☐) over equivalent pH range. **(b)** Linear plot of fluoride uptake verses zeta potential for samples where pH was equivalent to ± 0.1 pH unit. Experimental parameters as per Figure S34.

Models used to fit isotherm data

The Langmuir model

The Langmuir isotherm model, (Equation D2) assumes monolayer adsorption over a finite number of degenerate binding sites, with no interaction between adsorbed species.

$$q_e = \frac{q_{max} K_L C_e}{1 + K_L C_e} \quad \textbf{(Eqn. D2)}$$

In the Langmuir equation, q_{max} (mg g^{-1}) is the theoretical maximal uptake capacity of the adsorbent. K_L is a Langmuir Isotherm constant related to the favourability of adsorption. C_e (mg L^{-1}) is the fluoride concentration in solution at equilibria.

The Freundlich model

The Freundlich isotherm was originally purely an empirical model. However, it is now commonly quoted as being able to describe multilayer adsorption systems where adsorption sites are heterogeneous [10],

$$q_e = K_F C_e^{\frac{1}{n}} \quad \textbf{(Eqn. D3)}$$

where K_F and n are Freundlich isotherm constants. K_F is a measure of adsorption capacity and n is a factor of heterogeneity.

The Temkin model

The Temkin isotherm (Equation D4) has been applied to systems where the heat of adsorption decreases linearly as exchange sites are occupied, as a result of interactions between the sorbate species in solution and on the adsorbent surface [11],

$$q_e = \frac{RT}{b_T} \ln (A_T C_e) \quad \textbf{(Eqn. D4)}$$

where R is the ideal gas constant (8.314 $J \cdot K^{-1} \cdot mol^{-1}$), T is temperature (K), b_T is the molar enthalpy of adsorption ($kJ \cdot mol^{-1}$) and A_T is a Temkin isotherm constant ($L \cdot g^{-1}$). The term $\frac{RT}{b_T}$ is often represented by a single constant B, related to the heat of adsorption.

The Dubinin-Radushkevich model

The Dubinin-Radushkevich isotherm (Equation D5) assumes the adsorption follows a Gaussian distribution of binding energies and is used to determine whether chemisorption, ion-exchange or physisorption dominates the system [12],

$$q_e = q_{max}\, e^{-B_D\left[RT\ln\left(1+\frac{1}{C_e}\right)\right]^2} \quad \textbf{(Eqn. D5)}$$

where B_D is a D-R isotherm constant ($mol^2 \cdot J^2$). The mean free energy of sorption E_D ($J \cdot mol^{-1}$) can thus be obtained via Equation D6.

$$E_D = \frac{1}{\sqrt{2B_D}} \quad \textbf{(Eqn. D6)}$$

The model-fitting to the data and subsequent calculation of parameters associated with each isotherm was achieved using non-linear least-squares analysis. The Microsoft SOLVER programme was, according to the method of Billo [13]. The errors associated with the parameters and R^2 values were acquired using Billo's "SolvStat" Excel add-in.

Table D13. Key parameters obtained from fitting experimental data from main research article to isotherm models.

Model	Parameter	HHCP1-Ca	HHCP2-Ca
Langmuir	K_L	7.29 ± 2.80 (x 10^{-4})	4.52 ± 1.00
	q_{max} ($mg \cdot g^{-1}$)	240 ± 60	74.6 ± 5.4
	R^2	0.946	0.941
Freundlich	K_F ($mg \cdot g^{-1}$)	0.608 ± 0.400	4.42 ± 2.00
	n	1.35 ± 0.18	2.65 ± 0.48
	R^2	0.912	0.845
Temkin	A_T ($L \cdot g^{-1}$)	198 ± 17	781 ± 200
	b_T ($kJ \cdot mol^{-1}$)	1.13 ± 0.07	2.86 ± 0.27
	B	2.20 ± 0.13	0.867 ± 0.83
	R^2	0.977	0.939
Dubinin-Radushkevich	B_D ($mol^2 \cdot J^{-2}$)	1.74 ± 0.17 (x 10^{-8})	8.21 ± 1.20 (x 10^{-9})
	q_{max} ($mg \cdot g^{-1}$)	267 ± 34	96.2 ± 10
	E_D ($kJ \cdot mol^{-1}$)	5.36 ± 0.34	7.81 ± 0.79
	R^2	0.962	0.935

Table D14. Comparison on maximum uptake capacity values of polymers compared to other relevant sorbents reported in the literature.

Description of adsorbent	Calculated q_{max} ($mg \cdot L^{-1}$)	Concentration range ($mg \cdot L^{-1}$)	Reference
HHCP1	267 ± 34	50 – 2,000	This work
HHCP2	96.2 ± 10	50 – 2,000	This work
La-loaded commercial IX resin	187 ± 15	10 – 1,500	[9]
Al-loaded commercial IX resin	12.2	10 - 50	[14]
La-modified activated alumina	6.7	<1 - 20	[15]
SO_4^{2-} doped Fe_3O_4/Al_2O_3 nanoparticles	70.4	2 - 160	[16]
MgAl-CO_3 layered double hydroxide clay	318 ± 6	5 – 2,500	[17]
B and N containing conjugated microporous polymer	24	<1 – 50 (estimated from dataset)	[18]
Chitosan-coated perlite	64.1	5 - 25	[19]
Th-complexed bis[2-methacryloyloxy)-ethyl] phosphate polymer	4.32	1 - 10	[20]
Activated alumina	8.27	1 - 20	[21]
MIL-88A (MOF)	40.4	5 - 250	[22]

Determination of release of OH^- and Ca^{2+} from networks during fluoride uptake

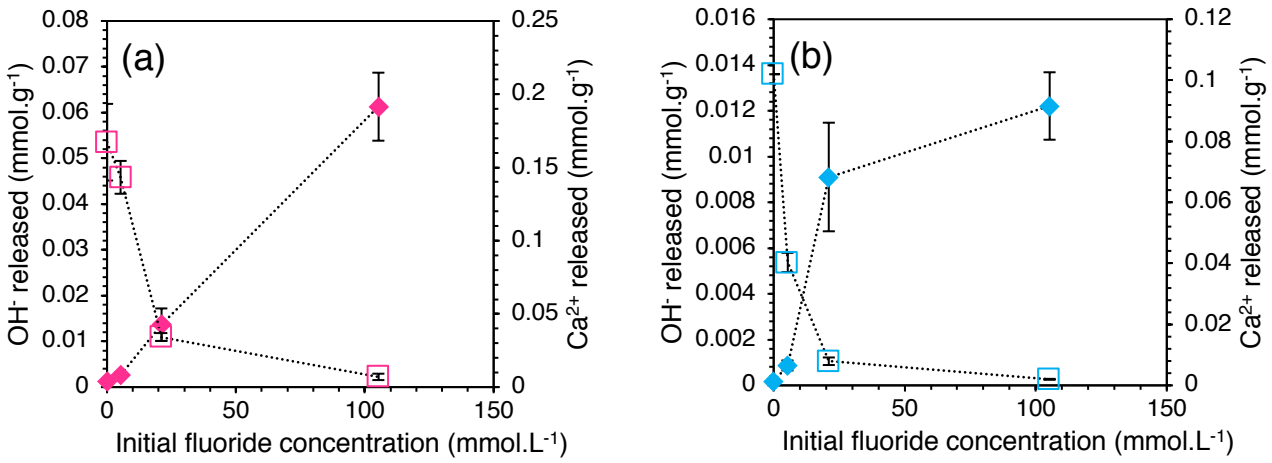

Fig. S36. Monitoring quantities of OH^- (◆) and Ca^{2+} (□) released into solution, as a function of initial fluoride solution concentration, during batch equilibrium experiments for (a) HHCP1-Ca and (b) HHCP2-Ca. Polymer mass = 100 mg. Solution volume = 25 mL. T = 18°C.

Models used to fit static kinetic data

The pseudo first-order (PFO) model

The PFO model (Equation D7) is used to describe adsorption data where the uptake behaviour is analogous to a first-order chemical reaction [23]. It is often used to successfully model physisorption mechanisms.

$$q_t = q_e\left(1 - e^{-k_1 t}\right)$$ (**Eqn. D7**)

where q_e is the uptake capacity at equilibrium, t is time in minutes and k_1 is the pseudo first-order rate constant in min^{-1}.

The pseudo second-order (PSO) model

The PSO model (Equation D8) is used to describe adsorption data where the uptake behaviour is analogous to a second-order chemical reaction [24]. It often fits chemisorption uptake data well. However, agreement with this model does not necessarily indicate that the mode of uptake is chemisorption [25],

$$q_t = \frac{k_2 q_e^2 t}{1 + k_2 q_e t}$$ (**Eqn. D8**)

where q_e is the uptake capacity at equilibrium, t is time in minutes and k_2 is the pseudo second-order rate constant in min^{-1} and $g \cdot mg^{-1} \cdot min^{-1}$. Additional parameters may be calculated from the PSO model, using the equations below (D9 and D10),

$$t_{1/2} = \frac{1}{k_2 q_e}$$ (**Eqn. D9**)

$$h_0 = k_2 q_e^2$$ (**Eqn. D10**)

where $t_{1/2}$ is the sorption half-time (min) and h_0 is the initial sorption rate ($mg \cdot g^{-1} \cdot min^{-1}$).

The Elovich model

This model (Equation D11) may be applied, using a simplification proposed by Chien and Clayton [26],

$$q_t = \frac{1}{\beta}\ln(t) + \frac{1}{\beta}\ln(\alpha\beta)$$ (**Eqn. D11**)

where α is the initial rate constant ($mg \cdot g^{-1} \cdot min^{-1}$) and β is a desorption constant ($mg \cdot g^{-1}$). Agreement with this model is often interpreted to mean that adsorption involves two or three simultaneous first-order reactions [26].

For these three models, fitting to the data and subsequent calculation of associated parameters and errors values was performed using SOLVER, as before.

The Boyd (film-diffusion) model

This model (Equation D12) considers the transport of the sorbate species through the hydrous film layer surrounding the adsorbent particle [27],

$$\ln(1 - F) = k_{fd}t \qquad \textbf{(Eqn. D12)}$$

where F is the fractional attainment of equilibrium at time t and k_{fd} is the film-diffusion rate constant (min^{-1}). Therefore, in a plot of $-\ln(1-C_t/C_i)$ vs t, a linear gradient would indicate that the uptake rate is controlled by the movement of adsorbate ions through the hydrous film layer surrounding the adsorbent particles (film-diffusion). A non-linear gradient would suggest the rate is controlled by the movement of the adsorbate within the pores of the resin beads (intra-particle-diffusion), or the chemical reaction at the surface [28].

The intra-particle model

This model (Equation D13) considers the movement of the sorbate species through the pores of the adsorbent particle to the active binding sites [29],

$$q_t = k_{id}t^{1/2} + C \qquad \textbf{(Eqn. D13)}$$

where k_{id} is the intra-particle-diffusion rate constant ($mg \cdot g^{-1} \cdot min^{-1/2}$) and C is a constant relating to the thickness of the adsorbent film layer. In a plot of of q_t vs $t^{1/2}$, a linear gradient, passing through the origin, indicates the adsorption is entirely controlled by intra-particle-diffusion [30].

For these two models, fitting to the data and generation of R^2 values was performed using simple linear regression.

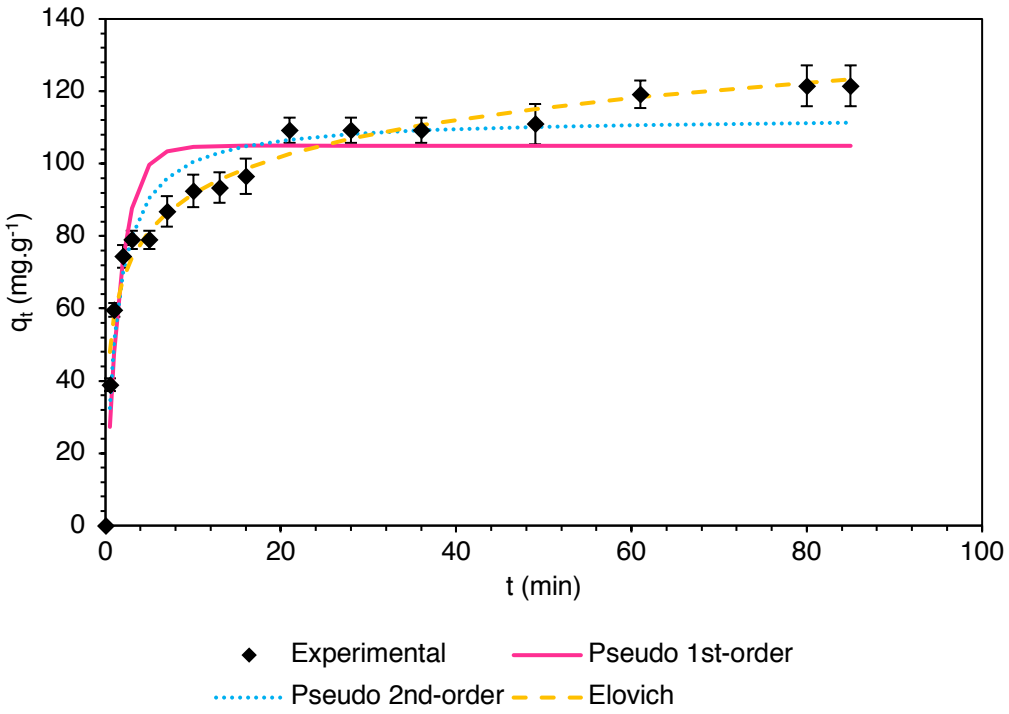

Fig. D37. Uptake of fluoride over time by HHCP1-Ca. Error bars represent 95% confidence limits from 3 replicate electrode measurements. Polymer mass = 2.00 g. Contact solution initial volume = 500 mL. Initial fluoride concentration = 2,000 $mg \cdot L^{-1}$. T = 18°C.

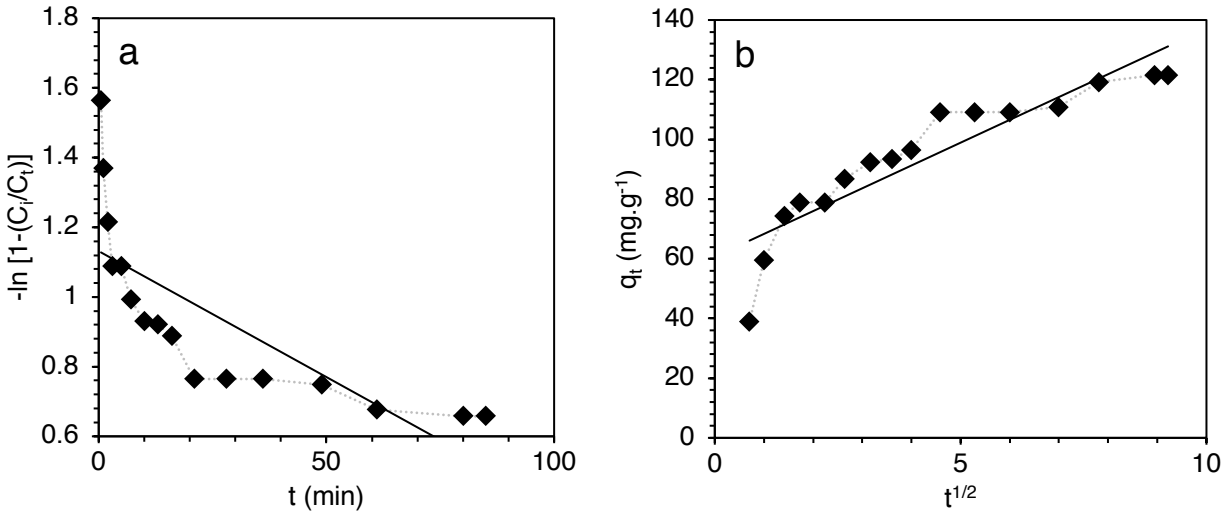

Fig. D38. Fitting of the above uptake data to **(a)** film diffusion and **(b)** intra-particle diffusion models.

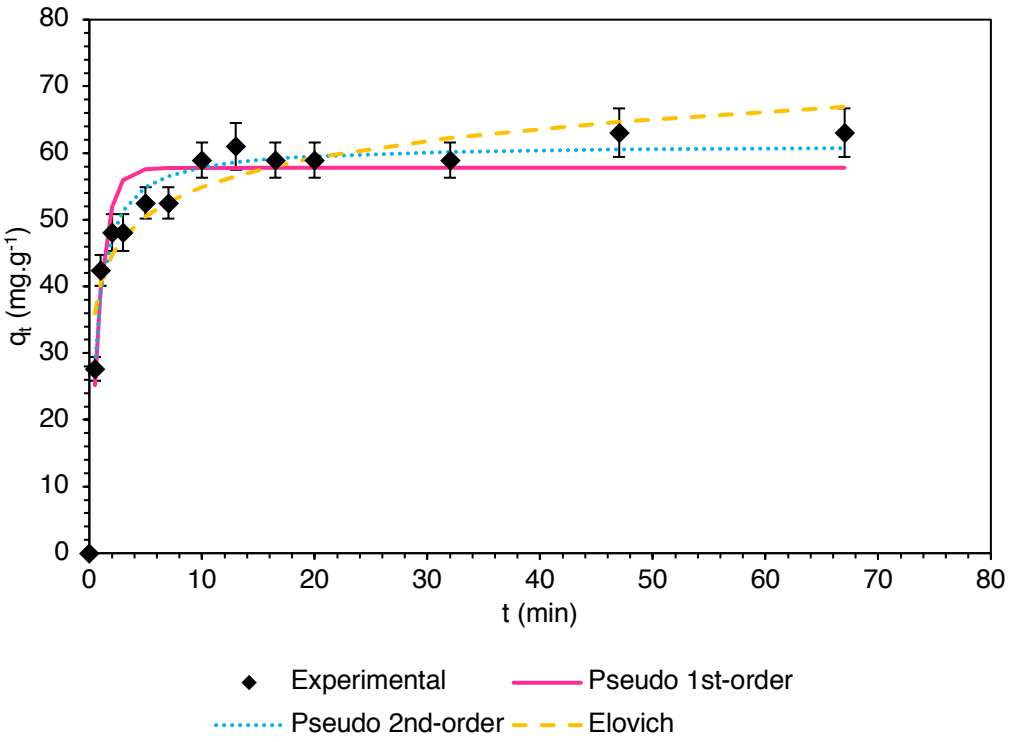

Fig. D39. Uptake of fluoride over time by HHCP2-Ca. Error bars represent 95% confidence limits from 3 replicate electrode measurements. Polymer mass = 2.00 g. Contact solution initial volume = 500 mL. Initial fluoride concentration = 2,000 mg·L^{-1}. T = 18°C.

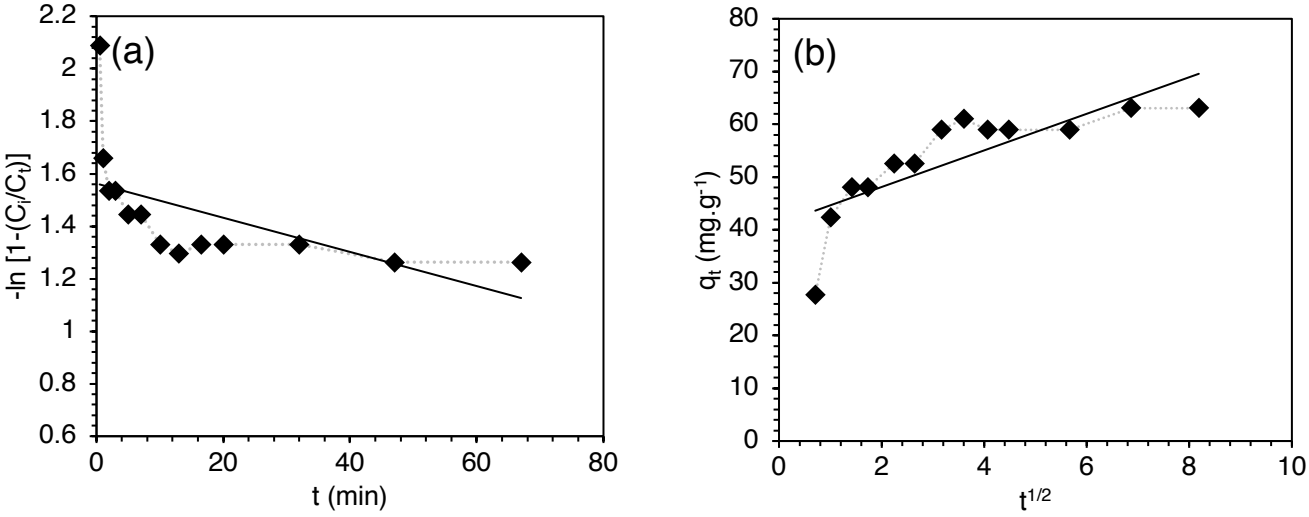

Fig. D40. Fitting of the above uptake data to **(a)** film diffusion and **(b)** intra-particle diffusion models.

Table D15. Extracted parameters from model-fitting to static kinetic data for both networks.

Model	Parameter	HHCP1-Ca	HHCP2-Ca
PFO	k_1 (min^{-1})	0.602 ± 0.13	1.15 ± 0.17
	q_e ($mg \cdot g^{-1}$)	105 ± 4	57.8 ± 17
	R^2	0.787	0.844
PSO	k_2 ($g \cdot mg^{-1} \cdot min^{-1}$)	7.15 ± 1.4 (x 10^{-3})	2.81 ± 0.36 (x 10^{-2})
	q_e ($mg \cdot g^{-1}$)	113 ± 3	61.3 ± 1.0
	h_0 ($mg \cdot g^{-1} \cdot min^{-1}$)	91.2 ± 18	105 ± 14
	$t_{1/2}$ (min)	1.24 ± 0.24	0.581 ± 0.076
	R^2	0.905	0.946
Elovich	α ($mg \cdot g^{-1} \cdot min^{-1}$)	3.84 ± 1.0 (x 10^{-2})	0.196 ± 0.039
	β ($mg \cdot g^{-1}$)	1,290 ± 60	3,000 ± 350
	R^2	0.971	0.872
Film diffusion	R^2	0.592	0.336
Intra-particle diffusion	R^2	0.829	0.627

Notes

For both networks, the plot of $-\ln(1-C_t/C_i)$ vs t does not yield a linear gradient. The plot of q_t vs $t^{1/2}$ also does not yield a linear gradient. Collectively, this indicates that intra-particle diffusion is not the rate-determining step and that film-diffusion or chemical reaction is more likely to be rate-controlling.

Dynamic breakthrough data

The fluoride breakthrough data for columns loaded with HHCP1-Ca and HHCP2-Ca was fitted with the empirical Dose-Response model (Equations D14 and D15) [31]

$$\frac{C}{C_i} = 1 - \frac{1}{1+\left(\frac{V_{eff}}{b}\right)^a} \qquad \textbf{(Eqn. D14)}$$

$$q_0 = \frac{bC_i}{m}$$ (**Eqn. D15**)

Where C is the concentration of fluoride in the effluent at a given point, C_i is the concentration of fluoride in the inlet stream, V_{eff} is the volume of solution eluted from the column (mL), a and b are constants of the Dose-Response model, q_0 is the theoretical maximum uptake capacity of the resin in a dynamic environment ($mg \cdot g^{-1}$) and m is the dry mass of resin (g).

Fitting to the data and subsequent calculation of associated parameters and errors values was performed using SOLVER, as before.

Table D16. Parameters returned from fitting dynamic breakthrough data for HHCP1-Ca and HHCP2-Ca to Dose-Response model. Polymer mass = 1.30 g. Inlet [F^-] = 2,000 $mg \cdot L^{-1}$. Flow rate = 2.75 $mL \cdot hr^{-1}$. T = 18°C.

Parameter	HHCP1-Ca	HHCP2-Ca
a	4.96 ± 0.20	3.06 ± 0.06
b	58.9 ± 0.5	22.0 ± 0.2
q_o ($mg \cdot g^{-1}$)	95.8 ± 0.8	58.4 ± 0.4
R^2	0.991	0.999

Selectivity and competition effects via ion chromatography analysis

A solution was made up, containing 1 mM of 8 common anions, as their Na salts (F^-, Cl^-, NO_3^-, Br^-, PO_4^{3-}, SO_4^{2-}, I^- and CO_3^{2-}). This solution was contacted by HHCP1-Ca and HHCP2-Ca, as described in the main article. The fluoride uptake was compared to control samples of 1 mM fluoride only. Pre-contact and post-contact anjon concentrations were determined by ion chromatography, as described in the main article. The instrument was calibrated with solutions of 1-10 $mg \cdot L^{-1}$ of the relevant anions, which were diluted from 1,000 $mg \cdot L^{-1}$ analytical standards, purchased from Fisher Scientific. The equilibrium uptake capacity for the various anions (q_e) in $mmol \cdot g^{-1}$ was calculated using the procedure described in the main research article. The distribution coefficient (K_D) for each anion was calculated as follows (Equation D16):

$$K_D = \overline{[X^-]} \Big/ [X^-]$$ (**Eqn. D16**)

where $\overline{[X^-]}$ is the concentration of anion immobilized by the polymer ($mmol \cdot g^{-1}$) and $[X^-]$ is the concentration remaining in solution at equilibrium ($mmol \cdot mL^{-1}$).

The separation factor (S.F.) is then calculated from Equation D17,

$$S.F._{(X/Y)} = K_{d(X)} \Big/ K_{d(Y)}$$ (**Eqn. D17**)

where X is the ion of interest and Y is a competing ion.

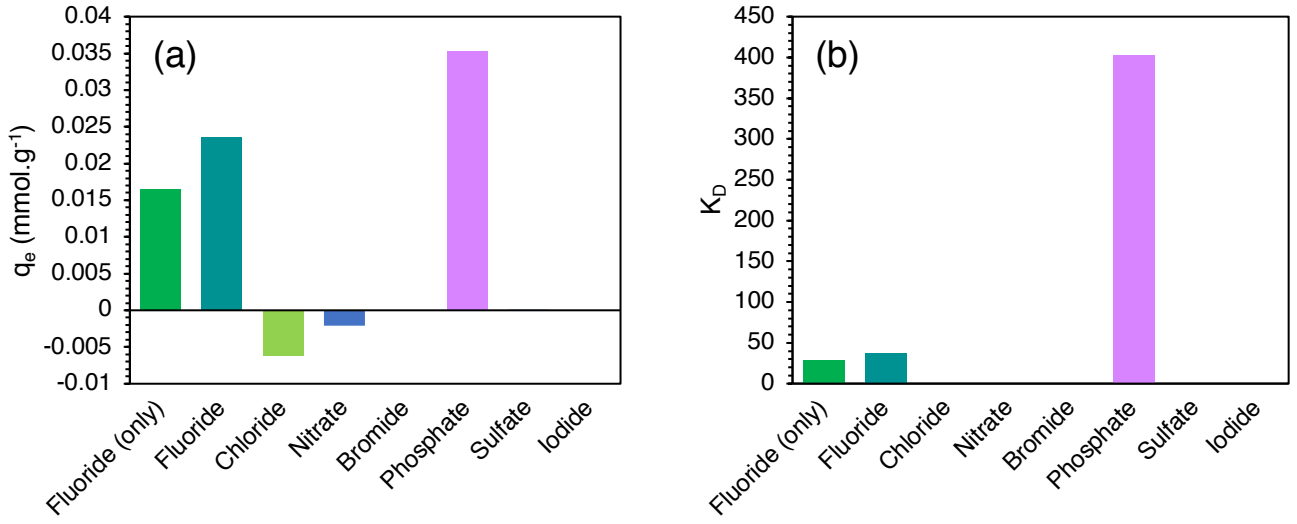

.

Fig. D41. (a) Uptake of common anions by HCCP1-Ca. **(b)** K_D values for each anion. Polymer mass = 100 mg. Contact solution volume = 25 mL. Initial concentration of anions = 1.00 mM. Contact time = 6 hr. T = 18°C.

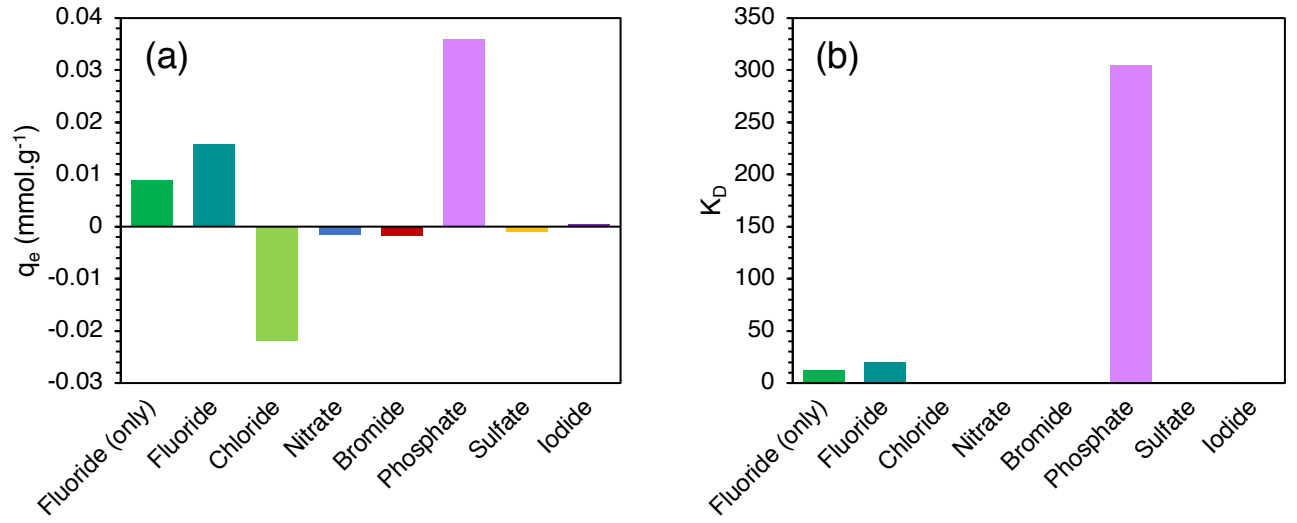

Fig. D42. (a) Uptake of common anions by HCCP2-Ca. **(b)** K_D values for each anion. Polymer mass = 200 mg. Contact solution volume = 10 mL. Initial concentration of anions = 1.00 mM. Contact time = 6 hr. T = 18°C.

The relevant S.F.s for fluoride vs the competing anions is shown in Table D17.

Table D17. Calculated S.F.s of HHCP1-Ca and HHCP2-Ca from K_D data for fluoride with respect to competing anions. Cl^- and NO_3^- are not presented as they were released into solution during the equilibrium process.

Network	**Separation Factor (F^-/competing anion)**			
	Br^-	**PO_4^{3-}**	**SO_4^{2-}**	**I^-**
HHCP1-Ca	>10,000	9.18 x 10^{-2}	1,130	>10,000
HHCP2-Ca	>10,000	6.40 x 10^{-2}	>10,000	23.5

Defluoridation performance of the polymers over several cycles

Regeneration of HHCP1-Ca and HHCP2-Ca was attempted, using the procedures described in the main article. The fluoride uptake capacities of the networks, after each desorption/adsorption cycle, were measured.

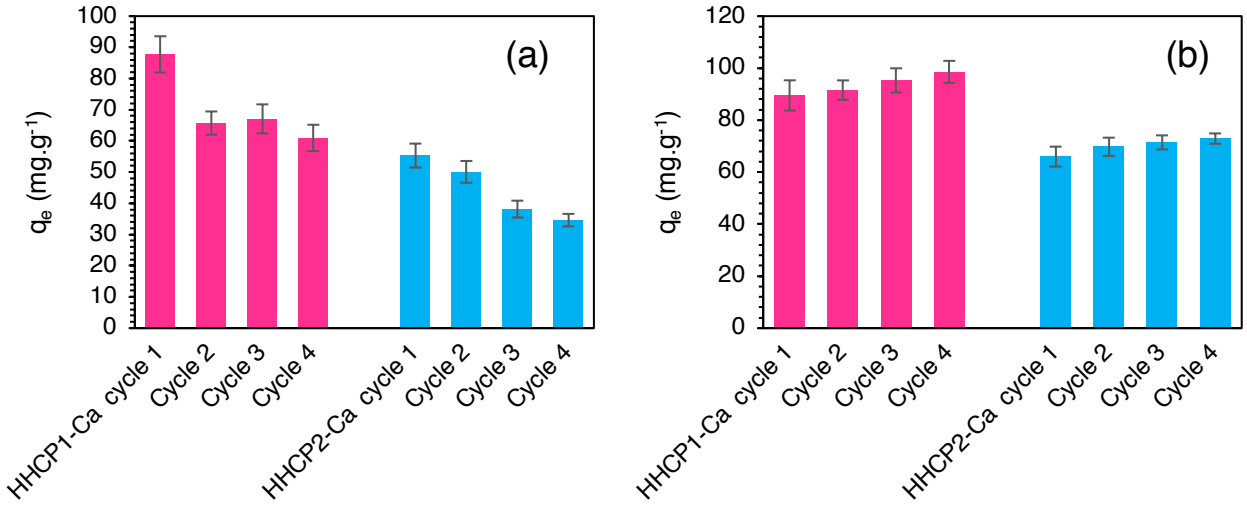

Fig. D43. Equilibrium uptake capacity of HHCP1-Ca and HHCP2-Ca over repeated cycles of fluoride-loading and desorption/regeneration attempts. **(a)** Treatment with 1 M NaOH. **(b)** Treatment with 1 M HNO_3, then reloading with Ca^{2+}. Polymer mass = 100 mg. Contact solution volume = 25 mL. Initial fluoride concentration = 2,000 mg·L^{-1}. Contact time = 6 hr. T = 18°C.

Note: "cycle 1" refers to the as-synthesised polymers, prior to any regeneration attempt.

Appendix D References

[1] R. Dawson, L.A. Stevens, T.C. Drage, C.E. Snape, M.W. Smith, D.J. Adams, A.I. Cooper, "Impact of water coadsorption for carbon dioxide capture in microporous polymer sorbents", *Journal of The American Chemical Society*, 2012, **134**, 10741-10744.

[2] R.H. Schlosberg, C.G. Scouten, "Organic-chemistry of calcium - formation and pyrolysis of hydroxycalcium phenoxides", *Energy & Fuels*, 1988, **2**, 582-585.

[3] F.A. Andersen, L. Brecevic, "Infrared-spectra of amorphous and crystalline calcium-carbonate", *Acta Chemica Scandinavica*, 1991, **45**, 1018-1024.

[4] M. Galvan-Ruiz, J. Hernandez, L. Banos, J. Noriega-Montes, M.E. Rodriguez-Garcia, "Characterization of calcium carbonate, calcium oxide, and calcium hydroxide as starting point to the improvement of lime for their use in construction", *Journal of Materials in Civil Engineering*, 2009, **21**, 694-698.

[5] M. Ni, B.D. Ratner, "Differentiation of calcium carbonate polymorphs by surface analysis techniques – An XPS and TOF-SIMS study", *Surface Interface Analysis*, **40** (2008) 1356-1361.

[6] D. Steele, E.R. Lippincott, "The crystal and solution vibrational spectra of biphenyl", *Journal of Molecular Spectroscopy*, 1961, **6**, 238-264.

[7] R. Ullah, I. Ahmad, Y. Zheng, "Fourier transform infrared spectroscopy of bisphenol A", *Journal of Spectroscopy*, **2016**, 1-5.

[8] R. Vinodh, P. Hemalatha, M. Ganesh, M.M. Peng, A. Abidov, M. Palanichamy, W.S. Chab, H.T. Jang, "Novel microporous hypercross-linked conjugated quinonoid chromophores with broad light absorption and CO_2 sorption characteristics", *RSC Advances*, 2014, **4**, 3668-3674.

[9] T. Robshaw, S. Tukra, D.B. Hammond, G.J. Leggett, M.D. Ogden, “Highly efficient fluoride extraction from simulant leachate of spent potlining via La-loaded chelating resin. An equilibrium study”, *Journal of Hazardous Materials*, 2019, **361**, 200-209.

[10] K.Y. Foo, B.H. Hameed, “Insights into the modeling of adsorption isotherm systems”, *Chemical Engineering Journal*, 2010, **156**, 2-10.

[11] M. Eriksson, I. Lundstrom, L.G. Ekedahl, “A model of the Temkin isotherm behavior for hydrogen adsorption at Pd-SiO_2 interfaces”, *Journal of Applied Physics*, 1997, **82**, 3143-3146.

[12] A.A. Inyinbor, F.A. Adekola, G.A. Olatunji, “Kinetics, isotherms and thermodynamic modeling of liquid phase adsorption of Rhodamine B dye onto *Raphia hookerie* fruit epicarp”, *Water Resources and Industry*, 2016, **15**, 14-27.

[13] E.J. Billo, *Excel for Chemists: A Comprehensive Guide*, 3rd ed., John Wiley, Hoboken, New Jersey, 2004.

[14] D.B. Bhatt, P.R. Bhatt, H.H. Prasad, K.M. Popat, P.S. Anand, “Removal of fluoride ion from aqueous bodies by aluminium complexed amino phosphonic acid type resins”, *Indian Journal of Chemical Technology*, 2004, **11**, 299-303.

[15] J.M. Cheng, X.G. Meng, C.Y. Jing, J.M. Hao, “La^{3+}-modified activated alumina for fluoride removal from water”, *Journal of Hazardous Materials*, 2014, **278**, 343-349.

[16] L.Y. Chai, Y.Y. Wang, N. Zhao, W.C. Yang, X.Y. You, “Sulfate-doped Fe_3O_4/Al_2O_3 nanoparticles as a novel adsorbent for fluoride removal from drinking water”, *Water Research*, 2013, **47**, 4040-4049.

[17] L. Lv, J. He, M. Wei, D.G. Evans, Z.L. Zhou, “Treatment of high fluoride concentration water by MgAl-CO_3 layered double hydroxides: Kinetic and equilibrium studies”, *Water Research*, 2007, **41,** 1534-1542.

[18] Z.P. Li, H. Li, H. Xia, X.S. Ding, X.L. Luo, X.M. Liu, Y. Mu, “Triarylboron-linked conjugated microporous polymers: Sensing and removal of fluoride ions”, *Chemistry-A European Journal*, 2015, **21**, 17355-17362.

[19] Y. Vijaya, M.V. Subbaiah, A.S. Reddy, A. Krishnaiah, “Equilibrium and kinetic studies of fluoride adsorption by chitosan coated perlite”, *Desalination and Water Treatment*, 2010, **20**, 272-280.

[20] N. Thakur, S.A. Kumar, D.N. Wagh, S. Das, A.K. Pandey, S.D. Kumar, A.V.R. Reddy, “Matrix supported tailored polymer for solid phase extraction of fluoride from variety of aqueous streams”, *Journal of Hazardous Materials*, 2012, **201**, 193-201.

[21] R. Leyva-Ramos, N.A. Medellin-Castillo, A. Jacobo-Azuara, J. Mendoza-Barron, L.E. Landin-Rodriguez, J.M. Martinez-Rosales, A. Aragon-Pina, “Fluoride removal from water solution by adsorption on activated alumina prepared from pseudo-boehmite”, *Journal of Environmental Engineering Management*, 2008, **18**, 301-309.

[22] F. Ke, G. Luo, P.R. Chen, J. Jiang, Q.Y. Yuan, H.M. Cai, C.Y. Peng, X.C. Wan, “Porous metal-organic frameworks adsorbents as a potential platform for defluoridation of water”, *Journal of Porous Materials*, 2016, **23**, 1065-1073.

[23] S. Lagergren, “Theorie der sogenannten adsorption gelosterstoffe”, *Svenska Vetenskapsakademiens Handlingar*, **24** (1898) 1-39.

[24] G. Blanchard, M. Maunaye, G. Martin, “Removal of heavy metals from waters by means of natural zeolites”, *Water Research*, 1984, **18**, 1501-1507.

[25] H.N. Tran, S.J. You, A. Hosseini-Bandegharaei, H.P. Chao, “Mistakes and inconsistencies regarding adsorption of contaminants from aqueous solutions: A critical review”, *Water Research*, 2017, **120**, 88-116.

[26] S.H. Chien, W.R. Clayton, “Application of Elovich equation to the kinetics of phosphate release and sorption in soils”, *Soil Science Society of America Journal*, 1980, **44**, 265-268.

[27] G.E. Boyd, A.W. Adamson, L.S. Myers Jr., “The exchange adsorption of ions from aqueous solutions by organic zeolites. 11. Kinetics”, *Journal of The American Chemical Society*, 1947, **69**, 2836-2848.

[28] T.J. Robshaw, R. Dawson, K. Bonser, M.D. Ogden, “Towards the implementation of an ion-exchange system for recovery of fluoride commodity chemicals”, Kinetic and dynamic studies, *Chemical Engineering Journal*, 2019, **367,** 149-159.

[29] W.J. Weber, J.C. Morris, “Kinetics of adsorption on carbon from solution”, *Journal of The Sanitary Engineering Division*, 1963, **89**, 31-60.
[30] S.E. Pepper, K.R. Whittle, L.M. Harwood, J. Cowell, T.S. Lee, M.D. Ogden, “Cobalt and nickel uptake by silica-based extractants”, *Separation Science and Technology*, 2018, **53**, 1552-1562.
[31] G.Y. Yan, T. Viraraghavan, M. Chen, “A new model for heavy metal removal in a biosorption column”, *Adsorption Science and Technology*, 2001, **19**, 25-43.